

https://dspace.org/

Lithium iron phosphate cathode materials: investigating the structural changes caused by synthetic modifications and doping

Thiebaut, Michelle

2022

https://hdl.handle.net/10539/34607

Downloaded from a DSpace repository. https://dspace.org/

Lithium iron phosphate cathode materials: Investigating the structural changes caused by synthetic modifications and doping

A thesis submitted to the Faculty of Science, University of the Witwatersrand, Johannesburg, in fulfilment of the requirements for the degree of Doctor of Philosophy

By

Michelle Thiebaut

June 2022

Declaration

I declare that this thesis is my own, unaided work. It is being submitted for the Degree of Doctor of Philosophy in the University of the Witwatersrand, Johannesburg. It has not been submitted before for any degree or examination in any other University



Candidate

(Michelle Thiebaut)

4 June 2022

Supervisor: Professor Caren Billing

Co-supervisors: Professor David Gordon Billing and Professor Deena Naidoo

Abstract

In this project, lithium iron phosphate ($LiFePO_4$) was synthesized by a hydrothermal method using homemade Teflon bombs as the reaction vessels. Changes in the $LiFePO_4$ structure were investigated when, applying a series of synthetic modifications. The synthesis was optimized using the developed methodology and infrastructure and phase pure $LiFePO_4$ was produced. Upon further characterization it was determined that although the products were phase pure, they were not defect free. This emphasized the importance of using a multi-technique approach to fully characterize and understand both the average and local structure, as well as identify the presence of amorphous phases. A series of synchrotron-based techniques were used, namely, X-ray absorption spectroscopy (XAS) using both X-ray near edge structure (XANES) and extended X-ray absorption fine structure (EXAFS), powder X-ray diffraction (PXRD) with Rietveld refinement, and to a lesser extent pair distribution function (PDF), together with laboratory instrumentation such as Mössbauer spectroscopy and Raman spectroscopy.

The main synthetic challenge was the elimination of air that causes the rapid oxidation of Fe^{2+} to Fe^{3+}. The presence of Fe^{3+} in the structure negatively influence the functioning of the material as a cathode, thus preventing oxidation is crucial and a large part of this project. Other factors that influenced the product was the lithium-ion addition rate during synthesis, where slower addition rates promote the formation of impurity phases as well as the oxidation to Fe^{3+}. To produce $LiFePO_4$ with the lowest amount of defects, cation disorder and Fe^{3+} content, it was found that all the precursor solutions needed to be purged with nitrogen before and during mixing until they were sealed in the reaction vessels, longer reaction times were preferential, and a lithium addition rate of one drop every 3 seconds appeared optimal.

After optimizing the synthetic route the possibility of doping (with Zn^{2+}) and co-doping (with Zn^{2+} and Co^{2+}) was investigated. It appeared that doping was possible using this method and there was no indication that either doping or co-doping specifically affected the Fe^{2+} content and no significant structural changes were noted.

Acknowledgements
I would like to thank the following people and institutions:

- The University of the Witwatersrand, National Research Foundation (NRF, South Africa), Department of Science and Innovation – Centre of Excellence (DSI-CoE, South Africa), Materials for Energy Research Group (MERG) and UKRI-GCRF START programme (Diamond Light Source, United Kingdom) for financial support.
- The School of Chemistry
- Prof's Caren Billing, Dave Billing and Deena Naidoo for the guidance, support and patience
- Gerrard Peters and Dr Rudolph Erasmus for always being willing to assist me.
- Dr David Pickup for the University of Kent for assisting me with my XAS analysis.
- The members in my research group
- Brookhaven National Laboratory, USA (beamline 28-ID-1 (PDF) at NSLS II).
- Diamond Light Source for the award of beam time as part of the Energy Materials Block Allocation Group SP14239.
- Mathias Kiefer, my best friend, for your continuous support, meme-sharing, jokes and long discussions about life and science. Without you I am not sure I would have been able to finish. SODACOVA.
- Dr Grace Ngubeni for all your guidance, support and listening ear. I appreciate you dearly my friend.
- My mother and brother for never complaining and always supporting me. I know it has not always been easy and I will forever be grateful.
- Lastly, I want to thank God. With the many blessings and constant reminders that I am never alone I was able to finish. This has been a journey of faith.

Trust in the Lord with all your heart and do not rely on your own understanding; in all your ways know Him, and He will make your paths straight (Proverbs 3: 5-6)

Conference proceedings that resulted from the work presented in this thesis

Poster presentations

Thiebaut M., Billing C., Billing D.G., **"Structure comparison of lithium iron cathode materials"** 9th International Conference of the African Materials Research Society, Gaborone, Botswana, 11-14 December 2017.

Thiebaut M., Billing C., Billing D.G., Naidoo D., "**Exploring air exposure as a major pitfall in producing $LiFePO_4$"** Indaba9 - International Union of Crystallography Conference, Skukuza, Kruger National Park, South Africa, 2-7 September 2018.

Thiebaut M., Billing C., Billing D.G., Naidoo D., **"Exploring air exposure as a major pitfall in producing $LiFePO_4$"** The Annual CoE-SM / AMSEM Student Presentation Workshop. University of the Witwatersrand, South Africa, 21 May 2018.

Thiebaut M., Billing C., Billing D.G., Naidoo D., **"Exploring air exposure as a major pitfall in producing $LiFePO_4$"** Energy Storage and Industry 4.0 Conference, KwaMaritane Bush Lodge, Pilansberg National Park, South Africa, 31 July - 2 August 2019.

Thiebaut M., Billing C., Billing D.G., Naidoo D., **"Exploring air exposure as a major pitfall in producing $LiFePO_4$"** SA-ESRF Light Source Conference, Johannesburg, Johannesburg Business School, South Africa, 11 – 13 November 2019.

Oral Presentation

Thiebaut M., Billing C., Billing D.G., Naidoo D., "**Effects of Li^+ addition rate during the synthesis of $LiFePO_4$: Combining X-ray diffraction and spectroscopy techniques to determine the average and local structure."** The 25th Congress of the International Union of Crystallography, Prague, Czech Republic, Hybrid conference (attended virtually),14 – 22 August 2021.

Paper submitted to Dalton Transactions (Manuscript ID - DT-ART-06-2022-001752)

Thiebaut M., D Naidoo, Billing D.G., C Billing., **The influence of the Li^+ addition rate during the hydrothermal synthesis of $LiFePO_4$ on the average and local structure.**

Table of Contents

Declaration 2
Abstract I
Acknowledgements II
Conference proceedings that resulted from the work presented in this thesis III
List of Figures VIII
List of Tables XVI
Chapter 1 1
Overview and literature review 1
1.1 Overview 1
1.2. The global energy crisis 1
1.3. Batteries as energy storage technologies 2
1.3.1. Lead-acid (PbO_2) 2
1.3.2. Nickel based batteries: Nickel - cadmium (NiCd) and nickel-metal hydride (Ni-MH) 3
1.3.3. Sodium sulphur (NaS) 3
1.3.4. Vanadium redox batteries (VRB) 3
1.3.5. Metal-air batteries (zinc-air and lithium-air) 4
1.4 Lithium-ion batteries (Li-ion) 4
1.4.1. Lithium-ion battery components 6
1.4.2. $LiFePO_4$ as a cathode material 12
1.5. Aims and objectives 18
1.6. References 20
Chapter 2 33
Synthetic methodology, instrumentation and theory of the characterisation methods 33
2.1 General outline of the synthetic method 33
2.1.1. Description of the reaction vessel: Teflon bombs 33
2.1.2 General outline of the synthesis 34
2.2. Instrumentation and data analysis methodology 35
2.2.1. Synchrotron powder X-ray diffraction 35
2.2.2. Pair distribution analysis 36
2.2.3 X-ray absorption spectroscopy 37
2.2.4. Mössbauer spectroscopy 40
2.2.5. Raman spectroscopy 40
2.2.6. Data visualization 41
2.3. Theory of the characterisation methods 41

2.3.1. Powder X-ray diffraction 41
2.3.2. Pair distribution function 46
2.3.3. X-ray absorption spectroscopy 48
2.3.4. Mössbauer Spectroscopy 64
2.3.5. Raman Spectroscopy 79
2.4 References: 82
Chapter 3 87
Characterization of $LiFePO_4$ and the use of commercial $LiFePO_4$ as a reference material. 87
3.1. Literature review of $LiFePO_4$ structure 87
3.1.1. Powder X-ray diffraction (PXRD) 87
3.1.2. X-ray absorption spectroscopy 89
3.1.3. Mössbauer spectroscopy 93
3.1.4. Raman Spectroscopy 94
3.2. Results and Discussion for C-$LiFePO_4$ 96
3.2.1. Powder X-ray diffraction 96
3.2.2. X-ray absorption spectroscopy 97
3.2.3. Mössbauer spectroscopy 101
3.2.4. Raman spectroscopy 102
3.3. Conclusion 105
3.4. References 105
Chapter 4 111
The chronicles of synthesising $LiFePO_4$ 111
4.1 Introduction 111
4.2 Experimental Procedure, Results, Discussion and Section Conclusions 114
4.2.1. Synthesis time 114
4.2.2. Percentage volume of the solution in the Teflon bombs 120
4.2.3. Determination of the Molar Ratio - *x*Li:Fe:PO_4 123
4.2.4. Individually purged samples 131
4.2.5. Controlling the exact volume to improve reproducibility 148
4.3. Conclusion 158
4.4. References 159
Chapter 5 165
Effects of Li^+ addition rate during the synthesis of $LiFePO_4$: Combining X-ray diffraction and spectroscopy techniques to determine average and local structure 165
5.1 Introduction 165
5.2. Experimental 165

5.3. Results and Discussion 166
5.3.1. Synchrotron radiation powder X-ray diffraction 166
5.3.2. X-ray absorption spectroscopy 173
5.3.3. Pair distribution function 188
5.3.4. Mössbauer spectroscopy 194
5.3.5. Raman spectroscopy 198
5.4. Conclusion 201
5.5. References 202
Chapter 6 207
The effect of air exposure during the synthesis of $LiFePO_4$ 207
6.1. Introduction 207
6.2. Sample preparation 208
6.3. Results and Discussion 208
6.3.1. Powder X-ray diffraction 208
6.3.2. Mössbauer spectroscopy 214
6.3.3. Raman Spectroscopy 218
6.4. Conclusion 221
6.5. References 222
Chapter 7 225
Doping with Zn^{2+} using a low cost and low energy synthetic route 225
7.1. Introduction 225
7.2. Sample preparation 226
7.3. Results and discussion 226
7.3.1. Powder X-ray diffraction 226
7.3.2. Raman Spectroscopy 232
7.3.3. X-ray absorption spectroscopy (XAS) 235
7.4. Conclusion 252
7.5. References 253
Chapter 8 258
Co-doping with Zn^{2+} and Co^{2+} using a low cost and low energy synthetic route 258
8.1. Introduction 258
8.2. Sample preparation 259
8.3. Results and discussion 259
8.3.1. Powder X-ray powder diffraction 259
8.3.2. Raman Spectroscopy 265
8.3.3. X-ray absorption spectroscopy 268

8.4. Conclusion 284
8.5. References 285
Chapter 9 289
General conclusions 289
A1. Synchrotron PXRD calibration using LaB_6 293
A2. Experimental components for XAS 294
A3. ^{57}Co decay scheme and the description of a Mossbauer spectrometer. 295
A3.1. Decay of ^{57}Co to ^{57}Fe 295
A3.2 Experimental setup 295
A.4. Mössbauer spectroscopy calibration 299
A5. Mössbauer data analyses using VindaD and $\chi 2$- values for fits 300
A6. Scripts used for PDF Gaussian fitting 304
A7 Integrating the 2-dimensional PXRD data to a 1-dimensional diffractogram 305
A8. Modifying the FEFF.inp to account for doping and co-doping by adding a single scattering path for the dopant 307
A9. References 310

List of Figures

Figure 1.1: Schematic diagram of the working principle of LIBs. 5
Figure 1.2: Different cell designs of batteries (left) are shown for (a) coin (b) cylindrical (c) prismatic and (d) pouch cells.[9,11] The schematics of the different components inside the cell are shown on the right.[12,13] 6
Figure 1.3: Crystal structure of $LiFePO_4$. FeO_6 octahedra are represented in blue, PO_4 tetrahedra are represented in pink, LiO_6 octahedra are represented in grey and the green spheres represents oxygen. Li^+ and Fe^{2+} occupy the M1 and M2 sites respectively. 12
Figure 1.4: The lithium channels are parallel to the b-axis. FeO_6 octahedra are represented in blue, PO_4 tetrahedra are represented in pink and Li^+ are represented by the grey spheres. The oxygen atoms have been removed for simplicity. Li^+ migration paths are indicated with A, B, C. 14
Figure 2.1: Diffracted beam emanating from a powdered sample showing the Debye-Scherrer cones.[33] 41
Figure 2.2: PDF of $LiFePO_4$. The blue plot corresponds to a Q_{max} of 10 whereas the pink plot corresponds to a Q_{max} of 20. The space resolution for the Q_{max} of 10 is lower. 47
Figure 2.3: The PDF of $LiFePO_4$ showing the different structural effects that can be determined independently of structure modeling.[44] 47
Figure 2.4: The photoelectron excitation process with the surrounding electron shells using the Bohr model.[29] 48
Figure 2.5: A schematic of the experimental setup for measurements in transmission mode. 49
Figure 2.6: An absorption spectrum of $LiFePO_4$ showing the different XANES and the EXAFS regions. The numbered regions will be described in (ii) below. 50
Figure 2.7: The first derivative spectrum of $LiFePO_4$. This spectrum can be used in most cases when choosing E_0. 55
Figure 2.8: The (a) absorption spectrum before normalization, (b) the pre-edge and post-edge regression lines used for normalization and (c) the normalized spectrum of $LiFePO_4$. 56
Figure 2.9: A plot of $LiFePO_4$ as (a) $\chi(k)$ function in k-space, (b) the magnitude of the Fourier transform (dashed) and the real parts of the Fourier Transform (solid). 58
Figure 2.10: The effect of different R_{bkg} values (a) 0.2, (b) 1 and (c) 2 on the background function and (d) the effect on different R_{bkg} values in the FT magnitude demonstrating the removal of Fourier Transform effects. 59
Figure 2.11: The effects of different k-weight on the χk function of $LiFePO_4$. The spectral weight changes with the k-weight. 60
Figure 2.12: A schematic showing the nuclear resonant absorption and nuclear resonance fluorescence observed in a recoil-free environment.[53] 65
Figure 2.13: The intensity distribution showing the emission spectral line centered around E_0. The mean lifetime of the excited state can be used to determine the natural line width.[53] 66
Figure 2.14: The movement of the $\gamma - ray$ due to the recoil energy if the nucleus was at rest before the emission. 67
Figure 2.15: A schematic illustrating the effect of the recoil on both the emission and absorption lines. These lines are separated by an energy of $2E_R$ and no overlap is observed between these lines.[53] 68
Figure 2.16: The amount of overlap between the emission and the absorption lines is responsible for the formation of a transmission spectrum.[33,53] 71
Figure 2.17: (a) Changes in the interactions between the nuclear charge and the electron density present at the nucleus for the bare, source and absorber and (b) the shift of the energy of the nuclear states due to the interactions producing the isomer shift.[58] 74
Figure 2.18: (a) The splitting of $I = 32$ with an energy separation of ΔEQ and (b) the Mössbauer spectrum that results from this splitting. The states can also be shifted and is indicated by the isomer shift.[58] 78

Figure 2.19: (a) The magnetic dipole splitting of ^{57}Fe and (b) the Mössbauer spectrum and intensities that results from this splitting.[58] 79
Figure 2.20: Different scattering processes that can occur upon photon interaction with a molecule.[64] 80
Figure 3.1: The olivine structure of $LiFePO_4$. Adapted from Strelstov et al.[12] 88
Figure 3.2: The XAS spectrum of $LiFePO_4$ can be divided into XANES and EXAFS. 90
Figure 3.3: The splitting of the energy levels for the metal d-orbitals. The 1s → 3d transition leads two different excited states.[25] 91
Figure 3.4: The XANES spectrum of $LiFePO_4$ can be divided into pre-edge, rising absorption edge and main absorption edge. 91
Figure 3.5: (a) The EXAFS oscillations for $LiFePO_4$ can be used for local structure determination. (b) The different coordination shells around the Fe absorbing atom in R-space for $LiFePO_4$. 92
Figure 3.6: Synchrotron diffractogram of C-LFP showing the observed (purple), calculated (green) and difference (black) plots generated from a Rietveld refinement analysis. Bragg reflections for $LiFePO_4$ are indicated by grey markers. The unmatched phase present is indicated in red. 97
Figure 3.7: Normalized Fe K-edge spectrum of C-LFP, $FePO_4 \bullet 4H_2O$ and Fe_2O_3 that were used as standards. 98
Figure 3.8: Normalized Fe K-edge spectrum of C-LFP. The pre-edge region (inset) and the main edge are indicated on the spectrum of C-LFP. 98
Figure 3.9: The FT magnitude of EXAFS $k3\chi(k)$ data for C-LFP showing the first, second and third coordination shells. 99
Figure 3.10: (a) The experimental Fe k^3-weighted $[k3\chi(k)]$ spectrum and (b) the experimental FT magnitude (top) and FT real (bottom) of the EXAFS $k3\chi(k)$ data (green) and the theoretical FEFF fit (maroon) of C-LFP. The fitting window here for (a) was 3 – 12.828 $Å^{-1}$ and for (b) 1.3 – 5 Å. 100
Figure 3.11: The Mössbauer spectrum of C-LFP when including three doublets and two sextet models to model the experimental data. 102
Figure 3.12: Raman spectra for the white particulates in C-LFP (W1/W2). The green arrow indicates the intense peak that could be associated with Fe_3O_4. 103
Figure 3.13: Raman spectra for the black phase in C-LFP (B1/B2). The green arrow indicates the intense peak that could be associated with Fe_3O_4. 103
Figure 4.1: Powder diffractogram of the 12hours-25 sample showing the observed (purple), calculated (green) and difference (black) plots generated from a Rietveld refinement analysis. Bragg reflections for $LiFePO_4$, Li_3PO_4, the Fe-impurity and $LiFePO_4(OH)$ are indicated with the grey, blue, yellow and red markers, respectively. (*) indicates an unidentified impurity. 115
Figure 4.2: Powder diffractogram of 48hours-25 showing the observed (purple), calculated (green) and difference (black) plots generated from a Rietveld Refinement analysis. Bragg reflections for $LiFePO_4$ and the Fe- impurity are indicated with the grey and yellow markers, respectively. (*) indicates an unidentified impurity. 115
Figure 4.3: Laboratory powder diffractogram of the 12hours-25 sample showing the observed (purple), calculated (green) and difference (black) plots generated from a Rietveld refinement analysis. The inset is indicated by the brown rectangle. Bragg reflections for $LiFePO_4$ are indicated with the grey. 117
Figure 4.4: Laboratory powder diffractogram of the 48hours-25 showing the observed (purple), calculated (green) and difference (black) plots generated from a Rietveld Refinement analysis. The inset is indicated by the brown rectangle. Bragg reflections for $LiFePO_4$ are indicated with the grey markers. 117
Figure 4.5: Mössbauer spectra for (a) the 12hours-25 and (b) the 48hours-25 samples showing the different environments present. 119

Figure 4.6: Powder diffractogram of the 48hours-50 sample showing the observed (purple), calculated (green) and difference (black) plots generated from a Rietveld Refinement analysis. Bragg reflections for $LiFePO_4$, Li_3PO_4 and the Fe-impurity are indicated with the grey, blue and yellow markers, respectively. (*) indicates the unidentified impurity.....121
Figure 4.7: Powder diffractogram of the 48hours-75 sample showing the observed (purple), calculated (green) and difference (black) plots generated from a Rietveld Refinement analysis. Bragg reflections for $LiFePO_4$, Li_3PO_4, the Fe-impurity and $LiFePO_4(OH)$ are indicated with the grey, blue, yellow and red markers, respectively. (*) indicates the unidentified impurity.....122
Figure 4.8: (a) Powder diffractogram of the LFP-2a (pink) and LFP-2b (green) samples showing the observed plots. Bragg reflections for $LiFePO_4$ are indicated with the black markers. 125
Figure 4.9: Powder diffractogram of the LFP-2.5a (pink) and LFP-2.5b (green) sample showing the observed plots. Bragg reflections for $LiFePO_4$ are indicated with the black markers. 125
Figure 4.10: Powder diffractogram of the LFP-3a sample showing the observed (purple), calculated (green) and difference (black) plots generated from a Rietveld Refinement analysis. Bragg reflections for $LiFePO_4$ and the Fe-impurity phase are indicated with the grey and yellow markers, respectively. 126
Figure 4.11: Powder diffractogram of the LFP-3b sample showing the observed (purple), calculated (green) and difference (black) plots generated from a Rietveld Refinement analysis. Bragg reflections for $LiFePO_4$ and the Fe-impurity phase are indicated with the grey and yellow markers, respectively. 126
Figure 4.12: Mössbauer spectrum of LFP-3b. 128
Figure 4.13: Raman spectrum and microscopic image (inset) of LFP-3b. 130
Figure 4.14: Powder diffractogram of the LFP-P1 sample showing the observed (purple), calculated (green) and difference (black) plots generated from a Rietveld Refinement analysis. Bragg reflections for $LiFePO_4$ are indicated with the grey markers.....132
Figure 4.15: Powder diffractogram of the LFP-P2 sample showing the observed (purple), calculated (green) and difference (black) plots generated from a Rietveld Refinement analysis. Bragg reflections for $LiFePO_4$ are indicated with the grey markers.....132
Figure 4.16: Comparison Fe K-edge XANES pre-edge region of the different standards purged samples.....135
Figure 4.17: Comparison of the XANES Fe K-edge rising absorption and main absorption edge for the $LiFePO_4$ standard and the purged samples.....136
Figure 4.18: LCF best fit (blue) of (a) LFP-P1 for the Fe K-edge XANES spectrum (pink) and (b) for LFP-P2 of the Fe K-edge XANES spectrum (olive green) along with the residual spectrum (grey). 137
Figure 4.19: Comparison of the Fe k^3-weighted $[k3\chi(k)]$ spectrum of the LFP-P1 and LFP-P2 synthesised samples. 138
Figure 4.20: The magnitude of the Fourier transform of EXAFS $k3\chi(k)$ data comparing the radial distance of the different coordination shells of the two purged samples. 139
Figure 4.21: (a) The experimental Fe k^3-weighted $[k3\chi(k)]$ spectrum and (b) the experimental FT magnitude (top) and FT real (bottom) of the EXAFS $k3\chi(k)$ data (green) and the theoretical FEFF fit (black) of LFP-P1. The fitting window is indicated with the vertical lines. 140
Figure 4.22: (a) The experimental Fe k^3-weighted $[k3\chi(k)]$ spectrum and (b) the experimental FT magnitude (top) and FT real (bottom) of the EXAFS $k3\chi(k)$ data (pink) and the theoretical FEFF fit (black) of LFP-P2. The fitting window is indicated with the vertical lines. 140
Figure 4.23: Mössbauer spectra for the (a) LFP-P1 and (b) LFP-P2 sample. 144
Figure 4.24: Raman spectrum and microscopic image (inset) of LFP-P1. The bottom inset is that of the poorly crystalline hematite. 146
Figure 4.25: Raman spectrum and microscopic image (inset) of LFP-P2. The bottom inset is that of the poorly crystalline hematite. 146

Figure 4.26: Powder diffractogram of the LFP-1 sample showing the observed (purple), calculated (green) and difference (black) plots generated from a Rietveld Refinement analysis. Bragg reflections for $LiFePO_4$ and Li_3PO_4 are indicated with the grey markers and blue markers, respectively 149
Figure 4.27: Powder diffractogram of the LFP-2 sample showing the observed (purple), calculated (green) and difference (black) plots generated from a Rietveld Refinement analysis. Bragg reflections for $LiFePO_4$ and the Fe-impurity are indicated with the grey and yellow markers, respectively 149
Figure 4.28: Powder diffractogram of the LFP-3 sample showing the observed (purple), calculated (green) and difference (black) plots generated from a Rietveld Refinement analysis. Bragg reflections for $LiFePO_4$ and Li_3PO_4 are indicated with the grey markers and blue markers, respectively 150
Figure 4.29: Mössbauer spectrum of the LFP-1 sample. 153
Figure 4.30: Mössbauer spectrum of the LFP-2 sample. 153
Figure 4.31: Mössbauer spectrum of the LFP-3 sample. 153
Figure 4.32: Raman spectrum and microscopic image (inset) of LFP-1. 156
Figure 4.33: Raman spectrum and microscopic image (inset) of LFP-2. 156
Figure 4.34: Raman spectrum and microscopic image (inset) of LFP-3. A broad peak at ~1350 cm^{-1} is circled in orange. 157
Figure 5.1: Synchrotron diffractogram of the 1sec $LiFePO_4$ sample showing the observed (purple), calculated (green) and difference (black) plots generated from a Rietveld Refinement analysis. Bragg reflections for $LiFePO_4$ are indicated with the grey markers. 166
Figure 5.2: Synchrotron diffractogram of the 2sec $LiFePO_4$ sample showing the observed (purple), calculated (green) and difference (black) plots generated from a Rietveld Refinement analysis. Bragg reflections for $LiFePO_4$ and Li_3PO_4 are indicated with the grey and the yellow markers respectively. (*) indicates unidentified peaks from impurity phase/s. 167
Figure 5.3: Synchrotron diffractogram of the 3sec_1 $LiFePO_4$ sample showing the observed (purple), calculated (green) and difference (black) plots generated from a Rietveld Refinement analysis. Bragg reflections for $LiFePO_4$ are indicated with the grey markers. 167
Figure 5.4: Synchrotron diffractogram of the 3sec_2 $LiFePO_4$ sample showing the observed (purple), calculated (green) and difference (black) plots generated from a Rietveld Refinement analysis. Bragg reflections for $LiFePO_4$ and Li_3PO_4 are indicated with the grey and the yellow markers respectively. 168
Figure 5.5: Synchrotron diffractogram of the 4sec $LiFePO_4$ sample showing the observed (purple), calculated (green) and difference (black) plots generated from a Rietveld Refinement analysis. Bragg reflections for $LiFePO_4$ are indicated with the grey markers. 168
Figure 5.6: Synchrotron diffractogram of the 5sec $LiFePO_4$ sample showing the observed (purple), calculated (green) and difference (black) plots generated from a Rietveld Refinement analysis. Bragg reflections for $LiFePO_4$ and Li_3PO_4 are indicated with the grey and the yellow markers respectively. (*) indicates unidentified peaks from impurity phase/s. 169
Figure 5.7: Normalized Fe K-edge spectra for all the varied Li^+ addition samples compared to that of the $LiFePO_4$ standard (black). These spectra are largely overlapped. 173
Figure 5.8: Comparison Fe K-edge XANES pre-edge region of the different standards and varied Li^+ addition rate samples. 174
Figure 5.9: Comparison of the $LiFePO_4$ standard with the different Li^+ addition samples of the XANES Fe K-edge rising absorption and main absorption edge. 176
Figure 5.10: LCF best fit (blue) of the 1sec of the Fe K-edge XANES spectrum (purple) along with the residual spectrum (grey). 178
Figure 5.11: LCF best fit (blue) of the 2sec of the Fe K-edge XANES spectrum (green) along with the residual spectrum (grey). 178
Figure 5.12: LCF best fit (blue) of the 3sec_1 of the Fe K-edge XANES spectrum (pink) along with the residual spectrum (grey). 178

Figure 5.13: LCF best fit (blue) of the 3sec_2sec of the Fe K-edge XANES spectrum (black) along with the residual spectrum (grey).....178
Figure 5.14: LCF best fit (blue) of the 4sec of the Fe K-edge XANES spectrum (pink) along with the residual spectrum (grey). 179
Figure 5.15: LCF best fit (blue) of the 5sec of the Fe K-edge XANES spectrum (black) along with the residual spectrum (grey). 179
Figure 5.16: Comparison of the Fe k^3-weighted [$k3\chi(k)$] spectrum of the different Li^+ addition rate samples.....180
Figure 5.17: The magnitude of the Fourier transform of EXAFS $k3\chi(k)$ data comparing radial distance of the different coordination shells of the different Li^+ addition rate samples.....181
Figure 5.18: (a) The experimental Fe k^3-weighted [$k3\chi(k)$] spectrum and (b) the experimental FT magnitude (top) and FT real (bottom) of the EXAFS $k3\chi(k)$ data (blue) and the theoretical FEFF fit (black) of the 1sec $LiFePO_4$. The fitting window is indicated with the vertical lines.....182
Figure 5.19: (a) The experimental Fe k^3-weighted [$k3\chi(k)$] spectrum and (b) the experimental FT magnitude (top) and FT real (bottom) of the EXAFS $k3\chi(k)$ data (red) and the theoretical FEFF fit (black) of the 2sec $LiFePO_4$. The fitting window is indicated with the vertical lines.....182
Figure 5.20: (a) The experimental Fe k^3-weighted [$k3\chi(k)$] spectrum and (b) the experimental FT magnitude (top) and FT real (bottom) of the EXAFS $k3\chi(k)$ data (purple) and the theoretical FEFF fit (black) of the 3sec_1 $LiFePO_4$. The fitting window is indicated with the vertical lines. 183
Figure 5.21: (a) The experimental Fe k^3-weighted [$k3\chi(k)$] spectrum and (b) the experimental FT magnitude (top) and FT real (bottom) of the EXAFS $k3\chi(k)$ data (olive) and the theoretical FEFF fit (black) of the 3sec_2 $LiFePO_4$. The fitting window is indicated with the vertical lines.....183
Figure 5.22: (a) The experimental Fe k^3-weighted [$k3\chi(k)$] spectrum and (b) the experimental FT magnitude (top) and FT real (bottom) of the EXAFS $k3\chi(k)$ data (pink) and the theoretical FEFF fit (black) of the 4sec $LiFePO_4$. The fitting window is indicated with the vertical lines.....183
Figure 5.23: (a) The experimental Fe k^3-weighted [$k3\chi(k)$] spectrum and (b) the experimental FT magnitude (top) and FT real (bottom) of the EXAFS $k3\chi(k)$ data (green) and the theoretical FEFF fit (black) of the 5sec $LiFePO_4$. The fitting window is indicated with the vertical lines.....184
Figure 5.24: The experimental PDF of the 3sec_1 $LiFePO_4$ sample using a fitting range of 1 – 30Å. The observed G(r) is indicated with the green circles, the calculated G(r) is indicated with the black solid line and the difference curve is indicated in red.....188
Figure 5.25: The experimental PDF of the 3sec_1 $LiFePO_4$ sample showing a fitting range of 1 – 6.5Å with the major interatomic bond distance contributions in real space. The observed G(r) is indicated with the green circles. 190
Figure 5.26: The observed G(r) of the different Li^+ addition rate $LiFePO_4$ samples using a r-range of 1 – 6.5Å. Different areas under discussion are labelled A – E and important structural features are indicated with yellow circles. 191
Figure 5.27: The proposed model for the increase in coordination number around the Fe atoms. Possible interatomic interactions are indicated with the dashed lines. Iron is represented by brown, lithium by green, phosphorous by purple and oxygen by red. 194
Figure 5.28: Mössbauer spectra of (from the bottom to the top) the 1sec, 3sec_1, 3sec_2 and 4sec Li^+ addition rate $LiFePO_4$ samples showing the different Fe environments present.....195
Figure 5.29: Raman spectrum and microscopic image (inset) of the 1sec $LiFePO_4$ sample.....198
Figure 5.30: Raman spectrum and microscopic image (inset) of the 2sec $LiFePO_4$ sample.....199
Figure 5.31: Raman spectrum and microscopic image (inset) of the 3sec_1 $LiFePO_4$ sample.....199
Figure 5.32: Raman spectrum and microscopic image (inset) of the 3sec_2 $LiFePO_4$ sample.....199
Figure 5.33: Raman spectrum of α-Fe_2O_3 in the 2sec $LiFePO_4$ sample.....200

Figure 6.1: Synchrotron diffractogram of the Air0 $LiFePO_4$ sample showing the observed (purple), calculated (green) and difference (black) plots generated from a Rietveld refinement analysis. Bragg reflections for $LiFePO_4$ are indicated with the blue makers. 209
Figure 6.2: Synchrotron diffractogram of the Air3min $LiFePO_4$ sample showing the observed (purple), calculated (green) and difference (black) plots generated from a Rietveld refinement analysis. Bragg reflections for $LiFePO_4$, Li_3PO_4 and the Fe impurity are indicated with the blue, orange and red markers, respectively. 209
Figure 6.3: Synchrotron diffractogram of the Air30min $LiFePO_4$ sample showing the observed (purple), calculated (green) and difference (black) plots generated from a Rietveld refinement analysis. Bragg reflections for $LiFePO_4$, Li_3PO_4, Fe impurity and tavorite are indicated with the blue, orange, red and green markers, respectively. (*) indicates an unidentified impurity phase. 210
Figure 6.4: Synchrotron diffractogram of the Air1hr $LiFePO_4$ sample showing the observed (purple), calculated (green) and difference (black) plots generated from a Rietveld refinement analysis. Bragg reflections for $LiFePO_4$, Li_3PO_4, Fe impurity and tavorite are indicated with the blue, orange, red and green markers, respectively. (*) indicates an unidentified impurity phase. 210
Figure 6.5: Synchrotron diffractogram of the Air4hr $LiFePO_4$ sample showing the observed (purple), calculated (green) and difference (black) plots generated from a Rietveld refinement analysis. Bragg reflections for $LiFePO_4$, Li_3PO_4, Fe impurity and Tavorite are indicated with the blue, orange, red and green markers, respectively. 211
Figure 6.6: Mössbauer spectra of (from the bottom to the top) the Air0, Air3min, Air30min, Air1hr and Air4hr $LiFePO_4$ samples showing the different Fe environments present. 215
Figure 6.7: The Fe^{3+} content increases with air exposure time. 217
Figure 6.8: Raman spectrum of the Air0 $LiFePO_4$ sample. 219
Figure 6.9: Raman spectrum of the Air3min $LiFePO_4$ sample. 219
Figure 6.10: Raman spectrum of the Air30min $LiFePO_4$ sample. 220
Figure 6.11: Raman spectrum of the Air1hr $LiFePO_4$ sample. 220
Figure 6.12: Raman spectrum of the Air4hr $LiFePO_4$ sample. 220
Figure 7.1: Synchrotron diffractogram of $LiFePO_4$ showing the observed (purple), calculated (green) and difference (black) plots generated from a Rietveld refinement analysis. Bragg reflections for $LiFePO_4$ and the Fe-impurity are indicated with the grey and yellow markers. 227
Figure 7.2: Synchrotron diffractogram of the 1Zn $LiFePO_4$ sample showing the observed (purple), calculated (green) and difference (black) plots generated from a Rietveld refinement analysis. Bragg reflections for $LiFePO_4$ and Li_3PO_4 are indicated with the grey markers and blue markers. 227
Figure 7.3: Synchrotron diffractogram of the 2.5Zn $LiFePO_4$ sample showing the observed (purple), calculated (green) and difference (black) plots generated from a Rietveld refinement analysis. Bragg reflections for $LiFePO_4$ and the Fe-impurity are indicated with the grey markers and blue markers. 228
Figure 7.4: Synchrotron diffractogram of the 3Zn $LiFePO_4$ sample showing the observed (purple), calculated (green) and difference (black) plots generated from a Rietveld refinement analysis. Bragg reflections for $LiFePO_4$, Li_3PO_4 and the Fe-impurity are indicated with the grey, blue and yellow markers respectively. 228
Figure 7.5: Variation in the volume as a function of Zn^{2+} concentration in terms of x:$LiFe_{1-x}Zn_xPO_4$. 230
Figure 7.6: Raman spectra for the undoped and Zn-doped $LiFePO_4$ samples. The peaks due to symmetric stretching of $PO43-$ vibrational mode at ~950 cm^{-1} (910 – 976 cm^{-1}) is given in the inset. 233
Figure 7.7: Normalized Fe K-edge spectra for the different Zn-doped samples (pink – undoped, black – 1Zn, green – 2.5Zn and blue – 3Zn) compared to that of the $LiFePO_4$ standard (purple). 235
Figure 7.8: Comparison Fe K-edge XANES pre-edge region of the different standards, and the undoped and Zn-doped $LiFePO_4$ samples. 236

Figure 7.9: Comparison of the $LiFePO_4$ standard with the different undoped and Zn-doped $LiFePO_4$ samples.....238
Figure 7.10: LCF best fit (coral) of the undoped $LiFePO_4$ sample of the Fe K-edge XANES spectrum (pink) along with the residual spectrum (grey).....239
Figure 7.11: LCF best fit (coral) of the 1Zn $LiFePO_4$ sample of the Fe K-edge XANES spectrum (black) along with the residual spectrum (grey).....239
Figure 7.12: LCF best fit (coral) of the 2.5Zn $LiFePO_4$ sample of the Fe K-edge XANES spectrum (green) along with the residual spectrum (grey).....240
Figure 7.13: LCF best fit (coral) of the 3Zn $LiFePO_4$ sample of the Fe K-edge XANES spectrum (blue) along with the residual spectrum (grey).....240
Figure 7.14: Comparison of the Fe k^3-weighted $[k3\chi(k)]$ spectrum of the different synthesised samples (undoped and Zn-doped samples).....242
Figure 7.15: The FT magnitude of EXAFS $k3\chi(k)$ data comparing radial distance of the different coordination shells of the undoped and Zn-doped samples.....243
Figure 7.16: (a) The experimental Fe k^3-weighted $[k3\chi(k)]$ spectrum and (b) the experimental FT magnitude (top) and FT real (bottom) of the EXAFS $k3\chi(k)$ data (pink) and the theoretical FEFF fit (maroon) of the undoped sample. The fitting range for (a) is 3 – 12.828 $Å^{-1}$ and for (b) 1.3 – 5 Å. ..244
Figure 7.17: (a) The experimental Fe k^3-weighted $[k3\chi(k)]$ spectrum and (b) the experimental FT magnitude (top) and FT real (bottom) of the EXAFS $k3\chi(k)$ data (black) and the theoretical FEFF fit (maroon) of the 1Zn sample. The fitting range for (a) is 3 – 12.828 $Å^{-1}$ and for (b) 1.3 – 5 Å.....244
Figure 7.18: (a) The experimental Fe k^3-weighted $[k3\chi(k)]$ spectrum and (b) the experimental FT magnitude (top) and FT real (bottom) of the EXAFS $k3\chi(k)$ data (green) and the theoretical FEFF fit (maroon) of the 2.5Zn sample. The fitting range for (a) is 3 – 12.828 $Å^{-1}$ and for (b) 1.3 – 5 Å.....245
Figure 7.19: (a) The experimental Fe k^3-weighted $[k3\chi(k)]$ spectrum and (b) the experimental FT magnitude (top) and FT real (bottom) of the EXAFS $k3\chi(k)$ data (blue) and the theoretical FEFF fit (maroon) of the 3Zn sample. The fitting range for (a) is 3 – 12.828 $Å^{-1}$ and for (b) 1.3 – 5 Å.....245
Figure 7.20: The changes in the (a) of interatomic distance and (b) the disorder of the first (Fe-O) coordination shell.....249
Figure 7.21: The changes in the (a) of interatomic distance and (b) the disorder of the second (Fe-P) coordination shell.....250
Figure 7.22: The changes in the (a) of interatomic distance and (b) the disorder of the third (Fe-Fe) coordination shell.....251
Figure 8.1: Synchrotron diffractogram of the undoped $LiFePO_4$ showing the observed (purple), calculated (green) and difference (black) plots generated from a Rietveld refinement analysis. Bragg reflections for $LiFePO_4$ and the Fe-impurity are indicated with the grey and yellow markers.....260
Figure 8.2: Synchrotron diffractogram of 2.5Zn – 3.5Co showing the observed (purple), calculated (green) and difference (black) plots generated from a Rietveld refinement analysis. Bragg reflections for $LiFePO_4$, Li_3PO_4 and the Fe-impurity are indicated with the grey, blue and yellow markers respectively. (*) indicates the unidentified impurity.....261
Figure 8.3: Synchrotron diffractogram of 3Zn – 3Co showing the observed (purple), calculated (green) and difference (black) plots generated from a Rietveld refinement analysis. Bragg reflections for $LiFePO_4$ and the Fe-impurity are indicated with the grey and yellow markers. 261
Figure 8.4: Synchrotron diffractogram of 4Zn – 2Co showing the observed (purple), calculated (green) and difference (black) plots generated from a Rietveld refinement analysis. Bragg reflections for $LiFePO_4$, Li_3PO_4, the Fe-impurity and $LiFePO_4(OH)$ are indicated with the grey, blue, yellow and red markers respectively. (*) indicates the unidentified impurity.....262
Figure 8.5: Raman spectra for the undoped and Zn^{2+} - Co^{2+} co-doped $LiFePO_4$ samples. The peaks due to symmetric stretching of $PO43-$ (950 – 951 cm^{-1}) are given in the inset (879 – 1118 cm^{-1}).....266

Figure 8.6: Normalized Fe K-edge spectra for the different Zn-doped samples compared to that of the $LiFePO_4$ – standard (purple). The spectra for undoped, 2.5Zn – 3.5Co, 3 Zn – 3Co and 4Zn – 2Co $LiFePO_4$ samples are indicated in pink, black, green and blue, respectively. 268
Figure 8.7: Comparison normalized Fe K-edge XANES pre-edge region of the different undoped and Zn^{2+}- Co^{2+} co-doped $LiFePO_4$ samples. 269
Figure 8.8: Comparison of the $LiFePO_4$ standard with the different undoped and Zn^{2+}- Co^{2+} co-doped $LiFePO_4$ samples. 270
Figure 8.9: LCF best fit (coral) of the undoped $LiFePO_4$ sample of the normalized Fe K-edge XANES spectrum (pink) along with the residual spectrum (grey). 271
Figure 8.10: LCF best fit (coral) of the 2.5Zn-3.5Co $LiFePO_4$ sample of the normalized Fe K-edge XANES spectrum (black) along with the residual spectrum (grey). 271
Figure 8.11: LCF best fit (coral) of the 3Zn-3Co $LiFePO_4$ sample of the normalized Fe K-edge XANES spectrum (green) along with the residual spectrum (grey). 272
Figure 8.12: LCF best fit (coral) of the 4Zn-2Co $LiFePO_4$ sample of the normalized Fe K-edge XANES spectrum (blue) along with the residual spectrum (grey). 272
Figure 8.13: Comparison of the Fe k^3-weighted [$k^3\chi(k)$] spectrum of the different synthesised samples (undoped and Zn^{2+}-Co^{2+}co-doped samples). 274
Figure 8.14: Phase corrected FT magnitude EXAFS $k^3\chi(k)$ data comparing radial distance of the different coordination shells of the undoped and Zn^{2+}-Co^{2+} co-doped samples. 274
Figure 8.15: (a) The experimental Fe k^3-weighted [$k3\chi(k)$] spectrum and (b) the experimental FT magnitude (top) and FT real (bottom) of the EXAFS $k3\chi(k)$ data (pink) and the theoretical FEFF fit (maroon) of the undoped sample. The fitting range for (a) was 3 – 12.350 Å $^{-1}$ and for (b) 1.3 – 5 .. 276
Figure 8.16: (a) The experimental Fe k^3-weighted [$k3\chi(k)$] spectrum and (b) the experimental FT magnitude (top) and FT real (bottom) of the EXAFS $k3\chi(k)$ data (black) and the theoretical FEFF fit (maroon) of the 2.5Zn-3.5Co sample. The fitting range for (a) was 3 – 12.350 Å $^{-1}$ and for (b) 1.3 – 5 Å 276
Figure 8.17: (a) The experimental Fe k^3-weighted [$k3\chi(k)$] spectrum and (b) the experimental FT magnitude (top) and FT real (bottom) of the EXAFS $k3\chi(k)$ data (green) and the theoretical FEFF fit (maroon) of the 3Zn-3Co sample. The fitting range for (a) was 3 – 12.350 Å $^{-1}$ and for (b) 1.3 – 5 Å 277
Figure 8.18: (a) The experimental Fe k^3-weighted [$k3\chi(k)$] spectrum and (b) the experimental FT magnitude (top) and FT real (bottom) of the EXAFS $k3\chi(k)$ data (blue) and the theoretical FEFF fit (maroon) of the 4Zn-2Co sample. The fitting range for (a) was 3 – 12.350 Å $^{-1}$ and for (b) 1.3 – 5 Å. 277
Figure 8.19: The changes in the interatomic distance of the first (Fe-O) coordination shell. 280
Figure 8.20: The changes in the disorder of the first (Fe-O) coordination shell. 281
Figure 8.21: The changes in the interatomic distance of the second (Fe-P) coordination shell. 282
Figure 8.22: The changes in the disorder of the second (Fe-P) coordination shell 282
Figure 8.23: The changes in the interatomic distance of the third (Fe-Fe) coordination shell. 283
Figure 8.24: The changes in the disorder of the third (Fe-Fe) coordination shell 283
Figure A1: The Rietveld refinement plot for the calibration of 28-ID-1 at BNL of NIST 660c (LaB_6) with a wavelength of 0.167057(4) Å. 293
Figure A2: The Rietveld refinement plot for the calibration of 28-ID-1 at BNL of NIST 660c (LaB_6) with a wavelength of 0.166316(1) Å. 293
Figure A3: The Rietveld refinement plot for the calibration of the Bruker D8 Advance of NIST 660c (LaB_6) with a wavelength of 0.709313(4) Å. 294
Figure A4: The decay scheme of ^{57}Co to ^{57}Fe producing a $\gamma - ray$ with energy 14.4 keV.[3] 295
Figure A5: A schematic of the experimental setup for transmission measurements.[4,5] 296
Figure A6: PHA spectrum for ^{57}Co showing the different energy lines. 298

Figure A7: PHA spectrum for ^{57}Co showing the selected 14.4 keV. 298
Figure A8: The Mössbauer spectrum of α-Fe foil showing the six line positions and the hyperfine splittings.[5] 299
Figure A9: The calibration spectrum of the α-Fe foil recorded in transmission mode. 300
Figure A10: A description of the different fields provided in the Vinda 'Spec-sheet'. 301
Figure A11: After loading of the spectrum the spectrum information as well as the plot is added to the different fields. Different models can be selected to account for the different environments. The objective is to minimize the chi-square by solving different parameters. 302
Figure A12: Error analysis box in Vinda. 302
Figure A13: An example of the Ipython window. 304
Figure A14: The script used for fitting a Gaussian model to a PDF peak. 305
Figure A15: The individual PDF peak and the Gaussian fit. 305
Figure A16: The information output after executing the script shown in Figure A14. 305
Figure A17: Integrating the 2-Dimensional data to produce a 1-Dimensional powder pattern for the calibrant LaB_6. The masked beam stop is shown in red. 306
Figure A18: Integrating the 2-Dimensional data to produce a 1-Dimensional powder pattern for the $LiFePO_4$ sample. The masked beam stop is shown in red. 306
Figure A19: The FEFF.inp of the undoped $LiFePO_4$ resulting in four different nearest neighbour Fe atoms (indicated in red). 307
Figure A20: The undoped $LiFePO_4$ produces one Fe scattering path (indicated in red) with a high ranking. 308
Figure A21: Adding Zn to the atom list (indicated in green) produces one Zn nearest neighbour (indicated in green) and three Fe nearest neighbours (indicated in red). 308
Figure A22: The Zn doped $LiFePO_4$ produces one Zn scattering path (indicated in green) with a very low ranking and one Fe scattering path (indicated in red) with a higher ranking. 309
Figure A23: Adding Zn (indicated in green) and Co (indicated in blue) to the atom list leads to one Zn nearest neighbour (indicated in green) one Co nearest neighbour (indicated in blue) and two Fe nearest neighbours (indicated in red). 309
Figure A24: The Zn doped and Co co-doped $LiFePO_4$ produces one Zn scattering path (indicated in green) and one Co scattering path (indicated in blue) both with a very low ranking and one Fe scattering path (indicated in red) with a higher ranking. 310

List of Tables

Table 1.1: Commonly used single dopants and the doping effect on the structure and electrochemical performance. 15
Table 1.2: Co-dopants and the doping effect on the structure as well as electrochemical performance. 16
Table 2.1: Refineable parameters for each phase present and the refineable global parameters (for the whole powder pattern):[40] 43
Table 2.2: Commonly used criteria to determine the quality of the fit.[40] 45
Table 2.3: Description of parameters that are used in the EXAFS equation (**eqn 2.16**), that contribute to the signal and the method of determination.[29,46] 52
Table 2.4: The fitting parameters, typical values and the correlations associated with the parameters.[30] 62
Table 2.5: Different molecular vibrations and the changes that are linked to the different vibrations.[63] 81
Table 3.1: The lattice parameters and volume when using a hydrothermal synthesis. 87
Table 3.2: $LiFePO_4$ interatomic distances (Å) as reported by other groups using PXRD data 89

Table 3.3: The average interatomic distance and average Debye-Waller factor as determined in literature for $LiFePO_4$ 93
Table 3.4: Hyperfine parameters (IS and QS) commonly found in literature for Fe^{2+} in $LiFePO_4$ 94
Table 3.5: Raman wavenumbers and the different assignments for $LiFePO_4$ found in literature. 95
Table 3.6: Rietveld error indices, lattice parameters and the volume for C-LFP 96
Table 3.7: Structural parameters determined using FEFF for the first, second and third coordination shells of C-LFP. 101
Table 3.8: Raman modes for the white and black particulates present in C-LFP. $LiFePO_4$ modes are shaded in grey, α-Fe_2O_3 in orange, Fe_3O_4 in green and the unidentified phases are not shaded. 104
Table 4.1: Reliability factors for each Rietveld refinement. 116
Table 4.2: Selected structural parameters of the refined $LiFePO_4$ structures for the different samples. 116
Table 4.3: Multiphase analysis (%) of the undoped $LiFePO_4$. 117
Table 4.4: The percentage Fe^{2+} occupying the Fe^{2+}site (M2), vacancies on the M2 site and Li^+ and Fe^{2+} occupying the Li^+ site (M1) in the refined $LiFePO_4$ structures. 118
Table 4.5: Different isomer shifts (δ – mm/s) and quadrupole splitting (ΔEQ – mm/s) for the 12 and 48 hour samples. 119
Table 4.6: Percentage contribution from each form of Fe and the total Fe in the 12 and 48 hour samples 119
Table 4.7: The full width half maximum line width (Γ – mm/s) value for the 12 and 48 hour samples. 120
Table 4.8: Rietveld error indices for LFP-3a and LFP-3b 126
Table 4.9: Selected structural parameters of the refined structures for the different samples 127
Table 4.10: The percentage Fe^{2+} occupying the M2 (Fe^{2+}) site, vacancies on the M2 site and Li^+ and Fe^{2+} occupying the M1 (Li^+) site in the refined $LiFePO_4$ structures. 127
Table 4.11: Different isomer shifts (δ – mm/s) and quadrupole splitting (ΔEQ – mm/s) for LFP-3b. 128
Table 4.12: Percentage contribution from each form of Fe and the total Fe in LFP-3b. 129
Table 4.13: The full width half maximum line width (Γ – mm/s) value for LFP-3b. 129
Table 4.14: Raman modes of LFP-3b with the assigned vibrational modes. 130
Table 4.15: Rietveld error indices for the different purged samples. 133
Table 4.16: Selected structural parameters of the refined structures for the different purged samples. 133
Table 4.17: The percentage Li occupying the Fe site (M2), vacancies on the M2 site and Fe occupying the M1 (Li) site in the refined $LiFePO_4$ structures. 133
Table 4.18: Interatomic bond distances of the refined structures 134
Table 4.19: The different pre-edge peak intensities and peak positions for the standards and purged samples 135
Table 4.20: The different main edge peak intensities and peak positions for the standards and the purged samples 137
Table 4.21: LCF goodness of fit parameters for the purged samples. 138
Table 4.22: LCF Percentage of the different components present in the purged samples. 138
Table 4.23: The reliability factor and energy shift of the purged samples. 140
Table 4.24: Structural parameters determined using FEFF for the first, second and third coordination shell of the purged samples. 142
Table 4.25: The average interatomic distance and average Debye-Waller factor of the different coordination shells. 142
Table 4.26: Different isomer shifts (δ – mm/s) and quadrupole splitting (ΔE_Q – mm/s) for the purged samples 144

Table 4.27: Percentage contribution from each form of Fe and the total Fe in the purged samples. . 145
Table 4.28: The full width half maximum line width (Γ – mm/s) value for the purged samples. 145
Table 4.29: Raman modes of the purged samples with the assigned vibrational modes. 147
Table 4.30: Rietveld error indices for LFP-1, LFP-2 and LFP-3. 150
Table 4.31: Multiphase analysis (%) of LFP-1, LFP-2 and LFP-3. 150
Table 4.32: Selected structural parameters of the refined structures for the different purged samples. 151
Table 4.33: The percentage Li occupying the M2 (Fe) site, vacancies on the M2 site and Fe occupying the M1(Li) site in the refined $LiFePO_4$ structures. 151
Table 4.34: Interatomic distances of the refined structures. 152
Table 4.35: Different isomer shifts (δ – mm/s) and quadrupole splitting (ΔE_Q – mm/s) for the purged samples..... 154
Table 4.36: Percentage contribution from each form of Fe and the total Fe in the purged samples. . 154
Table 4.37: The full width half maximum line width (Γ – mm/s) value for the purged samples. 155
Table 4.38: Raman modes of the purged samples with the assigned vibrational modes. 157
Table 5.1: Rietveld error indices for the varied Li^+ addition rate samples..... 169
Table 5.2: Selected structural parameters of the refined $LiFePO_4$ phases for the varied Li^+ addition rate samples..... 170
Table 5.3: The percentage $LiFePO_4$ and Li_3PO_4 obtained from a multiphase Rietveld refinement of the XRD of the Li^+ addition rate samples..... 170
Table 5.4: The percentage Li occupying the M2 (Fe) site, vacancies on the M2 site and Fe occupying the M1 (Li) site in the refined $LiFePO_4$ structures..... 171
Table 5.5: Interatomic bond distances (Å) of the varied Li^+ addition rate samples. 172
Table 5.6: The different pre-edge peak intensities and peak positions for the standards and the varied Li^+ addition rate samples..... 175
Table 5.7: The different main edge peak intensities and peak positions for the standards and the Li^+ addition rate samples..... 177
Table 5.8: LCF goodness of fit parameters for the Li^+ addition rate samples..... 178
Table 5.9: Percentage of the different components present in the varied Li^+ addition rate samples as determined from LCF. 179
Table 5.10: The reliability factor and energy shift of the varied Li^+ addition rate samples..... 182
Table 5.11: Structural parameters determined using FEFF for the first, second and third coordination shell of the Li^+ addition rate samples..... 185
Table 5.12: The average interatomic distance and average Debye-Waller factor of the different coordination shells. 187
Table 5.13: The peak positions for selected peaks to determine any changes in the interatomic bond distances for the Li^+ addition rate samples as compared to the fully analysed 3sec_1 sample. Blue indicates the shorter distances and orange indicates longer distances**.** 192
Table 5.14: The peak width (FWHM) for selected peaks to determine any changes in disorder for the Li^+ addition rate samples as compared to the fully analysed 3sec_1 sample. Blue possibly indicates a lower degree of disorder and orange possibly indicates a higher degree in disorder**.**..... 192
Table 5.15: The peak integral intensity for selected peaks to determine any changes in coordination number for the Li^+ addition rate samples as compared to the fully analysed 3sec_1 sample. Blue possibly indicates a lower coordination and orange possibly indicates a higher coordination. 193
Table 5.16: Different isomer shifts (δ – mm/s) and quadrupole splitting (ΔEQ – mm/s) for the varied Li^+ addition rate samples..... 196
Table 5.17: Percentage contribution from each form of Fe and the total Fe in the varied Li^+ addition rate samples..... 197

Table 5.18: The full width half maximum line width (Γ – mm/s) value for the varied Li^+ addition rate samples.....197
Table 5.19: Raman modes of the different Li^+ addition rate samples with the assigned vibrational modes. Intensities for the $\upsilon 1$ ($PO43-$) and $\upsilon 3$ ($PO43-$) modes are given in brackets. 200
Table 6.1: Rietveld error indices and selected structural parameters of $LiFePO_4$.....211
Table 6.2: The percentage of $LiFePO_4$ and impurity phases obtained from a multiphase Rietveld refinement of the samples. 212
Table 6.3: The percentage Li^+ occupying the M2 (Fe) site and Fe occupying the M1 (Li^+) site in the refined $LiFePO_4$ structures.....213
Table 6.4: Interatomic bond distances of the refined structures. 214
Table 6.5: Different isomer shifts (δ – mm/s) and quadrupole splitting (ΔE_Q – mm/s) for the different samples.....216
Table 6.6: Percentage contribution from each form of Fe to the total Fe in the different samples.....217
Table 6.7: The full width half maximum line width (Γ – mm/s) value for the different samples. 218
Table 6.8: Raman modes of the different air exposed samples with the assigned vibrational modes. 221
Table 7.1: Reliability factors for each Rietveld refinement. 229
Table 7.2: Multiphase analysis (%) of the undoped $LiFePO_4$ and doped samples.....229
Table 7.3: Lattice parameters and volume of the $LiFePO_4$ phase for the undoped and Zn-doped $LiFePO_4$ samples.....230
Table 7.4: Occupancy of Fe^{2+} on the M2 and Li and Fe^{2+}/Fe^{3+} on the M1 sites. 231
Table 7.5: The individual and average interatomic bond distances (Å) of M2-O, P-O and M1-O. 232
Table 7.6: Raman modes of the undoped and Zn^{2+} doped $LiFePO_4$ samples showing the assigned vibrational modes.....234
Table 7.7: The different pre-edge peak intensities and peak positions for the undoped and Zn-doped $LiFePO_4$ samples.....236
Table 7.8: The different main edge peak intensities and peak positions for the undoped and Zn-doped $LiFePO_4$ samples.....238
Table 7.9: LCF goodness of fit parameters for the undoped and Zn-doped $LiFePO_4$ samples.....239
Table 7.10: LCF weight percentage of the different components present in the undoped and Zn-doped $LiFePO_4$ samples.....240
Table 7.11: Amount of Fe that should be replaced for each doping percentage.....241
Table 7.12: The reliability factor and energy shift of the undoped and Zn-doped samples.....244
T**able 7.13:** Structural parameters determined using FEFF for the first, second and third coordination shells of the undoped and Zn-doped samples. 246
Table 7.14: The average interatomic distance and average Debye-Waller factor of the different coordination shells. 247
Table 8.1: Reliability factors for each Rietveld refinement. 262
Table 8.2: Multiphase analysis (%) for the undoped $LiFePO_4$ as well as the doped $LiFe_{1-x-y}Zn_xCo_yPO_4$. 262
Table 8.3: Lattice parameters and volume for the $LiFePO_4$ phase of the undoped and Zn^{2+} - Co^{2+} co-doped $LiFePO_4$ samples.....263
Table 8.4: Occupancy of Fe^{2+} on the M2 and Li and Fe^{2+} and/or Fe^{3+} on the M1 sites. 264
Table 8.5: The individual and average interatomic bond distances (Å) of M2-O, P-O and M1-O. 265
Table 8.6: Raman modes of the undoped and Zn^{2+}- Co^{2+} co-doped $LiFePO_4$ samples showing the assigned vibrational modes.....266

Table 8.7: The different pre-edge peak intensities and peak positions for the undoped and Zn^{2+}- Co^{2+} co-doped $LiFePO_4$ samples. 270
Table 8.8: The different main edge peak intensities and peak positions for undoped and Zn^{2+}- Co^{2+} co-doped $LiFePO_4$ samples. 271
Table 8.9: LCF goodness of fit parameters for the undoped and Zn^{2+}- Co^{2+} co-doped $LiFePO_4$ samples. 272
Table 8.10: LCF weight percentage of the different components present in the undoped and Zn^{2+}-Co^{2+} co-doped $LiFePO_4$ samples. 273
Table 8.11: The amount of Fe to be replaced by the co-dopants in the feff.inp file. 273
Table 8.12: The reliability factor and energy shift of the undoped and Zn^{2+}- Co^{2+} co-doped $LiFePO_4$ samples. 276
Table 8.13: Structural parameters determined using FEFF for the first, second and third coordination shells of the undoped and Zn^{2+}- Co^{2+} co-doped samples. 278
Table 8.14: The average interatomic distance and average Debye-Waller factor of the first coordination shell. 280
Table A1: Rietveld error indices for the calibration of 28-ID-1 at BNL of NIST 660c from the refinement of Figure A1. 293
Table A2: Rietveld error indices for the calibration of 28-ID-1 at BNL of NIST 660c from the refinement of Figure A2. 293
Table A3: Rietveld error indices for the calibration of the Bruker D8 Advance of NIST 660c (LaB_6) from the refinement of Figure A3. 294
Table A4: The determined $\chi 2$ value along with the sample name and the chapter the data was used in. 303

Chapter 1

Overview and literature review

1.1 Overview

$LiFePO_4$ has been shown to be a good replacement for modern-day cathode materials in rechargeable Li-ion batteries due to its low toxicity, low cost and higher operating voltages but it also has the disadvantage of poor electronic and ionic conductivity. A large volume of research published on this material has been focused on how to improve the ionic and electronic conductivity properties. However, limited research has been conducted on using a low cost, low energy synthetic route that produces minimum defects and understanding how this affects the synthesised material. A relatively simple hydrothermal route was investigated and optimized, and the structure of the material produced was investigated using both diffraction and spectroscopy techniques. This methodology was then further used to dope and co-dope the $LiFePO_4$ structure with divalent metal ions and the effects on the structure were assessed.

This chapter gives a brief literature review on rechargeable batteries, specifically Li-ion batteries and looking at the different components found in Li-ion batteries (LIBs) with a focus on the cathode materials. The different sections that will be covered include the different compositions, structure, advantages, disadvantages, common structural defects of the material, limitations and commercialization.

1.2. The global energy crisis

Energy is an essential global need and the demand for energy is increasing every year due to the increase in the population and the increase in technological and economic development. This increase in demand brings two different topics under discussion: the increase in the use of fossil fuels and the need for sustainable energy. Carbon dioxide (CO_2) emission from the use of fossil fuels is the main contributor to global warming which is a major global threat[1] and with the increase in energy demand there is a substantial increase in the CO_2 emission. According to The BP Statistical review of World Energy (2020)[2] for carbon emission to reach zero by 2050, there would have to be a constant decrease of about 2.6 gigatonnes of CO_2 emission for the next 25 years.[3] This indicates that there has to be a massive decrease in the use of fossil fuel. In 2019 there was a worldwide increase in the use of renewable energy sources, particularly wind and solar energy, which led to a decrease in carbon emission

compared to previous years[3] but the usage of oil and coal still remained the main source for the production of power and electricity.[3]

Several attempts have been made to reduce the emission of CO_2 by reducing the usage of fossil fuels and by creating a sustainable future and sustainable energy. To work towards sustainable energy means the responsible use of the earth's energy sources and the implementation of and reliable, affordable and accessible energy to everyone. These attempts involve using renewable sources, improving on existing or creating new energy conversion and storage technologies, and reducing energy wastage.

1.3. Batteries as energy storage technologies

Renewable energy sources like solar or wind are available intermittently making energy storage systems an important focus point. Having efficient storage systems allows for the storing of excess energy that can be used when the renewable energy sources are not available.[1] Different technologies can be used as efficient storage systems, such as electrical, chemical, mechanical, thermal and electrochemical energy storage systems.[1,4] Batteries are classified as part of the electrochemical energy storage systems and consists of two electrodes that are separated by the electrolyte.

Battery storage systems are important for a variety for reasons and can be used in electrical grids, electric and hybrid electric vehicles, wireless network systems, portable electronic systems, marine and aerospace applications.[1] These systems can provide quality, clean energy and back-up energy, they provide a safe supply of energy as well as the efficient generation of power.[5] Currently used battery storage systems include, but are not limited to, lead-acid, nickel-metal hydride and nickel-cadmium, sodium sulphur, vanadium redox, metal-air and lithium-ion batteries.[1,4,5] A brief description of each battery follows here, except for the Li-ion battery (LIB) which, is of interest in this project and will be discussed in greater detail in section 1.4.

1.3.1. Lead-acid (PbO_2)

PbO_2 batteries are still being used for industrial, automotive and household applications. The cathode material is made of lead dioxide (PbO_2), the anode material of metallic lead (Pb) and the electrolyte is a sulphuric acid solution.[1,4,5] The advantages of this battery is its energy efficiency (85 - 90%), low self-discharge, low maintenance costs and the robustness of the

battery. The disadvantages include the toxicity of lead, slow charging rate, low cycle life and low energy density (30 W h/kg).[1,5,6]

1.3.2. Nickel based batteries: Nickel - cadmium (NiCd) and nickel-metal hydride (Ni-MH)

The anode in a NiCd battery consist of Cd and that in a MH Ni-MH battery consists of MH. In both batteries the cathode is nickel-oxyhydroxide and the electrolyte is an alkaline solution[7]. Examples of the different metal hydrides (MH) include two different alloy classes: AB_5 (where, A = La, Ce, Nd and Pr, B = Ni, Mn and Co) and AB_2 (where, A = Zr and Ti, B = Ni, Cr and V).[7] The advantages of the NiCd battery are its capability to recharge fast and a long cycle life (3000 cycles) but the main disadvantage is the toxicity, high cost of cadmium and a memory effect.[1,4] The memory effect refers to a reduction in capacity that a battery exhibits when it is discharged to the same point every time before being charged again.[8,9] Lithium ion batteries generally do not suffer from this effect.[7] The advantages of the Ni-MH battery are its higher energy capacity (30 - 40% higher than NiCd), higher energy density, improved environmental friendliness and almost no memory effect. The disadvantages of this device are its high self-discharge rate, low service rate and overcharging ability that can lead to overheating.[4,5]

1.3.3. Sodium sulphur (NaS)

This stationary device is made of a molten sulphur cathode, a molten sodium anode and a solid beta-alumina ceramic electrolyte.[1,4,6] It provides good efficiency (>85%), long cycle capability (2500 cycles), high energy density (151 – 170 kW h/m^3), slow discharge (~6 hours), improved storage capacity, low cost and long life cycle (15 years).[1,4,5] The disadvantages are that this device can only be used as stationary storage systems (such as for wind farms and solar plants) due its high operating temperature (300 – 350 ºC), an external heating source is needed to start the charge and discharge electrochemical processes, and the safety risks associated with the device if the sodium is exposed to air and moisture. [1,4,5]

1.3.4. Vanadium redox batteries (VRB)

This device is classified as a flow battery. The active constituents of the battery are in solution (different ionic forms of vanadium) where an ion selective membrane separates the active constituents.[1,4,5] The advantages of this flow battery are a high tolerance to overcharging, deep charging without decreasing the cycle life, high efficiency (~85%), low maintenance cost, the ability to recover the capacity, no excessive amount of hydrogen is produced and improved

safety. The disadvantage of the VRB is the need for pumps, sensors and secondary containment which makes them suitable only for large scale energy storage applications.[1,4,5]

1.3.5. Metal-air batteries (zinc-air and lithium-air)

Metal-air batteries generate electricity by using oxygen (from air) in an electrochemical couple with an electropositive metal and an ionic liquid as the electrolyte.[1,4,10] The use of the metal-air batteries are limited to small scale usage only. The Zn-air battery is slightly more affordable and environmentally friendly than the Li-air battery, but the latter has a higher specific energy. The disadvantages of a metal-air battery are its low efficiency (~50%), low electrical recharging as well as the formation of dendrites caused by the CO_2 present in the air of the atmosphere.[1,4]

1.4 Lithium-ion batteries (Li-ion)

Batteries can either be classified as non-rechargeable (primary) or rechargeable (secondary). Both working principles are the same except that for rechargeable batteries the electrochemical reaction needed to produce the current is reversible. The current is produced by the flow of electrons which in turn is produced by the chemical reactions occurring at the positive and negative electrodes.[11] Different electrode materials and electrolytes affects the chemical reactions that occur and these are responsible for properties such as the voltage and how much energy the battery can store.[11] Li-ion batteries are classified as rechargeable batteries and consists of four components: the cathode, anode, electrolyte and separator.[10,12] A battery can exist in two different states: charged and discharged (Fig. 1.1). The discharged state is the initial state of the battery and the cathode material contains the Li^+-ions. Charging the battery by using an applied electric field pushes the electrons through the external circuit to the anode and drives the movement of the Li^+-ions through the electrolyte and separator to the anode.[10,12] Using the battery in devices causes it to discharge, allowing electrons to move through the external circuit and Li^+-ions to diffuse back to the cathode.[12]

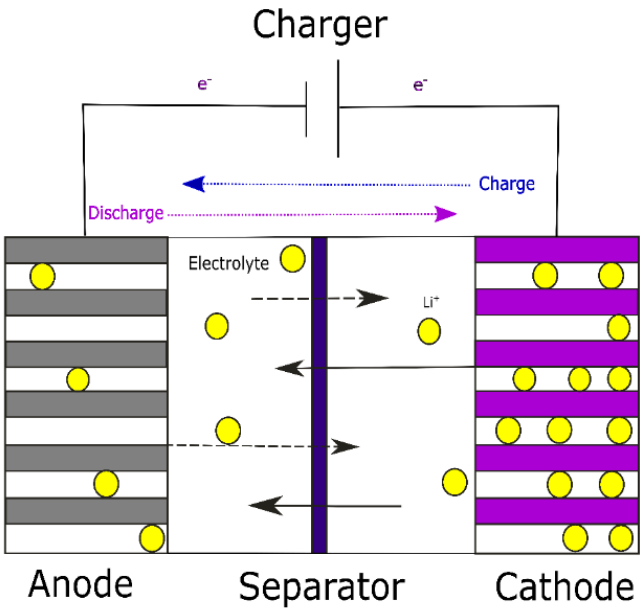

Figure 1.1: Schematic diagram of the working principle of LIBs.

A cell is a single electrochemical device whereas a battery is a group of different cells making them bigger in size. Batteries are manufactured in different cell designs with the most common designs being coin, cylindrical, prismatic (rectangular) and pouch cells (Fig. 1.2). Coin cells, cylindrical and prismatic cells all have hard casings whereas pouch cells do not.[13,14]

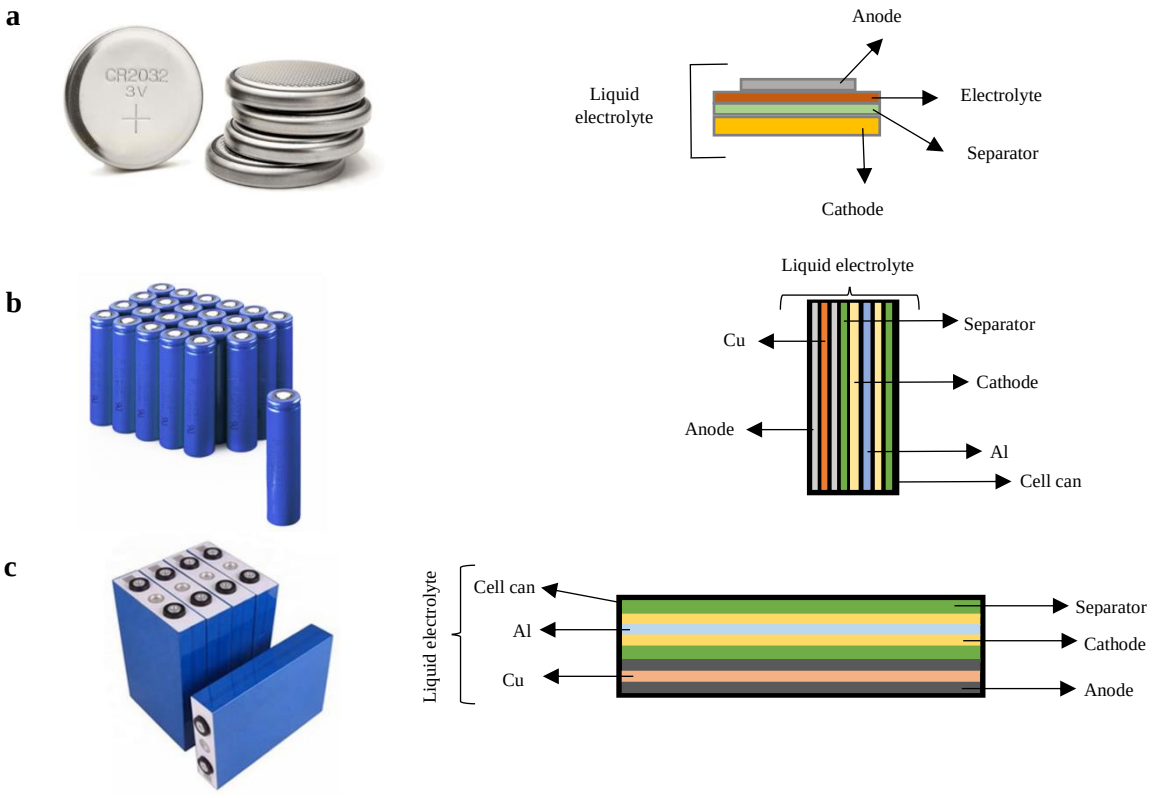

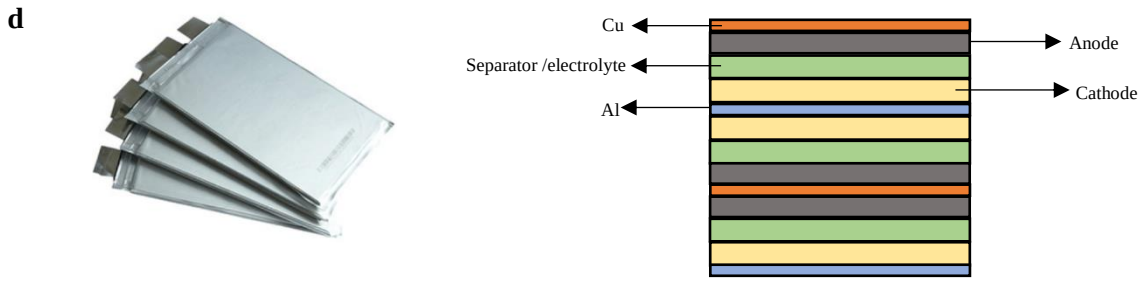

Figure 1.2: Different cell designs of batteries (left) are shown for (a) coin (b) cylindrical (c) prismatic and (d) pouch cells.[9,11] The schematics of the different components inside the cell are shown on the right.[12,13]

Coin cells are small, inexpensive to manufacture and are fairly safe devices designed to be compact for use in portable devices.[15] Although these are the most commonly manufactured cells, their low power makes them only useful for small electronic devices, such as wrist watches.[15] Cylindrical, prismatic and pouch cells are more commonly used in electric vehicles.[16] Cylindrical cells are safer due to the metal casing that improves the overall stability of the battery as well as the quicker manufacturing process that decreases the cost of the battery. The downside of the cylindrical cells is the complicated design that requires more interconnections.[17] The prismatic cells have a larger capacity than that of the cylindrical cells due to the design.[17] The casing is also more durable than that of the other cells. The pouch cells have a more flexible casing made of polymer coated aluminium[17] making the manufacturing process less expensive.[13] The packing of these cells is very important due to the absence of the metal casing making the cells more fragile.[13] The electrolyte used in these cells is a gel rather than liquid, making spillage less of a safety risk.[17]

1.4.1. Lithium-ion battery components

1.4.1.1. The anode material

Batteries that contain Li metal as the anode material are commonly referred to as lithium batteries and were somewhat commercialised in earlier rechargeable batteries.[12] The Li metal was very attractive as an anode and showed a high and promising theoretical capacity of ~3860 mAh/g and a negative electrochemical potential (-3.040 V vs SHE).[10,18] The common problems associated with these batteries are the inability to fully recharge[12] and the poor safety caused by the growth of Li dendrites on the anode that can lead to short circuiting and short life cycles of the batteries.[18–20] This increased safety risk has led to the elimination of Li metal

as the anode material by replacing it with a different material and by synthesising the cathode material in the charged state, meaning that it is the source of lithium ions. These types of batteries are referred to as lithium ion batteries.[10,12] Numerous studies have been done to find suitable anode materials. Among the anode materials that have been commercialised are carbon-based (graphite)[21–23] and lithium titanium dioxide ($Li_4Ti_5O_{12}$/LTO) anodes.[24–26] Graphite has been used as the anode in the majority of Li^+-ion batteries and can be classified as an intercalation compound forming LiC_6 during charging. This material showed good reversibility, a low gravimetric density, a high theoretical capacity (340 – 370 mAh/g), a low lithiation voltage and the improvement of both the safety and life cycle.[10,20,21] The main disadvantages of this material is the lower capacity compared to that of Li metal, the possible formation of dendrites due to a high charging rate and the side reactions between selected electrolytes and graphite.[10,27,28] These side reactions affect the battery capacity and have been researched extensively to find suitable electrolyte materials that are compatible with the anode material.[20,29] A synthetic carbon was mostly used as the anode material but was replaced with a natural graphite due to the high production cost and the high temperatures needed to produce the material.[20] LTO has a theoretical capacity of 175 mAh/g and reaches an actual capacity of ~150 mAh/g.[30] This material also has the ability for fast insertion and removal of Li^+ from the structure during charging, good cycle reversibility, is thermodynamically stable due to the stable operating voltage (1.5 V vs Li^+/Li) and almost no volume change occurs during the charging and discharging cycle.[25,31–35]. The main disadvantages of LTO are that the material suffers from low rate capability caused by a low diffusion coefficient ($\sim 2 \times 10^{-8}\,cm^2/s$ at 25°C)[30] and low electronic conductivity ($\sim 10^{-13} S/cm$ at 25°C).[31] Graphite or other carbon-based materials are still the chosen anode material for Li-ion batteries.

1.4.1.2. The electrolyte and the separator

The electrolyte transports the Li^+-ions between the anode and the cathode but does not allow for the flow of electrons.[10] It is important that the electrolyte is able to form of a solid electrolyte interphase (SEI) on the electrodes through the formation of stable compounds by side reactions.[36,37] This layer mainly depends on reactions occurring with the anode, is formed during the first few cycles, and is of importance as it prevents any other side reactions from occurring throughout the lifetime of the battery.[36,37] Other than the formation of the SEI, important characteristics for suitable electrolytes are: it should be a good ionic conductor and an electronic insulator, have a wide electrochemical window to avoid degradation, be inert to

other cell components, thermally stable, environmental friendly and low cost.[38] The different electrolyte types used in room temperature Li-based batteries are a) non-aqueous, b) aqueous, c) ionic liquids, d) polymer and e) hybrid electrolytes.[37] The focus here is on non-aqueous electrolytes that are most commonly used in commercial Li-ion batteries. The electrolyte is composed of a lithium salt ($LiPF_6$) dissolved in an organic carbonate or a mixture of organic carbonates such as[37,38] ethylene carbonate (EC) together with diethyl (DEC), dimethyl (DMC), propylene (PC) and/or ethyl-methyl (EMC) carbonate.[37,38]

The separator is a porous material that separates the anode and the cathode from one another but it is permeable to the Li^+-ions.[10,12,36,39] The design of the separator is very important for the battery performance and can affect properties such as the cycle life, power and energy density and the safety of the battery and prevents any short circuiting.[40] Important characteristics to take into account when either designing or selecting separators are the chemical stability, porosity, thickness, permeability, thermal stability, mechanical strength, wettability, thermal shrinkage, shutdown and the cost of producing the separator.[40,41] Celgard 3501, Solupor 7P03A and Separion S240P30 are examples of three commercial separators.[36] Celgard 3501 consists of a single polypropylene (PP) layer and is coated with surfactant, Solupor 7P03A consists of ultrahigh molecular weight polyethylene (PE) fibrils and Separion S240P30 is coated with polyethylene terephthalate (PET), Al_2O_3 and SiO_2.

1.4.1.3. The cathode material

The development of cathode materials have mainly been focused on two different categories of compounds namely conversion and intercalation compounds.[12]

(i) Conversion compounds:

The working principle behind these types of cathode materials are based on the ability of the material to undergo electrochemical conversions.[12] The structure is comprised of elements that are more abundant, inexpensive and environmental friendly such as chalcogenides, halogens (in their salt form) and transition metals (e.g. Fe or Cu).[42] These materials exhibit an increase in capacity[12,43] due to the use and availability of multiple valence states making them very attractive cathode materials. Two different conversion reactions can occur and involves the breaking and formation of new bonds and the production of electrons.[19,42] The first reaction includes high valence (valence state of 2+ or above) metal ions and halides (e.g. FeF_2). The element with the highest mobility (e.g. F^-) will diffuse out of the compound (e.g. FeF_2) and

form a bond with Li^+ (e.g. LiF) while the metal (e.g. Fe^{2+}) will form nanocomposite particles. These nanocomposites are then dispersed in LiF.[19,44] The second reaction involves the lithiation of S (Li_2S), Se (Li_2Se), Te (Li_2Te), Br_2 (LiBr) and I_2 (LiI) but the reaction only forms one phase – one single phase is converted into a different single phase.[42] Promising candidate materials for this type of battery are S/Li_2S CuF_2 and FeF_3.[42] S/Li_2S has the highest theoretical capacity, with a gravimetric capacity of 1166 – 1675 mA h/g and volumetric capacity of 1937 mA h/cm^3. CuF_2 offers higher theoretical potentials (3.55 V vs. Li/Li^+) and FeF_3 offers relatively high gravimetric (713 mA h/g) and volumetric (1937 – 2196 mA h/cm^3) capacities. Metal fluorides also have the advantage of providing maximum energy storage.[42] Although very promising, none of these conversion compounds have been commercialized yet due to the very low conductivity, interaction between the electrodes and the electrolyte,[45] the substantial volume change associated with the conversion reaction causing limited cyclability, limited reversibility and capacity loss[12,45] as well as the presence of voltage hysteresis which is detrimental to the battery efficiency.[12,43,45]

(ii) Intercalation compounds:

Most intercalation compounds have been widely commercialized and consist of different structures that accommodate the insertion and extraction of the Li^+-ions. Intercalation compounds rely on a single redox couple ($M^{(n+1)}/M^n$)[12] rather than having multiple valence states available for the reaction as shown with the conversion compounds.[12] The removal of the Li^+-ions from the cathode material results in the multivalent metal ion within this material undergoing a change in oxidation state to maintain charge neutrality, producing electrons and it should maintain its structural integrity.[46,47] Other important characteristics when searching for a suitable intercalation compound for rechargeable batteries includes being able to reversibly react with the lithium, have a high capacity, be able to operate at a high voltage, have high power density, be a good electronic conductor, low cost and environmentally friendly.[46] The different crystal structures that fall under intercalation compounds are layered (Li/TiS_2, $LiCoO_2$ and Ni-containing materials), spinel ($LiMn_2O_4$) and polyanion compounds (olivine - $LiFePO_4$).

Layered cathode materials are composed of alternating cation and anion sheets. The first commercialised layered cathode material was Li/TiS_2 and was commercialized by Exxon.[46] This material exhibited high cycle durability, a high Li^+ intercalation capacity of ~240 mAh/g, low operating voltage of ~2 V versus Li/Li^+ and an experimental capacity of 256 mAh/g.[20,48]

The cathode material was synthesised in the charged state (TiS_2) and Li metal was needed as the anode. This meant that the battery was accompanied by safety issues associated with the Li metal. Another safety issue associated with this material was the release of toxic gas (H_2S) upon exposure to moisture.[20] Although commercialized this material only found use in coin cells utilised in watches.[46]

The most common layered compound is $LiCoO_2$ (LCO) and was first investigated and tested by Mizushima *et.al.*[49], using an organic electrolyte that lowered the operating temperature to ambient temperatures making them more useable in devices.[49] This cathode material was first commercialised by SONY in 1990. The theoretical specific capacity of LCO is 274 mAh/g but only at an operating voltage of ~5 V versus Li/Li^+. [49] An operating voltage this high, however, oxidises the organic electrolyte and poses a safety risk by causing an unstable structure. In commercial cells the material exhibits a specific capacity of between 145 – 155 mAh/g at an operating voltage of 3.5 – 4 V versus Li/Li^+, [29,49] where lowering the voltage is the reason for lower actual specific capacity. The main advantage of LCO compared to TiS_2 is that the material is synthesised and produced in its discharged state and the cathode material already contained Li^+-ions eliminating the need for Li metal as the anode material which reduced the safety risk.[10]

Ni - based layered cathode materials derived from the same parent layered material: $LiNiO_2$ (LNO) and was tested in 1985 by Thomas *et al.*[50] LNO showed improved capacity and energy density[51] compared to that of LCO but exhibited poor thermal stability.[52,53] Another major problem with LNO was the migration of Ni^{2+} onto the Li^+ sites leading to poor rate performance.[52,54] Modifications to the parent material by substituting Ni^{2+} with different metals led to improved thermal stability and the commercialization of two different variations of cathode materials. $LiNi_xMn_yCo_zO_2$ (NMC) was first patented by Argonne National Laboratory (ANL)[55] and showed improved capacity and improved thermal stability due to the partial replacement of Ni^{2+} with both Mn^{4+} and Co^{2+}.[56] Abundant research has been done to determine the optimum ratio of each metal ion in NMC where the percentage of Ni^{2+} was the main metal with either a lower or higher Ni content.[56,57] NMC 333 (3-Ni, 3-Mn, 3-Co molar ratio) and NMC 532 (5-Ni, 3-Mn, 2-Co molar ratio) are the two Ni-poor cathode materials that have dominated the battery industry and the most promising materials for electric vehicles.[20] Having Ni-rich materials (more than 50%) led to an increase in the oxidation of the electrolyte as well as decreased the thermal stability of the material.[56,57] Ni-rich cathode materials that have been commercialized are NMC 622 (6-Ni, 2-Mn, 2-Co molar ratio) and NMC 811 (8-Ni, 1-Mn, 1-

Co molar ratio).[20] NMC on its own has been used by companies like Daimler (cell maker – Li-Tec) and Honda (cell maker – Toshiba) in the Smart and Fit vehicle models respectively.[16] NMC together with $LiMn_2O_4$ (LMO – discussed in the next section) has been used by companies like Fiat (cell maker – Samsung), Mitsubishi (cell maker – Li-Energy Japan) and Renault (cell maker – LG Chem) in the 500, i-MiEV and Zoe vehicle model, respectively.[16]

A different Ni-rich cathode material that has been commercialised is $LiNi_{0.8}Co_{0.15}Al_{0.05}O_2$ (NCA)[58] with a specific capacity of 180 mAh/g and an operating voltage of 3.7 V.[20,29] NCA exhibited improved energy density compared to NMC but was also plagued by lower discharge voltage.[29] The presence of Al^{3+} has to be kept at low percentages, usually between 5 – 10%, to inhibit capacity decay and improve battery safety. Percentages higher than 5 –10% inhibit Li^+ diffusion.[59] Due to the high Ni-content in this material it can exhibit limited cycle life caused by the formation of inactive materials on the surface of the cathode material a result of adsorption of moisture and CO_2 and the formation of Li_2CO_3 and LiOH caused by improper storage.[60] NCA exhibits an increase in thermal stability compared to that of the Ni-rich NMC 811 but a decrease compared to the Ni-poor NMC 333.[20,61] NCA on its own is used by Tesla (cell maker – Panasonic) in the Model S vehicle[16] but used together with LMO by Nissan (cell maker - Automotive Energy Supply Corporation (AESC)) in the Leaf vehicle models.[16]

In 1983 Thackeray *et al*.,[62,63] showed the 3D spinel structure of $LiMn_2O_4$ (LMO), with voltage of 3 – 4 V versus Li/Li^+ has a dual discharge plateau and it was considered as a major competitor to LCO. LMO (M = manganese) was cheaper to produce compared to that of LCO (C = cobalt), LMO was less toxic, it had improved thermal and cyclic stability and improved power density.[64,65] The stability at room temperature of the cathode was first tested with carbon anodes by Taracon *et al*.,[66,67] at Bellacore . The theoretical specific capacity was determined to be 148 mAh/g but in a working cell the capacity reached 110 – 120 mAh/g[29,68] at an operating voltage of 4.1 V[29,68] to ensure the stability during cycling.[69,70] Two other main challenges are: 1) the presence of the Jahn-Teller effect at lower voltages that causes cell degradation[68,71,72] and 2) disproportionation of $2Mn^{3+}$ into Mn^{2+} and Mn^{4+}. The disproportionation originates through the reactions that occur between LMO and the lithium salt ($LiPF_6$), the organic solvent and trace H_2O content and affects the battery performance by causing capacity loss,[73] structure degradation[74,75] and increases the charge transfer resistance by the migration of the Mn^{2+} and Mn^{4+} cations towards the anode.[73,75] LMO has been used together with other NMC and NCA in some electric vehicles.[16]

Polyanionic compounds consists of tetrahedral structures $[(XO_4)^{n-}$ or $(X_mO_{3m+1})^{n-}$ where X= P, S, As, Mo or W, to list a few, that are combined with transition metal polyhedral structures (MO_x) where strong covalent bonding occurs.[76] The advantages making these material types so attractive as cathode materials are the increased thermal stability due to the strong covalent bonding improving the safety of the battery as well as the high capacity that these materials possess.[76] The different polyanion compounds that are being investigated include phosphates, silicates, fluorophosphates, fluorosulphates and borates.[76] The cathode material of interest is $LiFePO_4$ and the next section will discuss this cathode material in further detail.

1.4.2. $LiFePO_4$ as a cathode material

Phospho-olivines were first investigated by Goodenough and his team for the use as a cathode material.[77] These materials have been thought of as a good replacement intercalation compound in Li^+-ion batteries. $LiFePO_4$ falls under the phospho-olivine group, has an orthorhombic structure and crystallises in the *Pnma* space group. It exhibits a slightly distorted hexagonal close packing oxygen array which has two different octahedral sites and a tetrahedral site (Fig. 1.3).[77–79]

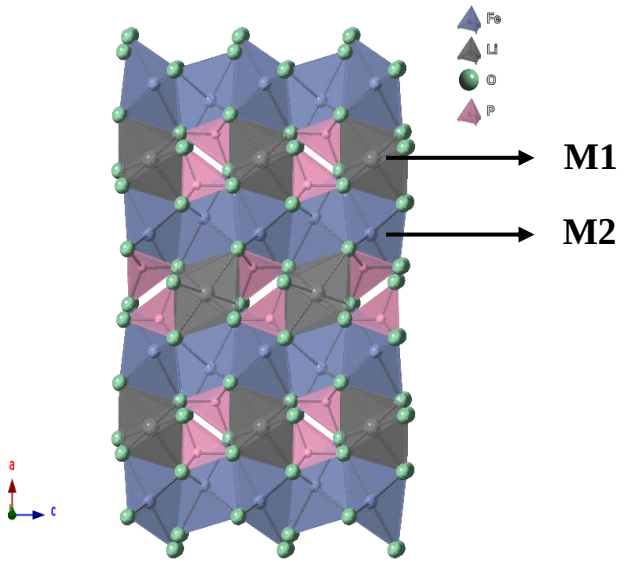

Figure 1.3: Crystal structure of $LiFePO_4$. FeO_6 octahedra are represented in blue, PO_4 tetrahedra are represented in pink, LiO_6 octahedra are represented in grey and the green spheres represents oxygen. Li^+ and Fe^{2+} occupy the M1 and M2 sites respectively.

The two octahedral sites are energetically distinguishable and are responsible for cation ordering.[80] Lithium occupies the M1 edge-sharing octahedral site where LiO_6 forms a chain along the b-axis [010] and lies on an inversion site (Fig. 1.3).[77,81] Iron occupies the M2 corner-sharing octahedral site where FeO_6 forms a zigzag pattern in the b/c plane and is located on a

mirror plane (Fig. 1.3)[77,81] and phosphorous (PO_4^{3-}) occupies the tetrahedral sites (PO_4).[78,80] Although Li^+ and Fe^{2+} both occupy octahedra sites, the average Li-O (M1-O) bond distances are shorter than that of the Fe-O (M2-O) bond distances.[77] The distance between neighbouring Li-O_6 (M1-O) octahedra are shorter than the distance between neighbouring Fe-O_6 (M2-O) octahedra. This shorter distance between neighbouring Li-O (M1-O) octahedra causes slight electrostatic repulsion and is responsible for more distortion around the M1 octahedra.[81] The presence of the PO_4 tetrahedra is advantageous for the cathode material in terms of the battery operation and the thermal stability. This is due to the electrostatic repulsion that exists between the Fe and P causing the weakening of the Fe-O bonds. This weakening of the bonds is responsible for the high operating voltage (3.5 V versus Li^+/Li).[77,80,82] The PO_4 tetrahedra also stabilize the structure due to the inductive effect by reducing the Fe-O covalent character and by the sharing of oxygen ions between iron and phosphorous.[77,83] This bonding sequence prevents oxygen from being released at elevated temperatures and reacting with the electrolyte[77,80] and provides thermal stability by providing protection against overcharging. Yamada et al.[83] showed that only 147 J/g of heat is released over a temperature range of 250 – 360 ºC when fully charged. This is very important when constructing a battery as most batteries are prone to accidental overheating.[84–86]

Chemical lithiation and delithiation of $LiFePO_4$ occurs via a two-phase system where the Fe^{2+} is oxidised to Fe^{3+} ($LiFePO_4 \rightleftarrows FePO_4$). The delithiation is accompanied by a 6.81% volume reduction [77,80,83,87] and both structures have the same 3-dimensional framework with similar lattice constants which allows the structure to stay intact.[77,80] The small volume change and the similarity in structure leads to the high cycle life of $LiFePO_4$.[77,85,88] During delithiation the olivine structure is theoretically able to utilise all the lithium in the structure and is stable over a wide range of lithium concentrations ($0 \leq x \leq 1$).[87] The Li^+ migration during lithiation and delithiation in the olivine type structure has been studied extensively and Li^+ diffuses only through a 1-dimensional tunnel.[78,89–91] By calculating the energy profiles of migration along path A [010], path B [001] and path C [101] (Fig. 1.4) the most favourable migration path can be determined. Path A is parallel to the b-axis (y-axis), path B is parallel to the c-axis (z-axis) and path C is across the Li^+ channels.[78,89,90] The energy and Li^+ jump distance was determined to be the lowest for migration along [010]. Path A has a distance of 2.9 – 3.0Å, path B has a distance of 4.6 – 4.7Å and path C has a distance of 5.6 – 5.8Å.[89,90] Due to the increase in the energy profile and the jump distance it would be difficult to cross channels due to the high

activation barrier and this confirms that Li^+ migration only occurs along the one-dimensional [010] channel in a curved trajectory.[78,89,90]

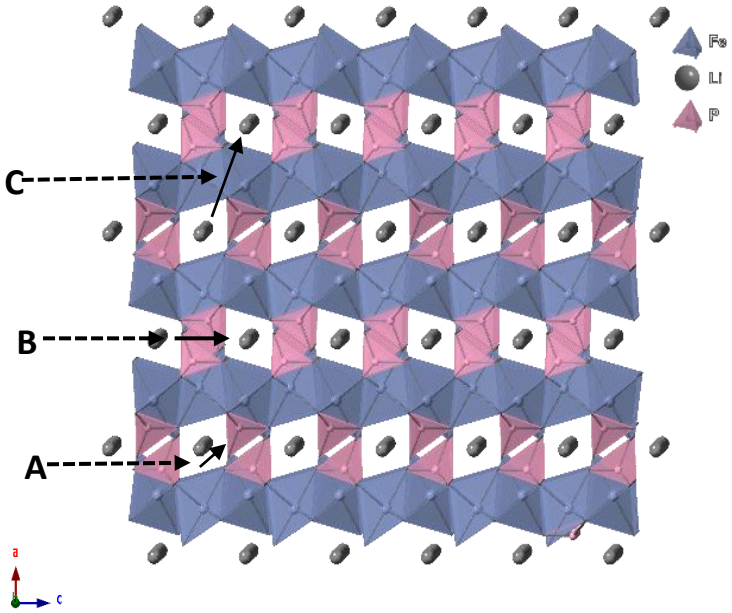

Figure 1.4: The lithium channels are parallel to the b-axis. FeO_6 octahedra are represented in blue, PO_4 tetrahedra are represented in pink and Li^+ are represented by the grey spheres. The oxygen atoms have been removed for simplicity. Li^+ migration paths are indicated with A, B, C.

Aside from the high operating voltage and the thermal stability, $LiFePO_4$ is considered a good cathode material due to its low cost, environmentally friendliness, excellent cycle life[77,78], good cyclic stability a theoretical capacity of 170 mAh/g[83] but a reversible capacity of 110 – 120 mAh/g.[77]

The major drawbacks of $LiFePO_4$ that affect the battery performance are poor electronic conductivity and poor ionic conductivity (poor lithium diffusion) at room temperature.[46,80,83,92–94] Poor electronic conductivity can be improved by coating particles with carbon,[93–95] or by dispersing conductive metals (e.g. copper or silver) in the active material[94] to increase electronic contact between particles. This enhances the surface electronic conductivity, decreases the resistance between particles and controls the particle growth. Poor ionic conductivity is improved by minimizing the particle size[83,93,95–97] and doping with metal ions.[98–104] Smaller particles provides a larger surface area, decrease the Li^+ diffusion distance and have a higher ability to support high current densities.[83,95,97] This enhances the bulk capacity, charge and discharge rate and overall electrochemical performance.[93–95,105]

Doping or co-doping with other metal ions can occur on the Li^+ site and the Fe^{2+} site or by anion doping on the O^{2-} site or by co-doping on these site. By introducing a dopant, the general

structure does not change but the electrochemical properties are modified and it can affect the crystal field which in turn affects the electronic structure of the metal and the electrochemical potential.[106] Doping on the Li^+ site increases the width of the 1-dimensional channel and decreases the charge transfer[107] but caution has to be taken when doping the Li site as there is a possibility that the dopant can block the diffusion channel. Doping on the Fe^{2+} site can increase both the ionic and electronic diffusion, facilitating the lithium migration and weakening the Li - O bonds.[108,109] Another doping site is the anion site. Doping on the O^{2-} site enhances the conductivity and suppresses antisite defects that facilitate the lithium migration by removing blockages in the channel.[98,103] There are several dopants that are known to improve the performance of $LiFePO_4$. Table 1.1 gives a list of the most commonly used single dopants and the dopant site and Table 1.2 gives a list of co-dopants used on either the lithium and iron, the iron or the iron and oxygen sites.

Other drawbacks decreasing the electrochemical performance include the sensitivity to moisture if not stored properly,[110–119] the inherent defects[91,117,120] and impurities present in $LiFePO_4$.[83,114,121] Impurities can lead to the extraction of Li^+ from the structure[115] as well as Fe dissolution risking the safety of the battery.[112,114,122] The inherent defects affect the electrochemical performance by blocking the 1-dimensional channel.[89,123] These drawbacks can be overcome by proper storage of $LiFePO_4$ and by synthesising and heat treatment in an inert atmosphere.[84,87,96,118,124–126] Heat treatment in an inert atmosphere of between 450 – 800ºC is an effective way of removing most defects and leads to ordering of the cations.[81,87]

Table 1.1: Commonly used single dopants and the doping effect on the structure and electrochemical performance.

Doping Site	Dopant	Doping effect
Li site	Na[99,127–129]	Improves reversible capacity, rate capability, ionic transport and electronic conductivity.
	K[100,130]	Improves the Li^+ diffusion coefficient by expanding Li^+ channels, decreases charge transfer resistance and improves cyclic performance.
	Mo[131]	Improves cyclic performance and battery capacity.
	Nd[132]	Improves the discharge capacity and cycling performance.
	Nb[133]	Improves rate capability and Li^+ migration.
Fe site	Zn^{2+}[101,134]	Increases structure stability, Li^+ intercalation/deintercalation, decreases charge transfer resistance, improves reversibility and Li^+ diffusion.

	Mg[108]	Improves cyclic stability, ionic and electronic conductivity, enhances reversibility and exhibit improved structure stability.
	V[135,136]	Improves cyclic stability, ionic and electronic conductivity, enhances reversibility and improves charge-discharge current.
	Cu[102,137–140]	Improves electronic conductivity, discharge capacity, rate and cyclic performance and reversibility.
	Ni[108,141,142]	Increases the stability of the structure, enhances Li^+ diffusion and improves electrical conductivity and cyclic ability and diminish electrode polarization.
	La[143–145]	Improves electronic conductivity, Li^+ migration, capacity performance, cyclic stability and decrease charge transfer resistance.
	Y[146]	Decrease polarization and increases exchange current density.
	Mn[147–150]	Improves electronic conductivity, reversible capacity, exhibits high reversibility and structure stability.
	Co[108,151–153]	Improves electronic conductivity, Li^+ migration, discharge and reversibility capacity.
O site	F[103,154,155]	Improves electronic conductivity and Li^+ diffusion, enhances rate capability and cycling performance, suppresses the formation of defects.
	Cl[104,156]	Improves Li^+ diffusion and reversibility.

Table 1.2: Co-dopants and the doping effect on the structure as well as electrochemical performance.

Doping site	Cathode/anode material	Doping Effects
Li and Fe-site	$Li_{0.99}Nb_{0.01}Fe_{0.97}Ti_{0.03}PO_4$/graphene	Improved discharge capacity, cycling stability and reversibility.[157]
	$Li_{0.97}Na_{0.03}Fe_{0.97}V_{0.03}PO_4$/C	Higher capacity, better conductivity enhanced structure stability, increased Li^+ diffusion.[158]
	$Li_{0.99}Zr_{0.0025}Fe_{0.99}Co_{0.01}PO_4$	Increase in stability, increased rate capacity and cyclic stability.[159]
	$Li_{0.97}Na_{0.02}K_{0.01}$FePO4/C	Cyclic ability and discharge capacity improved and that the diffusivity increased.[160]
	$Li_{0.97}Na_{0.03}Fe_{0.99}Ti_{0.03}PO_4$/C	Decrease in charge transfer resistance, increase in electrical conductivity and Li^+ diffusion.[161]
	$Li_{0.99}La_{0.01}Fe_{0.90}Ti_{0.1}PO_4$/carbon aerogel composite	Exhibit excellent high-rate electrochemical performance (low temperatures such as -20°C) and electronic conductivity.[162]
Fe-site	$LiFe_{0.905}V_{0.069}Ti_{0.025}PO_4$/C	Improved the electronic conductivity, Li^+ diffusion.[163]
	$LiFe_{0.9}V_{0.07}Ti_{0.03}PO_4$/C	Increase in discharge capacity and cyclic ability.[164]
	$LiFe_{0.94}Mg_{0.03}Cu_{0.03}PO_4$/C	Increase in conductivity, discharge capacity. Decrease in charge transfer resistance.[165]

	$LiFe_{0.95}Ni_{0.02}Mn_{0.03}PO_4/C$	Improved structural stability, electronic conductivity, Li^+ diffusion, cycling and rate capability. Decrease in charge transfer resistance.[166]
	$LiFe_{0.98}Ni_{0.01}Mn_{0.01}PO_4/C$	Increase in rateability, cyclic ability, discharge capacity.[167]
	$LiFe_{0.98}Ni_{0.01}Co_{0.01}PO_4/C$	Improved structure stability, cycling performance, particle morphology and rate capability.[168]
	$LiFe_{0.99}Mg_{0.001}Co_{0.001}PO_4$	Increase in ionic mobility, diffusion coefficient, discharge capacity and efficiency.[169]
	$LiFe_{0.985}Mg_{0.005}Ti_{0.01}PO_4$	High electrical conductivity, rate capability and cyclic stability.[170]
Fe and O-site	$LiFe_{1-x}Na_x(PO4)_{1-y}Cl_y$	Enhanced the initial capacity, coulombic efficiency, rate capability.[171]
	$LiFe_{0.95}V_{0.05}(PO_4)_{0.97}F_{0.03}/C$	Improved cycling performance, low charge transfer resistance, electrical conductivity, ion transport.[172]
	$LiFe_{0.92}Mg_{0.08}(PO_4)_{0.97}F_{0.03}/C$	Increased electrochemical performance (low temperature -20°C), increased diffusion coefficient. Reduced charge transfer resistance.[173]
	$LiFe_{0.94}Ti_{0.04}PO_{4-\sigma}\ N_{0.03}$	Increased rate performance.[174]

The hydrothermal synthetic route has shown to be a low energy and low cost synthesis producing small particle sizes but the main disadvantage is the formation of intrinsic structural defects. Two different structural defect models have been proposed to describe the possible cation disorder in these samples:[87,175] a lithium-iron mixing model or site exchange model $[(Li_{1-z}Fe_z)(Li_xFe_{1-x})PO_4]$ and a antisite defect model $[(Li_{1-z}Fe_zPO_4)$ or $(Li_xFe_{1-x})PO_4]$. The site exchange model involves the simultaneous replacement of $Fe^{2+}$with Li^+ on the M2 site and Li^+ with Fe^{2+} on the M1 site. The antisite defect involves the replacement of either Li^+ or Fe^{2+} on the M1 or M2 site, where the most common antisite defect is the replacement of Li^+ with Fe^{2+} on the M1 site (Fe_{Li} antisite defect). This defect exists due to an excess of iron in the structure.[87,175,176] Liu *et al*.[121] reported that in order for the Fe_{Li} antisite to form during synthesis, Li vacancies would have to form first as Fe^{2+} would only occupy the Li^+ sites under the right conditions.[121] The disordering caused by Fe^{2+} on the M1 site will cause additional electrostatic repulsion leading to structural instability and is thermodynamically unfavourable.[81] One of the major electrochemical consequences of the formation of Fe_{Li} antisites or site exchange is the blocking of the 1-dimensional Li^+ diffusion channels. This is a major cause for concern as there is only one channel along which Li^+ diffusion can occur and blocking this site affects the mobility, electrode capacity and the rate capability.[89,121,176–179] The oxidation of Fe^{2+} to Fe^{3+} is

another common defect present in $LiFePO_4$. Fe^{3+} can be incorporated into the $LiFePO_4$ structure in one of two ways:[180,181] 1) the replacement of Fe^{2+} with Fe^{3+} ($3Fe^{2+} \rightarrow 2Fe^{3+}$) leaving an Fe vacancy in the structure and 2) the replacement of both Li^+ and Fe^{2+} with Fe^{3+} ($LiFe^{2+} \rightarrow Fe^{3+}$). The latter causes a Li^+ vacancy on the M1.[180–182]

Although Goodenough and his team were the first to propose $LiFePO_4$ as a cathode material,[77] the commercialization of $LiFePO_4$ was a major patent battle between three different organisations, namely, A123 Systems Inc., University of Texas (Goodenough) and Nippon Telegraph and Telephone in Japan. A123 Systems Inc.[183] ended up being the company responsible for the patent in the early 2000's. $LiFePO_4$ has been used is some electric vehicles from companies like Coda (cell maker – Lishen Tianjin)[16] and Chevrolet (cell maker – A123)[29] for the Model EV and Spark vehicles, respectively. Currently China is a major user of $LiFePO_4$ in electric buses, electrical grids and in electric vehicles from the company BYD.[184–186]

1.5. Aims and objectives

The aims of this research were to synthesise $LiFePO_4$ using a low cost, low energy hydrothermal synthetic route. Homemade Teflon bombs have been successfully used in the past to synthesise porous borophosphates,[187] $[NH_4Fe(III)[BP_2O_8(OH)]$ and $M^I_xM^{II}_z(H_2O)_2[BP_2O_8].zH_2O$, and it is explored here whether these bombs can be used to successfully synthesise $LiFePO_4$. It was attempted to limit the formation of defects without having to include the heat-treatment step at higher temperatures which would require more energy usage by applying several modifications to the synthetic route.

To achieve this, the following the objectives will be addressed:

- Objective 1: To determine the structural characteristics if the commercial $LiFePO_4$ sample which will be used as standard when analysing the data in the X-ray absorption near edge structure (XANES) region.
- Objective 2: To optimise the parameters for the hydrothermal synthesis of $LiFePO_4$ using Teflon bombs.
- Objective 3: To investigate the effects of various impurities and an increasing Fe^{3+} content on the $LiFePO_4$ structure when samples are exposed to air for different durations during the synthesis.
- Objective 4: To investigate the possibility of using Teflon bombs to dope and co-dope on the Fe-site and the effect these dopants would have on the $LiFePO_4$ structure.

- Objective 5: To assess the complementary and differences in the techniques used in the characterisation of the synthesised samples.

The work in this thesis is broken up as follows:

Chapter 1 covers a literature review of different batteries, lithium ion batteries and the cathode materials found in the latter specifically $LiFePO_4$. Chapter 2 covers the general synthesis, instrumental and analysis parameters and a literature review of the different characterisation techniques that will be used.

Chapter 3 is separated into two sections. The first is a literature review on the structural aspects of $LiFePO_4$ and the second is the investigation into any structural differences (if any) between the information found in literature and that of a commercially obtained $LiFePO_4$ (C-LFP) sample which would be used as a standard for the XANES analysis. Synchrotron powder X-ray diffraction (PXRD) with Rietveld refinement, X-ray absorption spectroscopy (XAS) using both X-ray absorption near edge structure (XANES) and extended X-ray absorption fine structure (EXAFS), Mössbauer spectroscopy and Raman spectroscopy were used to characterised C-LFP.

Chapter 4 comprises of an investigation of the effect of varying several parameters during the synthesis process such as the synthesis time, the volume of the solution in the Teflon bombs, the ratio of the precursors and purging of the precursor solutions. The techniques that will be used to characterize the samples include synchrotron PXRD with Rietveld refinement, Mössbauer spectroscopy and Raman spectroscopy.

Chapter 5 shows the effects of varying the lithium addition rate to the remaining precursors on the structure, the Fe^{2+} content and the formation of impurity phases. Using this information an optimum addition rate was suggested and the reproducibility was investigated. To achieve this the structure of the synthesised samples were characterised using synchrotron PXRD, XAS with both XANES and EXAFS, Mössbauer and Raman spectroscopy.

Chapter 6 investigates the effects when the solutions were exposed to air for different waiting periods before the Teflon bombs were sealed and placed in the oven. This aided in determining how exposure to air affected the formation of impurity phases and its effect on the Fe^{2+} content. These samples were be characterized using synchrotron PXRD, Mössbauer and Raman spectroscopy.

Chapter 7 and Chapter 8 examines the possibility of doping (with Zn^{2+}) and co-doping (with Zn^{2+} and Co^{2+}) using the hydrothermal route. Changes in the average and local structure together with the Fe^{2+} content were investigated. These materials were characterised using synchrotron PXRD, XAS (XANES and EXAFS) and Raman spectroscopy.

1.6. References

1. Aneke, M. and Wang, M. Energy storage technologies and real life applications – A state of the art review. *Applied Energy*. **179**, 350–377 (2016).
2. BP Statistical Review of World Energy 2020 (2021). at: www.bp.com/statisticalreview.
3. Statistical Review of World Energy Home (2021). at: https://www.bp.com/en/global/corporate/energy-economics/statistical-review-of-world-energy.html
4. Mahlia, T. M. I., Saktisahdan, T. J., Jannifar, A., Hasan, M. H. and Matseelar, H. S. C. A review of available methods and development on energy storage; Technology update. *Renewable and Sustainable Energy Reviews*. **33** 532–545 (2014).
5. Hu, X., Zou, C., Zhang, C. and Li, Y. Technological Developments in Batteries: A Survey of Principal Roles, Types, and Management Needs. *IEEE Power and Energy Magazine*. **15,** 20–31 (2017).
6. Hadjipaschalis, I., Poullikkas, A. & Efthimiou, V. Overview of current and future energy storage technologies for electric power applications. *Renewable and Sustainable Energy Reviews*. **13**, 1513–1522 (2009).
7. Scott, K. Recycling: Nickel–Metal Hydride Batteries. *Encycl. Electrochem. Power Sources*, 199–208 (2009).
8. Greenway, Do NiMH Batteries Have A Memory- Need, Cycle Life, And Charging Guide_Greenway battery (2022). Available at: https://m.greenway-battery.com/news/Do-NiMH-Batteries-Have-A-Memory--Need,-Cycle-Life,-And-Charging-Guide-1652.html. (Accessed on 30 April 2022).
9. Panasonic Eneloop, The memory effect in batteries: what it is and how to prevent it (2022). Available at: https://www.panasonic-eneloop.eu/en/news/memory-effect-batteries-what-it-and-how-prevent-it. (Accessed on 30 April 2022).
10. Whittingham, M. S. History, evolution, and future status of energy storage. in *Proceedings of the IEEE*. **100,** 1518–1534 (2012)
11. Australian Academy of Science, How a battery works? (2022). Available at: https://www.science.org.au/curious/technology-future/batteries. (Accessed on 30 April 2022)
12. Ma, Y. Computer Simulation of Cathode Materials for Lithium Ion and Lithium Batteries: A Review. *Energy Environ. Mater.* **1**, 148–173 (2018).
13. Flash Battery, The best lithium cells for industry (2021). Available at: https://www.flashbattery.tech/en/cells-lithium-batteries-industrial/. (Accessed on: 12 January 2021)

14. Schröder, R., Aydemir, M. and Seliger, G. Comparatively Assessing different Shapes of Lithium-ion Battery Cells. *Procedia Manuf.* **8**, 104–111 (2017).7).

15. Microbattery, Lithium Coin Cells (2021). Available at: https://www.microbattery.com/coin-cells. (Accessed on 30 April 2022).

16. Anderman, M. Technical report: Assessing the Future of Hybrid and Electric Vehicles: The 2014 xEV Industry Insider Report, Advanced Automotive Batteries. http://www.ehcar.net/library/rapport/rapport022.pdf (2013).

17. Automotive News. The 3 main types of lithium ion battery cells (2021). Available at: https://www.autonews.com/shift/3-main-types-lithium-ion-battery-cells. (Accessed on: 20 January).

18. Xu, W., Wang, J., Ding, F., Chen, Xi., Nasybulin, E., Zhang, Y. and Zhang, J. G.. Lithium metal anodes for rechargeable batteries. *Energy and Environmental Science*. **7**, 513–537 (2014).

19. Nitta, N., Wu, F., Lee, J. T. and Yushin, G. Li-ion battery materials: Present and future. *Materials Today*. **18** (2015).

20. Li, M., Lu, J., Chen, Z. and Amine, K. 30 Years of Lithium-Ion Batteries. *Advanced Materials*. **30** (2018).

21. Flandrois, S. and Simon, B. Carbon materials for lithium-ion rechargeable batteries. *Carbon*. **37**, 165–180 (1999).

22. Besenhard, J. O. and Fritz, H. P. Cathodic reduction of graphite in organic solutions of alkali and NR^{4+} salts. *J. Electroanal. Chem.* **53**, 329–333 (1974).

23. Besenhard, J. O. The electrochemical preparation and properties of ionic alkali metal- and NR4-graphite intercalation compounds in organic electrolytes. *Carbon N. Y.* **14**, 111–115 (1976).

24. Ferg, E., Gummow, R. J., de Kock, A. and Thackeray, M. M. Spinel Anodes for Lithium-Ion Batteries. *J. Electrochem. Soc.* **141**, L147–L150 (1994).

25. Ohzuku, T., Ueda, A. and Yamamoto, N. Zero-Strain Insertion Material of Li $[Li_{1/3}Ti_{5/3}]O_4$ for Rechargeable Lithium Cells. *J. Electrochem. Soc.* **142**, 1431–1435 (1995).

26. Sun, X., Radovanovic, P. V. and Cui, B. Advances in spinel $Li_4Ti_5O_{12}$ anode materials for lithium-ion batteries. *New Journal of Chemistry*. **39**, 38–63 (2015).

27. Dey, A. N. and Sullivan, B. P. The Electrochemical Decomposition of Propylene Carbonate on Graphite. *J. Electrochem. Soc.* **117**, 222 (1970).

28. Arakawa, M. and Yamaki, J. I. The cathodic decomposition of propylene carbonate in lithium batteries. *J. Electroanal. Chem.* **219**, 273–280 (1987).

29. Blomgren, G. E. The Development and Future of Lithium Ion Batteries. *J. Electrochem. Soc.* **164**, A5019–A5025 (2017).

30. Zaghib, K., Simoneau, M., Armand, M. and Gauthier, M. Electrochemical study of $Li_4Ti_5O_{12}$ as negative electrode for Li-ion polymer rechargeable batteries. *J. Power Sources* **81**–**82**, 300–305 (1999).

31. Chen, C. H., Vaughey, J. T., Jansen, A. N., Dees, D. W., Kahaian, A. J., Goacher, T. and Thackeray, M. M. Studies of Mg-Substituted $Li_{4-x}Mg_xTi_5O_{12}$ Spinel Electrodes ($0 \leq x \leq 1$) for Lithium Batteries. *J. Electrochem. Soc.* **148**, A102 (2001).

32. Guo, X., Wang, C., Chen, M., Wang, J. and Zheng, J. Carbon coating of $Li_4Ti_5O_{12}$ using amphiphilic carbonaceous material for improvement of lithium-ion battery performance. *J. Power Sources* **214**, 107–112 (2012).

33. Zhou, T. P., Feng, X. Y., Guo, X., Wu, W. W., Cheng, S. and Xiang, H. F. Solid-state synthesis and electrochemical performance of Ce-doped $Li_4Ti_5O_{12}$ anode materials for lithium-ion batteries. *Electrochim. Acta* **174**, 369–375 (2015).

34. Vikram Babu, B., Vijaya Babu, K., Tewodros Aregai, G., Seeta Devi, L., Madhavi Latha, B., Sushma Reddi, M., Samatha, K. and Veeraiah, V. Structural and electrical properties of $Li_4Ti_5O_{12}$ anode material for lithium-ion batteries. *Results Phys.* **9**, 284–289 (2018).

35. Yi, T. F., Jiang, L. J., Shu, J., Yue, C. B., Zhu, R. S. and Qiao, H. B. Recent development and application of $Li_4Ti_5O_{12}$ as anode material of lithium ion battery. *J. Phys. Chem. Solids* **71**, 1236–1242 (2010).

36. Francis, C. F. J., Kyratzis, I. L. and Best, A. S. Lithium-Ion Battery Separators for Ionic-Liquid Electrolytes: A Review. *Adv. Mater.* **32**, 1904205 (2020).

37. Li, Q., Chen, J., Fan, L., Kong, X. and Lu, Y. Progress in electrolytes for rechargeable Li-based batteries and beyond. *Green Energy and Environment*. **1**, 18–42 (2016).

38. Xu, K. Nonaqueous liquid electrolytes for lithium-based rechargeable batteries. *Chem. Rev.* **104**, 4303–4417 (2004).

39. Orendorff, C. J. The role of separators in lithium-ion cell safety. *Electrochem. Soc. Interface* **21**, 61–65 (2012).

40. Zhang, S. S. A review on the separators of liquid electrolyte Li-ion batteries. *Journal of Power Sources*. **164**, 351–364 (2007).

41. Deimede, V. and Elmasides, C. Separators for Lithium-Ion Batteries: A Review on the Production Processes and Recent Developments. *Energy Technol.* **3**, 453–468 (2015)

42. Wu, F. and Yushin, G. Conversion cathodes for rechargeable lithium and lithium-ion batteries. *Energy and Environmental Science*. **10**, 435–459 (2017).

43. Ko, J. K., Wiaderek, K. M., Pereira, N., Kinnibrugh, T. L., Kim, J. R., Chupas, P. J., Chapman, K. W. and Amatucci, G. G. Transport, phase reactions, and hysteresis of iron fluoride and oxyfluoride conversion electrode materials for lithium batteries. *ACS Applied Materials and Interfaces*. **6** 10858–10869 (2014).

44. Wang, F., Yu, H. C., Chen, M. H., Wu, L., Pereira, N., Thornton, K., Van Der Ven, A., Zhu, Y., Amatucci, G. G. and Graetz, J. Tracking lithium transport and electrochemical reactions in nanoparticles. *Nat. Commun.* **3**, 1–8 (2012).

45. Kraytsberg, A. and Ein-Eli, Y. A critical review-promises and barriers of conversion electrodes for Li-ion batteries. *Journal of Solid State Electrochemistry*. **21**, 1907–1923 (2017).

46. Whittingham, M. S. Lithium batteries and cathode materials. *Chem. Rev.* **104**, 4271–4301 (2004).

47. Satyavani, T. V. S. L., Srinivas Kumar, A. and Subba Rao, P. S. V. Methods of synthesis and performance improvement of lithium iron phosphate for high rate Li-ion batteries: A review. *Eng. Sci. Technol. an Int. J.* **19**, 178–188 (2016)

48. Holleck, G. L. and Driscoll, J. R. Transition metal sulfides as cathodes for secondary lithium batteries-II. titanium sulfides. *Electrochim. Acta.* **22**, 647–655 (1977).

49. Mizushima, K., Jones, P. C., Wiseman, P. J. and Goodenough, J. B. Li_xCoO_2 ($0<x\leq1$): A new cathode material for batteries of high energy density. *Solid State Ionics* **3**–**4**, 171–174 (1981)..

50. Thomas, M. G. S. R., David, W. I. F., Goodenough, J. B. and Groves, P. Synthesis and structural characterization of the normal spinel $LiNi_2O_4$. *Mater. Res. Bull.* **20**, 1137–1146 (1985).

51. Liu, W., Oh, P., Liu, X., Lee, M. J., Cho, W., Chae, S., Kim, Y., Cho, J. Nickel-Rich Layered Lithium Transition-Metal Oxide for High-Energy Lithium-Ion Batteries. *Angew. Chemie - Int. Ed.* **54**, 4440–4457 (2015).

52. Arai, H., Okada, S., Sakurai, Y. and Yamaki, J. I. Thermal behavior of $Li_{1-y}NiO_2$ and the decomposition mechanism. *Solid State Ionics* **109**, 295–302 (1998).

53. Dahn, J. R., Fuller, E. W., Obrovac, M. and von Sacken, U. Thermal stability of Li_xCoO_2, Li_xNiO_2 and λ-MnO_2 and consequences for the safety of Li-ion cells. *Solid State Ionics* **69**, 265–270 (1994)

54. Rougier, A., Gravereau, P. and Delmas, C. Optimization of the Composition of the $Li_{1-z}Ni_{1+z}O_2$ Electrode Materials: Structural, Magnetic, and Electrochemical Studies. *J. Electrochem. Soc.* **143**, 1168–1175 (1996)

55. Thackeray, M. M., Johnson, C. S., Amine, K. and Kim, J. Lithium metal oxide electrodes for lithium cells and batteries. *Electrochem. and Solid-State Lett.* **16**, 117 (2001).

56. Bak, S. M., Hu, E., Zhou, Y., Yu, X., Senanayake, S. D., Cho, S. J., Kim, K. B., Chung, K. Y., Yang, X. Q. and Nam, K. W. Structural changes and thermal stability of charged $LiNi_xMn_yCo_zO_2$ cathode materials studied by combined in situ time-resolved XRD and mass spectroscopy. *ACS Appl. Mater. Interfaces* **6**, 22594–22601 (2014).

57. Jung, R., Metzger, M., Maglia, F., Stinner, C. and Gasteiger, H. A. Oxygen Release and Its Effect on the Cycling Stability of $LiNi_xMn_yCo_zO_2$ (NMC) Cathode Materials for Li-Ion Batteries . *J. Electrochem. Soc.* **164**, A1361–A1377 (2017).

58. Lee, K. K., Yoon, W. S., Kim, K. B., Lee, K. Y. and Hong, S. T. Characterization of $LiNi_{0.8}5Co_{0.10}M_{0.05}O_2$ (M = Al, Fe) as a cathode material for lithium secondary batteries. in *Journal of Power Sources* **97–98**, 308–312 (2001).

59. Madhavi, S., Subba Rao, G. V., Chowdari, B. V. R. and Li, S. F. Y. Effect of aluminum doping on cathodic behaviour of $LiNi_{0.7}Co_{0.3}O_2$. *J. Power Sources* **93**, 156–162 (2001).

60. Oh, P., Song, B., Li, W. and Manthiram, A. Overcoming the chemical instability on exposure to air of Ni-rich layered oxide cathodes by coating with spinel $LiMn_{1.9}Al_{0.1}O_4$. *J. Mater. Chem. A* **4**, 5839–5841 (2016).

61. Inoue, T. and Mukai, K. Roles of positive or negative electrodes in the thermal runaway of lithium-ion batteries: Accelerating rate calorimetry analyses with an all-inclusive microcell. *Electrochem. commun.* **77**, 28–31 (2017).

62. Thackeray, M. M., David, W. I. F., Bruce, P. G. and Goodenough, J. B. Lithium insertion into manganese spinels. *Mater. Res. Bull.* **18**, 461–472 (1983).

63. Gummow, R. J., de Kock, A. and Thackeray, M. M. Improved capacity retention in rechargeable 4 V lithium/lithium-manganese oxide (spinel) cells. *Solid State Ionics* **69**, 59–67 (1994).

64. Yoshio, M., Inoue, S., Hyakutake, M., Piao, G. and Nakamura, H. New lithiummanganese composite oxide for the cathode of rechargeable lithium batteries. *J. Power Sources* **34**, 147–152 (1991).

65. Lee, S., Cho, Y., Song, H.-K., Lee, K. T. and Cho, J. Carbon-Coated Single-Crystal $LiMn_2O_4$ Nanoparticle Clusters as Cathode Material for High-Energy and High-Power Lithium-Ion Batteries. *Angew. Chemie* **124**, 8878–8882 (2012).

66. Tarascon, J. M., Guyomard, D. and Baker, G. L. An update of the Li metal-free rechargeable battery based on $Li_{1+\chi}Mn_2O_4$ cathodes and carbon anodes. *J. Power Sources* **44**, 689–700 (1993).

67. Tarascon, J. M. and Guyomard, D. Li Metal-Free Rechargeable Batteries Based on $Li_{1+x}Mn_2O_4$ Cathodes ($0 \leq x \leq 1$) and Carbon Anodes. *J. Electrochem. Soc.* **138**, 2864–2868 (1991).

68. Thackeray, M. M. Structural Considerations of Layered and Spinel Lithiated Oxides for Lithium Ion Batteries. *J. Electrochem. Soc.* **142**, 2558–2563 (1995).

69. Wu, Y., Ma, C., Yang, J., Li, Z., Allard, L. F., Liang ,C. and Chi, M. Probing the initiation of voltage decay in Li-rich layered cathode materials at the atomic scale. *J. Mater. Chem. A* **3**, 5385–5391 (2015).

70. Zheng, J., Myeong, S., Cho, W., Yan, P., Xiao, Jie., Wang, C., Cho, J. and Zhang, J. G. Li- and Mn-Rich Cathode Materials: Challenges to Commercialization. *Advanced Energy Materials* **7**, (2017).

71. Thackeray, M. M. Manganese oxides for lithium batteries. *Progress in Solid State Chemistry* vol. 25 1–71 (1997).

72. Sun, Y. K., Jeon, Y. S. and Lee, H. J. Overcoming Jahn-Teller distortion for spinel Mn phase. *Electrochem. Solid-State Lett.* **3**, 7–9 (2000).

73. Xia, Y. and Yoshio, M. Studies on Li-Mn-O spinel system (obtained from melt-impregnation method) as a cathode for 4 V lithium batteries part IV. High and low temperature performance of LiMn2O4. *J. Power Sources* **66**, 129–133 (1997).

74. Du Pasquier, A., Blyr, A., Courjal, P., Larcher, D., Amatucci, G., Gérand, B. and Tarascon, J-M. Mechanism for Limited 55°C Storage Performance of $Li_{1.05}Mn1_{.95}O_4$ Electrodes. *J. Electrochem. Soc.* **146**, 428–436 (1999).

75. Robertson, A. D., Lu, S. H. and Howard, W. F. M^{3+}-Modified $LiMn_2O_4$ Spinel Intercalation Cathodes: II. Electrochemical Stabilization by. *J. Electrochem. Soc.* **144**, 3505–3512 (1997).

76. Gong, Z. and Yang, Y. Recent advances in the research of polyanion-type cathode materials for Li-ion batteries. *Energy and Environmental Science* vol. 4 3223–3242 (2011).

77. Padhi, A. K., Nanjundaswamy, K. S. and Goodenough, J. B. Phospho-olivines as Positive-Electrode Materials for Rechargeable Lithium Batteries. *J. Electrochem. Soc.* **144**, 1188 (1997).

78. Islam, M. S., Driscoll, D. J., Fisher, C. A. J. and Slater, P. R. Atomic-scale investigation of defects, dopants, and lithium transport in the $LiFePO_4$ olivine-type battery material. *Chem. Mater.* **17**, 5085–5092 (2005).

79. Franger, S., Le Cras, F., Bourbon, C. and Rouault, H. Comparison between different $LiFePO_4$ synthesis routes and their influence on its physico-chemical properties. in *Journal of Power Sources* **119–121**, 252–257 (2003).

80. Padhi, A. K., Nanjundaswamy, K. S., Masquelier, C., Okada, S. and Goodenough, J. B. Effect of structure on the Fe^{3+}/Fe^{2+} redox couple in iron phosphates. *J. Electrochem. Soc.* **144**, 1609–1613 (1997).

81. Chung, S. Y., Choi, S. Y., Yamamoto, T. and Ikuhara, Y. Atomic-scale visualization of antisite defects in $LiFePO_4$. *Phys. Rev. Lett.* **100**, 125502 (2008).

82. Rousse, G., Rodriguez-Carvajal, J., Patoux, S. and Masquelier, C. Magnetic Structures of the Triphylite $LiFePO_4$ and of Its Delithiated Form $FePO_4$. *Chem. Mater.* **15**, 4082–4090 (2003).

83. Yamada, A., Chung, S. C. and Hinokuma, K. Optimized $LiFePO_4$ for Lithium Battery Cathodes. *J. Electrochem. Soc.* **148**, A224 (2001)

84. Dokko, K., Shiraishi, K. and Kanamura, K. Identification of Surface Impurities on $LiFePO_4$ Particles Prepared by a Hydrothermal Process. *J. Electrochem. Soc.* **152**, A2199 (2005).

85. Haas, O., Deb, A., Cairns, E. J. and Wokaun, A. Synchrotron X-ray absorption study of $LiFePO_4$ electrodes. *J. Electrochem. Soc.* **152**, (2005).

86. Howard, W. F. and Spotnitz, R. M. Theoretical evaluation of high-energy lithium metal phosphate cathode materials in Li-ion batteries. *J. Power Sources* **165**, 887–891 (2007).

87. Chen, J. and Graetz, J. Study of Antisite Defects in Hydrothermally Prepared $LiFePO_4$ by in Situ X-ray Diffraction. *ACS Appl. Mater. Interfaces* **3**, 1380–1384 (2011).

88. Huang, X., Yan, S., Zhao, H., Zhang, L., Guo, R., Chang, C., Kong, X and Han, H. Electrochemical performance of $LiFePO_4$ nanorods obtained from hydrothermal process. *Mater. Charact.* **61**, 720–725 (2010).

89. Morgan, D., Van der Ven, A. and Ceder, G. Li Conductivity in Li_xMPO_4 (M = Mn, Fe, Co, Ni) Olivine Materials. *Electrochem. Solid-State Lett.* **7**, (2004).

90. Fisher, C. A. J., Prieto, V. M. H. and Islam, M. S. Lithium battery materials $LiMPO_4$ (M = Mn, Fe, Co, and Ni): Insights into defect association, transport mechanisms, and doping behavior. *Chem. Mater.* **20**, 5907–5915 (2008).

91. Gardiner, G. R. and Islam, M. S. Anti-site defects and ion migration in the $LiFe_{0.5}Mn_{0.5}PO_4$ mixed-metal cathode material. *Chem. Mater.* **22**, 1242–1248 (2010).

92. Andersson, A. S. and Thomas, J. O. The source of first-cycle capacity loss in $LiFePO_4$. *J. Power Sources* **97**, 498–502 (2001).

93. Huang, H., Yin, S. C. and Nazar, L. F. Approaching theoretical capacity of $LiFePO_4$ at room temperature at high rates. *Electrochem. Solid-State Lett.* **4**, (2001).

94. Croce, F., D' Epifanio, A., Hassoun, J., Deptula, A., Olczac, T. and Scrosati, B. A Novel Concept for the Synthesis of an Improved $LiFePO_4$ Lithium Battery Cathode. *Electrochem. Solid-State Lett.* **5**, A47 (2002).

95. Prosini, P. P., Zane, D. and Pasquali, M. Improved electrochemical performance of a $LiFePO_4$-based composite cathode. *Electrochim. Acta* **46**, 3517–3523 (2001).

96. Kuwahara, A., Suzuki, S. and Miyayama, M. Hydrothermal synthesis of $LiFePO_4$ with small particle size and its electrochemical properties. *J. Electroceramics* **24**, 69–75 (2010).

97. Goodenough, J. B. and Manivannan, V. Cathodes for Lithium-Ion Batteries : Some Comparisons. *Denki Kagaku oyobi Kogyo Butsuri Kagaku* **66**, 1173–1181 (1998).

98. Xu, J. and Chen, G. Effects of doping on the electronic properties of $LiFePO_4$: A first-principles investigation. *Phys. B Condens. Matter* **405**, 803–807 (2010).

99. Yin, X., Huang, K., Liu, S., Wang, H. and Wang, H. Preparation and characterization of Na-doped $LiFePO_4$/C composites as cathode materials for lithium-ion batteries. *J. Power Sources* **195**, 4308–4312 (2010).

100. Fang, X., Li, J., Huang, K., Liu, S., Huang, C., Zhuang, S and Zhang, J. Synthesis and electrochemical properties of K-doped $LiFePO_4$/C composite as cathode material for lithium-ion batteries. *J. Solid State Electrochem.* **16**, 767–773 (2012).

101. Liu, H., Cao, Q., Fu, L. J., Li, C., Wu, Y. P. and Wu, H. Q. Doping effects of zinc on $LiFePO_4$ cathode material for lithium ion batteries. *Electrochem. commun.* **8**, 1553–1557 (2006).

102. Jayaprakash, N., Kalaiselvi, N. and Periasamy, P. Synthesis and Characterization of $LiM_XFe_{1-X}PO_4$ (M = Cu, Sn; X = 0.02) Cathodes-A study on the Effect of Cation Substitution in LiFePO4. *Material. Int. J. Electrochem. Sci.* **3**, (2008).

103. Radhamani, A. V., Karthik, C., Ubic, R., Ramachandra Rao, M. S. and Sudakar, C. Suppression of $FeLi^{\bullet}$ antisite defects in fluorine-doped $LiFePO_4$. *Scr. Mater.* **69**, 96–99 (2013).

104. Yang, L., Jiao, L., Miao, Y. and Yuan, H. Improvement of electrochemical properties of $LiFePO_4$/C cathode materials by chlorine doping. in *Journal of Solid State Electrochemistry* vol. 13 1541–1544 (2009).

105. Yun, N. J., Ha, H. W., Jeong, K. H., Park, H. Y. and Kim, K. Synthesis and electrochemical properties of olivine-type $LiFePO_4$/C composite cathode material prepared from a poly(vinyl alcohol)-containing precursor. *J. Power Sources* **160**, 1361–1368 (2006).

106. Liu, C., Neale, Z. G. and Cao, G. Understanding electrochemical potentials of cathode materials in rechargeable batteries. *Mater. Today* **19**, (2016).

107. Xu, Z., Gao, L., Liu, Y. and Li, L. Review—Recent Developments in the Doped

$LiFePO_4$ Cathode Materials for Power Lithium Ion Batteries. *J. Electrochem. Soc.* **163**, A2600–A2610 (2016).

108. Wang, D., Li, H., Shi, S., Huang, X. and Chen, L. Improving the rate performance of $LiFePO_4$ by Fe-site doping. *Electrochim. Acta* **50**, 2955–2958 (2005).

109. Li, H., Wang, Z., Chen, L. and Huang, X. Research on Advanced Materials for Li-ion Batteries. *Adv. Mater.* **21**, 4593–4607 (2009).

110. Cuisinier, M., Martin, J. F., Dupré, N., Yamada, A., Kanno, R. and Guyomard, D. Moisture driven aging mechanism of $LiFePO_4$ subjected to air exposure. *Electrochem. commun.* **12**, 238–241 (2010).

111. Martin, J. F., Yamada, A., Kobayashi, G., Nishimura, S., Kanno, R., Guyomard, D. and Dupré, N. Air Exposure Effect on $LiFePO_4$. *Electrochem. Solid-State Lett.* **11**, A12 (2008).

112. Porcher, W., Moreau, P., Lestriez, B., Jouanneau, S., Le Cras, F. and Guyomard, D. Stability of $LiFePO_4$ in water and consequence on the Li battery behaviour. *Ionics (Kiel).* **14**, 583–587 (2008).

113. Porcher, W., Moreau, P., Lestriez, B., Jouanneau, S. and Guyomard, D. Is $LiFePO_4$ stable in water? *Electrochem. Solid-State Lett.* **11**, A4 (2008).

114. Yu, D. Y. W., Donoue, K., Kadohata, T., Murata, T., Matsuta, S. and Fujitani, S. Impurities in $LiFePO_4$ and their influence on material characteristics. *J. Electrochem. Soc.* **155**, (2008).

115. Cuisinier, M., Martin, J. F., Dupré, N., Kanno, R. and Guyomard, D. Elucidating the $LiFePO_4$ air aging mechanism to predict its electrochemical performance. *J. Mater. Chem.* **21**, 18575–18583 (2011).

116. Martin, J. F., Cuisinier, M., Dupré, N., Yamada, A., Kanno, R. and Guyomard, D. More on the reactivity of olivine $LiFePO_4$ nano-particles with atmosphere at moderate temperature. *J. Power Sources* **196**, 2155–2163 (2011).

117. Hamelet, S., Gibot, P., Casas-Cabanas, M., Bonnin, D., Grey, C. P., Cabana, J., Leriche, J. B., Rodriguez-Carvajal, J., Courty, M., Levasseur, S., Carlach, P., Van Thournout, M., Tarascon, J. M. and Masquelier, C. The effects of moderate thermal treatments under air on $LiFePO_4$-based nano powders. *J. Mater. Chem.* **19**, 3979–3991 (2009)

118. Delaporte, N., Trudeau, M. L., Bélanger, D. and Zaghib, K. Protection of $LiFePO_4$ against Moisture. *Materials (Basel).* **13**, 942 (2020).

119. Zaghib, K., Dontigny, M., Charest, P., Labrecque, J. F., Guerfi, A., Kopec, M., Mauger, A., Gendron, F. and Julien, C. M. Aging of LiFePO4 upon exposure to H 2 O. *J. Power Sources* **185**, 698–710 (2008).

120. Jensen, K. M. Ø., Christensen, M., Gunnlaugsson, H. P., Lock, N., Bøjesen, E. D., Proffen, T. and Iversen, B. B. Defects in Hydrothermally Synthesized $LiFePO_4$ and $LiFe_{1-x}Mn_xPO_4$ Cathode Materials. *Chemistry of Materials* **25**, 2282 - 2290 (2013).

121. Liu, J., Jiang, R., Wang, X., Huang, T. and Yu, A. The defect chemistry of $LiFePO_4$ prepared by hydrothermal method at different pH values. *J. Power Sources* **194**, 536–540 (2009).

122. Iltchev, N., Chen, Y., Okada, S. and Yamaki, J. $LiFePO_4$ storage at room and elevated temperatures. *J. Power Sources* **119**–**121**, 749–754 (2003).

123. Chen, J., Bai, J., Chen, H. and Graetz, J. In situ hydrothermal synthesis of $LiFePO_4$ studied by synchrotron X-ray diffraction. *J. Phys. Chem. Lett.* **2**, 1874–1878 (2011).

124. Sanchez, M. A. E., Brito, G. E. S., Fantini, M. C. A., Goya, G. F. and Matos, J. R. Synthesis and characterization of $LiFePO_4$ prepared by sol-gel technique. *Solid State Ionics* **177**, 497–500 (2006).

125. Tajimi, S., Ikeda, Y., Uematsu, K., Toda, K. and Sato, M. Enhanced electrochemical performance of $LiFePO_4$ prepared by hydrothermal reaction. in *Solid State Ionics* **175** 287–290 (2004).

126. Jugović, D., Mitrić, M., Cvjetićanin, N., Jančar, B., Mentus, Sl. and Uskoković, D. Synthesis and characterization of $LiFePO_4$/C composite obtained by sonochemical method. *Solid State Ionics* **179**, 415–419 (2008).

127. Liu, X., Chen, X., Zhao, Z. and Liang, X. Effect of Na^+ on Li extraction from brine using $LiFePO_4$/$FePO_4$ electrodes. *Hydrometallurgy* **146**, 24–28 (2014).

128. Chu-Ying, O., Wang, D., Shi, S., Wang, Z., Li, H., Huang, Z. and Chen, L. First Principles Study on $Na_xLi_{1-x}FePO_4$ As Cathode Material for Rechargeable Lithium Batteries. *Chinese Phys. Lett.* **23**, 61 (2006).

129. Xin, X., Li, H., Chang, Q. and Wang, W. Preparation and Investigation on Lattice Distortion and Electrochemical Performances of $Li_{0.95}Na_{0.05}FePO_4$/C. *Chinese J. Chem. Phys.* **25**, 429 (2012)

130. Chen, Z., Zhang, Z., Zhao, Q., Duan, J. and Zhu, H. Understanding the Impact of K-Doping on the Structure and Performance of $LiFePO_4$ /C Cathode Materials . *J. Nanosci. Nanotechnol.* **19**, 119–124 (2018).

131. Zhang, M., Jiao, L F., Yuan, H. T., Wang, Y. M., Guo, J., Zhao, M., Wang, W. and Zhou, X. D. The preparation and characterization of olivine $LiFePO_4$/C doped with MoO_3 by a solution method. *Solid State Ionics* **177**, 3309–3314 (2006).

132. Zhang, Q., Wang, S., Zhou, Z., Ma, G., Jiang, W., Guo, X. and Zhao, S. Structural and electrochemical properties of Nd-doped $LiFePO_4$/C prepared without using inert gas. *Solid State Ionics* **191**, 40–44 (2011).

133. Ma, Z., Shao, G., Wang, G., Zhang, Y. and Du, J. Effects of Nb-doped on the structure and electrochemical performance of $LiFePO_4$/C composites. (2013).

134. Shenouda, A. Y. and Liu, H. K. Studies on electrochemical behaviour of zinc-doped $LiFePO_4$ for lithium battery positive electrode. *J. Alloys Compd.* **477**, 498–503 (2009).

135. Wen, Y., Zeng, L., Tong, Z., Nong, L. and Wei, W. Structure and properties of $LiFe_{0.9}V_{0.1}PO_4$. *J. Alloys Compd.* **416**, 206–208 (2006).

136. Chen, M., Shao, L. L., Yang, H. B., Ren, T. Z., Du, G. and Yuan, Z. Y. Vanadium-doping of $LiFePO_4$/carbon composite cathode materials synthesized with organophosphorus source. *Electrochim. Acta* **167**, 278–286 (2015).

137. Lee, J., Kumar, P., Moudgil, B. M. and Singh, R. K. Electrochemical enhancement of $LiFePO_4$ as a cathode material by incorporating Cu flakes for lithium ion rechargeable

battery. *Solid State Ionics* **231**, 18–24 (2013).

138. Chang, Z. R., Lv, H. J., Tang, H., Yuan, X. Z. and Wang, H. Synthesis and performance of high tap density $LiFePO_4$/C cathode materials doped with copper ions. *J. Alloys Compd.* **501**, 14–17 (2010).

139. Feng, Z. S., Wang, L. L., Wang, Y., Chen, J. J., He, Z. Y., Ji, D. Y. and Zhang, Y. X. Improved electrochemical properties of $LiFePO_4$/Cu cathode material synthesized via an optimized two-step chemical process. *J. Alloys Compd.* **651**, 712–717 (2015).

140. Lee, S. B., Cho, S. H., Heo, J. B., Aravindan, V., Kim, H. S. and Lee, Y. S. Copper-substituted, lithium rich iron phosphate as cathode material for lithium secondary batteries. *J. Alloys Compd.* **488**, 380–385 (2009)

141. Liu, Y., Gu, Y. J., Luo, G. Y., Chen, Z. L., Wu, F. Z., Dai, X. Y., Mai, Y. and Li, J. Q. Ni-doped $LiFePO_4$/C as high-performance cathode composites for Li-ion batteries. *Ceram. Int.* (2020).

142. Zhang, W., Hu, Y., Tao, X., Huang, H., Gan, Y. and Wang, C. Synthesis of spherical $LiFePO_4$/C via Ni doping. *J. Phys. Chem. Solids* **71**, 1196–1200 (2010).

143. Cho, Y. Da, Fey, G. T. K. and Kao, H. M. Physical and electrochemical properties of La-doped $LiFePO_4$/C composites as cathode materials for lithium-ion batteries. *Journal of Solid State Electrochemistry* vol. 12 815–823 (2008).

144. Li, J. Z., Wang, S. Y., Wei, L. H., Liu, Z. and Tian, Y. W. Effective Enhancement of the Electrochemical Properties for $LiFePO_4$/C Cathode Materials by Lanthanum Doping. *Int. J. Electrochem. Sci* vol. **10**, (2015).

145. Cui, Y., Wang, M., Guo, R. and Xu, Z. Electrochemical performance of C-La^{3+} codoped $LiFePO_4$ synthesized by microwave heating. *Rare Met.* **28**, 127–131 (2009).

146. Chen, J., Wang, X., Ma, Z. and Shao, G. Effects of yttrium ion doping on electrochemical performance of $LiFePO_4$/C cathodes for lithium-ion battery. *Ionics (Kiel).* **21**, 2701–2708 (2015).

147. Nakamura, T., Miwa, Y., Tabuchi, M. and Yamada, Y. Structural and Surface Modifications of $LiFePO_4$ Olivine Particles and Their Electrochemical Properties. *J. Electrochem. Soc.* **153**, A1108 (2006).

148. Lin, Y., Zeng, B., Lin, Y., Li, X., Zhao, G., Zhou, Ting., Lai, H. and Huang, Z. Electrochemical properties of carbon-coated $LiFePO_4$ and $LiFe_{0.98}Mn_{0.02}PO_4$ cathode materials synthesized by solid-state reaction. *Rare Met.* **31**, 145–149 (2012).

149. Naik, A., Zhou, J., Gao, C., Liu, G. and Wang, L. Rapid and facile synthesis of Mn doped porous $LiFePO_4$/C from iron carbonyl complex. *J. Energy Inst.* **89**, 21–29 (2016).

150. Nakamura, T., Sakumoto, K., Okamoto, M., Seki, S., Kobayashi, Y., Takeuchi, T., Tabuchi, M. and Yamada, Y. Electrochemical study on Mn^{2+}-substitution in $LiFePO_4$ olivine compound. *J. Power Sources* **174**, 435–441 (2007).

151. Shanmukaraj, D., Wang, G. X., Murugan, R. and Liu, H. K. Electrochemical studies on $LiFe_{1-x}Co_xPO_4$/carbon composite cathode materials synthesized by citrate gel technique for lithium-ion batteries. *Mater. Sci. Eng. B Solid-State Mater. Adv. Technol.* **149**, 93–98 (2008).

152. Gao, H., Jiao, L., Yang, J., Qi, Z., Wang, Y. and Yuan, H. High rate capability of Co-doped $LiFePO_4$/C. *Electrochim. Acta* **97**, 143–149 (2013).

153. Song, J., Shao, G., Shi, M., Ma, Z., Song, W., Wang, C. and Liu, S. The effect of doping Co on the electrochemical properties of $LiFePO_4$/C nanoplates synthesized by solvothermal route. *Solid State Ionics* **253**, 39–46 (2013).

154. Lu, F., Zhou, Y., Liu, J. and Pan, Y. Enhancement of F-doping on the electrochemical behavior of carbon-coated $LiFePO_4$ nanoparticles prepared by hydrothermal route. *Electrochim. Acta* **56**, 8833–8838 (2011).

155. Pan, M., Lin, X. and Zhou, Z. Electrochemical performance of $LiFePO_4$/C doped with F synthesized by carbothermal reduction method using NH_4F as dopant. *J. Solid State Electrochem.* **16**, 1615–1621 (2012).

156. Sun, C. S., Zhang, Y., Zhang, X. J. and Zhou, Z. Structural and electrochemical properties of Cl-doped $LiFePO_4$/C. *J. Power Sources* **195**, 3680–3683 (2010).

157. Tian, Z., Zhou, Z., Liu, S., Ye, F. and Yao, S. Enhanced properties of olivine LiFePO4/graphene co-doped with Nb^{5+} and Ti^{4+} by a sol-gel method. *Solid State Ionics* **278**, 186–191 (2015).

158. Yang, X., Hu, Z. and Liang, J. Effects of sodium and vanadium co-doping on the structure and electrochemical performance of $LiFePO_4$/C cathode material for lithium-ion batteries. *Ceram. Int.* **41**, 2863–2868 (2015).

159. Gao, L., Xu, Z. and Zhang, S. The co-doping effects of Zr and Co on structure and electrochemical properties of $LiFePO_4$ cathode materials. *J. Alloys Compd.* **739**, 529–535 (2018).

160. Madram, A. R., Daneshtalab, R. and Sovizi, M. R. Effect of Na^+ and K^+ co-doping on the structure and electrochemical behaviors of $LiFePO_4$/C cathode material for lithium-ion batteries. *RSC Adv.* **6**, 101477–101484 (2016).

161. Shu, H., Wang, X., Wen, W., Liang, Q., Yang, X., Wei, Q., Hu, B., Liu, L., Liu, X., Song, Y., Zho, M., Bai, Y., Jiang, L., Chen, M., Yang, S., Tan, J., Liao, Y. and Jiang, H. Effective enhancement of electrochemical properties for $LiFePO_4$/C cathode materials by Na and Ti co-doping. *Electrochim. Acta* **89**, 479–487 (2013).

162. Zhang, H., Xu, Y., Zhao, C., Yang, X. and Jiang, Q. Effects of carbon coating and metal ions doping on low temperature electrochemical properties of $LiFePO_4$ cathode material. *Electrochim. Acta* **83**, 341–347 (2012).

163. Long, Y. F., Su, J., Cui, X. R., Lv, X. Y. and Wen, Y. X. Enhanced rate performance of $LiFePO_4$/C by co-doping titanium and vanadium. *Solid State Sci.* **48**, 104–111 (2015).

164. Lv, X. Y., Cui, X. R., Long, Y. F., Su, J. and Wen, Y. X. Optimization of titanium and vanadium co-doping in $LiFePO_4$/C using response surface methodology. *Ionics (Kiel).* **21**, 2447–2455 (2015).

165. Fan, C. L., Zhang, K. H. and Han, S. C. Comprehensive methods to enhance the electrochemical performances of $LiFe_{0.94}Mg_{0.03}Cu_{0.03}PO_4$/C cathode for lithium ion batteries. *Mater. Res. Bull.* **48**, 2497–2503 (2013).

166. Shu, H., Wang, X., Wu, Q., Hu, B., Yang, X., Wei, Q., Liang, Q., Bai, Y., Zhou, M., Wu, C., Chen, M., Wang, A. and Jiang, L. Improved electrochemical performance of

$LiFePO_4$/C cathode via Ni and Mn co-doping for lithium-ion batteries. *J. Power Sources* **237**, 149–155 (2013).

167. Zhang, X., Xu, X., Dong, H., Xu, Y. and Zhao, C. Hierarchical $LiFe_{0.98}MII_{0.02}PO_4$/C (MII= Ni, Mn, Mg) composites via co-doping for lithium ion batteries. *IOP Conf. Ser.: Earth Environ. Sci.* **189**, (2018).

168. Kiani, G. R., Boroomand, S., Khodabakhshi, R. & Esmaeili, M. A novel co-doped $LiFePO_4$/C cathode material, modified for enhanced high power density battery applications. *Microelectron. Eng.* **136**, 77–80 (2015).

169. Ding, Y. H. and Zhang, P. Effect of Mg and Co co-doping on electrochemical properties of LiFePO 4. *Trans. Nonferrous Met. Soc. China (English Ed.* **22**, s153–s156 (2012).

170. Tu, J., Wu, K., Tang, H., Zhou, H. and Jiao, S. Mg-Ti co-doping behavior of porous $LiFePO_4$ microspheres for high-rate lithium-ion batteries. *J. Mater. Chem. A* **5**, 17021–17028 (2017).

171. Wang, Z. H., Yuan, L. X., Wu, M., Sun, D. and Huang, Y. H. Effects of Na^+ and Cl^- co-doping on electrochemical performance in $LiFePO_4$/C. *Electrochim. Acta* **56**, 8477–8483 (2011).

172. Lv, Y. J., Huang, B., Tan, J. X., Jiang, S. Q., Zhang, S. F., and Wen, Y. Z. Enhanced low temperature electrochemical performances of $LiFePO_4$/C by V^{3+} and F^- co-doping. *Mater. Lett.* **229**, 349–352 (2018).

173. Huang, Y., Xu, Y. and Yang, X. Enhanced electrochemical performances of $LiFePO_4$/C by co-doping with magnesium and fluorine. *Electrochim. Acta* **113**, 156–163 (2013).

174. Su, W., Xu, K., Zhong, G., Wei, Z., Wang, C. and Meng, Y. Enhanced Electrochemical Performance of $LiFePO_4$ as Cathode for Lithium Ion Battery by Codoping with Titanium and Nitrogen. *Int. J. Electrochem. Sci* **12**, 6930–6939 (2017).

175. Jensen, K. M. Ø., Christensen, M., Gunnlaugsson, H. P., Lock, N., Bøjesen, E. D., Proffen, T. and Iversen, B. B. Defects in Hydrothermally Synthesized $LiFePO_4$ and $LiFe_{1-x}Mn_xPO_4$ Cathode Materials. *Chemistry of Materials* **25**, 2282 - 2290 (2013).

176. Sun, X. and Xu, Y. Fe excess in hydrothermally synthesized $LiFePO_4$. *Mater. Lett.* **84**, 139 - 142 (2012).

177. Ø. Jensen, K. M., Gunnlaugsson, H. P., Christensen, M. and Iversen, B. B. Mössbauer spectroscopy study of defects in hydrothermally synthesized $LiFePO_4$ cathode material. *Hyperfine Interact.* **226**, 73–78 (2014).

178. Chen, J., Bai, J., Chen, H. and Graetz, J. In Situ Hydrothermal Synthesis of $LiFePO_4$ Studied by Synchrotron X-ray Diffraction. *J. Phys. Chem. Lett.* **2**, 1874–1878 (2011).

179. Hoang, K. and Johannes, M. Tailoring Native Defects in $LiFePO_4$: Insights from First-Principles Calculations. *Chem. Mater.* **23**, 3003–3013 (2011).

180. Hannoyer, B., Prince, A. A. M., Jean, M., Liu, R. S. and Wang, G. X. Mössbauer study on $LiFePO_4$ cathode material for lithium ion batteries. *ICAME 2005* 767–772 (2006).

181. Andersson, A. S., Kalska, B., Häggström, L. and Thomas, J. O. Lithium extraction/insertion in $LiFePO_4$: An X-ray diffraction and Mössbauer spectroscopy study. *Solid State Ionics* **130**, 41–52 (2000).

182. Fransolet, A.-M., Antenucci, D., Speetjens, J.-M. and Tarte, P. An X-ray determinative method for the divalent cation ratio in the triphylite-lithiophilite series. *Mineral. Mag.* **48**, 373–381 (1984).

183. LeVine, S. The man who brought us the lithium-ion battery at the age of 57 has an idea for a new one at 92 — Quartz. (2015). at https://qz.com/338767/the-man-who-brought-us-the-lithium-ion-battery-at-57-has-an-idea-for-a-new-one-at-92/.

184. Olivetti, E. A., Ceder, G., Gaustad, G. G. and Fu, X. Lithium-Ion Battery Supply Chain Considerations: Analysis of Potential Bottlenecks in Critical Metals. *Joule* vol. 1 229–243 (2017).

185. International Energy Agency. Innovation in batteries and electricity storage: A global analysis based on patent data .(2020). at https://www.actu-environnement.com/media/pdf/news-36144-etude-oeb-batteries-brevets.pdf.

186. Sustainable Bus. LFP in China, NMC in Western countries. Electric bus market split between two battery technologies. (2019) at https://www.sustainable-bus.com/news/lfp-battery-industry-is-driven-by-chinese-electric-bus-market-reasons-for-a-dominance-bus/.

187. Mogodi, M. W. *Structure and thermoresponsive behaviour of porous and non-porous borophosphates*. Thesis (PhD). University of the Witwatersrand.(2016).

Chapter 2

Synthetic methodology, instrumentation and theory of the characterisation methods

2.1 General outline of the synthetic method

2.1.1. Description of the reaction vessel: Teflon bombs

The reaction vessels used were homemade Teflon bombs (Image 2.1a and 2.1b) which consisted of three different components: The screw on lid, the cap that was needed to seal the bombs and the sample cell as shown in Images 2.1a and b. The total volume of these bombs were ~ 18.5 mL and for the experimental procedure (as investigated) the volume used was ~4.6 mL (25% of the total volume as discussed in Chapter 4). After the manufacturing of these bombs, the sealing of the Teflon bombs had to be checked to ensure the proper to build-up of the desired pressure for the synthesis. To test this a certain amount of water was added to the bombs which were then placed in the oven (model FS0H4) at 120°C for 48 – 72 hours then removed from the oven and cooled to room temperature. The bombs were opened and the volume of the water inside the bombs were measured. If the volume remained the same in the bombs it had no leakages and no solution evaporated then the bombs could be used for the synthesis. However, if the volume decreased then the bombs had to be modified and the above test had to be repeated.

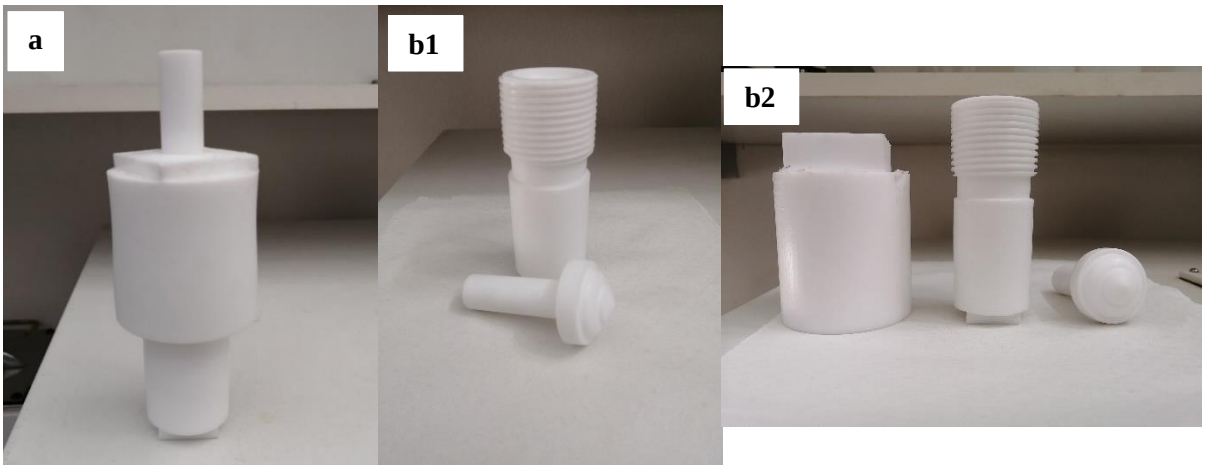

Image 2.1: (a) Fully assembled and (b1; b2) the deconstructed Teflon bombs used for the hydrothermal synthesis

2.1.2 General outline of the synthesis

A hydrothermal synthetic route[1] using the above mentioned homemade Teflon bombs was used to synthesise all samples. As determined in Chapter 4, a molar ratio of 3:1:1 (Li:Fe:PO_4) was used, where LiOH (98%, Sigma Aldrich) was used as the source of lithium, $FeSO_4 \bullet 7H_2O$ (99%, Sigma Aldrich) as the source of iron and 85% wt H_3PO_4 as the phosphorous source. The $FeSO_4 \cdot 7H_2O$ and H_3PO_4 were dissolved together in water, separately from the LiOH while under continuous stirring. The LiOH was then added drop wise to the $FeSO_4/H_3PO_4$ solution using a syringe. This mixture was then added to the Teflon bombs and placed in the oven (Image 2.2) at 120ºC for a fixed period of time as will be discussed. After removing the Teflon bombs from the oven, these were allowed to cool down to room temperature. The samples were then filtered, using vacuum filtration, washed 4-5 times with deionised water and placed in the oven on the filter paper at 70ºC for 24 hours to dry. The dried samples were then ground using an agate mortar and pestle and then placed in a vial and stored in a desiccator (the effects of storage conditions are discussed in the introduction of Chapter 6). The Teflon bombs had to be thoroughly cleaned after each synthesis. This was done by placing the complete deconstructed bomb in a 1:1 HCl solution. The solution was then heated with the bombs for 3 days and then removed and rinsed with water to ensure no sample remained on the walls on the Teflon bombs. Following rinsing procedure the bombs were placed in a 1:1 HNO_3 solution for a further three days then removed from the 1:1 HNO_3 solution, rinsed with deionised water and subsequently placed in deionised water for 4 days before being removed and dried.



Image 2.2: Teflon bombs placed in the oven for the desired reaction time and at the desired temperature.

Modifications to the general synthesis outlined above will be discussed in other chapters. Chapter 4 reviews the different modifications that were made to find the optimum synthetic conditions. These modifications include the volume of sample added to the bomb, the synthesis time of the reaction, the ratio of the lithium compared to the other reagents, purging of solutions and examination of the reproducibility of the synthesis. Chapter 5 will discuss how the optimum lithium addition rate was determined and reproducibility of the optimum addition rate. The final synthesis conditions noted in chapter 5 were then used to synthesise the samples investigated for chapters 7 and 8, with the exception of the addition of the dopants.

2.2. Instrumentation and data analysis methodology

2.2.1. Synchrotron powder X-ray diffraction

Synchrotron radiation powder X-ray diffraction (PXRD) data for Rietveld refinements were measured at the 28-ID-1 beamline of the National Synchrotron Light Source II (NSLS-II) at Brookhaven National Laboratory (BNL). Samples were loaded into Kapton capillaries and measurements were done at room temperature. Different phases were identified using the software package, DIFFRAC.SUITE EVA version 4.2.1.10 linked to the crystallography open database (COD).[2] Refinements and structure parameters were obtain by Rietveld refinement and was performed using the Bruker AXS TOPAS-Academic version 7[3] and Jedit 4.3.1[4] was used to construct the input files. The simple axial divergence model[5] was used to describe the asymmetry due to divergence and the peak shape was described using the Thompson-Cox-Hastings (TCHZ) Pseudo-Voight function[6] (discussed further in section 2.3.1.1) to describe both the Gaussian and Lorentzian contributions. To describe the background scattering a 4th order Chebychev polynomial function was used (also discussed in section 2.3.1.1). The structural parameters refined were the scale, lattice parameters, occupancy of iron and lithium, thermal displacement, fractional coordinates and both Gaussian and Lorentzian strain. The lattice parameters were left to refine throughout the refinement and the thermal displacement parameters were only allowed to refine between 0.1 Å and 1.5 Å.[5] As suggested for inorganic structures. As described on page 17, there are usually two different models that can be used to describe the cation disorder. During the refinement process both these models were considered. The occupancy of the cations especially Fe and Li to include the occupancy of another cation on the same site was refined as described by Dinnebier et al.[5] Including lithium on the Fe-site led to extremely high errors on this site, whereas including iron on the Li-site produced reasonable errors. This indicated that the model that best described the cation occupancy and

disorder is the antisite defect model. The starting model chosen was that of Streltsov *et al.*[7] This model was then modified using the data collected of a PXRD pure $LiFePO_4$ sample (labelled as LFP-P1) synthesised using the above mentioned synthetic route. The modified $LiFePO_4$ structure was then utilised as the starting model for all the other refined structures. Rietveld could not be used to distinguish between the presence of Fe^{2+} and Fe^{3+} and as such Mössbauer spectroscopy was used to evaluate the percentage of Fe^{2+} and Fe^{3+} present on these sites. The refinement process used for the inclusion of doping cations will be described in Chapter 7 and 8.

All preliminary PXRD measurements were performed on a Bruker D8 Advance with a Molybdenum X-ray source, the detector was a VANTEC-1-1-dimensional PSD detector and the X-ray generator had a voltage of 50 kV and a current of 30 mA with the presence of a Ni filter. The errors reported for this section are the fitting error and do not include the measurement error. The calibration for the synchrotron and the lab based measurements using LaB_6 is discussed in Appendix A1.

2.2.2. Pair distribution analysis

Total scattering data suitable for pair distribution function (PDF) analysis was also measured at the 28-ID-1 beamline of the NSLS-II at BNL using a wavelength of 0.1671 Å and a Q_{max} = 28 $Å^{-1}$. The 2D tiff images obtained were integrated using Fit2D[8] and PDF data was generated using PDFgetX3[9] and this data processing was performed at the synchrotron. Selected corrections to the data were made in xPDFSuite.[10] To refine data of both the calibrant and the sample, PDFGui[11] was used. LaB_6 (NIST 660c) was used as the calibrant and to determine the instrumental resolution parameters Q_{damp} (which accounts for the Gaussian damping due to the limited resolution of Q) and Q_{broad} (which accounts for the peak broadening due the increase in noise with Q).[12] The values of Q_{damp} = 0.014(2) $Å^{-1}$ and Q_{broad} = 0.014(3) $Å^{-1}$ were then fixed in further sample refinements. The refined parameters included the scale, *delta2* (to account for peak sharpening at low temperatures), the lattice parameters and atomic displacement parameters. PDF's to determine different interatomic distance contributions (Fe-O, P-O, Fe-P and Fe-Fe) were also calculated in PDFGui using the above mentioned instrumental parameters. Gaussian functions were fitted to selected peaks of interest.[5,13] Peak positions, integral peak intensity, full width at half maximum, as well as the errors, were determined using automated Python scripts similar to the peak selection software implemented in xPDFSuite (the script is shown in Appendix A6).[10] The reported errors for the peak positions,

integral peak intensity and full width at half maximum are the fitting errors and not the errors associated with the measurement.

2.2.3 X-ray absorption spectroscopy

Fe K-edge X-ray absorption spectra were collected at the B18 beamline, Diamond Light Source (DLS), Oxfordshire, United Kingdom. The storage ring energy was 3 eV with a top-up mode at nominal current of 300 mA. The beam was conditioned using a monochromator crystal [Si(111)], collimating Si mirrors coated in Pt and harmonics rejection mirrors. A full description can be found in Appendix A2. Standards with known oxidation states and geometry around the Fe atom was used, namely, $LiFePO_4$ (>97%, Sigma Aldrich), $FePO_4 \cdot 4H_2O$ (97%, Sigma Aldrich) and α-Fe_2O_3 (puriss, Riedel-de Haën). The $LiFePO_4$ standard was stored in a desiccator. Standards and the synthesised samples were ground and mixed with cellulose (Avicel PH-101, Sigma Aldrich) and pressed into 13 mm pellets at 1.5 ton. The cellulose to sample ratio was 5:1 for phosphates and 10:1 for α-Fe_2O_3. Data was collected in transmission mode with the first ionization chamber filled with nitrogen and the second and third ionization chamber filled with argon. Internal references (Fe foil) were used for the energy calibration at each scan and was performed at the synchrotron. Three scans of each standard and each sample were collected and both the data as well as the reference channel were imported for each scan to perform data processing. All the scans were aligned with the reference scan of the $LiFePO_4$ standard to enable comparison of edge energies. Thereafter the three aligned scans for each sample were merged into one scan. The threshold energy (E_0) was chosen to be the first maximum of the first derivative scan and is used as a reference for all parameters in XANES (X-ray absorption near edge structure) and EXAFS (extended X-ray absorption fine structure) analyses. Every scan was normalized and the background removed, R_{bkg} was set to 1. No spline clamps were used at low energy values, but a strong spline clamp was used at higher energy values. The merged scan for each sample were used for further analysis. Data processing, XANES analysis and linear combination fitting (LCF) was carried out using Athena[14], and Artemis[14] was used for EXAFS analysis. Peak positions were determined using the multiple peak fitting tool in Origin8[15] (2016) or using the curve and peak fitting software Fityk[16] (version 1.3.1).

2.2.3.1. XANES (pre-edge and edge region) and the use of linear combination fitting

To investigate the pre-edge region and to perform linear combination fitting (LCF) the three standards were used. LCF is a very useful tool to determine the major and minor components present in unknown samples.[17–20] Quantitative data as well as bonding characteristics of the absorbing atom can be determined. The standards provided three different bonding environments and characteristics, namely $Fe^{2+}O_6$ and $Fe^{3+}O_6$ in a slightly distorted environment and then $Fe^{3+}O_6$ in an environment with a higher degree of distortion. $LiFePO_4$ (with Fe^{2+}) shows the presence of the two peaks (t_{2g} and e_g) in the pre-edge region with a weak intensity that are caused by the break in the inversion symmetry due to the slightly distorted FeO_6 octahedra.[21–23] $FePO_4 \cdot 4H_2O$ is an amorphous powder[24] and Fe exists as Fe^{3+}. Mössbauer spectroscopy and previous XAS studies indicate that a $Fe^{3+}O_6$ octahedral environment exists in this phase.[23,24] Four of the oxygen atoms are bonded to phosphorous groups and the other two are bonded to the water groups. The α-Fe_2O_3 standard also has a $Fe^{3+}O_6$ octahedral arrangement.[23,25] The presence of the intense pre-edge peak indicates that the Fe^{3+} is in a much more distorted environment due to the Fe-Fe repulsion present in the structure.[26,27] For the LCF fits the weighting of each standard was kept between 0 and 1 and constrained to a sum of 1. No overall shift of E_0 was allowed.

2.2.3.2. EXAFS – Local structure determination

To emphasise oscillations at higher *k*-values a k^3-weighted Hanning window was utilised. This k-weight order enhances any structural information that could have been lost due to signal damping that occurs at higher *k*-values. The k-space was analysed over the k-range of 3 – 12.828 $Å^{-1}$. Beyond this range the data was noisy and was excluded from the fits. The R-space was analysed over the r-range of 1.3 – 5 Å. The minimum range was chosen to exclude peaks that are not related to the shortest interatomic bond distance and the maximum to include the largest interatomic distance. By increasing the distance of analysis, separating and identifying the different scattering contributions becomes difficult due to overlapping contributions.

The parameters that were refined for the determination of the local structure were the amplitude reduction factor (S_0^2), the energy shift (ΔE_0), the change in interatomic distance (ΔR) and the Debye-Waller factor (σ^2). The coordination number (CN) was not set to refine and was changed manually using knowledge of the known structure. The starting values for each of these

refineable parameters were the same as the starting values determined using Artemis and they were:[14] S_0^2 = 1.000, ΔE_0 = 0, ΔR = 0 and σ^2 = 0.003. These refined parameters led to the determination of the structural parameters such as coordination numbers (*N*), interatomic distances ($R = X_a - X_b$) and the Debye-Waller factor (σ^2). The errors associated with the interatomic distances and the Debye-Waller factor are the fitting errors and not the measurement error as seen with PXRD and PDF sections. To build the model used for the calculation of the scattering paths of the cluster of atoms using FEFF[28] the starting model that was used for $LiFePO_4$ was determined by Streltsov *et al.*[7] The cluster size used for the scattering path calculation was 7.038 Å and the longest path that was included was 5.0 Å.

All Fourier Transformed EXAFS were phase corrected. The first fitting model considered each scattering path with its own unique refineable description for ΔR. For this model $S_0^2$and ΔE_0 were refined throughout the fitting process but had the same refineable description and was thus kept the same for all scattering paths. σ^2 was also given a unique refineable description that was different for each scattering path thus determining the disorder individually for each added path however the results for this model showed that σ^2 had errors larger than the actual value. The σ^2 ± error values were only reasonable when the first coordination shell had six identical interatomic bond distances showing an undistorted octahedra. Other techniques such as Rietveld refinement of PXRD data and Mössbauer spectroscopy, for the samples discussed here, indicated that the structure showed that a distorted octahedra was present (as shown with results in Chapters 4 and 5). The first model was thus not adequate.

This led to the second model that was used for all the samples. This model also kept S_0^2 and ΔE_0 the same for all scattering paths with different σ^2 for every scattering path, but ΔR was only allowed to vary for each coordination shell. This model produced reasonable values for the σ^2 ± error and allowed for a distorted octahedron. A good *R*-factor for an acceptable EXAFS fit is less than 5%[29] but for a good fit it is less than 2%.[30] The energy shift (ΔE_0) parameter is very important to ensure that the energy grid used to compare the measured data of different samples with that of theoretical data are aligned. The energy shift is highly correlated to that of the path length and it is therefore very desirable to have small energy shift values (-10 eV < ΔE_0 < 10 eV).[31] The reduced χ^2 value was used to determine if any changes made to the model would significantly improve or worsen the fit.

2.2.4. Mössbauer spectroscopy

The Mössbauer spectra were recorded at room temperature, in transmission mode and using a ^{57}Co γ-ray source (30 mCi) and a multichannel analyser. An Fe foil was used to calibrate the isomer shift and the velocity and the analysis was performed using Vinda[32] (version 0.7) in Microsoft Excel. The two most common line shapes are the Lorentzian or a convolution of the Lorentzian line shape and Gaussian broadening and is called the Voigt. In this thesis a Voigt model was used to describe the line shape rather than a Lorentzian as the latter is used for an ideal case where all the Fe environments are identical but is not useful in cases where the geometry and distance in the polyhedral is different.[33,34] In this case all the Fe environments are not identical and due to the disorder present it deviates from the ideal line shape and a Lorentzian line shape was not used. Spectra for the different samples were fitted to a sum of Voigt doublets and each component was fitted with independent line widths to accommodate any differences in the phases due to disorder. Constraints were added to allow the minimum line width to be 0.275 mm/s and a maximum linewidth of 0.65 mm/s. These values were experimentally obtained through the calibration process. Gaussian Broadening effects were also included in the fit. Discrete doublets that does not really overlap were added in an attempt to not over fit the data. Modelling for the different spectra were performed based on the research and different environments determined by Amisse *et. al*.[35] and Li and Shinno.[36] Other cited literature in the different chapters were also used as a way to identify the different environments. These literature environments together with the other characterization techniques were then used to discuss the results. The experimental setup, calibration process and the fitting procedure, error analysis with the sample determined χ^2 values can be found in Appendices A3, A4 and A5, respectively.

2.2.5. Raman spectroscopy

Raman spectra were acquired using the 514.5 nm line of a Lexel Model 95-SHG argon ion laser as the excitation source. The Raman spectrometer was a Horiba LabRAM HR instrument equipped with an Olympus BX41 microscope attachment. The incident beam was focused onto the sample using a 100x objective (N.A. = 0.90) and the backscattered light was dispersed via a 600 lines/mm grating onto a liquid nitrogen cooled CCD detector. The software used for acquisitions was LabSpec v.5.[37] The incident beam power was kept low (~ 0.4 mW) to minimise any possible localised heating. Different sections as seen under the microscope were sampled within each sample especially if different coloured particulates were present. Each

colour was then sampled at least twice to get a good overall representation of the sample. Peak positions, selected full width at half maximum (FWHM) and selected relative intensities of the resulting spectra were determined using Fityk[16] (version 1.3.1). All peaks were fitted using a Lorentzian function. Selected spectra were included in this thesis.

2.2.6. Data visualization

All figures used to represent data were written in Notepad++ and then run through Python (v3.8.5) using the command shell iPython (v7.19.0). Matplotlib[38] was utilised as the visualization library.

2.3. Theory of the characterisation methods

2.3.1. Powder X-ray diffraction

Powder X-ray diffraction (PXRD) is a technique used for studying the atomic structures of materials. The crystallites in a powdered sample are (or should ideally be) randomly orientated and when the sample is placed in the path of an X-ray beam, the X-rays would be reflected off the lattice planes where the atoms reside and Miller indices (*hkl*) are used to describe the planes.[5] Diffraction from these planes would occur if Bragg's law (**eqn . 2.1**) is fulfilled by having the correct orientation:[39]

$$n\lambda = 2dsin\theta \qquad \textbf{(2.1)}$$

where n is the diffraction order and should be an integer, λ is the X-ray wavelength, d is the interplanar spacing of the lattice planes that are parallel to each other and θ is the diffraction angle between the incoming and diffracted X-ray beams. The diffracted X-rays at a certain 2θ angle would form the Debye-Scherrer cones (Fig. 2.1) and can be observed as a 1-dimensional diffractogram by integrating the 2-dimensional image produced by the Debye-Scherrer cones.[5]

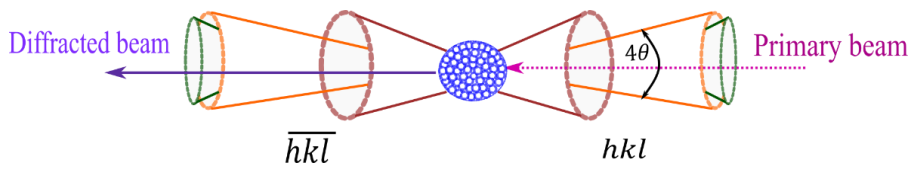

Figure 2.1: Diffracted beam emanating from a powdered sample showing the Debye-Scherrer cones.[33]

The Bragg equation can also be used to extract structural information and peak positions on a diffraction pattern.[5] A diffraction pattern is comprised of Bragg reflections and Bragg

intensities (I_{hkl}). The individual reflections display several properties, namely, positions, height, breadth and an integrated area. The Bragg intensities can be related to the same set of Miller indices when the same planes were responsible for them. There is a direct relationship between the Bragg intensity and the square of absolute structure factor:[40]

$$I_{hkl} \propto |F_{hkl}|^2. \quad \textbf{(2.2)}$$

The diffracted rays from the planes contain information, on the atoms in the structure, in the amplitude and phase. This information contributes to the intensity of the peaks and can be mathematically described as the structure factor (F_{hkl}). F_{hkl} is determined by the sum of neighbouring Bragg reflection contributions of the modeled structure. The structure factor can be expressed as:[40,41]

$$F_{hkl} = \sum_j N_j f_j \exp 2\pi i\left[hx_j + ky_i + lz_i\right] \exp\left[-M_j\right] \quad \textbf{(2.3 a)}$$

where N is the occupancy multiplier, f is the scattering factor, *hkl* are the Miller indices, x-y-z describes the position parameters and M_j is given as:

$$M_j = \frac{8\pi^2 \mu_s^2 sin^2\theta}{\lambda^2}. \quad \textbf{(2.3 b)}$$

The root-mean-square thermal displacement of the atom parallel to the diffraction vector is described by μ_s^2.

2.3.1.1. The Rietveld method

The refinement of crystal structures from powder diffraction data can be done using the Rietveld method to extract important structural information. The Rietveld method is an elegant approach to obtain the best possible fit of a model to the experimental data using a least-squares refinement. The goal is that the best fit between the calculated and the observed data is obtained for the entire powder pattern and this is found by simultaneously refining the parameters that lead to the determination of the crystal structure using the Bragg reflections.[40] A diffraction pattern is given in the form of the intensity measured at different step increments such as the scattering angle, i.e. Y_i vs. 2θ. The least-squares refinement is then performed to the calculated intensity, $Y_{c,i}$ in the diffraction pattern. Different structural and instrumental parameters are refined to optimize the fit (Table 2.1) and to determine $Y_{c,i}$ using:[40]

$$Y_{c,i} = s \sum_K L_K |F_K|^2 \, \phi(2\theta_i - 2\theta_K) P_K A + Y_{b,i} \quad \textbf{(2.4)}$$

Where s is the scale factor and summation across *K* that described the Miller indices (*h*, *k*, and *l*) for the Bragg reflections according to the following parameters: L_K is the Lorentz-Polarization and multiplicity factors, $|F_K|$ is the structure factor, ϕ is used to describe the reflection profile function, P_K describes the preferred orientation factor, *A* is the absorption factor and $Y_{b,i}$ describes the background intensity.

Table 2.1: Refineable parameters for each phase present and the refineable global parameters (for the whole powder pattern):[40]

Parameters for each phase	**Global parameters**
Fractional coordinates - x_m, y_m, z_m	$2\theta -$ error
Isotropic thermal parameters - B_m	Instrumental profile
The site-occupancy multiplier - N_m	Peak asymmetry
Scale factor	Background
Specimen-profile breadth parameters	Wavelength
Lattice Parameters	Specimen displacement
Overall temperature factor	Specimen transparency
Thermal parameters: Anisotropic	Absorption
Preferred orientation	
Profile parameters: Crystallite size and microstrain	
Extinction	

m indicates the mth atom in the unit cell

The best fit between the observed and calculated values is obtained by minimization of the residual function and can be described by the summation over all the steps using:[40]

$$S_y = \sum_i \left(w_i \left(Y_{o,i} - Y_{c,i} \right) \right)^2 \quad \textbf{(2.5)}$$

where $w_i = \frac{1}{Y_{oi}}$, $Y_{o,i}$ is used to describe the observed intensity at a step and $Y_{c,i}$ is used to described the calculated intensity at a step.

Peak profile function: The peak profile on the diffractogram would have contributions related to both the instrumental resolution function (IRF) as well as the microstructure such as the microstrain and domain size of the sample. The peak profile function accounts for the IRF contributions such as the emission profile and instrumental aberrations.[5] The most common peak profile functions used in refinements are Pearson VII, Gaussian, Lorentzian and modifications of these functions. The profile function used in this project for the refinements is the modified Thompson-Cox-Hasting Pseudo-Voight (TCHZ)[6] profile function and is described by:[6,40]

$$TCHZ = \eta L + (1-\eta)G \quad \textbf{(2.6 a)}$$

where η is the parameter that can be used to relate the individual Gaussian (G) and Lorentzian (L) contributions and can be expanded as follows:

$$\eta = 1.36603(\Gamma_L/\Gamma) - 0.47719(\Gamma_L/\Gamma)^2 + 0.1116(\Gamma_L/\Gamma)^3 \quad \textbf{(2.6 b)}$$

where Γ_L is described by:

$$\Gamma_L = Xtan\theta + \frac{Y}{cos\theta} \quad \textbf{(2.6 c)}$$

and Γ is described by

$$\Gamma = (\Gamma_G^5 + 2.69269\Gamma_G^4\Gamma_L + 2.42843\Gamma_G^3\Gamma_L^2 + 4.47163\Gamma_G^2\Gamma_L^3 + 0.07842\Gamma_G\Gamma_L^4 + \Gamma_G^5)^{1/5} \quad \textbf{(2.6 d)}$$

where $\Gamma_G$is:

$$\Gamma_G = \sqrt{Utan^2\theta + Vtan\theta + W + \frac{Z}{cos^2\theta}}. \quad \textbf{(2.6 e)}$$

The refineable parameters in this profile function are *U, V, W, X, Y* and *Z*. The microstrain and crystallite size for the contributing Gaussian parameters are described by *U* and *Z* and for the contributing Lorentzian parameters *X* and *Y*, respectively.[5]

The background function: The background at a certain point on the diffraction pattern can either be modelled using an empirical function, analytical function or by manually modelling the background. The background should always be refined as both the instrumental and sample effects can contribute to the background, these include scattering (thermal, diffuse, incoherent and inelastic) and disorder. A higher-order Chebyshev polynomial can be used so that the function is flexible enough to fit the features present in the background. The higher the order the higher the flexibility of the function.

How to identify a good fit?

A best-fit is reached when the residual **(eqn 2.5)** has been minimised. It is also extremely important that the fit makes both physical and chemical sense. To assess the quality of the fit that the refinement has reached, a set of criteria should be examined. The same criteria can also be used to assess how the fit is proceeding and when it can be stopped. *R*-factors are commonly used as part of this criteria along with the goodness-of-fit (Table 2.2). The *R*-factors give information about the observed and calculated intensities of the diffraction pattern.[40] Another important criteria that should not be overlooked is the visual assessment of the fit between the observed and calculated pattern together with the residual.[40,42] Visual inspection of the fit throughout the refinement can indicate when there are possible errors such as with the lattice parameters, the background shape, the scale factor and profile mismatches.[40] The visual fit and the chemical plausibility of the model can determine the quality of the fit that was produced through the refinement process.[42]

Table 2.2: Commonly used criteria to determine the quality of the fit.[40]

Criteria			Description
R-weighted pattern	$R_{wp} = \sqrt{\frac{\sum_i w_i (y_{o,i} - y_{c,i})^2}{\sum_i w_i (y_{o,i})^2}}$	**(2.7)**	This factor is great for gauging the refinement progress and is important due to the minimization term in the numerator. This factor can be misleading if the pattern background is high.
R-expected	$R_{exp} = \sqrt{\frac{N-P}{\sum_i w_i y_{o,i}^2}}$	**(2.8)**	N is the number of data points and P is the number of parameters in the refinement.
Goodness-of fit	$\chi^2 = \left(\frac{R_{wp}}{R_{exp}}\right)^2$	**(2.9)**	This factor should ideally be equal to one for a perfect fit. Generally, $\chi^2 > 1$ and becomes smaller as the fit between the observed and calculated intensities improve. If $\chi^2 < 1$ then one possible case that should be considered is that the counting errors are larger than the errors in the model. This could be caused by a high background or poor counting statistics. Large counting times could also influence χ^2 by increasing the R_{exp} and R_{wp} difference.[42]

The Durbin-Watson statistic	$d = \frac{\sum_{i=2}^{N}(\Delta y_i - \Delta y_{i-1})^2}{\sum_{i=1}^{N}\Delta y_i^2}$ **(2.10 a)** $\Delta y_i = y_{o,i} - y_{c,i}$ **(2.10 b)**	This is a correlation parameter that measures the correlations between y_i values and should ideally be 2. This value will be further away from 2 if there is mismatch present between the observed and calculated intensities.

While Bragg intensities are used for the other factors mentioned in Table 2.2, the R-Bragg factor (R_B in **eqn 2.11**) and the R-structure factor (R_F in **eqn 2.12**) are not based on the Bragg intensities. These factors are usually used for the refinements of single crystal diffraction.[40]

$$R_B = \frac{\sum|I_{o,K} - I_{c,K}|}{\sum I_{o,K}} \quad \textbf{(2.11)} \qquad R_F = \frac{\sum|I_{o,K}{}^{1/2} - I_{c,K}{}^{1/2}|}{\sum I_{o,K}{}^{1/2}} \quad \textbf{(2.12)}$$

2.3.2. Pair distribution function

The pair distribution function (PDF) has found great importance in characterising the local structure of materials and describes the bond length and interatomic distance distribution.[43] The PDF, *G(r)*, can be obtained from experimental data by obtaining the Fourier Transform of the scattering amplitude, *S(Q)*:[43]

$$G(r) = 4\pi r\,[\rho(r) - \rho_0] = \frac{2}{\pi}\int_0^{\infty} Q[S(Q) - 1]\,(Qr)\,dQ \quad \textbf{(2.13 a)}$$

where $\rho(r)$ and ρ_0 are the microscopic pair density and average number density respectively and Q is used to describe the magnitude of the scattering vector. Q can also be described in terms of the elastic scattering where the scattering angle is described using 2θ and the radiation wavelength is described by λ:

$$Q = \frac{4\pi sin\theta}{\lambda} \quad \textbf{(2.13 b)}$$

The real space resolution for the peaks on a PDF is highly influenced by Q (the scattering vector).[43] If the maximum Q (Q_{max}) is large then the real space resolution would show the splitting of peaks, but if the maximum Q is small then the peak splitting would be minimised resulting in peaks with maybe some shouldering (as illustrated in Fig. 2.2).[43] A large Q would also allow for structure analysis of the medium range in the structure and as such short and medium range order can be described using PDF.

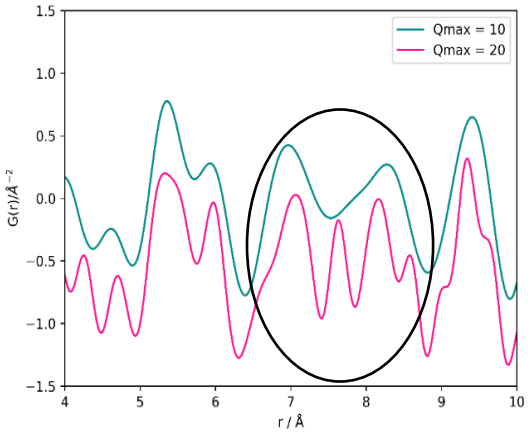

Figure 2.2: PDF of $LiFePO_4$. The blue plot corresponds to a Q_{max} of 10 whereas the pink plot corresponds to a Q_{max} of 20. The space resolution for the Q_{max} of 10 is lower.

2.3.2.1. Structural effects on the PDF

The experimental PDF displays some structural features such as the peak position, peak area, peak width and r_{max} (Fig. 2.3). These features can be determined independent of structure modeling.[44,45]

Peak position: The position of the peak on a PDF provides information on the bond-length and interatomic distances.[5,45]

Peak area: The peak area of the peak on a PDF provides information on the coordination, the occupancies and the scattering pair responsible for the peak.[5,44,45]

Peak width: The width of the peak provides information on the interatomic distance distribution of similar atomic pair contributing to the same peak i.e. the disorder present.[44,45]

r_{max}: The maximum distance at which peaks can be observed on the PDF can give an indication of the particle size.[44]

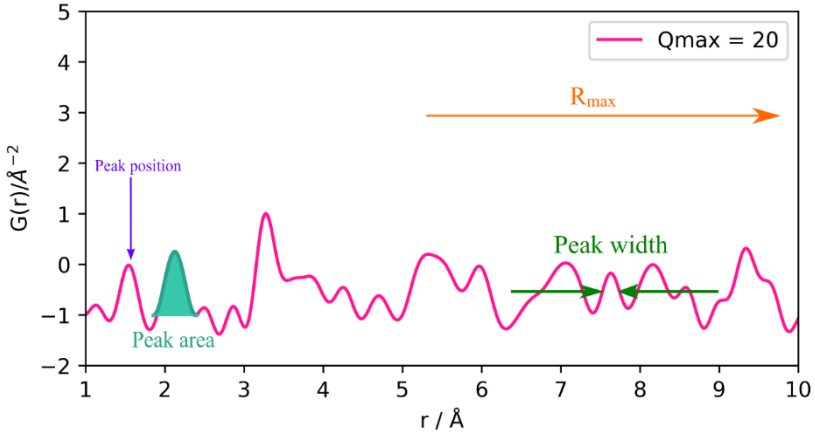

Figure 2.3: The PDF of $LiFePO_4$ showing the different structural effects that can be determined independently of structure modeling.[44]

2.3.3. X-ray absorption spectroscopy

X-ray absorption spectroscopy (XAS) is a technique that produces a signal based on element specific X-ray energy and can be described in two different regions: 1) X-ray absorption near edge structure (XANES) that provides information about the oxidation state and geometry and 2) the extended X-ray absorption fine structure (EXAFS) to determine the local structure around the energy specific element.[29,46]

2.3.3.1. Background on XAS

During an experiment a sample is exposed to a specific X-ray energy. If the binding energy of an element is matched by the X-ray energy then the electrons, on exposure, can either be excited into orbitals of a higher energy or into the continuum. If electrons are excited into the continuum then it is no longer associated with the atom (Fig. 2.4). The excited photoelectrons either leaves behind a hole or a core hole if the electrons were core electrons.[29] The transition of the electrons in higher energy orbitals to the core hole is called the relaxation process. The relaxation process is then accompanied by a release of energy in one of two ways:

1) The energy is released in the form of fluorescence radiation. The energy that is released from the transition is equal to the energy difference between the higher and lower energy orbitals and the transition energy is element specific.[29,46] Successive core holes are continuously filled for example the electron in the L-shell fills the hole in the K-shell then the electron in the M-shell fills the core hole in the L-shell.[29]

2) The energy can be released producing an Auger electron. The core hole is filled by a higher energy orbital electron and this electron loses the energy of the transition by emitting another electron (the Auger electron) that is either in the same or in a different shell.[29,46]

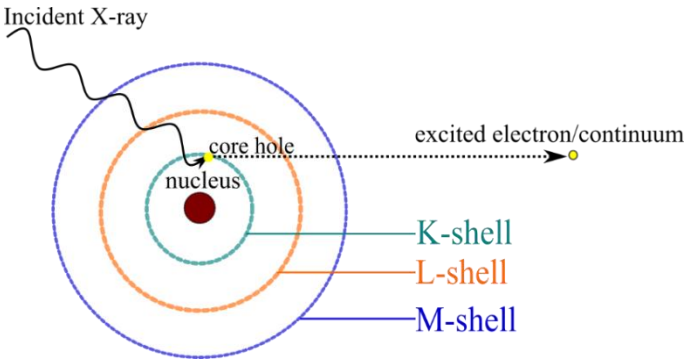

Figure 2.4: The photoelectron excitation process with the surrounding electron shells using the Bohr model.[29]

2.3.3.2. X-ray absorption coefficient

The absorption coefficient (μ) can be described using the following Beer-Lambert relationship:[29,46]

$$I_t = I_0^{-\mu x} \quad \textbf{(2.14)}$$

where I_t describes the transmitted X-ray intensity through the sample, I_0 is the X-ray intensity that the sample is exposed to and x is used to describe the thickness of the sample. I_t decreases exponentially with the thickness of x. If the sample is exposed to more X-rays then more X-rays will be transmitted through the sample.[29] The absorption coefficient can be described as the probability of the absorption of X-rays by the sample and XAS measures this probability (μ) over an energy range. If the energy of the incoming X-rays are the same as the energy required for electron excitation to an unoccupied orbital then the probability for absorption to take place increases dramatically.[29,46] The changes in the absorption coefficient are referred to as the different absorption edges of the spectrum by scanning over a range of energies.

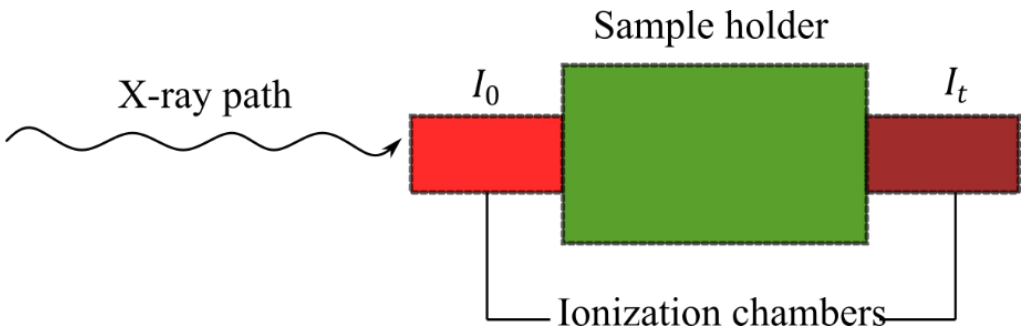

Figure 2.5: A schematic of the experimental setup for measurements in transmission mode.

2.3.3.3 Measurements in transmission mode

Transmission mode measurements allow for the X-ray intensity to be measured before the sample as well as after the X-ray beam was transmitted through the sample.[46] In the experimental setup (Fig. 2.5) ionization chambers are responsible for measuring I_0 and I_t. Transmission mode measurements require that the absorber atom (the element of interest) is present in high concentrations in the sample because if the concentration of the absorber atom is high then enough transmitted X-rays would be produced to allow for accurate measurements.[29]

2.3.3.4. Absorption edges

The absorption edges and binding energies are element specific where the atomic number and edge energy have a direct relationship – heavier atoms would have an increase in edge energy. The edge energy increases due to the increase in the binding energy for heavier atoms.[29] The electrons in the K-shell for example would have a larger energy than the electrons in the L-shell. An absorption spectrum can be divided into the following sections: XANES (pre-edge, edge, white line) and EXAFS (oscillations), as displayed in Figure 2.6. The pre-edge can be found before the sharp rise and the edge can be described as the sharp rise in the absorption spectrum that is due to the excitation of a core electron. The white line is a sharp feature that is on top of the edge and before the drop in the intensity of the oscillation region.[30]

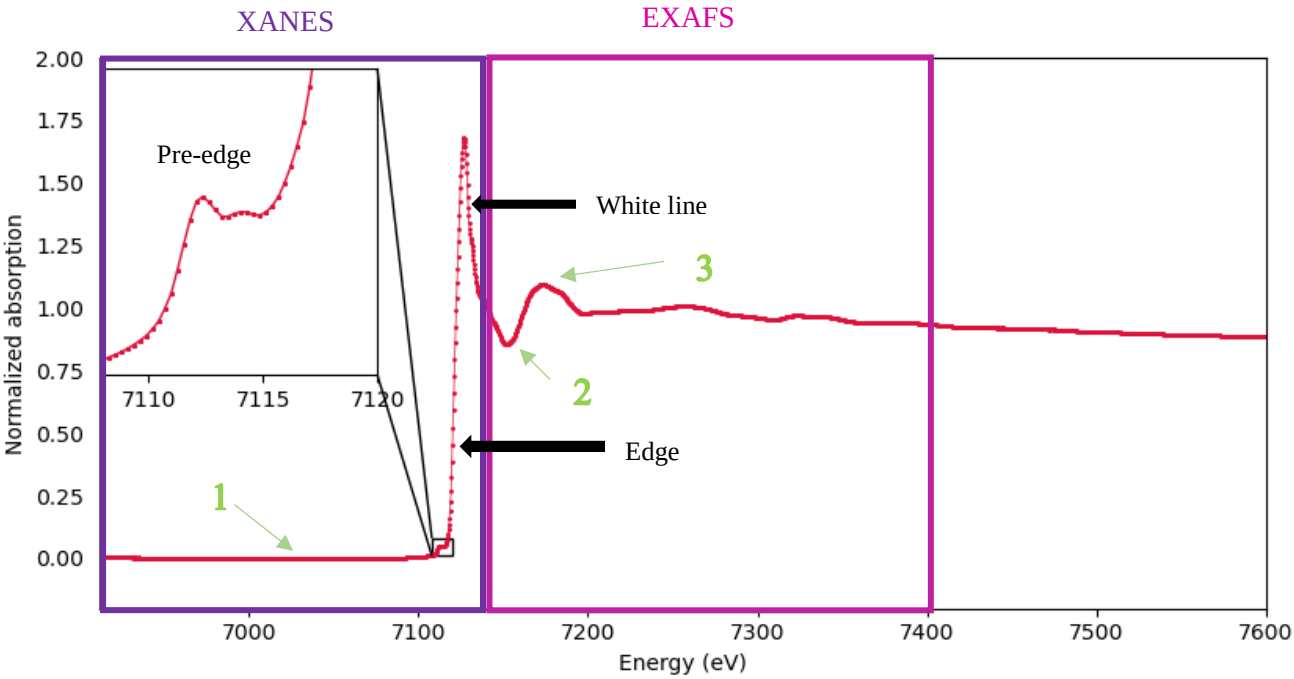

Figure 2.6: An absorption spectrum of $LiFePO_4$ showing the different XANES and the EXAFS regions. The numbered regions will be described in (ii) below.

(i) XANES spectra

The range used to identify the XANES region can be defined relative to the edge energy and ranges from -50 eV – 200 eV (Fig. 2.6). The absorption edge shape depends on the excitation of the photoelectron and the available density of states.[29] The features seen in the XANES spectrum is a result of the excited photoelectrons that can occupy the unoccupied orbitals and the changes in the density between the different states.[29] The nucleus (positive) is screened by the electrons (negative) in a neutral atom and when the oxidation state increased, the number of protons present are more than the number of electrons thus causing a lowering in the

remaining electron energy states. The lowering in the energy states results in the increase in the edge energy and more energy would be required to excite the core electrons. Changes in the oxidation state can also be accompanied by a change in the centrosymmetry of the absorber atom and this will also lead to changes in the features of the absorption edge.[29]

(ii) EXAFS spectra

The extended X-ray absorption fine structure can be used to determine the local structure and bonding environment around the absorber atom (Fig. 2.6).[29,46] This region extends ~1000 eV and higher above the absorption edge. The information that can be determined from this region is the identity of the surrounding atoms and the coordination numbers around the absorbing atoms, the interatomic distance between the absorber and neighbouring atoms and the degree of bonding disorder.[29,46] Using the absorber atom as the reference point, the photoelectrons that act like spherical waves move away from the absorber atoms (outgoing waves). The neighbouring atoms that surround the absorber atoms are in turn scattering these photoelectron waves (scattered waves). The probability of the absorber atom absorbing the X-ray is determined by the phase of the outgoing and scattered waves.

The X-ray scattering process can be described in three processes (Fig. 2.6 numbered in green):[29]

1. Below the absorption edge, no photoelectrons are produced, and no scattering can be observed.
2. For energies slightly above the edge, the wavelength of the photoelectron is longer and drop in the oscillatory part of the spectrum indicates that minimum absorption occurs and the outgoing and the scattered waves are out of phase.
3. As the energy increases to above the absorption edge, the kinetic energy (E_k) increases, and the wavelength of the photoelectron becomes shorter. The remaining energy after the electron is excited into the continuum is given to the photoelectron in the form of kinetic energy:[29]

$$E_k = E - E_0 \qquad \textbf{(2.15)}$$

where E can be described as the incident X-ray and E_0 as the electron binding energy.

The outgoing and the scattered waves become more in phase and can be identified as the maxima in the oscillatory region. The average distance between the absorber and neighbouring

atoms can be determined by the periodicity of the outgoing and scattered waves. For uncoordinated atoms the oscillations would not be present as the oscillations only occur with neighbouring atoms.

The EXAFS signal is produced from the different scattering paths of the photoelectron. The scattering paths can be followed from the absorber atom to one or more neighbouring atoms and then back to the absorber atom.[29] A group of atoms in a shell would contribute to the same component in the EXAFS signal and have the same radial distance. The number of atoms in the shell with the same component contribution and radial distance would be referred to as the coordination number in the shell.[29] The total spectrum is constructed by the sum of the scattering paths. The EXAFS equation can be used to describe the signal and each scattering path can be describe by:[29,46]

$$\chi_i(k) = \sum_i \frac{N_i S_0^2 f_{eff_i}(k)}{k R_i^2} sin[2kR_i + \varphi_i(k)] e^{-2\sigma_i^2 k^2} e^{\frac{2R_i}{\lambda(k)}} \quad \textbf{(2.16)}$$

where R_i, the half path length of the photoelectron for a single scattering event, can be further described as[29]

$$R_i = R_{0i} + \Delta R_i \quad \textbf{(2.16a)}$$

R_{0i} is the half path length that was used in the theoretical calculation and ΔR_i can be used to modify R_{0i}.

k^2 can also be used to describe the excess E_k of the photoelectron in wavenumbers using the following relationship[29]

$$k^2 = \frac{2m_e(E - E_0 + \Delta E_0)}{\hbar} \quad \textbf{(2.17)}$$

where m_e is the mass of an electron, $\hbar$ is Planck's constant, $E - E_0$ is measured in eV and is ~3.81k^2 and k is measured in Å^{-1}. The balance of the terms in **eqn 2.16** are described in Table 2.3.

Table 2.3: Description of parameters that are used in the EXAFS equation (**eqn 2.16**), that contribute to the signal and the method of determination.[29,46]

Term	Description	Method of determination
$f_{eff_i}(k)$	Describes the effective scattering amplitude and is the main reason for EXAFS being an element sensitive technique. For elements with similar electrons it can be difficult to distinguish	Calculated by FEFF

	between them based on the scattering amplitude as it depends strongly on the number of electrons. The more electrons present in the atoms the higher scattering amplitudes at higher wavenumbers.	
$N_i S_o^2$	N_i can either be described as the number of coordinating atoms for single scattering events or the number of identical paths for multiple scattering events. The difference in scattering path is indicated by the subscript. S_o^2 is the amplitude reduction factor. The slight relaxation of the electrons that remain after a core hole has been left by a photoelectron can be accounted for by S_o^2. Different elements have different S_o^2 values.	Modelling
$\frac{1}{R^2}$	The contribution to the EXAFS signal from a shell at a certain distance decreases with an increase in the distance from the absorber	Modelling
$sin[2kR_i + \varphi_i(k)]$	The oscillations of the signal and the phase can be described using this entire term. $2R_i$ describes the scattering path of the photoelectron as it reaches the neighbouring atoms and then travels back to the absorber atom. This term is then multiplied by the wavenumber, *k*, and is needed to determine the phase of the scattering event. A phase shift is caused by the interaction of the photoelectron with both the absorber and neighbouring atoms. This shift is described by the term $\varphi_i(k)$ and causes an approximate -0.5Å shift in the distance when calculating the Fourier Transform (FT). The wavelength of the photoelectron lengthens upon interaction with the atoms. The sine term is important for producing the FT and to show peaks that can be related to the different interatomic distances of the different shells surrounding the absorber atom. Due to the phase shift the peaks cannot directly be related to the distance unless phase corrected.	Modelling but $\varphi_i(k)$ is calculated by FEFF.
$e^{-2\sigma_i^2 k^2}$	σ^2 can be described as the mean-square displacement of the interatomic distance between the absorber and neighbouring atoms in the different shell or as the Debye-Waller factor. The	Modelling

	value determined for this term therefore produces the distance distribution between the absorber and coordinating atoms. σ^2 also accounts for the thermal and structural heterogeneity disorder.	
$e^{\frac{2R_i}{\lambda(k)}}$	This term depends on the mean free path of the photoelectron, $\lambda(k)$, and is the reason the EXAFS signal can be used to look at the different scattering contributions from atoms within a range of 10 Å.	$\lambda(k)$ has to be calculated by FEFF.
ΔR_i	This term describes the changes in interatomic distance between the starting model and the experimental data.	Modelling
ΔE_i	This term is used to align the energy scale between the measured and theoretical spectrum and relates to changes in the energy of the photoelectron.	Modelling

2.3.3.5 Data reduction for XANES and EXAFS analysis

To analyse the XANES region, data reduction up to the normalisation step is needed but to analyse the EXAFS spectra further processing should be included.[30]

(i) Truncation:

Truncation has to be performed if the data cannot be used above or below a certain point for example the presence of another edge in the dataset. Not removing these features could interfere with other data reduction steps and the analysis.[29,30]

(ii) Aligning the reference scans:

Reference data that was measured with the dataset can be used for aligning data and accounting for any drifts in the energy caused by changes with the monochromator.[29,30,47] Aligning the data to one another and to a common energy scale can also prevent energy resolution loss. It is common to use the derivative scan to align the scans and using the reference channels rather than the data to ensure that beam damage does not play a factor as is the case with some samples.[30] The individual shift that occurs after the samples are aligned to the reference spectrum is applied to the data scans.[29]

Merging the same scans in a dataset:

If multiple scans were taken of the same sample under the same conditions then these scans can be averaged by a process of merging.[30] Merging also has the benefit of reducing the noise and improving the signal of the merged scan. Merging provides an option of choosing the weighting of importance for each added scan as one scan could be noisier than the other scans.[30] A method that can be used is to give all the scans the same weighting and if a particular scan is too noisy and decreases the quality of the merged spectrum then it can be removed from the dataset.[30]

(iii) Choosing the E_0 value:

The energy needed to excite a core electron is referred to as the edge energy and E_0 can be considered as the energy reference spectrum.[29] The determination of E_0 involves choosing a certain point that can be used as the zero energy and that can be used to align the theoretical and experimental spectra.[30] E_0 can be selected in many ways but the method should be consistent and E_0 can be chosen using the derivative spectrum (that for $LiFePO_4$ is shown in Fig. 2.7) in one of the following ways:[30]

- Using the first maximum peak.
- Using the first peak.
- Using a well-defined peak.
- Using the derivative of the reference spectrum and choosing the peak.

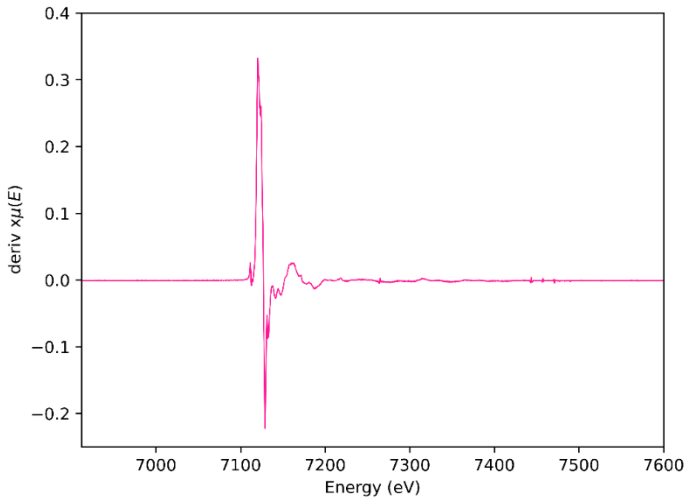

Figure 2.7: The first derivative spectrum of $LiFePO_4$. This spectrum can be used in most cases when choosing E_0.

(iv) Normalization:

Normalization is used to remove any interference in the spectrum that is not due to the chemical environment such as sample thickness or from the instrumentational and experimental setups. If normalized correctly then different spectra of different samples and environments regardless the measurement mode (eg. transmission or fluorescence) can be compared.[29,47] The pre-edge line can be used to define the region before the edge and the post-edge line can be utilised to describe the oscillatory region after the edge (Fig. 2.8a).[47] The regression of the pre-edge (using linear function) and the post-edge (using polynomial function) regions using all the data is part of the normalization process and the used function has to pass through the middle of the data in both regions of the spectrum.[47] By extrapolating the post-edge line to the chosen E_0 chosen as indicated above the edge step, $\Delta\mu_0$ can be determined (Fig. 2.8b).[46] The pre-edge line is first subtracted from the spectrum and the data along the pre-edge line is moved to y = 0. Normalization changes the spectrum such that it is moved between 0 (pre-edge region) and 1 (oscillations) by dividing the entire spectrum by $\Delta\mu_0$ (Fig 2.8c). Scaling of $\chi(k)$ for EXAFS analysis is done by also using $\Delta\mu_0$. After normalization, the spectrum should be flattened if it does not oscillate around 1. The flattening function is applied to the post-edge region by another subtraction of the pre-edge and the post-edge slopes.[29] Flattening the data results in no data change but the visualization of the normalized data is better.[47]

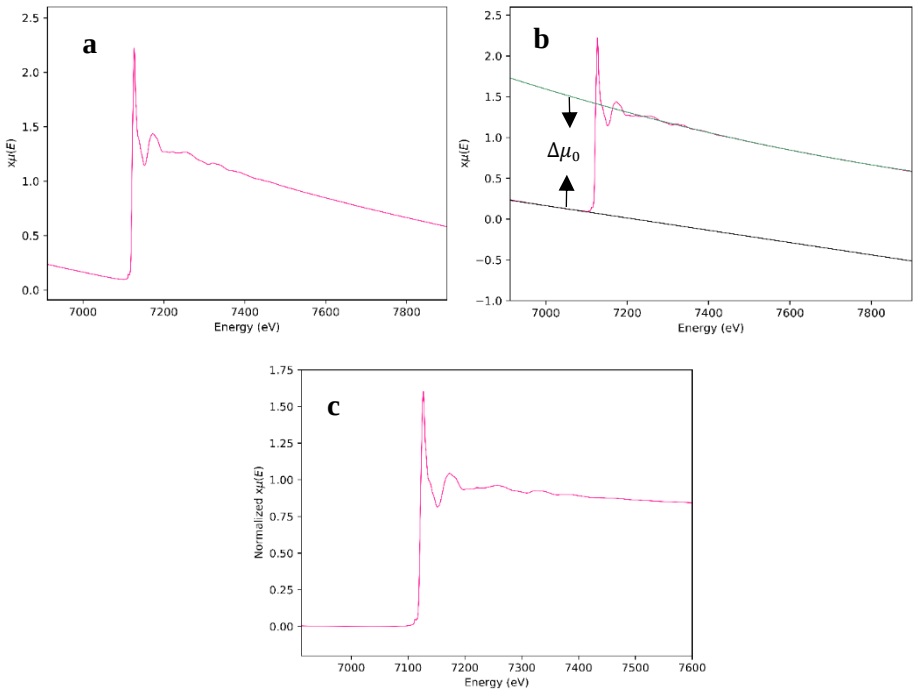

Figure 2.8: The (a) absorption spectrum before normalization, (b) the pre-edge and post-edge regression lines used for normalization and (c) the normalized spectrum of $LiFePO_4$.

(v) Converting $\chi(E)$ to$\chi(k)$:

Due to the creation of a photoelectron and its wave-like behaviour, EXAFS analysis uses wavenumber rather than the energy of the X-ray. To convert from energy $\chi(E)$ to wavenumber $\chi(k)$ the following relationship can be used:[29,30]

$$k = \sqrt{\frac{2m_e(E-E_0)}{\hbar}}. \quad \textbf{(2.18)}$$

The absorption coefficient would then also be described in terms of the wavenumber[46] $\chi(k)$ and can be plotted in *k*-space (Fig 2.9a).[47]

(vi) The basics of Fourier Transform

The information that can be found in an EXAFS spectrum can be looked at as the sum of different sine waves with each wave possessing its own amplitude and phase. The amplitude and the phase depends on two aspects: 1) the distance between the absorber and the coordinating atoms and 2) the type of atoms.[29] To separate each component into distances (*r*), the sine waves can be Fourier Transformed and separated into its Fourier components of amplitude and phase. The benefit of a Fourier Transform is that the coordinating atoms around the absorber atom can be separated and bonding information can be extracted. The Fourier components contain both the real and imaginary parts. The magnitude of the Fourier Transform (FT magnitude)[29] leads to the plot of $\chi(R)$ in *r*-space (Fig. 2.9b – dashed). A peak on the FT magnitude shows the different coordinating atoms that are at similar radial distances coordinating to the absorber atom and provides information about the atoms. Although the FT magnitude produces the radial distances of the coordinating atoms it is not a radial distribution function (RDF) as would be obtained when analysing PDF data.[29,30] The difference between the two concepts are due to the following:[29]

- The bond distance in EXAFS does not correspond directly with the first peak. The shifting of this peak depends on the type of atoms involved (Fe, O etc.)
- Multiple scattering paths affect the Fourier Transform but do not play a role in the RDF.
- The peak amplitude in EXAFS depends on different variables but for a RDF the amplitude relies on the coordination number.
- The amplitude becomes smaller with increasing radial distance from the absorber due to $\lambda(k)$ whereas once again the RDF amplitude is dependent on the coordination number.

Even though the distances are extracted from the Fourier Transform, the FT magnitude is still complex and hence the real (Fig. 2.9b – solid) or imaginary parts should also be modelled and shown during the EXAFS fit together with the $\chi(k)$ function (Fig. 2.9a).[29,46]

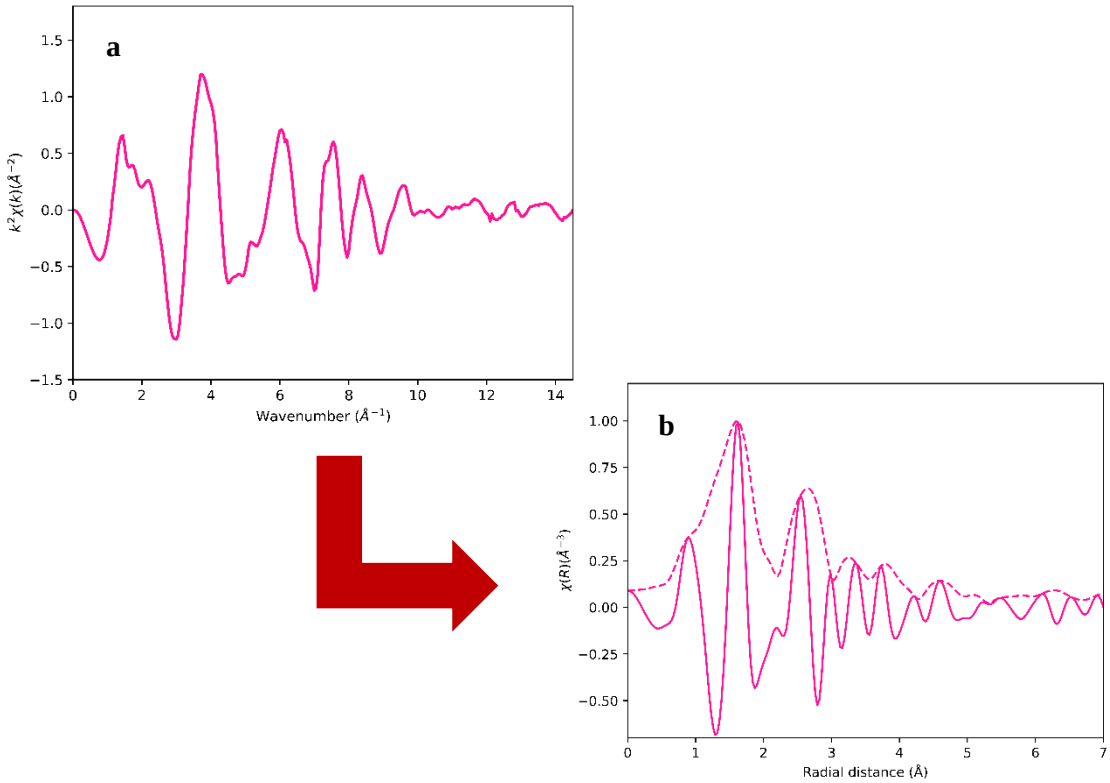

Figure 2.9: A plot of $LiFePO_4$ as (a) $\chi(k)$ function in k-space, (b) the magnitude of the Fourier transform (dashed) and the real parts of the Fourier Transform (solid).

(vii) Background function of a dataset

Further background removal has to be performed on the post-edge region in order to process any EXAFS data. A background function consists of splines. Splines are used as a way to minimise contributions made by the background and is used as a smoothing function. If the spline follows the data too closely some information in the oscillations will be removed together with the background function.[46] The spline function has to be able to remove Fourier Transform components in the lower *R* region such that below the shortest *R* distance there should be no contributing signal and does not affect the components in the higher *R*-region.[46] Currently an approach known as AUTOBK[48] (in Athena) is used to construct these functions (Fig. 2.10a-c). AUTOBK constructs background functions by using information provided in the lower *R*-region and uses cubic (third order) splines.[29] AUTOBK also uses the R_{bkg} parameter (the maximum frequency component) that is used to determine the value below which contributing components would be considered as part of the background and all

frequencies up to the R_{bkg} value would be removed (Fig. 2.10d).[29] R_{bkg} is commonly said to be about 1 – 1.5 Å or half the distance of the shortest atomic bond distance.[29,46]

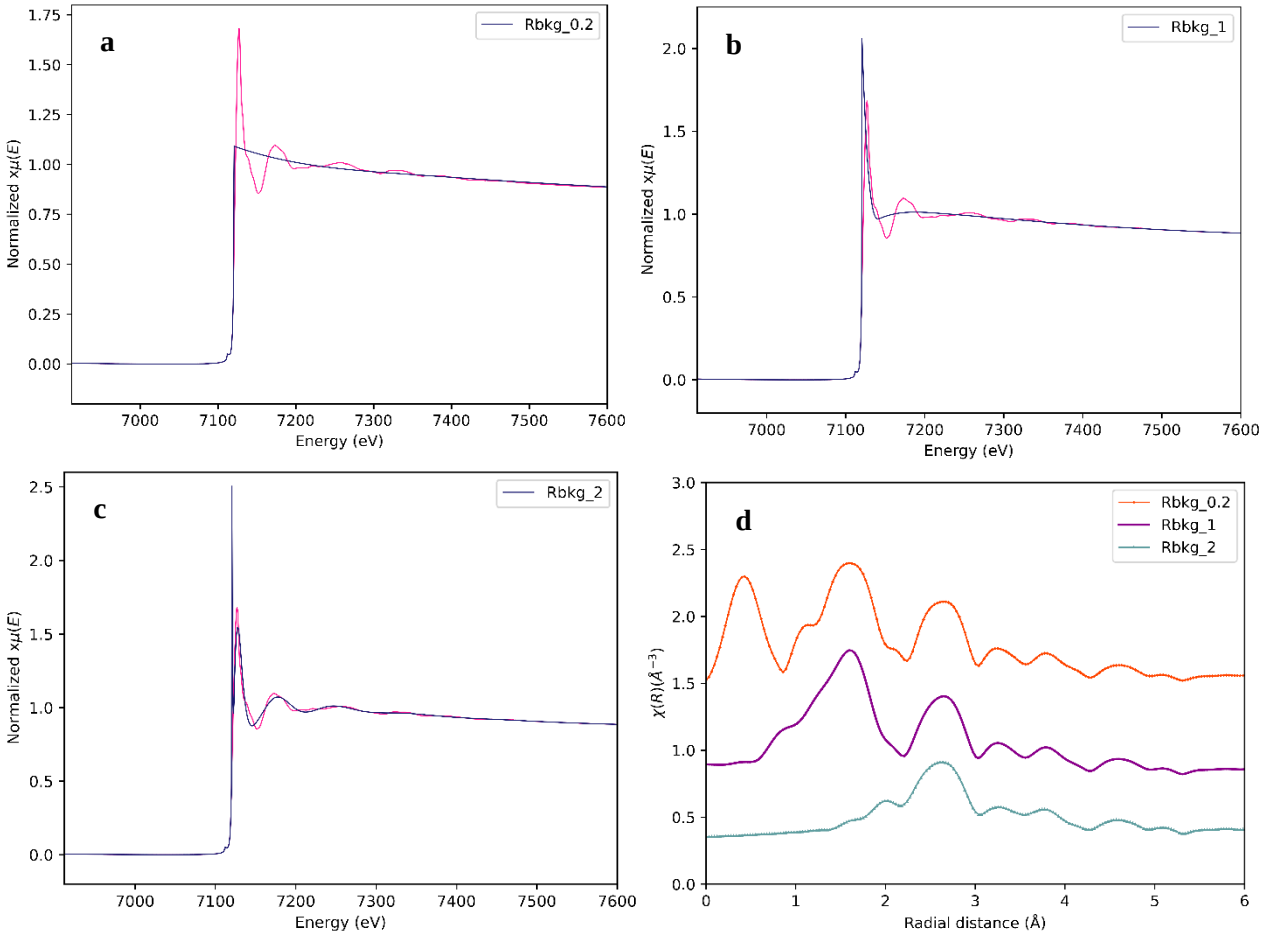

Figure 2.10: The effect of different R_{bkg} values (a) 0.2, (b) 1 and (c) 2 on the background function and (d) the effect on different R_{bkg} values in the FT magnitude demonstrating the removal of Fourier Transform effects.

(viii) <u>K-weights used for Fourier Transforms:</u>

The EXAFS signal that had been Fourier Transformed is written as FT[$\chi(k)$k^{kw}] with units Å^{-1-kw} and indicates $\chi(k)$ was multiplied by k using a k-weight (kw) of 1, 2 or 3 (k, k^2 or k^3) – before the Fourier Transform. The $\chi(k)$ function should usually undergo this process to compensate for the diminishing amplitude of the oscillations with an increase in energy.[29,46] The k-weight determines where the spectral weight would be and if the lower or upper range would be emphasised (Fig. 2.11)[29,47] for example k^1 the data would be emphasised at low k-values.

Increasing the k^{kw} would also increase the range where the information would be emphasised (Fig 2.11).[29] The correct *k*-weight to use should produce similar oscillations over the entire data range.[47]

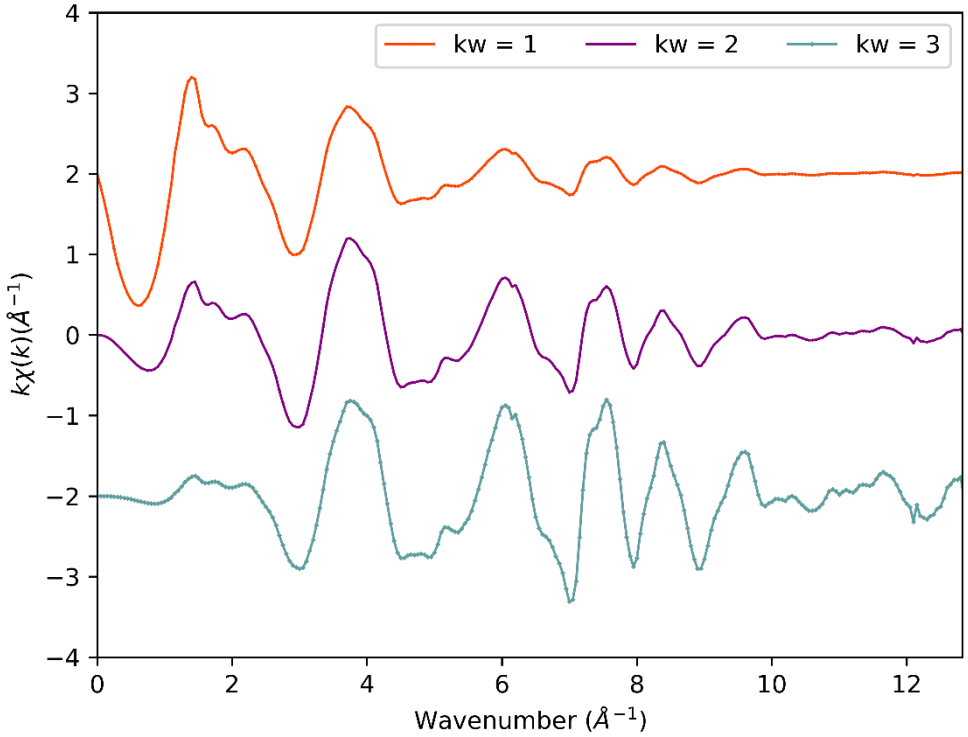

Figure 2.11: The effects of different k-weight on the $\chi(k)$ function of $LiFePO_4$. The spectral weight changes with the k-weight.

Different *k*-weights can also be used in a background function. The correct k-weight would produce a background function that cuts the oscillatory part of the spectrum down the middle, i.e. there is the same amount of oscillation on the top as there is below the line.[29] It is important to ensure that there is a balance between the *k*-weight chosen for the data and the *k*-weight chosen for the background function. Usually it is better to use a *k*-weight of 1 or 2 for the background function as it produces a balanced spectrum irrespective of the *k*-weight used in the data.[29]

(ix) Data ranges to use from the Fourier Transform:

When determining the data range that should be used for the analysis, any features not structure-related should be excluded. If noise plays a role in a specific area it could be indicated with a slight ripple in the spectrum. These ripples can therefore be used to indicate which ranges would be usable and to determine the upper range.[29] When moving beyond the upper limit, significant noise, as indicated by the high frequency ripples, will be present. The maximum

k-range is desirable as this produces the best spatial resolution for the best separation between neighbouring peaks.[29,47] Increasing the *k*-range resolves neighbouring peaks better at lower radial distances and might not have any affect at higher radial distances.[29]

(x) Determining the windows used for Fourier Transform:

Data ranges in terms of *k* extend from a low to a higher finite range whereas the range for the Fourier Transform is infinite thus indicating that zeros have to be added to the Fourier Transform range that is outside the *k*-range.[29] A step-function is used at the beginning and the end of this range as sharp changes occur where the values go from zero to non-zero and then back again to zero. To diminish and smooth this transition, the change in the data should be multiplied by a window that moderately allows the data from zero to reach the non-zero value and the non-zero value to go back to zero at the end of the range.[29,30] A Hanning-window is a common window function that can be used for this purpose. This window specifies the minimum and maximum values for the k-range as well as the width for this gradual transition. Values for this transition is usually between 1 – 2 Å.[29]

(xi) Information contained in a Fourier Transformed spectrum:

The Nyquist theorem can be used to determine the amount of information that can be found in both the original spectrum and the spectrum after it has been Fourier Transformed:[29,46]

$$N_{INP} = \frac{2}{\pi}\Delta k \Delta R + 1 \qquad \textbf{(2.19)}$$

where N_{INP} can be described as the number of independent data points, Δk is the Fourier Transform range and ΔR is the data analysis range. N_{INP} should be more than the number of variables needed for the fit with ideally twice as many N_{INP} than variables.

2.3.3.6 Linear combination fitting

The sum of the absorption from each of the species of the absorber atom present in the sample contributes to the final spectrum. Linear combination fitting (LCF), that is the sum of the linear combinations present in the sample, can be used to quantify this. [30] To determine the weighted sum for all the species, a library of standards representing all possible species present should be used.[29,30] Mathematically this process can be expressed for a certain energy range as:[29]

$$Model = \sum_i f_i\,(STD)_i \qquad \textbf{(2.20)}$$

The model would be the best representation of the least-square fit using the standards, f_i is the scaling factor applied to each standard to get the best representation and STD is the

standard. Commonly the scaling factor applied to the standard would be constrained to be positive and to sum to one.

(i) How to quantify the fit mismatch:

The fit mismatch can be quantified by either using the EXAFS *R*-factor or the χ^2.[30] The Internal XAFS Society Standards and Criteria Committee defines the EXAFS *R*-factor as:[30]

$$R_{IXS}^2 = 100 \times \frac{\sum_i^N (data_i - fit_i)^2}{\sum_i^N (data_i)^2} \ \%. \qquad \textbf{(2.21)}$$

The mismatch using χ^2 can be defined as:[30]

$$\chi^2 = \sum_{i=1}^{N_{inp}} \frac{(data_i - fit_i)^2}{\varepsilon_i^2} \qquad \textbf{(2.22)}$$

where ε is the uncertainty associated with a certain point.

2.3.3.7 Local structure determination

(i) Common fitting parameters, typical values and correlations.

The refineable parameters that are allowed to vary when performing an EXAFS fit are $\Delta R, N, \sigma^2, S_o^2$ and E_0. These parameters should be within an acceptable range for the final fit and the correlation between these refineable parameters should be minimised. This can be used as a guideline regarding the starting model and the progress of the fit. This information is summarised in Table 2.4.

Table 2.4: The fitting parameters, typical values and the correlations associated with the parameters.[30]

Parameter	Typical value	Effects	Correlations:
N	Positive	Coordination numbers and degeneracy cannot be negative.	S_o^2 and σ^2
S_o^2	0.70 – 1.05[49]	If S_0^2 for the model is either higher or lower than the typical value it could indicate distorted data or a questionable fit.	N and σ^2

σ^2	Never negative / 0.002 – 0.03 Å^2	Values outside this range could indicate that a different model should be used or sometimes that the added path does not contribute to the fit	N and S_o^2 The correlation can be reduced by increasing the *k*-range.
ΔR	0.1 Å	If the deviation between the experimental and starting model is larger than this distance then a different starting model is needed.	E_0 but in more complicated models then N, σ^2 and ΔR for other paths.
E_0	On the rising absorption edge but not on the pre-edge region.	Wrong reference energy	N and σ^2

(i) EXAFS models: Comparing two fits

The fitting process involves a least-square fit between the theoretical and experimental data and the fit provides important goodness-of-fit information that can be used to assess the fit. This information includes the *R*-factor, number of independent points (N_{inp}) and variables (N_{var}), chi-square (χ^2) and reduced chi-square (χ_v^2).[29] Different models can be compared to each other using the above mentioned goodness-of-fit information. The *R*-factor describes the mean-square misfit that exists between the fit and the data for the Fourier Transform components and can be described as:[29]

$$R_{factor} = \frac{\sum_i (data_i - fit_i)^2}{\sum_i (data_i)^2} \ \% . \qquad \textbf{(2.23)}$$

A good[30] to reasonable[29,30] fit has a R-factor of less than 0.02 (2%) and 0.05 (5%), respectively. The χ^2 can be described using:[29]

$$\chi^2 = \frac{N_{inp}}{N_{pts}} \sum_i \left(\frac{data_i - fit_i}{\varepsilon_i} \right)^2 \quad \textbf{(2.24)}$$

where N_{inp} is used to described the number of independent points, N_{pts} is used to describe the number of data points and ε_i is the uncertainties.

χ_v^2 can be used when models of the same dataset, same number of variables and the same *k*-range are used to compare consecutive fits and can be described as:[30]

$$\chi_v^2 = \frac{N_{inp}}{\nu N} \sum_{i=1}^{N} \frac{(data_i - fit_1)^2}{\varepsilon_1^2}. \quad \textbf{(2.25 a)}$$

This equation takes into account the degrees of freedom (ν):[29]

$$\nu = N_{inp} - N_{variables}. \quad \textbf{(2.25 b)}$$

Improvement to the fit should be significant for example $\chi_v^2(50) < \chi_v^2(100)$ but when the initial $\chi_v^2(52)$ and the final $\chi_v^2(50)$ then the models are too similar implies and no real improvement can be observed.[29] If a certain added path did not decrease χ_v^2 then the fit showed no improvement. [46]

2.3.4. Mössbauer Spectroscopy

Mössbauer spectroscopy has found many useful applications in solid state research such as material sciences, chemistry and physics.[50,51] Its widespread application have been due to its ability to provide information regarding a material's electronic structure, bonding properties, magnetic behaviour and molecular symmetry.[50] The success of this technique relies on the Mössbauer Effect that was discovered by Rudolph L. Mössbauer in 1957 and is based on the principle of recoilless nuclear resonance absorption of $\gamma-$ rays. This work earned him the Nobel Prize in Physics in 1961.[52]

2.3.4.1 Nuclear $\gamma - resonance$ emission and absorption

The emission of $\gamma-$ rays are observed when a parent isotope decays and produces a daughter nucleus with Z protons and N neutrons in the excited state (E_e). Upon the transition from the excited to the ground state (E_g), a $\gamma-$ ray with no recoil will have an energy of $E_0 = E_e -$

E_g.[53,54] The emitted $\gamma -$ ray can then be absorbed by another nucleus with the same Z and N and the absorber will then be in the excited state (Fig 2.12). This process is referred to as nuclear resonance absorption of $\gamma -$ rays or as the Mössbauer effect. To observe the Mössbauer effect certain conditions have to be met which will be discussed later.[53,54] Another process known as nuclear resonance fluorescence follows when the excited absorber atom transitions back to the ground state and a $\gamma -$ ray is again emitted that can occur via different routes (Fig. 2.12).[53]

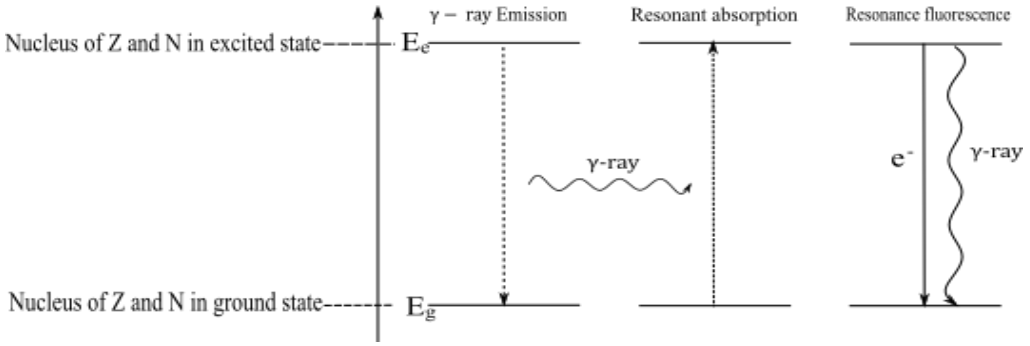

Figure 2.12: A schematic showing the nuclear resonant absorption and nuclear resonance fluorescence observed in a recoil-free environment.[53]

2.3.4.2 Spectral line shape and natural line width

The Heisenberg uncertainty principle can be used to evaluate the energy (E_0) of the transition. The ground state is stable and therefore has an infinite lifetime whereas the excited state has a finite lifetime. This leads to some uncertainty as to the exact energy for E_0 and can be denoted as ΔE using the uncertainty principle:[53]

$$\Delta E \Delta t \geq \hbar \quad \textbf{(2.26 a)}$$

where

$$\hbar = \frac{h}{2\pi} \quad \textbf{(2.26 b)}$$

where h is Planck's constant.

The time available to measure the energy (Δt) is related to the mean lifetime using the following relationship:[53,54]

$$\Delta t \approx \tau. \quad \textbf{(2.26 c)}$$

The spectral / emission line that is centered around E_0 forms due to the radiation as a function of the energy and can be expressed as an intensity distribution (Fig 2.13). A Lorentzian curve can be used to represent the intensity distribution described by the Breit-Wigner equation:[53,55,56]

$$I(E) = \frac{\Gamma/2\pi}{(E-E_0)^2 + \left(\Gamma/2\right)^2} \quad \textbf{(2.27)}$$

The same intensity distribution can be observed for the absorption spectral line. The natural width of the spectral lines can be determined by the mean lifetime of the excited state using the relationship shown by Weisskopf and Wigner:[53]

$$\Gamma\tau = \hbar \quad \textbf{(2.28)}$$

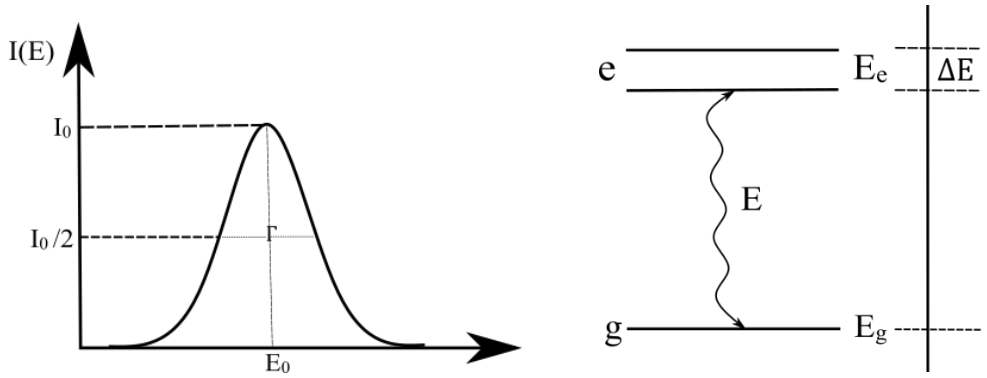

Figure 2.13: The intensity distribution showing the emission spectral line centered around E_0. The mean lifetime of the excited state can be used to determine the natural line width.[53]

The mean lifetime (τ) and the width of the transition line can be linked to the amount of resonance overlap that will occur. The lifetimes suitable for resonance overlap are $\sim 10^{-6} - 10^{-11}s$. Shorter lifetimes produce transition lines that are too broad with too much resonance overlap and a loss of resolution. The transition lines are smeared out and indistinguishable from the spectrum baseline.[33,53] Longer lifetimes produce transition lines that are too narrow and no resonance overlap will occur. If the spectral line for both the emission and absorption process are at the same energy (E_0) then maximum resonance absorption can occur.[33,53]

The shape of the absorption line, also known as the resonance cross section, can be given by the Breit-Wigner formula:[55]

$$\sigma(E) = \frac{\sigma_0 \Gamma^2}{[\Gamma^2 + 4(E-E_0)^2]} \quad \textbf{(2.29 a)}$$

where

$$\sigma_0 = \frac{\lambda^2}{2\pi} \cdot \frac{2I_e+1}{2I_g+1} \cdot \frac{1}{\alpha+1} \quad \textbf{(2.29b)}$$

is the maximum absorption cross section, $I_e \; and \; I_g$ are the nuclear spin quantum numbers for the excited and ground state, respectively, λ is the wavelength of the $\gamma -$ ray and α the internal conversion coefficient.

2.3.4.3 The Mössbauer Effect

The Mössbauer Effect depends significantly on the presence of the emission and absorption of $\gamma -$ rays occurring in a recoilless environment. A very important factor that determines if the recoilless absorption and emission will occur is the type of sample as this determines if the Mössbauer Effect will be observed. If a free nucleus or atom emits a $\gamma -$ ray, the nucleus will move in the opposite direction than that of the emitted $\gamma -$ ray due to the recoil energy (Fig 2.14).[53,54]

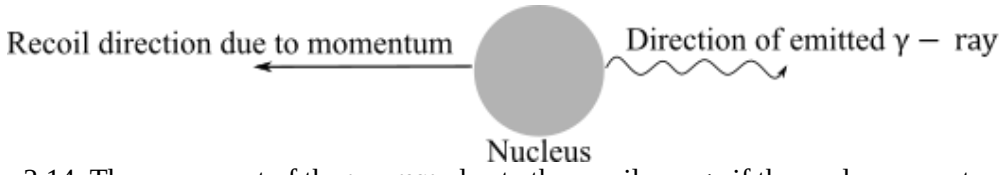

Figure 2.14: The movement of the $\gamma - ray$ due to the recoil energy if the nucleus was at rest before the emission.

The recoil energy after the emission of the $\gamma -$ ray can be determined using:[53]

$$E_R \; = \frac{1}{2} M v^2. \qquad \textbf{(2.30)}$$

The change in direction after emission is to conserve the momentum of the nucleus and would therefore be:[55]

$$p_n \; = -p_\gamma = -\frac{E_\gamma}{c} \qquad \textbf{(2.31)}$$

where p_n represent the momentum of the nucleus and p_γ the $\gamma -$ ray, respectively and c is the speed of light.

The energy of the emitted $\gamma -$ ray therefore has to take into account the recoil energy, E_R and would not be $E_\gamma = E_0$. The energy would be determined:[53]

$$E_\gamma \; = \; E_0 \; - \; E_R. \qquad \textbf{(2.32 a)}$$

Due to the large mass of the free atom nucleus, *M*, the recoil energy can be describe using the nonrelativistic approximation:[53]

$$E_R = \frac{p_n^2}{2M} \qquad \textbf{(2.32 b)}$$

And after substituting **(eqn 2.31)** E_R can be described as:

$$E_R = \frac{E_\gamma^2}{2Mc^2} \qquad \textbf{(2.32 c)}$$

Due to the recoil effect, there will be a shift in energy by E_R for both the emission and the absorption lines relative to E_0 (Fig. 2.15). The emission $\gamma-$ray would have an energy of $E_\gamma = E_0 - E_R$ and the recoil will cause a shift to lower energies (Fig. 2.15). The absorption process will also be affected by the recoil. For the absorption of the $\gamma-$ray to occur the energy would have to be $E_\gamma = E_0 + E_R$ causing a shift to higher energies for the absorption line (Fig. 2.15).[53] These two lines are now separated by $2E_R$ which is larger than the natural linewidth of most Mössbauer nuclides and due to the recoil the overlap between the transition lines would not occur and no resonant absorption would take place, hence the Mössbauer Effect would not be observed.[53]

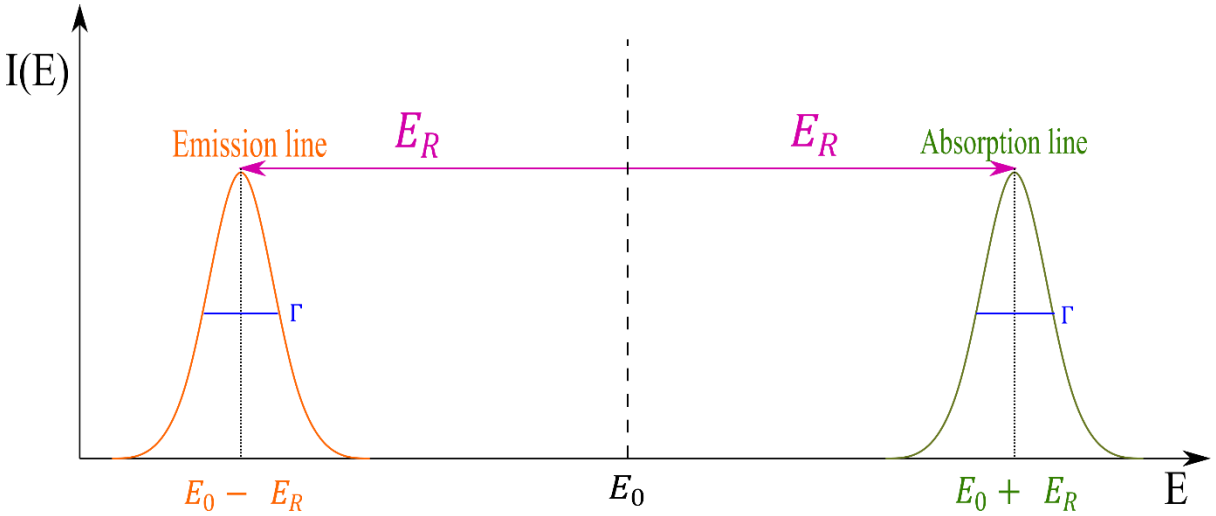

Figure 2.15: A schematic illustrating the effect of the recoil on both the emission and absorption lines. These lines are separated by an energy of $2E_R$ and no overlap is observed between these lines.[53]

Atoms that are constantly moving at a certain velocity (υ), such as atoms in a gas, emitting a $\gamma-$ray of energy E_γ in the same direction as the movement of the atoms would receive additional Doppler energy, E_D.[53]

The $\gamma-$ray energy that is emitted in this case is:[55]

$$E_\gamma = E_0 - E_R + E_D \quad \textbf{(2.33 a)}$$

where E_D is the Doppler energy and can be related to E_γ using:

$$E_D = \frac{v_n}{c} E_\gamma \quad \textbf{(2.33 b)}$$

where v_n refers to the velocity of the moving atom or nucleus

Gases do not all move with the same velocity and the $\gamma -$ ray of energy is therefore linked to the Doppler energy **(eqn 2.33 b)**. The $\gamma -$ ray energies are scattered statistically and can be attributed to the possibility that E_D can either be positive or negative and this causes Doppler broadening of the transition line. Doppler broadening can therefore be determined as:[54,55]

$$\overline{E_D} = E_\gamma (\overline{2E_K/Mc^2})^{1/2} \quad \textbf{(2.34)}$$

where E_K is the mean kinetic energy of the moving nucleus in the gas and E_D is taken over all angles (ϑ) that is between $\overrightarrow{p_\gamma}$ and $\overrightarrow{v_n}$.

The width of the Doppler broadening can also be determined in terms of E_R:[53]

$$\Gamma_D = 2\sqrt{E_R \cdot kT}. \quad \textbf{(2.35)}$$

Γ_D is either in the same order of magnitude or larger than that of E_R. The emission line (with the Doppler broadening) and the absorption line now only overlap in a small energy region indicating that there is a very low probability that resonance absorption would occur and that the Mössbauer Effect would be observed. If atoms are bound in the solid then there is a very high probability of nuclear resonance absorption occurring. In a solid, the atoms are bound in a lattice of certain mass, M. This mass is considered much larger than the mass of the free atom and the recoil energy is then considered negligible.[53,55]

2.3.4.4 Recoil-free fraction

Mössbauer nuclides that are bound in a solid lattice would not be allowed to recoil freely as seen in previous sections described above and the atom can only vibrate within the lattice. In a lattice, the recoil energy is converted into vibrational energy and is transferred to the lattice vibrational system. The energy disperses by heating the surroundings in the lattice while the atoms remain it their positions with no mean displacement of the nucleus.[53,54] Under these conditions, the recoil energy would be taken up by the whole lattice and there would also be no Doppler broadening.[53] There is a probability, *f*, that the lattice undergoes a zero-phonon

transition and that no lattice excitation occurs during the emission or absorption of the $\gamma-$ ray. The recoil-free fraction is the fraction of nuclear transitions for the emission and absorption of $\gamma-$ rays that can occur without any recoil.

The recoil-free fraction, f can be described by[55,57]

$$f = exp\left(\frac{E_R}{\hbar\omega_E}\right) = exp(-k^2 < x^2 >) \quad \textbf{(2.36)}$$

where k is the propagation vector and $< x^2 >$ is the mean-square displacement in the x-direction and ω_E describes the Einstein frequency.

The recoil-free fraction is also dependent on temperature and can also be determined using the Debye solid model where f is also generally referred to as the Debye-Waller factor:[54,55]

$$f = \exp\left[\frac{-6E_R}{k_B\Theta_D}\left\{\frac{1}{4} + \left(\frac{T}{\Theta_D}\right)^2 \int_0^{\Theta_D/T} \frac{x}{e^x - 1} dx\right\}\right] \quad \textbf{(2.37)}$$

where k_B is the Boltzmann factor and $\Theta_D = {\hbar\omega_D}/{k_B}$, the Debye temperature, and is a measure of the strength between bonds and with the following approximations the equation can be further reduced to:[54,55]

For $T \ll \Theta_D$ then $f = \exp\left[-\frac{E_R}{k_B\Theta_D}\left(\frac{3}{2} + \frac{\pi^2T^2}{\Theta_D^2}\right)\right]$ **(2.38 a)**

and for $T > \Theta_D$ $then$ $f = \exp\left(-\frac{6E_RT}{k_B\Theta_D^2}\right)$ **(2.38 b)**

The recoil-free fraction increases:[53,55]

1. by the decreasing the recoil/transition energy
2. by decreasing the temperature
3. by increasing Θ_D.

2.3.4.5 Mössbauer transmission spectrum and the Doppler shift

The overlap between the absorption and emission lines has to occur in order to produce a useable spectrum and therefore the Doppler shift has to be utilised by moving the source that causes changes in the energy. The Doppler shift relates the energy to the velocity and produces a transmission spectrum of the transmitted intensity as a function of velocity. The transmission spectrum is due to the detection of the 14.4 keV $\gamma-$ rays (nuclear decay scheme can be found in Appendix A3.1) that are absorbed by the absorber.[33] The emission spectrum is that of source

and is varied over a range of energies relative to that of the absorption spectrum for the absorber (Fig 2.16). To produce the transmission spectrum, the velocity of the source is varied as to have no overlap, some overlap or maximum overlap with the absorber. If there is no overlap then no resonant absorption occurs and if there is only a small amount of overlap then there is very little resonant absorption and the counting rates or transmission intensity would be large. The increase in overlap results in a decrease in the counting rate or the transmission intensity. Complete overlap between the emission spectrum and the absorption spectrum allows for maximum resonant absorption and the transmission intensity would be at a minimum (Fig 2.16). A greater overlap between the spectra results in the reduction of the transmission due to the resonant absorption.[33,53]

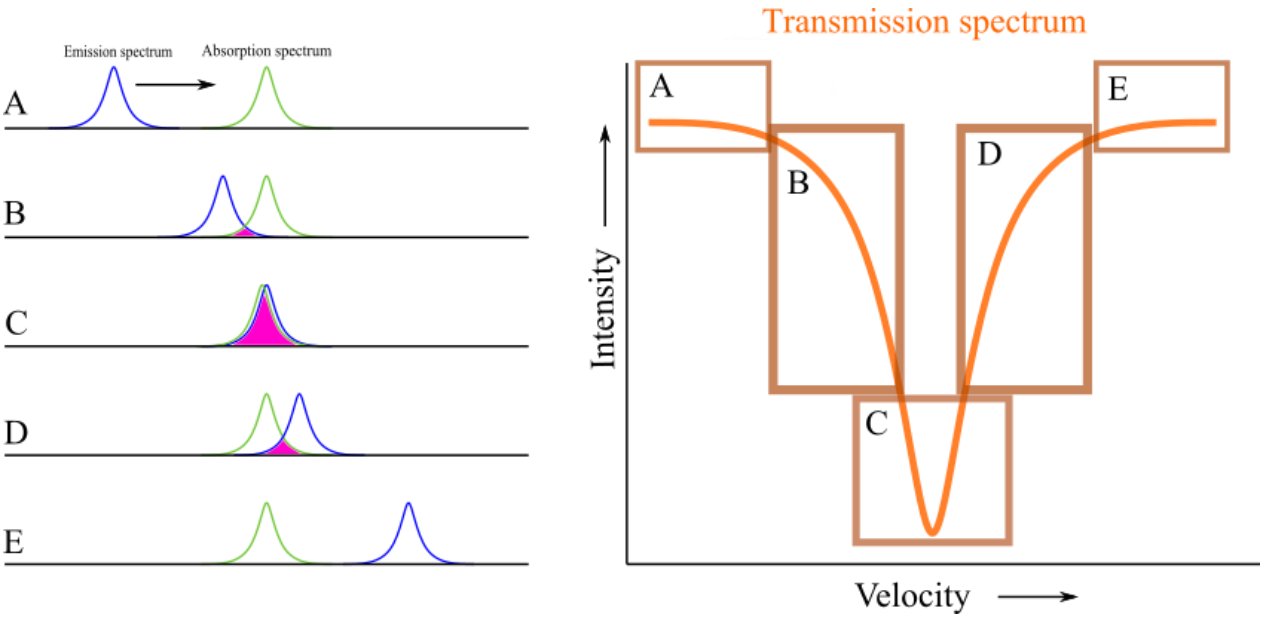

Figure 2.16: The amount of overlap between the emission and the absorption lines is responsible for the formation of a transmission spectrum.[33,53]

2.3.4.6 Hyperfine Interactions

The above explanations all involve a bare nucleus with no influence from a chemical environment. In real materials the Mössbauer nucleus experiences interactions from both the electric and magnetic fields. The fields affects the nuclear energy states and the interactions are referred to as nuclear hyperfine interactions.[58,59] The interaction between the nucleus and its surroundings cause changes in both the nuclear and electronic levels by either shifting or splitting of these levels. If the interaction only causes shifting of the nuclear energy levels, it is known as an electric monopole interaction ($e0$) but if it splits the levels into sublevels without any shifting then it is known as electric quadrupole ($e2$) and magnetic dipole ($m1$) interactions.[58,59]

The hyperfine interactions mentioned above can be observed in a Mössbauer spectrum and can be used to extract important information about the material and local environment. The position of the resonance lines give the isomer shift (δ) whereas $e2$ and $m1$ splits the resonance line of the transition between the degenerate nuclear levels and give rise to the electric quadrupole splitting (ΔE_Q) and the magnetic splitting (ΔE_M).[58,59]

2.3.4.6.1 Electric Hyperfine Interaction

The electrostatic interaction between the nucleus (charge Z_e) and the surroundings has a total energy that can be described as:[60]

$$E_{el} = \int \rho_n(r)V(r)\, d\tau \qquad \textbf{(2.39)}$$

The nuclear charge density, $\rho_n(r)$ at a certain point with set coordinates r = (x_1, x_2, x_3) and the Coulombic potential at a point r = (x_1, x_2, x_3) is described by $V(r)$ and the volume by $d\tau = dx_1 \cdot dx_2 \cdot dx_3$.

$V(r)$ can be further expanded using the Taylor series at the point r = 0:[60]

$$V(r) = V_0 + \sum_{i=1}^{3}\left(\frac{\partial V}{\partial x_i}\right)_0 x_i + \frac{1}{2}\sum_{i,j=1}^{3}\left(\frac{\partial^2 V}{\partial x_i \partial x_j}\right)_0 x_i x_j + \cdots \qquad \textbf{(2.40)}$$

by inserting **(2.39)** into **(2.40)** the following expression can be obtained:

$$E_{el} = V_0 \int \rho_n(r)\, d\tau + \sum_{i=1}^{3}\left(\frac{\partial V}{\partial x_i}\right)_0 \cdot \int \rho_n(r) x_i\, d\tau + \frac{1}{2}\sum_{i,j=1}^{3}\left(\frac{\partial^2 V}{\partial x_i \partial x_j}\right)_0 \cdot \int \rho_n(r) x_i x_j\, d\tau + \cdots \qquad \textbf{(2.41)}$$

The first term of **(eqn 2.41)** describes a point charge electrostatic interaction and second term describes the electric dipole interaction, but no dipole moment exists. Higher order terms represent very small interactions and nuclear moments and are can be considered negligible. The most important term is the third one and can be written as:[60]

$$E_3 = \frac{1}{2}\sum_{i,j=1}^{3} V_{ii} \cdot \int p_n(r) {x_i}^2\, d\tau = \frac{1}{2}\sum_{i=1}^{3} V_{ii} \cdot \int \rho_n(r)\left(x_i^2 - \frac{r^2}{3}\right) d\tau + \frac{1}{6}\sum_{i=1}^{3} V_{ii} \cdot \int \rho_n(r) r^2 d\tau \qquad \textbf{(2.42 a)}$$

where

$$r^2 = \sum_{i=1}^{3} x_i^2 \qquad \textbf{(2.42 b)}$$

With additional substitution and the inclusion of the nuclear quadrupole moment, **eqn 2.42a** can be rewritten as:

$$E = \frac{2}{3}\pi e|\psi(o)|^2 \int \rho_n(r) r^2 d\tau + \frac{1}{2}\sum_{i=1}^{3} V_{ii} \cdot \int \rho_n(r) \left(x_i^2 - \frac{r^2}{3}\right) d\tau \equiv E_I + E_Q \quad \textbf{(2.43)}$$

The first term in **(eqn 2.43)** labelled as E_I can be used to describe the electric monopole interaction and causes a shift in the nuclear energy levels. The second term **(eqn 2.43)** labelled as E_Q describes the electric quadrupole interaction and causes splitting of the degenerate nuclear energy levels.[60]

(A) Electric Monopole Interaction: The Mössbauer isomer shift

The electrostatic interaction between the electrons and the nuclear charge can be described as the electric monopole interaction. The p, d and f-electrons have an angular momentum that is non-zero and unlike the s-electrons they do not have the ability to penetrate the nucleus unless relativistic effects are considered. The s-electrons penetrating the nucleus have an electrostatic interaction with the nuclear charge.[60] The Coulombic interactions cause a shift in the nuclear state energy level. Using the first term of **(eqn 2.43)** the interaction energy can be expressed as:[60]

$$E_I = \frac{2}{3}\pi Z e^2 |\psi(o)|^2 \langle r^2 \rangle \equiv \delta E \quad \textbf{(2.44)}$$

where $|\psi(o)|^2$ describes the electron densities and $\langle r^2 \rangle$ is the square of the nuclear radius. The electrostatic shift, δE, is different for the ground and the excited states for nuclei with the same mass and the same charge. The difference is caused by the changes in the nuclear volume and the mean square of the radius, $< r^2 >$. The electrostatic shift and the energies for the excited state and the ground state for the Mössbauer nucleus would be different compared to the bare Mössbauer nucleus (Fig. 2.17). This phenomenon is responsible for the Mössbauer shift.[58] The Mössbauer nucleus in the excited state of the source would emit a $\gamma -$ ray photon of transition energy E_S and the absorber would emit a $\gamma -$ ray photon of a transition energy E_A. With the Doppler velocity the emission and absorption lines will only be observed when overlap occurs and the difference in the electrostatic shift will be observed. This shift is the isomer shift (Fig. 2.17b)and can be expressed as:[58]

$$\delta = \mathrm{E_S} - \mathrm{E_A} = \frac{2\pi}{5} Z e^2 \{|\psi(0)|^2{}_A - |\psi(0)|^2{}_S\}(\langle r_e{}^2 \rangle - \langle r_g{}^2 \rangle) \quad \textbf{(2.45)}$$

where $|\psi(0)|^2{}_s$ and $|\psi(0)|^2{}_A$ is the electronic charge density of the source and the absorber, respectively.

The difference between r_e and r_g is small such that $r_e - r_g = \delta R$ and $r_e + r_g = 2R$ and therefore equation **(eqn 2.46)** can be written as:

$$\delta = \frac{4}{5}\pi Z e^2 \{|\psi(0)|^2_A - |\psi(0)|^2_S\} \cdot R^2 \left(\frac{\delta R}{R}\right) \quad \textbf{(2.46)}$$

The difference in the electron densities between the source and the absorber are due to the different chemical environments that would also cause different transition energies and electrostatic shifts for E_S and E_A (Fig. 2.17).

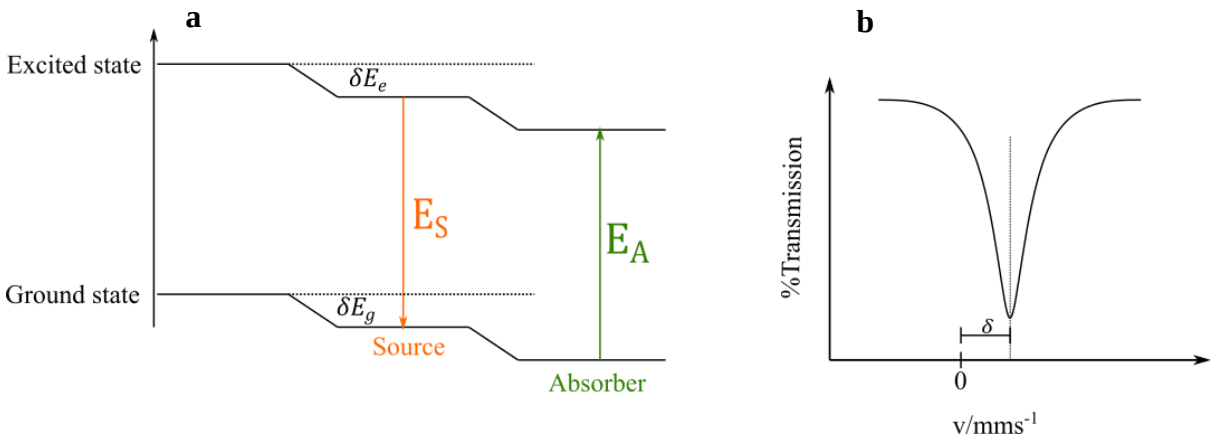

Figure 2.17: (a) Changes in the interactions between the nuclear charge and the electron density present at the nucleus for the bare, source and absorber and (b) the shift of the energy of the nuclear states due to the interactions producing the isomer shift.[58]

The change in the nuclear radius associated with the transition from the excited and ground states is described by the nuclear factor, $\left(\frac{\delta R}{R}\right)$ and can be either negative or positive for the Mössbauer nuclide. For[60]

- $\frac{\delta R}{R} > 0$ and $\delta > 0$; indicates that from the source to the absorber the nucleus exhibits an increase in the electron density
- $\frac{\delta R}{R} < 0$ and $\delta < 0$; indicates that there is a decrease in the electron density between the source and the absorber.

In an experiment the Doppler velocity needed to bring the source and absorber back into resonance can be described as:[60]

$$v_D = \left(\frac{4\pi c}{5E_\gamma}\right) Z e^2 R^2 \left(\frac{\delta R}{R}\right) \{|\psi(0)|^2_A - |\psi(0)|^2_S\} \quad \textbf{(2.47)}$$

If the same Mössbauer nuclide is used for a range of compounds then a standard source can be used and $|\psi(0)|^2{}_S$ can be seen as a constant:[58,60]

$$\delta = cons\left(\frac{\delta R}{R}\right)\{|\psi(0)|^2{}_A - C\} \quad \textbf{(2.48)}$$

(A1) Chemical information provided with the observed isomer shifts

The isomer shift relies in changes to the electron density, $|\psi(0)|^2$, and the penetration of the s-electrons in the nucleus. The density of the s-electrons are composed of two contributions: 1) the fully occupied s-orbitals and 2) the partially occupied valence electrons.[60] The electronic structure is strongly influenced by the valence contribution to the s-electron density. Chemical changes that could affect the electronic structure are the spin state, oxidation state as well as the bond properties.[58,60] The s-electron density would be influenced by valence shell changes either directly or indirectly. Altering the population of the s-electrons in the valence shell would directly influence $|\psi(0)|^2$ by changing the s-electron density and the s-electron density would be influenced indirectly because the p,d and f-like electrons that have a nonzero angular momentum bring about some shielding of the s-electrons. If the valence density increases, then the nuclear charge would attract the s-electrons less and the $|\psi(0)|^2$ would decrease. Similarly, the decrease in the valence density would have an increase in the attraction and would therefore increase $|\psi(0)|^2$.[60]

The effect the spin state and the oxidation state of iron complexes $\left(\frac{\Delta R}{R} < 0\right)$ have on the isomer shift leads to three important trends[33,58,61] The isomer shift is always in reference to a standard:

1) High spin complexes would have a higher isomer shift than low-spin and intermediated spin complexes.
2) Iron complexes with a high spin would show a more positive isomer shift with lower oxidation states than with higher oxidation states.
3) Iron complexes of a low spin have similar isomer shifts and therefor the isomer shift alone cannot be used to identify the oxidation state for a certain compound.
4) The bonding properties, such as strength of the $\sigma - \text{donor and the } \pi - \text{acceptor}$, and the geometry around the Mössbauer nucleus also affects the isomer shift:
    - Complexes with ionic ligands would have a higher isomer shift compared to the isomer shift complexes with covalent ligands.

- Octahedra (six) coordinated environments would exhibit a higher isomer shift compared to the lower coordinated environments such as tetrahedra (four).

(B) Electric Quadrupole Interaction: Quadrupole splitting

For the occurrence of the electric quadrupolar interaction it is necessary that the nuclear quadrupole moment can be observed as well as that the electric field gradient (EFG) be nonzero.[60] The second term in **(eqn 2.43)** is responsible for the splitting of nuclear energy levels that are degenerate and this is referred to as the quadrupole splitting (ΔE_Q). This term was not present when discussing the monopole interaction as the distribution for the nuclear charge was uniform;[60] but if a nuclear charge have a spin quantum number that is $I > \frac{1}{2}$ then the degeneracy would be lifted due the quadrupole interaction.[58] For nuclear states where $I = 0, \frac{1}{2}$, no quadrupole moments are observed.[58]

(B1) Nuclear quadrupole moment

The deviation from the spherical symmetry and the change in the nuclear states can be measured by the electric quadrupole moment. The nuclear quadrupole moment can be described by:[60]

$$Q_{ij} = \int \rho_n(r)\left(x_i x_j - \delta_{ij} r^2\right) d\tau \qquad \textbf{(2.49)}$$

where ρ_n describes the nuclear charge, x_{ij} are used the described the r coordinates on a Cartesian system and δ_{ij} is the Kronecker symbol.

To describe the quadrupole moment of the nucleus, the nuclear constant, *Q*, can be used because of the definite angular momentum and the charge distributions that is cylindrical symmetric. If $Q_{ij} = 0$ for off-diagonal elements and the *z*-axis is the preferred orientation axis then the quadrupole moment for a cylindrical nucleus can be given by:[58,59]

$$Q \equiv \frac{1}{e}\int \rho_n(r)(z^2 - x^2)d\tau = \frac{1}{e}\int \rho_n(r)(3z^2 - r^2)d\tau = \frac{1}{e}\int \rho_n(r) r^2 (3\cos^2\theta - 1)d\tau \qquad \textbf{(2.50)}$$

where $z = r\cos\theta$ and θ is the polar angle between the z (the axis of symmetry) and vector $\vec{r}$. This equation shows that for an elongated nuclei $Q > 0$, for an oblate or flattened nuclei $Q < 0$ and for a spherical charge distribution $Q = 0$.[60]

(B2) Electric field gradient (EFG)

Quadrupole interaction energy can be used to obtain information regarding the electronic and molecular structure. Changes in these structures originates from changes in the electric field gradient (EFG) and describes the interaction between the quadrupole moment $\left(I > \frac{1}{2}\right)$ and the electric field. The alteration of the EFG by physical and chemical changes are important when interpreting the ΔE_Q.[60]

The total EFG has 2 main contributions:[60]

1) Lattice contributions: The Mössbauer atom is surrounded by charges from distant ions in a non-cubic symmetry.
2) Valence electron contributions: The uneven distribution of electrons in the valence shell between the Mössbauer atom and the ligands surrounding it.

(B3) Quadrupole splitting

The (*2I + 1*)-fold magnetic substrates are split due to the electric quadrupole interaction and no energy shifts are associated with this electric quadruple interaction. The eigenvalues E_Q can be determined by the first-order perturbation matrix:[59,60]

$$E_Q = \frac{eQV_{zz}}{4I(2I-1)}\left[3m_i^2 - I(I+1)\right]\sqrt{1+\frac{\eta^2}{3}} \qquad \textbf{(2.51 a)}$$

The nuclear magnetic spin quantum number, $m_i = I, I-1, I-2, \ldots, -I$, V_{zz} describes the one of the principal tensor components and the asymmetry parameter (η) can be described by:[58–60]

$$\eta = \frac{V_{xx} - V_{yy}}{V_{zz}} \qquad 0 \leq \eta \leq 1 \qquad \textbf{(2.51 b)}$$

For ^{57}Fe (14.4 keV) the electric quadrupole interaction of the ground $\left(I = \frac{1}{2}\right)$ and excited $\left(I = \frac{3}{2}\right)$ state can be explained as follows: For $I = \frac{1}{2}$ there is no quadrupole moment present but for $I = \frac{3}{2}$ there is a quadrupole moment leading to the splitting of the excited state into two doubly degenerate states (Fig. 2.18a) i.e. $\left|\frac{3}{2}, \pm\frac{3}{2}\right\rangle$ and $\left|\frac{3}{2}, \pm\frac{1}{2}\right\rangle$. The energy difference between the degenerate states can be described as:[58,60]

$$\Delta E_Q = E_Q\left(\pm\frac{3}{2}\right) - E_Q\left(\pm\frac{1}{2}\right) = \frac{eQV_{zz}}{2} \quad \textbf{(2.52)}$$

A quadrupole doublet would be observed for a ^{57}Fe experiment. These lines are separated by the quadrupole splitting (Fig. 2.18a) and can provide information about the structure such as the bond properties and the local symmetry around the site of interest.[58,60]

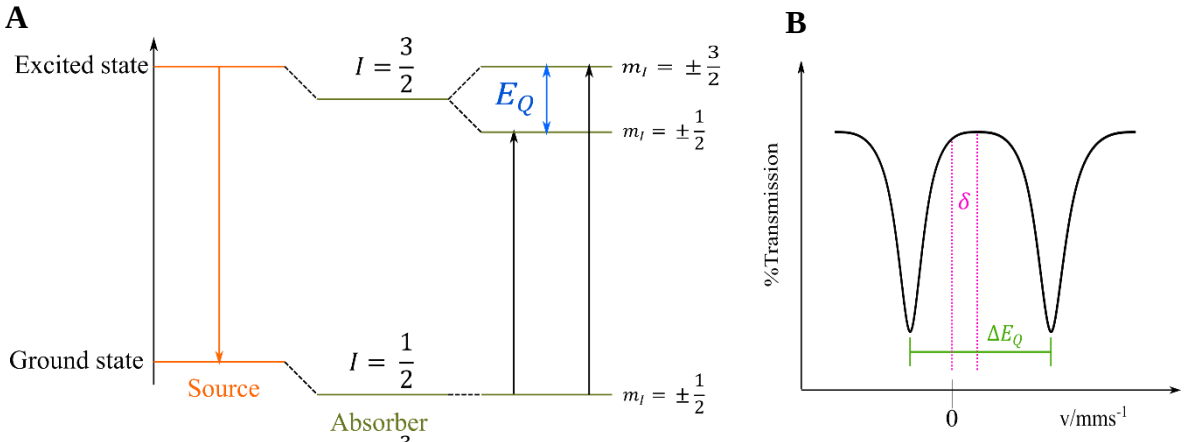

Figure 2.18: (a) The splitting of $I = \frac{3}{2}$ with an energy separation of ΔE_Q and (b) the Mössbauer spectrum that results from this splitting. The states can also be shifted and is indicated by the isomer shift.[58]

(C) Magnetic Hyperfine Interactions

The magnetic dipole interaction exists when there is an interaction between a magnetic field and a nucleus that has a spin quantum number $I > 0$ and is described using the Hamiltonian:[58]

$$\hat{H}_m = -\hat{\vec{\mu}} \cdot \hat{\vec{B}} = -g_N \mu_N \hat{I} \cdot \hat{\vec{B}} \quad \textbf{(2.53)}$$

where $\vec{\mu}$ is the magnetic dipole moment, $\vec{B}$ is the magnetic induction, g_N describes the Landé factor and $\mu_N = \frac{e\hbar}{2M_p c}$ where M_p is the mass of a proton.

The eigenvalue E_m by the first order perturbation matrix diagonalization produces:[58,59]

$$E_m(m_I) = \frac{-\mu B m_I}{I} = -g_N \mu_N B m_I. \quad \textbf{(2.54)}$$

Nuclear states are split into *2I + 1* non-degenerate substates $|I, m_I\rangle$ if the spin quantum number is *I*. This split is a result of the magnetic dipole interaction (nuclear Zeeman effect) and the magnetic dipole transitions $(\Delta I = 1, \Delta m = 0, \pm 1)$ for $\gamma - \text{ray transitions}$ are those allowed by the selection rules.[58] The magnetic dipole interaction for ^{57}Fe the ground state $\left(I = \frac{1}{2}\right)$ splits

into two substates and the excited state $\left(I = \frac{3}{2}\right)$ splits into four substates (Fig 2.19a). There are six allowable transitions due to the selection rules as mentioned above and a resonance sextet with 3:2:1:1:2:3 relative intensities (Fig. 2.19b) is produced. These line intensities follow this intensity pattern due to the magnetic field even distribution with respect to the propagation of the $\gamma-$ ray. The magnetic field acting on the nucleus can be determined by the hyperfine splitting.[58] Information on the spin interaction processes such as electron configuration, magnetic moment and relaxation and the spin value[62] that can be obtained from the magnetic dipole splitting.

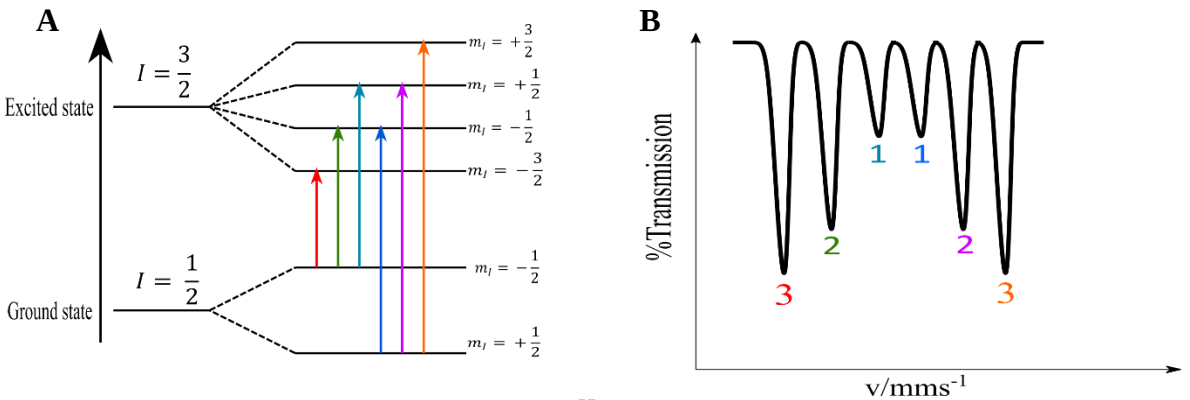

Figure 2.19: (a) The magnetic dipole splitting of ^{57}Fe and (b) the Mössbauer spectrum and intensities that results from this splitting.[58]

2.3.5. Raman Spectroscopy

Raman spectroscopy is a non-destructive technique that utilizes the vibrational modes to investigate the chemical and structural properties of a material.[63] This technique is very versatile and can be used to study powders, solids, liquids, gels and gasses. It has found great importance in different fields such as chemistry, geology, archaeology and pharmaceutics[64] and can be used to characterise materials as long as molecular bonds exist in the sample. Raman spectroscopy relies on the scattering of light and the interaction between the photon and the molecule after the sample is exposed to a laser source.[64] This interaction can be described in terms of three different scattering processes (as illustrated in Fig 2.20):[63,64]

1. Rayleigh scattering: This type of scattering can be identified where the molecule shows no change in energy upon photon interaction. The photon before the interaction (incident) and the photon after the interaction (scattered) would both have the same energy and wavelength. This scattering process also occurs the most frequently.

2. Raman scattering: Raman scattering can be divided into Stokes and Anti-Stokes Raman scattering. Stokes scattering occurs when the molecule gains energy upon photon interaction and the photon that is scattered away from the molecule thus loses energy and has an increased wavelength. The energy gain of the molecule causes an increase in vibrational levels. The opposite occurs for Anti-Stokes scattering. The molecule loses energy after the interaction with the photon whereby the photon that is scattered would gain energy and have a decreased wavelength. The loss in energy of the molecule causes the vibrational energy to relax. These scattering processes do not occur as often as Rayleigh scattering. Between Stokes and Anti-Stokes Raman scattering; Stokes scattering is more likely to occur making this scattering process more intense and more measurable.

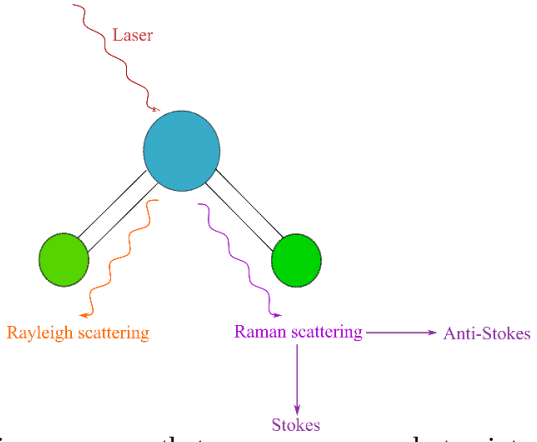

Figure 2.20: Different scattering processes that can occur upon photon interaction with a molecule.[64]

A Raman spectrum is constructed using the change in frequency between the intensity of the radiation that was scattered and the incident radiation.[63] This difference is also referred to as a Raman shift and a spectrum would be a plot of the intensities and the Stokes-shifted frequencies, reported in wavenumber with Raman active modes present on the spectrum (Fig 2.21).[63,64] The position of the peaks can be used as a chemical fingerprint which is unique to a particular material, and can thus be used as either an identification or comparative tool.[64]

Raman spectroscopy can be used to investigate intramolecular and crystal lattice vibrations. The vibrational energy of the molecules or crystals can be related to the frequency shifts.[63] This relationship makes Raman spectroscopy a very useful tool as the vibrational energy can be influenced by the different atomic environments, the bond order, disorder, crystal symmetry

and the local environment. Molecular vibrations can be classified as either stretching, bending, out-of-plane, rocking, wagging and twisting (Table 2.5).

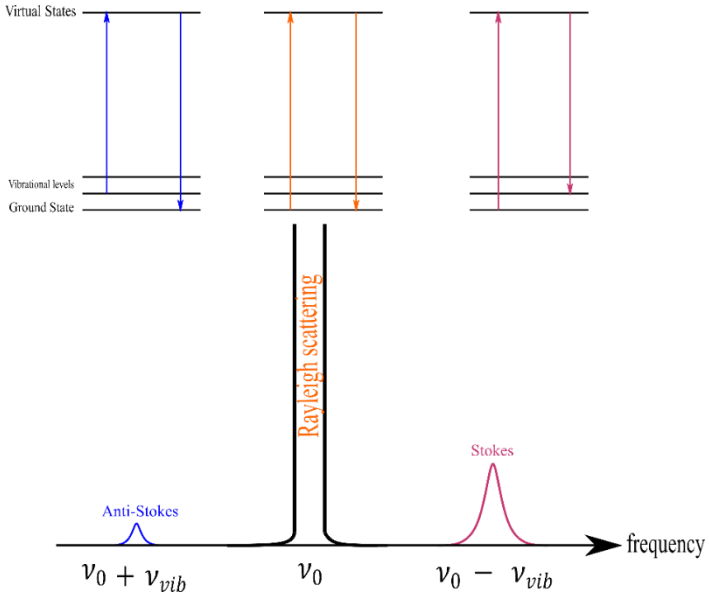

Figure 2.21: The energy level diagrams for Rayleigh and Raman scattering and the scattering at a frequency ν_0 as well as ν_{vib} representing the molecular vibrations. [63]

Table 2.5: Different molecular vibrations and the changes that are linked to the different vibrations.[63]

Molecular vibration:	Changes that occur:	
Stretching	Bond length	Changes in the bond length and angle.
Bending	Bond angle between atoms.	
Out-of-plane	Atoms moving in and out of the plane.	
Rocking	Angle between the molecule and a group of atoms in the molecule.	No change in the bond lengths or the angle.
Wagging	A change in the plane - the plane that runs through the molecule and the plane that runs through a group of atoms.	

Twisting	A change in planes between two groups of atoms.

2.3.3.1 Concentration and crystallinity:

The peak intensity can be used to make conclusions about both the concentration and the crystallinity. There exists a direct relationship between the peak intensity and the concentration. Peaks that are sharp and intense usually indicate crystalline and peaks that broader and less intense usually denoted amorphous substances.[64]

2.4 References:

1. Yang, S., Zavalij, P. Y. and Stanley Whittingham, M. Hydrothermal synthesis of lithium iron phosphate cathodes. *Electrochem. commun.* **3**, 505–508 (2001).
2. Graulis, S., Chateigner, D., Downs, R. T., Yokochi, A. F.T., Quirós, M., Lutterotti, L., Manakova, E., Butkus, J., Moeck, P. and Le Bail, A. Crystallography Open Database - An open-access collection of crystal structures. *J. Appl. Crystallogr.* **42**, 726–729 (2009).
3. Coelho, A. A. TOPAS and TOPAS-Academic: An optimization program integrating computer algebra and crystallographic objects written in C++: An. *J. Appl. Crystallogr.* **51**, 210–218 (2018).
4. jEdit - Programmer's Text Editor - overview. http://www.jedit.org/index.php.
5. Dinnebier, R., Leineweber, A. and Evans, J. *Rietveld refinement: practical powder diffraction pattern analysis using TOPAS*. (2018).
6. Thompson, P., Cox, D. E. and Hastings, J. B. Rietveld refinement of Debye–Scherrer synchrotron X-ray data from Al_2O_3. *J. Appl. Crystallogr.* **20**, 79–83 (1987).
7. Streltsov, V. A., Belokoneva, E. L., Tsirelson, V. G. and Hansen, N. K. Multipole analysis of the electron density in triphylite, $LiFePO_4$, using X-ray diffraction data. *Acta Crystallogr. Sect. B* **49**, 147–153 (1993).
8. Hammersley, A. P. FIT2D: A multi-purpose data reduction, analysis and visualization program. *J. Appl. Crystallogr.* **49**, 646–652 (2016).
9. Juhás, P., Davis, T., Farrow, C. L. and Billinge, S. J. L. PDFgetX3: A rapid and highly automatable program for processing powder diffraction data into total scattering pair distribution functions. *J. Appl. Crystallogr.* **46**, 560–566 (2013).
10. Yang, X., Juhas, P., Farrow, C. L. and Billinge, S. J. L. xPDFsuite: an end-to-end software solution for high throughput pair distribution function transformation, visualization and analysis. (2014).
11. Farrow, C. L., Juhas, P., Liu, J. W., Bryndin, D., Boin, E. S., Bloch, J., Proffen, Th. and

Billinge, S. J.L. PDFfit2 and PDFgui: Computer programs for studying nanostructure in crystals. *J. Phys. Condens. Matter* **19**, 335219 (2007).

12. Farrow, C. L., Juhás, P., Liu, J W., Bryndin, D., Božin, E S., Bloch, J., Proffen, T. H. and Billinge, S J L. PDFgui user guide. Available at: http://www.diffpy.org (2016).

13. Billinge, S. J. L. The rise of the X-ray atomic pair distribution function method: a series of fortunate events. *Philos. Trans. R. Soc. A Math. Phys. Eng. Sci.* **377**, 20180413 (2019).

14. Ravel, B. and Newville, M. ATHENA, ARTEMIS, HEPHAESTUS: Data analysis for X-ray absorption spectroscopy using IFEFFIT. *Journal of Synchrotron Radiation*. **12**, 537–541 (International Union of Crystallography, 2005).

15. OriginLab - Origin and OriginPro - Data Analysis and Graphing Software. https://www.originlab.com/.

16. Wojdyr, M. Fityk: A general-purpose peak fitting program. *J. Appl. Crystallogr.* **43**, 1126–1128 (2010).

17. Kelly, S. D. and Ravel, B. EXAFS analysis with self-consistent atomic potentials. *AIP Conference Proceedings*, **882**, 135–137 (AIP, 2007).

18. Keating, J., Sankar, G., Hyde, T. I., Kohara, S. and Ohara, K. Elucidation of structure and nature of the PdO-Pd transformation using in situ PDF and XAS techniques. *Phys. Chem. Chem. Phys.* **15**, 8555–8565 (2013).

19. Etschmann, B. E., Donner, E., Brugger, J., Howard, D. L., de Jonge, M. D., Paterson, D., Naidu, R., Scheckel, K. G., Ryan, C. G. and Lombi, E. Speciation mapping of environmental samples using XANES imaging. *Environ. Chem.* **11**, 341 (2014).

20. Gaur, A., Shrivastava, B. D. and Khalid, S. Copper K-edge XANES of Cu(I) and Cu(II) oxide mixtures Related content Study of XAFS spectroscopic methods of speciation using mixtures of Cu(I) and Cu(II) chlorides. *J. Phys. Conf. Ser.* **190,** 012084 (2009).

21. Wilke, M., Farges, F., Petit, P. E., Brown, G. E. and Martin, F. Oxidation state and coordination of Fe in minerals: An Fe K-XANES spectroscopic study. *Am. Mineral.* **86**, 714–730 (2001).

22. Haas, O., Deb, A., Cairns, E. J. and Wokaun, A. Synchrotron X-ray absorption study of $LiFePO_4$ electrodes. *J. Electrochem. Soc.* **152**, (2005).

23. Deb, A., Bergmann, U., Cairns, E. J. and Cramer, S. P. X-ray absorption spectroscopy study of the Li_xFePO_4 cathode during cycling using a novel electrochemical in situ reaction cell. *J. Synchrotron Radiat.* **11**, 497–504 (2004).

24. Delacourt, C., Poizot, P., Bonnin, D. and Masquelier, C. Lithium-Insertion Mechanism in Crystalline and Amorphous $FePO_4 \cdot nH_2O$. *J. Electrochem. Soc.* **156**, A595 (2009).

25. Glatzel, P., Mirone, A., Eeckhout, S. G., Sikora, M. and Giuli, G. Orbital hybridization and spin polarization in the resonant 1s photoexcitations of α-Fe_2O_3. *Phys. Rev. B - Condens. Matter Mater. Phys.* **77**, 115133 (2008).

26. De Groot, F., Vankó, G. and Glatzel, P. The 1s x-ray absorption pre-edge structures in transition metal oxides. *J. Phys. Condens. Matter* **21**, 104207–104214 (2009).

27. Pailhé, N., Wattiaux, A., Gaudon, M. and Demourgues, A. Impact of structural

features on pigment properties of α-Fe_2O_3 haematite. *J. Solid State Chem.* **181**, 2697–2704 (2008).

28. Zabinsky, S. I., Rehr, J. J., Ankudinov, A., Albers, R. C. and Eller, M. J. Multiple-scattering calculations of x-ray-absorption spectra. *Phys. Rev. B* **52**, 2995–3009 (1995).

29. Kelly, S. D., Hesterberg, D. and Ravel, B. *Analysis of Soils and Minerals Using X-ray Absorption Spectroscopy*. 387–463 (John Wiley & Sons, Ltd, 2015)

30. Calvin, S. *XAFS for Everyone* . (CRC Press, 2013).

31. Kelly, S. D. and Ravel, B. EXAFS energy shift and structural parameters. in *AIP Conference Proceedings* **882**, 132–134 , 2007.

32. Gunnlaugsson, H. P. Spreadsheet based analysis of Mössbauer spectra. *Hyperfine Interact.* **237**, 79 (2016).

33. Dyar, M. D., Agresti, D. G., Schaefer, M. W., Grant, C. A. & Sklute, E. C. Mössbauer spectroscopy of Earth and planetary materials. *Annual Review of Earth and Planetary Sciences* vol. 34 83–125 (2006).

34. Dyar, M. D. Mössbauer Spectroscopy.(2022). Available at: https://serc.carleton.edu/research_education/geochemsheets/techniques/mossbauer.html. (Accessed on 30 April 2022).

35. Amisse, R., Sougrati, M. T., Stievano, L., Davoisne, C., Dražič, G., Budič, B., Dominko, R. and Masquelier, C. Singular Structural and Electrochemical Properties in Highly Defective $LiFePO_4$ Powders. *Chem. Mater.* **27**, 4261–4273 (2015).

36. Li, Z. and Shinno, I. Next nearest neighbor effects in triphylite and related phosphate minerals. *Mineral. J.* **19**, 99–107 (1997).

37. LabRAM User Guide An Introduction to the Software and Hardware. (2004). at https://www.tcd.ie/Physics/research/groups/1d-nanostructures/resources/equipment/Raman.pdf.

38. Hunter, J. D. Matplotlib: A 2D graphics environment. *Comput. Sci. Eng.* **9**, 90–95 (2007).

39. Dinnebier, R. E. and Billinge, S. J. L. *Powder Diffraction: Theory and Practice*. 1–20 (The Royal Society of Chemistry, 2008).

40. Young, R. A. *The Rietveld Method*. 1–38 (Oxford University Press, 1993).

41. Thompson, M. *Synthesis and characterisation of d-Bi_2O_3 related materials stabilised by substitutions of Ca, Ga, Nb and Re.* (The University of Birmingham, 2010).

42. Toby, B. H. R factors in Rietveld analysis: How good is good enough? . *Powder Diffr.* **21**, 67–70 (2006).

43. Proffen, T., Billinge, S. J. L., Egami, T. and Louca, D. Structural analysis of complex materials using the atomic pair distribution function - A practical guide. *Zeitschrift fur Kristallographie* **218**, 132–143 (2003).

44. Chapman, K. W. Emerging operando and X-ray pair distribution function methods for energy materials development. *MRS Bull.* **41**, 231–238 (2016).

45. Billinge, S. J. L. *Powder Diffraction: Theory and Practice*. 464–493 (Royal Society of

Chemistry, 2008).

46. Newville, M. Fundamentals of XAFS. *Rev. Mineral. Geochemistry* **78**, 33–74 (2014).

47. ATHENA: XAS Data Processing — Athena 0.9.26 documentation. https://bruceravel.github.io/demeter/documents/Athena/index.html.

48. Newville, M., Liviņ, P., Yacoby, Y., Rehr, J. J. and Stern, E. A. Near-edge x-ray-absorption fine structure of Pb: A comparison of theory and experiment. *Phys. Rev. B* **47**, 14126–14131 (1993).

49. Li, G. G., Bridges, F. and Booth, C. H. X-ray-absorption fine-structure standards: A comparison of experiment and theory. *Physical Review B*. **52**, 6332–6348 (1995).

50. Gutlich, P., Schröder, C. and Schünemann, V. Mössbauer spectroscopy-An indispensable tool in solid state research. *Spectroscopy Europe* **24**, 21 - 31(2012).

51. Royal Society of Chemistry. Introduction to Mossbauer Spectroscopy. (2021). at: https://www.rsc.org/membership-and-community/connect-with-others/through-interests/interest-groups/mossbauer/.

52. Rudolf Mössbauer - Nobel Lecture: Recoilless Nuclear Resonance Absorption of Gamma Radiation. (2021). at https://www.nobelprize.org/prizes/physics/1961/mossbauer/lecture/.

53. Gütlich, P., Bill, E. and Trautwein, A. X.*Mössbauer Spectroscopy and Transition Metal Chemistry*. 7–24 (Springer Berlin Heidelberg, 2011).

54. Gibb, T. C. *Principles of Mössbauer Spectroscopy*. 1–21 (Springer Netherlands, 1976).

51. Gütlich, P., Link, R. and Trautwein, A. *Mössbauer Spectroscopy and Transition Metal Chemistry*. 4–12 (Springer-Verlag Berlin Heidelberg, 1978).

55. Gütlich, P., Link, R. & Trautwein, A. Basic Physical Concepts. in *Mossabauer Spectroscopy and Transition Metal Chemistry* vol. Series Volume 3 4–12 (Springer-Verlag Berlin Heidelberg, 1978).

56. Breit, G. & Wigner, E. Capture of slow neutrons. *Phys. Rev.* **49**, 519–531 (1936).

57. Lamb, W. E. Capture of neutrons by atoms in a crystal. *Phys. Rev.* **55**, 190–197 (1939).

58. Gütlich, P., Bill, E. & Trautwein, A. X. *Mössbauer Spectroscopy and Transition Metal Chemistry*. 73–135 (Springer Berlin Heidelberg, 2011).

59. Gibb, T. C. *Principles of Mössbauer Spectroscopy*. 22–44 (Springer US, 1976).

60. Gütlich, P., Link, R. & Trautwein, A. *Mössbauer Spectroscopy and Transition Metal Chemistry*. 13–40 (Springer-Verlag Berlin Heidelberg, 1978).

61. Byrne, J. M. and Kappler, A. *Analytical Geomicrobiology*. 314–338 (Cambridge University Press, 2019).

62. Yang, Q. and Chen, C. *Nuclear Analytical Techniques for Metallomics and Metalloproteomics.*128–162 (Royal Society of Chemistry, 2010).

63. Baddour-Hadjean, R. & Pereira-Ramos, J. P. Raman microspectrometry applied to the study of electrode materials for lithium batteries. *Chem. Rev.* **110**, 1278–1319 (2010).

64. HORIBA. What is Raman Spectroscopy? (2021) at https://www.horiba.com/en_en/raman-imaging-and-spectroscopy/.

Chapter 3

Characterization of $LiFePO_4$ and the use of commercial $LiFePO_4$ as a reference material.

$LiFePO_4$ has been used commercially as a cathode material in lithium-ion batteries (LIBs) mostly to power various electronic devices and certain electrical vehicles.[1,2] One of the aims of this project was to investigate how the synthesis process affects the average and local structure of $LiFePO_4$. Commercially available $LiFePO_4$ (Sigma Aldrich, >97% pure) was used as a reference material for the XANES region of the XAS data. To fully understand the characteristics of this material, the structure was also further analysed by other techniques used in this study. This chapter is divided into two different sections: 1) a literature review of the $LiFePO_4$ structure and 2) a study of the structural differences between the commercial $LiFePO_4$ (C-$LiFePO_4$) and that reported in literature.

3.1. Literature review of $LiFePO_4$ structure

3.1.1. Powder X-ray diffraction (PXRD)

3.1.1.1.Lattice parameters and cell volume

$LiFePO_4$ crystallises in the *Pnma* space group and the orthorhombic crystal system where $a \neq b \neq c$. Table 3.1 contains a summary of the lattice parameters and unit cell volume of $LiFePO_4$ that was obtained when using a hydrothermal synthesis and will also be used as a comparison for the parameters obtained for the synthesised material in the chapters to follow. $LiFePO_4$ is cited to contain no antisite defects when the volume ranges from 290 – 291.4 $Å^3$. [3–5]

Table 3.1: The lattice parameters and volume when using a hydrothermal synthesis.

Reference	*a* (Å)	*b* (Å)	*c* (Å)	Volume ($Å^3$)
Yang *et al.*[6]	10.381(7)	6.013(5)	4.716(3)	294.38*
Chen *et al.*[7]	10.3319(1)	6.0040(1)	4.6939(1)	291.18(1)
Prince *et al.*[8]	10.3095(7)	5.9993(4)	4.6932(3)	290.27(3)
Chen *et al.*[9]	10.3447(9)	6.0033(5)	4.6964(4)	291.66(4)
Kuwahara *et al.*[10]	10.3280(5)	6.0040(3)	4.6936(2)	291.05(2)
Sun and Xu[11]	10.3323(7)	6.0061(8)	4.6928(8)	291.2312(0)
#Chen and Graetz[5]	10.303(1)	5.987(1)	4.670(1)	289.87(5)
$Chen and Graetz[5]	10.3658(6)	6.0037(3)	4.7124(3)	293.27(2)

*Manually calculated and not determined by the group, # After heat treatment, $ before heat treatment.

3.1.1.2. Interatomic bond distances of $LiFePO_4$

The $LiFePO_4$ structure consists of different polyhedral structures (FeO_6, PO_4 and LiO_6) with different interatomic distances (Fig. 3.1).[12] The FeO_6 octahedra consists of 4 equatorial and 2 axial positions and 4 different interatomic distances (Table 3.2). The Wyckoff lattice sites for Li, Fe and P are 4a, 4c and 4c, respectively and for the three oxygen positions O1, O2 and O3 the sites are 4c, 4c and 8d, respectively.[13,14] The longer Fe – O(3) bonds are bonded to the two O(3) atoms that forms the short edge of the octahedra and is edge shared with the PO_4 tetrahedra.[15] The PO_4 tetrahedra have significantly shorter bond distances than both the FeO_6 and LiO_6 octahedra (Table 3.2). The basal plane of the PO_4 tetrahedra [O(3) – O(3) – O(2)] shares oxygen atoms with both Fe [O(3) and O(3)] and Li [O(3) and O(2)] and can be used to investigate both the geometry and orientation of the FeO_6 and LiO_6.[12] P - O distances can also give an indication of the distortion around the PO_4 tetrahedra.[16] The average Li-O interatomic bond distance (Table 3.2) can aid in determining which sample could possibly exhibit better Li^+ mobility. If the average bond distance is longer it implies that the Li channels are wider.[16] The Li – Li interatomic distance together with the O(1) – O(2) interatomic distance of the LiO_6 octahedra can also be used to describe the geometry of the channel. Better ionic conductivity can be achieved if the Li – Li distances are shorter and O(1) – O(2) interatomic distances are longer.[16]

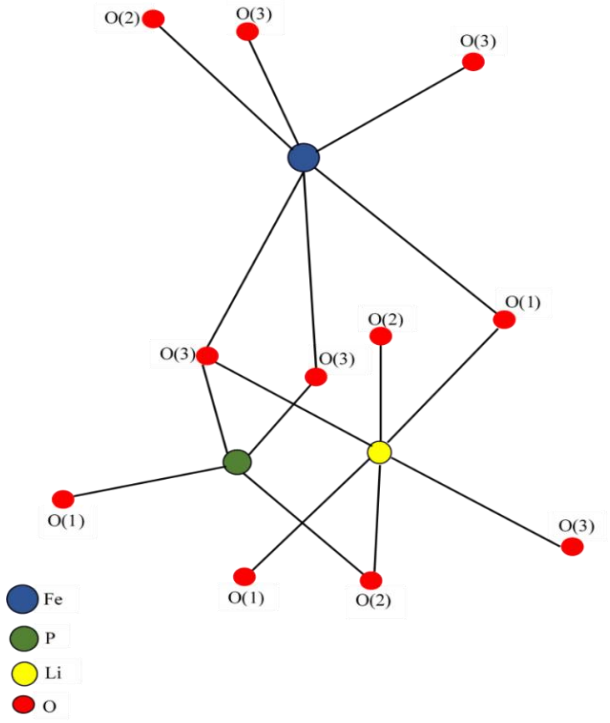

Figure 3.1: The olivine structure of $LiFePO_4$. Adapted from Strelstov et al.[12]

Table 3.2: $LiFePO_4$ interatomic distances (Å) as reported by other groups using PXRD data

	Streltsov *et al.* [12]	**Rousse *et al.*** [17] **and Islam *et al.*** [18]	**Prince *et al.*** [8]	**Jugović *et al.*** [16]
M2 – O(1)	2.204(2)	2.199	2.196(9)	2.197(3)
M2 – O(2)	2.108(2)	2.115	2.086(9)	2.084(2)
M2 – O(3) (×2)	2.251(1)	2.253	2.224(5)	2.248(2)
M2 – O(3) (×2)	2.064(2)	2.061	2.080(6)	2.082(2)
Average M2–O	**2.157**	**2.157**	**2.148**	**2.157**
P – O(1)	1.524(2)	1.525	1.555(6)	1.521(4)
P – O(2)	1.538(2)	1.539	1.577(9)	1.618(2)
P – O(3) (×2)	1.556(1)	1.558	1.554(6)	1.560(2)
Average P – O	**1.544**	**1.545**	**1.560**	**1.565**
M1 – O(1) (×2)	2.171(1)	2.174	ND*	2.172(2)
M1 – O(2) (×2)	2.087(1)	2.086	ND*	2.066(3)
M1 – O(3) (×2)	2.189(1)	2.194	ND*	2.143(2)
Average M1 – O	**2.149**	**2.151**	**ND***	**2.127**

ND* = Not determined by the group

Streltsov *et al.*[12] determined the interatomic bond distances using single crystal X-ray diffraction whereas Rousse *et al.*[17], Islam *et al.*[18], Prince *et al.*[8] and Jugović *et al.*[16] used powder X-ray diffraction (PXRD) to determine the interatomic bond distances. No other phases except $LiFePO_4$ were detected using PXRD. The interatomic bond distances in Table 3.2 will be compared with those determined in this work in the chapters to follow.

3.1.2. X-ray absorption spectroscopy

X-ray absorption spectroscopy (XAS) is a very useful tool to determine the oxidation state and local geometry around the absorbing atom; it is also important to probe the local structure.[19–21] XAS spectra can be divided into two parts (Fig. 3.2): X-ray absorption near edge structure (XANES) and extended X-ray absorption fine structure (EXAFS). To investigate the valence state, geometry and local structure of $LiFePO_4$ the Fe K-edge was used. Fe is the absorbing atom whereas the K-edge refers to the absorption of the X-rays by the 1s core electrons.[19,22,23]

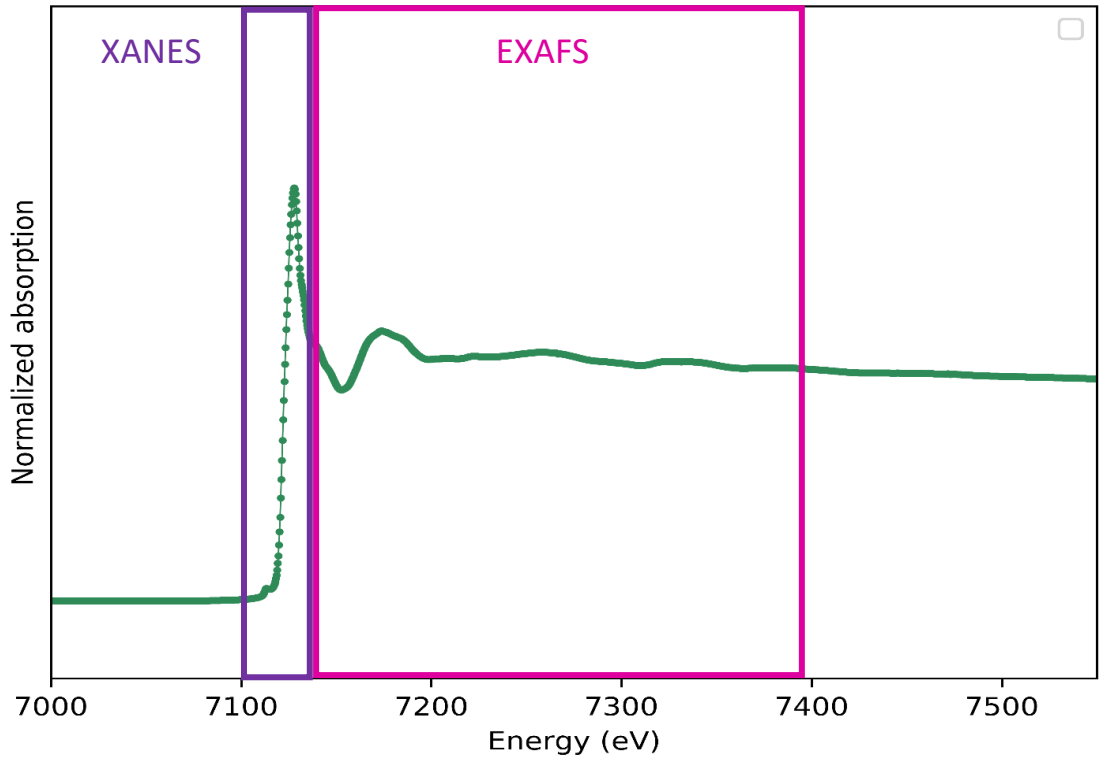

Figure 3.2: The XAS spectrum of $LiFePO_4$ can be divided into XANES and EXAFS.

3.1.2.1.XANES

XANES is an effective way of determining the valence state as well as the changes in geometry around of Fe and can be divided into the pre-edge, absorption edge and the main edge.[24–27] The pre-edge peaks arise due to the $1s \rightarrow 3d$ unoccupied orbital transition.[24] For a compound with a centrosymmetric non-distorted octahedron, the transition is quadrupole allowed but dipole forbidden and the pre-edge features would be of very low intensity and barely visible.[28–30] When the central atom is surrounded by ligands two of the five *d* metal orbitals, namely, d_z^2 and $d_{x^2-y^2}$ are directed towards the ligand whereas the other three orbitals, namely, d_{xy}, d_{yz} and d_{zx} are directed between the ligands.[31] The energy of the electron depends on the direction of the orbital and subsequently, the energy for the d_z^2 and $d_{x^2-y^2}$ orbitals would be raised due the repulsion field caused by the ligands and the energy for the d_{xy}, d_{yz} and d_{zx} orbitals would not be influenced as much. The energy would split into two energy levels with (i) d_z^2 and $d_{x^2-y^2}$ and (ii) d_{xy}, d_{yz} and d_{zx} being degenerate (Fig. 3.3). Three orbitals are thus lower in energy and denoted t_{2g} and two orbitals are higher in energy and represented as e_g (Fig 3.3).[31]

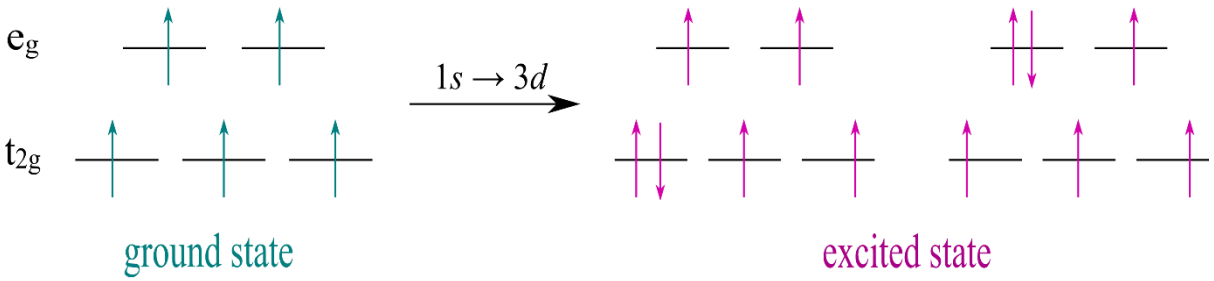

Figure 3.3: The splitting of the energy levels for the metal d-orbitals. The 1s → 3d transition leads two different excited states.[25]

In $LiFePO_4$ the distortion around Fe reduces the symmetry from an O_h to C_s which breaks the inversion centre of the octahedra and causes mixing of the 3*d* – 4*p* orbitals of the Fe metal and produces a crystal-field that splits the 3*d* states into two energy levels[25] and causes the 1*s* → 3*d* transition to become partially dipole allowed and two weak peaks[32] are present in the pre-edge region (Fig. 3.4).[20,28,29,33] The pre-edge peaks of $LiFePO_4$ are at ~ 7112 eV (t_{2g})[20,25] and at ~7114 eV (e_g).[20,25] A change in oxidation state from Fe^{2+} to Fe^{3+} is indicated by a shift in the peaks to higher energy and a change in geometry and distortion around Fe is indicated by an increase in intensity.[20,25,32,34,35]

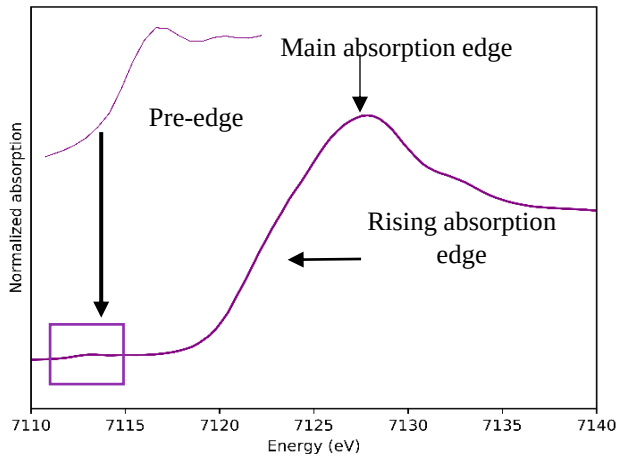

Figure 3.4: The XANES spectrum of $LiFePO_4$ can be divided into pre-edge, rising absorption edge and main absorption edge.

The rising absorption edge and the main edge corresponds to the to the 1s → 4p and the 1s → continuum transition [24] which occurs at ~7125 - 7127 eV for $LiFePO_4$ (Fig. 3.4).[30,36] The extreme increase in intensity of the absorption edge follows after the electrons are excited to unoccupied p-orbitals.[37] The rising absorption edge as well as the main absorption edge can be used to determine the oxidation state of Fe. As with the pre-edge region a change in oxidation state from Fe^{2+} to Fe^{3+} would show a peak shift to a higher energy.[20,34,38]

3.1.2.2.EXAFS

EXAFS follows the main absorption edge and can be identified by small oscillations. These oscillations can provide information of the local structure in $LiFePO_4$ (Fig. 3.5a).[39,40] by determining the interatomic distances, coordination numbers and the Debye-Waller factor around the Fe absorbing atom with the nearest neighbour coordination shells.[20,25,27,30,41] The Debye-Waller factor is a good indication of the disorder in the local structure around Fe.[27,39,40,42]

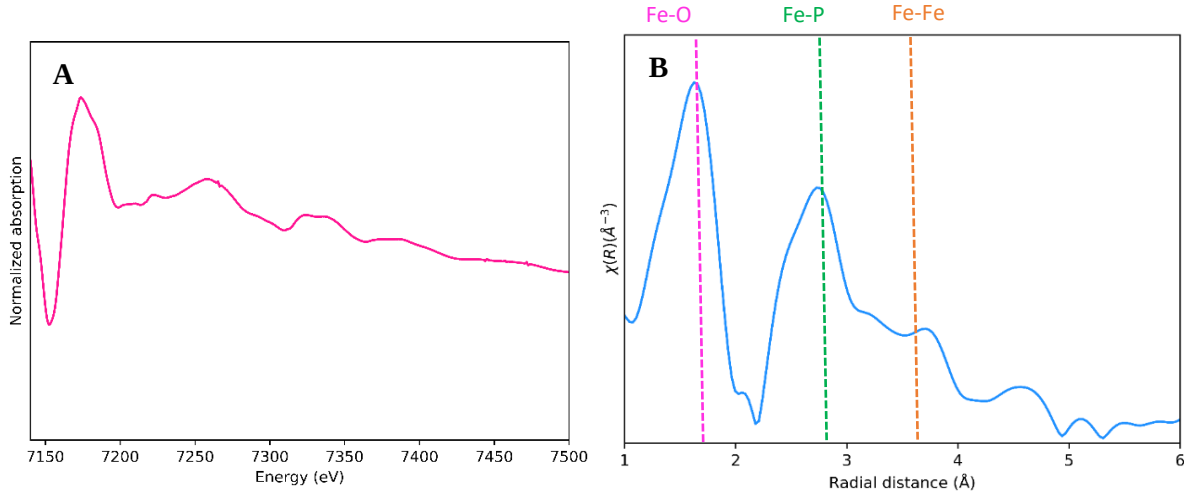

Figure 3.5: (a) The EXAFS oscillations for $LiFePO_4$ can be used for local structure determination. (b) The different coordination shells around the Fe absorbing atom in R-space for $LiFePO_4$.

The different coordination shells around Fe can also be determined (Fig. 3.5b). The first strong peak around 1.8 Å corresponds to the scattering process of the oxygen coordination shell (Fe-O). The second major peak around 2.8 Å corresponds to the phosphorous coordination shell (Fe-P) and the third peak around 3.6 Å corresponds to the iron coordination shell (Fe-Fe).[20,25,30,40,43] Table 3.3 contains the average interatomic distances and average disorder as determined by other research groups and will be used to compared the EXAFS models determined in the chapters to follow.

Table 3.3: The average interatomic distance and average Debye-Waller factor as determined in literature for $LiFePO_4$.

Reference	Coordination shell	Coordination number	Interatomic distance (Å)	Debye-Waller factor (Å²)
Haas *et al.*[25]	Fe-O	6	2.13	0.0037
	Fe-P	5	3.15	0.0046
	Fe-Fe	4	4	0.0055
Hsu *et al.*[41]	Fe-O	6	2.15	0.0082
	Fe-P	5	3.25	0.0049
	Fe-Fe	4	3.94	0.0096
Deb *et al.*[20]	Fe-O	6	2.13	0.0028
	Fe-P	5	3.15	0.0045
	Fe-Fe	4	4	0.0054
[#]Zhao *et al.*[42]	Fe-O	6	2.09	0.0083

[#] Research group only did EXAFS modelling on the first coordination shell.

3.1.3. Mössbauer spectroscopy

Mössbauer spectroscopy is a very sensitive technique for determining the Fe phases with different valence states and local environments and involves the observation of the electronic states of the different Fe environments.[44] To evaluate the different environments, it is important to quantify/consider three different parameters: isomer shift (IS = δ), quadrupole splitting (QS = ΔE_Q)[44] and full width at half maximum line width (Γ).[13,45–47] The isomer shift evaluates the change in electron density of the chemical environment[44] whereas the quadrupole splitting evaluates the charge distribution around the Fe nucleus and is sensitive to distortion in the oxygen environment in this work.[48] full width at half maximum line width is a useful indicator to probe the local structural disorder as well as the quadrupolar effects.[45–47] In $LiFePO_4$ the major doublet is that of Fe^{2+} in a slightly distorted octahedral (M2 site) environment. The hyperfine parameters of this doublet is δ = 1.20 – 1.22 mm/s, ΔE_Q = 2.95 – 2.98 mm/s[45] and Γ = 0.2 – 0.3 mm/s.[13,47] Fe^{2+} in a slightly distorted octahedral environment exhibits a very high ΔE_Q due to the high $3d^6$ configuration and the asymmetric (distorted) environment of the octahedra[44] compared to that of the Fe^{3+} (δ = 0.44 mm/s, ΔE_Q = 0.7 – 0.9 mm/s),[47] where Fe^{3+} has a d^5 electron configuration.[49] Table 3.4 lists the hyperfine parameters for Fe^{2+} in $LiFePO_4$ that are commonly found in literature.

Table 3.4: Hyperfine parameters (IS and QS) commonly found in literature for Fe^{2+} in $LiFePO_4$

Reference Papers	δ (mm/s)	ΔE_Q (mm/s)
Amisse *et al.*[50]	1.22	2.95
Yamada *et al.*[44]	1.22	2.95
Kuwahara *et al.*[10]	1.22	2.96
Prince *et al.*[8]	1.20	2.96
Porcher *et al.*[51]	1.23	2.94
Martin *et al.*[52]	1.24	2.96
Cuisinier *et al.*[53]	1.22	2.97
Sanchez *et al.*[46]	1.21	2.98
Hamelet *et al.*[47]	1.22	2.95
Maccario *et al.*[13]	1.22	2.95
Xia *et al.*[54]	1.22	2.97
Andersson *et al.*[55]	1.22	2.96

3.1.4. Raman Spectroscopy

$LiFePO_4$ has 36 Raman active optical modes. The vibrational modes of $LiFePO_4$ can be divided into internal and external optic modes.[56–58] The internal modes of $LiFePO_4$ corresponds to the intramolecular vibrations of PO_4^{3-} anions (tetrahedra) and exists between 400 – 1100 cm^{-1} (Table 3.5). The vibrational motion of the internal modes can be described in terms of the symmetry of P-O: the P-O symmetric stretching (υ_1), symmetric O-P-O bending (υ_2), antisymmetric P-O stretching (υ_3) and antisymmetric O-P-O bending (υ_4).[57,59] The external modes refers to the translational motion of Fe^{2+} and the PO_4^{3-} rotational motion and occurs below 400 cm^{-1} (Table 3.5). These modes can also be referred to as lattice vibrations.[57–59] Any Li^+ motion is only IR active and is Raman inactive.[56] The region below 400cm^{-1} is also expected to contain the lithium cage modes. The cage mode refers to the motion that lithium ions undergo due to the potential energy environment caused by the oxygen and phosphate neighbouring atoms.[56,57] No specific band can be assigned to the lithium cage mode and the lithium motion contributes very little to (υ_1) and (υ_3) whereas (υ_2) and (υ_4) involve some lithium motion.[56]

Table 3.5: Raman wavenumbers and the different assignments for $LiFePO_4$ found in literature.

Wavenumbers (/cm)			Assignment
Burba & Frech[56]	**Paraguassu *et al.***[60]	**Wu *et al.***[57]	
107	106	112	
151	147		
161	157	153	
199	195	175	PO_4^{3-} rotational and Fe^{2+} translational motion
226		228	
245	249	245	
292		297	
410		402	
447	442	445	
499			ν_2 (PO_4^{3-} symmetric bending)
513			
572	571		
595	586	593	
612	628		ν_4 (PO_4^{3-} asymmetric bending)
631		637	
657			
953	949	949	ν_1 (PO_4^{3-} symmetric stretching)
999	995	995	
1071	1067	1067	ν_3 (PO_4^{3-} asymmetric stretching)
	1079		

3.2. Results and Discussion for C-$LiFePO_4$

3.2.1. Powder X-ray diffraction

The sample was measured using both a laboratory diffractometer and synchrotron PXRD. The results shown in this section are only those from the synchrotron. The X-ray wavelength was determined to be 0.166316(1) Å using LaB_6 (NIST 660c) to calibrate the instrument. The structure of C-LFP was refined by starting with a structure resolved by Streltsov *et al.*[12] and the refined parameters were the scale, lattice parameters, thermal displacement parameters and Lorentzian microstrain. The Rietveld error indices, lattice parameters and the volume are presented in Table 3.6. However, not all the peaks in the measured diffraction pattern were accounted for in this refinement indicating that $LiFePO_4$ was not the only phase present (Fig. 3.6 – indicated with red), but higher resolution data would be necessary to determine if the peak at ~ 3.3 Å is actually two overlapped peaks, one being the impurity and the other $LiFePO_4$. The same impurity peak was observed in the preliminary laboratory PXRD data. Common $LiFePO_4$ impurities such as Fe_2O_3, Fe_3O_4 and Li_3PO_4 did not match the impurity present. Other than the impurity peak, the sample shows crystalline features and the synthetic method is most probably a solid state route or one where the sample was heat-treated. The error indices in Table 3.6 could be improved if the impurity was matched to a phase. The lattice parameters and the volume (Table 3.6) were comparable to those determined by other groups (Table 3.1)[3,8,11] possibly indicating that the impurity present does not have a large effect on the lattice parameters or volume. $LiFePO_4$ is thought to be defect-free (including antisite defects) when the volume ranges from 290 – 291.4 $Å^3$ [3–5] indicating that the structure is possibly free of most defects.

Table 3.6: Rietveld error indices, lattice parameters and the volume for C-LFP

R_{wp}	15.17
R_p	13.42
R_{exp}	9.20
GOF	1.13
***a* (Å)**	10.329(9)
***b* (Å)**	6.0086(5)
***c* (Å)**	4.6916(4)
Volume ($Å^3$)	291.19(4)
R_{wp}	15.17
R_p	13.42

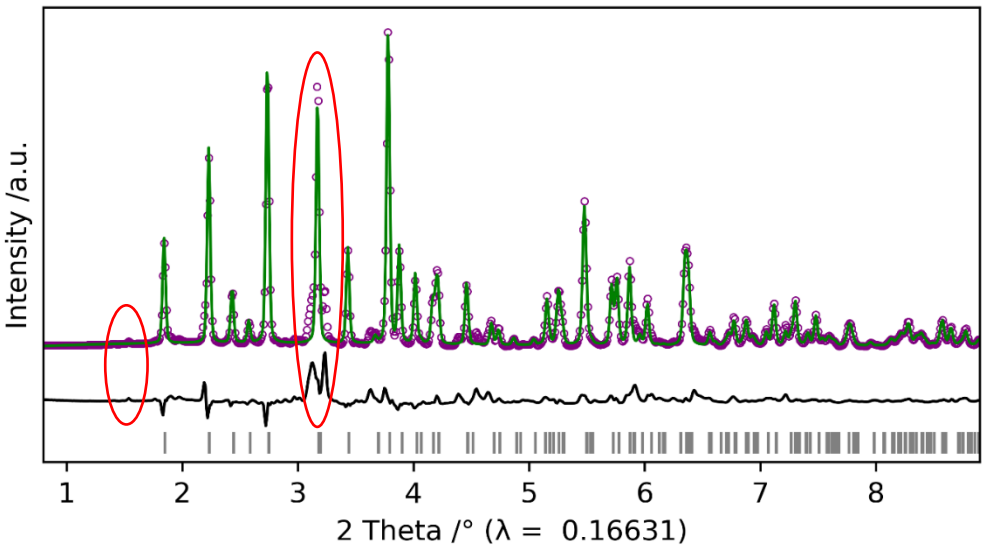

Figure 3.6: Synchrotron diffractogram of C-LFP showing the observed (purple), calculated (green) and difference (black) plots generated from a Rietveld refinement analysis. Bragg reflections for $LiFePO_4$ are indicated by grey markers. The unmatched phase present is indicated in red.

3.2.2. X-ray absorption spectroscopy

3.2.2.1.XANES

XAS Fe K-edge was collected for C-$LiFePO_4$ and two other standards with Fe^{3+} present namely $FePO_4$•$4H_2O$ and α-Fe_2O_3 (Fig. 3.7). Synchrotron PXRD investigated the average structure and XAS, with both XANES and EXAFS, was used to look at the local Fe environment of C-$LiFePO_4$. This is important as C-$LiFePO_4$ is used as a standard to compare the XANES of the synthesised samples in the chapters that follow. The pre-processing of the XANES data is described in section 2.2.3. of chapter 2. The t_{2g} (7112.2 eV) and e_g (7114.1 eV) peaks are both present in the sample (Fig. 3.8 inset). These two peaks can be used to identify $LiFePO_4$ due to the distortion present in the $Fe^{2+}O_6$ octahedra.[20,25] The main absorption edge (Fig. 3.8) is at ~ 7126.97 eV and this position is commonly associated with Fe^{2+}.[30] Using the peak position of the pre-edge and main absorption edge showed that very little Fe^{2+} has been oxidised Fe^{3+}. The peak positions for the standards containing Fe^{3+} ($FePO_4$•$4H_2O$ and α-Fe_2O_3) were determined to be 7114.3 eV and 7114.4 eV, respectively for the pre-edge region (Fig. 3.7) and 7131.9 eV and 7133.8 eV for the main absorption edge (Fig. 3.7), respectively.

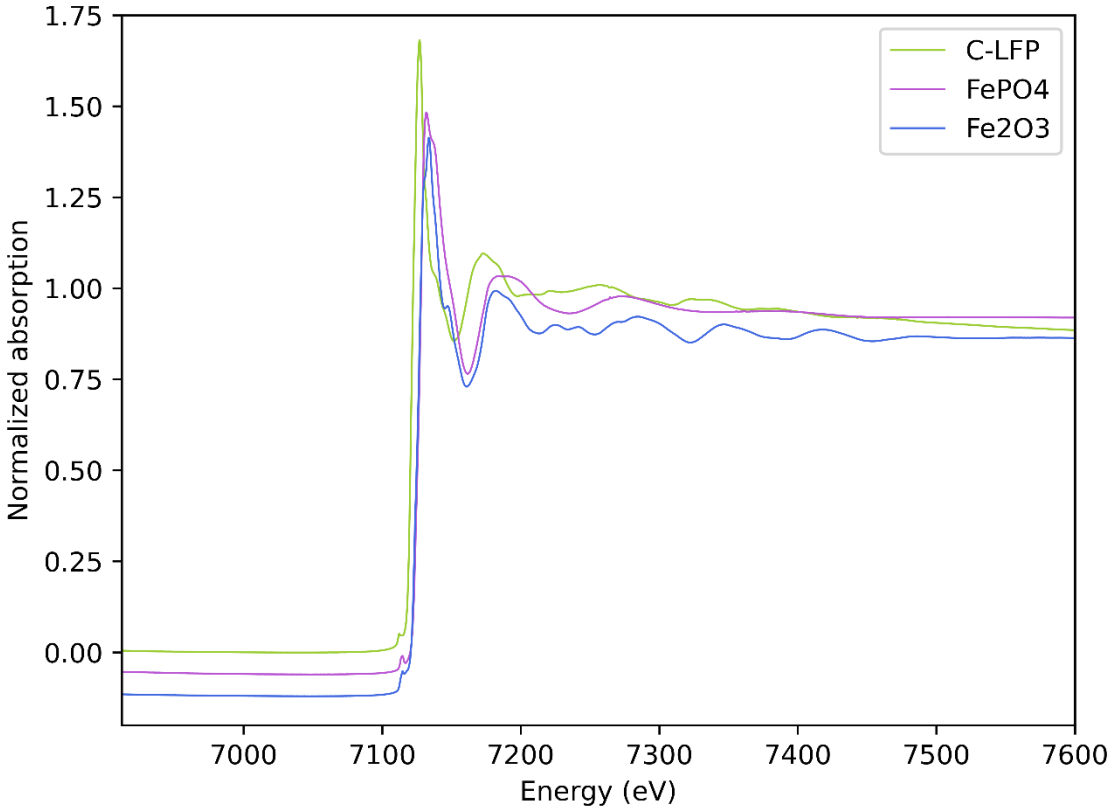

Figure 3.7: Normalized Fe K-edge spectrum of C-LFP, $FePO_4 \cdot 4H_2O$ and Fe_2O_3 that were used as standards.

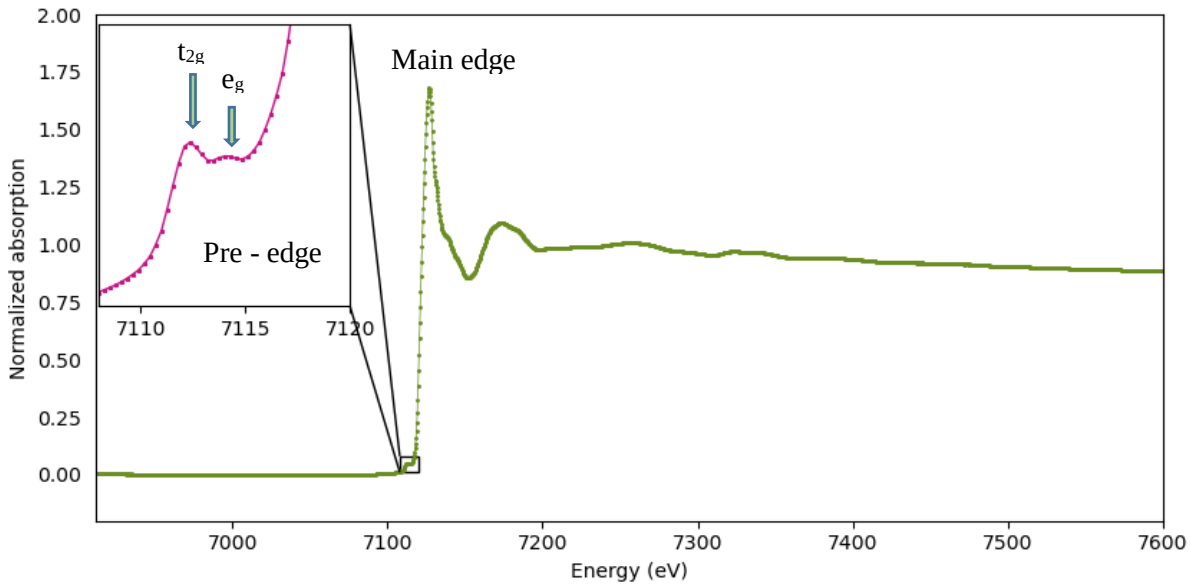

Figure 3.8: Normalized Fe K-edge spectrum of C-LFP. The pre-edge region (inset) and the main edge are indicated on the spectrum of C-LFP.

3.2.2.2. EXAFS

The fitting parameters used for the modelling of C-$LiFePO_4$ is described in section 2.2.3.2. and all Fourier Transformed (FT) EXAFS spectra were phase corrected. C-LFP showed the

presence of all three the peaks relating to the different coordination shells present in $LiFePO_4$ (Fig. 3.9). The first coordination shell was identified as oxygen, the second coordination shell was phosphorous and the third coordination shell was iron.[20,25,41] Three different Fe-O scattering paths (Fe-O1, Fe-O2 and Fe-O3) were used for the modelling. The combination between these paths that gave the lowest χ^2- value for the first coordination shell was Fe-O1 and Fe-O2.After each combination the reduced χ^2- value as well as the error were assessed. A good *R*-factor is generally less than 0.05 (5%)[61] and ΔE_o should ideally be -10 eV < ΔE_0 < 10 eV.[62] For this sample the *R*-factor was 0.0086, the value of S_o^2 was 0.91(8) and the ΔE_o was 0.22(1.07).

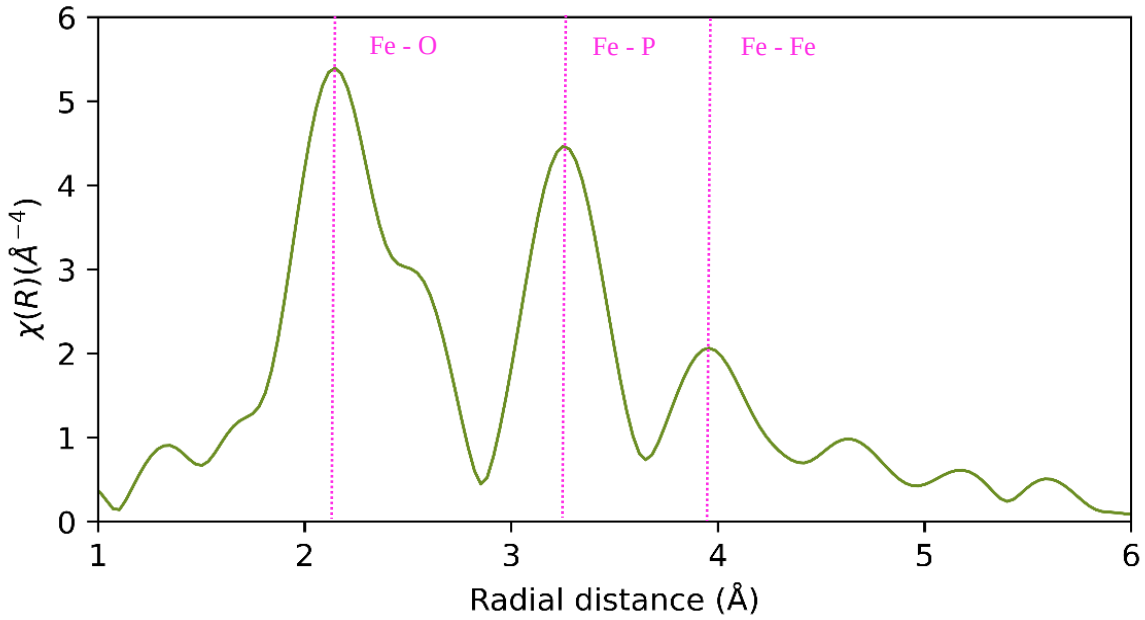

Figure 3.9: The FT magnitude of EXAFS $k^3\chi(k)$ data for C-LFP showing the first, second and third coordination shells.

To describe the fit and the experimental data the $k^3\chi(k)$ plot, the magnitude of the Fourier Transform (FT magnitude) and the real space of the Fourier Transform (FT real) is provided (Fig. 3.10). The Fe-O coordination shell had a coordination number of six[20,25,41] and had two different interatomic bond distances which differed by 0.09 Å (Table 3.7). Using a coordination of six matched the intensity of the first peak in Figure 3.10a. This was consistent with the synchrotron PXRD results (Table 3.2) and XAS studies performed by other research groups (Table 3.3). Three interatomic bond distances were longer and the other three were shorter which gives a distorted octahedra as seen from the signal produced in the pre-edge region. The degree of disorder (as indicated by the Debye-Waller factor) was slightly larger for the longer interatomic bond distances (Table 3.7). The average Fe-O interatomic bond distance (2.11 Å)

was similar to those determined for other local structures and the average disorder (0.010 Å^2) was slightly larger (Table 3.3).[20,25,41] The Fe-P coordination shell had a coordination number of five.[20,25,41] This shell consisted of one shorter and four longer interatomic bond distances, differing by 0.42 Å. The disorder in both the Fe-O and Fe-P shells were similar. The average interatomic distance (3.17 Å) was only slightly longer and the average disorder (0.007 Å^2) was larger than the reported values (Table 3.3).[20,25] The Fe-Fe coordination shell had a coordination number of four[20,25,41] and consisted of two longer and two shorter interatomic distances. The disorder in the Fe-Fe coordination shell is also similar for both interatomic distances which, differed by 0.62 Å. The average interatomic distance (4.24 Å) and average disorder (0.007 Å^2) for the Fe-Fe coordination shell was both slightly longer and larger, respectively than the values reported by other groups (Table 3.3).[20,25] The misfits that can be observed between the experimental data and the fit indicates that there are some deviations between the C-LiFePO$_4$ and the model used.

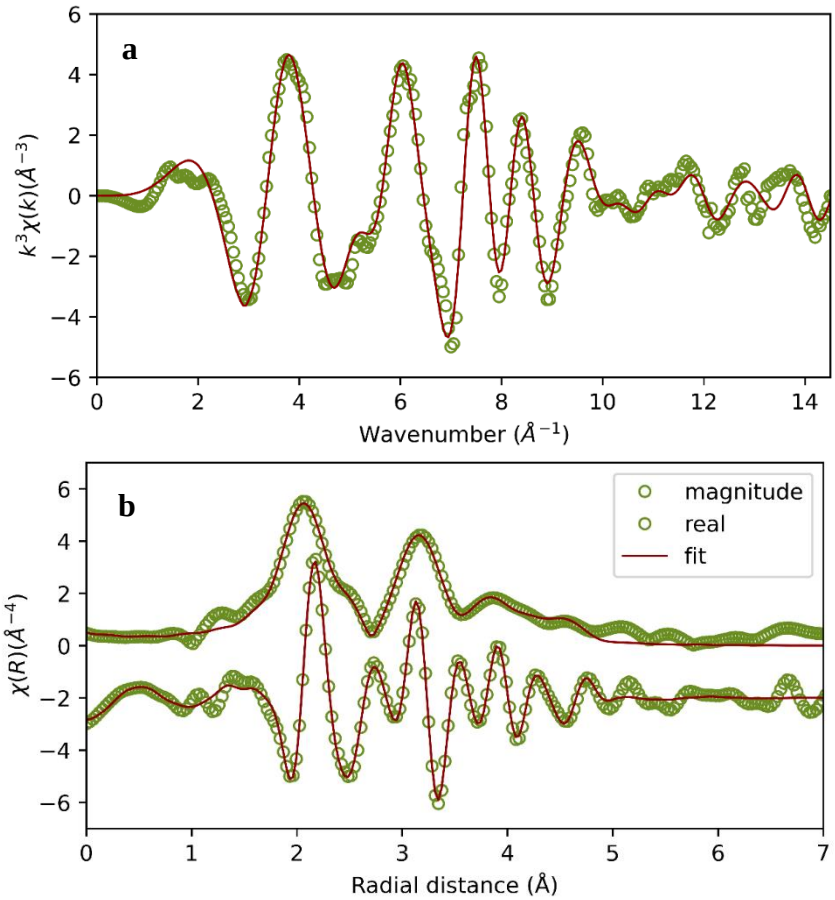

Figure 3.10: (a) The experimental Fe k^3-weighted [$k^3\chi(k)$] spectrum and (b) the experimental FT magnitude (top) and FT real (bottom) of the EXAFS $k^3\chi(k)$ data (green) and the theoretical FEFF fit (maroon) of C-LFP. The fitting window here for (a) was 3 – 12.828 Å^{-1} and for (b) 1.3 – 5 Å.

Table 3.7: Structural parameters determined using FEFF for the first, second and third coordination shells of C-LFP.

Sample	Shell	Coordination number	Average interatomic distance (Å)	Debye-Waller factor (Å^2)
C-LFP	Fe-O1	3	2.15(2)	0.011(4)
	Fe-O2	3	2.06(2)	0.008(2)
	Fe-P1	1	2.83(1)	0.008(3)
	Fe-P2	4	3.25(1)	0.007(1)
	Fe-Fe1	2	3.83(1)	0.007(2)
	Fe-Fe2	2	4.65(1)	0.008(3)

3.2.3. Mössbauer spectroscopy

Mössbauer spectroscopy was used to investigate the Fe^{2+} environment in C-LFP and to Mössbauer spectroscopy was used to investigate the Fe^{2+} environment in C-LFP and to determine if any other iron environments are present but because of the nature of the sample it is expected that Fe^{2+} characteristic of $LiFePO_4$ would be present in this sample. Fe^{2+} in the $LiFePO_4$ structure produces an isomer shift (δ) of 1.20 – 1.23 mm/s and a quadrupole splitting (ΔE_Q) of 2.94 – 2.98 mm/s (Table 3.4).[13,44,46,47,50] In this work, using a Pseudo Voigt doublet to fit Fe^{2+} in the spectra from C-LFP showed a δ = 1.22(1) mm/s and ΔE_Q = 2.94(1) mm/s (Fig. 3.11) and accounted for 66(6)% of the total Fe. To improve the fit two other doublets was added – one Fe^{2+} and one Fe^{3+} environment. The Fe^{2+} is Fe on the M2 site but because of the smaller ΔE_Qthis environment is more distorted[50] (δ = 1.21(1) mm/s and ΔE_Q = 2.49(1) mm/s) and accounts for 26(4)% of the Fe in the sample. The Fe^{3+} is Fe on the M1[47,50] site (δ = 1.48(1) mm/s and ΔE_Q = 0.69(1) mm/s) where Fe^{3+} replaced Li^+ and accounted for 2(1)% of the total Fe. Two Lorentzian sextets were also added to the fit but did not account for all the smaller peaks on either side of the doublet. The first sextet had B_{hf} = 48.3(1) T, δ = 0.27(1) mm/s and ΔE_Q = -0.01(1) mm/s and accounted for 2(1)% of the total Fe and the second sextet had B_{hf} = 45.2(5) T, δ = 0.62(1) mm/s and ΔE_Q = 0.08(1) mm/s accounted for 4(1)% of the total Fe. These parameters did not match to those of α-Fe_2O_3.[47] Fe^{2+} on the M1 site was also added during analysis but the hyperfine parameters[63] could not be matched and did not improve the fit. The final χ^2 was 9.61 indicating that there were other environments that were not accounted for.

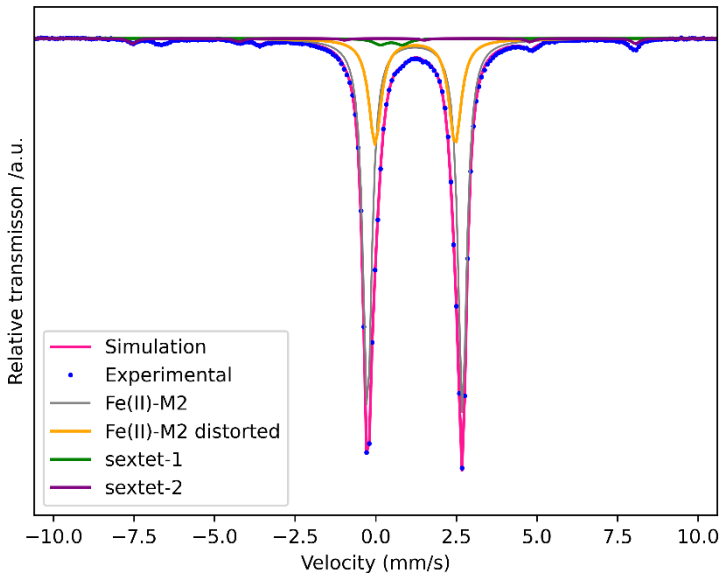

Figure 3.11: The Mössbauer spectrum of C-LFP when including three doublets and two sextet models to model the experimental data.

3.2.4. Raman spectroscopy

Two different coloured particulates (white and black) were identified in C-LFP under the optical microscope used on the Raman spectrograph (Fig. 3.12 and Fig. 3.13 insets). Both the white (Fig. 3.12 and Table 3.8) and black (Fig. 3.13 and Table 3.8) particulates were analysed by Raman spectroscopy and the vibrational modes for $LiFePO_4$ were identified in both (Table 3.8 – coloured in grey).[56,57,60] These modes were also identified by Burba and Frech,[56] Paraguassu *et al.*,[60] and Wu *et al.*[57] summarised in Table 3.5. The impurity peaks that were detected are also indicated in Table 3.8. The peaks indicated in orange could be associated with some of the peaks found for hematite (α-Fe_2O_3).[64] The peaks indicated in green could be associated with two peaks found for magnetite (Fe_3O_4)[64] and the most intense of these peaks also showed an increase in concentration for the black particulate compared to the white particulate (indicated with the green arrow on Figs. 3.12 and 3.13). The impurity denoted with (*) in Table 3.8 has not been identified.

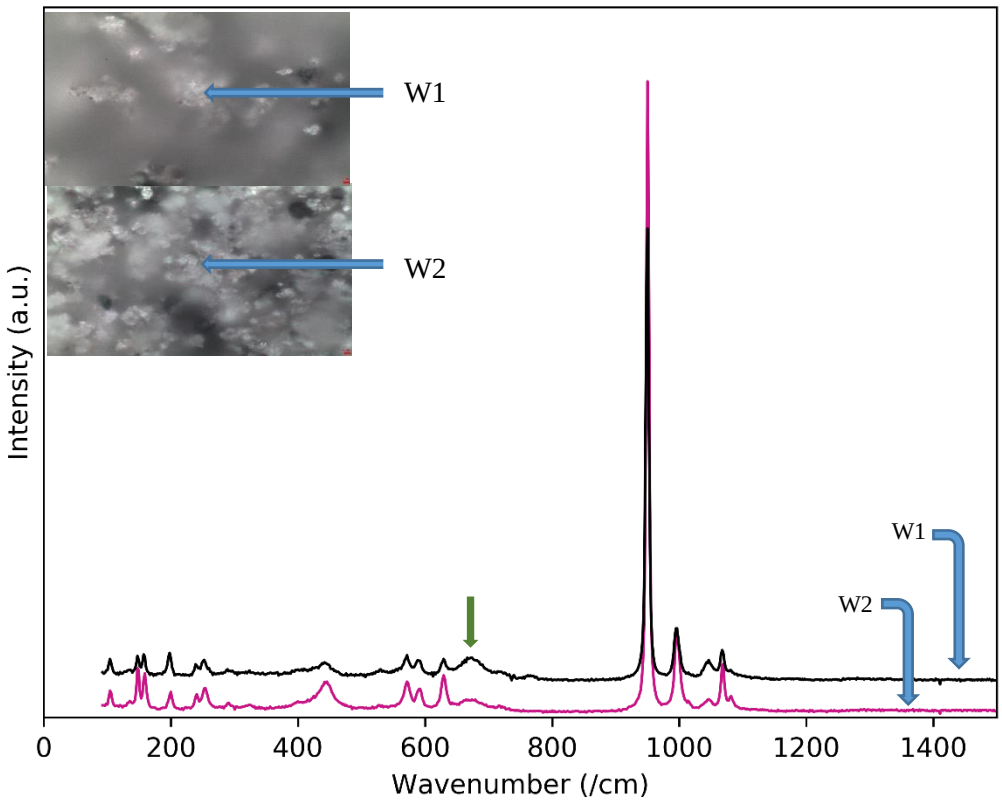

Figure 3.12: Raman spectra for the white particulates in C-LFP (W1/W2). The green arrow indicates the intense peak that could be associated with Fe_3O_4.

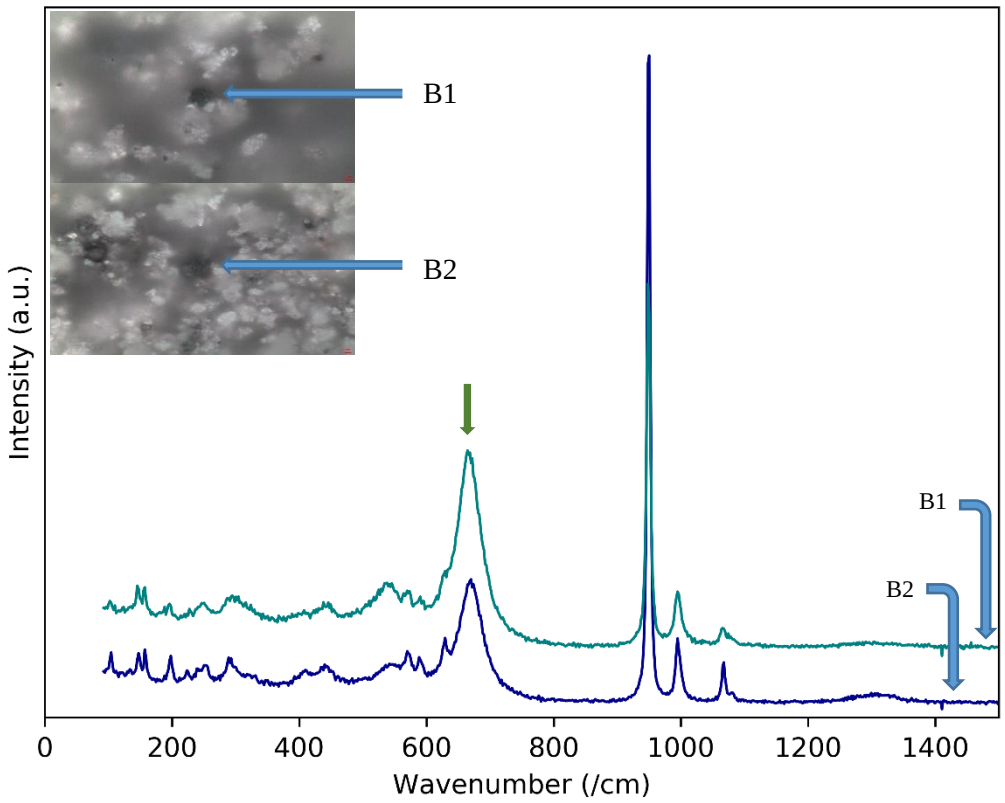

Figure 3.13: Raman spectra for the black phase in C-LFP (B1/B2). The green arrow indicates the intense peak that could be associated with Fe_3O_4.

Table 3.8: Raman modes for the white and black particulates present in C-LFP. $LiFePO_4$ modes are shaded in grey, α-Fe_2O_3 in orange, Fe_3O_4 in green and the unidentified phases are not shaded.

Wavenumbers(/cm)				Assignment
C-LFP (W1)	**C-LFP (W2)**	**C-LFP (B1)**	**C-LFP (B1)**	
104	**104**	**103**	**102**	
134*		134*		
148	**147**	**147**	**146**	
158	**157**	**157**	**156**	PO_4^{3-} rotational and Fe^{2+} translational motion
199	**197**	**197**	**195**	
		223	227	
240	**239**			
253	251	254	247	
290	289	291	299	
		408		
444	**443**	**441**	**442**	υ_2 (PO_4^{3-})
	530	549		
571	**571**	**571**	**571**	
591	**589**	**590**	**591**	
629	**629**	**628**	**626**	υ_4 (PO_4^{3-})
672	672	669	667	
719*	720*			
949	**950**	**948**	**947**	υ_1 (PO_4^{3-})
998	**998**	**995**	**995**	
1045*	1045*			υ_3 (PO_4^{3-})
1068	**1067**	**1066**	**1067**	
1082*		1080*		
		1306	1307	

3.3. Conclusion

Different average and local structure techniques were used to characterise a commercially available $LiFePO_4$ material. From PXRD (with Rietveld refinement) some unidentified peaks that were not accounted for by the $LiFePO_4$ structure were observed. The pre-edge and main edge peaks observed from XAS showed no major peak shifts, compared to literature, signifying that the Fe^{2+} was the main oxidation state present and the local structure was as predicted from previous work and could not be used to identify the impurity. The interatomic distances and disorder did show some deviation to the previously reported values but this could simply be due to the difference in the synthetic method or it may be due to the impurity. Mössbauer spectroscopy also clearly showed Fe^{2+} as the main oxidation state, but also that $LiFePO_4$ was not the only Fe environment present in C-LFP. There was another Fe^{2+} environment that was more distorted than the Fe^{2+} M2 site in $LiFePO_4$ as well as two other Lorentzian sextets that could account for the Fe^{3+} present in the sample. Unfortunately, not all the peaks on either side of the doublet could be accounted for, indicating another possible environment present in the sample. Raman spectroscopy showed that $LiFePO_4$ was present together with an unidentified phase as well certain peaks that could be allocated to α-Fe_2O_3 and Fe_3O_4 with the other peaks possibly overlapping with that of $LiFePO_4$. It was interesting to note that the commercial sample clearly contained impurities (said to be >97% pure) showing that it is not straight-forward to synthesise the pure material. The fact that impurities were noted by PXRD, the least sensitive of these technique, shows that the quantity was at a percentage level on average. The impurity phase(s) could clearly affect the electrochemical performance to some extent, although this aspect was not investigated in this work.

3.4. References

1. Liang, Q., Yue, H., Wang, S., Yang, S., Lam, Kwok ho. and Hou, X. Recycling and crystal regeneration of commercial used LiFePO4 cathode materials. *Electrochim. Acta* **330**, 135323 (2020).

2. Wang, W. and Wu, Y. An overview of recycling and treatment of spent $LiFePO_4$ batteries in China. *Resources, Conservation and Recycling*, **127**, 233–243 (2017).

3. Chen, J., Wang, S. and Whittingham, M. S. Hydrothermal synthesis of cathode materials. *J. Power Sources* **174**, 442–448 (2007).

4. Chen, J., Bai, J., Chen, H. and Graetz, J. In situ hydrothermal synthesis of $LiFePO_4$ studied by synchrotron X-ray diffraction. *J. Phys. Chem. Lett.* **2**, 1874–1878 (2011).

5. Chen, J. and Graetz, J. Study of Antisite Defects in Hydrothermally Prepared $LiFePO_4$ by in Situ X-ray Diffraction. *ACS Appl. Mater. Interfaces* **3**, 1380–1384 (2011).

6. Yang, S., Zavalij, P. Y. and Whittingham, S. M. Hydrothermal synthesis of lithium iron phosphate cathodes. *Electrochem. commun.* **3**, 505–508 (2001).

7. Chen, J., Bai, J., Chen, H. and Graetz, J. In Situ Hydrothermal Synthesis of $LiFePO_4$ Studied by Synchrotron X-ray Diffraction. *J. Phys. Chem. Lett.* **2**, 1874–1878 (2011).

8. Prince, A. A. M., Mylswamy, S., Chan, T. S., Liu, R. S., Hannoyer, B., Jean, M., Shen, C. H., Huang, S. M., Lee, J. F. and Wang, G. X. Investigation of Fe valence in $LiFePO_4$ by Mössbauer and XANES spectroscopic techniques. *Solid State Commun.* **132**, 455–458 (2004).

9. Chen, J., Yue, H., Wang, S., Yang, S., Lam, K. and Hou, X. The hydrothermal synthesis and characterization of olivines and related compounds for electrochemical applications. *Solid State Ionics* **178**, 1676–1693 (2008).

10. Kuwahara, A., Suzuki, S. and Miyayama, M. Hydrothermal synthesis of $LiFePO_4$ with small particle size and its electrochemical properties. *J. Electroceramics* **24**, 69–75 (2010).

11. Sun, X. and Xu, Y. Fe excess in hydrothermally synthesized $LiFePO_4$. *Mater. Lett.* **84**, 139 - 142 (2012).

12. Streltsov, V. A., Belokoneva, E. L., Tsirelson, V. G. and Hansen, N. K. Multipole analysis of the electron density in triphylite, $LiFePO_4$, using X-ray diffraction data. *Acta Crystallogr. Sect. B* **49**, 147–153 (1993).

13. Maccario, M., Croguennec, L., Wattiaux, A., Suard, E., Le Cras, F. and Delmas, C. C-containing $LiFePO_4$ materials - Part I: Mechano-chemical synthesis and structural characterization. *Solid State Ionics* **179**, 2020–2026 (2008).

14. Shi, S., Zhang, H., Ke, X., Ouyang, C., Lei, M. and Chen, L. First-principles study of lattice dynamics of $LiFePO_4$. *Phys. Lett. Sect. A Gen. At. Solid State Phys.* **373**, 4096–4100 (2009).

15. Yiming, W., Giuli, G., Moretti, A., Nobili, F., Fehr, K. T., Paris, E. and Marassi, R. Synthesis and characterization of Zn-doped $LiFePO_4$ cathode materials for Li-ion battery. *Mater. Chem. Phys.* **155**, 191–204 (2015)

16. Jugović, D., Cvjetićanin, N., Mitrić, M. and Mentus, S. Comparison between different LiFePO4 synthesis routes. in *Materials Science Forum*, **555**, 225–230 (2007).

17. Rousse, G., Rodriguez-Carvajal, J., Patoux, S. and Masquelier, C. Magnetic Structures of the Triphylite $LiFePO_4$ and of Its Delithiated Form $FePO_4$. *Chem. Mater.* **15**, 4082–4090 (2003).

18. Islam, M. S., Driscoll, D. J., Fisher, C. A. J. and Slater, P. R. Atomic-scale investigation of defects, dopants, and lithium transport in the $LiFePO_4$ olivine-type battery material.

Chem. Mater. **17**, 5085–5092 (2005).

19. Penner-Hahn, J. E. X-ray absorption spectroscopy in coordination chemistry. in *Coordination Chemistry Reviews* **190–192**, 1101–1123 (1999).

20. Deb, A., Bergmann, U., Cairns, E. J. and Cramer, S. P. X-ray absorption spectroscopy study of the Li_xFePO_4 cathode during cycling using a novel electrochemical in situ reaction cell. *J. Synchrotron Radiat.* **11**, 497–504 (2004).

21. White, E. W. and McKinstry, H. A. Chemical Effect on X-Ray Absorption-Edge Fine Structure. *Advances in X-Ray Analysis* 376–392 (1966).

22. McBreen, J. The application of synchrotron techniques to the study of lithium-ion batteries. *J. Solid State Electrochem.* **13**, 1051–1061 (2009).

23. Waychunas, G. A., Apted, M. J. and Brown, G. E. X-ray K-edge absorption spectra of Fe minerals and model compounds: Near-edge structure. *Phys. Chem. Miner.* **10**, 1–9 (1983).

24. Shulman, G. R., Yafet, Y., Eisenberger, P. and Blumberg, W. E. Observations and interpretation of x-ray absorption edges in iron compounds and proteins. *Proc. Natl. Acad. Sci. U. S. A.* **73**, 1384–1388 (1976).

25. Haas, O., Deb, A., Cairns, E. J. & Wokaun, A. Synchrotron X-ray absorption study of $LiFePO_4$ electrodes. *J. Electrochem. Soc.* **152**, (2005).

26. Lengke, M. F., Ravel, B., Fleet, M. E., Wanger, G., Gordon, R. A. and Southam, G. Precipitation of gold by the reaction of aqueous gold(III) chloride with cyanobacteria at 25-80°C - Studied by X-ray absorption spectroscopy. Can. J. Chem. **85**, 651–659 (2007).

27. Lin, F., Liu, Y., Yu, X., Cheng, L., Singer, A., Shpyrko, O. G., Xin, H. L., Tamura, N., Tian, C., Weng, T. C., Yang, X. Qing., Meng, Y. S., Nordlund, D., Yang, W. and Doeff, M. M. Synchrotron X-ray Analytical Techniques for Studying Materials Electrochemistry in Rechargeable Batteries. Chemical Reviews **117**, 13123–13186 (2017).

28. Westre, T. E., Kennepohl, P., DeWitt, J. G., Hedman, B., Hodgson, K. O. and Solomon, E. I. A multiplet analysis of Fe K-edge 1s → 3d pre-Edge features of iron complexes. *J. Am. Chem. Soc.* **119**, 6297–6314 (1997).

29. Randall, C. R., Shu, L., Chiou, Y. M., Hagen, K. S., Ito, M., Kitajima, N., Lachicotte, R. J., Zang, Y. and Que, L. X-ray Absorption Pre-Edge Studies of High-Spin Iron(II) Complexes. *Inorg. Chem.* **34**, 1036–1039 (1995).

30. Deb, A., Bergmann, U., Cairns, E. J. and Cramer, S. P. Structural investigations of $LiFePO_4$ electrodes by Fe X-ray absorption spectroscopy. *J. Phys. Chem. B* **108**, 7046–7051 (2004).

31. Griffith, J. S. and Orgel, L. E. Ligand-field theory. *Q. Rev. Chem. Soc.* **11**, 381–393 (1957).

32. Wilke, M., Farges, F., Petit, P. E., Brown, G. E. and Martin, F. Oxidation state and coordination of Fe in minerals: An Fe K-XANES spectroscopic study. *Am. Mineral.* **86**, 714–730 (2001).

33. De Groot, F., Vankó, G. and Glatzel, P. The 1s x-ray absorption pre-edge structures in transition metal oxides. *J. Phys. Condens. Matter* **21**, 104207–104214 (2009).

34. Wong, J., Lytle, F. W., Messmer, R. P. and Maylotte, D. H. K-edge absorption spectra of selected vanadium compounds. *Phys. Rev. B* **30**, 5596–5610 (1984).

35. Roe, A. L., Schneider, D. J., Mayer, R. J., Pyrz, J. W., Widom, J. and Que, L. X-ray Absorption Spectroscopy of Iron-Tyrosinate Proteins. *J. Am. Chem. Soc.* **106**, 1676–1681 (1984).

36. Park, K. S., Kang, K. T., Lee, S. B., Kim, G. Y., Park, Y. J. and Kim, H. G. Synthesis of $LiFePO_4$ with fine particle by co-precipitation method. *Mater. Res. Bull.* **39**, 1803–1810 (2004).

37. Yano, J. and Yachandra, V. K. X-ray absorption spectroscopy. *Photosynthesis Research*, **102**, 241–254 (2009).

38. Nam, K., Bak, S., Hu, E., Yu, X., Zhou, Y., Wang, X., Wu, L., Zhu, Y., Chung, K. and Yang, X. Combining In Situ Synchrotron X-Ray Diffraction and Absorption Techniques with Transmission Electron Microscopy to Study the Origin of Thermal Instability in Overcharged Cathode Materials for Lithium-Ion Batteries. *Adv. Funct. Mater.* **23**, 1047–1063 (2013).

39. Rehr, J. J. and Albers, R. C. Theoretical approaches to x-ray absorption fine structure. *Rev. Mod. Phys.* **72**, 621–654 (2000).

40. Dominko, R., Bele, M., Goupil, J. M., Gaberscek, M., Hanzel, D., Arcon, I. and Jamnik, J. Wired porous cathode materials: A novel concept for synthesis of $LiFePO_4$. Chem. Mater. **19**, 2960–2969 (2007).

41. Hsu, K. F., Hu, S. K., Chen, C. H., Cheng, M. Y., Tsay, S. Y., Chou, T. C., Sheu, H. S., Lee, J. F. and Hwang, B. J. Formation mechanism of $LiFePO_4$/C composite powders investigated by X-ray absorption spectroscopy. J. Power Sources 192, 660–667 (2009).

42. Zhao, T., Chu, W., Zhao, H., Liang, X., Xu, W., Yu, M., Xia, D. and Wu, Z. XAS study of $LiFePO_4$ synthesized by solid state reactions and hydrothermal method. in *Nuclear Instruments and Methods in Physics Research, Section A: Accelerators, Spectrometers, Detectors and Associated Equipment* **619**, 122–127 (2010).

43. Giorgetti, M., Berrettoni, M., Scaccia, S. and Passerini, S. Characterization of sol-gel-synthesized $LiFePO_4$ by multiple scattering XAFS. *Inorg. Chem.* **45**, 2750–2757 (2006).

44. Yamada, A., Chung, S. C. and Hinokuma, K. Optimized $LiFePO_4$ for Lithium Battery Cathodes. *J. Electrochem. Soc.* **148**, A224 (2001).

45. Hirose, K., Honma, T., Doi, Y., Hinatsu, Y. and Komatsu, T. Mössbauer analysis of Fe ion state in lithium iron phosphate glasses and their glass-ceramics with olivine-type $LiFePO_4$ crystals. *Solid State Commun.* **146**, 273–277 (2008).

46. Sanchez, M. A. E., Brito, G. E. S., Fantini, M. C. A., Goya, G. F. and Matos, J. R. Synthesis and characterization of $LiFePO_4$ prepared by sol-gel technique. *Solid State Ionics* **177**, 497–500 (2006).

47. Hamelet, S., Gibot, P., Casas-Cabanas, M., Bonnin, D., Grey, C. P., Cabana, J., Leriche, J. B., Rodriguez-Carvajal, J., Courty, M., Levasseur, S., Carlach, P., Van Thournout, M., Tarascon, J. M. and Masquelier, C. The effects of moderate thermal treatments under air on $LiFePO_4$-based nano powders. *J. Mater. Chem.* **19**, 3979–3991 (2009).

48. Delacourt, C., Poizot, P., Bonnin, D. and Masquelier, C. Lithium-Insertion Mechanism in Crystalline and Amorphous $FePO_4 \cdot nH_2O$. *J. Electrochem. Soc.* **156**, A595 (2009).

49. Hannoyer, B., Prince, A. A. M., Jean, M., Liu, R. S. & Wang, G. X. Mössbauer study on $LiFePO_4$ cathode material for lithium ion batteries. in *ICAME 2005* 767–772 (Springer Berlin Heidelberg, 2006).

50. Amisse, R., Sougrati, M. T., Stievano, L., Davoisne, C., Dražič, G., Budič, B., Dominko, R. and Masquelier, C. Singular Structural and Electrochemical Properties in Highly Defective $LiFePO_4$ Powders. *Chem. Mater.* **27**, 4261–4273 (2015).

51. Porcher, W., Moreau, P., Lestriez, B., Jouanneau, S., Le Cras, F. and Guyomard, D. Stability of $LiFePO_4$ in water and consequence on the Li battery behaviour. *Ionics (Kiel).* **14**, 583–587 (2008).

52. Martin, J. F., Yamada, A., Kobayashi, G., Nishimura, S., Kanno, R., Guyomard, D. and Dupré, N. Air Exposure Effect on $LiFePO_4$. *Electrochem. Solid-State Lett.* **11**, A12 (2008).

53. Cuisinier, M., Martin, J. F., Dupré, N., Yamada, A., Kanno, R. and Guyomard, D. Moisture driven aging mechanism of $LiFePO_4$ subjected to air exposure. *Electrochem. commun.* **12**, 238–241 (2010).

54. Xia, X., Wang, Z. and Chen, L. Regeneration and characterization of air-oxidized $LiFePO_4$. *Electrochem. commun.* **10**, 1442–1444 (2008).

55. Andersson, A. S., Kalska, B., Häggström, L. and Thomas, J. O. Lithium extraction/insertion in LiFePO4: An X-ray diffraction and Moessbauer spectroscopy study. Solid State Ionics 130, 41–52 (2000).

56. Burba, C. M. and Frech, R. Raman and FTIR Spectroscopic Study of Li_xFePO_4 ($0 \leq x \leq 1$). *J. Electrochem. Soc.* **151**, A1032 (2004).4).

57. Wu, J., Krishna Phani Dathar, G., Sun, C., Theivanayagam, M. G., Applestone, D., Dylla, A. G., Manthiram, A., Henkelman, G., Goodenough, J. B. and Stevenson, K. J. In situ Raman spectroscopy of $LiFePO_4$: size and morphology dependence during charge and self-discharge. *IOP Publ. Nanotechnol. Nanotechnol.* **24**, 424009–424018

(2013).

58. Paques-Ledent, M. T. and Tarte, P. Vibrational studies of olivine-type compounds-II Orthophosphates, -arsenates and -vanadates $A^{I}B^{II}X^{V}O_4$. *Spectrochim. Acta Part A Mol. Spectrosc.* **30**, 673–689 (1974).

59. Baddour-Hadjean, R. and Pereira-Ramos, J. P. Raman microspectrometry applied to the study of electrode materials for lithium batteries. *Chem. Rev.* **110**, 1278–1319 (2010).

60. Paraguassu, W., Freire, P. T. C., Lemos, V., Lala, S. M., Montoro, L. A. and Rosolen, J. M. Phonon calculation on olivine-like $LiMPO_4$ (M = Ni, Co, Fe) and Raman scattering of the iron-containing compound. *J. Raman Spectrosc.* **36**, 213–220 (2005).

61. Kelly, S. D., Hesterberg, D. & Ravel, B. *Analysis of Soils and Minerals Using X-ray Absorption Spectroscopy*. 387–463 (John Wiley & Sons, Ltd, 2015).

62. Kelly, S. D. & Ravel, B. EXAFS energy shift and structural parameters. in *AIP Conference Proceedings* **882**, 132–134 (2007).

63. Li, Z. and Shinno, I. Next nearest neighbor effects in triphylite and related phosphate minerals. *Mineral. J.* **19**, 99–107 (1997).

64. de Faria, D. L. A. and Lopes, F. N. Heated goethite and natural hematite: Can Raman spectroscopy be used to differentiate them? *Vib. Spectrosc.* **45**, 117–121 (2007).

Chapter 4

The chronicles of synthesising $LiFePO_4$

4.1 Introduction

$LiFePO_4$ can be synthesised using either solid state or solution based syntheses.[1] The solid state synthesis produces well-ordered and crystalline materials with the main disadvantages being the very high energy and time consuming process that produces large particles and low purity products.[1] The most common solid state-based syntheses include solid state, mechano-chemical activation and carbo-thermal treatment.[1]

The solid state synthetic route involves the thorough mixing of stoichiometric amounts of the iron precursors ($FeC_2O_4•2H_2O$, $Fe(CH_3COO_2)$, $FePO_4(H_2O)_2$), the lithium precursors ($LiOH•2H_2O$, Li_2CO_3, LiF, CH_3COOLi, LiOH) and the phosphorus precursors ($NH_4H_2PO_4$, $(NH_4)_2HPO_4$).[1–9] Mixing can occur using either ball-milling or a mortar and pestle with or without the addition of a solvent.[2–9] Heat treatment of the mixed samples can occur either through a one step or two step process in a reducing atmosphere. The first heat treatment generally occurs between 320 – 800ºC for 3 – 10 hours and the second step occurs between 400 – 800ºC for 6 – 24 hours and the sample is reground between heating steps.[2–9] The temperature is an important parameter during synthesis and affects the crystallinity and the particle size.[1]

Mechano-chemical activation involves the chemical activation of stoichiometric amounts of the precursors such as FeC_2O_4, dried $Fe_3(PO4)_2•5H_2O$ ($FeSO_4•7H_2O$ + Na_3PO_4) and $FeC_2O_4•2H_2O$ as the iron precursors, Li_2CO_3 and Li_3PO_4 as the lithium precursor and $(NH_4)_2HPO_4$ and $NH_4H_2PO_4$ as the phosphorous source with the use of high energy ball-milling.[1,10–13] The ball-milling time varies between 10 min – 24 hours[12–16] and the resulting mixed product is then heat-treated for any time between 15 min – 10 hours at temperatures between 400– 800ºC.[12–16] Heat treatment usually occurs under an atmosphere of N_2 or H_2/Ar mixture. The heat treatment conditions are important to limit the formation of impurities.[1,10] This synthetic procedure produces well crystallised materials, small and uniform particles and utilises lower heat treatment temperatures due to the initial chemical activation. The temperature needed for crystallization was reduced to 432°C rather than the original 502°C.[14] The disadvantage of this route is the possible contamination of LiFePO4 for the ball-milling medium[1] and the energy intensive and time consuming process.[10]

Carbothermal treatment uses an iron(III)-precursor with the required addition of a carbon source for the reduction of iron(III).[1,10] The iron (Fe_2O_3, $FePO_4$, $FePO_4•4H_2O$), lithium (Li_2CO_3, $LiOH•H_2O$, LiH_2PO_4) and phosphorous ($NH_4H_2PO_4$, $FePO_4$, $FePO_4•4H_2O$, LiH_2PO_4) precursors together with a carbon source (carbon black, glucose) is mixed thoroughly and ground together using either high energy ball-milling or a mortar and pestle.[17–21] The mixture is then placed in a temperature controlled furnace for 8 – 12 hours at 560– 750ºC in either a N_2 or Ar atmosphere.[17–21] This synthetic route is considered more cost efficient when using the slightly cheaper iron(III) rather than iron(II) precursor[10] and produces fine, uniform particles.[1] The important parameters to control during synthesis is the temperature, reducing agents and precursors and to ensure that all the precursors remain in contact.[1]

Solution based syntheses are usually performed at lower temperatures and thereby utilising less energy to produce LiFePO4. Small and uniform particles are formed as well more uniform carbon coating when added to improve the electronic conductivity of the material.[1] The most common solution-based syntheses include sol-gel, co-precipitation and hydrothermal.[1]

For a sol-gel synthesis, the precursors such as iron powder, $FeC_2O_4•2H_2O$ as the Fe precursor, $LiNO_3$ as the lithium precursor and $(NH_4)H_2PO_4$ as the phosphorous precursor are mixed together with citric acid or a citrate precursor aqueous solution (chelating agent) to form a homogenous mixture.[1,22,23] The mixed solution is then heated on a hotplate under continuous stirring until a gel is formed. The gel is then dried at 60 – 140ºC for 12 hours – 1 week to form a powder.[22–29] The dried powder is then ground in a mortar and pestle followed by heat treatment under an inert atmosphere for 15 min – 20 hours at 400 – 850ºC.[22–29] The important parameters to control during the sol-gel synthesis is temperature, reaction time and the pH of the solution. No mention is made of the actual pH of the solution.[1] These parameters affect the particle morphology. Sol-gel syntheses produce high purity products and small particles.[1]

For a co-precipitation synthesis stoichiometric amounts of the aqueous lithium precursor (LiOH) is added to a solution containing stoichiometric amounts of the aqueous iron ($(NH_4)_2Fe(SO_4)_2•6H_2O$) and phosphorous (H_3PO_4, $NH_4H_2PO_4$) precursors while under continuous stirring.[14,30,31] The precursors co-precipitate under the right pH conditions and form a slurry. The slurry is then washed and dried to form amorphous $LiFePO_4$.[14,30–32] The above process can be performed under an N_2 atmosphere. To produce crystalline $LiFePO_4$ the powder is heat-treated for 12 – 18 hours at 550 – 800ºC under a N_2 or Ar atmosphere.[14,30–32] It is important to control the pH (no mention of the pH value) during a co-precipitation synthetic

route. Co-precipitation produces well crystallised powders with small particles of high purity, but it can also produce a wide variety of particle sizes depending on the conditions.[1]

All the precursors ($FeSO_4•7H_2O$, $LiOH•H_2O$, $LiOH$, H_3PO_4, $(NH_4)_3PO_4$, $(NH_4)_3PO_4•3H_2O$) have to be in solution when using a hydrothermal synthesis by dissolving the precursors in distilled water. After mixing of the precursors, the homogenous solution is then added to a stainless steel autoclave[1,33,34] and a reaction temperature of 120 – 220ºC is applied for 2 – 24 hours.[2,35–43] The precipitate that forms during the reaction has to be washed either with water or with solvents such as ethanol and acetone. The precipitate is dried for 1 – 24 hours at 40 – 100ºC and can be performed in air or under vacuum. [2,35–43] An additional heat treatment under an argon or nitrogen atmosphere can be added and should be performed if carbon was added. The important parameters to control during a hydrothermal synthesis is the reaction rate, temperature and the concentration of the precursors.[1] This synthetic route produces small particles,[1,35,36,40,43] which is a very low energy consuming[1,34,39,44,45] and inexpensive[34,44] process but inherent defects in the structure are common.[34,41,44–46]

This chapter focuses on the developmental stages of the hydrothermal approach used (described in section 2.1.2.) to optimise the reaction time, reaction temperature as well as applying different strategies to improve the reproducibility of the product. PXRD was used to determine the average structure as well as identify the different phases. Rietveld refinement was only performed on selected samples. The refinements were used to determine phase percentages, structural defects as well as interatomic bond distances. XAS was used to determine the oxidation state, distortion around the iron atom and EXAFS analysis to determine the local structure and the disorder around the iron atom. Mössbauer spectroscopy was utilised to determine the different type of iron environments as well as the total percentage of Fe^{2+} present in the $LiFePO_4$ environment and Raman spectroscopy was used to identify $LiFePO_4$ as well any other possible amorphous impure phases present. This synthesis is low cost and low energy because of the use of teflon bombs rather than the commercially used autoclave and the reaction temperature which is a much lower than the temperatures normally used for other syntheses as described above. For each modification applied to the synthesis the changes in the experimental procedure, results, discussion and a conclusion is given before continuing with the next modification. Preliminary PXRD data was obtained using a laboratory diffractometer, as shown with the 12hours-25 and 48hours-25 sample, before collecting synchrotron PXRD data described in this chapter.

4.2 Experimental Procedure, Results, Discussion and Section Conclusions

4.2.1. Synthesis time

To determine the optimum reaction time two different samples were prepared at two different reaction times. The same synthesis as outlined in section 2.1.2. was used with the only modification applied was the synthesis time. The Teflon bombs were filled to 25% of their total volume for both the samples. After adding the solution to the Teflon bombs the bombs were placed in the oven at 120°C for 12 hours and 48 hours, respectively.

The diffraction patterns of the samples heated for 12 hours (**12hours-25,** where 25 represents the % filling of the bombs) (Fig. 4.1) and 48 hours (**48hours-25)** (Fig. 4.2) were refined to compare the average structure. The X-ray wavelength used in the refinement was 0.166316(4) Å. The reliability factors for the refinement are given in Table 4.1. There is slight variation between the two samples indicating that the refineable parameters accounted for similar features in both samples. The other two samples, **48hours-50** and **48hours-75**, given in Tables 4.1 – 4.4 will be discussed in the section to follow. Both samples indexed as $LiFePO_4$. The 48hours-25 sample (Fig. 4.2) showed sharper peaks than that of 12hours-25 (Fig. 4.1) and also a higher degree of purity as shown with the multiphase refinement. The 12hours-25 sample had slightly more intensity mismatches indicating that there were other structural defects that were not accounted for. The lattice parameters for $LiFePO_4$ were refined throughout the refinement whereas the lattice parameters and the thermal parameters for the impure phase were only refined once (not shown here). The refined lattice parameters and volume for both samples are given in Table 4.2 and is smaller for the 12hours-25. These parameters are similar to those determined by other groups that used a hydrothermal synthesis.[37–40,44] A summary of these parameters can also be found in Table 3.1.

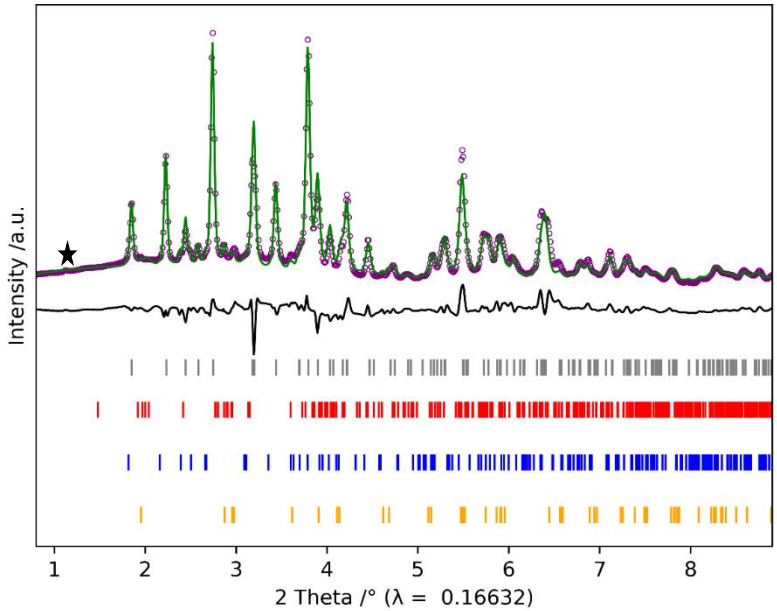

Figure 4.1: Powder diffractogram of the 12hours-25 sample showing the observed (purple), calculated (green) and difference (black) plots generated from a Rietveld refinement analysis. Bragg reflections for $LiFePO_4$, Li_3PO_4, the Fe-impurity and $LiFePO_4(OH)$ are indicated with the grey, blue, yellow and red markers, respectively. (*) indicates an unidentified impurity.

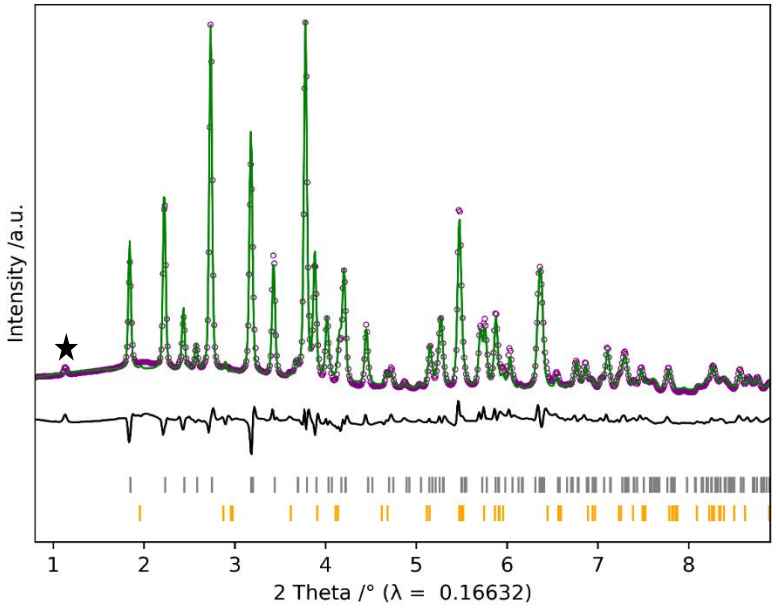

Figure 4.2: Powder diffractogram of 48hours-25 showing the observed (purple), calculated (green) and difference (black) plots generated from a Rietveld Refinement analysis. Bragg reflections for $LiFePO_4$ and the Fe- impurity are indicated with the grey and yellow markers, respectively. (*) indicates an unidentified impurity.

Table 4.1: Reliability factors for each Rietveld refinement.

	R_{wp}	R_p	R_{exp}	GOF
12hours-25	7.81	5.60	16.01	0.49
48hours-25	6.73	5.21	18.18	0.37
48hours-50	6.89	5.22	16.68	0.41
48hours-75	6.99	5.36	15.64	0.45

Table 4.2: Selected structural parameters of the refined $LiFePO_4$ structures for the different samples.

Sample	a (Å)	b (Å)	c (Å)	Volume ($Å^3$)
12hours-25	10.30(2)	5.9613(9)	4.7030(8)	288.64(8)
48hours-25	10.335(8)	5.9907(5)	4.7043(4)	291.25(4)
48hours-50	10.331(8)	5.9838(5)	4.7029(4)	291.73(4)
48hours-75	10.338(8)	5.9859(4)	4.7048(4)	291.15(3)

A multiphase Rietveld analysis showed that $LiFePO_4$ was the major phase in both the 12hours-25 sample and the 48hours-25 sample (Table 4.3). Four different impurity phases were identified in 12hours-25 (Table 4.3) – tavorite ($LiFePO_4(OH)$), lithiophosphate (Li_3PO_4), an Fe-impurity (s.g. $I4_1/a$, #88) and an unidentified phase (indicated with * on Figs. 4.1 and 4.2.). The Fe-impurity that was matched to these peaks had a chemical formula of $Fe_{3.44}(PO_4)_{1.98}O_{2.08}$ as studied by Schmid-Beurmann[47] as part of a solid solution series of $\beta - Fe_2(PO_4)O$ and $Fe_4(PO_4)_3(OH)_3$. The phase identified is closer to the $Fe_4(PO_4)_3(OH)_3$ endmember as no hydrogen was present in the chemical formula. This phase is part of the tetragonal space group and the octahedra present contains both Fe^{2+} and Fe^{3+} on the 8f site. These cations are distorted over the octahedra sites.[47] This phase will be referred to as the Fe-impurity throughout. Two different impurity phases were identified in 48hours-25 (Table 4.3) – the Fe-impurity (s.g. $I4_1/a$, #88) and the same unidentified phase (indicated with * on Fig 2) as shown in Figure 1. Comparing the intensity of the peak (*) in Figure 4.1 and Figure 4.2, the peak is more defined in Figure 4.2 indicating that the impurity is present in a higher percentage in 48hours-25. The Fe-impurity, which is the lowest phase present in both 12hours-25 and 48hours-25, was not detected in both samples using laboratory instrumentation (Figs. 4.3 and 4.4) but was detected using with the synchrotron (Figs. 4.1. and 4.2) No other phases except $LiFePO_4$ was detected

in the laboratory PXRD. The unidentified phase was not evident possibly due to the limited 2theta range of the instrument as seen in Figure 4.3 and Figure 4.4. This highlights the advantages of using synchrotron data.

Table 4.3: Multiphase analysis (%) of the undoped $LiFePO_4$.

	$LiFePO_4$	**Fe-impurity**	**Li_3PO_4**	**$LiFePO_4(OH)$**
12hours-25	89.65	1.05	2.95	6.36
48hours-25	99.18	0.82	-	-
48hours-50	96.73	0.58	2.68	-
48hours-75	86.60	6.39	4.63	2.38

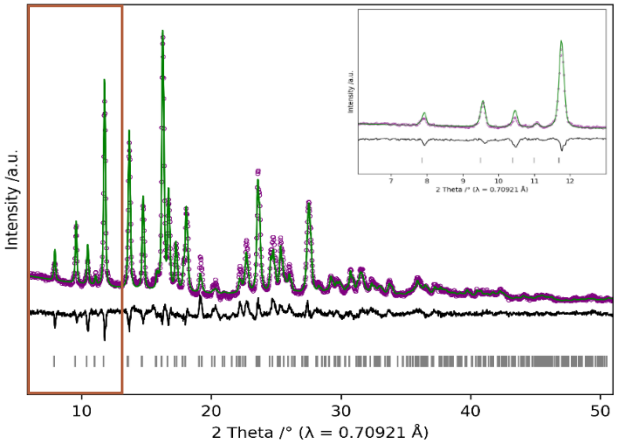

Figure 4.3: Laboratory powder diffractogram of the 12hours-25 sample showing the observed (purple), calculated (green) and difference (black) plots generated from a Rietveld refinement analysis. The inset is indicated by the brown rectangle. Bragg reflections for $LiFePO_4$ are indicated with the grey.

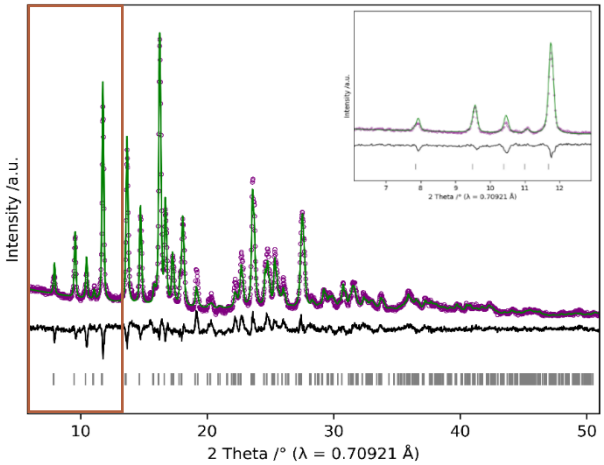

Figure 4.4: Laboratory powder diffractogram of the 48hours-25 showing the observed (purple), calculated (green) and difference (black) plots generated from a Rietveld Refinement analysis. The inset is indicated by the brown rectangle. Bragg reflections for $LiFePO_4$ are indicated with the grey markers.

Refining the occupancies of the M2 and the M1 site showed that neither site was fully occupied with Fe^{2+} or Li^{+}, respectively (Table 4.4). No Li^{+} was found on the M2 site although this site showed the presence of vacancies in both samples. The 48hours-25 had the highest percentage of Fe^{2+} or Fe^{3+} (referred to as Fe) occupying this M2 site as well as a higher percentage of Li^{+} occupying the M1 site.

Table 4.4: The percentage Fe^{2+} occupying the M2 site (Fe^{2+}), vacancies on the M2 site and Li^{+} and Fe^{2+} occupying the M1 site (Li^{+}) in the refined $LiFePO_4$ structures.

Sample	12hours-25	48hours-25	48hours-50	48hours-75
M2 (Fe) occupancy	96(2)	98(1)	98(1)	98(2)
M2 (Fe) vacancy	4	2	2	2
M1 (Li^{+}) occupancy	88(1)	92.7(8)	92.2(8)	92(1)
M1 (Fe) occupancy	12(1)	7.3(7)	7.8(8)	8(1)

Mössbauer spectroscopy was used to determine the oxidation state of the Fe atom as well as the different Fe environments presents in the sample. It was also used to indicate how much Fe^{2+} was present in the $LiFePO_4$ samples. Three different Fe environments were identified using Voigt doublets (Fig. 4.5a and Fig. 4.5b). Two different Fe^{2+} environments and one Fe^{3+} environment was identified in the both 12hours-25 and 48hours-25 samples. The first site is Fe^{2+} in $LiFePO_4$ (Table 4.5)[5,9,41,48–52] in a distorted octahedral environment and is already distorted due to the sharing of oxygen by both the iron and the phosphorous. The second site is assigned to Fe^{2+} in a more distorted $LiFePO_4$ environment (Table 4.5)[49,52] which is even more distorted than the environment commonly found in $LiFePO_4$. The deviation in quadrupole splitting (ΔE_Q) indicates an increase in distortion.[49,52] The third environment is that of Fe^{3+} present on the M2 site present as defects in the structure[48,49,51,52] (Table 4.5). The ΔE_Q is slightly larger than that of Fe^{3+} present on the M1 site.[49,50,52]

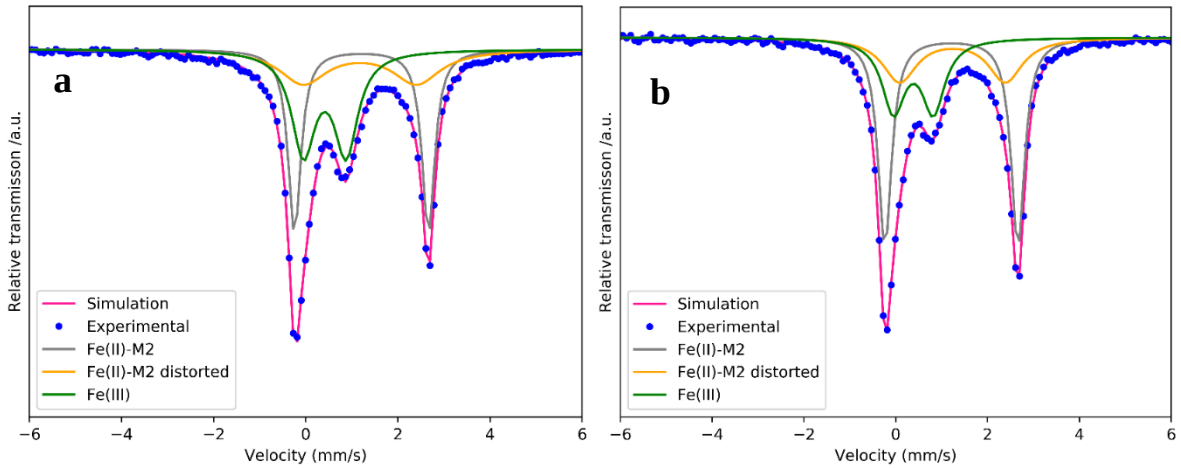

Figure 4.5: Mössbauer spectra for (a) the 12hours-25 and (b) the 48hours-25 samples showing the different environments present.

Table 4.5: Different isomer shifts (δ – mm/s) and quadrupole splitting (ΔE_Q – mm/s) for the 12 and 48 hour samples.

	Fe(II) – M2		**Fe(II) –M2 distorted**		**Fe(III)**	
	δ	ΔE_Q	δ	ΔE_Q	δ	ΔE_Q
12hours-25	1.21(1)	2.91(1)	1.17(1)	2.46(2)	0.41(1)	0.92(1)
48hours-25	1.21(1)	2.90(1)	1.24(1)	2.30(1)	0.39(1)	0.87(1)

The total Fe^{2+} (Table 4.6) is most abundant in the 48hours-25 sample. The Fe^{2+} in the less distorted $LiFePO_4$ is the major phase in the 48hours-25 sample but not for the 12hours-25 sample. Fe^{2+} in $LiFePO_4$ and Fe^{3+} were identified as the major phases in 12hours-25. The increase of Fe^{3+} in the 12hours-25 was also seen by PXRD where there were more Fe^{3+} impurity phases present (Table 4.3).

Table 4.6: Percentage contribution from each form of Fe and the total Fe in the 12 and 48 hour samples.

	Fe(II) – M2	**Fe(II) –M2 distorted**	**Fe(III)**	**Total Fe**	
				Fe^{2+}	**Fe^{3+}**
12hours-25	37(5)	25(3)	38(5)	62	38
48hours-25	47(9)	28(6)	25(5)	75	25

The disorder around the $Fe^{2+}$and Fe^{3+} atoms (Table 4.7) were probed using the full width at half maximum line width Lorentzian contribution (Γ). $Fe^{2+}$and Fe^{3+} in an ordered environment has a Γ of 0.2 – 0.3 mm/s as determined by other studies.[49,50,53] The disorder for Fe^{2+} in the less distorted environment is similar for both samples. The more distorted Fe^{2+} and the Fe^{3+} environments show a higher disorder around the $Fe^{2+}$and Fe^{3+} atom. The increase in disorder for Fe^{2+} in a more distorted $LiFePO_4$ environment and Fe^{3+} can be caused by the distribution of Fe^{3+} on the Li and Fe^{2+} site.[49,50] The larger Γ can usually be observed for Fe^{3+} and can be associated with Fe^{3+} distributed on the M2 site, the presence of amorphous Fe^{3+} phases and surface defects that contain Fe^{3+}.[50] The larger Γ observed for Fe(II) – M2 distorted could be an effect of the more distorted environment and possibly Fe^{3+} on this site as well.

Table 4.7: The full width half maximum line width (*Γ* – mm/s) value for the 12 and 48 hour samples.

	Fe(II) – M2	**Fe(II) –M2 distorted**	**Fe(III)**
12hours-25	0.33(1)	1.24(2)	0.61(1)
48hours-25	0.35(1)	0.89(1)	0.60(1)

PXRD and Mössbauer spectroscopy was used to determine the optimum synthesis time between the 12 and 48 hour samples. The 48 hour sample was determined to be the most promising. Rietveld refinements showed that the 48hours-25 sample had the least amount of impurities, the highest percentage of Fe on the M2 site and Li occupying the M1 site. Mössbauer spectroscopy also showed that the 48hours-25 had the highest percentage of Fe^{2+} and the lowest percentage of Fe^{3+}.

4.2.2. Percentage volume of the solution in the Teflon bombs

The extent to which the bomb is filled should influence the pressure in the bomb when heated at 120 °C. To determine the percentage to which the bombs should be filled, to produce the desired product, they were filled to - 25% (the previous synthesis was used), 50% and 75% and the general outlined synthesis described section 2.1.2. was used. All the samples were placed in the oven at 120 °C for 48 hours. The longer time was sufficient for the larger sample volumes to heat up.

Based on the antisite defect analysis as well as the total Fe^{2+} in both samples determined using Mössbauer spectroscopy as shown in the previous section the more optimal synthesis time was determined to be 48 hours. To determine what the optimum filling percentage of the Teflon bombs (as this could affect the pressure in the bomb), samples were prepared by also filling these to 50% and 75% of the total volume. XRD and Rietveld analysis were performed on the 50% filled: **48hours-50** (Fig. 4.6) and 75% filled: **48hours-75** (Fig. 4.7) samples. The same refinement method and X-ray wavelength was used for these samples as described in section 4.2.1.2.1. Rietveld error indices can be found in Table 4.1 for ease of comparison to that of the 48hour-25 sample discussed in the previous section. All the peaks in the different samples were accounted for except for the same unidentified impure phase found in the 48hours-25 sample (Fig. 4.1). A few minor intensity mismatches were present indicating that not all the structural features were accounted for in the refinement.

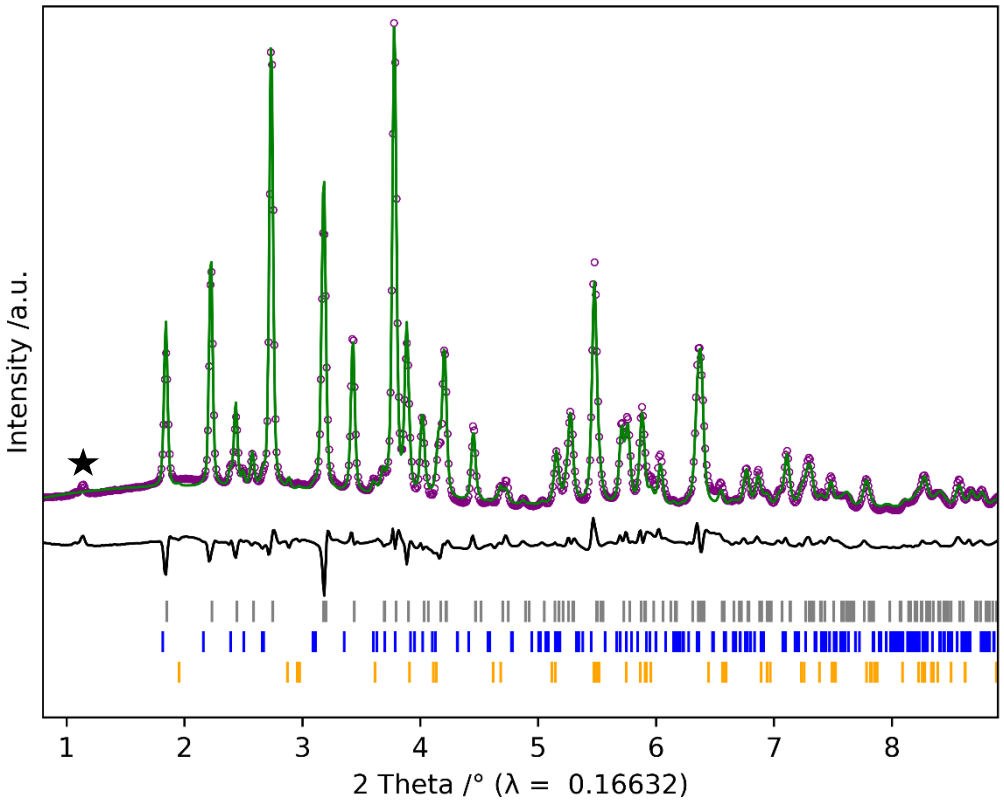

Figure 4.6: Powder diffractogram of the 48hours-50 sample showing the observed (purple), calculated (green) and difference (black) plots generated from a Rietveld Refinement analysis. Bragg reflections for $LiFePO_4$, Li_3PO_4 and the Fe-impurity are indicated with the grey, blue and yellow markers, respectively. (*) indicates the unidentified impurity.

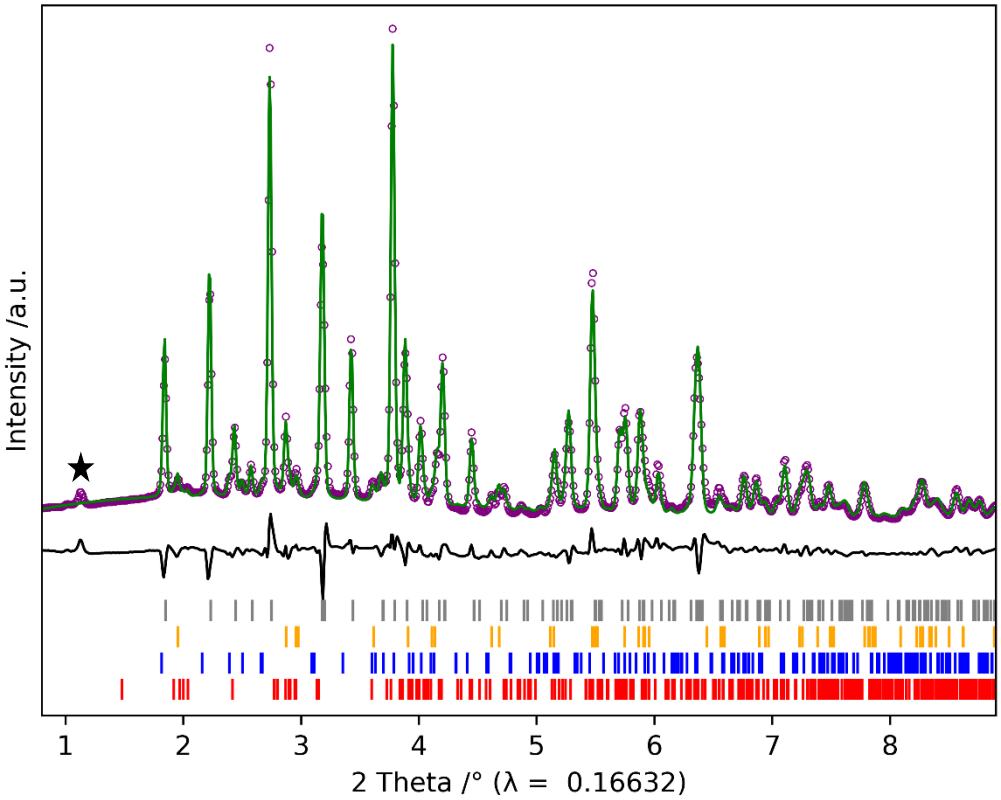

Figure 4.7: Powder diffractogram of the 48hours-75 sample showing the observed (purple), calculated (green) and difference (black) plots generated from a Rietveld Refinement analysis. Bragg reflections for $LiFePO_4$, Li_3PO_4, the Fe-impurity and $LiFePO_4(OH)$ are indicated with the grey, blue, yellow and red markers, respectively. (*) indicates the unidentified impurity.

There was no significant difference between the lattice parameters (Table 4.2) for the 48hours-25, 48hours-50 and 48hours-75 samples, which compares well to those reported by other groups (Table 3.1).[37–40,44]. $LiFePO_4$ was present as the major phase in all three samples, but with the 48hours-75 sample having almost 10% less $LiFePO_4$ than the other two samples (Table 4.3). Li_3PO_4 and the same Fe-impurity were present in both the 48hours-50 and 48hours-75 samples, with $LiFePO_4(OH)$ also being present in the 48hours-75 sample. The same unidentified phase (indicated with *) is present in all the samples with a possible variation in the percentage of this phase present.

Refining the M2 (Fe^{2+}) and M1 (Li^+) sites of the $LiFePO_4$ component in the samples showed that for all three 48hours samples the M2 (Fe^{2+}) site was not fully occupied with 2% vacancies present (Table 4.4). The 48hours-50 and 48hours-75 samples show similar percentages of Li^+ occupying the M1 site (~92.2 and ~92%, respectively), whereas the 48hours-25 sample (92.7%) had a slightly higher percentage of Li^+ occupying the M1 site.

The 48hours-25 sample contained the least presence of defects and impurities (0.82%), and hence further syntheses were done using a 25% filling of the Teflon bombs and at a 48 hour heating time.

4.2.3. Determination of the Molar Ratio - *x*Li:Fe:PO_4

Determining the optimum lithium molar ratio is important as a lithium deficient system can lead to poor electrochemical performance and a lithium excess system could lead to the formation of impurity phases.[54,55] More detailed information on these studies can be found in section 5.1. To determine the optimum lithium molar ratio *x*Li:Fe:PO_4, different ratios (x = 2, 2.5, 3) were used to potentially eliminate the formation of impurity phases. The synthesis was conducted largely under a nitrogen atmosphere (Image 4.1), to eliminate phases cause by air exposure, by purging the solutions but still using the general synthesis outline as described in section 2.1.2. The flow rate N_2 was slow enough, 47kPa, to allow for the slow bubbling so that no solution splashed on the sides of the vessel. The deionised water used for the dissolution of $FeSO_4$•$7H_2O$ and LiOH was not purged but the water used to rinse the sample vessel with was purged. Water was added to the LiOH first since LiOH dissolved relatively slow and then also added to the $FeSO_4$•7H2O/H_3PO_4 mixture while the LiOH solution was under continuous purging and stirring. After the dissolution of both the Fe^{2+}-salt and LiOH the solutions were left to purge further under continuous stirring for another 5 minutes. The Teflon bombs were purged for 10 minutes. The empty Teflon bomb had N_2 flowing through so that minimal air entered the cell when the solution mixture was added. The LiOH solution was added dropwise to the $FeSO_4$/H_3PO_4 solution using a syringe. After the addition, the mixture was thoroughly mixed and purged for another 5 minutes producing a thick blueish-grey mixture. The solution was added to the Teflon bomb after which purged water was then used to rinse the vessel and subsequently also added to the bomb. The bomb was then tightly sealed and placed in the oven at 120°C for 48hours.

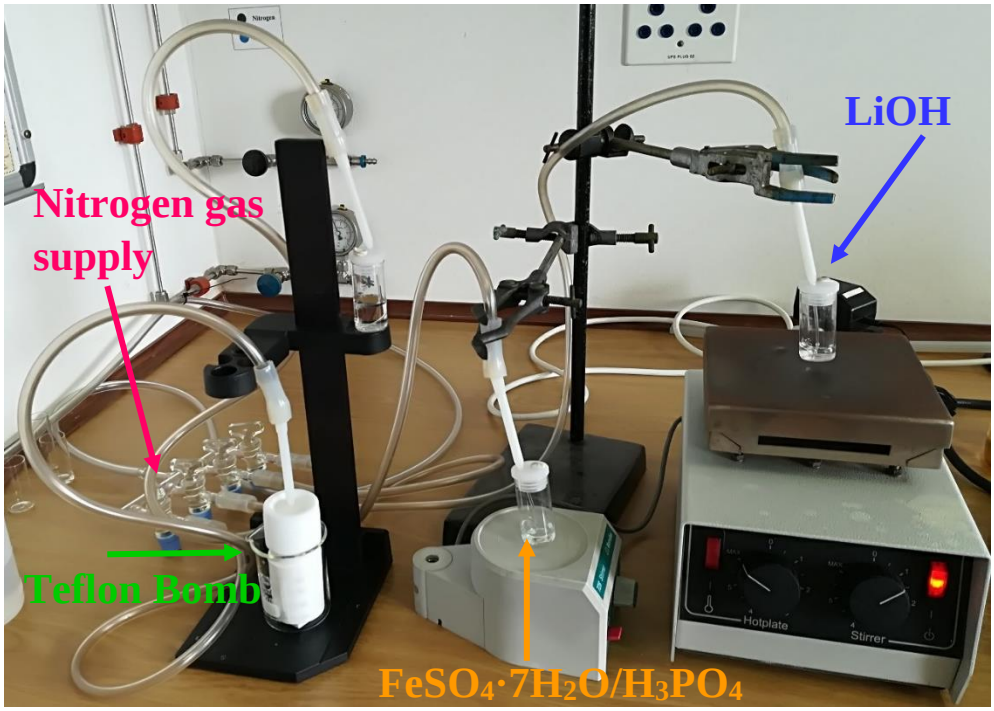

Image 4.1: Synthetic setup to allow for the purging of the LiOH and $FeSO_4 \cdot H_2O/H_3PO_4$ solution.

Samples prepared using varying ratios of added Li^+, namely *x*Li:Fe:PO_4 where *x*=2, 2.5 and 3. The samples were named **LFP-2**, **LFP-2.5** and **LFP-3**, respectively; **a** and **b** indicate duplicate samples. These samples were analysed by XRD (X-ray wavelength of 0.166316(4) Å) and Mössbauer spectroscopy. It is expected that the Fe^{3+} content should decrease due to the effect of purging the solutions to remove the effect of air exposure. Rietveld analysis was not performed on LFP-2a/b (Fig. 4.8) and LFP-2.5a/b (Fig. 4.9) samples since phase identification showed that there were multiple other phases present together with the $LiFePO_4$ phase. The broad underlying peak seen at ~2° is most likely amorphous phases present. The impurity phases in LFP-2a and b were similar, and those in LFP-2.5a and b were comparable, although discrepancies between the sets of LFP-2 and LFP-2.5 samples were noted.

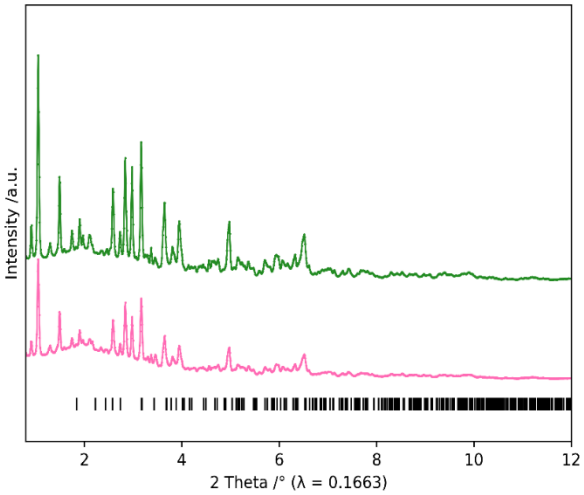

Figure 4.8: (a) Powder diffractogram of the LFP-2a (pink) and LFP-2b (green) samples showing the observed plots. Bragg reflections for $LiFePO_4$ are indicated with the black markers.

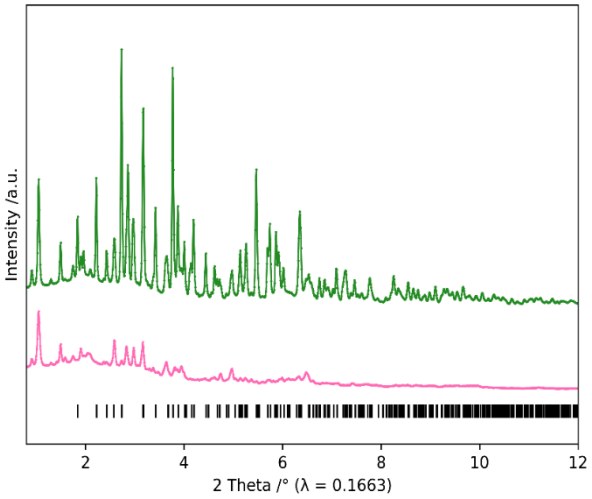

Figure 4.9: Powder diffractogram of the LFP-2.5a (pink) and LFP-2.5b (green) sample showing the observed plots. Bragg reflections for $LiFePO_4$ are indicated with the black markers.

Rietveld analysis was used to investigate LFP-3a (Fig. 4.10) and LFP-3b (Fig. 4.11). All peaks were accounted for during this refinement taking into account both $LiFePO_4$ and the Fe-impurity phase described in section 4.2.1. The Fe-impurity phase was not present in the laboratory data for LFP-3b. The Rietveld error indices can be found in Table 4.8. The error indices for both samples are very similar. There are some peak intensities mismatches and could be due to some defects not being accounted for during the refinement.

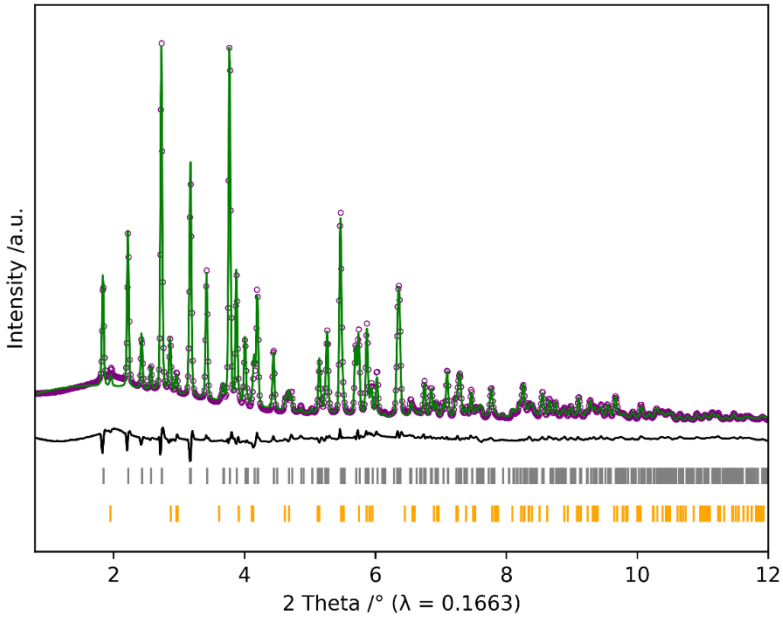

Figure 4.10: Powder diffractogram of the LFP-3a sample showing the observed (purple), calculated (green) and difference (black) plots generated from a Rietveld Refinement analysis. Bragg reflections for $LiFePO_4$ and the Fe-impurity phase are indicated with the grey and yellow markers, respectively.

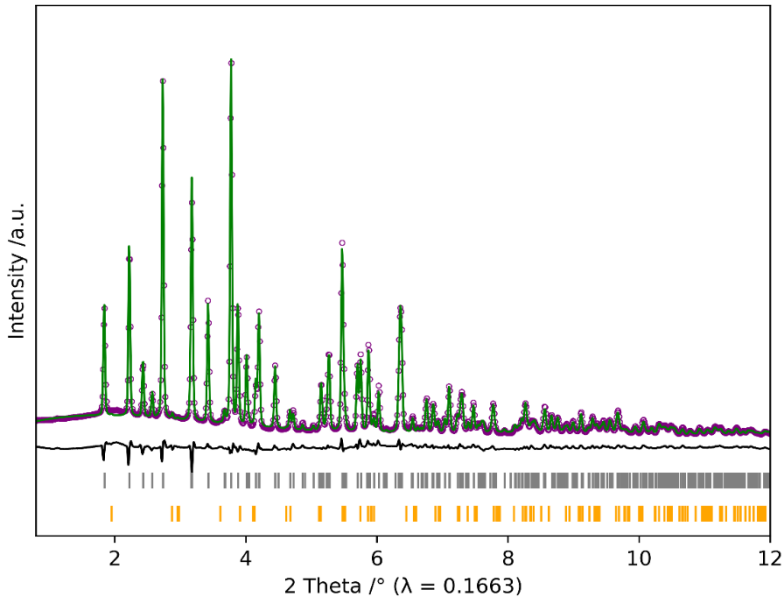

Figure 4.11: Powder diffractogram of the LFP-3b sample showing the observed (purple), calculated (green) and difference (black) plots generated from a Rietveld Refinement analysis. Bragg reflections for $LiFePO_4$ and the Fe-impurity phase are indicated with the grey and yellow markers, respectively.

Table 4.8: Rietveld error indices for LFP-3a and LFP-3b.

	R_{wp}	R_p	R_{exp}	GOF
LFP-3a	5.42	4.17	20.89	0.26
LFP-3b	5.38	4.20	18.47	0.29

The lattice parameters and volume (Table 4.9) were refined for both samples. The lattice parameters showed no significant difference but the volume for the LFP-3a sample revealed a larger volume. The lattice parameters were similar to the values reported in literature for hydrothermal syntheses. [37,39,40,44,56] The lattice parameters range are a = 10.30 − 10.38 Å, b = 5.98 − 6.01 Å, c = 4.67 − 4.72 Å with a volume of 289 − 293 Å^3.[37,39,40,44,56] A summary of the lattice parameters and volume can be found in Table 3.1. A multiphase Rietveld analysis showed that $LiFePO_4$ was the major phase in both the LFP-3a and LFP-3b samples. The minor phase was identified as the Fe-impurity in both the LFP-3a (6.71%) and LFP-3b (0.56%) samples and adding this phase to the refinement improved the fit for both samples.

Table 4.9: Selected structural parameters of the refined structures for the different samples

Sample	a (Å)	b (Å)	c (Å)	Volume (Å^3)
LFP-3a	10.359(5)	5.9978(3)	4.7117(2)	292.8(3)
LFP-3b	10.347(4)	5.9941(2)	4.7064(2)	291.9(2)

For the $LiFePO_4$ phase, the occupancy of the M2 (Fe) site and the M1 (Li^+) site was also refined (Table 4.10). The M2 site was fully occupied for LFP-3a but not for LFP-3b. No Li^+ was present on the LFP-3b M2 site indicating the presence of vacancies. Vacancies form when Fe^{2+} is replaced by Fe^{3+}.[57] The M1 (Li^+) site was also not fully occupied for both samples but LFP-3b had a lower percentage of Fe^{2+} and/or Fe^{3+} occupying this site possibly indicating fewer blockages of the Li^+ diffusion channel.

Table 4.10: The percentage Fe^{2+} occupying the M2 (Fe^{2+}) site, vacancies on the M2 site and Li^+ and Fe^{2+} occupying the M1 (Li^+) site in the refined $LiFePO_4$ structures.

	LFP-3a	LFP-3b
M2 (Fe) occupancy	100	98.7(7)
M2 (Fe) vacancy	-	1.3
M1 (Li^+) occupancy	91.6(6)	94.3(4)
M1 (Fe) occupancy	8.4(5)	5.4(4)

Mössbauer spectroscopy was performed on the $LiFePO_4$ sample with the lowest percentage of the impurity phase present – LFP-3b (Fig. 4.12). Four different Voigt doublets were used to

model the spectrum indicating that there were four different environments present - two different Fe^{2+} and two different Fe^{3+} environments.

The two different Fe^{2+} sites are present on the M2 site of $LiFePO_4$ with a different degree of octahedron distortion (Table 4.11), as before. The site with a larger quadrupole splitting, ΔE_Q, value indicates that the Fe^{2+} is in the normal slightly distorted M2 site in $LiFePO_4$.[5,9,41,48–52] The Fe^{2+} with the smaller ΔE_Q value indicates a higher degree of distortion around the Fe atom in $LiFePO_4$.[49,52] The Fe^{3+} with the smaller ΔE_Q (Table 4.11) is characteristic of Fe^{3+} present on the M1 (Li^+) site[49,50,52] and the Fe^{3+} with the larger ΔE_Q value is characteristic of Fe^{3+} present on the M2 site that can present itself as defects (Table 4.11).[48,49,51,52] These defects can also be present as superparamagnetic hematite.[58] Raman spectroscopy will be used to determine this possibility. The Fe^{3+} located on the M1 site is expected to have the lower ΔE_Q due to the increase in distortion. In the $LiFePO_4$ structure the M1 Li^+ site is already more distorted than the M2 Fe site[59,60] indicating that if the Li^+ (ionic radius of 0.76 pm) is replaced with the Fe^{3+} atom (ionic radius of 0.65 pm)[61] that is much smaller than the Li^+ it could be expected to have more distortion.[46]

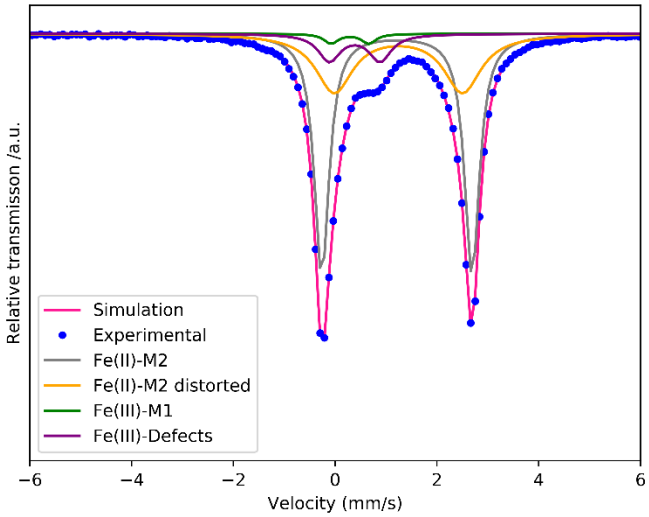

Figure 4.12: Mössbauer spectrum of LFP-3b.

Table 4.11: Different isomer shifts (δ – mm/s) and quadrupole splitting (ΔE_Q – mm/s) for LFP-3b.

	Fe(II) – M2		**Fe(II) –M2 distorted**		**Fe(III) –M1**		**Fe(III) – M2 / Defects**	
	δ	ΔE_Q	δ	ΔE_Q	δ	ΔE_Q	δ	ΔE_Q
LFP-3b	1.21(1)	2.95(1)	1.24(1)	2.52(1)	0.29(1)	0.74(1)	0.39(1)	0.99(1)

Fe^{2+} found in $LiFePO_4$ in the less distorted octahedron was identified as the major Fe phase in the sample (Table 4.12), but a significant amount of the distorted phase was also present. Only 2.1(2)% of the 5.4(4)% as shown with PXRD (Table 4.10) Fe on the M1 site was determined to be Fe^{3+} indicating that the rest of the Fe present on this site is Fe^{2+}. The Fe^{3+} on the M2 site (9.9(1)%) is the major source of Fe^{3+} in the sample.

Table 4.12: Percentage contribution from each form of Fe and the total Fe in LFP-3b.

	Fe(II) – M2	**Fe(II) –M2 distorted**	**Fe(III) –M1**	**Fe(III) – M2/Defects**	**Total Fe**	
					Fe^{2+}	**Fe^{3+}**
LFP-3b	56(6)	33(4)	2(1)	9(1)	89	11

The disorder (full width half maximum line width) reported for Fe^{2+} and Fe^{3+} in an ordered environment is 0.2 – 0.3 mm/s.[49–51,53] The lowest degree of disorder is present on the Fe^{2+} in $LiFePO_4$ environment and Fe^{3+} on the M1 site (Table 4.13). As expected, Fe^{2+} in a more distorted $LiFePO_4$ site has a very high degree of disorder and could be caused by an already distorted environment. Fe^{3+} on the M2 site / defect site also shows a higher degree of disorder and is caused by the distribution of both Fe^{3+} and Fe^{2+} on the M2 position (Table 4.13).[49,50]

Table 4.13: The full width half maximum line width (Γ – mm/s) value for LFP-3b.

	Fe(II) – M2	**Fe(II) –M2 distorted**	**Fe(III) –M1**	**Fe(III) – M2/Defects**
LFP-3b	0.35(1)	0.88(1)	0.33(2)	0.52(1)

Raman spectroscopy on the LFP-3b sample was also performed and all the external and internal modes of $LiFePO_4$ were identified (Fig. 4.13 and Table 4.14).[62–64] The PO_4^{3-} tetrahedra remain undistorted and evident by the clearly defined 950 cm^{-1} (υ_1 (PO_4)), 998 cm^{-1} and 1068 cm^{-1} (υ_3 (PO_4)) peaks and could indicate a stable $LiFePO_4$ structure (Fig. 4.11).[64] It is important that the PO_4 remains undistorted as it stabilizes the structure by reducing the Fe-O covalent character through the indicative effect.[9,65] These peaks exist due to the symmetric (υ_1) and asymmetric (υ_3) stretching respectively. Three different coloured phases (white, reddish and black) were present in the microscopic image (Fig. 4.13 inset). The white phase was identified as $LiFePO_4$ whereas the other two phases could not be identified due to poorly defined peaks.

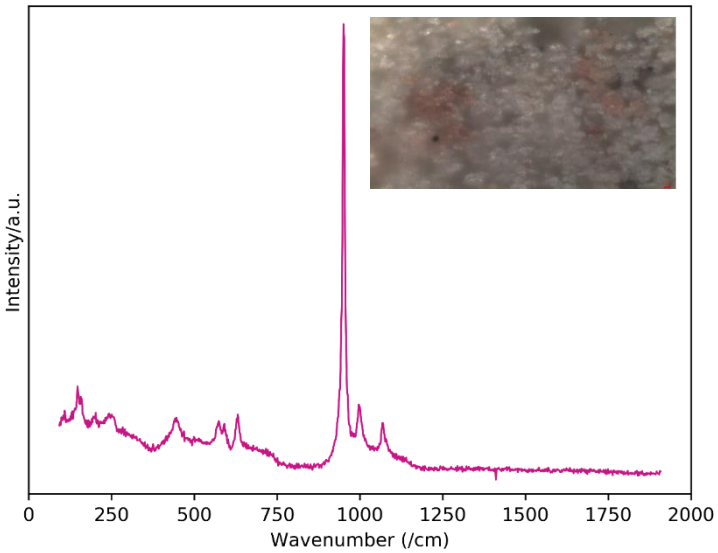

Figure 4.13: Raman spectrum and microscopic image (inset) of LFP-3b.

Table 4.14: Raman modes of LFP-3b with the assigned vibrational modes.

Wavenumbers(/cm)	Assignment
104 150 198 245	PO_4^{3-} rotational and Fe^{2+} translational motion
445	υ_2 (PO_4^{3-})
576 600 630	υ_4 (PO_4^{3-})
950	υ_1 (PO_4^{3-})
998 1069	υ_3 (PO_4^{3-})

In conclusion, the first objective was to determine the optimum lithium ratio (xLi:Fe:PO_4) and the second objective was to limit the effect that air exposure has during synthesis by purging

the solutions with N_2. The different Li^+ ratios were x = 2, 2.5 and 3. The ratios where x = 2 and 2.5 produced a highly mixed phase sample although $LiFePO_4$ was present in both samples. The ratio x = 3 gave a product where $LiFePO_4$ was the major phase present together with a small percentage of the Fe-impurity phase making this ratio the optimum ratio to use. Purging the solutions was also very beneficial. PXRD analysis of the LFP-3b (Table 4.10) showed that the defects on the Li^+ M1 site decreased compared to that of the 48hours-25 sample (Table 4.4). Mössbauer spectroscopy also showed that purging improved the percentage Fe^{2+} in the LFP-3b sample compared to the 48hour-25 sample. The percentage Fe^{2+} in the less distorted octahedra increased from 47.19% to 55.38% and the total Fe^{2+} percentage in the sample increased from 73.34% to 88.63%. The samples synthesised from this point on were all synthesised with a Li^+ ratio of x = 3 and by purging the solutions during synthesis.

4.2.4. Individually purged samples

To investigate the reproducibility the methodology as described in sections 2.1.2. and 4.2.3. was applied with a synthesis time of 48 hours, a Teflon bomb percentage filled to 25%, a Li^+ ratio of x = 3 and purging the solutions during synthesis. Two samples that were synthesised on two different occasions were used to investigate the reproducibility of this modified synthesis. These samples were labelled as **LFP-P1** and **LFP-P2** where P1 and P2 refers to the purged sample from the first and second synthesis, respectively.

XRD was performed on both LFP-P1 and LFP-P2. Rietveld refinement was performed on both LFP-P1 (Fig. 4.14) and LFP-P2 (Fig. 4.15). LFP-P1 was measured using an X-ray wavelength of 0.166316(1) Å and LFP-P2 with an X-ray wavelength of 0.167057(4) Å. All the peaks were accounted for and it was found that $LiFePO_4$ was the only phase present in both samples. This phase purity indicated that the purging was beneficial for this synthesis as well. The Rietveld error indices for both the refinements can be found in (Table 4.15). There were slight intensity mismatches on different peaks for both LFP-P1 and LFP-P2 samples and suggested that there were some structural features or defects that were not fully accounted for. The intensity mismatches were similar to the intensity mismatches in section 4.2.3.

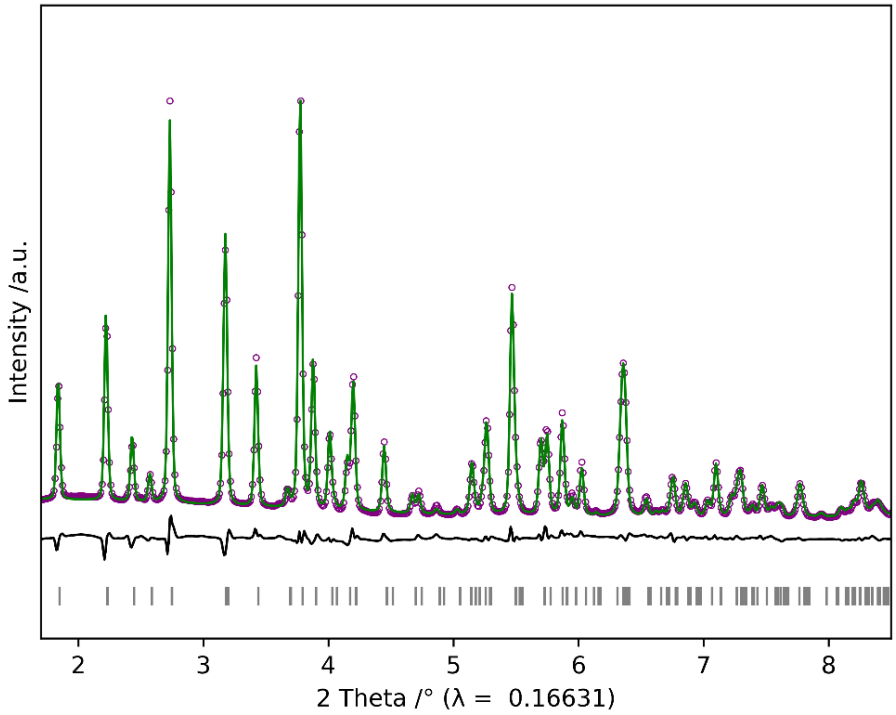

Figure 4.14: Powder diffractogram of the LFP-P1 sample showing the observed (purple), calculated (green) and difference (black) plots generated from a Rietveld Refinement analysis. Bragg reflections for $LiFePO_4$ are indicated with the grey markers.

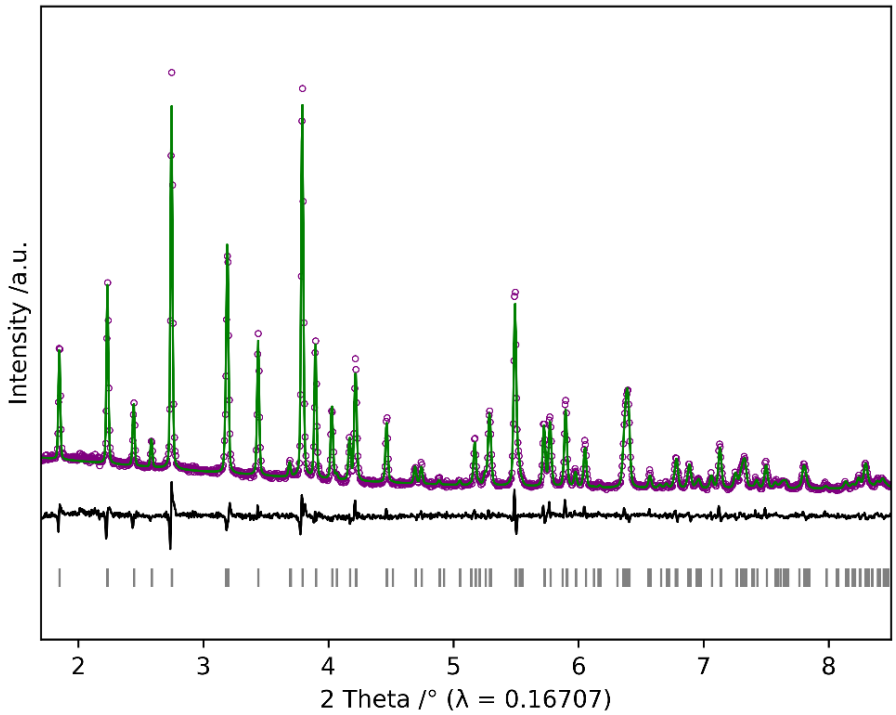

Figure 4.15: Powder diffractogram of the LFP-P2 sample showing the observed (purple), calculated (green) and difference (black) plots generated from a Rietveld Refinement analysis. Bragg reflections for $LiFePO_4$ are indicated with the grey markers.

Table 4.15: Rietveld error indices for the different purged samples.

	R_{wp}	R_p	R_{exp}	GOF
LFP-P1	5.96	4.72	16.94	0.35
LFP-P2	7.92	6.21	75.55	0.10

The lattice parameters (Table 4.16) were comparable to that other hydrothermal synthesis studies.[37,39,40,44,56] A summary of these values can be found in Table 3.1. The refined lattice parameters and volume was almost the same for both samples. The volume of LFP-P1 and LFP-P2 is slightly larger than that of the 48hours-25 (Table 4.2) and LFP-3b (Table 4.9) samples which could be an indication of the presence of more defects in the LFP-P1 and LFP-P2 samples.[44,66]

Table 4.16: Selected structural parameters of the refined structures for the different purged samples.

Sample	a (Å)	b (Å)	c (Å)	Volume ($Å^3$)
LFP – P1	10.352(5)	5.9953(3)	4.7080(2)	292.1(2)
LFP – P2	10.357(3)	5.9963(2)	4.7094(2)	292.5(2)

The M2 (Fe^{2+}) and M1 (Li^+) sites were refined to determine the occupancy, defects as well as the formation of vacancies (Table 4.17). The M2 (Fe^{2+}) site was not fully occupied and vacancies were present to a small extent for both samples. The M1 site was also not fully occupied and some of the Li^+ was replaced with either Fe^{2+} or Fe^{3+}. LFP-P1 and LFP-P2 have similar M2 and M1 occupancy percentages and vacancies. This show improved reproducibility compared to the LFP-3a and LFP-3b samples (Table 4.10) that had more variation.

Table 4.17: The percentage Li occupying the M2 site (Fe), vacancies on the M2 site and Fe occupying the M1 (Li) site in the refined $LiFePO_4$ structures.

	LFP – P1	LFP – P2
M2 (Fe) occupancy	98.7(8)	98.5(6)
M2 (Fe) vacancy	1.3	1.5
M1 (Li^+) occupancy	91.8 (5)	91.2(3)
M1 (Fe) occupancy	8.2(4)	8.8(3)

The M2-O, P-O and M1-O interatomic bond distances for both samples were also refined using the PXRD data (Table 4.18). A summary of the different M2-O, P-O and M1-O interatomic bond distances can be found in Table 3.2. The average M2-O interatomic bond distance is shorter[4,5,67,68] than the reported Fe-O interatomic bond distance indicating the presence of Fe^{3+}-O bonds in the synthesised structures.[69] A study by Gibot *et al*.[69] showed that the Fe^{2+}-O distance was 2.157 Å and Fe^{3+}-O distance was 2.147 Å. LFP-P1 shows a shorter M2-O distance than that for LFP-P2 indicating that there is possibly more Fe^{3+} present in LFP-P1.[69] The average P-O interatomic bond distance was longer for the synthesised samples than those reported for P-O in the $LiFePO_4$ structure.[4,5,67,68] LFP-P2 had a shorter interatomic P-O bond distance and suggests that the LFP-P2 structure is slightly more stable than that of LFP-P1 due to the stabilization of the PO_4 tetrahedra.[70,71] LFP-P1 had a slightly longer average M1-O interatomic bond distance respectively.[67,68]. The longer average interatomic M1-O bond distance indicates a volume expansion of the LiO_6 octahedra which is a consequence of the volume contraction of the FeO_6 octahedron due to the presence of the Fe^{3+}-O bonds.[72]

Table 4.18: Interatomic bond distances of the refined structures

	LFP – P1	**LFP – P2**
M2 – O(1)	2.170	2.202
M2– O(2)	2.053	2.068
M2– O(3) (×2)	2.037	2.048
M2 – O(3) (×2)	2.224	2.219
Average M2–O	**2.124**	**2.134**
P – O(1)	1.552	1.544
P – O(2)	1.634	1.611
P – O(3) (×2)	1.608	1.598
Average P – O	**1.600**	**1.588**
M1 – O(1) (×2)	2.178	2.172
M1 – O(2) (×2)	2.102	2.095
M1– O(3) (×2)	2.203	2.206
Average M1 – O	**2.161**	**2.158**

X-ray absorption spectroscopy (XAS) was used to investigate these samples further. The pre-edge, rising absorption edge and the main edge was used to investigate any changes in oxidation state and distortion around the Fe^{2+} and/or Fe^{3+} atom. Both LFP-P1 and LFP-P2 have the presence of the t_{2g} and e_g peaks (Fig. 4.16) that are also present in $LiFePO_4$ standard sample, with similar peak positions and intensities (Table 4.19).[5,22,24,73,74] The intensities of the second peak (the e_g peak) are slightly higher than for the $LiFePO_4$ standard. This increase in intensity can possibly be a result of an increase in the Fe^{3+} content or a slight increase in distortion.[75,76] Linear combination fitting (LCF) and Mössbauer spectroscopy was used to further investigate the changes in Fe^{3+} content. This increase in intensity is slightly higher for LFP-P1 than LFP-P2 and could be accompanied by peak broadening.

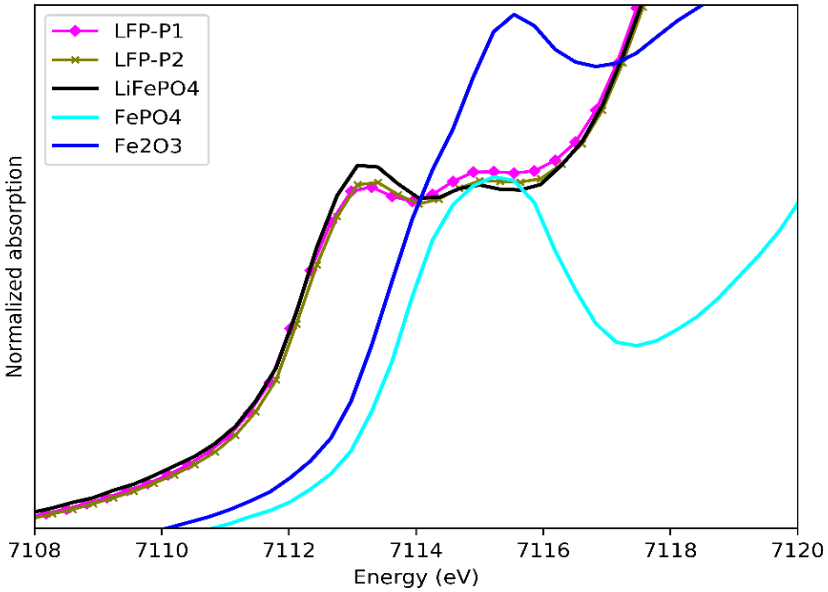

Figure 4.16: Comparison Fe K-edge XANES pre-edge region of the different standards purged samples.

Table 4.19: The different pre-edge peak intensities and peak positions for the standards and purged samples

Sample	Peak position 1 (eV)	Peak intensity 1 (au)	Peak position 2 (eV)	Peak intensity 2 (au)
$LiFePO_4$	7112.95	0.0480	7115.20	0.0457
$FePO_4$	-	-	7115.72	0.0469
Fe_2O_3	-	-	7115.22	0.0642
LFP-P1	7112.98	0.0455	7114.91	0.0476
LFP-P2	7113.08	0.0462	7115.07	0.0464

The rising absorption edge (Fig. 4.17) showed a slight shift to higher energy compared to that of the $LiFePO_4$ standard for both samples. The shift to slightly higher energy values indicates that both the samples do not only have Fe^{2+} present but also a small percentage of Fe^{3+} is also present.[24,74,75]

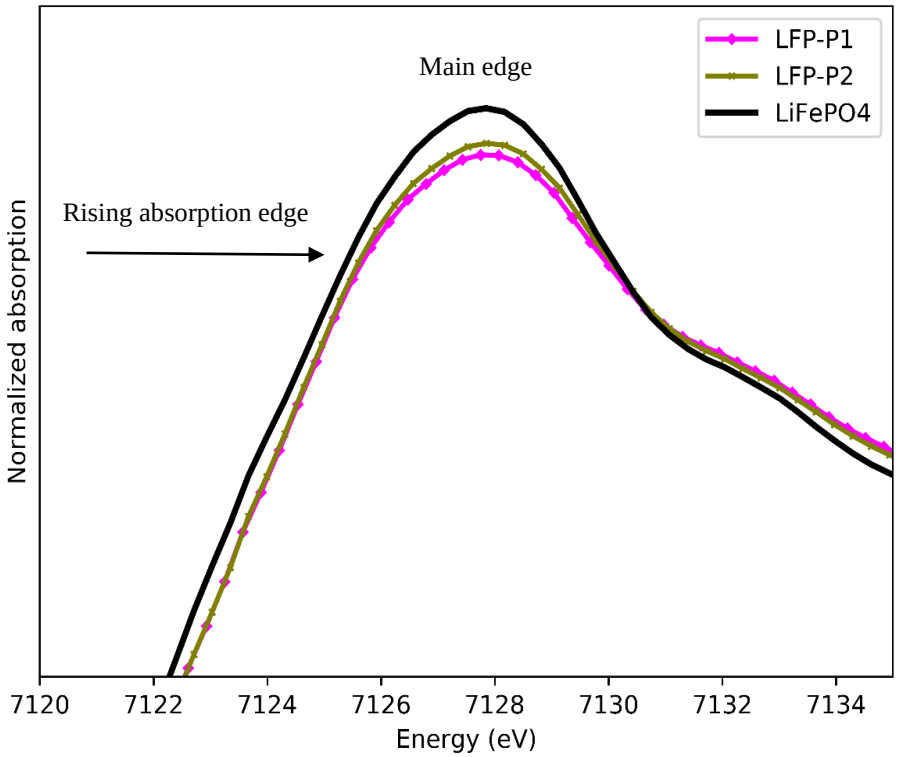

Figure 4.17: Comparison of the XANES Fe K-edge rising absorption and main absorption edge for the $LiFePO_4$ standard and the purged samples.

There is no peak shift of the main absorption edge (Fig. 4.17 and Table 4.20) compared to that of the $LiFePO_4$ standard indicating that there is no major difference in oxidation state.[24,74,75] The main absorption edge does show a similar drop in intensity for both LFP-P1 and LFP-P2. This drop in intensity indicates that there is a possible increase in disorder around the Fe atoms.[2] EXAFS has to be used to investigate the possible increase in disorder and also to determine if there are any changes in the local structure.

Table 4.20: The different main edge peak intensities and peak positions for the standards and the purged samples.

Sample	Peak position (eV)	Peak intensity (au)
$LiFePO_4$	7127.8	1.59
$FePO_4$	7133.0	1.46
α-Fe_2O_3	7134.3	1.44
LFP-P1	7127.9	1.53
LFP-P2	7127.8	1.55

Linear combination fitting was performed on the XANES region of both LFP-P1 (Fig. 4.18a) and LFP-P2 (Fig. 4.18b). A complete discussion of the standards used can be found in section 2.2.3.1. The fitting range for the purged samples were between 7103 – 7154 eV. The R-factor and chi-square values are relatively small and both the LFP-P1 and LFP-P2 show good fits (Table 4.21).[77] The LFP-P1 sample showed a higher degree of mismatch between the fitted data and the experimental data than the LFP-P2 sample which only shows a very small mismatch. There is possibly another Fe^{2+} or Fe^{3+} phase present in LFP-P1 with different bonding characteristics that were not accounted for using this set of standards. Adding different standards, standards that are more phase pure (discussed in section 3.2) and a bigger library of standards could possibly improve the accuracy of both fits.

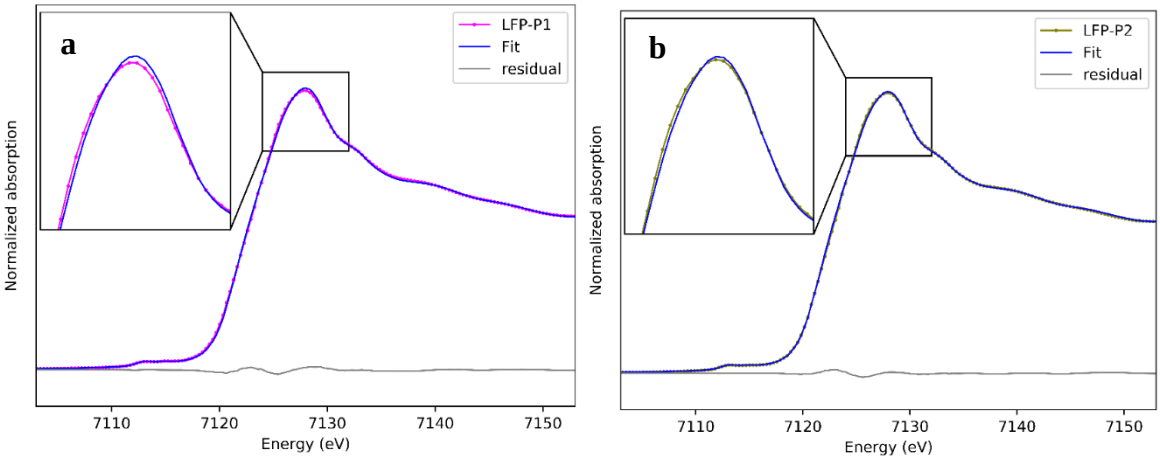

Figure 4.18: LCF best fit (blue) of (a) LFP-P1 for the Fe K-edge XANES spectrum (pink) and (b) for LFP-P2 of the Fe K-edge XANES spectrum (olive green) along with the residual spectrum (grey).

Table 4.21: LCF goodness of fit parameters for the purged samples.

Sample	R-factor	Chi-square
LFP-P1	0.0001644	0.00674
LFP-P2	0.0001062	0.00436

From these fits it was determined that both samples are mixed phase having both Fe^{2+} and Fe^{3+} sources. The major phase in both samples was identified as $LiFePO_4$ with only a difference of 0.6% between LFP-P2 and LFP-P1 (Table 4.17). LFP-P1 had Fe^{3+} in the slightly distorted ($FePO_4$) octahedra and Fe^{3+} in the more distorted (α-Fe_2O_3) octahedra environment present. The LFP-P2 sample only had one source of Fe^{3+} in a more distorted octahedra environment (α-Fe_2O_3). These results for LFP-P1 and LFP-P2 are consistent with the presence of shorter Fe^{3+}-O interatomic bond distances determined from the refinements of the PXRD data (Table 4.18).

Table 4.22: LCF Percentage of the different components present in the purged samples.

Sample	$Fe^{2+}O_6$ ($LiFePO_4$)	$Fe^{3+}O_6$ ($FePO_4$)	$Fe^{3+}O_6$ (Fe_2O_3)
LFP-P1	92.3(3)	4(1)	4(1)
LFP-P2	92.9(1)	-	7.1(1)

Looking at the EXAFS region the k-space plots for LFP-P1 and LFP-P2 (Fig. 4.19) had the same peaks present with similar features indicating that the local structure was the same for LFP-P1 and LFP-P2.[2]

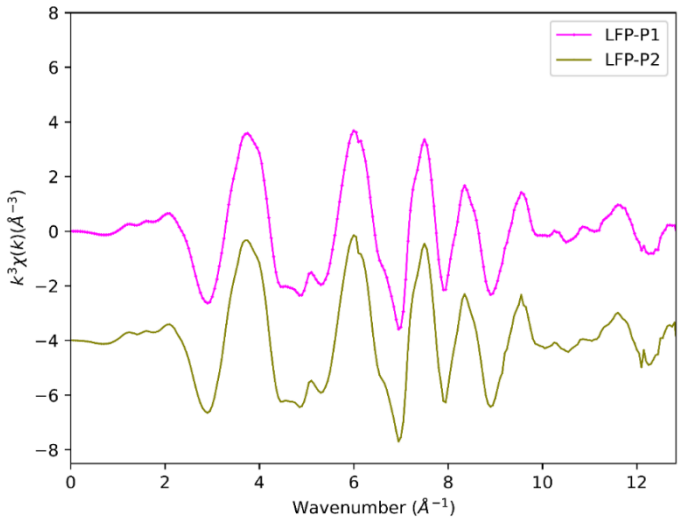

Figure 4.19: Comparison of the Fe k^3-weighted $[k^3\chi(k)]$ spectrum of the LFP-P1 and LFP-P2 synthesised samples.

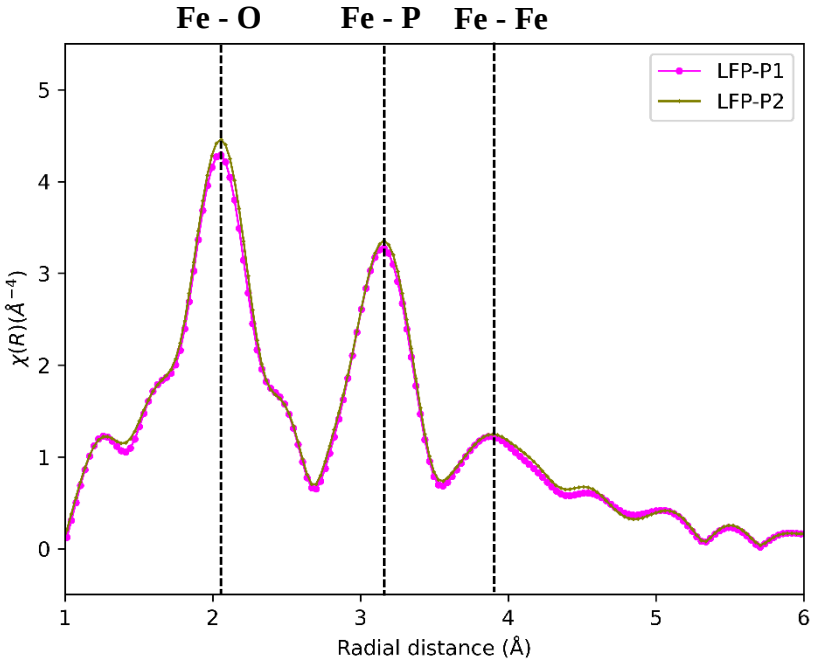

Figure 4.20: The magnitude of the Fourier transform of EXAFS $k^3\chi(k)$ data comparing the radial distance of the different coordination shells of the two purged samples.

EXAFS fitting was performed by calculating theoretical scattering paths generated by FEFF6 code[78] using the structure resolved by Streltsov[67] as a starting model. The coordination number, interatomic distance between the absorbing atom and neighbouring atoms (X_a – X_b) and the Debye Waller factor (σ^2) were determined using these different scattering paths. The magnitude of the Fourier Transform (FT magnitude) was used to identify the different coordination shells (Fig. 4.20). The FT EXAFS were phase corrected for both LFP-P1 and LFP-P2 using the strongest scattering path. The first peak (~2.1Å) corresponds to the scattering process of the closest oxygen (Fe-O) coordination shell, the second peak (~3.2Å) to the phosphorous (Fe-P) coordination shell and the third and fourth peaks (~3.9Å) to the iron (Fe-Fe) coordination shell.[22,24,73,74] Both LFP-P1 and LFP-P2 showed the presence of all three coordination shells (Fig. 4.20) of $LiFePO_4$. The drop in intensity in the FT magnitude (Fig. 4.20) can be linked to a change in the increase in disorder around the Fe atom.[2] The shape of the plot of the magnitude of the Fourier transform of both LFP-P1 and LFP-P2 are similar to that of the $LiFePO_4$ standard and thus indicates that there is no change in local structure.[2,22]

The local structure as described above were determined for the Fe-O, Fe-P and Fe-Fe coordination shells for the LFP-P1 and LFP-P2 samples (Figs. 4.21 – 4.22). The fitting procedure used can be found in section 2.2.3.2. The same scattering paths were used for both samples – mostly single and one multiple scattering paths. The R-factor (Table 4.23) for all the samples were less than 5% indicating that this was an acceptable fit.[79] The selected E_0 starting

values determined using ATHENA[78] also serve as an indication of the reliability of the data processing. This can be assessed by determining the value of ΔE_0 (Table 4.23). This parameter is correlated to the path length and is considered to be reliable if it is in the range -10 eV < ΔE_0 < 10 eV,[80] which is the case here. The amplitude reduction factor (S_0^2) for LFP-P1 and LFP-P2 is 0.93(8) and 0.84(9), respectively.

Table 4.23: The reliability factor and energy shift of the purged samples.

Sample	R-factor (%)	ΔE_0 (eV)
LFP-P1	0.47	-0.04(8)
LFP-P2	0.58	-2.4(9)

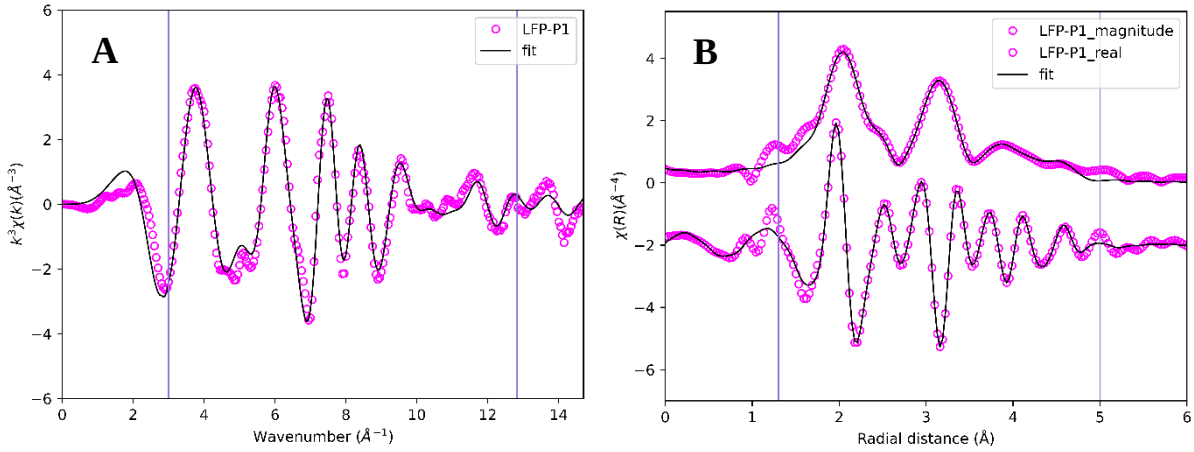

Figure 4.21: (a) The experimental Fe k^3-weighted $[k^3\chi(k)]$ spectrum and (b) the experimental FT magnitude (top) and FT real (bottom) of the EXAFS $k^3\chi(k)$ data (green) and the theoretical FEFF fit (black) of LFP-P2. The fitting window is indicated with the vertical lines.

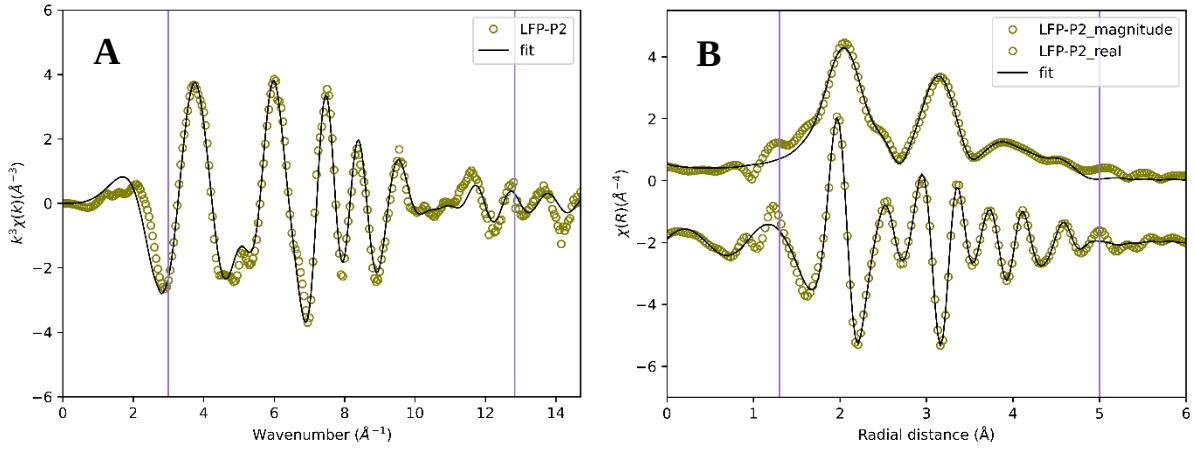

Figure 4.22: (a) The experimental Fe k^3-weighted $[k^3\chi(k)]$ spectrum and (b) the experimental FT magnitude (top) and FT real (bottom) of the EXAFS $k^3\chi(k)$ data (pink) and the theoretical FEFF fit (black) of LFP-P1. The fitting window is indicated with the vertical lines.

Table 4.24 contains information regarding the different shells, coordination number and individual interatomic bond distances and the individual Debye-Waller factor whereas Table 4.25 contains a summary of the average interatomic distances and the average Debye-Waller factor for the different coordination shells. A similar summary of the average interatomic distances and disorder as determined by other research groups can be found in Table 3.3.[2,22,73,74] The first coordination shell was oxygen with a coordination number of six. To obtain the best fit, data for LFP-P1 was fitted using a three-shell model that had three different interatomic distances. Data for LFP-P2 was fitted using a two-shell model with two different interatomic distances – four longer and two shorter (Table 4.24). The interatomic distances for LPF-P1 and LFP-2 are similar and within the error associated (Table 4.25). The average interatomic distance as determined by other groups have slight variation but are also within the experimental error. In general there was a slightly higher degree of disorder around the longer interatomic distance than the shorter distances (Table 4.24). The average disorder is very similar for the two samples and within the errors associated with them but the disorder is larger than the disorder reported by other groups, these are in the range of $0.0028 - 0.0083$ $Å^2$.[22,73,74]

The second coordination shell was phosphorous with coordination number of five (Table 4.24). This shell was fitted using a two-shell model. LFP-P1 had two shorter and three longer interatomic distances whereas the LFP-P2 had one shorter and four longer interatomic distances. LFP-P1 had a shorter average interatomic distance than LFP-P2 (Table 4.25). The average interatomic distance for LFP-P2 was also more similar to the average interatomic distance determined by other research groups.[22,73,74] There is a higher degree of disorder present around the longer interatomic distances (Table 4.24). Both samples exhibited a higher degree of disorder than the reported values (Table 4.25) for this coordination shell. This average disorder was also double the disorder reported ($0.0045 - 0.0046$ $Å^2$).[22,73,74] Compared to the reported studies both samples probably have more defects present in the structure in the first and second coordination shell leading to the higher degree of disorder.

The third coordination shell was iron with a coordination number of four and was fit using a two-shell model. Both LFP-P1 and LFP-P2 showed two longer and two shorter interatomic distances (Table 4.24). The individual interatomic Fe-Fe distances for the two samples are almost the same. The average interatomic Fe-Fe distances are longer than the reported values for the iron shell.[22,73,74] The average disorder was the same for both samples (Table 4.25) but the reported disorder in other works ($0.0054 - 0.0096$ $Å^2$)[22,73,74] was lower.

Table 4.24: Structural parameters determined using FEFF for the first, second and third coordination shell of the purged samples.

Sample	Shell	Coordination number	Interatomic distance (Å)	Debye-Waller factor ($Å^2$)
LFP-P1	Fe-O1	2	2.20(2)	0.014(8)
	Fe-O2	2	2.11(2)	0.017(9)
	Fe-O3	2	2.06(2)	0.007(3)
	Fe-P	2	2.834(8)	0.014(2)
	Fe- P	3	3.258(8)	0.007(1)
	Fe-Fe	2	3.84(1)	0.011(2)
	Fe-Fe	2	4.66(1)	0.014(4)
LFP-P2	Fe-O1	4	2.13(1)	0.012(3)
	Fe-O2	2	2.03(1)	0.009(2)
	Fe-P	1	2.821(8)	0.008(2)
	Fe- P	4	3.245(8)	0.008(1)
	Fe-Fe	2	3.82(2)	0.011(3)
	Fe-Fe	2	4.64(2)	0.012(4)

Table 4.25: The average interatomic distance and average Debye-Waller factor of the different coordination shells.

Shell	Sample	Average interatomic distance (Å)	Average Debye-Waller factor ($Å^2$)
Fe-O	LFP-P1	2.12	0.012
	LFP-P2	2.10	0.011
Fe-P	LFP-P1	3.088	0.0098
	LFP-P2	3.160	0.0080
Fe-Fe	LFP-P1	4.25	0.013
	LFP-P2	4.23	0.012

Disorder in the samples could either be caused by defects such as some of the Fe^{2+} occupying both M2 and M1 octahedral sites in the sample or by a decrease in crystallinity.[2] All the samples showed some degree of disorder in all the coordination shells (Table 4.24). Rietveld analysis showed that some $Fe^{2+}$and/or Fe^{3+} (Table 4.17) occupied the M1 site in both samples (around 8-9% site occupancy) and Figure 4.14 and Figure 4.15 displayed sharp well-defined peaks indicating good crystallinity. It was determined that LFP-P1 had a higher degree of disorder and this corroborates what was shown in the main edge (Fig. 4.17) and the FT magnitude (Fig. 4.20) where both showed a decrease in intensity. The oxygen and phosphorous coordination shells had different interatomic distance coordination for LFP-P1 and LFP-P2. LFP-P1 had a higher intensity and possible larger energy for the e_g peak (Fig. 4.16). This could be due to the different bonding distribution attributed to the difference in the interatomic distance coordination number present in the two samples. The LFP-P1 sample had 3 different interatomic distances whereas the LFP-P2 sample only had two different interatomic distances. This could have an effect on the interaction between the orbitals (e_g orbitals) that are in the direction of the ligand and experiences the repulsive field of the oxygen ligands[81] causing a change in the peak for the two different samples in the pre-edge region (Fig. 4.16).

The Mössbauer spectra for these two purged samples were analysed as before with five different Voigt doublets to determine the different Fe environments present – two different Fe^{2+} and two different Fe^{3+} sites (Fig 4.23) in both samples. The two Fe^{2+} sites are present in $LiFePO_4$ but the one site is less distorted (higher ΔE_Q value) than the other site (Table 4.26). The Fe^{3+} environments were that of Fe^{3+} on the M1 site and Fe^{3+} on the M2 site that can be present as defects in the structure (Table 4.26). A full description of these four sites was given in section 4.2.3. Another Fe environment were determined to be present in these samples. This site corresponds to Fe^{2+} on the M1 site that possibly replaced some of the Li^+ on the site.[82] The δ of the environment is similar to that of the previously described Fe^{2+} environments but the ΔE_Q is much smaller (Table 4.26). The ΔE_Q = 0.93 mm/s recorded for LFP-P2 where Fe^{3+} is on the M2 site is larger than the same site for other synthesised samples and could indicate a less distorted environment due to the increase in ΔE_Q.[52] No Fe^{3+} containing impurity phases were identified using PXRD but Fe^{3+} impure phases were identified using linear combination fitting implying that amorphous or poorly crystalline Fe^{3+} was present in both samples. Defects could correspond to that of superparamagnetic hematite.[58]

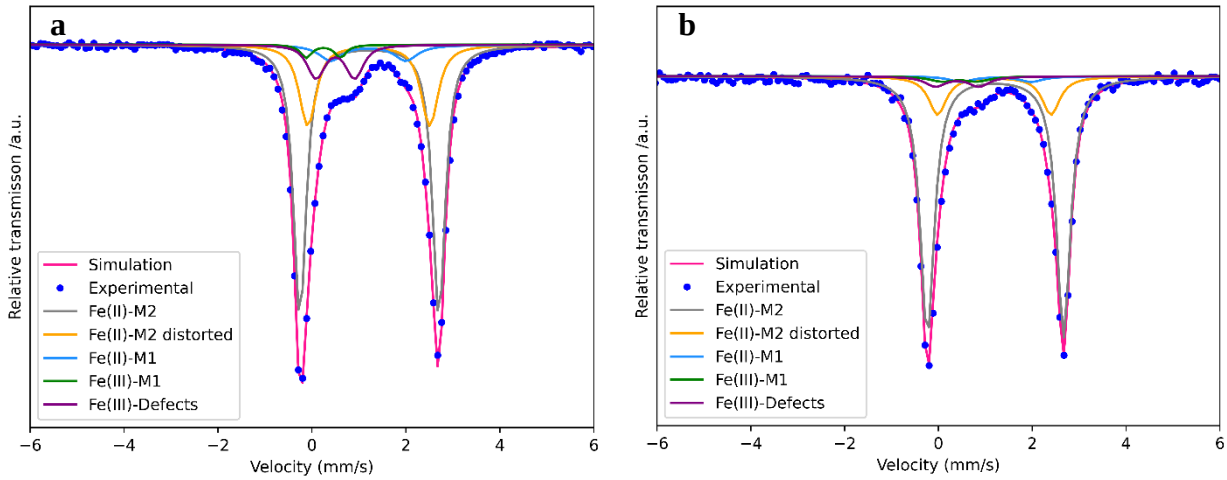

Figure 4.23: Mössbauer spectra for the (a) LFP-P1 and (b) LFP-P2 sample.

Table 4.26: Different isomer shifts (δ – mm/s) and quadrupole splitting (ΔE_Q – mm/s) for the purged samples.

	Fe(II) – M2		**Fe(II) –M2 distorted**		**Fe(II) –M1**		**Fe(III) –M1**		**Fe(III) – M2/Defects**	
	δ	ΔE_Q	δ	ΔE_Q	δ	ΔE_Q	δ	ΔE_Q	δ	ΔE_Q
LFP-P1	1.22(1)	2.96(1)	1.21(1)	2.60(1)	1.20(2)	1.60(4)	0.24(1)	0.73(2)	0.50(1)	0.82(2)
LFP-P2	1.22(1)	2.91(1)	1.19(1)	2.42(2)	1.23(7)	1.50(1)	0.45(8)	0.75(1)	0.40(3)	0.93(5)

LFP-P2 had the highest percentage of overall Fe^{2+} (Table 4.27). Fe^{2+} in $LiFePO_4$ was identified as the major phase in both samples and LFP-P2 had a higher percentage of this Fe^{2+} than LFP-P1. LFP-P1 had a higher percentage of Fe^{2+} in a more distorted M2 environment whereas LFP-P2 had a smaller percentage of Fe^{2+} on the M1 site. Both samples had similar percentages of Fe^{3+} on the M1 site whereas LFP-P1 had the highest percentage of Fe^{3+} on the M2 site. This aids in supporting the presence of Fe^{3+}-O interatomic distances present in both samples. According to the XRD results, LFP-P1 had a shorter average interatomic M2-O distance (Table 4.18) and the results in Table 4.27 show a higher percentage of Fe^{3+} on the M2 site. Rietveld analysis determined that there was 8.2(4)% Fe on the M1 site in LFP-P1 and Mössbauer spectroscopy indicated that 6(1)% of this was Fe^{2+} and 3(1)% was Fe^{3+}. Similarly, for LFP-P2, 3(1)% and 3(1)% of the 8.8(3)% Fe on the M1 site was Fe^{2+} and Fe^{3+}, respectively.

Table 4.27: Percentage contribution from each form of Fe and the total Fe in the purged samples.

	Fe(II) – M2	Fe(II) –M2 distorted	Fe(II) – M1	Fe(III) –M1	Fe(III) - Defects	Total Fe	
						Fe^{2+}	Fe^{3+}
LFP-P1	59(8)	23(5)	6(1)	3(1)	9(2)	88	12
LFP-P2	76(8)	14(3)	3(1)	3(1)	4(1)	93	7

Comparing the total Fe^{2+} and Fe^{3+} as determined using the LCF results (Table 4.22) and the Mössbauer spectroscopy results (Table 4.27), it is seen that LCF gives higher results for the total Fe^{2+} for LFP-P1. The results determined using these two techniques for LFP-P2 were similar for the total Fe^{2+} and Fe^{3+} present (with a difference of 0.1% for Fe^{2+}) whereas LFP-P1 deviated by 4.3% for the total Fe^{2+} and 4% for the total Fe^{3+}. This deviation can be explained by the mismatch seen for the LCF analysis for LFP-P1 and not for LFP-P2.

The disorder around the Fe atom in the different environments (Table 4.28) were probed using the full width at half maximum line width (Γ) and that for an ordered Fe environment the Γ is typically between 0.2 – 0.3 mm/s.[49–51,53] LFP-P1 had a lower degree of disorder for all the environments when compared to LFP-P2. Fe^{2+} and Fe^{3+} on the M1 site and Fe^{3+} present on the M2 site showed the highest degree of disorder.

Table 4.28: The full width half maximum line width (Γ – mm/s) value for the purged samples.

	Fe(II) – M2	Fe(II) –M2 distorted	Fe(II) –M1	Fe(III) –M1	Fe(III) – M2/Defects
LFP-P1	0.300(1)	0.381(5)	0.60(3)	0.28(3)	0.35(1)
LFP-P2	0.356(2)	0.45(2)	0.6(2)	0.6(2)	0.53(9)

The internal and external Raman modes for $LiFePO_4$ [62–64] (Table 4.29) were identified and assigned for both LFP-P1 (Fig. 4.24) and LFP-P2 (Fig. 4.25) and these are effectively the same as was seen for the LFP-3a sample in Table 4.14. The peak positions for LFP-P1 are slightly shifted toward higher wavenumbers. The well defined υ_1 (PO_4^{3-}) (~950 cm^{-1}) and υ_3 (PO_4^{3-}) (~998 cm^{-1} and 1068 cm^{-1}) peaks indicate that the PO_4^{3-} tetrahedron remains undistorted for both samples.[64] The microscopic images (Fig 4.22 inset and Fig 4.23 inset) showed two coloured phases. The major phase is the shiny-white phase as has been identified as $LiFePO_4$.

The reddish/brown phase could possibly be hematite.[83] This phase was very poorly crystallised and not all the peaks were defined, except for two peaks at ~227 cm^{-1} and 246 cm^{-1} (inset spectra of Fig. 4.24) and a very small, broad hump at ~1350 cm^{-1} (inset spectra of Fig. 4.24 and 4.25) which is present in hematite indicating an amorphous phase. Hematite was also identified in both LFP-P1 and LFP-P2 using Mössbauer spectroscopy.

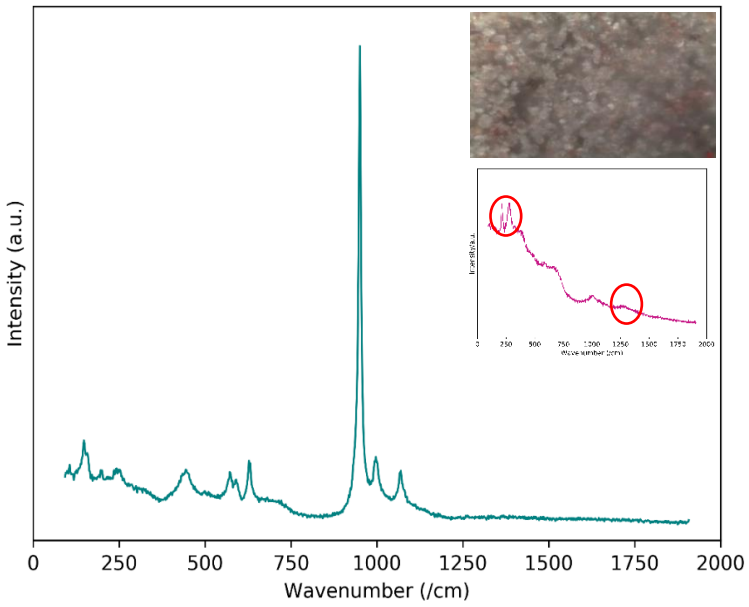

Figure 4.24: Raman spectrum and microscopic image (inset) of LFP-P1. The bottom inset is that of the poorly crystalline hematite.

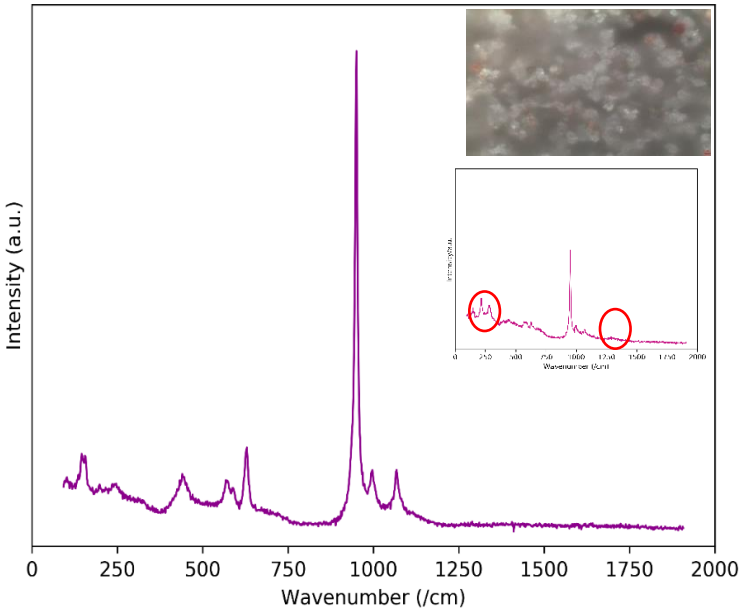

Figure 4.25: Raman spectrum and microscopic image (inset) of LFP-P2. The bottom inset is that of the poorly crystalline hematite.

Table 4.29: Raman modes of the purged samples with the assigned vibrational modes.

Wavenumbers(/cm)		Assignment
LFP-P1	**LFP-P2**	
100	100	PO_4^{3-} rotational and Fe^{2+} translational motion
149	146	
196	198	
244	243	
441	440	υ_2 (PO_4^{3-})
572	570	υ_4 (PO_4^{3-})
591	589	
628	627	
950	949	υ_1 (PO_4^{3-})
997	996	υ_3 (PO_4^{3-})
1068	1067	

In conclusion for this section, the average and local structure was used to thoroughly investigate the reproducibility of the modified synthetic route. XRD showed that LFP-P1 and LFP-P2 had very similar lattice parameters, volume and percentage occupancies for both the M2 site and the M1 site. The interatomic distances had some variability but was also very similar for both samples. The XANES region showed similar pre-edge and main edge peak shifts for both LFP-P1 and LFP-P2. Linear combination fitting was performed on both samples and it was determined that the total Fe^{2+} and Fe^{3+} was basically the same for these samples but that there was possibly another Fe^{3+} bonding environment present in LFP-P1. From the EXAFS fit that was performed on both LFP-P1 and LFP-P2 it was shown that both samples had similar interatomic distances and disorder present. The variation between these samples were within the experimental error. Mössbauer spectroscopy identified the same four Fe environments in both samples. The major difference between LFP-P1 and LFP-P2 was for Fe^{2+} and Fe^{3+} content

for these environments in the samples. LFP-P2 had 5.15% more Fe^{2+} than LFP-P1. Raman spectroscopy also showed that these structures were the same. The same modes could be identified for both samples indicating similar crystallinity. Taking all the techniques into consideration, LFP-P1 and LFP-P2 showed great reproducibility.

4.2.5. Controlling the exact volume to improve reproducibility

The variation in Fe^{2+} content between samples as seen from the Mössbauer spectroscopy results in section 4.2.4 showed the need to further improve the reproducibility between samples. The same synthesis was used as for the Li^{+} ratio (section 4.2.3) and the individually purged samples (section 4.2.4). A ratio of 3:1:1 ($Li:Fe:PO_4$), 25% volume filled Teflon bomb and a reaction time of 48 hours was used. The following changes were made to this synthesis: the water used for the dissolution of the precursors was purged before (± 70min) and throughout the experiment and a micro-pipette rather than a plastic syringe was used to add the exact volume needed to dissolve the precursors. The preparation method after the samples were removed for the oven is the same as stated in section 2.1.2.

Three replicate samples were prepared in exactly the same way and the diffraction patterns determined for each: **LFP-1** (Fig. 4.26), **LFP-2** (Fig.4.27) and **LFP-3** (Fig.4.28). An X-ray wavelength of 0.166316(1) Å was used. LFP-3 had a poor-quality fit compared to that of LFP-1 and LFP-2. This can also be seen graphically (Figs. 4.26 – 4.28).[84] The decrease in the quality of the fit indicated that LFP-3 had more structural defects that cannot be accounted for. The Rietveld error indices can be found in Table 4.30. $LiFePO_4$ was identified as the phase in all the samples, but there were also impurity phases present in all the samples. Unexpectedly the impurity was Li_3PO_4 for LFP-1 and LFP-3, but the Fe-impurity that was discussed in section 4.2.1 was present in LFP-2 (Table 4.31). The Li_3PO_4 content present in LFP1 and LFP-3 are very similar. The fact that inconsistencies in the product was found where the reproducibility was the main focus shows that the hydrothermal synthesis route is more complicated that initially realised and that there are other factors at play.

.

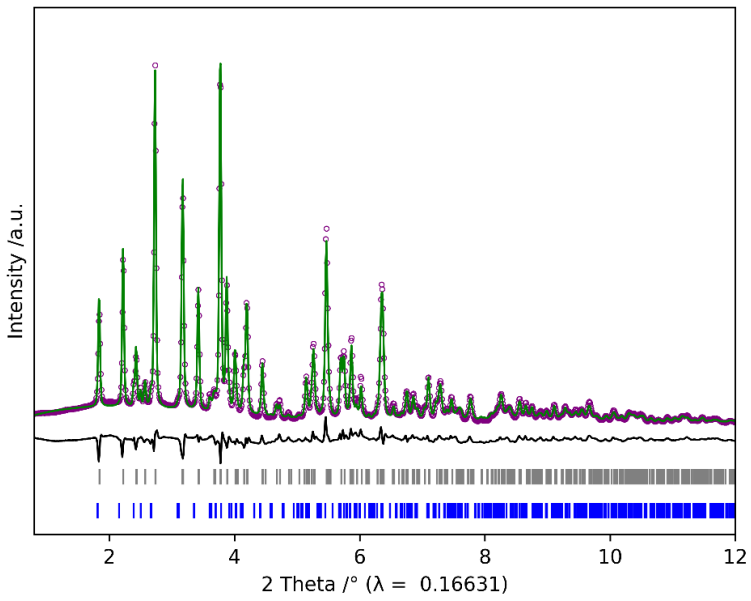

Figure 4.26: Powder diffractogram of the LFP-1 sample showing the observed (purple), calculated (green) and difference (black) plots generated from a Rietveld Refinement analysis. Bragg reflections for $LiFePO_4$ and Li_3PO_4 are indicated with the grey markers and blue markers, respectively

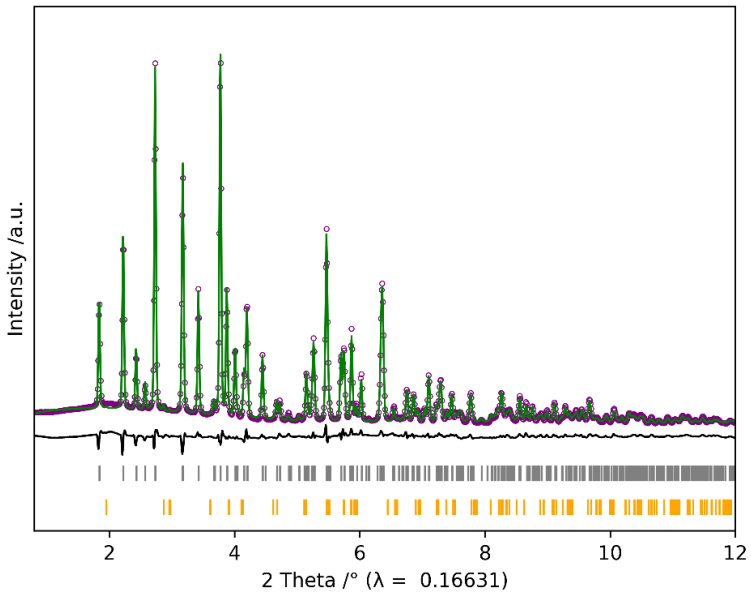

Figure 4.27: Powder diffractogram of the LFP-2 sample showing the observed (purple), calculated (green) and difference (black) plots generated from a Rietveld Refinement analysis. Bragg reflections for $LiFePO_4$ and the Fe-impurity are indicated with the grey and yellow markers, respectively

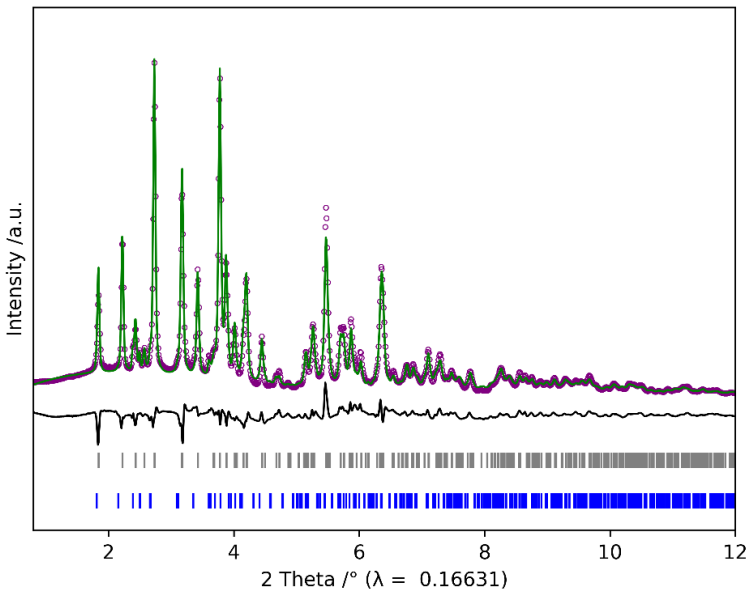

Figure 4.28: Powder diffractogram of the LFP-3 sample showing the observed (purple), calculated (green) and difference (black) plots generated from a Rietveld Refinement analysis. Bragg reflections for $LiFePO_4$ and Li_3PO_4 are indicated with the grey markers and blue markers, respectively

Table 4.30: Rietveld error indices for LFP-1, LFP-2 and LFP-3.

Sample	R_{wp}	R_p	R_{exp}	GOF
LFP – 1	6.41	5.17	16.0	0.40
LFP – 2	5.40	4.26	17.86	0.30
LFP – 3	7.09	5.46	15.94	0.44

Table 4.31: Multiphase analysis (%) of LFP-1, LFP-2 and LFP-3.

Sample	$LiFePO_4$	Li_3PO_4	Fe-impurity
LFP –1	95.73	4.27	-
LFP –2	99.42	-	0.58
LFP –3	96.06	3.94	-

For the $LiFePO_4$ phase, there is very slight to no variation between the lattice parameters and volume of the three samples (Table 4.32). The refined lattice parameters and volume were similar to those reported in literature for $LiFePO_4$ synthesised using a hydrothermal synthesis.[37,39,40,44,56] A summary of these results can be found in Table 3.1. The similarity in results indicate that the impurities have little effect on the lattice parameters and volume.

Table 4.32: Selected structural parameters of the refined structures for the different purged samples.

Sample	a (Å)	b (Å)	c (Å)	Volume (Å^3)
LFP –1	10.354(7)	6.0021(4)	4.7091(3)	292.6(3)
LFP –2	10.353(4)	5.9995(2)	4.7061(2)	292.3(2)
LFP –3	10.34(1)	5.9980(7)	4.7059(6)	291.9(6)

Neither the M2 (Fe^{2+}) site nor the M1 (Li^+) site was fully occupied with Fe^{2+} and Li^+, respectively (Table 4.33). No Li^+ was present on the M2 site although vacancies were present site. There was some variation in the occupancy of Fe between the samples with LFP-3 having a lower percentage of Fe^{2+} occupying the M2 site and the higher percentage vacancies then denotes a higher percentage of Fe^{3+} on this site.[57] $Fe^{2+}$and/or Fe^{3+} was present on the M1 site with the amount varying between the samples. LFP-3 had the lowest percentage of Li^+ occupying the M1 site and the highest percentage of Fe^{3+} and/or Fe^{2+} on this site whereas LFP-2 had the highest percentage of Li^+ on the M1 site. Overall, there were minor differences between LFP-1 and LFP-2.

Table 4.33: The percentage Li occupying the M2 (Fe) site, vacancies on the M2 site and Fe occupying the M1(Li) site in the refined $LiFePO_4$ structures.

	LFP –1	LFP –2	LFP –3
M2 (Fe) occupancy	98(1)	98.5(6)	96(2)
M2 (Fe) vacancy	2	1.5	4
M1 (Li) occupancy	90.1(8)	94.2(4)	89(2)
Fe on the M1 site	9.9(7)	5.8(3)	11(1)

The average interatomic bond distances were determined for all three samples for M2-O, M1-O and P-O (Table 4.34). There were only slight variations between these interatomic distances for the different samples. These distances were then compared to that of $LiFePO_4$ structures reported in literature.[4,5,67,68] A summary of these results can be found in Table 3.2. The synthesised M2-O interatomic bond distance were smaller than those found in literature.[4,5,67,68] This indicates that all the samples have some degree of Fe^{3+}-O causing an overall contraction of the FeO_6 octahedron.[69] LFP-1 and LFP-2 had the longest interatomic bond distance and it

could be concluded that these samples would have a lower degree of Fe^{3+}-O bonds compared to that of LFP-3. This is consistent with the percentage of vacancies and the presence of Fe^{3+} (Table 4.32) where LFP-3 was predicted to have a higher degree of Fe^{3+} present. Mössbauer spectroscopy was used to determine the percentage of Fe^{3+} present on both the M2 and M1 sites for these samples and the results will be compared shortly. LFP-3 also had the largest M1-O interatomic bond distance since the contraction of the FeO_6 octahedron would cause the expansion of the LiO_6 octahedron.[72] Compared to literature LFP-1 and LFP-3 have longer average interatomic M1-O bond distances[4,67,68] than LFP-2. The average P-O interatomic bond distance is longer for the synthesised samples than the bond distances reported for other $LiFePO_4$ structures.[4,5,67,68] LFP-3 had the longest interatomic bond distance and LFP-2 the shortest.

Table 4.34: Interatomic distances of the refined structures.

	LFP –1	**LFP –2**	**LFP –3**
M2 – O(1)	2.160	2.175	2.113
M2 – O(2)	2.038	2.058	1.984
M2 – O(3) (×2)	2.026	2.052	2.010
M2 – O(3) (×2)	2.231	2.225	2.239
Average M2–O	**2.119**	**2.131**	**2.099**
P – O(1)	1.545	1.547	1.580
P – O(2)	1.660	1.624	1.702
P – O(3) (×2)	1.623	1.589	1.643
Average P – O	**1.613**	**1.587**	**1.642**
M1 – O(1) (×2)	2.189	2.182	2.180
M1 – O(2) (×2)	2.107	2.100	2.133
M1 – O(3) (×2)	2.207	2.198	2.200
Average M1 – O	**2.168**	**2.160**	**2.171**

Mössbauer spectroscopy was performed on all three samples to compare the Fe^{2+} and Fe^{3+} content. The five different Voigt doublets were used to identify the same four different Fe environments as described on section 4.2.3 and 4.2.4 (Figs 4.29 – 4.31) and the results are given in Table 4.35.

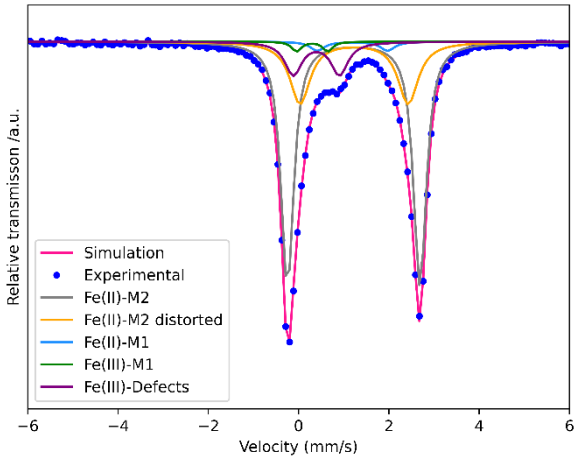

Figure 4.29: Mössbauer spectrum of the LFP-1 sample.

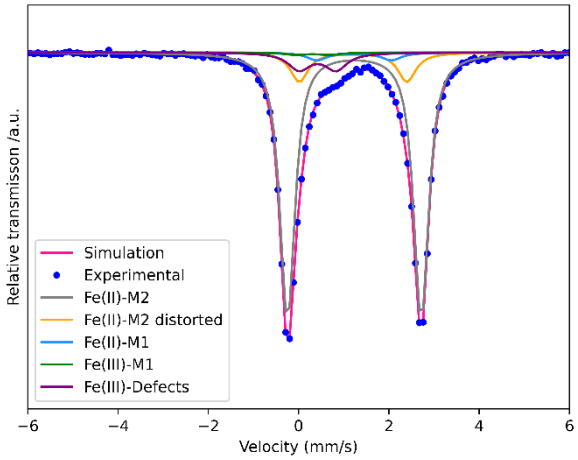

Figure 4.30: Mössbauer spectrum of the LFP-2 sample.

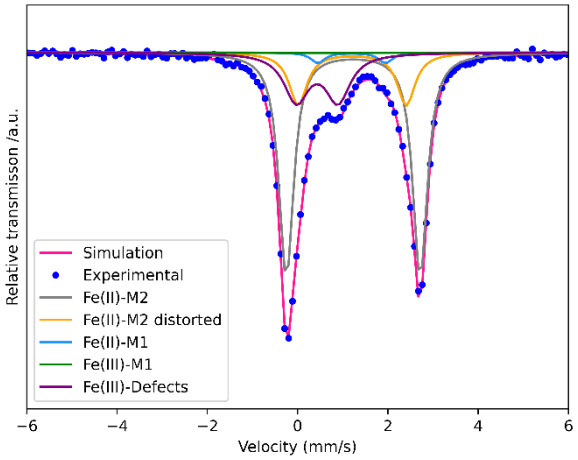

Figure 4.31: Mössbauer spectrum of the LFP-3 sample.

Table 4.35: Different isomer shifts (δ – mm/s) and quadrupole splitting (ΔE_Q – mm/s) for the purged samples.

	Fe(II) – M2		**Fe(II) – M2 distorted**		**Fe(II) –M1**		**Fe(III) –M1**		**Fe(III) – M2/Defects**	
	δ	δ	δ	ΔE_Q	δ	ΔE_Q	δ	ΔE_Q	δ	ΔE_Q
LFP-1	1.22(1)	2.94(1)	1.23(1)	2.40(1)	1.19(1)	1.56(3)	0.30(1)	0.69(2)	0.39(1)	1.02(1)
LFP-2	1.23(1)	2.96(1)	1.21(1)	2.38(1)	1.23(2)	1.65(4)	0.30(1)	0.75(2)	0.42(1)	0.81(2)
LFP-3	1.23(1)	2.97(1)	1.21(1)	2.40(1)	1.20(2)	1.50(4)	0.35(1)	0.50(7)	0.43(1)	0.92(1)

Considering the total $Fe^{2+}$and Fe^{3+} (Table 4.36) LFP-2 had the highest percentage of total Fe^{2+} and LFP-3 had the lowest percentage of Fe^{2+}. LFP-2 also had the lowest percentage of Fe^{2+} in the more distorted $LiFePO_4$ environment. Comparing the Mössbauer spectroscopy results for Fe^{2+} and Fe^{3+} on the M1 site to that of the Fe occupying the M1 site determined using PXRD (Table 4.33) it can be seen that not all the Fe has been accounted for indicating that another phase/environment might be present. Comparing the percentage of Fe^{3+} on the M2 site, LFP-3> LFP-1> LFP-2 and this is order is consistent with the PXRD results in terms of percentage vacancies on the M2 site. Determining the percentage of Fe^{3+} on the M2 site also supports the statement that LFP-3 has a higher degree of Fe^{3+}-O bonds as indicated by the shortest Fe-O interatomic bond distance. LFP-2 had the longest average Fe-O interatomic bond distance as well as the lowest percentage of Fe^{3+} on the M2 site.

Table 4.36: Percentage contribution from each form of Fe and the total Fe in the purged samples.

	Fe(II) – M2	**Fe(II) –M2 distorted**	**Fe(II) – M1**	**Fe(III) –M1**	**Fe(III) - Defects**	**Total Fe**	
						Fe^{2+}	**Fe^{3+}**
LFP-1	60(8)	24(3)	3(1)	2(1)	11(1)	87	13
LFP-2	78(8)	10(1)	3(1)	1(1)	8(1)	91	9
LFP-3	58(8)	17 (5)	3(1)	1(1)	21(6)	78	22

The disorder around the Fe atom in the different environments were also determined (Table 4.37). Fe^{2+} in the less distorted site for $LiFePO_4$ and Fe^{3+} on the M1 site for LFP-1 had the lowest degree of disorder, although it was still slightly higher than that reported for an ordered Fe environment.[49,50,53] There is a slight variation in the extent of disorder between the different samples in each environment.

Table 4.37: The full width half maximum line width (Γ – mm/s) value for the purged samples.

	Fe(II) – M2	**Fe(II) –M2 distorted**	**Fe(II) –M1**	**Fe(III) –M1**	**Fe(III) – M2/Defects**
LFP-1	0.32(1)	0.53(1)	0.37(2)	0.23(2)	0.44(1)
LFP-2	0.35(1)	0.48(1)	0.53(5)	0.60(1)	0.57(2)
LFP-3	0.38(1)	0.47(1)	0.38(4)	0.60(1)	0.63(1)

Raman spectroscopy found that the $LiFePO_4$ internal and external modes[62–64] were identified for LFP-1 (Fig. 4.32) and LFP-2 (Fig. 4.33). The peaks at lower wavenumbers could not be identified for LFP-3 (Fig. 4.34) and only υ_4 (PO_4^{3-}), υ_1 (PO_4^{3-}) and υ_3 (PO_4^{3-}) could be detected (Table 4.38). The drop in the intensity for these peaks and the disappearance of the internal mode for LFP-3 suggested that there was a decrease in crystallinity and ordering as suspected with PXRD.[64] The difference in peak shape and intensity, in the region 0 – 750 cm^{-1}, between LFP-1 (Fig. 4.32) and LFP-2 (Fig. 4.33) could be due to differences in the crystallinity as well as overlapping amorphous phases. The PXRD diffractograms of LFP-1 (Fig. 4.26) and LFP-2 (Fig.4.27) show very slight differences in peak sharpness and broadness, also revealing possible changes in the crystallinity. Mössbauer spectroscopy (Figs 4.29 and 4.30) indicated that LFP-1 had a higher Fe^{3+} content which could indicate the presence of amorphous phases causing overlapping peaks in the Raman spectra. LFP-3 (Fig. 4.34, inset) contained less of the white phase identified as $LiFePO_4$ than for the other samples. Li_3PO_4 (not shown here) and a poorly crystalline phase that has a broad peak at ~1350 cm^{-1} (Fig. 4.34) was identified in the LFP-3 sample. Li_3PO_4 was also identified in the sample using XRD and the poorly crystalline phase could be the source of Fe^{3+} identified using Mössbauer spectroscopy as superparamagnetic hematite with hyperfine parameters similar to that of Fe(III)- M2 Defects (Table 4.35).[58] There were other phases also present in LFP-1 and LFP-2 but they could not be identified due to low crystallinity and no distinct peaks. The Raman modes can be found in Table 4.37.

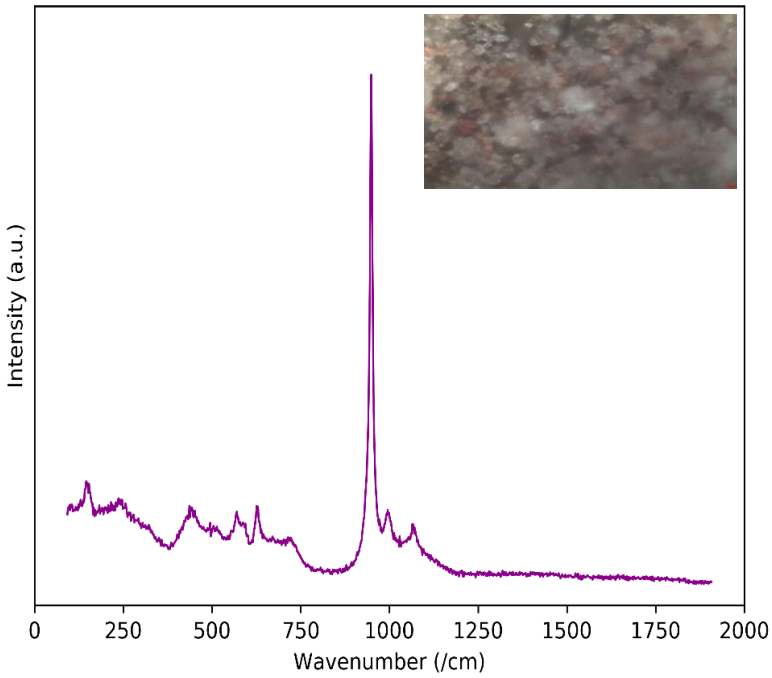

Figure 4.32: Raman spectrum and microscopic image (inset) of LFP-1.

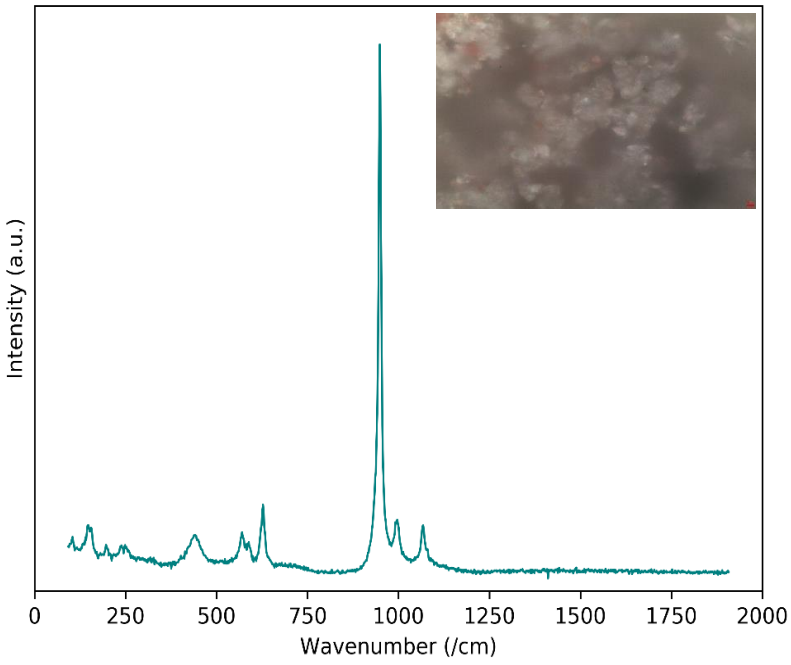

Figure 4.33: Raman spectrum and microscopic image (inset) of LFP-2.

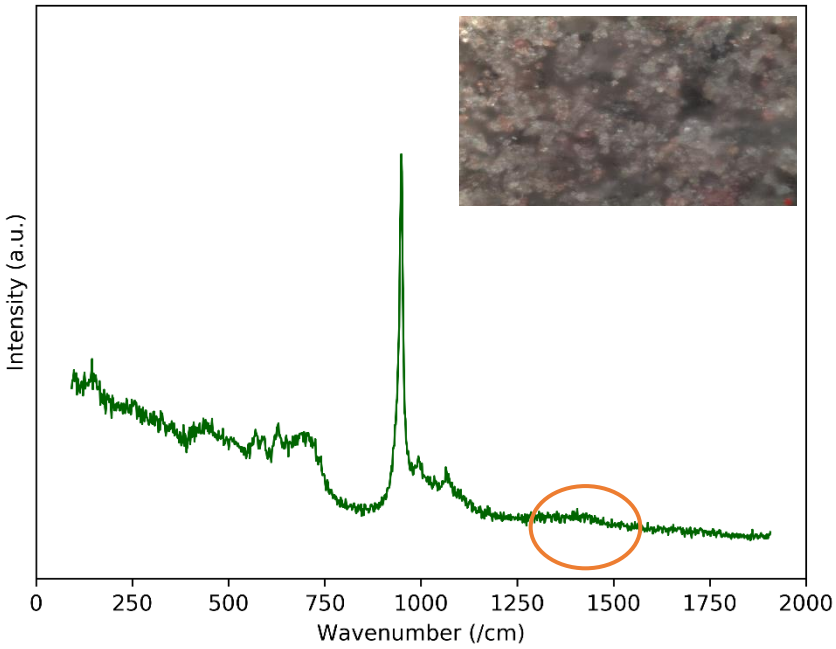

Figure 4.34: Raman spectrum and microscopic image (inset) of LFP-3. A broad peak at ~1350 cm^{-1} is circled in orange.

Table 4.38: Raman modes of the purged samples with the assigned vibrational modes.

Wavenumbers(/cm)			Assignment
LFP-1	**LFP-2**	**LFP-3**	
96	100		PO_4^{3-} rotational and Fe^{2+} translational motion
149	147	145	
195	197		
240	245		
439	440		υ_2 (PO_4^{3-})
569	571	575	υ_4 (PO_4^{3-})
590	589		
627	627	629	
948	948	948	υ_1 (PO_4^{3-})
995	995	993	υ_3 (PO_4^{3-})
1068	1067	1062	

In conclusion, XRD showed that impurities were present in all three samples. In LFP-1 and LFP-3, only $LiFePO_4$ and Li_3PO_4 were present and no Fe-containing impurities whereas LFP-2 had the Fe-impurity together with $LiFePO_4$. The lattice parameters and volume were similar for all three samples. LFP-1 and LFP-2 had similar M2 occupancies but there were variations between the M1 occupancies for all three samples. Mössbauer spectroscopy identified the same four Fe environments. The Fe^{2+} and Fe^{3+} content showed a significant variation between the three samples especially compared to the samples discussed in section 4.2.4. The difference between the highest and lowest Fe^{2+} content was 10.6%. This was not an improvement on the difference between the samples as discussed in section 4.2.4. Raman spectroscopy determined that the structure for LFP-1 and LFP-2 were similar and all the internal and external modes could be identified but for LFP-3 the crystallinity decreased and some modes could not be identified. In general, LFP-1 and LFP-2 were more similar in structure whereas LFP-3 had both a higher percentage of defects and a lower percentage of Fe^{2+}. Overall, the reproducibility was not improved using this synthetic modification and the reproducibility within a sample set was poor and Li_3PO_4 is now present in the sample.

4.3. Conclusion

This chapter looked at the synthesis time, percentage volume to which the bombs were filled as well as the ratio of the Li^+ added for synthesising $LiFePO_4$. This chapter also looked at the reproducibility between samples as well as how to improve reproducibility. The sample produced by filling the bomb to 25% of the total volume and heated at 120°C for 48 hours had the lowest amount of defects and Fe^{3+} present and these parameters were therefore used for the subsequent syntheses. The optimum Li^+ ratio was also found to be 3:1:1 ($Li:Fe:PO_4$). To reduce the impurities and defects, especially due to the oxidation of Fe^{2+} to Fe^{3+}, solutions were purged throughout the synthesis. Purging did increase the total percentage of Fe^{2+} but a small percentage of Fe^{3+} was still present in all the purged samples. The total percentage of Fe^{3+} was still lower for the purged than unpurged samples. There were slight differences between the samples when investigating reproducibility. The local structure, disorder, interatomic distances (different interatomic distance coordination) were very similar for the purged samples but the total $Fe^{2+}$and/or Fe^{3+} content did vary somewhat. Attempting to improve the reproducibility showed that there was still variability and that there could be additional factors playing a role in the hydrothermal synthesis of these samples.

4.4. References

1. Satyavani, T. V. S. L., Srinivas Kumar, A. and Subba Rao, P. S. V. Methods of synthesis and performance improvement of lithium iron phosphate for high rate Li-ion batteries: A review. *Eng. Sci. Technol. an Int. J.* **19**, 178–188 (2016).
2. Zhao, T., Chu, W., Zhao, H., Liang, X., Xu, W., Yu, M., Xia, D. and Wu, Z. XAS study of $LiFePO_4$ synthesized by solid state reactions and hydrothermal method. *Nuclear Instruments and Methods in Physics Research, Section A: Accelerators, Spectrometers, Detectors and Associated Equipment* **619**, 122–127 (2010).
3. Martin, J. F., Yamada, A., Kobayashi, G., Nishimura, S., Kanno, R., Guyomard, D. and Dupré, N. Air Exposure Effect on $LiFePO_4$. *Electrochem. Solid-State Lett.* **11**, A12 (2008).
4. Jugović, D., Cvjetićanin, N., Mitrić, M. and Mentus, S. Comparison between different $LiFePO_4$ synthesis routes. in *Materials Science Forum* **555**, 225–230 (2007).
5. Prince, A. A. M., Mylswamy, S., Chan, T. S., Liu, R. S., Hannoyer, B., Jean, M., Shen, C. H., Huang, S. M., Lee, J. F. and Wang, G. X. Investigation of Fe valence in $LiFePO_4$ by Mössbauer and XANES spectroscopic techniques. *Solid State Commun.* **132**, 455–458 (2004).
6. Hannoyer, B., Prince, A. A. M., Jean, M., Liu, R. S. and Wang, G. X. Mössbauer study on $LiFePO_4$ cathode material for lithium ion batteries. *ICAME* 767–772 (2006).
7. Dong, Y. Z., Zhao, Y. M., Chen, Y. H., He, Z. F. and Kuang, Q. Optimized carbon-coated $LiFePO_4$ cathode material for lithium-ion batteries. *Mater. Chem. Phys.* **115**, 245–250 (2009).
8. Yamada, A., Koizumi, H., Sonoyama, N. and Kanno, R. Phase change in Li_xFePO_4. *Electrochem. Solid-State Lett.* **8**, A409 (2005).
9. Yamada, A., Chung, S. C. and Hinokuma, K. Optimized $LiFePO_4$ for Lithium Battery Cathodes. *J. Electrochem. Soc.* **148**, A224 (2001).
10. Zhang, W. J. Structure and performance of $LiFePO_4$ cathode materials: A review. *Journal of Power Sources* **196**, 2962–2970 (2011).
11. Franger, S., Le Cras, F., Bourbon, C. and Rouault, H. $LiFePO_4$ synthesis routes for enhanced electrochemical performance. *Electrochem. Solid-State Lett.* **5**, A231 (2002).
12. Shin, H. C., Cho, W. Il and Jang, H. Electrochemical properties of the carbon-coated $LiFePO_4$ as a cathode material for lithium-ion secondary batteries. *J. Power Sources* **159**, 1383–1388 (2006).
13. Kim, J. K., Cheruvally, G., Ahn, J. H., Hwang, G. C. and Choi, J. B. Electrochemical properties of carbon-coated $LiFePO_4$ synthesized by a modified mechanical activation process. *J. Phys. Chem. Solids* **69**, 2371–2377 (2008).
14. Franger, S., Le Cras, F., Bourbon, C. and Rouault, H. Comparison between different $LiFePO_4$ synthesis routes and their influence on its physico-chemical properties. in *Journal of Power Sources* **119–121**, 252–257 (2003).

15. Franger, S., Le Cras, F., Bourbon, C. and Rouault, H. $LiFePO_4$ Synthesis Routes for Enhanced Electrochemical Performance. *Electrochem. Solid-State Lett.* **5**, A231 (2002).

16. Kosova, N. and Devyatkina, E. On mechanochemical preparation of materials with enhanced characteristics for lithium batteries. in *Solid State Ionics* **172**, 181–184 (2004).

17. Zhu, B. Q., Li, X. H., Wang, Z. X. and Guo, H. J. Novel synthesis of $LiFePO_4$ by aqueous precipitation and carbothermal reduction. *Mater. Chem. Phys.* **98**, 373–376 (2006).

18. Mi, C. H., Cao, G. S. and Zhao, X. B. Low-cost, one-step process for synthesis of carbon-coated $LiFePO_4$ cathode. *Mater. Lett.* **59**, 127–130 (2005).

19. Wang, L., Liang, G. C., Ou, X. Q., Zhi, X. K., Zhang, J. P. and Cui, J. Y. Effect of synthesis temperature on the properties of $LiFePO_4$/C composites prepared by carbothermal reduction. *J. Power Sources* **189**, 423–428 (2009).

20. Liu, H., Wang, Z. X., Li, X. H., Guo, H. J., Peng, W. J., Zhang, Y. H and Hu, Q. Y. Synthesis and electrochemical properties of olivine $LiFePO_4$ prepared by a carbothermal reduction method. *J. Power Sources* **184**, 469–472 (2008).

21. Barker, J., Saidi, M. Y.and Swoyer, J. L. Lithium iron(II) phospho-olivines prepared by a novel carbothermal reduction method. *Electrochem. Solid-State Lett.* **6**, A53 (2003).

22. Hsu, K. F., Hu, S. K., Chen, C. H., Cheng, M. Y., Tsay, S. Y., Chou, T. C., Sheu, H. S., Lee, J. F. and Hwang, B. J. Formation mechanism of $LiFePO_4$/C composite powders investigated by X-ray absorption spectroscopy. *J. Power Sources* **192**, 660–667 (2009).

23. Hsu, K. F., Tsay, S. Y. and Hwang, B. J. Physical and electrochemical properties of $LiFePO_4$/carbon composite synthesized at various pyrolysis periods. in *Journal of Power Sources* **146**, 529–533 (2005).

24. Deb, A., Bergmann, U., Cairns, E. J. and Cramer, S. P. Structural investigations of $LiFePO_4$ electrodes by Fe X-ray absorption spectroscopy. *J. Phys. Chem. B* **108**, 7046–7051 (2004).

25. Dominko, R., Bele, M., Goupil, J. M., Gaberscek, M., Hanzel, D., Arcon, I. and Jamnik, J. Wired porous cathode materials: A novel concept for synthesis of $LiFePO_4$. *Chem. Mater.* **19**, 2960–2969 (2007).

26. Rho, Y.-H., Nazar, L. F., Perry, L. and Ryan, D. Surface Chemistry of $LiFePO_4$ Studied by Mössbauer and X-Ray Photoelectron Spectroscopy and Its Effect on Electrochemical Properties. *J. Electrochem. Soc.* **154**, A283 (2007).

27. Dominko, R., Goupil, J. M., Bele, M., Gaberscek, M., Remskar, M., Hanzel, D. and Jamnik, J. Impact of the Carbon Coating Thickness on the Electrochemical Performance of $LiFePO_4$/C Composites. *J. Electrochem. Soc.* **152**, A607 (2005).

28. Arumugam, D., Paruthimal Kalaignan, G. and Manisankar, P. Synthesis and electrochemical characterizations of nano-crystalline $LiFePO_4$ and Mg-doped $LiFePO_4$ cathode materials for rechargeable lithium-ion batteries. *J. Solid State Electrochem.* **13**, 301–307 (2009).

29. Dominko, R., Goupil, J. M., Bele, M., Gaberscek, M., Remskar, M., Hanzel, D. and Jamnik, J. Impact of the Carbon Coating Thickness on the Electrochemical Performance

of $LiFePO_4$/C Composites. *J. Electrochem. Soc.* **152**, A607 (2005).

30. Park, K. S., Son, J.T., Chung, H.T., Kim, S.J., Lee, C.H. and Kim, H.G. Synthesis of $LiFePO_4$ by co-precipitation and microwave heating. *Electrochem. commun.* **5**, 839–842 (2003).

31. Arnold, G., Garche, J., Hemmer, R., Ströbele, S., Vogler, C. and Wohlfahrt-Mehrens, M. Fine-particle lithium iron phosphate $LiFePO_4$ synthesized by a new low-cost aqueous precipitation technique. in *Journal of Power Sources* **119–121**, 247–251 (2003).

32. Ding, Y., Jiang, Y., Xu, F., Yin, J., Ren, H., Zhuo, Q., Long, Z. and Zhang, P. Preparation of nano-structured $LiFePO_4$/graphene composites by co-precipitation method. *Electrochem. commun.* **12**, 10–13 (2010).

33. Ruiz-Jorge, F., Benítez, A., Fernández-García, S., Sánchez-Oneto, J. and Portela, J. R. Effect of Fast Heating and Cooling in the Hydrothermal Synthesis on $LiFePO_4$ Microparticles . *Ind. Eng. Chem. Res.* **59**, 9318–9327 (2020).

34. Chen, J., Bai, J., Chen, H. and Graetz, J. In situ hydrothermal synthesis of $LiFePO_4$ studied by synchrotron X-ray diffraction. *J. Phys. Chem. Lett.* **2**, 1874–1878 (2011).

35. Tajimi, S., Ikeda, Y., Uematsu, K., Toda, K. and Sato, M. Enhanced electrochemical performance of $LiFePO_4$ prepared by hydrothermal reaction. in *Solid State Ionics* **175**, 287–290 (2004).

36. Dokko, K., Shiraishi, K. and Kanamura, K. Identification of Surface Impurities on $LiFePO_4$ Particles Prepared by a Hydrothermal Process. *J. Electrochem. Soc.* **152**, A2199 (2005).

37. Sun, X. and Xu, Y. Fe excess in hydrothermally synthesized $LiFePO_4$. *Mater. Lett.* **84**, 139 - 142 (2012).

38. Chen, J. and Whittingham, M. S. Hydrothermal synthesis of lithium iron phosphate. *Electrochem. commun.* **8**, 855–858 (2006).

39. Yang, S., Zavalij, P. Y. and Stanley Whittingham, M. Hydrothermal synthesis of lithium iron phosphate cathodes. *Electrochem. commun.* **3**, 505–508 (2001).

40. Kuwahara, A., Suzuki, S. and Miyayama, M. Hydrothermal synthesis of $LiFePO_4$ with small particle size and its electrochemical properties. *J. Electroceramics* **24**, 69–75 (2010).

41. Jensen, K. M. Ø., Christensen, M., Gunnlaugsson, H. P., Lock, N., Bøjesen, E. D., Proffen, T. and Iversen, B. B. Defects in Hydrothermally Synthesized $LiFePO_4$ and $LiFe_{1-x}Mn_xPO_4$ Cathode Materials. *Chemistry of Materials* **25**, 2282 - 2290 (2013)

42. Huang, X., Yan, S., Zhao, H., Zhang, L., Guo, R., Chang, C., Kong, X and Han, H. Electrochemical performance of $LiFePO_4$ nanorods obtained from hydrothermal process. *Mater. Charact.* **61**, 720–725 (2010).

43. Shiraishi, K., Dokko, K. and Kanamura, K. Formation of impurities on phospho-olivine $LiFePO_4$ during hydrothermal synthesis. *J. Power Sources* **146**, 555–558 (2005).

44. Chen, J. and Graetz, J. Study of Antisite Defects in Hydrothermally Prepared $LiFePO_4$ by in Situ X-ray Diffraction. *ACS Appl. Mater. Interfaces* **3**, 1380–1384 (2011).

45. Bini, M., Ferrari, S., Capsoni, D., Mustarelli, P., Spina, G., Giallo, F. D., Lantieri, M., Leonelli, ., Rizzuti, A. and Massarotti, V. Pair distribution function analysis and Mössbauer study of defects in microwave-hydrothermal $LiFePO_4$. *RSC Adv.* **2**, 250–258 (2012).

46. Ø. Jensen, K. M., Gunnlaugsson, H. P., Christensen, M. and Iversen, B. B. Mössbauer spectroscopy study of defects in hydrothermally synthesized $LiFePO_4$ cathode material. *Hyperfine Interact.* **226**, 73–78 (2014).

47. Schmid-Beurmann, P. Synthesis and phase characterization of a solid solution series between β-$Fe_2(PO_4)O$ and $Fe_4(PO_4)_3(OH)_3$. *J. Solid State Chem.* **153**, 237–247 (2000).

48. Xia, X., Wang, Z. and Chen, L. Regeneration and characterization of air-oxidized $LiFePO_4$. *Electrochem. commun.* **10**, 1442–1444 (2008).

49. Hamelet, S., Gibot, P., Casas-Cabanas, M., Bonnin, D., Grey, C. P., Cabana, J., Leriche, J. B., Rodriguez-Carvajal, J., Courty, M., Levasseur, S., Carlach, P., Van Thournout, M., Tarascon, J. M. and Masquelier, C. The effects of moderate thermal treatments under air on $LiFePO_4$-based nano powders. *J. Mater. Chem.* **19**, 3979–3991 (2009).

50. Maccario, M., Croguennec, L., Wattiaux, A., Suard, E..,Le Cras, F. and Delmas, C. C-containing $LiFePO_4$ materials - Part I: Mechano-chemical synthesis and structural characterization. *Solid State Ionics* **179**, 2020–2026 (2008).

51. Cuisinier, M., Martin, J. F., Dupré, N., Yamada, A., Kanno, R. and Guyomard, D. Moisture driven aging mechanism of $LiFePO_4$ subjected to air exposure. *Electrochem. commun.* **12**, 238–241 (2010).

52. Amisse, R., Sougrati, M. T., Stievano, L., Davoisne, C., Dražič, G., Budič, B., Dominko, R. and Masquelier, C. Singular Structural and Electrochemical Properties in Highly Defective $LiFePO_4$ Powders. *Chem. Mater.* **27**, 4261–4273 (2015).

53. Cuisinier, M., Martin, J. F., Dupré, N., Kanno, R. and Guyomard, D. Elucidating the $LiFePO_4$ air aging mechanism to predict its electrochemical performance. *J. Mater. Chem.* **21**, 18575–18583 (2011).

54. Axmann, P., Stinner, C., Wohlfahrt-Mehrens, M., Mauger, A., Gendron, F. and Julien, C. M. Nonstoichiometric $LiFePO_4$: Defects and Related Properties. Chem. Mater. **21**, 1636–1644 (2009).

55. Wu, Y. J., Gu, Y. J., Chen, Y. B., Liu, H. Q. and Liu, C. Q. Effect of lithium phosphate on the structural and electrochemical performance of nanocrystalline $LiFePO_4$ cathode material with iron defects. *Int. J. Hydrogen Energy* **43**, 2050–2056 (2018)

56. Chen, J. and Whittingham, M. S. Hydrothermal synthesis of lithium iron phosphate. *Electrochem. commun.* **8**, 855–858 (2006).

57. Andersson, A. S., Kalska, B., Häggström, L. and Thomas, J. O. Lithium extraction/insertion in $LiFePO_4$: An X-ray diffraction and Moessbauer spectroscopy study. *Solid State Ionics* **130**, 41–52 (2000).

58. Sánchez, L. C., Arboleda, J. D., Saragovi, C., Zysler, R. D. and Barrero, C. A. Magnetic and structural properties of pure hematite submitted to mechanical milling in air and ethanol. *Phys. B Condens. Matter* **389**, 145–149 (2007).

59. Chung, S. Y., Choi, S. Y., Yamamoto, T. and Ikuhara, Y. Atomic-scale visualization of antisite defects in LiFePO4. *Phys. Rev. Lett.* **100**, 125502 (2008).

60. Liu, Z., Dong, D., Liu, M., Sui, Y., Su, W., Qian, Z. and Li, Z. Quadrupole splitting distributions in purpurite and related minerals. *Hyperfine Interact.* **163**, 13–27 (2005).

61. Shannon, R. D. Revised effective ionic radii and systematic studies of interatomic distances in halides and chalcogenides. *Acta Crystallogr. Sect. A* **32**, 751–767 (1976).

62. Burba, C. M. & Frech, R. Raman and FTIR Spectroscopic Study of Li[sub x]FePO[sub 4] (0≤x≤1). *J. Electrochem. Soc.* **151**, A1032 (2004).

63. Paraguassu, W., Freire, P. T. C., Lemos, V., Lala, S. M., Montoro, L. A. and Rosolen, J. M. Phonon calculation on olivine-like $LiMPO_4$ (M = Ni, Co, Fe) and Raman scattering of the iron-containing compound. *J. Raman Spectrosc.* **36**, 213–220 (2005).

64. Wu, J., Krishna Phani Dathar, G., Sun, C., Theivanayagam, M. G., Applestone, D., Dylla, A. G., Manthiram, A., Henkelman, G., Goodenough, J. B. and Stevenson, K. J. In situ Raman spectroscopy of $LiFePO_4$: size and morphology dependence during charge and self-discharge. *IOP Publ. Nanotechnol. Nanotechnol.* **24**, 424009–424018 (2013).

65. Padhi, A. K., Nanjundaswamy, K. S. and Goodenough, J. B. Phospho-olivines as Positive-Electrode Materials for Rechargeable Lithium Batteries. *J. Electrochem. Soc.* **144**, 1188 (1997).

66. Chen, J., Wang, S. and Whittingham, M. S. Hydrothermal synthesis of cathode materials. *J. Power Sources* **174**, 442–448 (2007).

67. Streltsov, V. A., Belokoneva, E. L., Tsirelson, V. G. and Hansen, N. K. Multipole analysis of the electron density in triphylite, $LiFePO_4$, using X-ray diffraction data. *Acta Crystallogr. Sect. B* **49**, 147–153 (1993).

68. Islam, M. S., Driscoll, D. J., Fisher, C. A. J. and Slater, P. R. Atomic-scale investigation of defects, dopants, and lithium transport in the $LiFePO_4$ olivine-type battery material. *Chem. Mater.* **17**, 5085–5092 (2005).

69. Gibot, P., Casas-Cabanas, M., Laffont, L., Levasseur, S., Carlach, P., Hamelet, S., Tarascon, J. M. and Masquelier, Christian. Room-temperature single-phase Li-insertion/extraction in nanoscale Li_xFePO_4. *Nat. Mater.* **7**, 741–747 (2008).

70. Shu, H., Wang, X., Wu, Q., Hu, B., Yang, X., Wei, Q., Liang, Q., Bai, Y., Zhou, M., Wu, C., Chen, M., Wang, A. and Jiang, L. Improved electrochemical performance of $LiFePO_4$/C cathode via Ni and Mn co-doping for lithium-ion batteries. *J. Power Sources* **237**, 149–155 (2013).

71. Gao, H., Jiao, L., Yang, J., Qi, Z., Wang, Y. and Yuan, H. High rate capability of Co-doped $LiFePO_4$/C. Electrochim. Acta **97**, 143–149 (2013).

72. Liu, Z. and Huang, X. Factors that affect activation energy for Li diffusion in $LiFePO_4$: A first-principles investigation. *Solid State Ionics* **181**, 907–913 (2010).

73. Haas, O., Deb, A., Cairns, E. J. and Wokaun, A. Synchrotron X-ray absorption study of $LiFePO_4$ electrodes. *J. Electrochem. Soc.* **152**, (2005).

74. Deb, A., Bergmann, U., Cairns, E. J. and Cramer, S. P. X-ray absorption spectroscopy

study of the Li_xFePO_4 cathode during cycling using a novel electrochemical in situ reaction cell. *J. Synchrotron Radiat.* **11**, 497–504 (2004).

75. Wong, J., Lytle, F. W., Messmer, R. P. and Maylotte, D. H. K-edge absorption spectra of selected vanadium compounds. *Phys. Rev. B* **30**, 5596–5610 (1984).

76. Roe, A. L., Schneider, D. J., Mayer, R. J., Pyrz, J. W., Widom, J. and Que, L. X-ray Absorption Spectroscopy of Iron-Tyrosinate Proteins. *J. Am. Chem. Soc.* **106**, 1676–1681 (1984).

77. Etschmann, B. E., Donner, E., Brugger, J., Howard, D. L., de Jonge, M. D., Paterson, D., Naidu, R., Scheckel, K. G., Ryan, C. G. and Lombi, E. Speciation mapping of environmental samples using XANES imaging. *Environ. Chem.* **11**, 341 (2014).

78. Ravel, B. and Newville, M. ATHENA, ARTEMIS, HEPHAESTUS: Data analysis for X-ray absorption spectroscopy using IFEFFIT. in *Journal of Synchrotron Radiation* **12** 537–541 (2005).

79. Kelly, S. D., Hesterberg, D. and Ravel, B. *Analysis of Soils and Minerals Using X-ray Absorption Spectroscopy*. 387–463 (John Wiley & Sons, Ltd, 2015).

80. Kelly, S. D. and Ravel, B. EXAFS energy shift and structural parameters. *AIP Conference Proceedings* **882**, 132–134 (2007).

81. Griffith, J. S. and Orgel, L. E. Ligand-field theory. *Q. Rev. Chem. Soc.* **11**, 381–393 (1957).

82. Li, Z. & Shinno, I. Next nearest neighbor effects in triphylite and related phosphate minerals. *Mineral. J.* **19**, 99–107 (1997).

83. de Faria, D. L. A. and Lopes, F. N. Heated goethite and natural hematite: Can Raman spectroscopy be used to differentiate them? *Vib. Spectrosc.* **45**, 117–121 (2007)

84. Toby, B. H. R factors in Rietveld analysis: How good is good enough? . *Powder Diffr.* **21**, 67–70 (2006).

Chapter 5

Effects of Li^+ addition rate during the synthesis of $LiFePO_4$: Combining X-ray diffraction and spectroscopy techniques to determine average and local structure

5.1 Introduction

$LiFePO_4$ exhibits poor lithium ion diffusion, and hence conductivity, due to the diffusion only occurring through the 1-dimensional channel.[1–4] Due to this disadvantage, the formation of side phases and the lithium content plays a critical role during synthesis. A study conducted by Axmann[5] showed that a lithium deficient system negatively affects the electrochemical properties and that the side phase Li_3PO_4 readily forms in a lithium excess system as the lithium combines with the phosphate group. Li_3PO_4 has been shown to be an excellent ion conductor but has been determined to be electrochemically inert as a side phase in $LiFePO_4$.[5,6] Another research group[7] determined that although an excess of lithium could readily form Li_3PO_4 there was a small balance where the right lithium excess can suppress the formation of impurities. The method development stage for this hydrothermal synthesis indicated that an excess lithium ratio of 3:1:1 (Li^+:Fe^{2+}:PO_4^{3-}) was the optimum synthesis condition (section 4.2.3) where the high lithium content produced a favourable basic solution.[7] It was therefore important to determine how the addition rate of the excess lithium affects the formation of the final product. In this chapter the effect of lithium (Li^+) addition was investigated during synthesis. The different Li+ addition rates showed the presence of different impurities, different percentage occupancies on the M2 and M1 site as well as Fe^{2+} content. The local structure remained the same but showed variation in the interatomic distances and Debye-Waller factors.

5.2. Experimental

The synthesis described in section 4.2.4 and section 4.2.5 was used with some modifications to investigate the effect of the Li^+ addition on the final product. Deionised water was purged for 1 hour and 30 min (~75 mL) before the synthesis and for the duration of the synthesis. All materials were dissolved using the purged water. After the dissolution of both the LiOH and the $FeSO_4/H_3PO_4$, a Li^+ drop was added every 1, 2, 3, 4 and 5 seconds to the $FeSO_4/H_3PO_4$ solution using a Pasteur pipette. After the addition of LiOH to the $FeSO_4/H_3PO_4$ solution the mixture was thoroughly mixed and purged for another 5 minutes. The rest of the synthesis was described in section 2.1.2.

5.3. Results and Discussion

5.3.1. Synchrotron radiation powder X-ray diffraction

Diffraction patterns were collected on the 1, 2, 3, 4 and 5 second Li^+ addition rate samples. These samples will be referred to as **1sec**, **2sec**, **3sec**, **4sec** and **5sec**. The 3sec sample showed the best preliminary XRD results when the data was collected on the lab diffractometer and therefore another 3sec sample was added to investigate the reproducibility of this addition rate. These samples will be referred to as **3sec_1** and **3sec_2** (duplicate). Rietveld refinement was conducted on all the above-mentioned addition rate (Figs. 5.1 – 5.6) using an X-ray wavelength of 0.167057(4) Å. Graphically it can be seen that the 2sec and 5sec samples have a poorer fit than the other samples. The Rietveld error indices (Table 5.1) also showed this except for the 3sec_1 sample where the main mismatches that affected the error indices was a cause of the intensity dropping below the baseline (3º, 3.5º and 4.9º where ° is given in 2theta). This was not sample related as it was not seen in the laboratory data. It could possibly be due to dead pixels and incorrect masking done at the synchrotron facility.

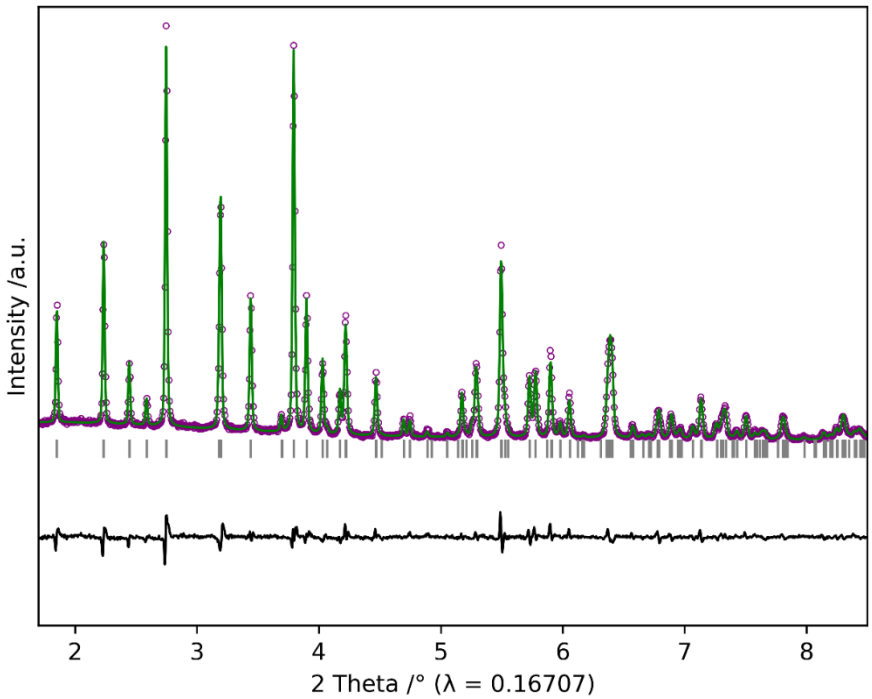

Figure 5.1: Synchrotron diffractogram of the 1sec $LiFePO_4$ sample showing the observed (purple), calculated (green) and difference (black) plots generated from a Rietveld Refinement analysis. Bragg reflections for $LiFePO_4$ are indicated with the grey markers.

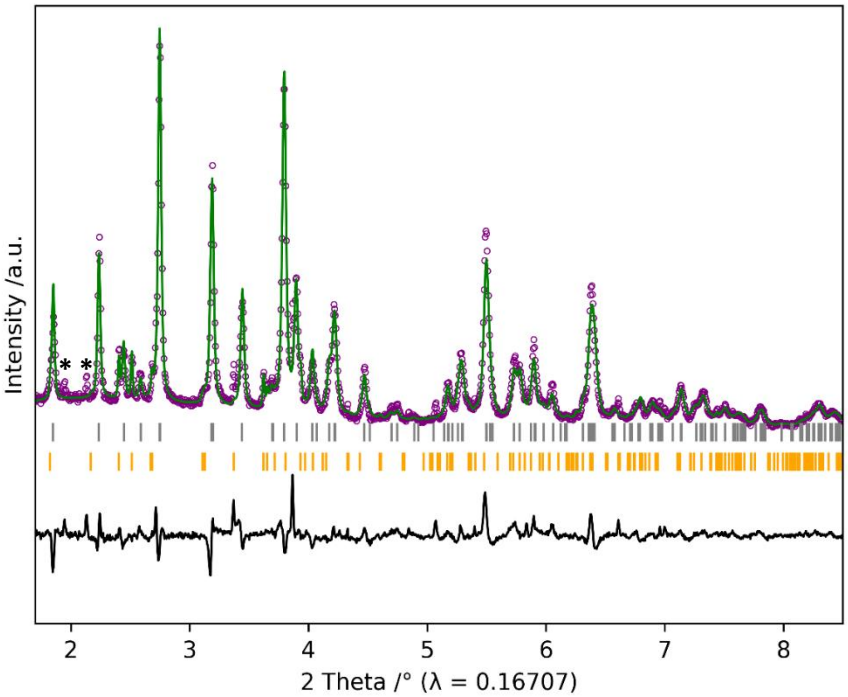

Figure 5.2: Synchrotron diffractogram of the 2sec $LiFePO_4$ sample showing the observed (purple), calculated (green) and difference (black) plots generated from a Rietveld Refinement analysis. Bragg reflections for $LiFePO_4$ and Li_3PO_4 are indicated with the grey and the yellow markers respectively. (*) indicates unidentified peaks from impurity phase/s.

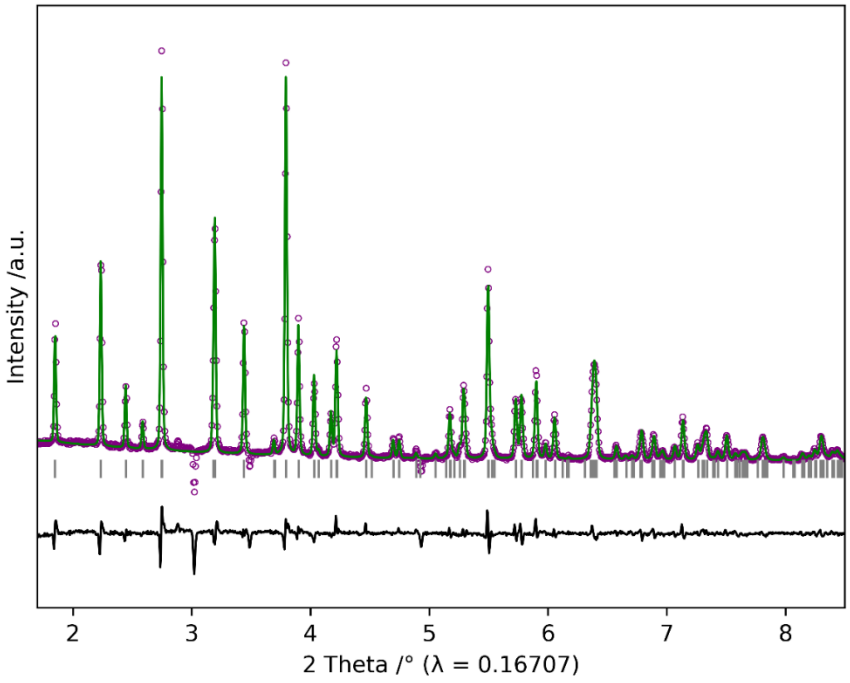

Figure 5.3: Synchrotron diffractogram of the 3sec_1 $LiFePO_4$ sample showing the observed (purple), calculated (green) and difference (black) plots generated from a Rietveld Refinement analysis. Bragg reflections for $LiFePO_4$ are indicated with the grey markers.

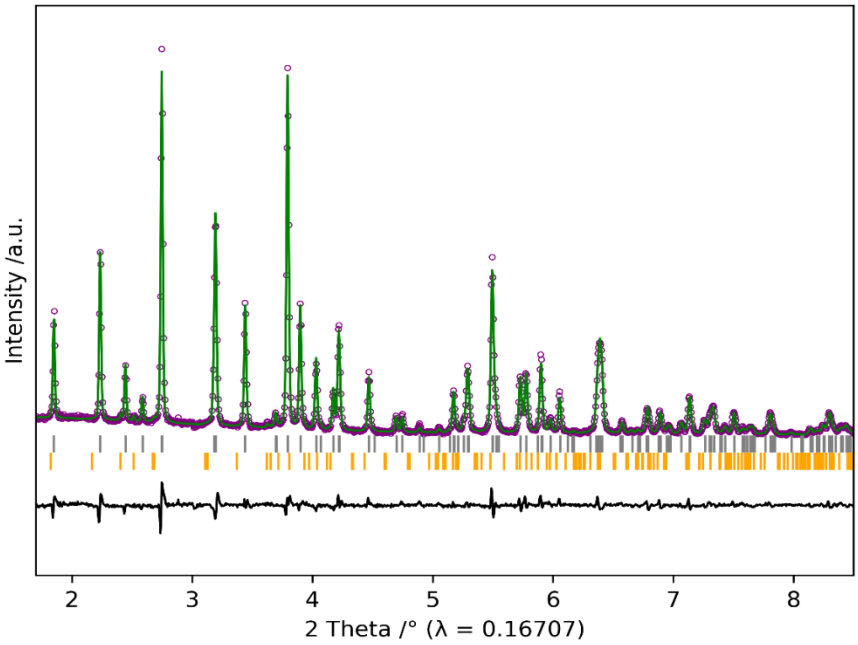

Figure 5.4: Synchrotron diffractogram of the 3sec_2 $LiFePO_4$ sample showing the observed (purple), calculated (green) and difference (black) plots generated from a Rietveld Refinement analysis. Bragg reflections for $LiFePO_4$ and Li_3PO_4 are indicated with the grey and the yellow markers respectively.

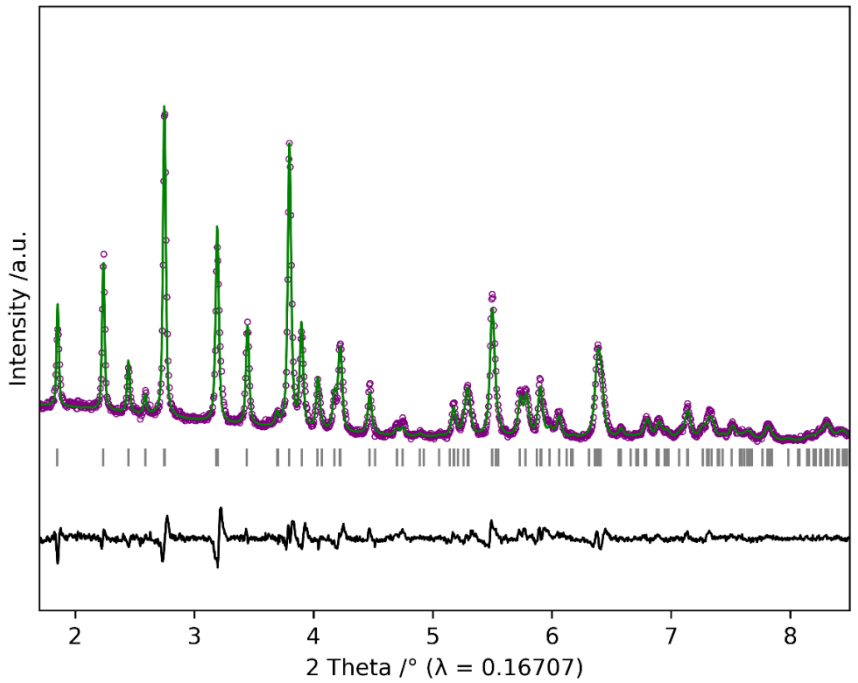

Figure 5.5: Synchrotron diffractogram of the 4sec $LiFePO_4$ sample showing the observed (purple), calculated (green) and difference (black) plots generated from a Rietveld Refinement analysis. Bragg reflections for $LiFePO_4$ are indicated with the grey markers.

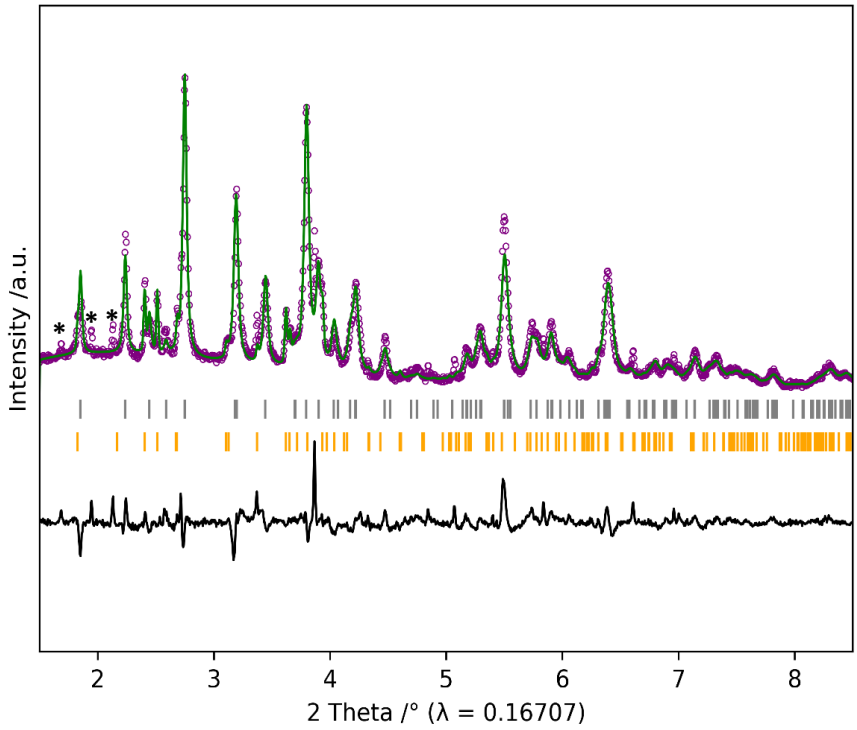

Figure 5.6: Synchrotron diffractogram of the 5sec $LiFePO_4$ sample showing the observed (purple), calculated (green) and difference (black) plots generated from a Rietveld Refinement analysis. Bragg reflections for $LiFePO_4$ and Li_3PO_4 are indicated with the grey and the yellow markers respectively. (*) indicates unidentified peaks from impurity phase/s.

Table 5.1: Rietveld error indices for the varied Li^+ addition rate samples.

Sample	R_{wp}	R_p	R_{exp}	GOF
1sec	7.23	5.72	55.64	0.13
2sec	9.17	6.63	51.63	0.18
3sec_1	15.42	7.75	59.89	0.26
3sec_2	6.90	5.47	57.09	0.12
4sec	8.11	6.23	64.41	0.13
5sec	9.50	6.72	52.14	0.18

The lattice parameters and the volume for each structure were also refined (Table 5.2). The refined lattice parameters as well as the volume are similar to those determined from previous studies (Table 3.1).[8–14] The lattice parameters were the same within the error with a slight variation in the volume especially for the 2sec and 5sec sample. A multiphase refinement was performed on all the samples. The identified phases present in the samples were $LiFePO_4$ and Li_3PO_4 (Table 5.3). $LiFePO_4$ was identified as the main phase in all the samples. No Li_3PO_4 was found in the 1sec, 3sec_1 and 4sec samples and only a very small amount of Li_3PO_4 in the 3sec_b sample although no Li_3PO_4 in the 3sec_b sample was detected in the laboratory data.

The 5sec and the 2sec samples had the highest percentage of Li_3PO_4 present. These two samples also showed the presence of an additional unidentified phase present. In the 2sec sample the peaks can be seen at 1.94º and 2.13º (indicated with *) and for the 5sec sample the peaks are present at 1.68º, 1.94º and 2.13º (indicated with *). The position of the peaks indicate that it could be the same impurity phase. The slightly higher, more defined and additional peak at 1.68° indicates that there could be a higher percentage of this phase present in the 5sec sample.

Table 5.2: Selected structural parameters of the refined $LiFePO_4$ phases for the varied Li^+ addition rate samples.

Sample	a (Å)	b (Å)	c (Å)	Volume (Å^3)
1sec	10.349(3)	5.9940(2)	4.7066(1)	291.97(2)
2sec	10.35(6)	5.9992(6)	4.7031(5)	291.91(5)
3sec_1	10.349(6)	5.9938(3)	4.7056(3)	291.88(3)
3sec_2	10.349(3)	5.9947(2)	4.7064(1)	291.99(2)
4sec	10.329(8)	5.9899(5)	4.7022(4)	290.92(4)
5sec	10.34(2)	5.989(1)	4.6995(9)	291.13(9)

Table 5.3: The percentage $LiFePO_4$ and Li_3PO_4 obtained from a multiphase Rietveld refinement of the XRD of the Li^+ addition rate samples.

Sample	$LiFePO_4$	Li_3PO_4
1sec	100	-
2sec*	92.02	7.98
3sec_1	100	-
3sec_2	98.15	1.85
4sec	100	-
5sec*	80.83	19.17

* Percentages exclude the additional impurity phase

To investigate the presence of structural defects, the data for all the samples were refined for both site exchange defects and antisite defects.[14] All samples comprise of a small percentage of Fe on the M1 (Li^+) site and no Li^+ on the M2 (Fe^{2+}) site and (Table 5.4). This corresponds to antisite defects rather than site exchange defects.[14] The M2 site was not fully occupied and as no Li^+ was found on this site which it indicates that vacancies were formed (Table 5.4). The replacement of some Fe^{2+} with Fe^{3+} could be responsible for the formation of the vacancies in

order to retain charge neutrality.[15] The M1 site was also refined to determine the amount of Li^+ that occupies this site and it was found that it was partially occupied by either Fe^{2+} or Fe^{3+} ions. The oxidation state of Fe on the M1 and M2 sites was determined using Mössbauer spectroscopy and will be discussed shortly. The 3sec_1 sample has the highest percentage of Li^+ occupying the M1 site, and hence the lowest percentage of Fe on the M1 site and the 5sec and the 2sec samples have the highest percentage of Fe occupying the M1 site. These samples could possibly exhibit poor electrochemical performance due to the blocking of the 1-dimensional Li^+ diffusion channels.[4,13,16] From these results, the 5sec sample was the least desirable- it had the lowest percentage of Fe on the M2 site and, since it had the highest percentage of Fe vacancies, it would also suggest that it had a higher amount of Fe^{3+} occupying the M2 site. This sample also showed the highest percentage of Fe occupying the M1 site.

Table 5.4: The percentage Li occupying the M2 (Fe) site, vacancies on the M2 site and Fe occupying the M1 (Li) site in the refined $LiFePO_4$ structures.

	1sec	**2sec**	**3sec_1**	**3sec_2**	**4sec**	**5sec**
M2 (Fe) occupancy	99.13(7)	96.6(2)	98.93(9)	99.035	96.3(2)	95.3(2)
M2 (Fe) vacancy	0.87	3.4	1.07	0.965	3.7	4.7
M1 (Li) occupancy	91.14(3)	86.5(1)	92.49(6)	91.18(3)	89.89(9)	83.1(2)
Fe on the M1 site	8.9(3)	13.5(1)	7.51(5)	8.81(7)	10.11(9)	16.9(1)

The refined M2-O, P-O and M1-O interatomic bond distances (Table 5.5) deviate slightly from the interatomic bond distances reported in literature (Table 3.2).[3,9,17,18] XRD did not detect any impurities in the samples from literature. For well crystallized $LiFePO_4$ with very little Fe^{3+} present the Fe-O interatomic bond distance ranges between $2.157 - 2.172$ Å[19,20] whereas the average Fe^{3+}-O interatomic bond distance for $FePO_4$ is 2.045Å[20] The average M2-O interatomic bond distances are shorter than the reported values ($2.148 - 2.157$ Å). The shorter bonds are indicative of the presence of Fe(III)-O bonds in the structure.[19,20] The 3sec_1 sample has the largest M2-O interatomic bond distance and indicates that the 3sec_1 sample has the lowest percentage of Fe(III)-O bonds. The 5sec sample has the shortest average M2-O interatomic bond distance almost closer to that of $FePO_4$ indicating that there are possibly more Fe^{3+}-O bonds present than in the other samples. This ties in with the parameters presented for

this sample in Table 5.4. The average P-O interatomic bond distance for the synthesised samples are larger than the reported values (1.544 − 1.565 Å).[3,9,17,18,21] The P-O interatomic bond distance can be used to investigate any changes in the stability of the $LiFePO_4$ structure. A shorter interatomic bond distance suggests a more stable structure.[22–24] The 3sec_1 sample had an interatomic bond distance closest to that of the reported values. The 5 sec sample exhibited the longest interatomic bond distance that deviated quite significantly from the reported value, as would be expected. The average M1-O interatomic bond distance for these synthesised samples is larger than the values reported in literature (2.127 − 2.151 Å).[3,17,18,21] A larger M1-O interatomic bond distance correlates to the shorter Fe-O interatomic bond distance for the metal on the M2 site.[20] This explains the large Li-O_6 interatomic distance for the 5sec sample that contains the higher degree of Fe^{3+}-O bonds.

Table 5.5: Interatomic bond distances (Å) of the varied Li^+ addition rate samples.

	1sec	**2sec**	**3sec_1**	**3sec_2**	**4sec**	**5sec**
M2 – O(1)	2.187	2.107	2.211	2.194	2.131	2.068
M2 – O(2)	2.057	1.998	2.059	2.056	2.009	1.994
M2 – O(3) (×2)	2.041	2.002	2.048	2.042	2.004	1.967
M2 – O(3) (×2)	2.238	2.267	2.232	2.240	2.266	2.280
Average M2–O	**2.134**	**2.107**	**2.138**	**2.136**	**2.113**	**2.093**
P – O(1)	1.540	1.580	1.546	1.543	1.573	1.599
P – O(2)	1.633	1.700	1.614	1.629	1.668	1.714
P – O(3) (×2)	1.600	1.649	1.592	1.599	1.628	1.686
Average P – O	**1.593**	**1.645**	**1.586**	**1.593**	**1.624**	**1.671**
M1 – O(1) (×2)	2.177	2.183	2.162	2.174	2.175	2.181
M1 – O(2) (×2)	2.093	2.121	2.094	2.092	2.119	2.117
M1 – O(3) (×2)	2.185	2.172	2.193	2.184	2.169	2.181
Average M1 – O	**2.152**	**2.159**	**2.150**	**2.150**	**2.154**	**2.160**

The interatomic bond distance analysis confirmed what was given in Table 5.4. The presence of the vacancies confirms that there is Fe^{3+} present in all the samples and the 5sec sample has the highest percentage of vacancies exhibited the most Fe^{3+}.

5.3.2. X-ray absorption spectroscopy

The general shape of the normalized spectra (Fig. 5.7) for the varied Li^+ addition rate samples are the same and similar to that of $LiFePO_4$ – standard. XANES and EXAFS were investigated separately.

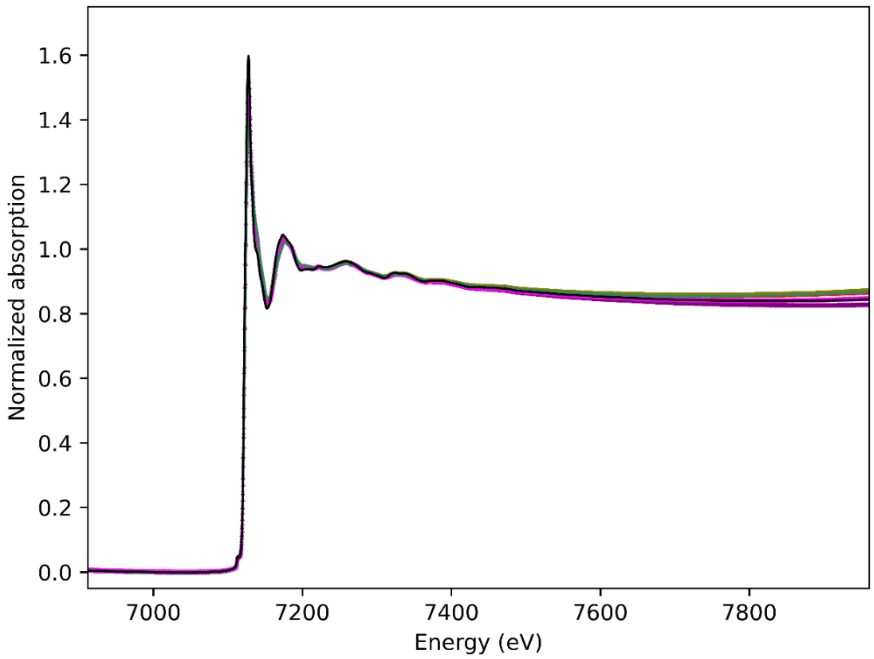

Figure 5.7: Normalized Fe K-edge spectra for all the varied Li^+ addition samples compared to that of the $LiFePO_4$ standard (black). These spectra are largely overlapped.

5.3.2.1. XANES

(i) Pre-edge

The pre-edge region exists due to the 1s → 3d dipole transition.[25] Three different standards ($LiFePO_4$ – Fe^{2+}, $FePO_4•4H_2O$ – Fe^{3+} and α-Fe_2O_3 – Fe^{3+} with an increase in the octahedron distortion) were used for the XANES pre-edge analysis (Fig. 5.8). A full discussion of the structural differences of these standards are in section 2.2.3.1.

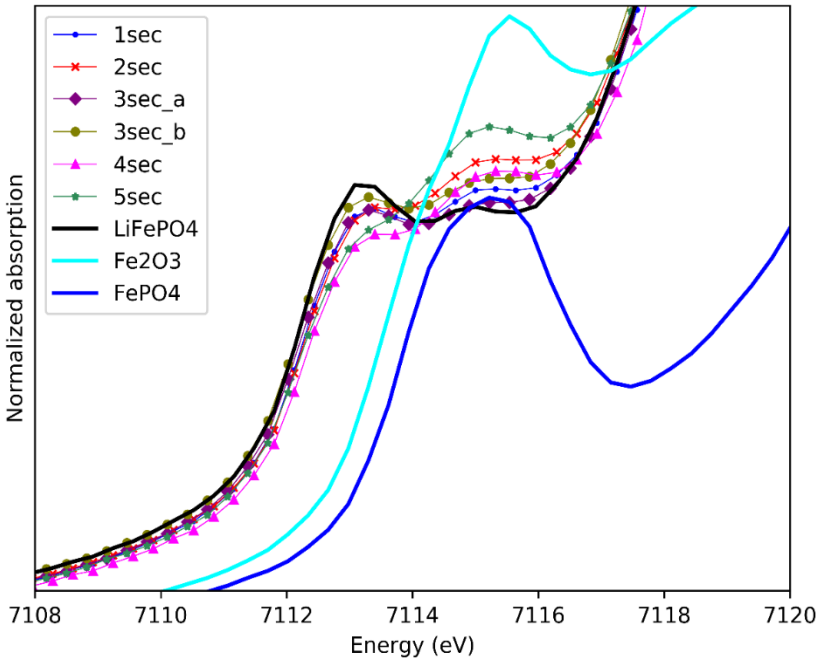

Figure 5.8: Comparison Fe K-edge XANES pre-edge region of the different standards and varied Li^+ addition rate samples.

The standards were used to assess the oxidation states and the geometry around the Fe^{2+}/Fe^{3+} atom in the synthesised samples. Comparing the synthesised samples with that of the $LiFePO_4$ standard, it showed that all samples exhibit the t_{2g} (7112 eV) and e_g (7115 eV) peak energies (Fig. 5.8 and Table 5.6),[26,27] although the energy position for the synthesised samples was at ~7113 eV and not at 7112 eV as reported in literature.[9,26,28,29] This could be an indication of possible mixed phases present as the exact position which depends on the ligands present in the sample as well as the amount of mixing in the samples between the two different oxidation states.[27,30] The peak positions for the $LiFePO_4$ standard could also be slightly different than the reported values due to the impurity phase present. The standard was discussed in section 3.2.2.1. The 4sec and 5 sec samples showed changes in the peak shape. The 4sec sample showed a less pronounce t_{2g} peak compared to the other samples and 5sec sample also showed a less pronounced t_{2g} peak to the point where it almost disappears and a more pronounced e_g peak compared to the other samples. The 4sec and 5sec samples could possibly have higher amounts of Fe^{3+}. The peaks ~7115 eV can either represent the e_g $LiFePO_4$ peak or the presence of (Fe^{3+}).[9,28] All samples show an increase of this peak intensity as well as some broadening as compared to the $LiFePO_4$ standard, this could indicate (1) an increase in distortion around the Fe atom [27,31,32] (Table 5.6), or (2) that there is a possible change in coordination number around the Fe^{3+} atom that further removes the inversion symmetry around the Fe atom,[30,33] or (3) a

change in bonding distribution affecting the e_g orbitals that experience the repulsion field of the ligands.[34] The change in bonding distribution is for example the shorter distances occupying the axial position in some samples whereas in other the longer distances occupy the axial position or a mixture thereof. The pre-edge region corroborates the information in Table 5.4 that was determined using XRD. Although the 4sec sample was phase pure (Fig. 5.5) there were quite a few defects or amorphous phases present in this sample that was not detected using PXRD (Table 5.4) and that could have an effect on the distortion around the Fe atom. A similar link can be seen between the 2sec and the 5sec samples and the 1sec and 3sec_1 sample. The samples with similar defects have similar intensities in the pre-edge region.

Table 5.6: The different pre-edge peak intensities and peak positions for the standards and the varied Li^+ addition rate samples.

Sample	Peak position 1 (eV)	Peak intensity 1 (au)	Peak position 2 (eV)	Peak intensity 2 (au)
$LiFePO_4$	7112.95	0.0480	7115.20	0.0457
$FePO_4$	-	-	7115.22	0.0469
Fe_2O_3	-	-	7115.72	0.0642
1sec	7113.17	0.0452	7115.57	0.0477
2sec	7113.08	0.0447	7115.93	0.0506
3sec_1	7113.08	0.0450	7115.64	0.0466
3sec_2	7113.03	0.0469	7115.58	0.0488
4sec	7113.77	0.0423	7115.52	0.0494
5sec	7113.22	0.0427	7115.49	0.0537

(ii) Rising absorption edge and main absorption edge:

The rising absorption and the main absorption edge can be used to determine if there is a change in oxidation state (Fig. 5.9 and Table 5.7).[27,31] A change in oxidation state from Fe^{2+} to Fe^{3+} will cause a shift to higher energy due to the electrons being more strongly bound to the nucleus and more energy is needed to excite the electrons in a Fe^{3+} state.[27,28,31] The peak position of the main absorption edge (Table 5.7) for the $LiFePO_4$ standard is at 7127.8 eV. This value is similar to those reported by other research groups as discussed in section 3.1.2.1.[28,35] The Fe^{3+} standards ($FePO_4$•$4H_2O$ and α-Fe_2O_3) have higher peak positions between positions between 7133 – 7134 eV (Table 5.7). The comparison of the main edge for all three standards are shown in Figure 3.7. The rising absorption edge of the samples synthesised shows that there is a slight shift to higher energy as compared to that of the $LiFePO_4$ standard (Fig 5.9). This indicates that

the majority of Fe is Fe^{2+} as the Fe^{3+} standards have a rising absorption edge that is higher in energy. The synthesised samples could be a mixture of Fe^{2+} and Fe^{3+} where the ratio of Fe^{3+} increases with an increase in the energy of the absorption edge and the increasing Fe^{3+} content is according to: 1sec, both 3sec samples < 2sec < 4sec < 5sec samples. The 1sec and both 3sec samples are all located at 7127.9 eV indicating the presence of Fe^{2+} similar to $LiFePO_4$-standard. Changes in oxidation state and the different ratios of oxidation states can be further investigated using linear combination fitting (LCF).

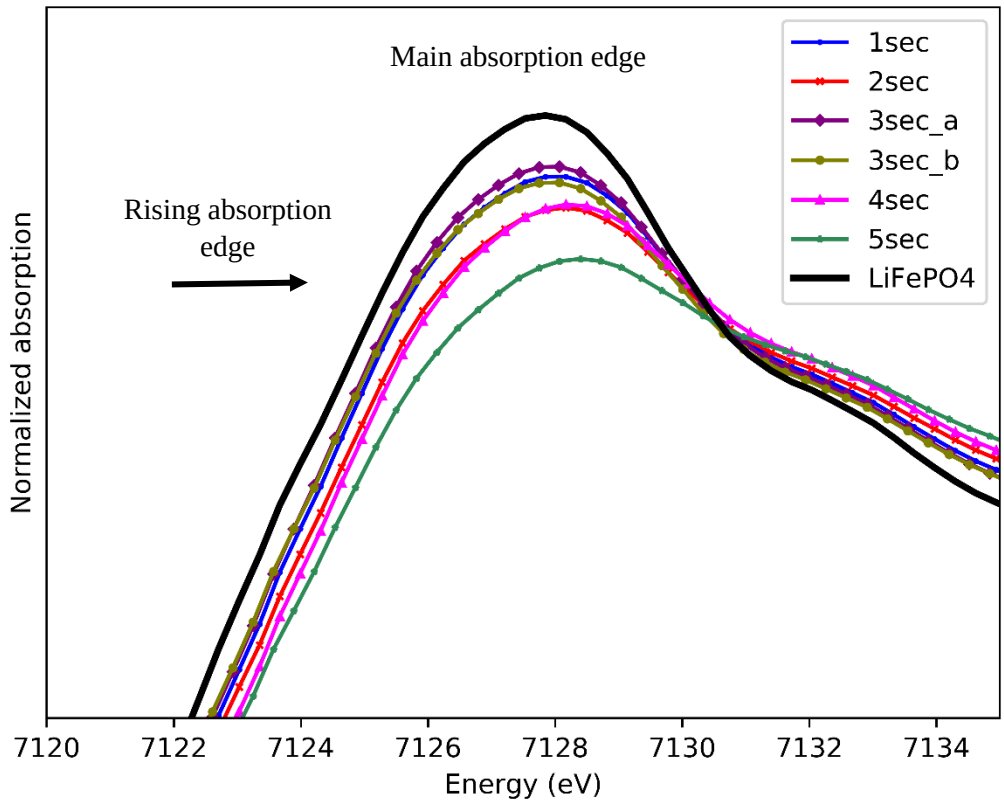

Figure 5.9: Comparison of the $LiFePO_4$ standard with the different Li^+ addition samples of the XANES Fe K-edge rising absorption and main absorption edge.

The change in intensity of the main absorption edge can also be a way of predicating if there is disorder in the local structure of the synthesised samples.[36] All samples show a slight drop in intensity compared to that of the $LiFePO_4$ standard and it can therefore be predicted that all the samples will exhibit some degree of disorder in the local structure (Fig 5.9 and Table 5.7). This suggests that the 1sec and both 3sec samples could exhibit the least amount of disorder as their intensity is slightly lower than the $LiFePO_4$ standard. The 5sec sample had the most extreme drop in peak intensity and therefore exhibits the highest degree of disorder in the local structure. A possible source of the disorder is the Fe on the Li^+ (M1) site and Fe^{3+} on the Fe^{2+}

(M2) site.[36] Both the presences of Fe on the M1 site and of Fe^{3+} was confirmed by XRD as shown in Table 5.4 and Table 5.5. The same trend seen for the drop in intensity was observed seen in the previously mentioned Tables. EXAFS analysis was used to further investigate the change in local structure and disorder as the XANES region only gives possible indications.

Table 5.7: The different main edge peak intensities and peak positions for the standards and the Li^+ addition rate samples.

Sample	Peak position (eV)	Peak intensity (au)
$LiFePO_4$	7127.8	1.59
$FePO_4$	7133.0	1.46
Fe_2O_3	7134.3	1.44
1sec	7127.9	1.52
2sec	7128.2	1.47
3sec_1	7127.9	1.53
3sec_2	7127.9	1.50
4sec	7128.3	1.47
5sec	7128.5	1.39

(iii) Linear Combination Fitting

Linear Combination Fitting (LCF) is a very useful tool to analyse XANES data to determine the major and minor components present in unknown samples[37–40] and all three standards were used to perform the fitting to determine the quantity of the bonding characteristics rather than the standard as a phase. The three different bonding environments and characteristics that are considered here are $Fe^{2+}O_6$ in a slightly distorted environment, $Fe^{3+}O_6$ also in a slightly distorted environment (similar to that of Fe^{2+} in $LiFePO_4$) and $Fe^{3+}O_6$ in an environment with a higher degree of distortion. These standards are discussed in section 2.2.3.1. LCF was performed on all the samples (Figs 5.10 – 5.15). The 1sec, 3sec_1 and 4sec sample show good LCF fits using the proposed bonding environments (Fig 5.10, 5.12 and 5.14). The 2sec sample showed a slight mismatch of over fitted data at the peak whereas the 3sec_2 and the 5sec samples showed a higher degree of mismatch (Fig 5.11, 5.13 and 5.15). Even with the slight mismatches, the goodness of fit parameters (Table 5.8) are reasonably small[38] for all the samples. The goodness of fit can also be seen visually by comparing the experimental and fitted data, and looking at the difference curves of the LCF. The accuracy of the fits can be improved if a more representative or wider set of standards were used, for example Fe_3O_4 that have both

Fe^{2+} and Fe^{3+} present. There are some changes in bonding properties between the 3sec_1 and 3sec_2 samples as indicated by the slight fitting mismatch present in 3sec_2.

Table 5.8: LCF goodness of fit parameters for the Li^{+} addition rate samples.

Sample	R-factor	Chi-square
1sec	0.0000848	0.0034
2sec	0.0001194	0.0047
3sec_1	0.0000975	0.0039
3sec_2	0.0002758	0.0117
4sec	0.0001521	0.0061
5sec	0.0003650	0.0142

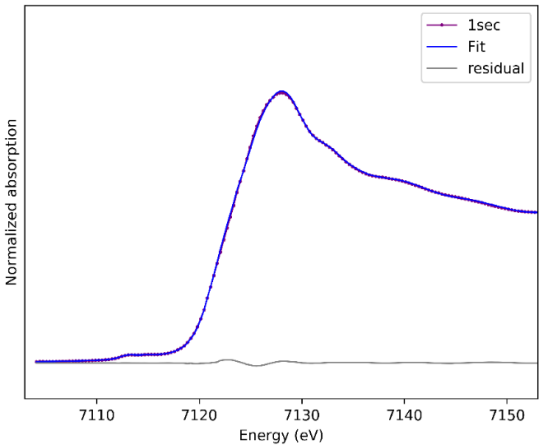

Figure 5.10: LCF best fit (blue) of the 1sec of the Fe K-edge XANES spectrum (purple) along with the residual spectrum (grey).

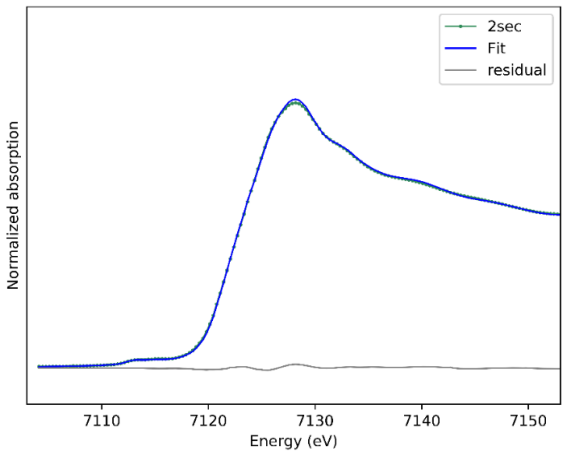

Figure 5.11: LCF best fit (blue) of the 2sec of the Fe K-edge XANES spectrum (green) along with the residual spectrum (grey).

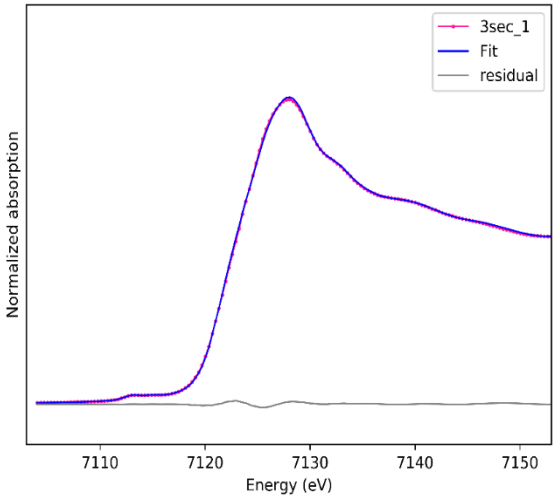

Figure 5.12: LCF best fit (blue) of the 3sec_1 of the Fe K-edge XANES spectrum (pink) along with the residual spectrum (grey).

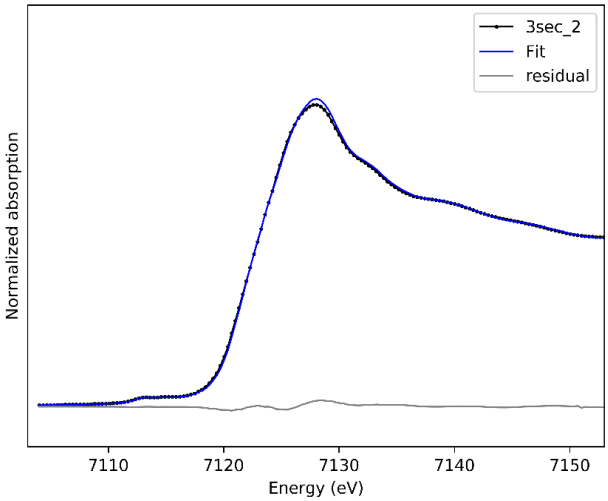

Figure 5.13: LCF best fit (blue) of the 3sec_2 of the Fe K-edge XANES spectrum (black) along with the residual spectrum (grey).

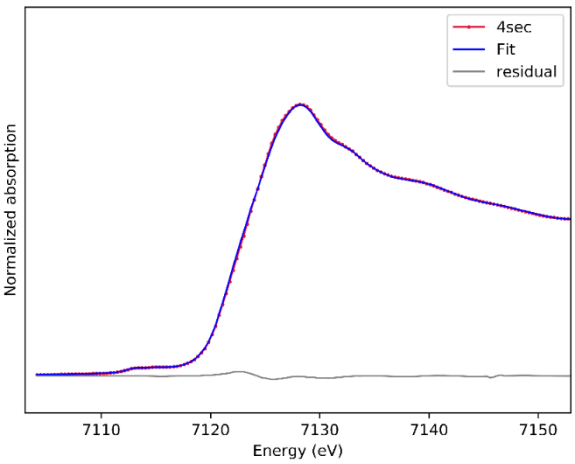

Figure 5.14: LCF best fit (blue) of the 4sec of the Fe K-edge XANES spectrum (pink) along with the residual spectrum (grey).

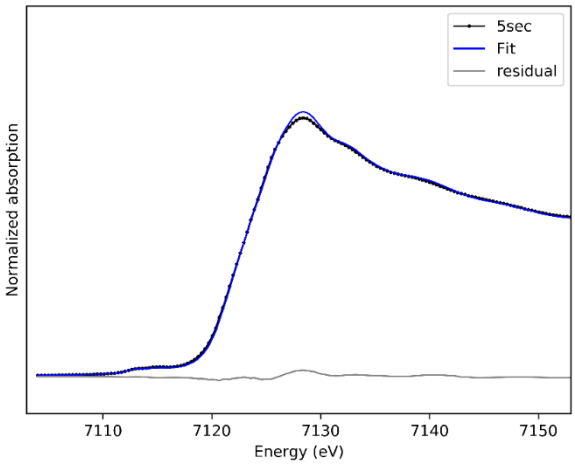

Figure 5.15: LCF best fit (blue) of the 5sec of the Fe K-edge XANES spectrum (black) along with the residual spectrum (grey).

All samples exhibit a mixture of Fe^{2+} and Fe^{3+} components as predicted by evaluating the pre-edge features (Fig. 5.8 Table 5.9). The 3sec_1, 3sec_2 and 1sec samples have the highest percentage of Fe^{2+} in an environment similar to that of $LiFePO_4$-standard. The 5sec sample has the lowest percentage of Fe^{2+} present. The 3sec_2 has no $Fe^{3+}O_6$ ($FePO_4$) present in the sample. The inclusion of the $Fe^{3+}O_6$ ($FePO_4$) bonding sequence led to a high error on the percentage and a different bonding sequence might need to be included or the bonding sequence of this sample has small differences compared to the given standards. The presence of Fe^{2+} and Fe^{3+} given in Table 5.9 confirms the trend as seen in Table 5.4. The 2sec, 4sec and 5sec samples has the highest percentage of Fe^{3+} presence as was predicted by the percentage vacancies present on the M2 site.

Table 5.9: Percentage of the different components present in the varied Li^+ addition rate samples as determined from LCF.

Sample	$Fe^{2+}O_6$ ($LiFePO_4$)	$Fe^{3+}O_6$ (Fe_2O_3)	$Fe^{3+}O_6$ ($FePO_4$)
1sec	88.6(2)	8.6(9)	2.8(8)
2sec	83.7(2)	10.5(1)	5.8(1)
3sec_1	90.8(1)	7.6(1)	1.6(9)
3sec_2	89.7(2)	10.3(2)	-
4sec	81.6(3)	9.1(1)	9.3(1)
5sec	75.6(3)	11.1(2)	13.4(2)

5.3.2.2. EXAFS

EXAFS was utilised to determine if and to what extent the local structure around Fe changes with the changes in the lithium addition rate. The k-weight, window, k-ranges and r-ranges are the same as those discussed in section 2.2.3.2. A comparison of the k-space (Fig. 5.16) showed that there is a slight decrease in the intensity and the disappearance of some features of the oscillations between the different Li^+ addition rate samples. The peak shapes are similar indicating similar local structures with only slight variations possibly in disorder.

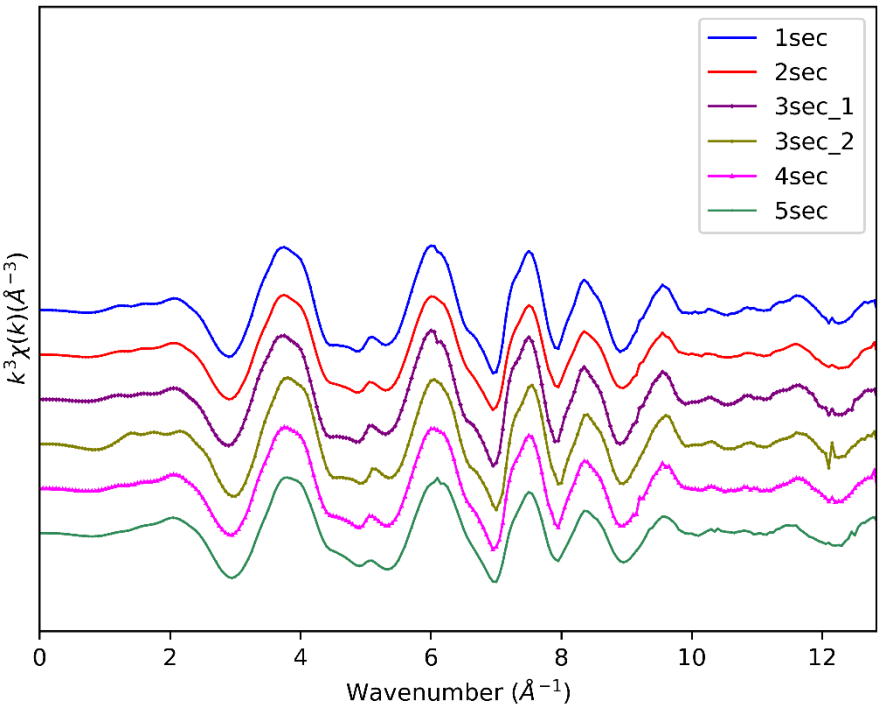

Figure 5.16: Comparison of the Fe k^3-weighted $[k^3\chi(k)]$ spectrum of the different Li^+ addition rate samples.

Performing a Fourier Transform on the k^3-range produces the real parts of the Fourier transform (FT real) and the magnitude of Fourier transform (FT magnitude) and the of EXAFS $k^3\chi(k)$ data as explained in section 2.3.3.5 (vii). This indicates the different scattering processes (due the coordination shells) of the neighbouring atoms around the Fe atom (Fig. 5.17).

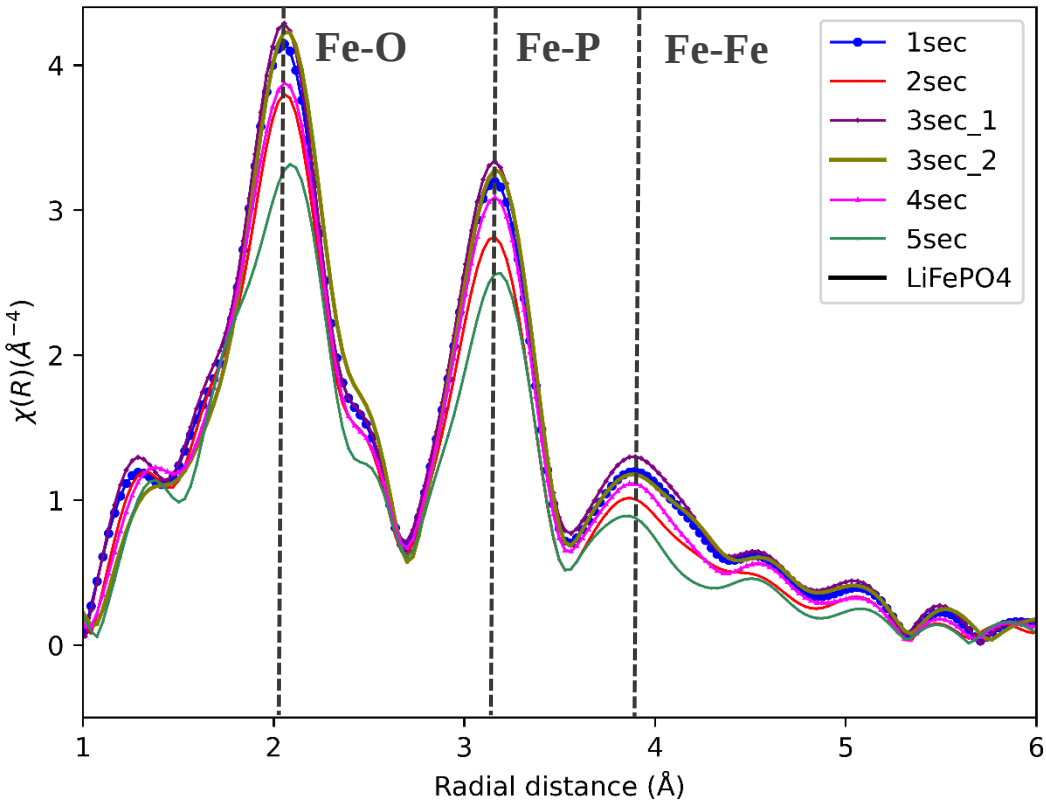

Figure 5.17: The magnitude of the Fourier transform of EXAFS $k^3\chi(k)$ data comparing radial distance of the different coordination shells of the different Li^+ addition rate samples.

Analyses were performed on the first three coordination shells. The same shells as seen in Chapter 3 and 4 were seen here. The first, second and third scattering process corresponded to the Fe-O coordination shell, Fe-P coordination shell Fe-Fe coordination shell. All the synthesised samples show the presence of these coordination shells (Fig. 5.17). The shape of the magnitude of the Fourier transform of the 1 – 5sec samples are similar indicating that there is no major change in the local structure but possibly a change in disorder.

Local structure determination:

Due to the general shape of the spectra in Figure 5.7, with a good comparison to the $LiFePO_4$ standard, the starting model for all the Li^+ addition rate samples were $LiFePO_4$. Refined parameters used for the determination of the local structure was the change in interatomic bond distance (ΔR – the adjustment in interatomic bond distance), the interatomic bond distances (X_a – X_b), the Debye-Waller factor (σ^2), the energy shift (ΔE_0) and the amplitude reduction factor (S_0^2). These parameters were determined using the fitting procedure described in section 2.2.3.1. The R-factors (Table 5.10) determined for the EXAFS results were less than 2% indicating a good fit.[41] The ΔE_o parameters (Table 5.10) as determined from the EXAFS fits

were also within the acceptable range (-10 eV < ΔE_0 < 10 eV)[42] and S_0^2 was between 0.76 – 0.90. The fitted k-space, FT magnitude and FT real for the 1sec – 5sec samples are shown in Figures 5.18 – 5.23.

Table 5.10: The reliability factor and energy shift of the varied Li^+ addition rate samples.

Sample	R-factor (%)	ΔE_0 (eV)
1sec	0.44	-0.8(8)
2sec	0.44	-0.4(9)
3sec_1	0.52	-1.2(8)
3sec_2	0.45	0.9(8)
4sec	0.35	-0.3(8)
5sec	0.58	-2.8(8)

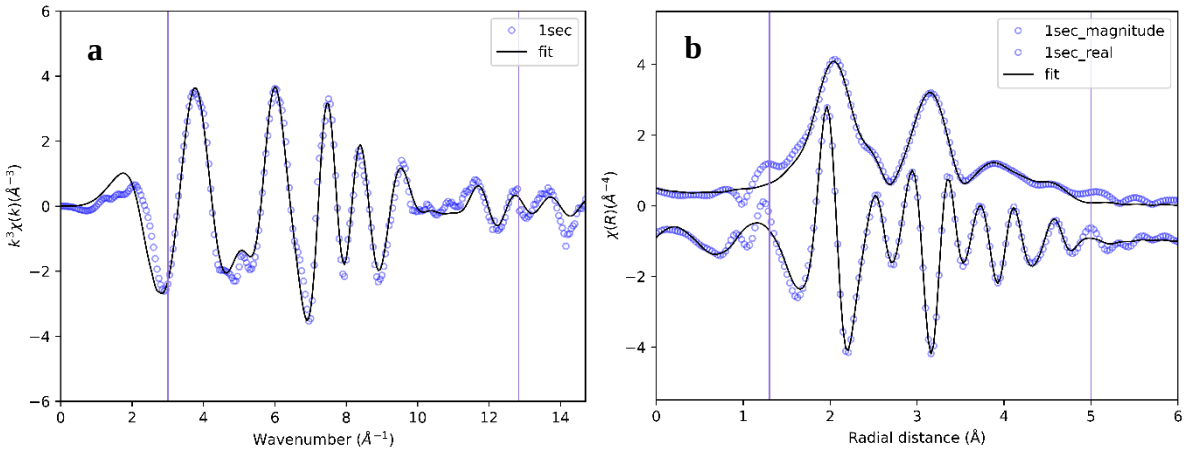

Figure 5.18: (a) The experimental Fe k^3-weighted $[k^3\chi(k)]$ spectrum and (b) the experimental FT magnitude (top) and FT real (bottom) of the EXAFS $k^3\chi(k)$ data (blue) and the theoretical FEFF fit (black) of the 1sec $LiFePO_4$. The fitting window is indicated with the vertical lines.

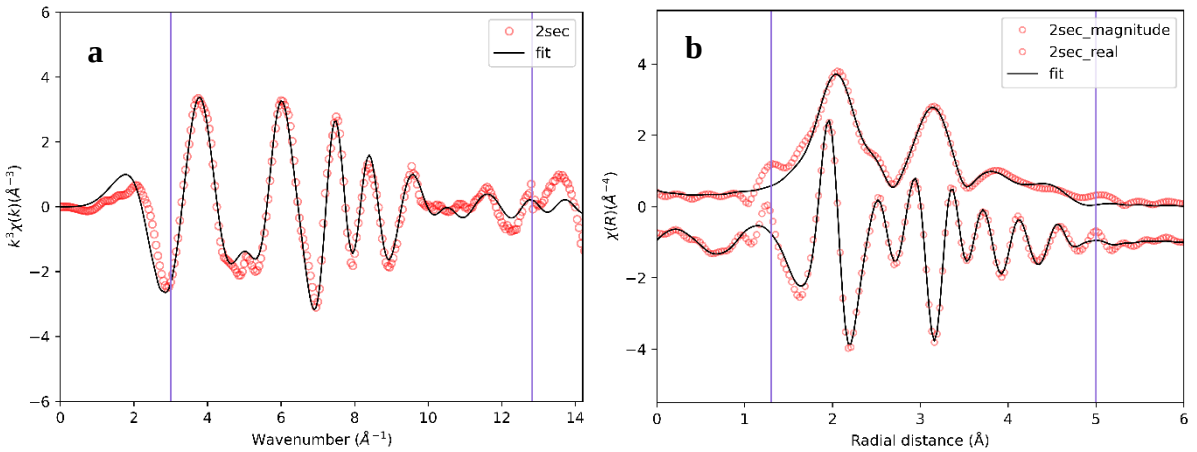

Figure 5.19: (a) The experimental Fe k^3-weighted $[k^3\chi(k)]$ spectrum and (b) the experimental FT magnitude (top) and FT real (bottom) of the EXAFS $k^3\chi(k)$ data (red) and the theoretical FEFF fit (black) of the 2sec $LiFePO_4$. The fitting window is indicated with the vertical lines.

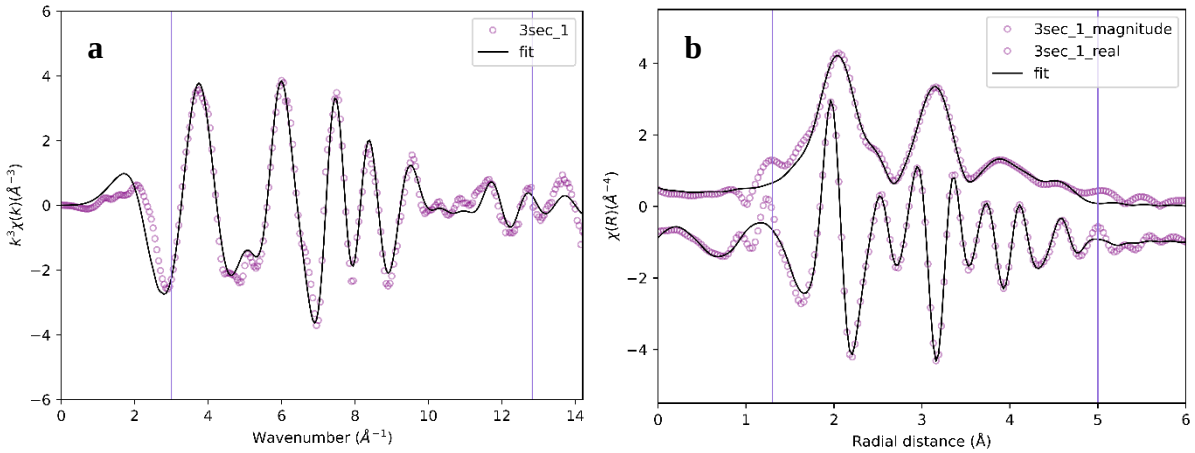

Figure 5.20: (a) The experimental Fe k^3-weighted $[k^3\chi(k)]$ spectrum and (b) the experimental FT magnitude (top) and FT real (bottom) of the EXAFS $k^3\chi(k)$ data (purple) and the theoretical FEFF fit (black) of the 3sec_1 $LiFePO_4$. The fitting window is indicated with the vertical lines.

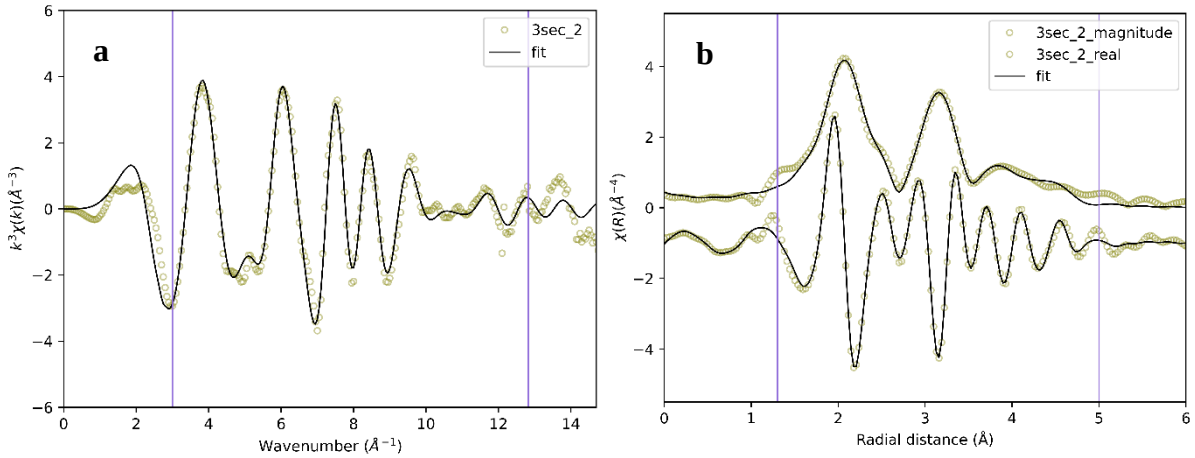

Figure 5.21: (a) The experimental Fe k^3-weighted $[k^3\chi(k)]$ spectrum and (b) the experimental FT magnitude (top) and FT real (bottom) of the EXAFS $k^3\chi(k)$ data (olive) and the theoretical FEFF fit (black) of the 3sec_2 $LiFePO_4$. The fitting window is indicated with the vertical lines.

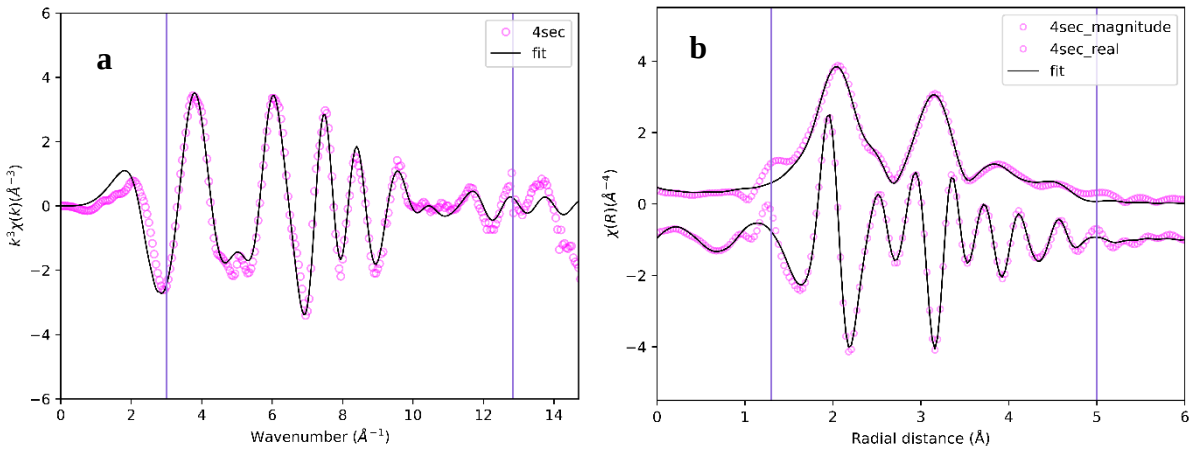

Figure 5.22: (a) The experimental Fe k^3-weighted $[k^3\chi(k)]$ spectrum and (b) the experimental FT magnitude (top) and FT real (bottom) of the EXAFS $k^3\chi(k)$ data (pink) and the theoretical FEFF fit (black) of the 4sec $LiFePO_4$. The fitting window is indicated with the vertical lines.

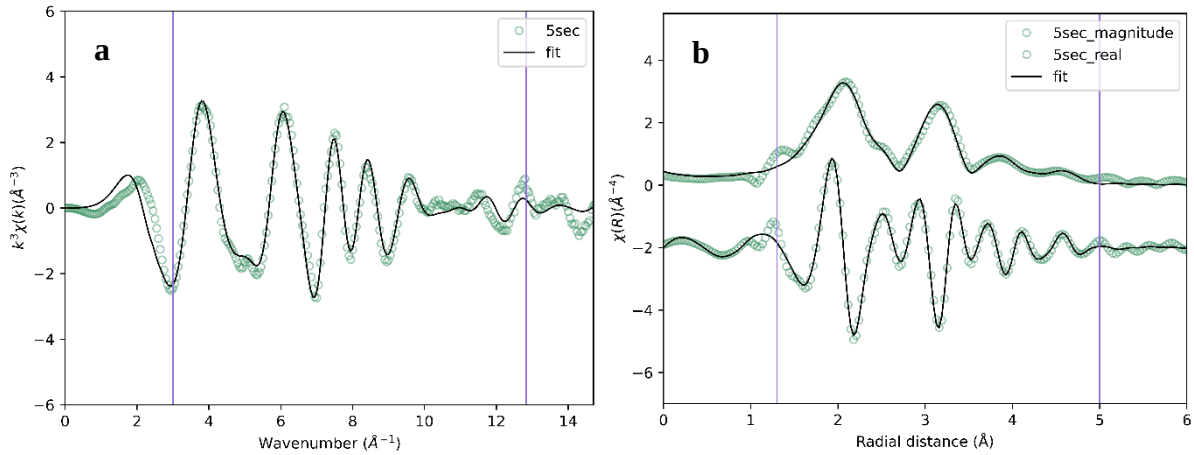

Figure 5.23: (a) The experimental Fe k^3-weighted $[k^3\chi(k)]$ spectrum and (b) the experimental FT magnitude (top) and FT real (bottom) of the EXAFS $k^3\chi(k)$ data (green) and the theoretical FEFF fit (black) of the 4sec $LiFePO_4$. The fitting window is indicated with the vertical lines.

Table 5.11 contains the individual coordination shells, coordination numbers (CN), interatomic bond distance and the Debye-Waller factors (disorder) determined for each sample and Table 5.12 contains the average interatomic distances and the average Debye-Waller factors. The interatomic bond distances for the Fe-O coordination shell (Table 5.11) in the 1sec, 2sec, 3sec_1 and 4sec samples had the same bonding distribution (two longer and four shorter interatomic distances). The 3sec_2 sample had four longer and two shorter interatomic distances and the longer distance (~2.12 Å) is shorter than longer distance (~2.21 Å) determined for the other samples. The 5sec sample has one longer and five shorter interatomic bond distances. Both interatomic distances of the 5sec sample were shorter than the individual distances determined for the other samples. These small variations in the distances and the combination of the different axial or equatorial positions could cause changes in the distortion of the octahedron around the Fe-orbitals (t_{2g} and e_g).[34] This could possibly explain the features seen in the pre-edge region (Fig. 5.8). There is slight variation between the individual disorder (Table 5.11) for the Fe-O coordination shell for the different samples except for the 3sec_2 and the 5sec sample. The individual disorder for the longer and the shorter distance for the 3sec_2 and 5sec, respectively is larger than the disorder of the other samples.

All samples except the 5sec sample had two shorter and three longer interatomic distances for the Fe-P coordination shell (Table 5.11). The 5sec sample had one shorter and four longer interatomic distances. The distance for the 1sec – 4sec samples is very similar but shorter for the 5sec sample. The 1sec – 4sec samples had more disorder around the longer interatomic distance but the 5sec sample had similar disorder around both the longer and shorter interatomic distances (Table 5.11). For the Fe-Fe coordination shell, the 1sec – 4sec samples

had two shorter and two longer interatomic distances (Table 5.11) and the 5sec sample had one longer and three shorter interatomic distances. The distances for the longer and shorter interatomic distances show little variation. The individual disorder was similar around all the interatomic distances (Table 5.11).

Table 5.11: Structural parameters determined using FEFF for the first, second and third coordination shell of the Li^+ addition rate samples.

Sample	Shell	Coordination number	Interatomic distance (Å)	Debye-Waller factor ($Å^2$)
1sec	Fe-O1	2	2.21(1)	0.013(5)
	Fe-O3	4	2.07(1)	0.010(1)
	Fe-P	2	2.835(7)	0.012(1)
	Fe- P	3	3.259(7)	0.007(1)
	Fe-Fe	2	3.84(1)	0.011(2)
	Fe-Fe	2	4.66(1)	0.013(4)
2sec	Fe-O1	2	2.21(1)	0.015(6)
	Fe-O3	4	2.07(1)	0.011(1)
	Fe-P	2	2.837(7)	0.013(1)
	Fe- P	3	3.261(7)	0.008(1)
	Fe-Fe	2	3.83(1)	0.012(1)
	Fe-Fe	2	4.65(1)	0.017(6)
3sec_1	Fe-O1	2	2.21(1)	0.013(6)
	Fe-O3	4	2.07(1)	0.009(1)
	Fe-P	2	2.835(7)	0.012(2)
	Fe- P	3	3.260(7)	0.006(1)
	Fe-Fe	2	3.84(1)	0.011(2)
	Fe-Fe	2	4.66(1)	0.012(4)
3sec_2	Fe-O2	4	2.12(1)	0.020(5)
	Fe-O3	2	2.08(1)	0.009(2)
	Fe-P	2	2.836(7)	0.014(2)
	Fe- P	3	3.261(7)	0.007(1)

	Fe-Fe	2	3.83(1)	0.011(2)
	Fe-Fe	2	4.65(1)	0.015(6)
4sec	Fe-O1	2	2.20(1)	0.015(6)
	Fe-O3	4	2.06(1)	0.011(1)
	Fe-P	2	2.835(7)	0.013(1)
	Fe- P	3	3.260(7)	0.007(1)
	Fe-Fe	2	3.83(1)	0.011(1)
	Fe-Fe	2	4.65(1)	0.015(4)
5sec	Fe-O2	1	2.092(9)	0.008(4)
	Fe-O1	5	2.048(9)	0.017(3)
	Fe-P	1	2.817(6)	0.009(2)
	Fe- P	4	3.241(6)	0.0089(9)
	Fe-Fe	1	3.81(2)	0.011(4)
	Fe-Fe	3	4.64(2)	0.017(3)

The average Fe-O interatomic bond distance (Table 5.12) for the 1sec – 4sec samples are within the range reported by other research groups (2.09 – 2.15 Å).[26,27,29,36] The average interatomic bond distance for the 5sec sample was shorter than both the other samples and the reported range. This shortening could be caused by the higher percentage of Fe^{3+} present as determined using XRD (Table 5.4). The average disorder in the Fe-O coordination shell was larger than the reported disorder (0.0028 – 0.0083 $Å^2$).[26,27,29,36] The 3sec_2 and 5sec samples had the highest degree of disorder present. The average Fe-P interatomic distance (Table 5.12) was shorter than the distance reported in literature (3.15 – 3.25 Å)[26,27,29] for the 1sec – 4sec sample whereas the distance for the 5sec sample that falls within the reported range. The average disorder for the Fe-P coordination shell was larger than the reported average disorder (0.0045 – 0.0049 $Å^2$).[26,27,29] The average Fe-Fe interatomic distance (Table 5.12) was the same for all the samples except for the 5sec sample. The distance reported in literature (3.94 – 4.00 Å)[26,27,29] is shorter than for the synthesised samples. The average disorder in the Fe-Fe coordination shell (Table 5.12) is larger than disorder reported for this coordination shell (0.0054 – 0.0096 $Å^2$).[26,27,29] The 5sec sample had the highest degree of average disorder.

Table 5.12: The average interatomic distance and average Debye-Waller factor of the different coordination shells.

Shell	Sample	Average interatomic distance (Å)	Average Debye-Waller factor ($Å^2$)
Fe-O	1sec	2.11	0.011
	2sec	2.09	0.011
	3sec_1	2.10	0.010
	3sec_2	2.11	0.016
	4sec	2.09	0.011
	5sec	2.055	0.016
Fe-P	1sec	3.084	0.009
	2sec	3.085	0.010
	3sec_1	3.087	0.009
	3sec_2	3.086	0.010
	4sec	3.084	0.009
	5sec	3.156	0.009
Fe-Fe	1sec	4.25	0.012
	2sec	4.25	0.014
	3sec_1	4.25	0.012
	3sec_2	4.25	0.013
	4sec	4.25	0.013
	5sec	4.43	0.016

All the coordination shells exhibit some degree of disorder. The Fe-O and Fe-Fe coordination shells have a higher degree of disorder than the Fe-P coordination shell. The presence of the disorder can be caused by either defects such as antisite defects or a decrease in crystallinity.[36] This was noticed with XRD for the 2sec (Fig. 5.2), 4sec (Fig. 5.5) and 5sec (Fig. 5.6) samples as seen with the noisier difference curve and the increase in the peak width. Rietveld analysis determined that there was $Fe^{2+}$and Fe^{3+} present on the Li^+ site in all the samples. This could be the major cause of the disorder present in the samples. The high degree of disorder present in 3sec_2 could be caused by the different interatomic distance ordering. The 2sec, 4sec and 5sec samples had a higher degree of disorder in the Fe-O and could be caused by the Fe^{2+}/Fe^{3+} replacing more Li^+ (Table 5.4).

5.3.3. Pair distribution function

Structure analysis of the 3sec_1 $LiFePO_4$ sample:

The pair distribution function, G(r) for the 3sec_1 $LiFePO_4$ sample can be seen in Figure 5.24. $LiFePO_4$ was the only phase used in the refinement and the fitting range was from 1 – 30 Å. Other known phases such as Li_3PO_4, Fe_3O_4, α-Fe_2O_3 and the Fe-impurity (as discussed in Chapter 4) was added to the fit. The addition of these phases to the refinement made no change to the fit. Regions at low r-ranges (<5 Å) as well as between 5 Å – 15 Å show more peak mismatch compared to the r-range above 15Å. This mismatch between the observed and calculated curve could be caused by the replacement of iron by lithium[43] – it can be assumed to be an amorphous species as no replacement on the M2 site was observed using Bragg Rietveld. Thus the peak mismatches could be due to additional amorphous phases present.[43] The r-range between 15 – 30 Å does not exhibit the same amount of mismatch and it can therefore be assumed that the same bulk features and increased cation ordering was observed.

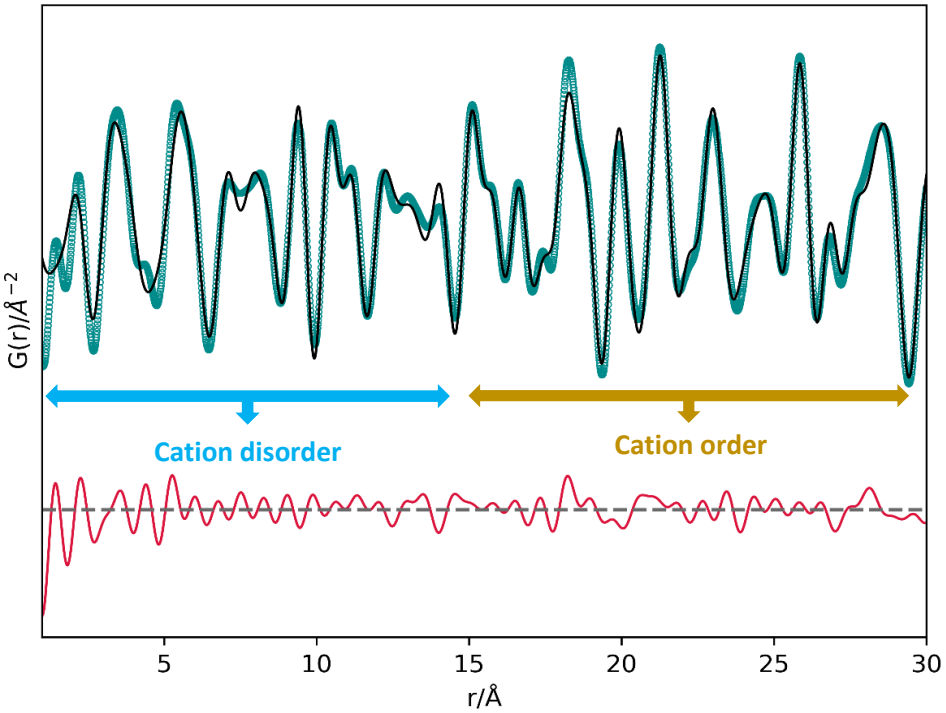

Figure 5.24: The experimental PDF of the 3sec_1 $LiFePO_4$ sample using a fitting range of 1 – 30Å. The observed G(r) is indicated with the green circles, the calculated G(r) is indicated with the black solid line and the difference curve is indicated in red.

The PDF refinement together with the calculated bonding distributions the first P-O, Fe-O, Fe-P and Fe-Fe interatomic bond distances could be identified and this can be seen in Figure 5.25 focusing on the r-range between 1 – 6.5Å. The assignment of the peaks to different bonding contributions becomes increasingly more difficult for a r-range beyond 6.5 Å due to the increase in overlapping bonding contributions.[44–46] Not much can be discerned about the lithium in the sample due to the weak X-ray scattering factor of lithium.[47] The P-O, Fe-O and Fe-P interatomic bond distances was identified at similar distances by Jensen *et al*.[43] using PDF but no mention was made of the first Fe-Fe interatomic bond distance. The first P-O interatomic bond distance was identified at 1.46 Å and the first Fe-O distance was identified at a distance of 2.19 Å. The third peak at 3.46 Å contains major contributions from both the first Fe-P as well as the first Fe-Fe interatomic bond distance. Calculated PDF's for the Fe-P and the Fe-Fe contributions show that the first Fe-P peak is at 3.22 Å and the first Fe-Fe peak is at 3.81 Å. The shouldering at 4.26 Å originates from a Fe-P interatomic bond distance and the peak at 5.53 Å originates from a combination of Fe-P (5.48 Å) and Fe-Fe (5.64 Å) contributions. The average interatomic bond distances obtained using EXAFS were shorter for the first Fe-O (2.10 Å - first coordination shell) and the first Fe-P (3.087 Å - second **c**oordination shell) were shorter and longer first Fe-Fe (4.25 Å - third coordination shell) as compared to the distances obtained with PDF. Comparing some of the individual bond distances determined using EXAFS (Table 5.11) to those determined using PDF showed similar distances. The Fe-O interatomic bond distance with a coordination number of two was 2.19 Å, the Fe-P interatomic distance with a coordination number of three was 3.260 Å and the Fe-Fe interatomic distance with a coordination number of two was 3.84 Å. The difference between the interatomic distances for the different techniques could due (1) additional amorphous phases present in the PDF leading to a non-ideal structure that was not picked up with EXAFS due to the element specific nature of EXAFS[48] or (2) the mixed oxidation state of Fe (Fe^{2+}/Fe^{3+}) in the different samples cause the interatomic bond distances to appear shorter when using EXAFS analysis.[49] Overall, the EXAFS and PDF fits were not ideal fits and some variation is expected between the fits.

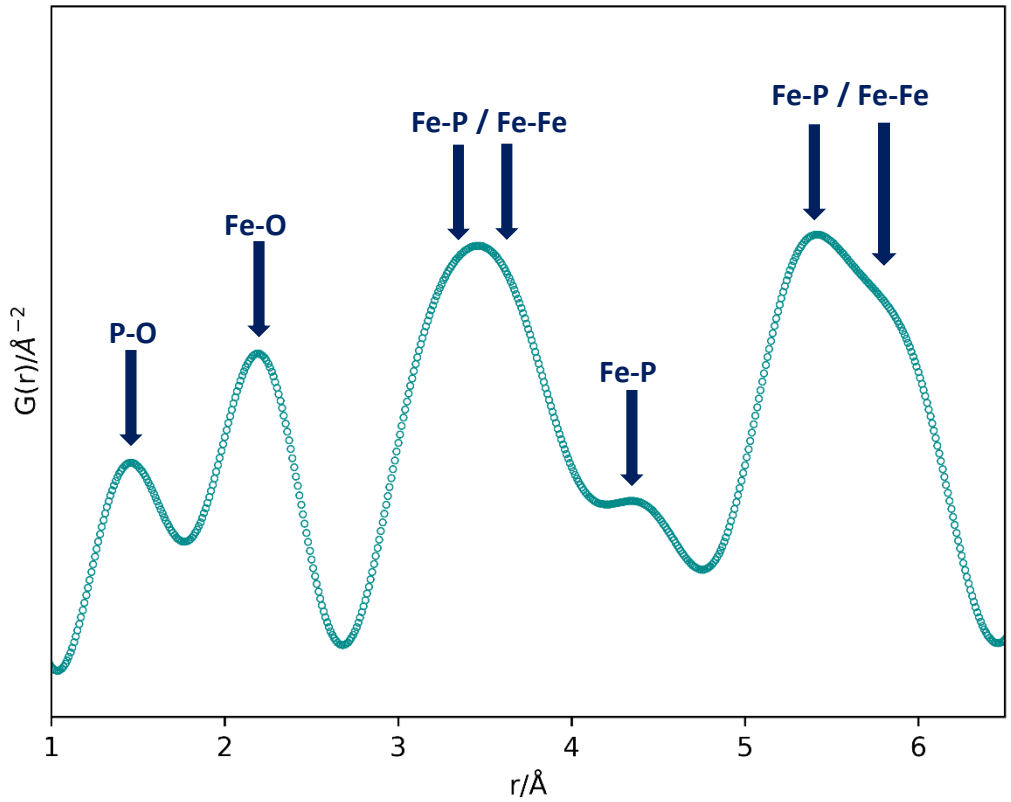

Figure 5.25: The experimental PDF of the 3sec_1 $LiFePO_4$ sample showing a fitting range of 1 – 6.5Å with the major interatomic bond distance contributions in real space. The observed G(r) is indicated with the green circles.

Model-independent analysis of the lithium addition rate samples:

To investigate the changes in the structure caused by changing the Li^+ addition rate during synthesis a model independent analysis of the observed G(r) of the different samples was used. In general, four different features are considered when investigating changes in the real structure without a model: (1) the peak positions, (2) the peak integral intensities, (3) the peak width and (4) the maximum distance at which a peak is observed.[44,50] The features under discussion for this particular dataset are the peak positions (Table 5.13), the peak widths full, width at half maximum – FWHM (Table 5.14) and the relative peak integral intensities (Table 5.15) for the different sections of the PDF's (A – E) indicated on Figure 5.26. The different sections on Figure 5.26 also corresponds to the different bonding contributions shown in Figure 5.25.

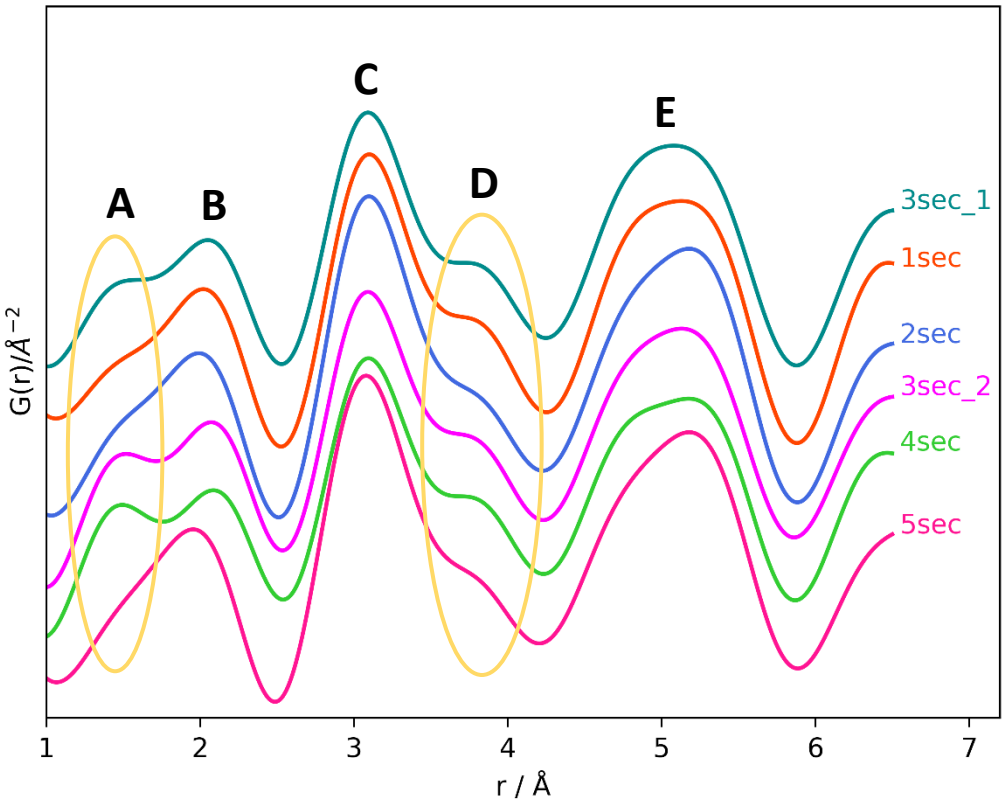

Figure 5.26: The observed G(r) of the different Li^+ addition rate $LiFePO_4$ samples using a r-range of 1 – 6.5Å. Different areas under discussion are labelled A – E and important structural features are indicated with yellow circles.

The peaks labelled Section A in Figure 5.26 corresponds to the interatomic bond distance of P-O for the different samples.[44,45,49,51,52] There is a systematic disappearance of this peak for the 1sec, 2sec and 5sec samples. The disappearance of this peak indicate an increase in defect concentration for these samples.[53] A similar feature can be seen for the Fe-P interatomic distance - section D in Figure 5.26. The disappearance for this shoulder is less pronounced than that of Section A but this is also an indication of an increase in defect concentration for the 2sec and 5sec samples.[53]

The peak positions can give possible information on the interatomic distances regarding the different sections indicated on Figure 5.26. [44,45,49,51,52] A summary of the changes in the peak positions and distances was given in Table 5.13. The peak positions were compared to that of the 3sec_1 sample but the 2sec and 5sec samples showed the smallest distance for Fe-O interatomic bond distances which was also observed using XRD as shown in Table 5.5.

Table 5.13: The peak positions for selected peaks to determine any changes in the interatomic bond distances for the Li^+ addition rate samples as compared to the fully analysed 3sec_1 sample. Blue indicates the shorter distances and orange indicates longer distances**.**

	A	B (Fe-O)	C (Fe-P/Fe-Fe)	D	E (Fe-P/Fe-Fe)
3sec_1	-	2.0460(4)	3.0922(1)	-	5.0717(7)
1sec	-	2.0160(5)	3.1009(2)	-	5.109(1)
2sec	-	1.9880(4)	3.0982(1)	-	5.077(5)
3sec_2	-	2.0678(5)	3.0922(2)	-	5.108(2)
4sec	-	2.0828(4)	3.0958(1)	-	5.110(4)
5sec	-	1.9429(9)	3.0803(2)	-	5.141(3)

The peak width can be used as a way to estimate any changes in the disorder between samples.[44,46,54]. These changes were summarised in Table 5.14 as a comparison to that of the 3sec_1 sample. Increasing values indicates a possible increase in the disorder and decreasing values indicate a possible decrease. There was slight variation between the values for Section C and Section E. Section B which relates to the Fe-O interatomic bond distance showed more variation between the different samples.

Table 5.14: The peak width (FWHM) for selected peaks to determine any changes in disorder for the Li^+ addition rate samples as compared to the fully analysed 3sec_1 sample. Blue possibly indicates a lower degree of disorder and orange possibly indicates a higher degree in disorder**.**

	A	B (Fe-O)	C (Fe-P/Fe-Fe)	D	E (Fe-P/Fe-Fe)
3sec_1	-	0.284(5)	0.401(5)	-	0.81(1)
1sec	-	0.65(1)	0.410(6)	-	0.83(1)
2sec	-	0.303(6)	0.38(2)	-	0.85(1)
3sec_2	-	0.240(6)	0.400(6)	-	0.79(1)
4sec	-	0.230(7)	0.393(5)	-	0.86(1)
5sec	-	0.375(8)	0.417(7)	-	0.88(1)

The peak integral intensity was used as an indication of any changes in the coordination number around the central atom.[44,53–55] Larger peak intensities could be an indication of the coordination number increasing and smaller peak intensities could be an indication of the

coordination number decreasing. A summary of the changes observed for the different sections are provided in Table 5.15. This method shows changes in the coordination number between samples that was not observed with the EXAFS modelling of these samples.

Table 5.15: The peak integral intensity for selected peaks to determine any changes in coordination number for the Li^+ addition rate samples as compared to the fully analysed 3sec_1 sample. Blue possibly indicates a lower coordination and orange possibly indicates a higher coordination.

	A	B (Fe-O)	C (Fe-P/Fe-Fe)	D	E (Fe-P/Fe-Fe)
3sec_1	-	0.147(2)	0.588(6)	-	0.791(9)
1sec	-	0.564(3)	0.647(7)	-	0.87(1)
2sec	-	0.176(3)	0.75(4)	-	0.93(1)
3sec_2	-	0.139(3)	0.570(6)	-	0.77(1)
4sec	-	0.114(2)	0.546(6)	-	0.719(9)
5sec	-	0.263(4)	0.730(9)	-	0.93(1)

Referring back to the e_g peak in the pre-edge region for XANES (Fig. 5.8), possible explanations were given for the increase in the Fe^{2+}/Fe^{3+} peak (~7115 eV) intensity. Firstly, the change in addition rate causes an increase in distortion[27,31,32] around the Fe atom resulting in a similar environment to that of α-Fe_2O_3. Secondly, the varied addition rate causes a change in the coordination number which causes the increase in intensity due to the break in the inversion symmetry around the Fe atom.[30,33] Thirdly, the different bonding distributions could affect the intensity and possibly the distortion. Changes in PDF peaks can also be used to distinguish between distortion and a possible change in coordination number. A study conducted by Willinger *et al*,[54] suggested that the distortion in an octahedral environment can be identified by both the decrease in integral intensity accompanied by an increase in peak width. That trend was not observed for these samples using model-independent analysis. The PDF peaks showed an increase in both the integral intensity (increase in the amount of atomic pairs contributing to that distances[54,56]) and the peak width (increase in the distribution of the interatomic bond distance[46,54]) for the same peak. This could indicate that the change in the peak is caused by the two different effects rather than only distortion. It is proposed that a change in coordination number occurs due to the presence of Fe^{3+} on the M2 site, where the Fe^{3+} atom has a smaller ionic radius than the of Fe^{2+} atom.[57] This increase in oxidation state is accompanied by an increase in electronegativity[58] as well as a further increase in the distortion around the FeO_6

octahedra. The increase in electronegativity and this distortion could cause the oxygen from the neighbouring atoms to be pulled toward the Fe^{3+} atom and form an interatomic interaction that is seen as a change in coordination number (Figure 5.27). The distortion of the local structure would also then cause other atomic pairs (Fe-P and Fe-Fe) to have a similar increase in the coordination number. The decrease in coordination would therefore be an indication of a less distorted structure than the 3sec_1 sample. Additional modelling, such as big-box reverse Monte Carlo (RMC) modelling, is necessary to determine the change in coordination number as well as the probability of this change occurring and to assess the changes in disorder.

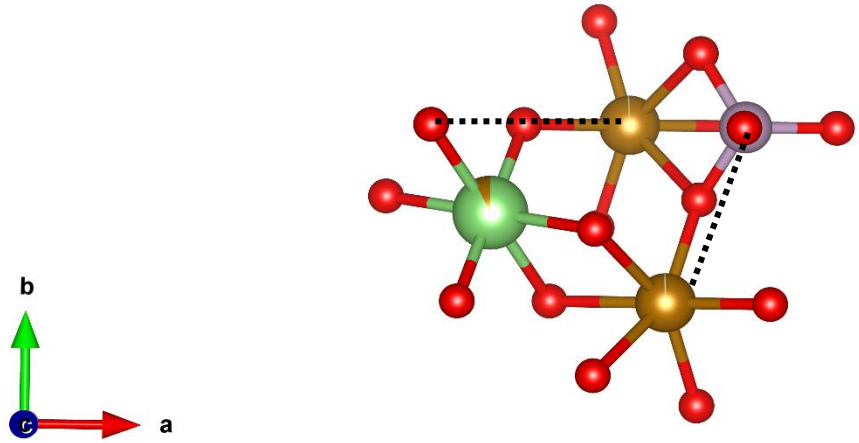

Figure 5.27: The proposed model for the increase in coordination number around the Fe atoms. Possible interatomic interactions are indicated with the dashed lines. Iron is represented by brown, lithium by green, phosphorous by purple and oxygen by red.

5.3.4. Mössbauer spectroscopy

Since the 1sec, 3sec_1, 3sec_2 and the 4sec samples showed the best XRD and XAS results, Mössbauer Spectroscopy was used to investigate further the valence state of the iron phases in these samples.

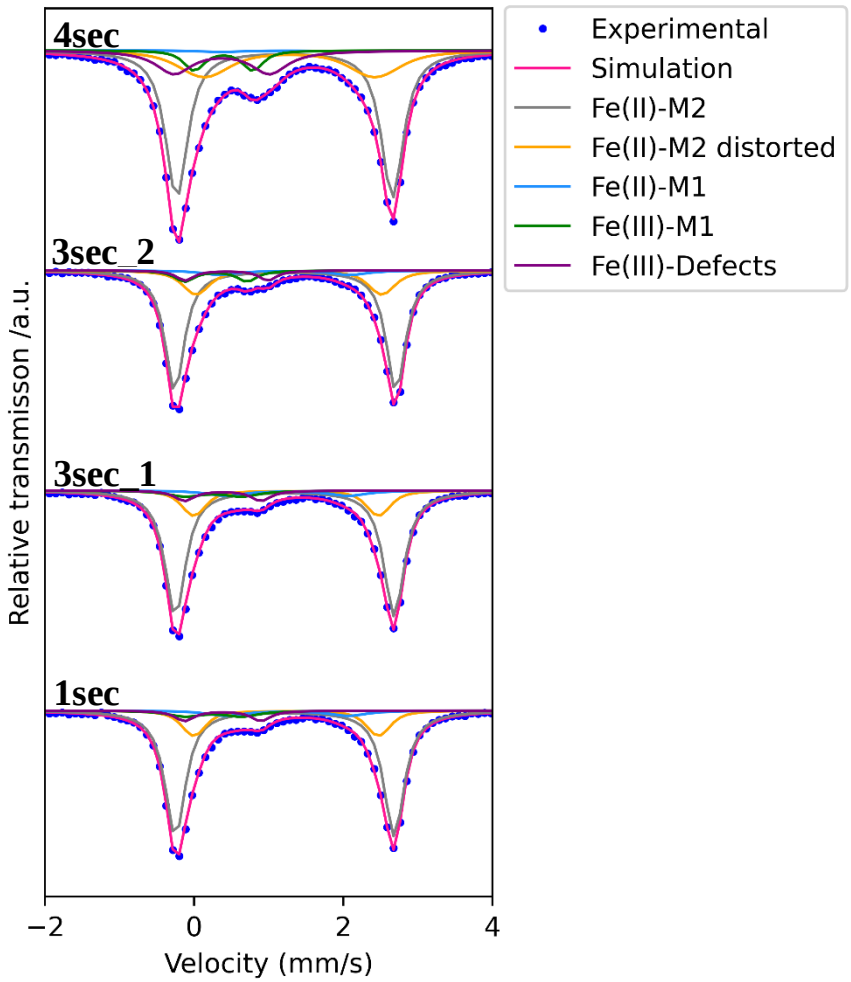

Figure 5.28: Mössbauer spectra of (from the bottom to the top) the 1sec, 3sec_1, 3sec_2 and 4sec Li^+ addition rate $LiFePO_4$ samples showing the different Fe environments present.

The same five doublets as seen in chapter 4 were used to fit the experimental data in all four samples (Fig. 5.28). Three of the Fe environments have a valence state of 2+ and the other two environments have a valence state of 3+. The one Fe^{2+} in all the samples have an isomer shift (δ) in the range 1.22 – 1.23 mm/s and a quadrupole splitting (ΔE_Q) = 2.89 – 2.96 mm/s (Table 5.16). This phase corresponds to Fe^{2+} occupying the M2 site in a slightly distorted octahedron and is present in $LiFePO_4$ and is referred to as Fe(II)-M2.[2,9,12,59–62] The 4sec sample has a slightly lower ΔE_Q than the other samples and could indicate a more distorted environment.[59,62] The 3sec_1 sample has the highest percentage of Fe^{2+} in the M2 slightly distorted ($LiFePO_4$) environment and the 4sec the lowest (Table 5.17). The second Fe^{2+} phase have similar δ values and lower ΔE_Q values compared to those in the first Fe^{2+} environment. This environment has δ = 1.23 – 1.28 mm/s and ΔE_Q = 2.29 – 2.47mm/s (Table 5.16) and is referred to as Fe(II)-M2 distorted. The ΔE_Q values of the samples have slightly lower values than the reported value (2.64 mm/s).[59] This environment corresponds to Fe^{2+} occupying the M2 site in $LiFePO_4$ but in

a more distorted environment.[59] The 1sec sample has the highest percentage and 3sec_2 sample has the lowest percentage of Fe^{2+} in this environment (Table 5.17). The third Fe^{2+} environment had a δ = 1.21 – 1.25 mm/s and ΔE_Q = 1.64 – 1.74 mm/s (Table 5.16). This corresponds to Fe2+ occupying the M1 site and replacing lithium.[63] The isomer shift is characteristic of Fe^{2+} in an octahedral arrangement but the quadrupole splitting is smaller. The 1sec sample had the highest percentage of this environment and the 4sec sample the lowest percentage (Table 5.17). Both these Fe^{3+} environments have similar δ values but different Δ values depending on the distortion and the environment (Table 5.16). The ΔE_Q values are lower than that of the Fe^{2+} environments. The one Fe^{3+} environment has a δ = 0.26 – 0.39 mm/s and ΔE_Q = 0.72 – 0.79 mm/s (Table 5.16). The δ for the 1sec, 3sec_1 and 3sec_2 samples are slightly lower than those recorded (0.40 – 0.50 mm/s).[59,61,62] This environment corresponds to Fe^{3+} occupying in the M1 site in a LiO_6 octahedron and is referred to as Fe(III)-M1.[59,61,62] The 1sec sample has the lowest and the 4sec sample has the highest percentage (Table 5.17). The total Fe percentage (Table 5.17) on the M1 site is higher for the 1sec (2.1%) and 3sec_2 (2.18%) than the occupancy determined using PXRD. This could possibly indicate amorphous Fe that PXRD could not detect. PXRD also showed that the 3sec_1 sample (0.51%) and the 4sec sample (8.9%) had a higher percentage of Fe present than the amount determined with Mössbauer spectroscopy. This could indicate an additional phase or environment that was not accounted for.

Table 5.16: Different isomer shifts (δ – mm/s) and quadrupole splitting (ΔE_Q – mm/s) for the varied Li^+ addition rate samples.

	Fe(II) – M2		**Fe(II) – M2 distorted**		**Fe(II) –M1**		**Fe(III) –M1**		**Fe(III) – M2/Defects**	
	δ	δ	δ	ΔE_Q	δ	ΔE_Q	δ	ΔE_Q	δ	ΔE_Q
1sec	1.22(1)	2.93(1)	1.23(1)	2.47(1)	1.25(2)	1.64(4)	0.26(1)	0.76(2)	0.38(1)	1.02(1)
3sec_1	1.23(1)	2.96(1)	1.24(1)	2.45(1)	1.21(3)	1.67(5)	0.27(1)	0.72(2)	0.41(1)	0.99(2)
3sec_2	1.23(1)	2.96(1)	1.26(1)	2.46(1)	1.22(2)	1.74(5)	0.28(1)	0.77(1)	0.42(1)	1.04(1)
4sec	1.21(1)	2.89(1)	1.28(1)	2.29(1)	1.23(3)	1.74(4)	0.39(1)	0.79(1)	0.37(1)	1.28(1)

The second Fe^{3+} environment has a δ = 0.37 – 0.42 mm/s and ΔE_Q = 0.99 – 1.28 mm/s (Table 5.16). This environment corresponds to structural defects in the form of Fe^{3+} on the M2 site and is referred to as Fe(III)-M2 Defects.[59,62,64,65] The 3sec_1 sample has the lowest and the 4sec

sample have the highest percentage (Table 5.17). The larger ΔE_Q between the two Fe^{3+} environments is most likely due to a less distorted environment around Fe^{3+}. The 3sec_1 sample had the highest percentage of total Fe^{2+} and the 4sec sample the lowest. These results followed a similar trend as determined with XRD. The XRD results showed that the 4sec sample should have the highest percentage of Fe^{3+} present on both the M1 and the M2 site, as well as overall in the sample.

Table 5.17: Percentage contribution from each form of Fe and the total Fe in the varied Li^+ addition rate samples.

	Fe(II) – M2	Fe(II) –M2 distorted	Fe(II) – M1	Fe(III) –M1	Fe(III) - Defects	Total Fe	
						Fe^{2+}	Fe^{3+}
1sec	68(8)	15(3)	6(1)	5(1)	6(1)	89	11
3sec_1	71(8)	16(3)	4(1)	3(1)	6(1)	91	9
3sec_2	67(8)	17(2)	5(1)	6(1)	5(1)	89	11
4sec	56(8)	21(4)	1(1)	7(1)	15(3)	78	22

The full width at half maximum line width (Γ) is a great tool to determine if there is any disorder present around the different Fe ions (Table 5.18). In these samples, all environments exhibited some degree of disorder around the Fe^{2+}/Fe^{3+} atom. The disorder around Fe(II) – M2, Fe(III) – M1 and Fe(III) – M2 is slightly larger than those reported for a ordered iron environment (0.2 – 0.3 mm/s).[61,62,66] The Fe(II) – M1 had a higher disorder for all the samples. This could be caused by the difference in the radii between Fe^{2+} and Li^+. The disorder for the Fe(II)-M2 distorted and Fe(III)-M2/Defects environment for the 4sec sample has a much higher degree of disorder than the same environment for the other samples.

Table 5.18: The full width half maximum line width (Γ – mm/s) value for the varied Li^+ addition rate samples.

	Fe(II) – M2	Fe(II) –M2 distorted	Fe(II) –M1	Fe(III) –M1	Fe(III) – M2/Defects
1sec	0.32(1)	0.28(1)	0.60(4)	0.56(4)	0.32(1)
3sec_1	0.31(1)	0.41(2)	0.65(6)	0.31(2)	0.35(2)
3sec_2	0.30(1)	0.34(1)	0.56(2)	0.31(1)	0.28(1)
4sec	0.33(1)	0.60(1)	0.60(1)	0.28(1)	0.59(1)

The total Fe^{2+} in the $LiFePO_4$ M2 environment determined using Mössbauer spectroscopy to the percentage determined by LCF (Table 5.9) shows good correlation. The 1sec, 3sec_1, 3sec_2 and 4sec sample show 0.40%, 0.20%, -0.70% and -3.60% difference between the Mössbauer spectroscopy results and those determined by LCF.

5.3.5. Raman spectroscopy

The Raman spectra with the corresponding microscopic images (Fig 5.29 – 5.32 and insets) were obtained for the 1sec, 2sec, 3sec_1 and 3sec_2 samples. All the peaks (Table 5.19) were matched to the different internal and external modes of $LiFePO_4$.[67–69] A summary of these modes as described in literature was given in Table 3.5. The peak at ~950 cm^{-1} that corresponds to the symmetric stretching and the peaks at ~996 cm^{-1} and ~1064 cm^{-1} that correspond to the asymmetric stretching are well defined and indicate that the PO_4^{3-} tetrahedra remain undistorted in all the samples.[69]

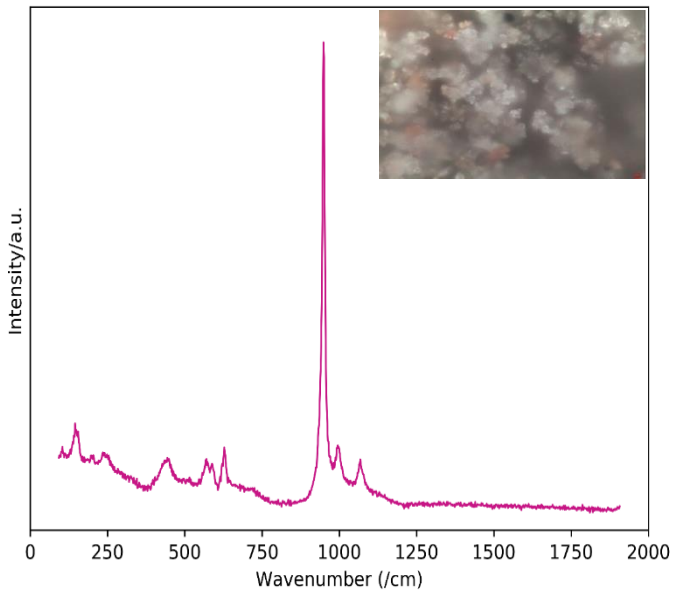

Figure 5.29: Raman spectrum and microscopic image (inset) of the 1sec $LiFePO_4$ sample

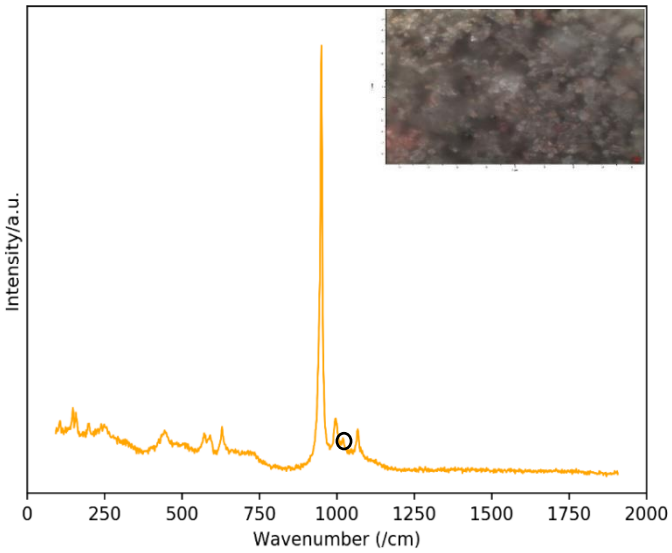

Figure 5.30: Raman spectrum and microscopic image (inset) of the 2sec $LiFePO_4$ sample.

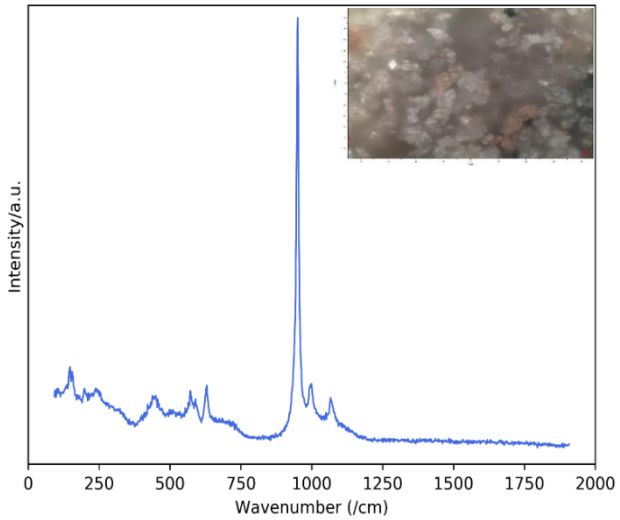

Figure 5.31: Raman spectrum and microscopic image (inset) of the 3sec_1 $LiFePO_4$ sample.

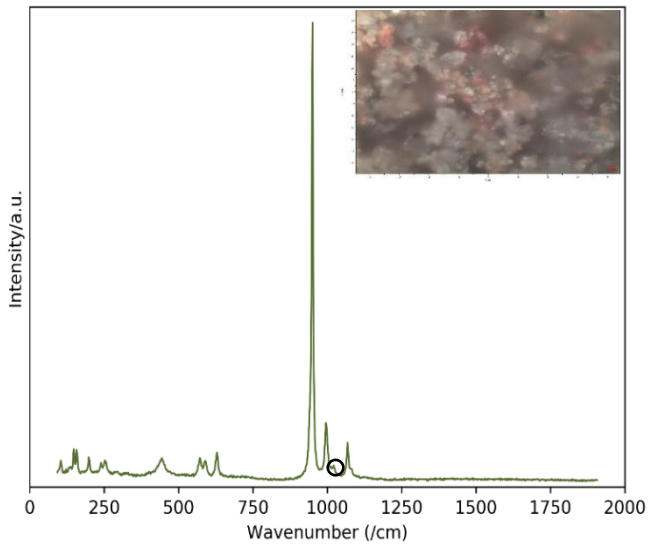

Figure 5.32: Raman spectrum and microscopic image (inset) of the 3sec_2 $LiFePO_4$ sample.

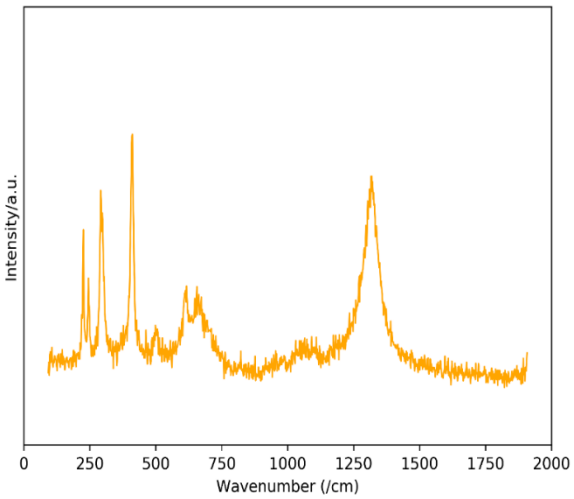

Figure 5.33: Raman spectrum of α-Fe_2O_3 in the 2sec $LiFePO_4$ sample.

Table 5.19: Raman modes of the different Li^+ addition rate samples with the assigned vibrational modes. Intensities for the υ_1 (PO_4^{3-}) and υ_3 (PO_4^{3-}) modes are given in brackets.

Wavenumbers (/cm)				**Assignment**
1sec	**2sec**	**3sec_1**	**3sec_2**	
100	104	98	104	PO_4^{3-} rotational and Fe^{2+} translational motion
148	147	146	147	
155	157	156	157	
194	197	199	198	
242	244	239	238	
439	443	442	443	υ_2 (PO_4^{3-})
569	571	571	571	υ_4 (PO_4^{3-})
589	590	589	590	
627	629	629	629	
948 (1568.7)	949 (1677.4)	949 (1862.8)	949 (3897.6)	υ_1 (PO_4^{3-})
996 (160.3)	996 (182.1)	997 (185.1)	994 (453.7)	υ_3 (PO_4^{3-})
1067 (83.23)	1068(106.1)	1064 (94.9)	1067 (257.4)	

The microscopic images (Insets Fig 5.29 – 5.32) show that there are three different phases in all the samples, indicated by, a shiny-white, red-brown and a black phase. The $LiFePO_4$ phase has been identified by the white colour. The phases indicated by red and black could not be identified due to the lack of defined peaks except for the red phase in the 2sec sample which was identified as hematite (α-Fe_2O_3)[13,70,71] (Fig. 5.33) and had well defined peaks. Superparamagnetic hematite was present in the 1sec, 3sec_1, 3sec_2 and 4 sec samples (Table 5.16). It is therefore possible that the same phase is present in all the samples but possibly to a lesser extent thus giving less defined peaks. Since there was no α-Fe_2O_3 identified in the samples using XRD it can be concluded that this phase is either amorphous or present in very small little amounts. The 2sec (Fig. 5.30) and 3sec_2 (Fig. 5.32) samples showed small peaks at 1019 cm^{-1} and 1020 cm^{-1} (circled in black) which could be due to the formation of Li_3PO_4.[72] Li_3PO_4 was identified in both the 2sec and the 3sec_2 samples using XRD.

5.4. Conclusion

To determine if the Li^+ addition rate has any effect on the local and average structure of the final product – Rietveld analysis of the XRD data, XAS, PDF and Mössbauer and Raman spectroscopy were conducted. All samples had defects present and some of these defects could be inherent to the hydrothermal synthetic method, such as Fe on the M1 (Li^+) site. The Li^+ addition rate does have an effect on the antisite defects such as Fe on the M1 site as well as the vacancies on the M2 site. LCF and Mössbauer spectroscopy also determined that the addition rate had an effect on the Fe^{2+} content. Some amorphous α-Fe_2O_3 and Li_3PO_4 was identified using Raman spectroscopy. The local structure as determined using XAS showed that there are some interatomic distance changes resulting in the increased distortion of the Fe-O octahedra as there are different combinations of the bond distances and possibly different axial and equatorial positions. There was no change in the coordination shells or coordination numbers of the local structure. PDF independent model analysis showed more structural changes than XAS but additional modelling (big-box RMC) is needed to fully understand these changes. The 3sec_1 and 3sec_2 samples were used to also investigate the reproducibility. The 3sec_2 sample had a small percentage of Li_3PO_4 present as determined with both XRD and Raman spectroscopy that was not detected in the 3sec_1 sample. Similar occupancies on the M2 and M1 site as well as interatomic distances were determined using XRD. Different pre-edge intensities were seen for the 3sec_1 and 3sec_2 samples. This could be a cause of the different interatomic distance combination as seen with EXAFS. LCF and Mössbauer spectroscopy

showed that a similar Fe^{2+} content was present in the sample although 3sec_1 had a slightly higher content. Based on the discrepancies noted it is difficult to distinguish which addition rate is optimal, where in this case the 1sec and 3sec samples gave the best results compared to the 2sec and especially the 5sec sample which was the least desirable sample.

5.5. References

1. Padhi, A. K., Nanjundaswamy, K. S., Masquelier, C., Okada, S. and Goodenough, J. B. Effect of structure on the Fe^{3+}/Fe^{2+} redox couple in iron phosphates. *J. Electrochem. Soc.* **144**, 1609–1613 (1997).
2. Yamada, A., Chung, S. C. and Hinokuma, K. Optimized $LiFePO_4$ for Lithium Battery Cathodes. *J. Electrochem. Soc.* **148**, A224 (2001).
3. Islam, M. S., Driscoll, D. J., Fisher, C. A. J. and Slater, P. R. Atomic-scale investigation of defects, dopants, and lithium transport in the $LiFePO_4$ olivine-type battery material. *Chem. Mater.* **17**, 5085–5092 (2005).
4. Morgan, D., Van der Ven, A. and Ceder, G. Li Conductivity in Li_xMPO_4 (M = Mn, Fe, Co, Ni) Olivine Materials. *Electrochem. Solid-State Lett.* **7**, (2004).
5. Axmann, P., Stinner, C., Wohlfahrt-Mehrens, M., Mauger, A., Gendron, F. and Julien, C. M. Nonstoichiometric $LiFePO_4$: Defects and Related Properties. Chem. Mater. **21**, 1636–1644 (2009).
6. Wu, Y. J., Gu, Y. J., Chen, Y. B., Liu, H. Q. and Liu, C. Q. Effect of lithium phosphate on the structural and electrochemical performance of nanocrystalline $LiFePO_4$ cathode material with iron defects. *Int. J. Hydrogen Energy* **43**, 2050–2056 (2018).
7. He, L. and Zhao, Z. Effect of excess Li^+ in solution on $LiFePO_4$ preparation via wet chemical method. *J. Alloys Compd.* **688**, 386–391 (2016).
8. Chen, J., Bai, J., Chen, H. and Graetz, J. In Situ Hydrothermal Synthesis of $LiFePO_4$ Studied by Synchrotron X-ray Diffraction. *J. Phys. Chem. Lett.* **2**, 1874–1878 (2011).
9. Prince, A. A. M., Mylswamy, S., Chan, T. S., Liu, R. S., Hannoyer, B., Jean, M., Shen, C. H., Huang, S. M., Lee, J. F. and Wang, G. X. Investigation of Fe valence in LiFePO4 by Mössbauer and XANES spectroscopic techniques. Solid State Commun. **132**, 455–458 (2004).
10. Yang, S., Zavalij, P. Y. and Stanley Whittingham, M. Hydrothermal synthesis of lithium iron phosphate cathodes. *Electrochem. commun.* **3**, 505–508 (2001).
11. Chen, J., Vacchio, M. J., Wang, S., Chernova, N., Zavalij, P. Y. and Whittingham, M. S. The hydrothermal synthesis and characterization of olivines and related compounds for electrochemical applications. *Solid State Ionics* **178**, 1676–1693 (2008).
12. Kuwahara, A., Suzuki, S. and Miyayama, M. Hydrothermal synthesis of $LiFePO_4$ with small particle size and its electrochemical properties. *J. Electroceramics* **24**, 69–75 (2010).
13. Sun, X. and Xu, Y. Fe excess in hydrothermally synthesized LiFePO4. Mater. Lett. 84,

139 - 142 (2012).

14. Chen, J. and Graetz, J. Study of Antisite Defects in Hydrothermally Prepared $LiFePO_4$ by in Situ X-ray Diffraction. *ACS Appl. Mater. Interfaces* **3**, 1380–1384 (2011).

15. Andersson, A. S., Kalska, B., Häggström, L. and Thomas, J. O. Lithium extraction/insertion in $LiFePO_4$: An X-ray diffraction and Mössbauer spectroscopy study. *Solid State Ionics* **130**, 41–52 (2000).

16. Liu, J., Jiang, R., Wang, X., Huang, T. and Yu, A. The defect chemistry of $LiFePO_4$ prepared by hydrothermal method at different pH values. *J. Power Sources* **194**, 536–540 (2009).

17. Streltsov, V. A., Belokoneva, E. L., Tsirelson, V. G. and Hansen, N. K. Multipole analysis of the electron density in triphylite, $LiFePO_4$, using X-ray diffraction data. *Acta Crystallogr. Sect. B* **49**, 147–153 (1993).

18. Jugović, D., Cvjetićanin, N., Mitrić, M. and Mentus, S. Comparison between different $LiFePO_4$ synthesis routes. in *Materials Science Forum* **555**, 225–230 (2007).

19. Gibot, P., Casas-Cabanas, M., Laffont, L., Levasseur, S., Carlach, P., Hamelet, S., Tarascon, J. M. and Masquelier, Christian. Room-temperature single-phase Li-insertion/extraction in nanoscale LixFePO4. Nat. Mater. **7**, 741–747 (2008).

20. Liu, Z. and Huang, X. Factors that affect activation energy for Li diffusion in $LiFePO_4$: A first-principles investigation. *Solid State Ionics* **181**, 907–913 (2010).

21. Rousse, G., Rodriguez-Carvajal, J., Patoux, S. and Masquelier, C. Magnetic Structures of the Triphylite $LiFePO_4$ and of Its Delithiated Form $FePO_4$. *Chem. Mater.* **15**, 4082–4090 (2003).

22. Shu, H., Wang, X., Wu, Q., Hu, B., Yang, X., Wei, Q., Liang, Q., Bai, Y., Zhou, M., Wu, C., Chen, M., Wang, A. and Jiang, L. Improved electrochemical performance of $LiFePO_4$/C cathode via Ni and Mn co-doping for lithium-ion batteries. J. Power Sources **237**, 149–155 (2013).

23. Gao, H., Jiao, L., Yang, J., Qi, Z., Wang, Y. and Yuan, H. High rate capability of Co-doped $LiFePO_4$/C. Electrochim. Acta **97**, 143–149 (2013).

24. Lu, Y., Shi, J., Guo, Z., Tong, Q., Huang, W. and Li, B. Synthesis of $LiFe_{1-x}Ni_xPO_4$/C composites and their electrochemical performance. *J. Power Sources* **194**, 786–793 (2009).

25. Shulman, G. R., Yafet, Y., Eisenberger, P. and Blumberg, W. E. Observations and interpretation of x-ray absorption edges in iron compounds and proteins. *Proc. Natl. Acad. Sci. U. S. A.* **73**, 1384–1388 (1976).

26. Haas, O., Deb, A., Cairns, E. J. and Wokaun, A. Synchrotron X-ray absorption study of $LiFePO_4$ electrodes. *J. Electrochem. Soc.* **152**, (2005).

27. Deb, A., Bergmann, U., Cairns, E. J. and Cramer, S. P. X-ray absorption spectroscopy study of the Li_xFePO_4 cathode during cycling using a novel electrochemical in situ reaction cell. *J. Synchrotron Radiat.* **11**, 497–504 (2004).

28. Deb, A., Bergmann, U., Cairns, E. J. and Cramer, S. P. Structural investigations of $LiFePO_4$ electrodes by Fe X-ray absorption spectroscopy. *J. Phys. Chem. B* **108**, 7046–

7051 (2004).

29. Hsu, K. F., Hu, S. K., Chen, C. H., Cheng, M. Y., Tsay, S. Y., Chou, T. C., Sheu, H. S., Lee, J. F. and Hwang, B. J. Formation mechanism of $LiFePO_4$/C composite powders investigated by X-ray absorption spectroscopy. J. Power Sources 192, 660–667 (2009).

30. Wilke, M., Farges, F., Petit, P. E., Brown, G. E. and Martin, F. Oxidation state and coordination of Fe in minerals: An Fe K-XANES spectroscopic study. *Am. Mineral.* **86**, 714–730 (2001).

31. Wong, J., Lytle, F. W., Messmer, R. P. and Maylotte, D. H. K-edge absorption spectra of selected vanadium compounds. *Phys. Rev. B* **30**, 5596–5610 (1984).

32. Roe, A. L., Schneider, D. J., Mayer, R. J., Pyrz, J. W., Widom, J. and Que, L. X-ray Absorption Spectroscopy of Iron-Tyrosinate Proteins. *J. Am. Chem. Soc.* **106**, 1676–1681 (1984).

33. Westre, T. E., Kennepohl, P., DeWitt, J. G., Hedman, B., Hodgson, K. O. and Solomon, E. I. A multiplet analysis of Fe K-edge 1s → 3d pre-Edge features of iron complexes. *J. Am. Chem. Soc.* **119**, 6297–6314 (1997).

34. Griffith, J. S. & Orgel, L. E. Ligand-field theory. *Q. Rev. Chem. Soc.* **11**, 381–393 (1957).

35. Park, K. S., Son, J.T., Chung, H.T., Kim, S.J., Lee, C.H. and Kim, H.G. Synthesis of $LiFePO_4$ by co-precipitation and microwave heating. *Electrochem. commun.* **5**, 839–842 (2003).

36. Zhao, T., Chu, W., Zhao, H., Liang, X., Xu, W., Yu, M., Xia, D. and Wu, Z. XAS study of $LiFePO_4$ synthesized by solid state reactions and hydrothermal method. in *Nuclear Instruments and Methods in Physics Research, Section A: Accelerators, Spectrometers, Detectors and Associated Equipment* **619**, 122–127 (2010).

37. Kelly, S. D. and Ravel, B. EXAFS analysis with self-consistent atomic potentials. *AIP Conference Proceedings* **882**, 135–137 (2007).

38. Keating, J., Sankar, G., Hyde, T. I., Kohara, S. and Ohara, K. Elucidation of structure and nature of the PdO-Pd transformation using in situ PDF and XAS techniques. *Phys. Chem. Chem. Phys.* **15**, 8555–8565 (2013).

39. Etschmann, B. E., Donner, E., Brugger, J., Howard, D. L., de Jonge, M. D., Paterson, D., Naidu, R., Scheckel, K. G., Ryan, C. G. and Lombi, E. Speciation mapping of environmental samples using XANES imaging. *Environ. Chem.* **11**, 341 (2014).

40. Gaur, A., Shrivastava, B. D. and Khalid, S. Copper K-edge XANES of Cu(I) and Cu(II) oxide mixtures. *J. Phys. Conf. Ser.* **190,** 012084 (2009).

41. Calvin, S. *XAFS for Everyone*.(CRC Press, 2013).

42. Kelly, S. D. and Ravel, B. EXAFS energy shift and structural parameters. *AIP Conference Proceedings* **882**, 132–134 (2007).

43. Jensen, K. M. Ø., Christensen, M., Gunnlaugsson, H. P., Lock, N., Bøjesen, E. D., Proffen, T. and Iversen, B. B. Defects in Hydrothermally Synthesized $LiFePO_4$ and $LiFe_{1-x}Mn_xPO_4$ Cathode Materials. *Chemistry of Materials* **25**, 2282 - 2290 (2013)

44. Chapman, K. W. Emerging operando and X-ray pair distribution function methods for energy materials development. *MRS Bull.* **41**, 231–238 (2016).

45. Coduri, M., Brunelli, M., Scavini, M., Allieta, M., Masala, P., Capogna, L., Fischer, H. E. and Ferrero, C. Rare Earth doped ceria: A combined X-ray and neutron pair distribution function study. *Zeitschrift fur Krist.* **227**, 272–279 (2012).

46. Bordet, P. Local structure studies using the pair distribution function. *EPJ Web Conf.* **104**, 01003 (2015).

47. Bini, M., Ferrari, S., Capsoni, D., Mustarelli, P., Spina, G., Giallo, F. D., Lantieri, M., Leonelli, ., Rizzuti, A. and Massarotti, V. Pair distribution function analysis and Mössbauer study of defects

48. Meral, C., Benmore, C. J. and Monteiro, P. J. M. The study of disorder and nanocrystallinity in C-S-H, supplementary cementitious materials and geopolymers using pair distribution function analysis. *Cement and Concrete Research* **41** 696–710 (2011).

49. Jensen, K. M. Ø., Andersen, H. L., Tyrsted, C., Bøjesen, E. D., Dippel, A. C., Lock, N., Billinge, S. J. L., Iversen, B. B. and Christensen, M. Mechanisms for iron oxide formation under hydrothermal conditions: An in situ total scattering study. *ACS Nano* **8**, 10704–10714 (2014).

50. Wang, X., Tan, S., Yang, X. Q. and Hu, E. Pair distribution function analysis: Fundamentals and application to battery materials. *Chinese Phys. B* **29**, 28802 (2020).

51. Knox, K. R., Abeykoon, A. M.M., Zheng, H., Yin, W. G., Tsvelik, A. M., Mitchell, J. F., Billinge, S. J.L., Bozin, E. S. Local structural evidence for strong electronic correlations in spinel $LiRh_2O_4$. *Phys. Rev. B - Condens. Matter Mater. Phys.* **88**, 174114 (2013).

52. Mohideen, M. I., Allan, P. K., Chapman, K. W., Hriljac, J. A. and Morris, R. E. Ultrasound-driven preparation and pair distribution function-assisted structure solution of a copper-based layered coordination polymer. *Dalt. Trans.* **43**, 10438–10442 (2014).

53. Wiaderek, K. M., Borkiewicz, O. J., Pereira, N., Ilavsky, J., Amatucci, G. G., Chupas, P. J. and Chapman, K. W. Mesoscale effects in electrochemical conversion: Coupling of chemistry to atomic- and nanoscale structure in iron-based electrodes. *J. Am. Chem. Soc.* **136**, 6211–6214 (2014).

54. Willinger, E., Massué, C., Schlögl, R. and Willinger, M. G. Identifying Key Structural Features of IrO_x Water Splitting Catalysts. *J. Am. Chem. Soc.* **139**, 12093–12101 (2017)

55. Petkov, V., Difrancesco, R. G., Billinge, S. J. L., Acharya, M. and Foley, H. C. Local structure of nanoporous carbons. *Philos. Mag. B Phys. Condens. Matter; Stat. Mech. Electron. Opt. Magn. Prop.* **79**, 1519–1530 (1999).

56. Proffen, T., Petkov, V., Billinge, S. J. L. and Vogt, T. Chemical short range order obtained from the atomic pair distribution function. *Zeitschrift fur Krist.* **217**, 47–50 (2002).

57. Shannon, R. D. Revised effective ionic radii and systematic studies of interatomic distances in halides and chalcogenides. *Acta Crystallogr. Sect. A* **32**, 751–767 (1976).

58. Li, K. and Xue, D. Estimation of electronegativity values of elements in different valence states. *J. Phys. Chem. A* **110**, 11332–11337 (2006).

59. Amisse, R., Sougrati, M. T., Stievano, L., Davoisne, C., Dražič, G., Budič, B., Dominko, R. and Masquelier, C. Singular Structural and Electrochemical Properties in Highly Defective $LiFePO_4$ Powders. *Chem. Mater.* **27**, 4261–4273 (2015).

60. Porcher, W., Moreau, P., Lestriez, B., Jouanneau, S., Le Cras, F. and Guyomard, D. Stability of $LiFePO_4$ in water and consequence on the Li battery behaviour. *Ionics (Kiel).* **14**, 583–587 (2008).

61. Maccario, M., Croguennec, L., Wattiaux, A., Suard, E..,Le Cras, F. and Delmas, C. C-containing $LiFePO_4$ materials - Part I: Mechano-chemical synthesis and structural characterization. *Solid State Ionics* **179**, 2020–2026 (2008).

62. Hamelet, S., Gibot, P., Casas-Cabanas, M., Bonnin, D., Grey, C. P., Cabana, J., Leriche, J. B., Rodriguez-Carvajal, J., Courty, M., Levasseur, S., Carlach, P., Van Thournout, M., Tarascon, J. M. and Masquelier, C. The effects of moderate thermal treatments under air on $LiFePO_4$-based nano powders. *J. Mater. Chem.* **19**, 3979–3991 (2009).

63. Li, Z. & Shinno, I. Next nearest neighbor effects in triphylite and related phosphate minerals. *Mineral. J.* **19**, 99–107 (1997).

64. Cuisinier, M., Martin, J. F., Dupré, N., Yamada, A., Kanno, R. and Guyomard, D. Moisture driven aging mechanism of $LiFePO_4$ subjected to air exposure. *Electrochem. commun.* **12**, 238–241 (2010)..

65. Xia, X., Wang, Z. and Chen, L. Regeneration and characterization of air-oxidized $LiFePO_4$. *Electrochem. commun.* **10**, 1442–1444 (2008).

66. Cuisinier, M., Martin, J. F., Dupré, N., Kanno, R. and Guyomard, D. Elucidating the $LiFePO_4$ air aging mechanism to predict its electrochemical performance. *J. Mater. Chem.* **21**, 18575–18583 (2011).

67. Burba, C. M. and Frech, R. Raman and FTIR Spectroscopic Study of Li_xFePO_4 ($0 \leq x \leq 1$). *J. Electrochem. Soc.* **151**, A1032 (2004).

68. Paraguassu, W., Freire, P. T. C., Lemos, V., Lala, S. M., Montoro, L. A. and Rosolen, J. M. Phonon calculation on olivine-like $LiMPO_4$ (M = Ni, Co, Fe) and Raman scattering of the iron-containing compound. *J. Raman Spectrosc.* **36**, 213–220 (2005).

69. Wu, J., Krishna Phani Dathar, G., Sun, C., Theivanayagam, M. G., Applestone, D., Dylla, A. G., Manthiram, A., Henkelman, G., Goodenough, J. B. and Stevenson, K. J. In situ Raman spectroscopy of $LiFePO_4$: size and morphology dependence during charge and self-discharge. *IOP Publ. Nanotechnol. Nanotechnol.* **24**, 424009–424018 (2013).

70. de Faria, D. L. A. and Lopes, F. N. Heated goethite and natural hematite: Can Raman spectroscopy be used to differentiate them? *Vib. Spectrosc.* **45**, 117–121 (2007)..

71. Dokko, K., Shiraishi, K. and Kanamura, K. Identification of Surface Impurities on $LiFePO_4$ Particles Prepared by a Hydrothermal Process. *J. Electrochem. Soc.* **152**, A2199 (2005).

72. Popovic, L., Manoun, B., de Waal, D., Nieuwoudt, M. K. and Comins, J. D. Raman spectroscopic study of phase transitions in Li_3PO_4. *J. Raman Spectrosc.* **34**, 77–83 (2003).

Chapter 6

The effect of air exposure during the synthesis of $LiFePO_4$

6.1. Introduction

It is important to understand the impact of air/moisture on $LiFePO_4$ during synthesis and during storage to avoid the formation of impurities that could affect the performance of the cathode material in a battery. The effect of air/moisture exposure after synthesis and during storage has been extensively studied by numerous research groups. Porcher *et al.*[1,2] investigated the stability of $LiFePO_4$ in water by varying time, pH and $LiFePO_4$ concentration. These studies showed the formation of Li_3PO_4 at the grain boundary as well as an increase in the Fe^{3+} content. It was concluded that $LiFePO_4$ should be stored in a dry atmosphere. The formation of the side phase (tavorite - $LiFePO_4(OH)$) that formed in storage in 120ºC hot air for 30 days were investigated by Cuisinier *et al.*[3] This study concluded that severe oxidation is due to long term exposure but following heat treatment of $LiFePO_4$ can be restored. Martin *et al*.[4] investigated the intrinsic properties of $LiFePO_4$ by avoiding air exposure during synthesis as well as during characterization. The effect of air exposure during synthesis has not been investigated as extensively, although Amisse *et al*.[5] probed the structural and electrochemical changes when an aqueous solution of $FeSO_4$ was exposed to air for 20 hours before synthesis. The resulting defective $LiFePO_4$ exhibited a volume reduction and a cationic distribution between the M2 and M1 sites (antisite defects). Impurities can be classified as either intrinsic or extrinsic impurities.[6] Intrinsic impurities are formed during synthesis which is dependent on the synthetic route. Extrinsic impurities are usually formed after synthesis during the storage or aging processes.[6] Previous publications were searching mainly for the effect and formation of extrinsic impurities. The presence of inactive impurities have an effect on the electrochemical properties by blocking the 1D Li^+ diffusion channel, as well as being responsible for the extraction of lithium from the active material and causing a decrease in the specific capacity and energy density.[2,3,6] Iron dissolution of $LiFePO_4$ in the electrolyte is an additional problem and can be caused by impurities containing Fe^{3+} that can form a cluster on the anode. The formation of the cluster on the anode can affect the battery safety and lifetime.[2,7] Aging of the active material usually leads to the formation of α-Fe_2O_3 which is the most common Fe^{3+} impurity.[3] This chapter explores the effect of air exposure during synthesis by exposing the samples to air for different times.

6.2. Sample preparation

The $FeSO_4 \cdot 7H_2O$ and H_3PO_4 was dissolved in water separately from the LiOH while under continuous stirring. The LiOH was then added drop wise to the iron solution using a syringe, ensuring a molar ratio of 3:1:1 ($Li:Fe:PO_4$), as described in section 2.1.2. For all the samples the Teflon bombs were filled to 25% of the total volume and placed in the oven at 120°C for 48 hours. To demonstrate the effect of air exposure during synthesis, one sample was purged and 4 other samples were exposed to air for different time periods. The purged sample was synthesised as described in section 4.2.3.

Waiting Period – No purging was done on the samples during this period. After the addition of LiOH to the $FeSO_4/H_3PO_4$ solution the sample was exposed to air for 3 min, 30 min, 1 hour or 4 hours, while continuously stirring, before being added to the Teflon bombs.

6.3. Results and Discussion

6.3.1. Powder X-ray diffraction

Diffractograms were collected for the five purged (**Air0**) and exposed to air for: 3 min (**Air3min**), 30 min (**Air30min**), 1 hour (**Air1hr)** and the 4 hours (**Air4hr**) samples. It was expected that Air0 sample would show very small percentages of impurities due to the purging of the solutions whereas as the air exposed samples would contain higher percentages and more impurities as the exposure time increases. Rietveld analysis was conducted for all samples (Figs. 6.1 – 6.5). The Air4hr sample (Fig. 6.5) was poorly crystalline and not all the peaks could be identified. Phases common to all samples were used for the refinement. An X-ray wavelength of 0.167057(4) Å was used for all the refinements. The Rietveld error indices can be found in Table 6.1. Graphically, the difference curve worsen for the air exposed samples and it can be seen that the fit quality decreases with air exposure time.[8] Due to the poorly defined peaks of the Air4hr sample (Fig 6.5) information such as the lattice parameters, occupancies and interatomic distances could not be reliably determined.

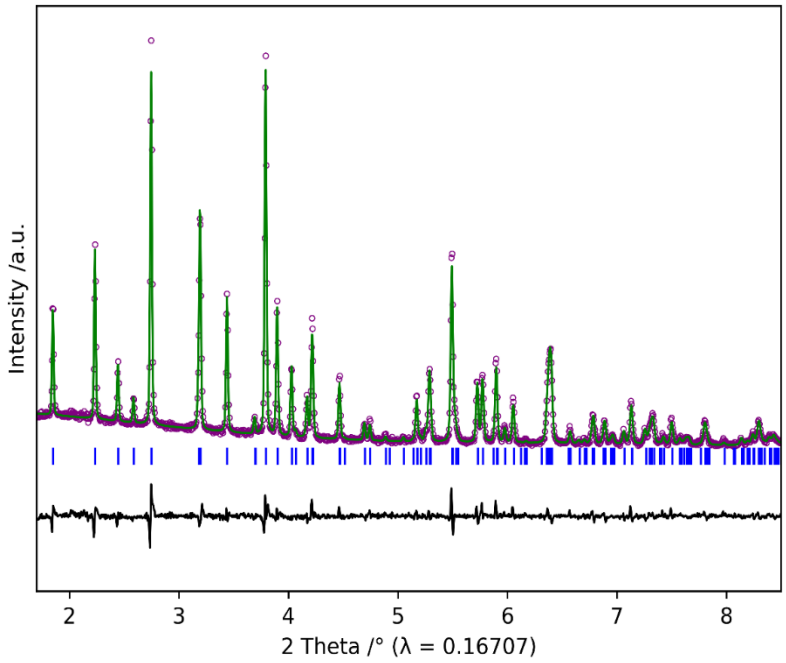

Figure 6.1: Synchrotron diffractogram of the Air0 $LiFePO_4$ sample showing the observed (purple), calculated (green) and difference (black) plots generated from a Rietveld refinement analysis. Bragg reflections for $LiFePO_4$ are indicated with the blue makers.

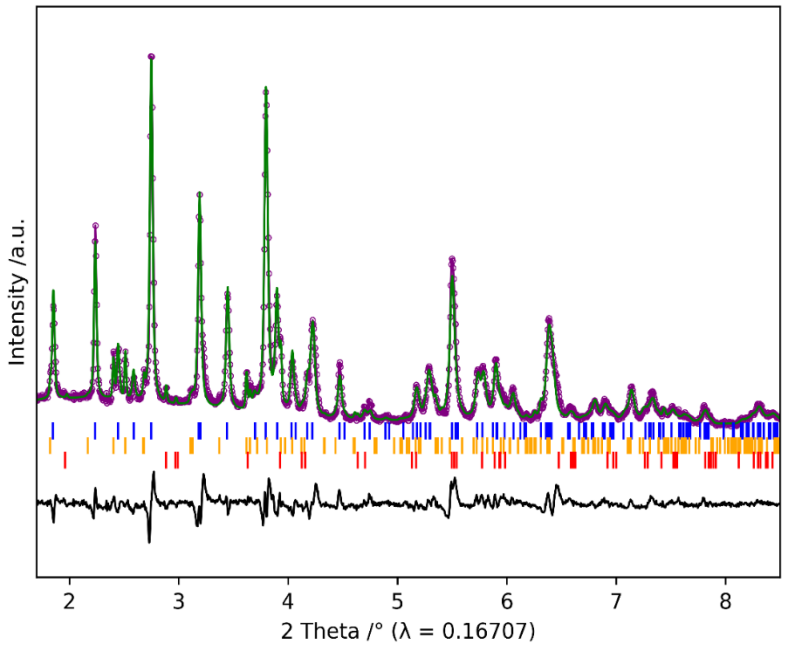

Figure 6.2: Synchrotron diffractogram of the Air3min $LiFePO_4$ sample showing the observed (purple), calculated (green) and difference (black) plots generated from a Rietveld refinement analysis. Bragg reflections for $LiFePO_4$, Li_3PO_4 and the Fe impurity are indicated with the blue, orange and red markers, respectively.

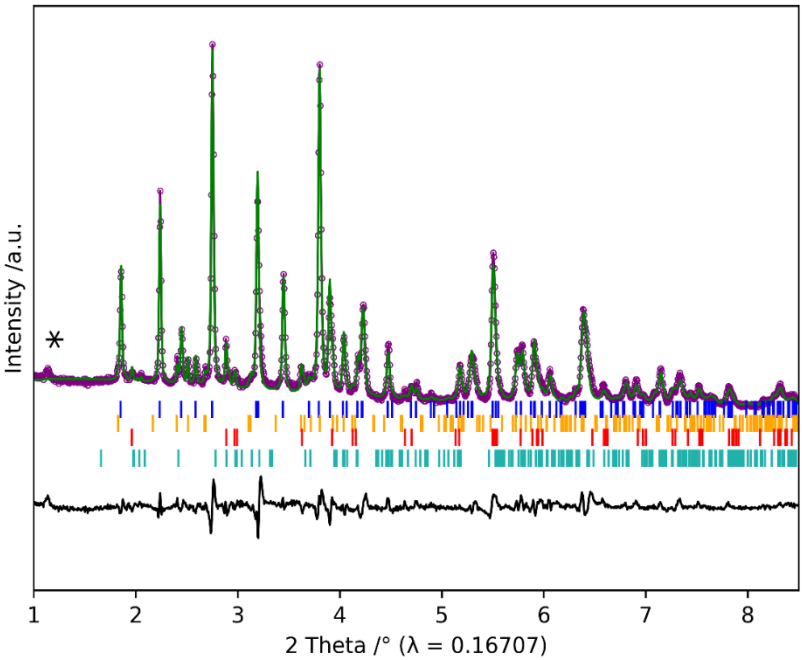

Figure 6.3: Synchrotron diffractogram of the Air30min $LiFePO_4$ sample showing the observed (purple), calculated (green) and difference (black) plots generated from a Rietveld refinement analysis. Bragg reflections for $LiFePO_4$, Li_3PO_4, Fe impurity and tavorite are indicated with the blue, orange, red and green markers, respectively. (*) indicates an unidentified impurity phase.

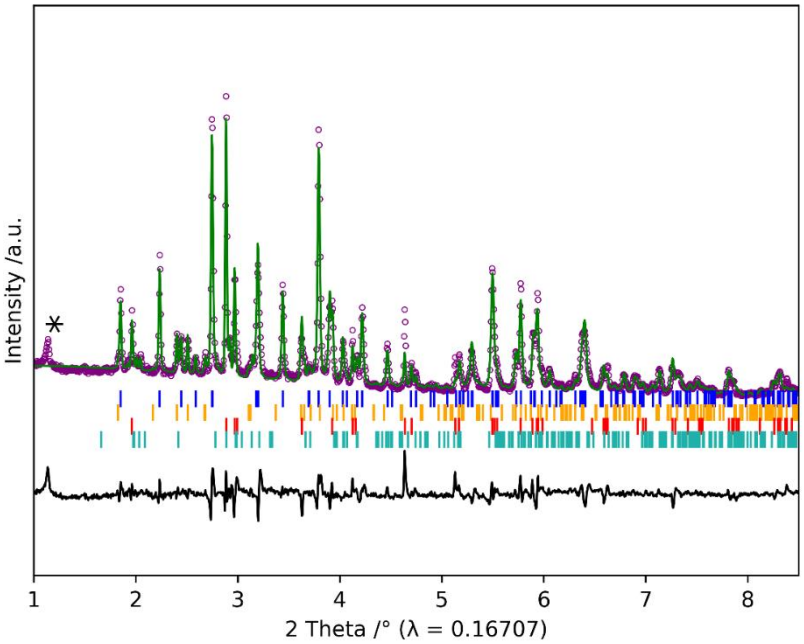

Figure 6.4: Synchrotron diffractogram of the Air1hr $LiFePO_4$ sample showing the observed (purple), calculated (green) and difference (black) plots generated from a Rietveld refinement analysis. Bragg reflections for $LiFePO_4$, Li_3PO_4, Fe impurity and tavorite are indicated with the blue, orange, red and green markers, respectively. (*) indicates an unidentified impurity phase.

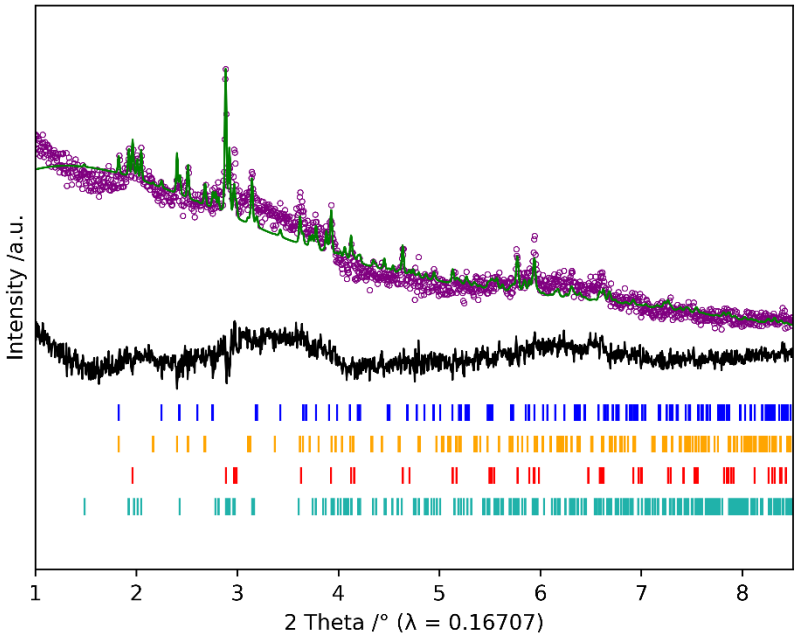

Figure 6.5: Synchrotron diffractogram of the Air4hr $LiFePO_4$ sample showing the observed (purple), calculated (green) and difference (black) plots generated from a Rietveld refinement analysis. Bragg reflections for $LiFePO_4$, Li_3PO_4, Fe impurity and Tavorite are indicated with the blue, orange, red and green markers, respectively.

Table 6.1: Rietveld error indices and selected structural parameters of $LiFePO_4$.

	Air0	**Air3min**	**Air30min**	**Air1hr**	**Air4hr**
R_{wp}	7.63	9.21	8.57	9.73	8.11
R_p	5.99	7.24	6.75	7.54	6.58
R_{exp}	69.21	52.97	55.44	56.17	69.70
GOF	0.11	0.17	0.15	0.17	0.11
a (Å)	10.356(3)	10.31(1)	10.315(8)	10.345(9)	-
b (Å)	5.9961(2)	5.9929(6)	5.9874(4)	5.9849(5)	-
c (Å)	4.7093(2)	4.6996(5)	4.6975(4)	4.7069(4)	-
V (Å^3)	292.4(3)	290.6(5)	290.1(4)	291.4(5)	-

The impurity phases detected and identified can be found in Table 6.2. As expected, no impurities were found in the Air0 sample due to purging however the amount of impurity phases in the air exposed samples increased with exposure time. As the initial air exposure time increases, the percentage of $LiFePO_4$ decreases and the percentage of impurity phases increases. The impurity phases present are Li_3PO_4, a Fe impurity ($Fe_{3.44}O_{10}P_{1.98}$ –$I4_1/a$, #88) and $LiFePO_4(OH)$ (Table 6.2) and an identified phase. Li_3PO_4 and $LiFePO_4(OH)$ are known side phases where the air/moisture effects have been investigated.[1–3] The Fe-impurity has been seen in other samples and was discussed in section 4.1.2 and the unidentified phase was also present in samples where the solutions were not purged as discussed in sections 4.1.2 and 4.1.3

(Figs. 4.1−4.5). In the Air3min air exposed sample, the Fe-impurity phase was added which improved the fit although it is present in a very small amount. $LiFePO_4(OH)$ improved the fit of both the Air30min and 1hour samples. In the Air30min and Air1hr samples an unidentified impurity phase is present (* peak at about 1.12º on Figs. 6.3 and 6.4). This peak becomes more prominent in the 1hour sample indicating that the amount of this phase present in the sample increases over time. The Air4hr sample contained the least amount $LiFePO_4$ and the highest percentage of Fe^{3+}-containing impurity phases. Li_3PO_4 was also identified in the sample.

The lattice parameters and volume obtained for the $LiFePO_4$ phase (Table 6.1) were comparable to the values reported in literature.[9–15] A complete summary of these values can be found in Table 3.1. The reported a-lattice constant ranges from 10.303 – 10.381 Å, the b- lattice constant from 5.987 – 6.013 Å and the c-lattice constant from 4.6928 – 4.716 Å. There is a slight decrease in the cell volume for the Air3min and Air30min samples compared to the purged sample with the Air30min sample exhibiting the highest degree of volume contraction. This could serve as an indication of an increase in structural defects and disorder.[5,16] These structural defects are most likely caused by the presence of Fe^{3+} in the structure[4], Li and Fe vacancies or due to Fe^{3+} occupying the M1 (Li) site.[16]

Table 6.2: The percentage of $LiFePO_4$ and impurity phases obtained from a multiphase Rietveld refinement of the samples.

Sample	$LiFePO_4$	Li_3PO_4	Fe Impurity	$LiFePO_4OH$
Air0	100	-	-	-
Air3min	91.15	8.08	0.76	-
Air30min*	89.86	5.67	2.38	2.09
Air1hr*	62.93	11.43	19.20	6.44
Air4hr	12.09	26.85	23.13	37.92

*not including the unidentified impurity phase

The best fits were achieved when using the Fe_{Li} antisite defect for the synthesised samples (Table 6.3). The M2 (Fe) site and the M1 (Li^+) site were refined to determine the percentage occupancy on each site and whether any vacancies were present. The M2 (Fe) site was not fully occupied for the Air0, Air3min and Air30min samples but was fully occupied for the Air1hr sample. The Air30min and Air3min samples had the highest percentage of vacancies present on the M2 site. Vacancies form when Fe^{2+} is replaced with Fe^{3+}.[17] The higher percentage of Fe^{3+} present in the Air3min and Air 30min samples could explain why this sample has the

smallest cell volume and why the Air0 and Air1hr samples showed a bigger cell volume because samples with a smaller cell volume have a higher percentage of defects present.[4] The M1 site was not fully occupied with Li^+ for any of the synthesised samples (Table 6.3). The Air30min sample had the lowest percentage of Fe^{2+} and/or Fe^{3+} present on the M1 site. The Air3min and Air1hr samples had the lowest percentage of Li^+ and hence the highest percentage Fe^{2+} and/or Fe^{3+} on the M1 site. This would lead to poor electrochemical performance due to the Fe^{2+} and/or Fe^{3+} blocking the Li^+ channel.[14,18,19] Mössbauer spectroscopy will aid in determining the oxidation states of Fe on the different sites as well as percentage of Fe^{3+} on the Li^+ site.

Table 6.3: The percentage Li^+ occupying the M2 (Fe) site and Fe occupying the M1 (Li^+) site in the refined $LiFePO_4$ structures.

	Air0	**Air3min**	**Air30min**	**Air1hr**
M2 site	99.0(6)	98(2)	98(1)	100
Vacancies on M2 site	1	2	2	-
M1 site	90.9(3)	89(2)	92.3(9)	89(1)
Fe on the M1 site	9.1(3)	11(1)	7.7(8)	11(1)

The calculated interatomic bond distances of FeO_6, LiO_6 and PO_4 were also determined from the Rietveld analysis (Table 6.4). The average interatomic M2-O bond distance is slightly shorter than those of Fe-O recorded in literature (Table 3.2).[11,20–22] This slight deviation is likely caused by the presence of Fe^{3+}–O bonds (which have a shorter interatomic bond distance than the Fe^{2+}-O bonds) in the synthesised samples.[23] The Air0 sample had the longest interatomic bond distance whereas the Air3min and Air30min samples had the shortest interatomic bond distance, an indication that there are less Fe^{3+}-O bonds and Fe^{3+} ions on the M2 site as confirmed by the M2 vacancies in the Air0 sample (Table 6.3). The contraction of the FeO_6 octahedra will cause the expansion of the LiO_6 octahedra as noted. The synthesised samples exhibit longer M1-O interatomic bond distances (Table 6.4) compared to those reported in literature.[20–22] The average P-O interatomic bond (Table 6.4) distance for the synthesised samples were longer than those reported in literature[11,20–22] and can be used to make assumptions about the stability of the $LiFePO_4$ structure. A shorter interatomic bond distance, as observed for the Air0 sample, indicated a more stable structure.[24–26]

Table 6.4: Interatomic bond distances of the refined structures.

	Air0	**Air3min**	**Air30min**	**Air1hr**
M2 – O(1)	2.205	2.137	2.156	2.146
M2 – O(2)	2.060	2.006	2.011	2.076
M2 – O(3) (×2)	2.050	1.989	2.012	1.999
M2 – O(3) (×2)	2.231	2.263	2.245	2.286
Average M2 – O bond length	**2.138**	**2.108**	**2.114**	**2.132**
P – O(1)	1.543	1.551	1.543	1.527
P – O(2)	1.627	1.686	1.666	1.683
P – O(3) (×2)	1.592	1.645	1.622	1.607
Average P – O bond length	**1.589**	**1.632**	**1.613**	**1.606**
M1 – O(1) (×2)	2.171	2.189	2.184	2.231
M1 – O(2) (×2)	2.094	2.117	2.116	2.058
M1– O(3) (×2)	2.191	2.190	2.184	2.159
Average M1 – O bond length	**2.152**	**2.165**	**2.161**	**2.149**

6.3.2. Mössbauer spectroscopy

Mössbauer spectroscopy was used to determine the possible Fe environments present in the five samples and the effect of air exposure on the Fe^{2+} content. It is expected that the Air0 sample will have the highest total percentage of Fe^{2+} present whereas this percentage would decrease as the exposure time increased. Using the isomer shift (δ) to indicate the oxidation state and the quadrupole splitting (ΔE_Q) to indicate the extent of the distortion,[16] a maximum of five different iron environments were identified. All five environments are present in the Air0 (Fig. 6.6), Air3min (Fig. 6.6), Air30min (Fig. 6.6) samples, but only three environments are present in the Air1hr sample (Fig. 6.6) and two in the Air4hr (Fig. 6.6) air exposed sample. These environments have been identified and discussed in other chapters.

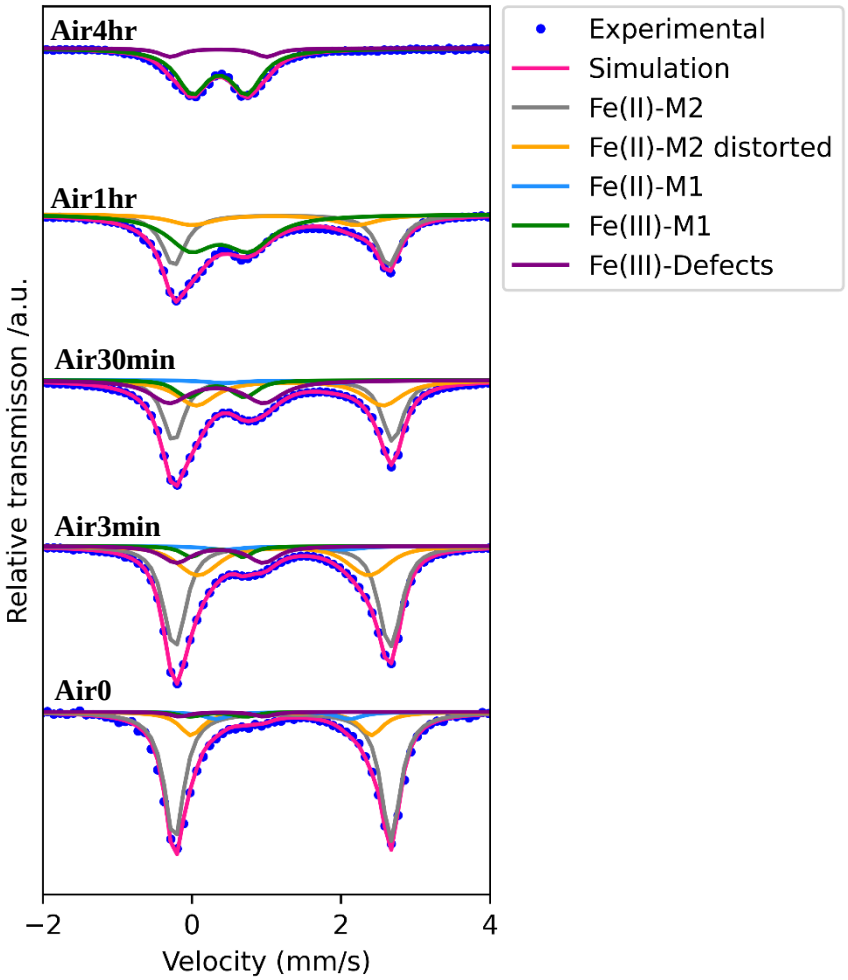

Figure 6.6: Mössbauer spectra of (from the bottom to the top) the Air0, Air3min, Air30min, Air1hr and Air4hr $LiFePO_4$ samples showing the different Fe environments present.

The different δ and ΔE_Q values can be found in Table 6.5. The main contribution of Fe in all the samples except the Air4hr sample is Fe^{2+} with δ ranging 1.20 – 1.22 mm/s and ΔE_Q between 2.88 – 2.94 mm/s. This is characteristic of Fe^{2+} in a slightly distorted FeO_6 environment (M2 site) in $LiFePO_4$.[2,3,5,11,13,16,27,28] The high ΔE_Q value is due to the local asymmetric environment and the high spin configuration of the $3d^6$ electrons.[11,27] The other Fe environments found in the structure are possibly due to distortions and other structural defects. Fe with δ between 1.20 – 1.24 mm/s and ΔE_Q between 2.34 – 2.51 mm/s is characteristic of Fe^{2+} on the M2 site but in a more distorted environment.[5] The ΔE_Q value of the samples are lower than those reported in literature and could be due to an increase in distortions.[5,16] The δ and ΔE_Q for the Air1hr sample is a bit lower than the reported values for Fe in this environment. This could be a result of impurity phases present with $LiFePO_4$. Another Fe^{2+} environment with an δ = 1.18 – 1.23 mm/s and ΔE_Q = 1.49 – 1.80 mm/s can be characterised as Fe^{2+} on the M1 site.[29] The

quadrupole splitting indicates changes in the distortion around the octahedra caused by the replacement of Li^+ with Fe^{2+}. Two Fe environments were also present with similar δ values but different ΔE_Q values. The one Fe^{3+} environment has δ values between 0.35 – 0.38 mm/s and ΔE_Q between 0.60 – 0.78 mm/s. These parameters are characteristic of Fe^{3+} present on the M1 (anti) site octahedra.[5,16,28] The second Fe^{3+} environment exhibits a δ value between 0.33 – 0.40 mm/s and a ΔE_Q between 1.08 – 1.26 mm/s. These parameters corresponds to Fe^{3+} occupying the M2 site the octahedral environment in the form of structural defects.[3,5,16,30] This environment can also be characteristic of superparamagnetic hematite.[31] No Fe^{3+} occupying the M2 site was identified in the Air1hour sample. This was also seen with PXRD. Air4hr showed no Fe^{2+} phases. $LiFePO_4(OH)$, hematite and the Fe-impurity are all Fe^{3+}-containing phases and it also then implies that all the Fe in the $LiFePO_4$ phase is fully oxidised. These phases, excluding hematite, were all identified using PXRD. Figure 6.6 clearly showed that there is not a doublet with a quadrupole splitting as large as the one characteristic of Fe^{2+} in $LiFePO_4$.

Table 6.5: Different isomer shifts (δ – mm/s) and quadrupole splitting (ΔE_Q – mm/s) for the different samples.

	Fe(II) – M2		**Fe(II) – M2 distorted**		**Fe(II) –M1**		**Fe(III) –M1**		**Fe(III) – M2/Defects**	
	δ	δ	δ	ΔE_Q	δ	ΔE_Q	δ	ΔE_Q	δ	ΔE_Q
Air0	1.22(1)	2.91(1)	1.20(1)	2.42(2)	1.22(3)	1.80(5)	0.35(4)	0.75(6)	0.40(4)	1.13(8)
Air3 min	1.21(1)	2.89(1)	1.22(1)	2.29(1)	1.23(2)	1.60(4)	0.34(1)	0.70(1)	0.38(1)	1.16(1)
Air30 min	1.22(1)	2.94(1)	1.31(1)	2.51(1)	1.18(2)	1.49(4)	0.33(1)	0.76(1)	0.33(1)	1.26(1)
Air1 hr	1.21(1)	2.88(1)	1.00(1)	2.34(2)	-	-	0.40(1)	0.73(1)	-	-
Air4 hr	-	-	-	-	-	-	0.38(1)	0.62(1)	0.37(1)	1.12(1)

The percentage contribution from the Fe^{2+} and Fe^{3+} as well as the total percentage present in the samples are given in Table 6.6. XRD detected no other phases except $LiFePO_4$ in the Air0 sample. The Fe^{3+} defects must therefore be amorphous in this sample.

Table 6.6: Percentage contribution from each form of Fe to the total Fe in the different samples.

	Fe(II) – M2	Fe(II) –M2 distorted	Fe(II) – M1	Fe(III) –M1	Fe(III) - Defects	Total Fe	
						Fe^{2+}	Fe^{3+}
Air0	73(8)	16(3)	5(1)	3(1)	3(1)	94	6
Air3min	53(7)	26(4)	4(1)	5(1)	12(2)	83	17
Air30min	35(4)	37(3)	3(1)	11(1)	24(2)	75	35
Air1hr	35(4)	23(3)	0	42(5)	0	58	42
Air4hr	0	0	0	49(3)	51(3)	0	100

The amount of Fe^{2+} that is oxidised to Fe^{3+} during air exposure increased with air exposure time (Table 6.6). The initial oxidation of Fe^{2+} to Fe^{3+} for the Air0 to Air3min samples seem to be more rapid than the oxidation that occurs for the Air30min – Air4hr samples (Fig. 6.7). The latter show an almost linear trend until all the Fe^{2+} has been converted to Fe^{3+}. The rapid oxidation at the initial stages of the synthesis indicates the difficulty of producing $LiFePO_4$ with only Fe^{2+} present. To overcome this problem a reductant can be added to the samples during synthesis but this addition has to be accompanied by heat treatment steps under reducing atmospheres. The total Fe^{2+} percentage in $LiFePO_4$ follows a similar trend as determined with the XRD phase analysis (Table 6.2) but not as determined when refining the occupancies. The Fe on the M2 or the M1 site is somewhat expected as Mössbauer spectroscopy is more sensitive to the different oxidation states and the specific local environments, whereas XRD only refines for Fe.

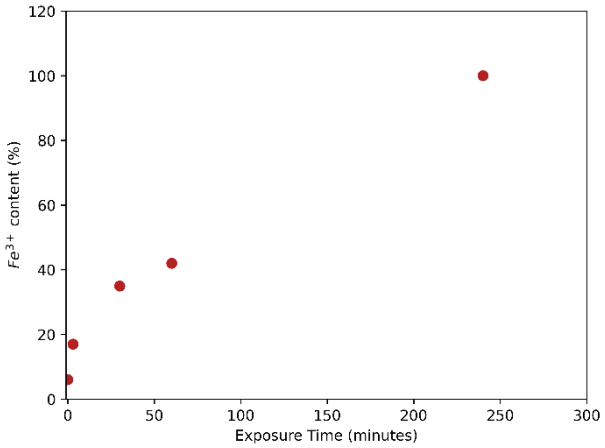

Figure 6.7: The Fe^{3+} content increases with air exposure time.

Disorder around the different Fe^{2+} and/or Fe^{3+} environments can also be investigated using the full width half maximum line width (Γ – mm/s) where Γ between 0.20 – 0.30 mm/s indicates a discrete (ordered) iron environment.[16,28,32] All the synthesised samples show at least some slight disorder around the Fe atom in all the environments (Table 6.7). As expected, the Γ values are much higher for the Fe^{2+} in the M2 site that is more distorted and with an increase in disorder around the Fe octahedral as air exposure time increases. The disorder of Fe^{3+} in the samples are similar to the disorder recorded in literature for a Fe^{3+} environment.[3,16,28] The Fe^{3+} environment is sensitive to the neighbouring atoms as well as the cation distribution and could explain why the disorder is higher for this site.[16,28]

Table 6.7: The full width half maximum line width (Γ – mm/s) value for the different samples.

	Fe(II) – M2	**Fe(II) –M2 distorted**	**Fe(II) –M1**	**Fe(III) –M1**	**Fe(III) – M2/Defects**
Air0	0.36(1)	0.57(2)	0.39(4)	0.45(8)	0.50(9)
Air3min	0.28(1)	0.43(1)	0.60(3)	0.30(1)	0.41(1)
Air30min	0.29(1)	0.60(1)	0.60(3)	0.28(1)	0.60(1)
Air1hr	0.32(1)	0.60(2)	-	0.60(1)	-
Air4hr	-	-	-	0.30(1)	0.54(1)

6.3.3. Raman Spectroscopy

It is expected that Raman spectroscopy will show the presence of any amorphous phases especially in the air exposed samples as well as the possible decrease in crystallinity. Multiple spots were sampled to be able to obtain a good representation of the entire sample. The spectra shown here were of the spot that showed the most crystalline $LiFePO_4$. The quality of the Raman spectra decreases with air exposure time (Figs. 6.8 – 6.12) indicating a decrease in crystallinity. The Raman spectrum of the Air0 sample could be identified as $LiFePO_4$ (Table 6.8) with the peaks corresponding to the translational and rotational motion of Fe^{2+} and PO_4^{3-}, respectively (internal modes) as well as the PO_4^{3-} (υ_2), (υ_4), (υ_1) and (υ_3) modes (external modes).[33] The internal modes could not be identified in the air exposed samples. This disappearance or decrease in the intensity of some of the peaks could indicate a decrease in crystallinity as well as the amount of $LiFePO_4$ present in these samples. In the Air3min, Air30min and Air4hr air exposed samples show the presence of PO_4^{3-} (υ_1) and (υ_3) modes (Table 6.8). These peaks do not necessarily correspond to that of $LiFePO_4$ and could overlap

with other phases. In the Air3min and Air4hr samples the peak at 944 cm^{-1} that are indicated in green in Table 6.8 correspond to a peak in Li_3PO_4.[34] This peak is at wavenumbers that are too low to be $LiFePO_4$. PXRD also detected Li_3PO_4 in the Air3min sample and in the Air4hr sample (Figs. 6.2, Fig. 6.5 and Table 6.3). The peaks at 1019 cm^{-1} and 1049 cm^{-1} in the Air3min and 1021 cm^{-1} in the Air4hr samples indicated in yellow in Table 6.8 correspond to peaks seen in $LiFePO_4(OH)$.[35] No $LiFePO_4(OH)$ was detected using XRD in the Air3min sample indicating that this phase is amorphous but this phase was identified in Air4hr (Table 6.2). The Air3min sample also shows a broad peak at around 1376 cm^{-1} shown in orange in Table 6.8, which can indicate the presence of α-Fe_2O_3[36] although no other peaks corresponding to α-Fe_2O_3 were identified.[14,37] Superparamagnetic hematite (Table 6.5) was identified with Mössbauer spectroscopy in all the samples except for in the Air1hr sample. There is a possibility that amorphous $LiFePO_4$ is present in the 4hour sample which could not be identified using PXRD. The 1hour sample only possesses the peak at 951cm^{-1} (PO_4^{3-} (υ_1) mode). The microscopic images (Figs. 6.8 – 6.12, inset) show the variation in phases that occur due to the exposure to air during synthesis.

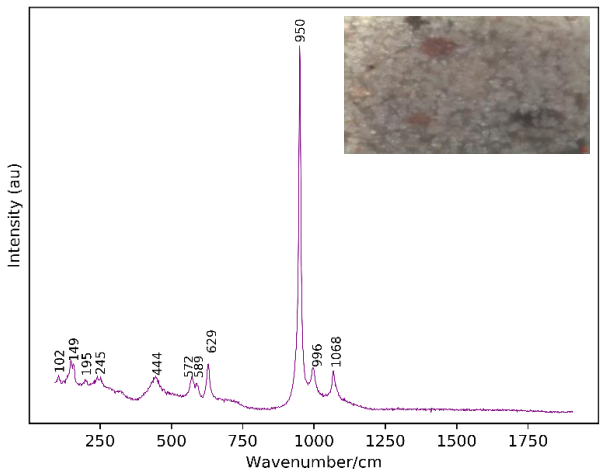

Figure 6.8: Raman spectrum of the Air0 $LiFePO_4$ sample.

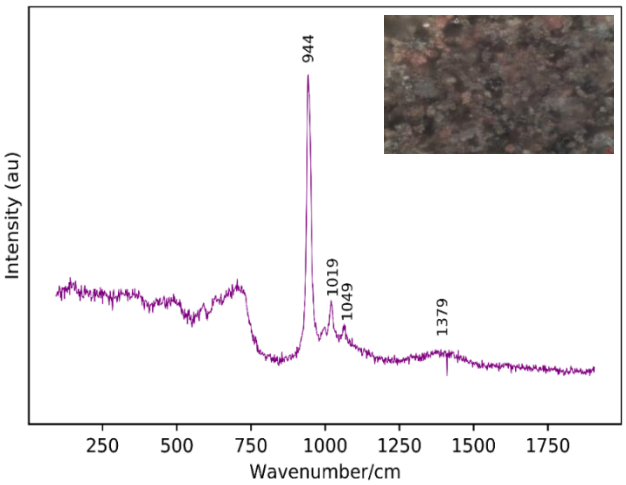

Figure 6.9: Raman spectrum of the Air3min $LiFePO_4$ sample.

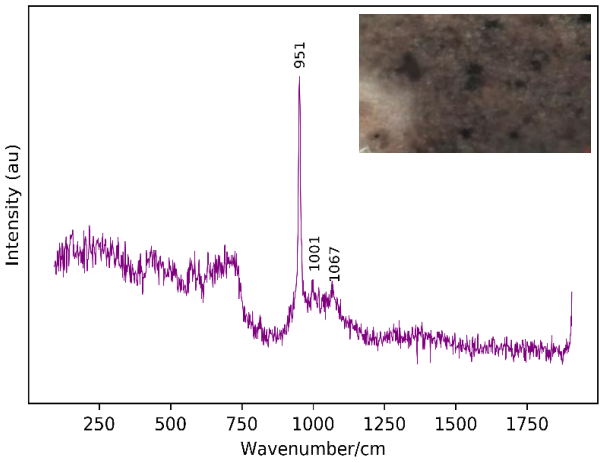

Figure 6.10: Raman spectrum of the Air30min $LiFePO_4$ sample.

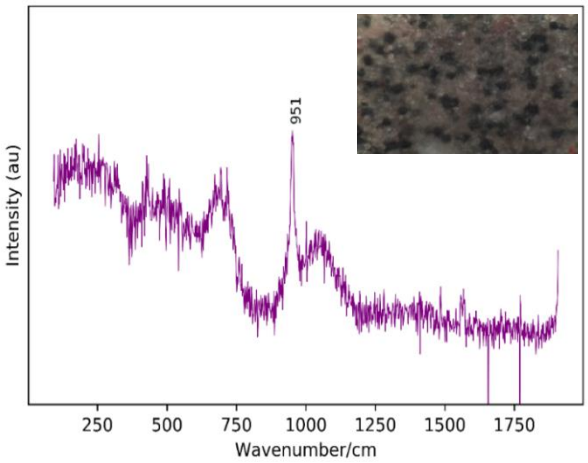

Figure 6.11: Raman spectrum of the Air1hr $LiFePO_4$ sample.

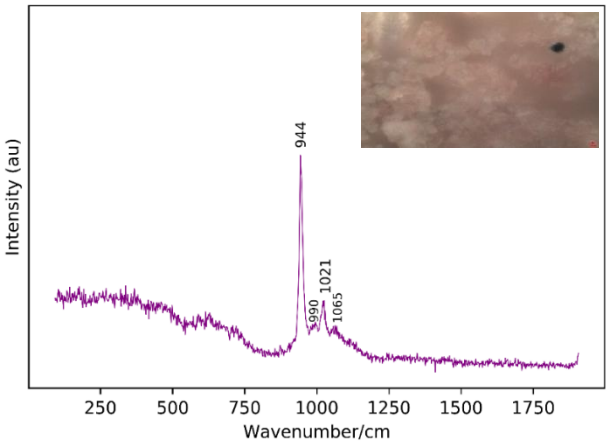

Figure 6.12: Raman spectrum of the Air4hr $LiFePO_4$ sample.

Table 6.8: Raman modes of the different air exposed samples with the assigned vibrational modes.

Air0	Air3min	Air30min	Air1hr	Air4hr	Assignment
102					
149					**Translations of Fe^{2+}, PO_4^{3-} and rotations**
195					
245					
444					**ν_2 (PO_4^{3-} symmetric bending)**
572					
589					**ν_4 (PO_4^{3-} asymmetric bending)**
629					
950	944	951	951	944	**ν_1 (PO_4^{3-} symmetric stretching)**
996		1001		990	
	1019			1021	**ν_3 (PO_4^{3-} asymmetric stretching)**
1068	1049	1067		1065	
	1376				**Fe_2O_3**

6.4. Conclusion

The effect of air exposure during synthesis was investigated by examining the average and local environments. From Rietveld analysis it was concluded that there is a decrease in the percentage of $LiFePO_4$ with air exposure. The percentage of the Fe-containing impurities also increased with time and this could be an effect of oxidation occurring in the sample. Even by purging the sample (Air0) and trying to eliminate oxygen it was seen that the hydrothermal synthetic route has inherent flaws even when synthesising under an inert N_2 environment. From Mössbauer spectroscopy it was determined that the amount of defects in the structure also increased with air exposure and that all the Fe^{2+} was oxidised in the 4hours due to air exposure. It is possible that complete oxidation occurs sooner than 4 hours. Raman spectroscopy indicated that the internal modes could not be identified in the air exposed samples and that crystallinity decreases with an increase in air exposure time. Peaks corresponding to Li_3PO_4, $LiFePO_4(OH)$ and α-Fe_2O_3 were identified in the 3min sample and Li_3PO_4 and $LiFePO_4(OH)$

in the Air4hr sample. In conclusion, exposing the samples to air during synthesis has a detrimental effect on the purity and the integrity of the $LiFePO_4$ structure since an increase in defects and a decrease in crystallinity was observed.

6.5. References

1. Porcher, W., Moreau, P., Lestriez, B., Jouanneau, S. and Guyomard, D. Is $LiFePO_4$ stable in water? *Electrochem. Solid-State Lett.* **11**, A4 (2008).
2. Porcher, W., Moreau, P., Lestriez, B., Jouanneau, S., Le Cras, F. and Guyomard, D. Stability of $LiFePO_4$ in water and consequence on the Li battery behaviour. *Ionics (Kiel).* **14**, 583–587 (2008).
3. Cuisinier, M., Martin, J. F., Dupré, N., Yamada, A., Kanno, R. and Guyomard, D. Moisture driven aging mechanism of $LiFePO_4$ subjected to air exposure. *Electrochem. commun.* **12**, 238–241 (2010).
4. Martin, J. F., Yamada, A., Kobayashi, G., Nishimura, S., Kanno, R., Guyomard, D. and Dupré, N. Air Exposure Effect on $LiFePO_4$. *Electrochem. Solid-State Lett.* **11**, A12 (2008).
5. Amisse, R., Sougrati, M. T., Stievano, L., Davoisne, C., Dražič, G., Budič, B., Dominko, R. and Masquelier, C. Singular Structural and Electrochemical Properties in Highly Defective $LiFePO_4$ Powders. *Chem. Mater.* **27**, 4261–4273 (2015).
6. Yu, D. Y. W., Donoue, K., Kadohata, T., Murata, T., Matsuta, S. and Fujitani, S. Impurities in $LiFePO_4$ and their influence on material characteristics. *J. Electrochem. Soc.* **155**, (2008).
7. Iltchev, N., Chen, Y., Okada, S. and Yamaki, J. $LiFePO_4$ storage at room and elevated temperatures. *J. Power Sources* **119**–**121**, 749–754 (2003).
8. Toby, B. H. R factors in Rietveld analysis: How good is good enough? . *Powder Diffr.* **21**, 67–70 (2006).
9. Yang, S., Zavalij, P. Y. and Stanley Whittingham, M. Hydrothermal synthesis of lithium iron phosphate cathodes. *Electrochem. commun.* **3**, 505–508 (2001).
10. Chen, J., Bai, J., Chen, H. and Graetz, J. In situ hydrothermal synthesis of LiFePO4 studied by synchrotron X-ray diffraction. *J. Phys. Chem. Lett.* **2**, 1874–1878 (2011).
11. Prince, A. A. M., Mylswamy, S., Chan, T. S., Liu, R. S., Hannoyer, B., Jean, M., Shen, C. H., Huang, S. M., Lee, J. F. and Wang, G. X. Investigation of Fe valence in $LiFePO_4$ by Mössbauer and XANES spectroscopic techniques. *Solid State Commun.* **132**, 455–458 (2004).
12. Chen, J., Vacchio, M. J., Wang, S., Chernova, N. Zavalij, P. Y. and Whittingham, M. S. The hydrothermal synthesis and characterization of olivines and related compounds for electrochemical applications. *Solid State Ionics* **178**, 1676–1693 (2008).
13. Kuwahara, A., Suzuki, S. and Miyayama, M. Hydrothermal synthesis of $LiFePO_4$ with small particle size and its electrochemical properties. *J. Electroceramics* **24**, 69–75

(2010).

14. Sun, X. and Xu, Y. Fe excess in hydrothermally synthesized $LiFePO_4$. *Mater. Lett.* **84**, 139 - 142 (2012).

15. Chen, J. and Graetz, J. Study of Antisite Defects in Hydrothermally Prepared $LiFePO_4$ by in Situ X-ray Diffraction. *ACS Appl. Mater. Interfaces* **3**, 1380–1384 (2011).

16. Hamelet, S., Gibot, P., Casas-Cabanas, M., Bonnin, D., Grey, C. P., Cabana, J., Leriche, J. B., Rodriguez-Carvajal, J., Courty, M., Levasseur, S., Carlach, P., Van Thournout, M., Tarascon, J. M. and Masquelier, C. The effects of moderate thermal treatments under air on $LiFePO_4$-based nano powders. *J. Mater. Chem.* **19**, 3979–3991 (2009).

17. Andersson, A. S., Kalska, B., Häggström, L. and Thomas, J. O. Lithium extraction/insertion in $LiFePO_4$: An X-ray diffraction and Moessbauer spectroscopy study. *Solid State Ionics* **130**, 41–52 (2000).

18. Morgan, D., Van der Ven, A. and Ceder, G. Li Conductivity in Li_xMPO_4 (M = Mn, Fe, Co, Ni) Olivine Materials. *Electrochem. Solid-State Lett.* **7**, (2004

19. Liu, J., Jiang, R., Wang, X., Huang, T. and Yu, A. The defect chemistry of $LiFePO_4$ prepared by hydrothermal method at different pH values. *J. Power Sources* **194**, 536–540 (2009).

20. Streltsov, V. A., Belokoneva, E. L., Tsirelson, V. G. and Hansen, N. K. Multipole analysis of the electron density in triphylite, $LiFePO_4$, using X-ray diffraction data. *Acta Crystallogr. Sect. B* **49**, 147–153 (1993).

21. Islam, M. S., Driscoll, D. J., Fisher, C. A. J. and Slater, P. R. Atomic-scale investigation of defects, dopants, and lithium transport in the $LiFePO_4$ olivine-type battery material. *Chem. Mater.* **17**, 5085–5092 (2005).

22. Jugović, D., Cvjetićanin, N., Mitrić, M. and Mentus, S. Comparison between different $LiFePO_4$ synthesis routes. in *Materials Science Forum* vol. 555 225–230 (2007).

23. Gibot, P., Casas-Cabanas, M., Laffont, L., Levasseur, S., Carlach, P., Hamelet, S., Tarascon, J. M. and Masquelier, Christian. Room-temperature single-phase Li-insertion/extraction in nanoscale Li_xFePO_4. *Nat. Mater.* **7**, 741–747 (2008).

24. Shu, H., Wang, X., Wu, Q., Hu, B., Yang, X., Wei, Q., Liang, Q., Bai, Y., Zhou, M., Wu, C., Chen, M., Wang, A. and Jiang, L. Improved electrochemical performance of $LiFePO_4$/C cathode via Ni and Mn co-doping for lithium-ion batteries. *J. Power Sources* **237**, 149–155 (2013).

25. Gao, H., Jiao, L., Yang, J., Qi, Z., Wang, Y. and Yuan, H. High rate capability of Co-doped LiFePO4/C. Electrochim. Acta **97**, 143–149 (2013).

26. Lu, Y., Shi, J., Guo, Z., Tong, Q., Huang, W. and Li, B. Synthesis of $LiFe_{1-x}Ni_xPO_4$/C composites and their electrochemical performance. *J. Power Sources* **194**, 786–793 (2009).

27. Yamada, A., Chung, S. C. and Hinokuma, K. Optimized $LiFePO_4$ for Lithium Battery Cathodes. *J. Electrochem. Soc.* **148**, A224 (2001).

28. Maccario, M., Croguennec, L., Wattiaux, A., Suard, E..,Le Cras, F. and Delmas, C. C-containing $LiFePO_4$ materials - Part I: Mechano-chemical synthesis and structural

characterization. *Solid State Ionics* **179**, 2020–2026 (2008).

29. Li, Z. and Shinno, I. Next nearest neighbor effects in triphylite and related phosphate minerals. *Mineral. J.* **19**, 99–107 (1997).

30. Xia, X., Wang, Z. and Chen, L. Regeneration and characterization of air-oxidized $LiFePO_4$. *Electrochem. commun.* **10**, 1442–1444 (2008).

31. Sánchez, L. C., Arboleda, J. D., Saragovi, C., Zysler, R. D. and Barrero, C. A. Magnetic and structural properties of pure hematite submitted to mechanical milling in air and ethanol. *Phys. B Condens. Matter* **389**, 145–149 (2007).

32. Cuisinier, M., Martin, J. F., Dupré, N., Kanno, R. and Guyomard, D. Elucidating the $LiFePO_4$ air aging mechanism to predict its electrochemical performance. *J. Mater. Chem.* **21**, 18575–18583 (2011).

33. Burba, C. M. and Frech, R. Raman and FTIR Spectroscopic Study of Li_xFePO_4 ($0 \leq x \leq 1$). *J. Electrochem. Soc.* **151**, A1032 (2004).

34. Popovic, L., Manoun, B., de Waal, D., Nieuwoudt, M. K. and Comins, J. D. Raman spectroscopic study of phase transitions in Li_3PO_4. *J. Raman Spectrosc.* **34**, 77–83 (2003).

35. Marx, N., Croguennec, L., Carlier, D., Bourgeois, L., Kubiak, P., Le Cras, F. and Delmas, C. Structural and electrochemical study of a new crystalline hydrated iron(iii) phosphate $FePO_4 \cdot H_2O$ obtained from $LiFePO_4(OH)$ by ion exchange. *Chem. Mater.* **22**, 1854–1861 (2010).

36. de Faria, D. L. A. and Lopes, F. N. Heated goethite and natural hematite: Can Raman spectroscopy be used to differentiate them? *Vib. Spectrosc.* **45**, 117–121 (2007).

37. Dokko, K., Shiraishi, K. and Kanamura, K. Identification of Surface Impurities on $LiFePO_4$ Particles Prepared by a Hydrothermal Process. *J. Electrochem. Soc.* **152**, A2199 (2005).

Chapter 7

Doping with Zn^{2+} using a low cost and low energy synthetic route

7.1. Introduction

Doping has been shown to improve drawbacks like poor ionic and electronic conductivity as well as stabilizing the $LiFePO_4$ structure.[1–4] Stabilization is an important feature that prevents the lattice from collapsing during and de-intercalation process.[2,5] The orthorhombic structure of $LiFePO_4$ consists of the two energetically distinguishable M1 (Li^+) and M2 (Fe^{2+}) octahedra and one phosphorous tetrahedra.[6,7] Doping can occur either on the M1, M2 for cationic dopants or the oxygen site in PO_4^{3-} for anionic dopants. A summary of the different dopants used in the different $LiFePO_4$ sites can be found Table 1.1. Doping on the M1 site could cause a blockage in the diffusion channel[8] but doping on the M2 site could stabilize the structure as well as enhance the electrochemical performance.[2, 5,9] Isovalent cations (M^{2+}) would easily replace and occupy the M2 site.[10]

Doping with zinc (Zn^{2+}) on this site using different concentrations has been investigated by several groups. Yiming *et al*.[11] investigated the doping effect over the range $0 \leq x \leq 0.26$ on $LiFe_{1-x}Zn_xPO_4$. The samples were synthesised using a wet chemistry method followed by thermal treatment in a reducing atmosphere. Samples that showed increased capacity and reduced electrode polarization when x = 0.01, 0.03 and 0.1. Zhao *et al*.[12] used a solid state synthetic route to synthesise $LiFe_{1-x}Zn_xPO_4$ over the range ($x \leq 1.0$). The lower Zn^{2+} (x = 0.1, 0.2, 0.3) concentration gave a single-phased $LiFePO_4$ product and the $LiFe_{0.7}Zn_{0.3}PO_4$ sample showed improved conductivity. The doping concentration range of $LiFe_{1-x}Zn_xPO_4$ where x = 0.02, 0.05 and 0.07 was synthesised using a microwave-assisted liquid phase route and was investigated by Bilecka *et al*.[13] These authors found that the $LiFe_{0.98}Zn_{0.02}PO_4$ sample showed improved rate capability. Shenouda *et al*.[5] doped in the range x = 0.015, 0.025 and 0.05 using ZnO as the Zn^{2+} precursor. The samples were ball-milled under an argon atmosphere. It was determined that the $LiFe_{0.975}Zn_{0.025}PO_4$ sample was the optimum concentration that enhanced the conductivity and improved the structure stability.

This chapter focuses on the possibility of doping with Zn^{2+} using a low energy, low cost hydrothermal synthesis in Teflon bombs and to study the effect this has on the structure of $LiFePO_4$. The average and local structure of $LiFePO_4$ and $LiFe_{1-x}Zn_xPO_4$ (x = 0.01, 0.025 and 0.03) was thus fully investigated using synchrotron powder X-ray diffraction with Rietveld

analysis, Raman spectroscopy (average structure) and X-ray absorption spectroscopy using both XANES and EXAFS (local structure).

7.2. Sample preparation

A molar ratio of $3_{Li}: 1 - x_{\mathrm{Fe}}: x_{Zn}: 1_{PO_4}$ was used for the doped samples. The methodology described in section 5.2 was used to synthesise these samples. The precursor used as the dopant was $Zn(NO_3)_2 \bullet 6H_2O$ (98%, Sigma Aldrich). The dopant was dissolved in unpurged deionised water before the commencement of the experiment but the other precursors (LiOH, $FeSO_4 \bullet 7H_2O$ and H_3PO_4) were dissolved with purged water. The Zn^{2+}-solution was added to the purged $FeSO_4/H_3PO_4$ solution and the LiOH was then added dropwise (one Li^+ drop every 3 seconds). The bombs were filled to 25% and placed in the oven at 120 °C for 48 hours.

7.3. Results and discussion

7.3.1. Powder X-ray diffraction

Rietveld refinement analysis was performed on the XRD data obtained to determine the average structure of $LiFePO_4$ and the Zn-doped $LiFePO_4$ samples. Zn-doped ($LiFe_{1-x}Zn_xPO_4$) samples were abbreviated according to the doping concentration: 1Zn, 2.5Zn and 3Zn for x = 0.01, 0.025 and 0.03, respectively. X-ray wavelength of 0.166316(1) Å was used for all the refinements with the results shown in Figures 7.1 – 7.4 and the Rietveld error indices in Table 7.1. $LiFePO_4$ was identified as the main phase in all samples and indexed as the orthorhombic crystal system *Pnma* (#62). Two other minor impurity phases (~6 %) were identified in the samples, namely, lithiophosphate (Li_3PO_4) and the Fe-impurity ($I4_1/a$, #88) (Table 7.2). This impurity was also identified in sections 4.2.1 – 4.2.5. None of the impure phases contain the dopant and it can be assumed that Zn^{2+} was incorporated into the $LiFePO_4$ structure. It was also assumed that the Zn^{2+} prefers the M2 site in $LiFePO_4$ and that the Zn^{2+} was successfully incorporated into the structure during the refinement process by keeping the occupancy of the M2 site fixed. The assumption was made based on three reasons: 1) M^{2+} cations such as Zn^{2+} prefer the M2 site,[10] (2) due to the similar scattering factors for Fe^{2+} and Zn^{2+} these atoms and not distinguishable by PXRD[11] and (3) because of the extremely low doping percentages refining the doping site lead to high occupancy errors. The high errors and occupancy values were also seen for Fe on the M2 site.

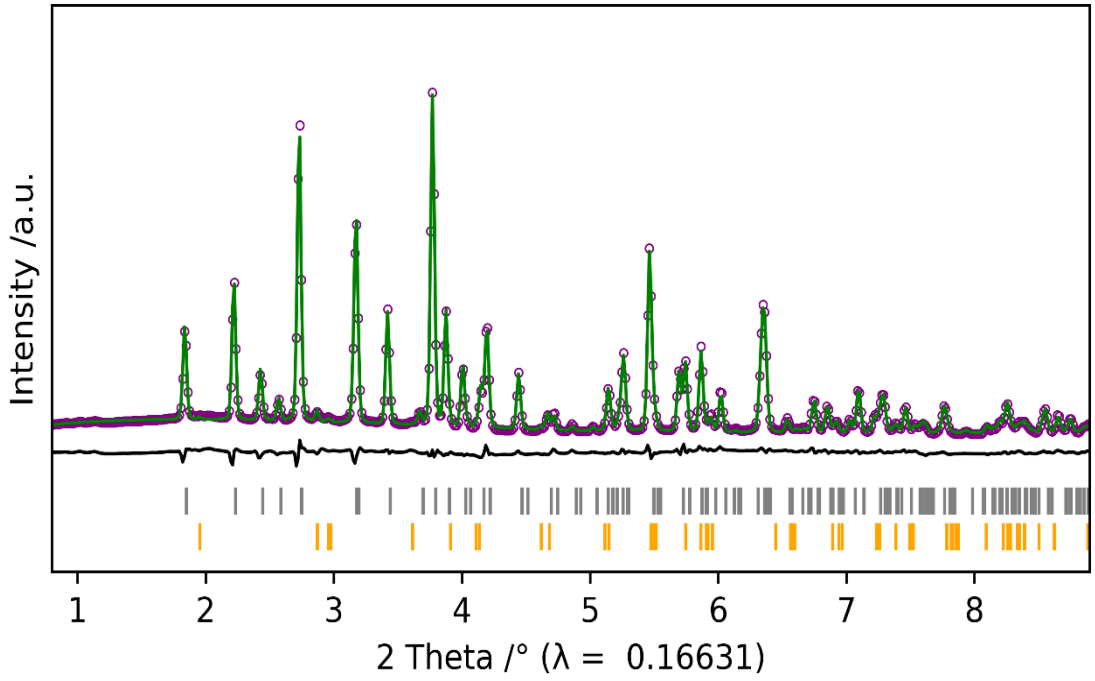

Figure 7.1: Synchrotron diffractogram of $LiFePO_4$ showing the observed (purple), calculated (green) and difference (black) plots generated from a Rietveld refinement analysis. Bragg reflections for $LiFePO_4$ and the Fe-impurity are indicated with the grey and yellow markers.

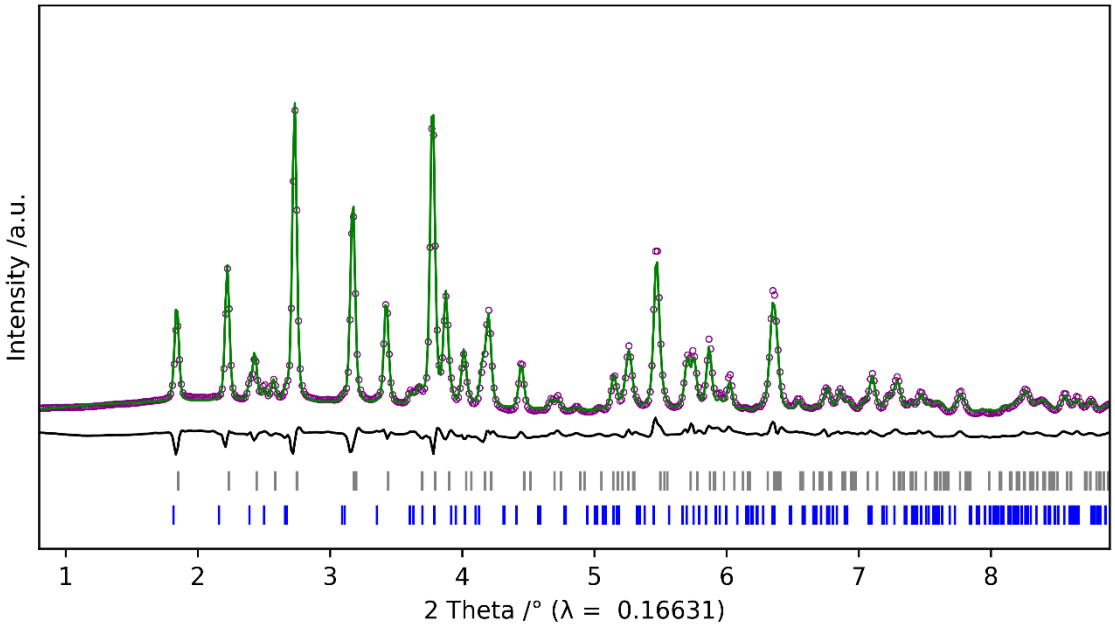

Figure 7.2: Synchrotron diffractogram of the 1Zn $LiFePO_4$ sample showing the observed (purple), calculated (green) and difference (black) plots generated from a Rietveld refinement analysis. Bragg reflections for $LiFePO_4$ and Li_3PO_4 are indicated with the grey markers and blue markers.

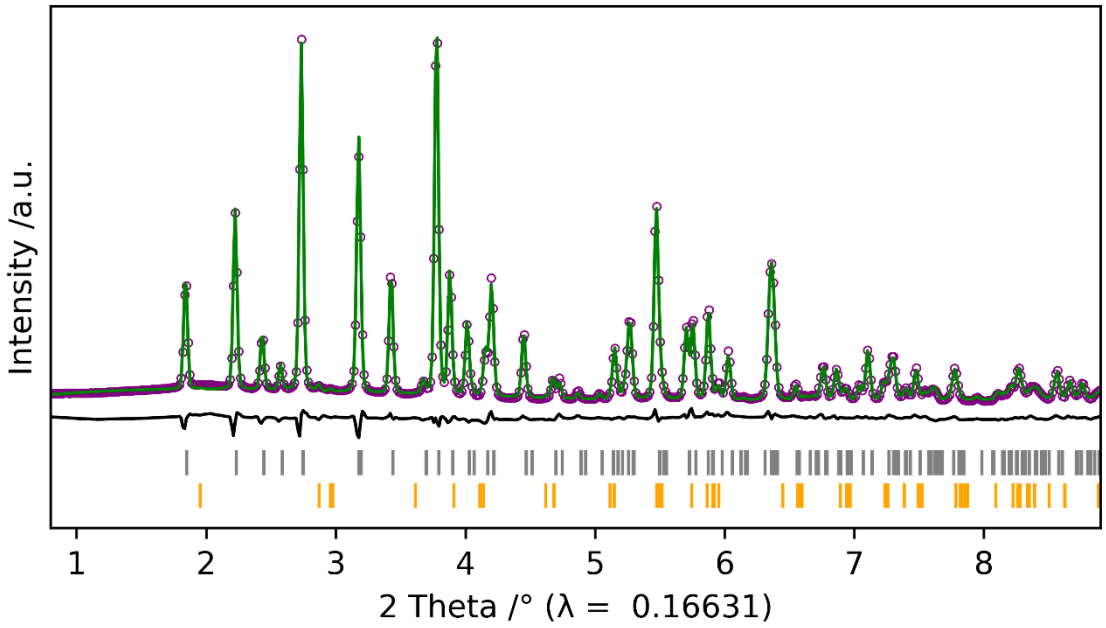

Figure 7.3: Synchrotron diffractogram of the 2.5Zn $LiFePO_4$ sample showing the observed (purple), calculated (green) and difference (black) plots generated from a Rietveld refinement analysis. Bragg reflections for $LiFePO_4$ and the Fe-impurity are indicated with the grey markers and blue markers.

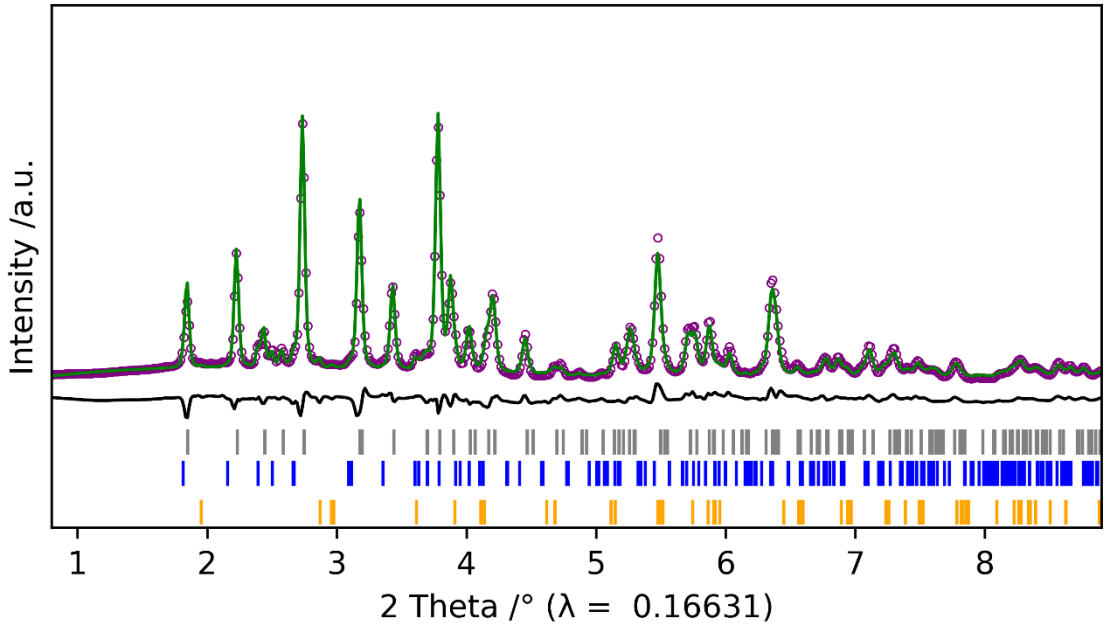

Figure 7.4: Synchrotron diffractogram of the 3Zn $LiFePO_4$ sample showing the observed (purple), calculated (green) and difference (black) plots generated from a Rietveld refinement analysis. Bragg reflections for $LiFePO_4$, Li_3PO_4 and the Fe-impurity are indicated with the grey, blue and yellow markers respectively.

Table 7.1: Reliability factors for each Rietveld refinement.

	R_{wp}	R_p	R_{exp}	GOF
$LiFePO_4$	5.06	3.94	16.92	0.30
1Zn	6.50	5.27	15.56	0.42
2.5Zn	5.29	4.14	16.14	0.33
3Zn	6.76	5.39	15.19	0.44

Table 7.2: Multiphase analysis (%) of the undoped $LiFePO_4$ and doped samples.

	$LiFePO_4$	**Fe-impurity**	**Li_3PO_4**
$LiFePO_4$	98.65	1.35	-
1Zn	95.90	-	4.10
2.5Zn	99.32	0.68	-
3Zn	93.99	0.82	5.19

There is a disagreement in literature as to the effect that Zn^{2+} doping has on the lattice parameters and volume of the unit cell for $LiFePO_4$. Shenouda *et al.*[5] and Liu *et al.*[2] showed that the lattice parameters increase with Zn^{2+} concentration, whereas Yiming *et al.*[11], Baster *et al.*[15] and Zhao *et al.*[12] showed that the lattice parameters decrease with Zn^{2+} concentration, as was found in this study. In the study conducted by Yiming *et al.*[11], the a-lattice and b-lattice constants showed a decrease of 10.329 – 10.313 Å and 6.007 – 6.005 Å, respectively and the c-lattice constant remained constant at ~ 4.695Å over the concentration range of 0 – 5%. The doping study conducted by Zhao *et al.*[12] over the same concentration range found that the a-lattice and b-lattice parameters also decreased from 10.321 – 10.272 Å and 6.002 – 5.983 Å, respectively but in this case the c-lattice constant increased slightly (4.688 – 4.694 Å) with doping concentrations. The refined lattice parameters and the volume for the undoped and Zn-doped samples can be found in Table 7.3. The lattice parameters for the doped samples are only slightly smaller than of the undoped $LiFePO_4$, except for the 1Zn b-lattice constant. This can suggest successful incorporation of Zn^{2+} into the $LiFePO_4$ lattice. Zn^{2+} has a slightly smaller ionic radius (0.74Å) compared to that of high spin Fe^{2+} (0.78Å) in an octahedral environment[15] and explains this decrease. The c-lattice constant shows a slight decrease which can possibly be an effect of the impurities present as seen in section 6.3.1 where the lattice parameters decreased.

Table 7.3: Lattice parameters and volume of the $LiFePO_4$ phase for the undoped and Zn-doped $LiFePO_4$ samples.

	x	a (Å)	b (Å)	c (Å)	Volume (Å^3)
$LiFePO_4$	0	10.367(5)	6.0029(3)	4.7132(2)	293.31(2)
1Zn	0.01	10.347(9)	6.0035(5)	4.7067(4)	292.37(4)
2.5Zn	0.025	10.345(4)	5.9964(3)	4.7063(2)	291.96(2)
3Zn	0.03	10.331(2)	5.9979(6)	4.7024(5)	291.37(6)

The a-lattice constant for 3Zn is not as constant as that for the 1Zn and 3Zn sample as would be expected when doping (Table 7.3).[11] This deviation could be an effect of the impurities present as the 3Zn sample had the highest percentage of impurities present. The shortening of the b-lattice constant showed a shortening of the Li^+ diffusion pathway and could lead to improved Li^+ mobility.[16,17] The 2.5Zn sample exhibited the smallest b-lattice constant and could possibly exhibit the best electrochemical performance based purely in the results of the lattice constants. The unit cell volume for the undoped $LiFePO_4$ is larger than the volume in previous sections. This sample could contain more defects or additional amorphous phases that were not detected using XRD. The unit cell volume for the doped samples are smaller than that determined for the undoped $LiFePO_4$ and decreases linearly with Zn^{2+} concentration (Fig. 7.5), thus obeying Vergard's law similar to the findings in the doping study conducted by Yiming *et al.*[11]

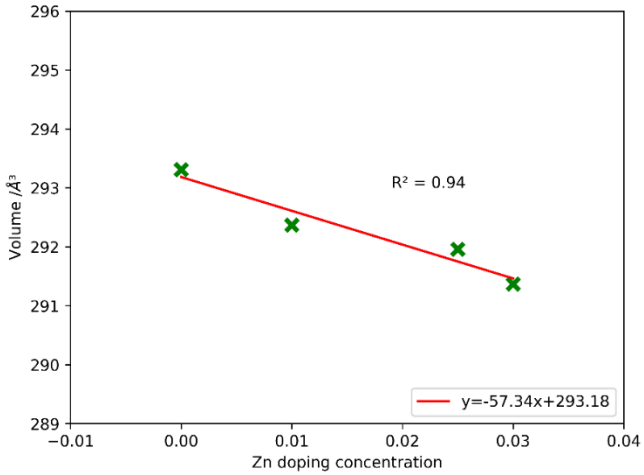

Figure 7.5: Variation in the volume as a function of Zn^{2+} concentration in terms of x:$LiFe_{1-x}Zn_xPO_4$.

One of the problems that could arise during de-intercalation is the possibility that the $LiFePO_4$ structure could collapse. The collapse is caused by the change in ionic radii when changing

from Fe^{2+} (0.78Å) to Fe^{3+} (0.65Å).[2] This would clearly affect the Li^+ diffusion and effect the reproducibility of the battery as re-intercalation of Li^+ into the structure would become more difficult.[5] Inserting Zn^{2+} (0.74 Å), with a radius closer to that of Fe^{2+}, that remains unchanged during de-intercalation into the structure should stabilize the structure to some extent[2,5] and is larger than Fe^{3+}.

The occupancy on the M2 site was kept fixed throughout the refinement but the synthesised samples showed the presence of antisite defects on the M1 site (Table 7.4). The high Fe content on the M1 site could possibly be due an excess of Fe in the structure from amorphous impurities or the Fe-impurity. The 1Zn and 3Zn sample had the highest percentage of $Fe^{2+}$and or Fe^{3+} on the M1 site. The 2.5Zn samples had the lowest percentage of defects present on the M1 site. This sample also had the lowest percentage impurities present (Table 7.2).

Table 7.4: Occupancy of Fe^{2+} on the M2 and Li and Fe^{2+}/Fe^{3+} on the M1 sites.

	M2 site	**M1 (Li^+) site**	**M1 (Fe^{2+}/Fe^{3+}) site**
$LiFePO_4$	99.14(7)	92.07(4)	7.93(34)
1Zn	99	89.97(9)	10.07(8)
2.5Zn	97.5	94.64(4)	5.36(36)
3Zn	97	90.11(11)	9.89(1)

The average interatomic bond distances of M2-O (Fe/Zn-O), P-O and M1-O also gave information regarding the effect of doping on the structure. The refined interatomic bond distances for Fe-O and Zn-O were the same. The individual and average bond distances can be found in Table 7.5. The incorporation of Zn^{2+} into the structure caused widening of the Li^+ diffusion channels by lengthening the average M1-O interatomic bond distances. Widening of the diffusion channels allow for easier intercalation and de-intercalation.[10,17–19] The lengthening of the M1-O interatomic bond distances compared to that of the undoped $LiFePO_4$ (2.132 Å) can be seen for all the doped samples (2.157 – 2.167 Å). The interatomic distances for a similar study, where the Zn^{2+}-doping for concentrations between 1 – 30%, was 2.136 – 2.147 Å.[11] The shortening of the M2-O and P-O average interatomic bond distances could be used to predict the structure stabilization due to doping.[10,19,20] 1Zn and 3Zn shows the highest degree of shortening of the M2-O interatomic bond distance. The 2.5Zn sample shows shortening of the average P-O interatomic bond distances. The P-O interatomic bond distances were similar to the reported values (1.500 – 1.530 Å) but the M2-O interatomic bond distances

were shorter (2.168 – 2.170 Å). This difference could be an effect of Fe^{3+} occupying the M2 site causing a shortening in the interatomic bond distances.[22] The shrinking of the FeO_6 octahedra leads to the expansion of the LiO_6 and this could also explain why the M1-O interatomic bond distances is longer than the reported ones.[23] To determine whether diffusion was improved a cell has to be assembled and tested.

Table 7.5: The individual and average interatomic bond distances (Å) of M2-O, P-O and M1-O.

	$LiFePO_4$	**1Zn**	**2.5Zn**	**3Zn**
M2 – O(1)	2.177	2.159	2.179	2.148
M2 – O(2)	2.069	2.043	2.068	2.024
M2 – O(3) (×2)	2.044	2.038	2.044	2.025
M2– O(3) (×2)	2.228	2.231	2.231	2.233
Average M2–O	**2.132**	**2.124**	**2.133**	**2.115**
P – O(1)	1.550	1.547	1.540	1.540
P – O(2)	1.629	1.649	1.617	1.660
P – O(3) (×2)	1.602	1.609	1.595	1.620
Average P – O	**1.600**	**1.604**	**1.587**	**1.610**
M1 – O(1) (×2)	2.184	2.181	2.180	2.182
M1 – O(2) (×2)	2.010	2.106	2.093	2.113
M1 – O(3) (×2)	2.202	2.204	2.197	2.205
Average M1– O	**2.132**	**2.164**	**2.157**	**2.167**

7.3.2. Raman Spectroscopy

Raman analysis was performed on the undoped, 1Zn, 2.5Zn and 3Zn $LiFePO_4$ samples (Fig. 7.6). The $LiFePO_4$ vibrational modes[24–26] were identified and assigned for all the samples (Table 7.6). A summary of these modes, used for comparison, can be found in Table 3.5. The lower wavenumber or fingerprint region is slightly more challenging to assign as these peaks are not well defined and can disappear if data consists of an excess of noise, and as such not much information could be extracted from this region.[27] The peak due to symmetric stretching of P-O (Fig. 7.6, inset) at around ~950 cm^{-1} can be used to determine if there is an increase or

decrease in the degree of ordering in the structure due to doping.[27,28] This can be investigated by determining the full width at half maximum (FWHM) of this peak. The FWHM was 7.92, 7.89, 7.53 and 7.09 cm^{-1} for the undoped, 1Zn, 2.5Zn and 3Zn samples, respectively. This indicates that there was in increase in ordering for the doped samples compared to that of the undoped sample.

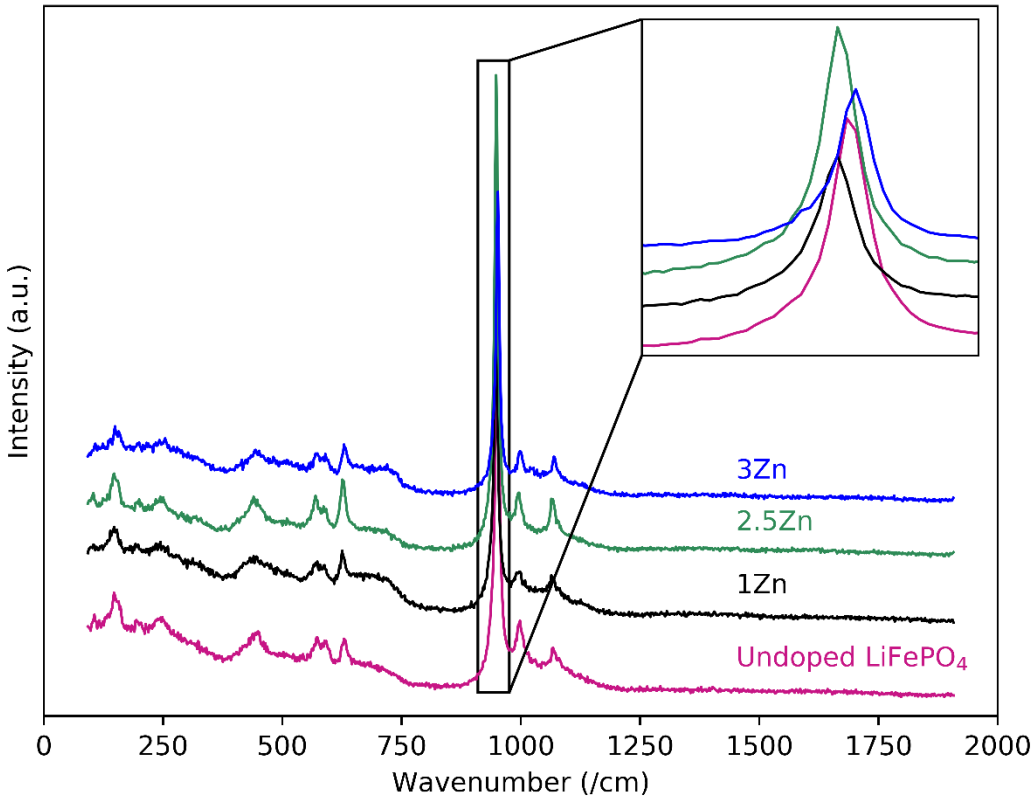

Figure 7.6: Raman spectra for the undoped and Zn-doped $LiFePO_4$ samples. The peaks due to symmetric stretching of PO_4^{3-} vibrational mode at ~950 cm^{-1} (910 – 976 cm^{-1}) is given in the inset.

The shift in peak position of the symmetric stretching of the PO_4^{3-} tetrahedra can be used to assess any changes in the P-O interatomic bond distance (Table 7.6). A blue shift in wavenumber (higher wavenumber) indicates a shortening of this bond distance[29,30] whereas the red shift in wavenumber (lower wavenumber) indicates an increase in this bond distance.[29,30] The undoped and the 3Zn sample showed an increase in the stability of the structure caused by the shortening of the P-O bond distance.[10,19,20] This was different than the distances determined using PXRD (Table 7.5)

Table 7.6: Raman modes of the undoped and Zn^{2+} doped $LiFePO_4$ samples showing the assigned vibrational modes.

Wavenumbers (/cm)				Assignment
Undoped $LiFePO_4$	**1Zn**	**2.5Zn**	**3Zn**	
103	95	95	106	PO_4^{3-} rotational and Fe^{2+} translational motion
150	147	149	153	
197	192	197	197	
243	244	244	253	
446	453	441	443	υ_2 (PO_4^{3-})
572	569	569	572	υ_4 (PO_4^{3-})
591	586	589	592	
630	627	628	631	
950	948	948	951	υ_1 (PO_4^{3-})
998	995	995	998	υ_3 (PO_4^{3-})
1068	1066	1067	1070	

Raman spectroscopy can also be used to determine if any impurities are present that were undetectable using XRD. The Raman microscopic images (Image 7.1) showed that three different distinguishable phases, were present in the samples. The majority of the shiny white coloured phase was identified as $LiFePO_4$. The phase tavorite, $LiFePO_4(OH)$[31] (black phase), was present in the undoped sample whereas the 1Zn sample had α-Fe_2O_3[32] (reddish/brown phase) as well as Li_3PO_4[33] (shiny white phase) present. No $LiFePO_4(OH)$ and α-Fe_2O_3 was identified using XRD. The 2.5Zn had poorly crystalline $LiFePO_4(OH)$ (black phase) present and the 3Zn sample contained traces of possibly α-Fe_2O_3 (reddish/brown phase) and a poorly crystalline or low concentration unidentified impurity (reddish/white phase) with sharp peaks at 951 cm^{-1} and 971 cm^{-1}.

.

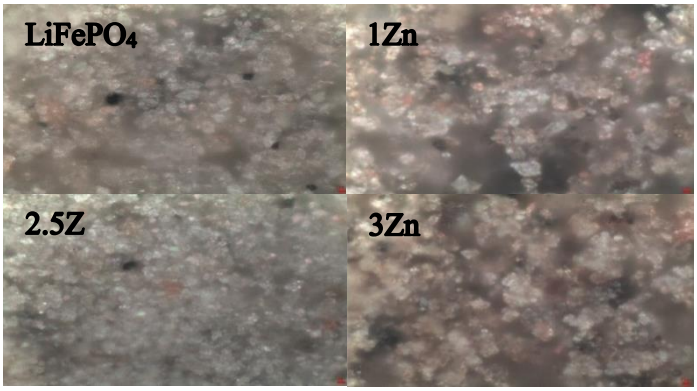

Image 7.1: Raman microscopic images of the undoped and Zn-doped $LiFePO_4$ samples

7.3.3. X-ray absorption spectroscopy (XAS)

The normalized Fe K-edge spectra (Fig. 7.7) for all the Zn-doped samples have the same general shape to that of the $LiFePO_4$ standard.

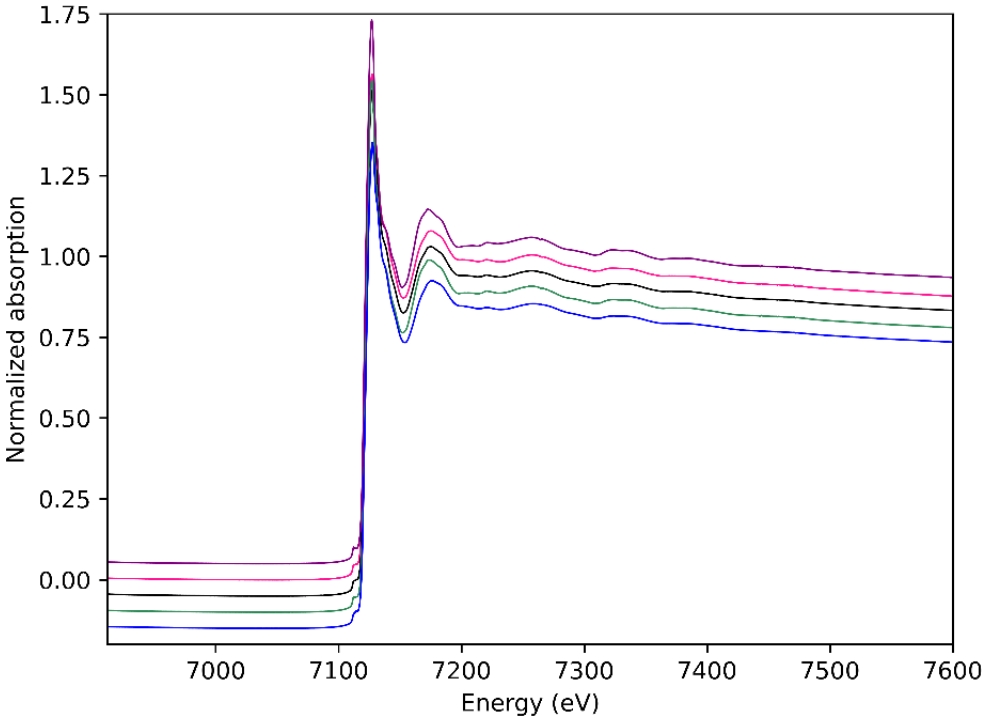

Figure 7.7: Normalized Fe K-edge spectra for the different Zn-doped samples (pink – undoped, black – 1Zn, green – 2.5Zn and blue – 3Zn) compared to that of the $LiFePO_4$ standard (purple).

(i) XANES:

The pre-edge region can be used to assess any changes in the Fe oxidation state upon doping as well as the changes around the Fe environment by comparing peak positions and intensities. The same three standards were used to visually compare the pre-edge region. As a reminder, the $LiFePO_4$ standard has Fe^{2+} in a slightly distorted octahedral environment and shows two

small peaks around 7112 eV (t_{2g}) and 7115 eV (e_g).[34,35] $FePO_4•4H_2O$ contains Fe^{3+} in an octahedral environment with similar distortion as seen by similar intensities on Figure 7.8.[34–36] α-Fe_2O_3 has Fe^{3+} in a more distorted octahedral environment indicated by the increase in intensity (Fig. 7.8).[35,37] A more detailed description of the pre-edge features and the different features of the standards can be found in section 2.2.3.1.

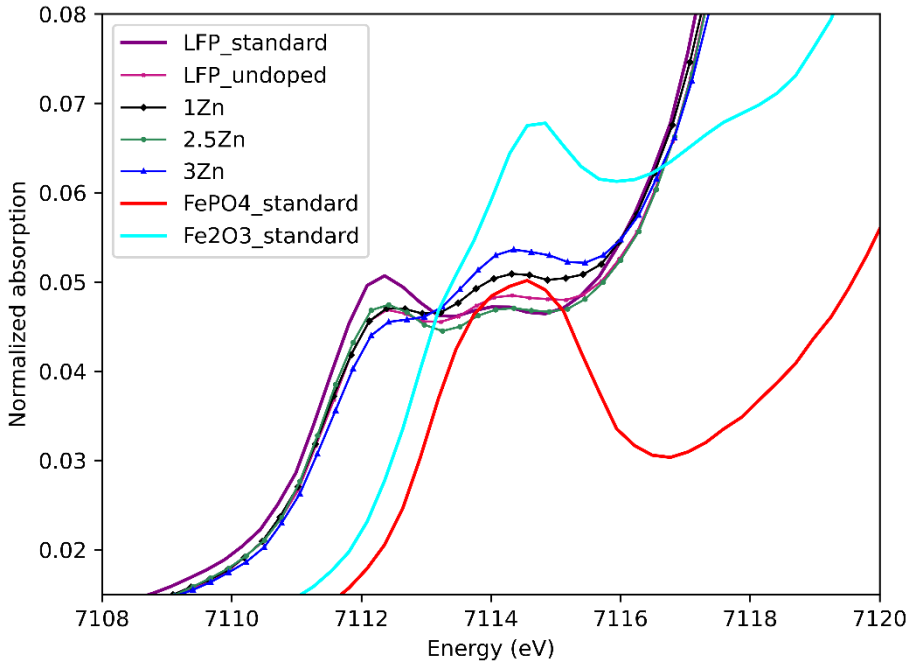

Figure 7.8: Comparison Fe K-edge XANES pre-edge region of the different standards, and the undoped and Zn-doped $LiFePO_4$ samples.

Table 7.7: The different pre-edge peak intensities and peak positions for the undoped and Zn-doped $LiFePO_4$ samples.

Sample	Peak position 1 (eV)	Peak intensity 1 (au)	Peak position 2 (eV)	Peak intensity 2 (au)	Peak 2 broadness (eV)
$LiFePO_4$	7112.19	0.050	7114.09	0.048	0.880
$FePO_4$	-	-	7114.27	0.050	-
Fe_2O_3	-	-	7114.43	0.067	-
Undoped	7112.21	0.048	7114.07	0.050	0.909
1Zn	7112.13	0.048	7113.92	0.052	1.08
2.5Zn	7113.08	0.049	7114.10	0.048	0.930
3Zn	7112.07	0.045	7114.03	0.055	1.28

All the undoped and Zn-doped samples showed both the peaks present in the $LiFePO_4$ samples with similar peak positions for the synthesised samples but a difference in peak intensities for both peaks (Fig. 7.8 and Table 7.7). The peak at ~7112 eV (t_{2g} peak) for all the synthesised samples shows a decrease in intensity compared to that of the $LiFePO_4$ standard (Fig. 7.8). This decrease in intensity could indicate a decrease in Fe^{2+} concentration.[38] This corroborates the XRD results that showed that the 2.5Zn had the lowest percentage of impurities (Table 7.2) as well as the least amount of M1 site defects (Table 7.4). The 3Zn would have the least amount of Fe^{2+} looking at the largest drop in intensity. This was also seen by the shortest Fe-O interatomic distance (Table 7.5) determined by XRD possibly indicating the presence of more Fe^{3+} in the sample. The second peak at ~7114 eV, that corresponds to the e_g peak, shows the slightly lower intensity peak of $LiFePO_4$ as well as the Fe^{3+} peaks of $FePO_4 \bullet 4H_2O$ and α-Fe_2O_3. This peak shows an increase in intensity as well as peak broadening (Table 7.7) for all the samples compared to the $LiFePO_4$ standard. The 2.5Zn sample shows very similar intensities to that of the $LiFePO_4$ peak. The undoped, 1Zn and 3Zn samples show an increase in the peak intensities, respectively. This increase in intensity could indicate an increase in Fe^{3+} concentration or possibly an increase in distortion around the Fe^{3+} environment present in the samples.[39] The distortion could be similar to that of Fe^{3+} in α-Fe_2O_3 but not as extreme. The peak broadening indicates larger energies for the synthesised samples[34] and because this peak is related to the interaction of the orbitals in the direction of the oxygen atoms and their repulsive field[40] – this could indicate changes in the bonding environments. The linear combination fitting analysis can be used to further determine the amount of Fe^{2+} and Fe^{3+} in the samples, as will be discussed below.

The rising and main absorption edges can also be used to assess any changes in the oxidation state[35,41,42] and the possible increase in disorder[42] (Fig. 7.9 and Table 7.8). The shift slightly to higher energies for the rising absorption edge indicates that some of the Fe^{2+} has been oxidised in the synthesised samples compared to that of the $LiFePO_4$ standard. The 2.5Zn sample would have the highest percentage of Fe^{2+} present as indicated by the pre-edge region and the XRD analysis. The undoped $LiFePO_4$ and the 1Zn sample overlap and would have similar amounts of Fe^{3+}, whereas the 3Zn would have the most Fe^{3+} present. There is only a slight shift to higher energies for the main absorption edge suggesting that some of the Fe^{2+} has been oxidised to Fe^{3+}. The shift is not as severe compared to the Fe^{3+} standards (Table 7.8) indicating that not all the Fe^{2+} has been oxidised to Fe^{3+}. The drop in intensity could indicate an increase in disorder.[42] Using this method of prediction it can be seen on Figure 7.9 that all the synthesised

samples would possibly exhibit an increase in the disorder of the Fe-environment. The 2.5Zn sample would have the least disorder and the 3Zn the highest degree of disorder. The undoped $LiFePO_4$ and the 1Zn still overlap in Figure 7.9 and should have a similar degree of disorder. The amount of Fe^{2+} and/or Fe^{3+} present in the sample can be quantitatively looked at using LCF and the degree of disorder can only be quantified when looking at the local structure using EXAFS.

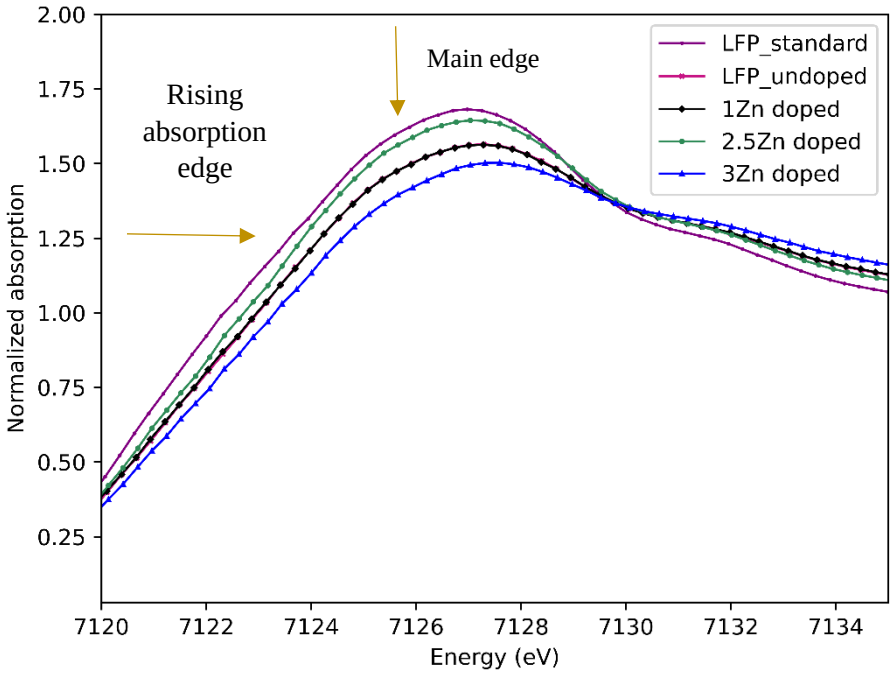

Figure 7.9: Comparison of the $LiFePO_4$ standard with the different undoped and Zn-doped $LiFePO_4$ samples.

Table 7.8: The different main edge peak intensities and peak positions for the undoped and Zn-doped $LiFePO_4$ samples.

Sample	Peak position (eV)	Peak intensity (au)
$LiFePO_4$	7126.97	1.68
$FePO_4$ (not indicated)	7131.92	1.54
Fe_2O_3 (not indicated)	7133.75	1.53
Undoped	7127.26	1.56
1Zn	7127.28	1.56
2.5Zn	7127.08	1.64
3Zn	7217.48	1.50

Linear combination fitting (LCF):

The same three standards were used for LCF and the results are shown in Figures. 7.10 – 7.13. All three standards have slightly different octahedral bonding characteristics. The differences in oxidation state and the degree of distortion would be able to give more information about the different environments in the synthesised samples, although this phase might not be present in the sample. LCF was performed over the energy range of 7102 – 7152 eV, the weights of the components were summed to 1 and no overall E_o shift was allowed. All the combinations of the different standards were fitted and the combinations that gave positive weights for each standard as well as small errors for each component were used. The goodness-of-fit parameters that were used to assess the fit was the R-factor and the reduced chi-square value. Both are relatively low[44] except for the reduced chi-square of the 2.5Zn sample indicating a greater mismatch between the model using the standards and the experimental results (Table 7.9).

Table 7.9: LCF goodness of fit parameters for the undoped and Zn-doped $LiFePO_4$ samples.

Sample	$LiFePO_4$ ($Fe^{2+}O_6$)	Fe_2O_3 ($Fe^{3+}O_6$)	$FePO_4$ ($Fe^{3+}O_6$)
Undoped	85(2)	8(1)	7(1)
1Zn	85(2)	8(1)	7(1)
2.5Zn	94(2)	-	6(1)
3Zn	77(1)	11(1)	12(1)

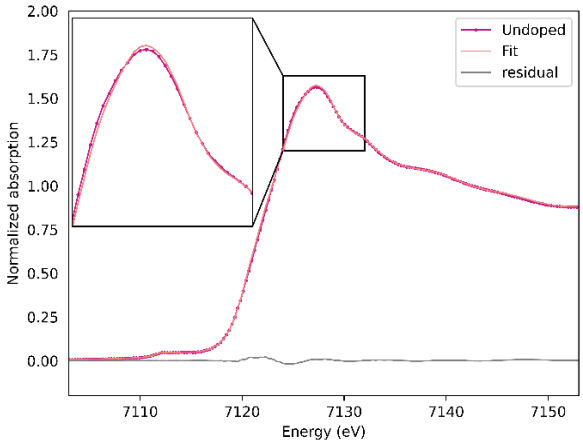

Figure 7.10: LCF best fit (coral) of the undoped $LiFePO_4$ sample of the Fe K-edge XANES spectrum (pink) along with the residual spectrum (grey).

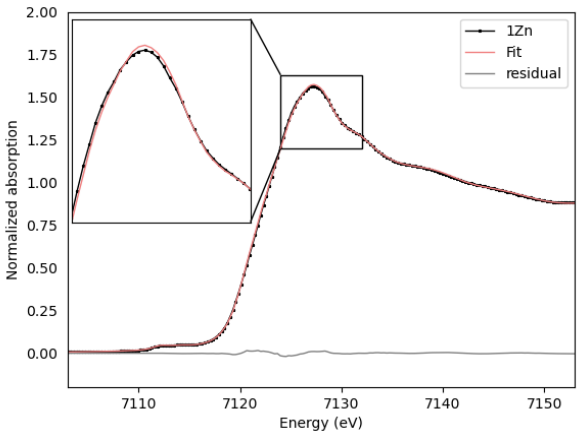

Figure 7.11: LCF best fit (coral) of the 1Zn $LiFePO_4$ sample of the Fe K-edge XANES spectrum (black) along with the residual spectrum (grey).

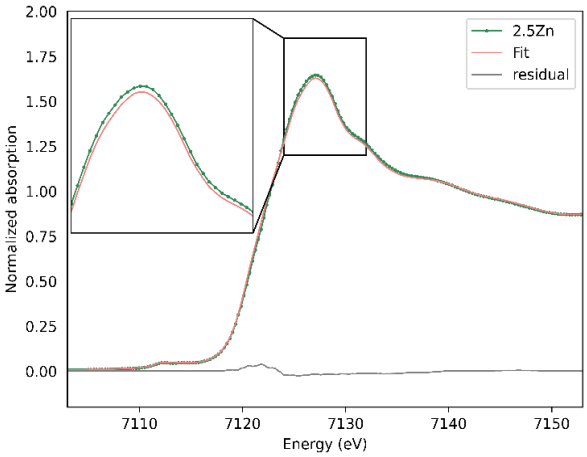

Figure 7.12: LCF best fit (coral) of the 2.5Zn $LiFePO_4$ sample of the Fe K-edge XANES spectrum (green) along with the residual spectrum (grey).

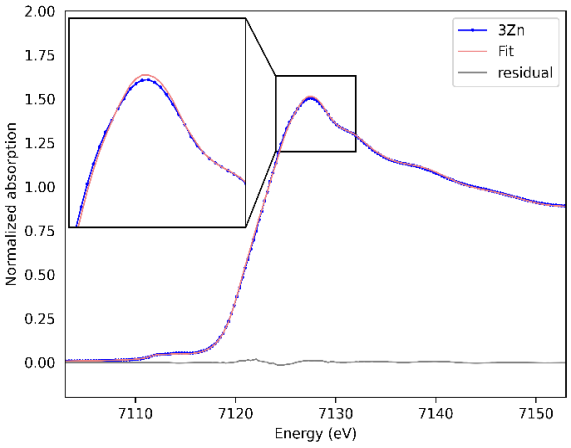

Figure 7.13: LCF best fit (coral) of the 3Zn $LiFePO_4$ sample of the Fe K-edge XANES spectrum (blue) along with the residual spectrum (grey).

Table 7.10: LCF weight percentage of the different components present in the undoped and Zn-doped $LiFePO_4$ samples.

Sample	R-factor	Chi-square
Undoped	0.0001182	0.000033
1Zn	0.0000892	0.000025
2.5Zn	0.0004130	0.000128
3Zn	0.0000823	0.000023

The calculated standard weights for each component present in each sample can be found in Table 7.10. The LCF calculated that the 2.5Zn had the highest Fe^{2+} weight. The 3Zn sample had the lowest Fe^{2+} weight of all the synthesised samples. The undoped and the 1Zn had very similar Fe^{2+} weights. The Fe^{2+} weights calculated with LCF followed a similar trend as determined by the pre-edge peak at ~7112 eV (Fig. 7.8) and the rising absorption edge (Fig.7. 9). All the synthesised samples had Fe^{3+} present. The trend predicted by the pre-edge peak at ~7114 eV can also someway be linked to the calculated Fe^{3+} weights (Fig. 7.8). The 3Zn sample was seen to have the highest intensity (Fig. 7.8) and can be correlated to having the highest Fe^{3+} (Fe_2O_3) weight present. The same was observed for 1Zn as well. The 2.5Zn sample had the lowest percentage of Fe^{3+} and it can be seen that the peak at 7114 eV (Fig. 7.8) is similar to that of $LiFePO_4$. The 2.5Zn sample had only one form of Fe^{3+} present, Fe^{3+} in the less distorted $FePO_4•4H_2O$ environment, and could explain the low intensity of this peak that is similar to that of the $FePO_4•4H_2O$ peak intensity. The undoped $LiFePO_4$ sample had both

forms of Fe^{3+} present and this could explain why this sample had a higher intensity than 2.5Zn. All the synthesised samples showed a mismatch between the measured data and the fit and can be seen from the insets in Figure 7.10 – 7.13 inset and the residual spectra, where the larger mismatch for the 2.5Zn sample is evident. The mismatch present in all the samples indicate that there was a bonding environment or species that was not included in the set of standards or that the samples had slight differences to that of the standards. The accuracy of the fit can be improved by having a larger and more diverse set of standards to identify all the constituents.[45]

(ii) EXAFS

EXAFS was used to probe the local structure and the disorder around the Fe-atoms and to determine if doping has any effect on the local Fe environment. The FT-EXAFS were all phase corrected. To account for the addition of a dopant a method outlined in the Artemis user guide[46,47] was used. In $LiFePO_4$ there are four nearest iron neighbours and when including the dopant, thus one needs to determine the number of (if any) iron atoms that would need to be replaced with zinc atoms (using equation 1). Table 7.11 contains the replacement values for each doping percentage.

$$Amount\ of\ iron\ atoms\ to\ be\ replaced = (dopant\ percentage) \times (nr\ of\ nearest\ neighbour\ iron\ atoms) \quad \textbf{(1)}$$

Table 7.11: Amount of Fe that should be replaced for each doping percentage.

Doping percentage	Replacement
1	0.04
2.5	0.1
3	0.12

If this value is not a whole number, then one either need to underestimate or overestimate the value. Both approaches were considered. In this case, overestimating the value would lead to replacing one whole iron site (25%) with zinc and underestimating the site would approximate the replacement of no sites. The dopant was added to the feff.inp file and given its own identity under the potential list. This would then add a single scattering zinc path. The modification of the feff.inp is given in Appendix A8.1. Including this scattering path when accounting for the overestimation led to high errors for the Debye-Waller factors for the metal atoms even with the correction of the amplitude reduction factor to account for the actual doping percentage of

the nearest zinc scattering path. The first nearest neighbour scattering path also had a low ranking indicating that the path is not important to the fit and the inclusion of this scattering path did not improve the fit. This leads to the possible conclusion that the doping concentration is below the detection limit of the software. The results presented in the next section is for the underestimation of zinc to zero.

Comparing the different $k^3\chi(k)$ spectra (Fig. 7.14) could indicate any changes in the local structure and local disorder. There are no major changes between the undoped and doped samples but minor changes in the intensity indicates that there could be changes in the local disorder for the synthesised samples.[42]

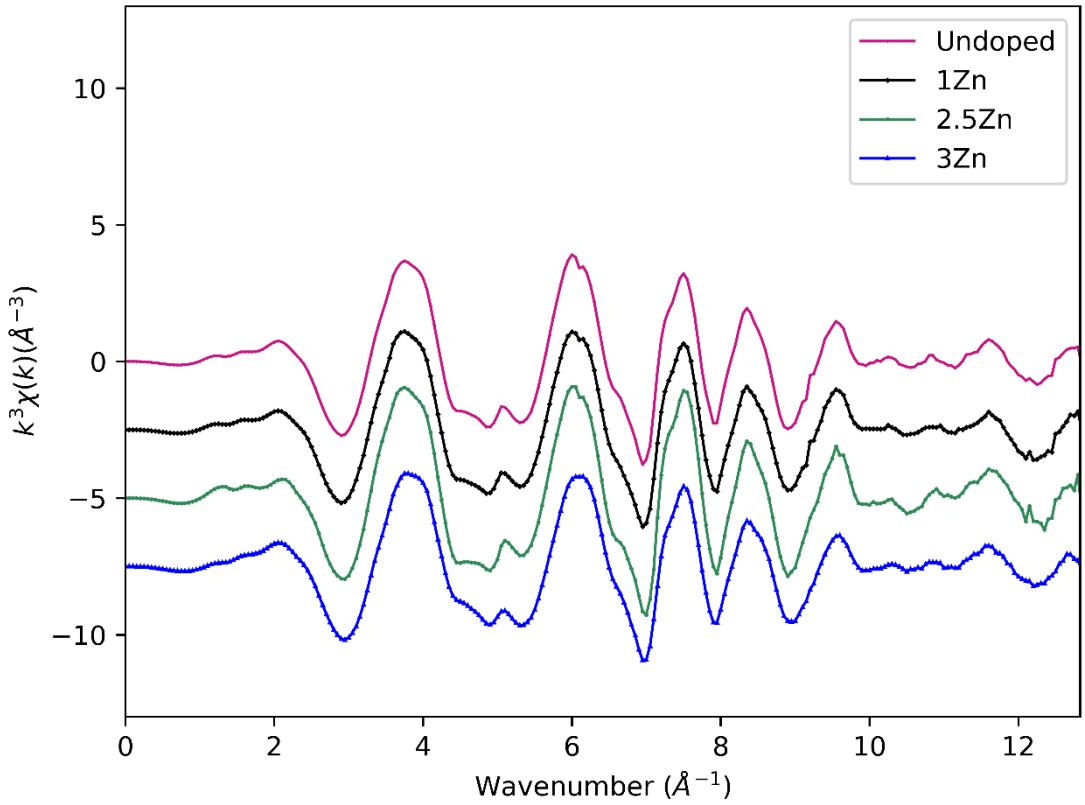

Figure 7.14: Comparison of the Fe k^3-weighted [$k^3\chi(k)$] spectrum of the different synthesised samples (undoped and Zn-doped samples).

Comparing the FT magnitude of the undoped sample with that of the doped samples (Fig. 7.15) was also used to predict any changes in the local structure. The three coordination shells indicated were present in all the synthesised samples and no major changes in the shape of the peaks of the FT magnitude is present indicating no major change in the local structure for the undoped and doped samples. The shouldering of the first peak is more pronounced for the doped than for the undoped samples. This could possibly indicate changes in the bond distance distribution. The shift in the peak positions (Fig. 7.15) could indicate changes in the interatomic

bond distances. There also seems to be a correlation between the peak shifts observed in Fig 7.14/15 and the doping concentration where an increase in concentration leads to an increase in the radial distance.

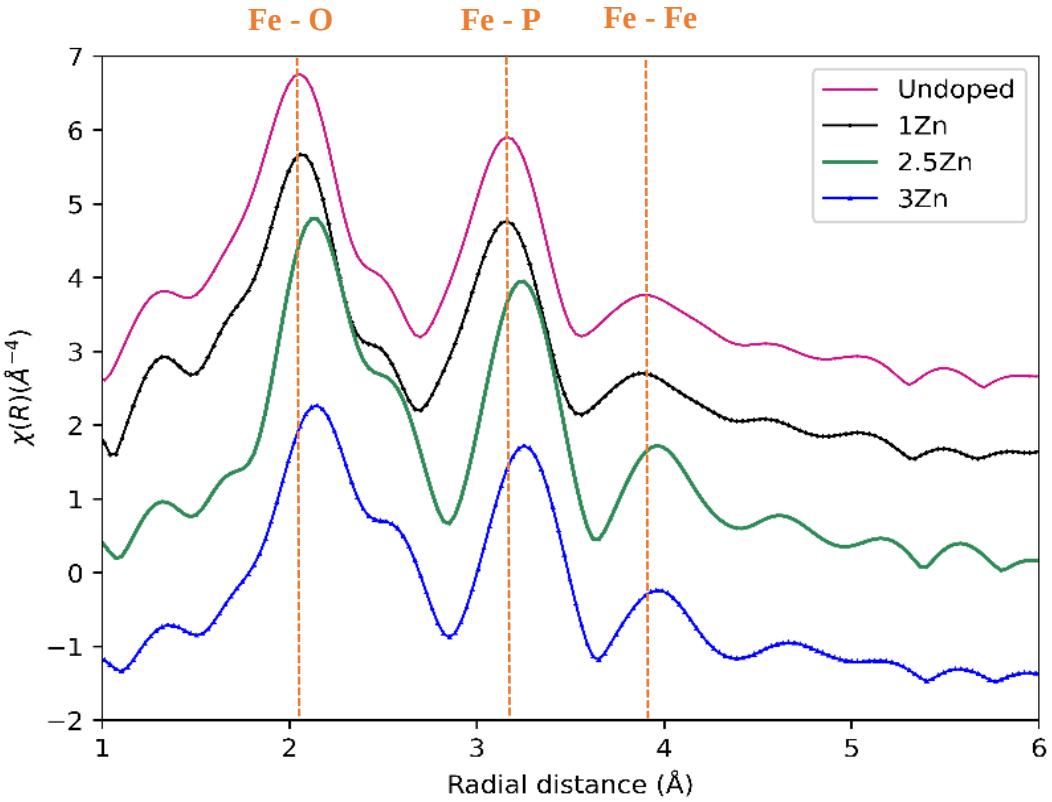

Figure 7.15: The FT magnitude of EXAFS $k^3\chi(k)$ data comparing radial distance of the different coordination shells of the undoped and Zn-doped samples.

Local Structure Determination:

The local structure was determined for all samples (Figs 7.16 – 7.19). Due to the similarity of the normalized spectra (Fig. 7.7) between the standard and the synthesised samples, the same starting model ($LiFePO_4$) was used for the local structure determination. The parameters determined for each sample was the amplitude reduction factor (S_o^2), the energy shift (ΔE_o), the adjustment of the half path length of the path (ΔR) and the Debye-Waller factor (σ^2 – mean square variation in the path length). The same fitting procedure described in section 2.2.3.2 was used to model the EXAFS data for this set of samples. The R-factor for all the fits was less than 2%.[45,38] The ΔE_o parameter was -10 eV < ΔE_0 < 10 eV for all the fits (Table 7.12)[48] and the value of S_o^2 for the samples was between 0.72 – 0.85.

Table 7.12: The reliability factor and energy shift of the undoped and Zn-doped samples.

Sample	R-factor (%)	E_0 (eV)	ΔE_0 (eV)
Undoped	0.58	7122.83	-2.4(9)
1Zn	0.65	7122.83	-2.4(9)
2.5Zn	0.67	7122.00	-2(1)
3Zn	0.54	7122.83	-1.4(9)

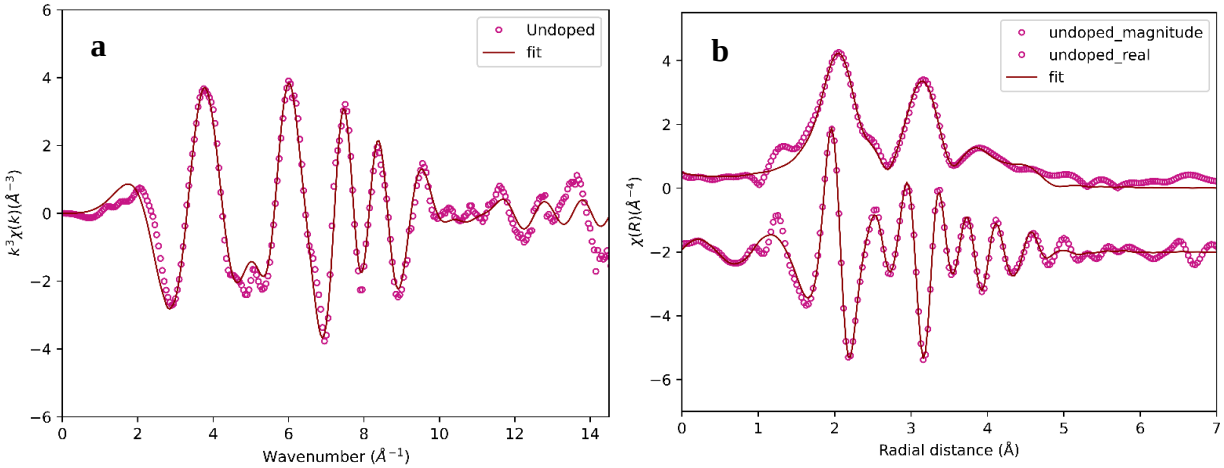

Figure 7.16: (a) The experimental Fe k^3-weighted $[k^3\chi(k)]$ spectrum and (b) the experimental FT magnitude (top) and FT real (bottom) of the EXAFS $k^3\chi(k)$ data (pink) and the theoretical FEFF fit (maroon) of the undoped sample. The fitting range for (a) is 3 – 12.828 Å^{-1} and for (b) 1.3 – 5 Å.

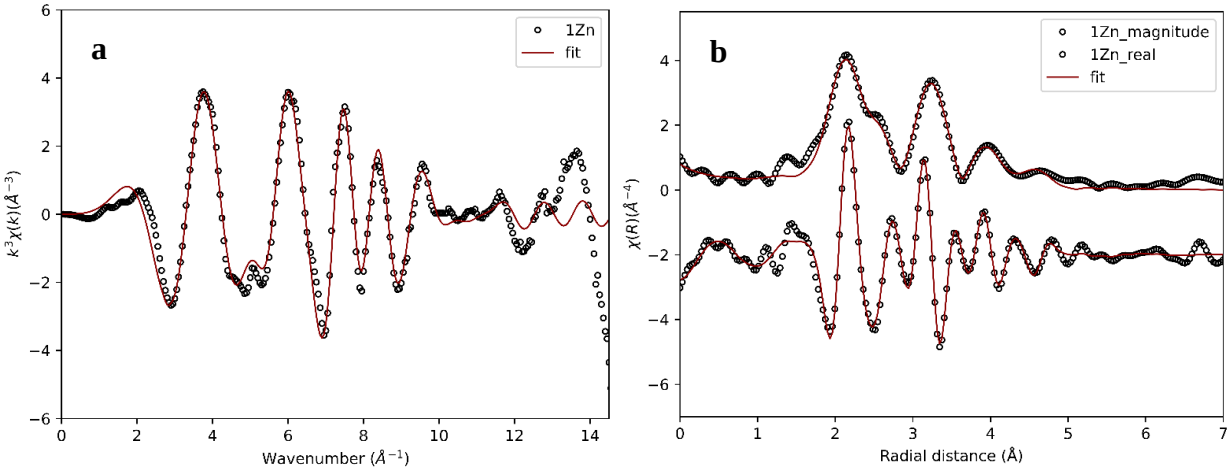

Figure 7.17: (a) The experimental Fe k^3-weighted $[k^3\chi(k)]$ spectrum and (b) the experimental FT magnitude (top) and FT real (bottom) of the EXAFS $k^3\chi(k)$ data (black) and the theoretical FEFF fit (maroon) of the 1Zn sample. The fitting range for (a) is 3 – 12.828 Å^{-1} and for (b) 1.3 – 5 Å.

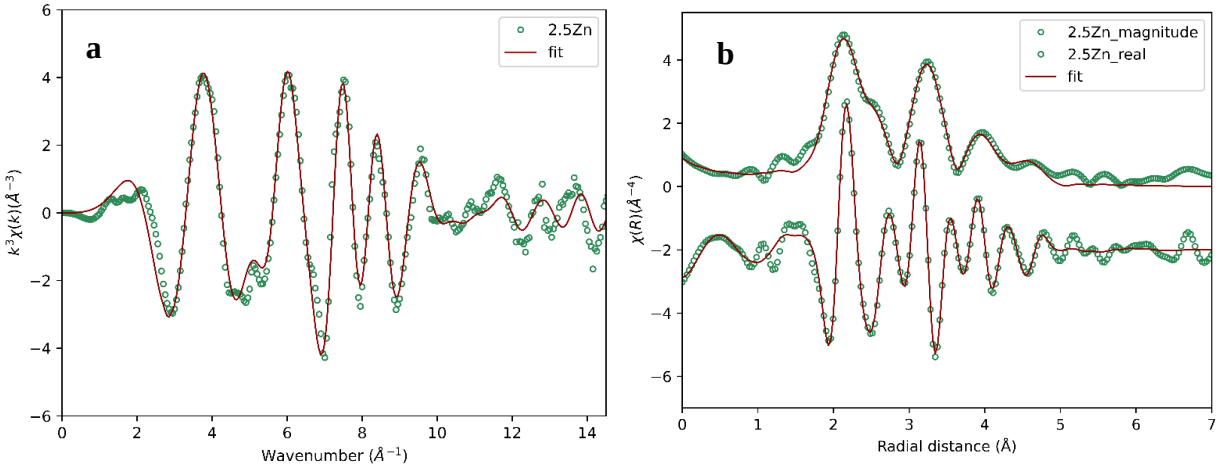

Figure 7.18: (a) The experimental Fe k^3-weighted $[k^3\chi(k)]$ spectrum and (b) the experimental FT magnitude (top) and FT real (bottom) of the EXAFS $k^3\chi(k)$ data (green) and the theoretical FEFF fit (maroon) of the 2.5Zn sample. The fitting range for (a) is 3 – 12.828 Å^{-1} and for (b) 1.3 – 5 Å

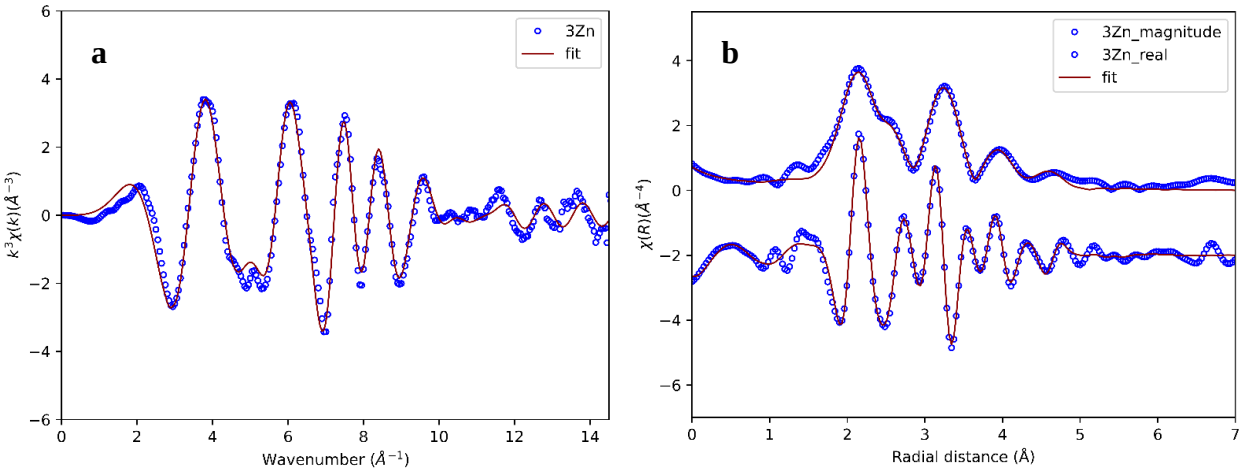

Figure 7.19: (a) The experimental Fe k^3-weighted $[k^3\chi(k)]$ spectrum and (b) the experimental FT magnitude (top) and FT real (bottom) of the EXAFS $k^3\chi(k)$ data (blue) and the theoretical FEFF fit (maroon) of the 3Zn sample. The fitting range for (a) is 3 – 12.828 Å^{-1} and for (b) 1.3 – 5 Å.

As none of the coordination shells exhibited any peak flattening or splitting for the FT magnitude (Fig. 7.15) that the local structure remained the same for the undoped and doped samples.[49] This was also shown with the EXAFS analysis. The first coordination shell was oxygen and had a coordination number of six for all the samples.[34,35,49] This coordination shell was fitted using a two shell model for all the samples and there was some variation in the distance distribution. The undoped, 1Zn and 2.5Zn samples had four longer and two shorter interatomic distances and the 3Zn sample had three shorter and three longer interatomic distances (Table 7.13). The second coordination shell was phosphorous and had a coordination number of five[34,35,49] for all the samples and consisted of one shorter and four longer interatomic distances. The third and last coordination shell was iron and had a coordination number of four[34,35,49] for all the samples. The shell consisted of two longer and two shorter

interatomic distances (Table 7.13). Table 7.14 contains the average interatomic distance for each coordination shell. The changes in radial distances as seen in Figure 7.15 were not reflected in the actual interatomic distances determined using EXAFS modelling (Table 7.13 and Table 7.14). Other factors might be affecting the Fourier Transform and the FT magnitude that was not accounted for in the modelling such as the presence of Fe^{3+} in the structure or the dopants that were not added to the actual model due to the low concentrations. These dopants were not included in the model (as discussed earlier as well as in Appendix A8) as including Zn in the scattering paths produced unrealistic values and errors.

T**able 7.13:** Structural parameters determined using FEFF for the first, second and third coordination shells of the undoped and Zn-doped samples.

Sample	Shell	Coordination number	Average interatomic distance (Å)	Debye-Waller factor ($Å^2$)
Undoped	Fe-O2	4	2.09(1)	0.013(5)
	Fe-O3	2	2.05(1)	0.011(6)
	Fe-P1	1	2.823(8)	0.007(2)
	Fe-P2	4	3.248(8)	0.007(1)
	Fe-Fe1	2	3.82(1)	0.009(1)
	Fe-Fe2	2	4.64(1)	0.012(4)
1Zn	Fe-O1	4	2.12(1)	0.011(2)
	Fe-O2	2	2.02(1)	0.009(3)
	Fe-P1	1	2.819(8)	0.007(2)
	Fe-P2	4	3.244(8)	0.007(1)
	Fe-Fe1	2	3.82(1)	0.009(2)
	Fe-Fe2	2	4.64(1)	0.012(4)
2.5Zn	Fe-O1	4	2.12(1)	0.011(2)
	Fe-O2	2	2.03(1)	0.008(3)
	Fe-P1	1	2.82(1)	0.007(2)
	Fe-P2	4	3.24(1)	0.007(1)
	Fe-Fe1	2	3.814(9)	0.008(2)
	Fe-Fe2	2	4.635(9)	0.010(4)
3Zn	Fe-O1	3	2.12(1)	0.011(2)
	Fe-O2	3	2.03(1)	0.010(2)
	Fe-P1	1	2.820(8)	0.007(2)
	Fe-P2	4	3.245(8)	0.0074(9)
	Fe-Fe1	2	3.82(1)	0.009(1)
	Fe-Fe2	2	4.64(1)	0.012(4)

Table 7.14: The average interatomic distance and average Debye-Waller factor of the different coordination shells.

Shell	Sample	Average interatomic distance (Å)	Average Debye-Waller factor (Å^2)
Fe-O	Undoped	2.08	0.012
	1Zn	2.09	0.010
	2.5Zn	2.09	0.010
	3Zn	2.08	0.011
Fe-P	Undoped	3.160	0.007
	1Zn	3.159	0.007
	2.5Zn	3.16	0.007
	3Zn	3.160	0.007
Fe-Fe	Undoped	4.23	0.011
	1Zn	4.23	0.011
	2.5Zn	4.23	0.009
	3Zn	4.23	0.011

No EXAFS studies where the Zn^{2+}-doping on the $LiFePO_4$ structure using the Fe K-edge was found and therefor another study by Tabassam *et al.*[50] and Minicucci *et al.*[51] was used as a comparison. In these studies replacement of Fe^{2+} with Ni^{2+} was investigated. The Ni^{2+} (0.69 Å) radius is smaller than that of Fe^{2+} (0.78 Å) similar to this study of Zn^{2+} (0.74 Å).[15] Tabassam *et al.*[50] investigated the effect of Ni^{2+}-doping ($LiFe_{1-x}Ni_xPO_4$ where, $0 < x < 0.15, 0.9, 1.0$) on the FeO_6 octahedron and it was determined that the doping concentration did not have an effect on the average interatomic distance using the Fe K-edge. The Fe-O interatomic distances were between 2.11 – 2.12 Å for the shorter distances and between 2.17 – 2.19 Å for the longer distances over the doping concentration. It was also determined that the structural disorder (0.0075 – 0.011 Å^2) for the shorter interatomic bond distance did not change much with the change in Ni^{2+} content.[50] To determine the size of the Ni-O octahedra and the interatomic distances, the Ni K-edge was used. Minicucci *et al.*[51] also investigated $LiFe_{1-x}Ni_xPO_4$ (where $x = 0.03, 0.05, 0.01, 0.015$) using both the Fe and Ni K-edges for the first (Fe/Ni-O) and second (Fe/Ni-P) coordination shells only. It was determined that the average interatomic distance for the nearest neighbour was constant with different doping concentration for both the FeO_6 (2.23 Å) and NiO_6 (0.02 – 0.03 shorter than Fe-O) octahedra for the shorter interatomic distances but that the doping had an effect on the longer interatomic distances. The shorter Fe-O and Ni-O distances are ~2.10 Å and longer Fe-O and Ni-O distances ranges between 2.30 – 2.33 Å and 2.24 – 2.45 Å, respectively over the doping range.

These changes caused more distortion in the octahedra (for $x < 0.15$) for both FeO_6 and NiO_6 where the latter was more affected. For the Fe-P/Ni-P coordination shell it was determined that doping has a larger effect on the shorter interatomic distances that on the longer interatomic distances. Further the effect was larger for Ni-P than for Fe-P. The longer interatomic distances ranged between 3.26 – 3.31 Å and 3.26 – 3.28 Å and the shorter interatomic distances ranged between 2.80 – 2.86 Å and 2.80 – 2.89 Å for Ni-P and Fe-P, respectively. Minicucci *et al.*[51] also showed that the disorder of the Fe-P coordination had little variation between doping concentrations. The disorder was between 0.0035 – 0.005 $Å^2$ and 0.010 – 0.0125 $Å^2$ for the longer and the shorter interatomic distances, respectively.

The results from this EXAFS experiment showed that the FeO_6 octahedra are distorted in the undoped and Zn-doped samples due to the two different interatomic distances and that the doping concentration did not have a notable effect on the average interatomic distance and is practically constant (Table 7.14). Minicucci *et al.*[51] also determined that the FeO_6 octahedra were naturally distorted and this was also consistent with the results found by Tabassam *et al.*[50] This study determined that the longer Fe-O interatomic distances were longer for the doped samples than for the undoped samples and the shorter Fe-O interatomic distances were shorter for the doped samples than for the undoped samples (Table 7.13 and Fig. 7.20). These changes in the octahedra show an increase the distortion due to doping. The structural disorder for the doped samples showed that the shorter interatomic distances had more variation between the doped samples than the disorder between the longer interatomic distances (Fig. 7.20). This disorder decreases slightly for the doped samples. The Fe-P coordination shell showed very little changes in the longer and the shorter Fe-P interatomic distances and had no variation in the disorder present in this shell (Table 7.13 and Fig. 7.21). The Fe-Fe coordination shell showed little to no variation in the shorter or longer interatomic distance (Table 7.13 and Fig. 7.22). The disorder decreased upon doping for both the shorter and longer interatomic distances but the shorter interatomic distance had more variation in the disorder between doping concentrations than the longer interatomic distances.

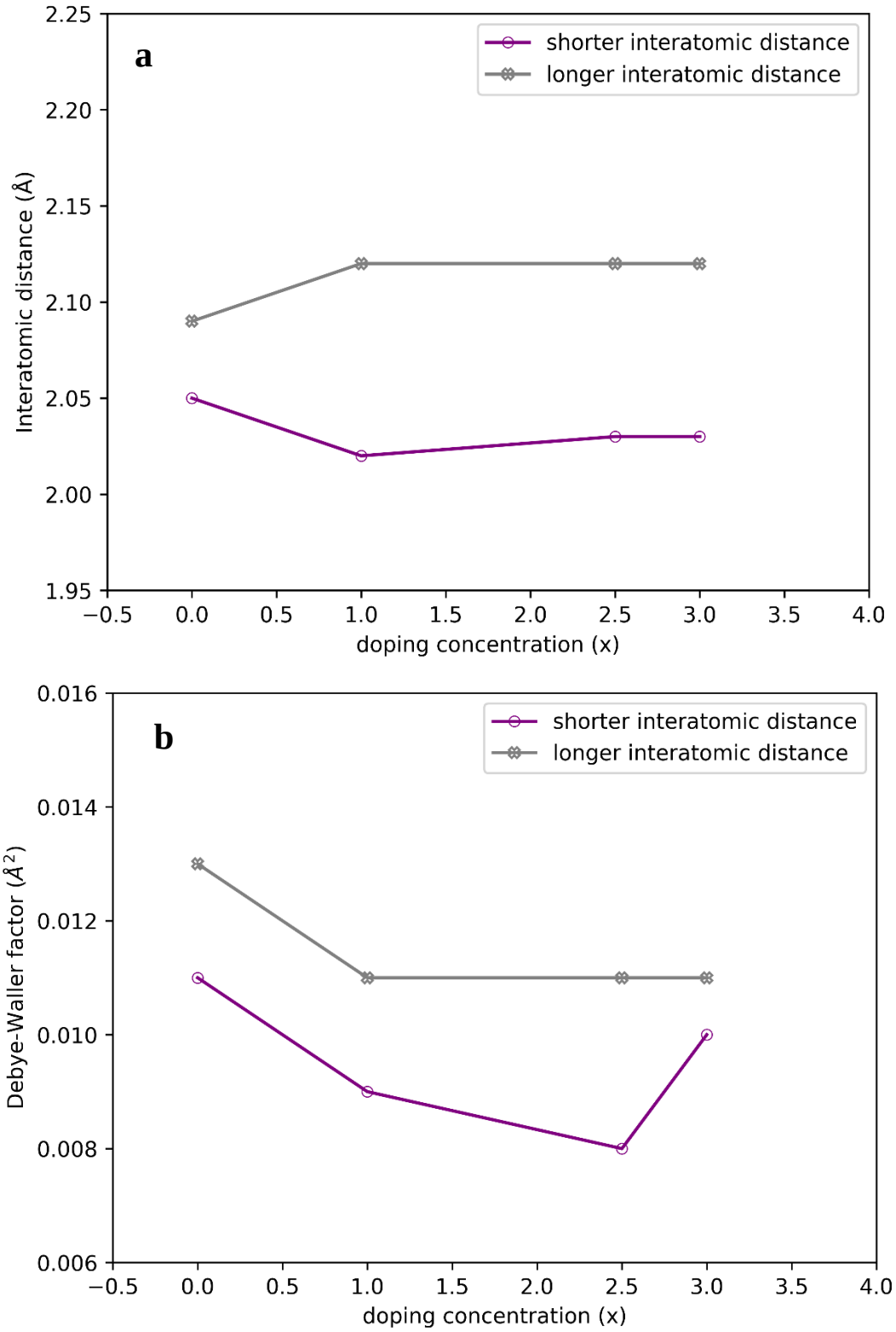

Figure 7.20: The changes in the (a) of interatomic distance and (b) the disorder of the first (Fe-O) coordination shell.

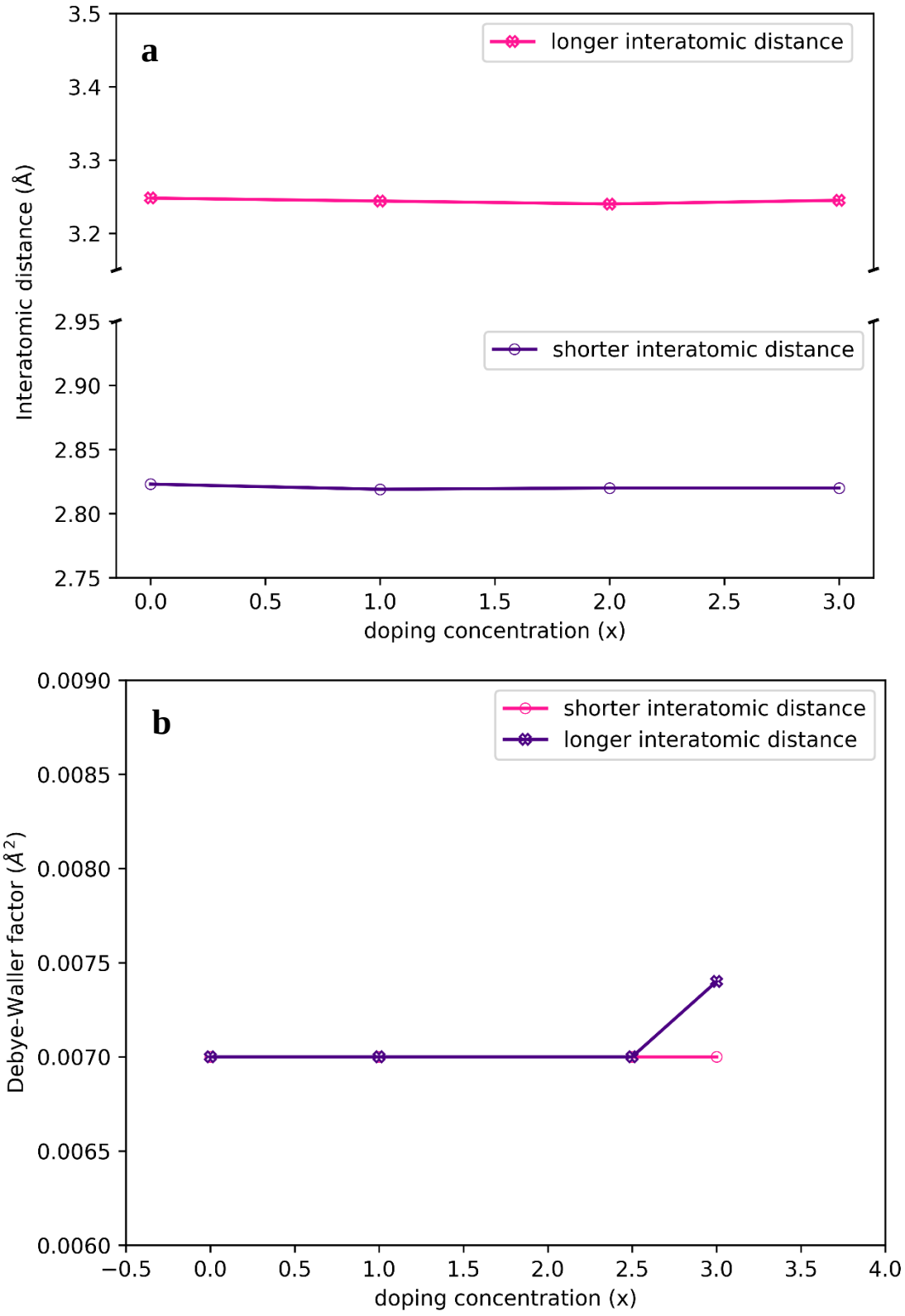

Figure 7.21: The changes in the (a) of interatomic distance and (b) the disorder of the second (Fe-P) coordination shell.

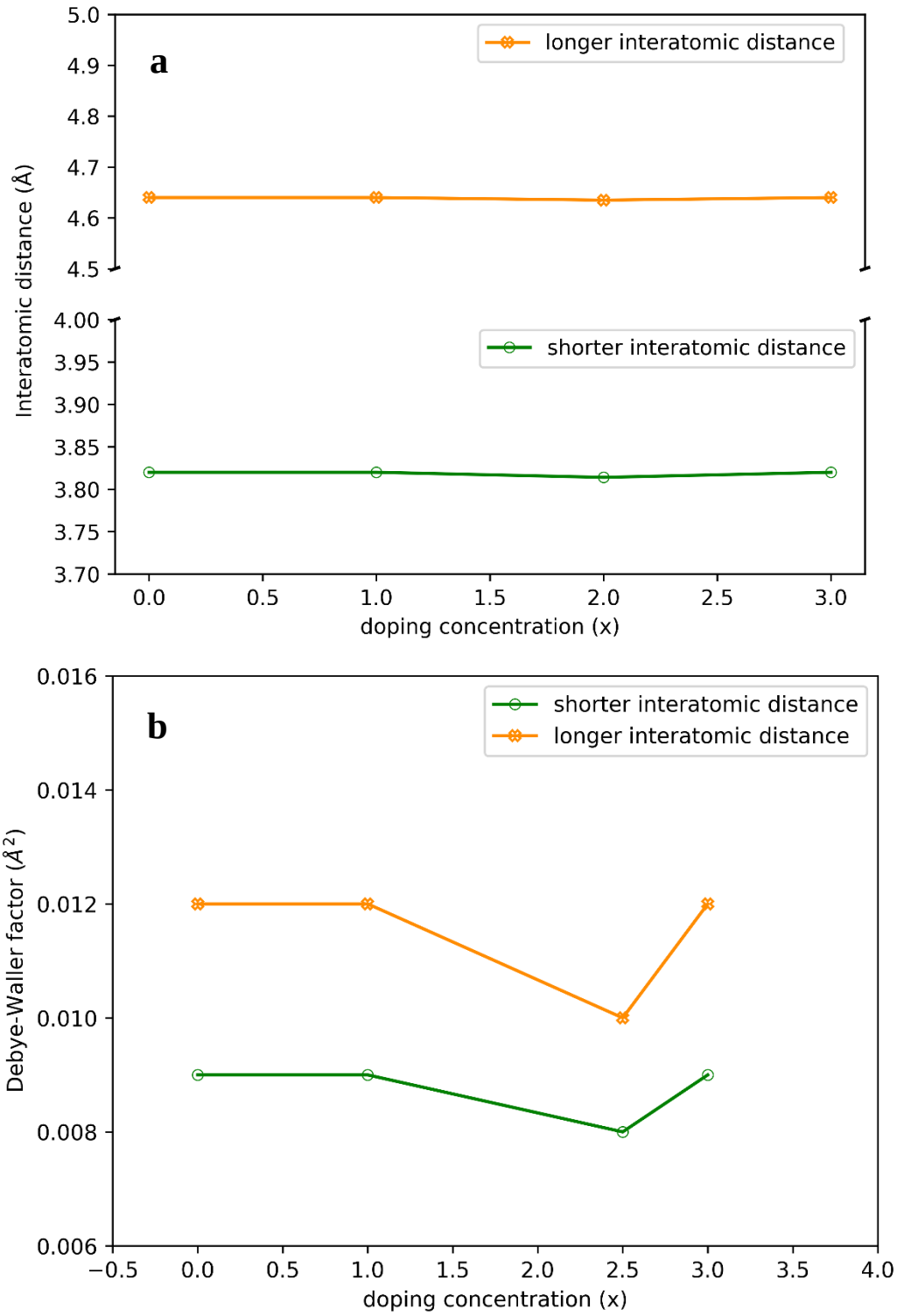

Figure 7.22: The changes in the (a) of interatomic distance and (b) the disorder of the third (Fe-Fe) coordination shell.

7.4. Conclusion

Doping with Zn^{2+} using a hydrothermal synthesis employed in this work was investigated. The defects present in the undoped sample, as shown with the presence of Fe on the M1 site and the 14.6% Fe^{3+}, indicates that the synthetic route has inherent problems. There was also ~2% of the Fe-impurity present in this sample as well as only 85.4% Fe^{2+} whereas the rest is Fe^{3+}. The same defects are probably present in the doped samples as well. The 1Zn sample showed that no Fe-containing impurities were detected with XRD but the b-lattice constant did not decrease as with the other doping percentages. The 1Zn sample had the highest percentage of Fe on the M1 site. XAS showed that there was an increase in the intensity of the e_g peak and possibly an increase in the distortion around the octahedron. Fe^{3+} was identified in these samples and only 85.4% was Fe^{2+}. These phases are possibly amorphous as only Fe^{2+} was identified using XRD. No change in the bonding distributions were observed for for the undoped, 1Zn and 2.5Zn samples and showed four longer and two shorter interatomic distances. The lattice parameters and volume are smaller than the undoped sample. The 2.5Zn sample had the lowest percentage of impurities present and was identified as the Fe-impurity that contains both Fe^{3+} and Fe^{2+}, the lowest percentage of Fe on the M1 site and the highest percentage of Fe^{2+} (93.6%). Amorphous $LiFePO_4(OH)$ was identified in this sample. The intensity of the e_g peak was similar to that of the $LiFePO_4$ standard. In the 3Zn sample Li_3PO_4 was the only impurity identified but had the highest percentage impurity present. The lattice parameters and volume were smaller than that of the undoped sample and the Fe-O interatomic bond distance was the shortest for this sample indicating the presence of more Fe^{3+}. LCF determined that the 3Zn sample had the lowest percentage of Fe^{2+} (77%) present confirming the XRD trend. The e_g peak for 3Zn in the pre-edge region showed the greatest increase in intensity and had the broadest peak indicating a change in bonding distribution. EXAFS analysis showed that 3Zn had three longer and three shorter Fe-O interatomic distances rather than the four longer and two shorter interatomic distances as in the case for the undoped, 1Zn and 2.5Zn samples. This change in the bonding distribution could increase the distortion around the e_g orbitals for the metal and the oxygen ligands.

On hindsight, the filtrate should be analysed using an element specific technique to ensure that all the added dopant was incorporated successfully into the structure, but from the data analysed the doped samples clearly reflected some changes as compared to that for the undoped samples. The impurities could be due to the unpurged Zn^{2+}-solution and purging the solution might

eliminate the impurities. EXAFS analysis using Fe K-edge showed that doping with zinc does not change or effect the local structure to a large extent which was expected for the low concentrations used and was similar to the comparative study used. Minor difference in the interatomic distance and disorder was observed between samples. To determine what extent Zn^{2+} doping would affect the Zn-O, Zn-P and Zn-Zn interatomic distances and disorder, an experiment using Zn K-edge would be useful as well as provide to more information on the local and medium range structure and effects of doping. Determining these effects would also be able to provide information on the structure and transport properties. Investigating the de-intercalated material could give more information on whether the Zn^{2+} stabilizes the structure. This chapter has illustrated that doping is possible using this synthetic method although there are defects that are inherent to this low cost, low energy synthesis.

7.5. References

1. Xu, J. and Chen, G. Effects of doping on the electronic properties of $LiFePO_4$: A first-principles investigation. *Phys. B Condens. Matter* **405**, 803–807 (2010).
2. Liu, H., Cao, Q., Fu, L. J., Li, C., Wu, Y. P. and Wu, H. Q. Doping effects of zinc on $LiFePO_4$ cathode material for lithium ion batteries. *Electrochem. commun.* **8**, 1553–1557 (2006).
3. Jayaprakash, N., Kalaiselvi, N. and Periasamy, P. Synthesis and Characterization of $LiM_XFe_{1-X}PO_4$ (M = Cu, Sn; X = 0.02) Cathodes-A study on the Effect of Cation Substitution in LiFePO4 *Material*. *Int. J. Electrochem. Sci* **3**, 476 - 488 (2008).
4. Xu, Z., Gao, L., Liu, Y. and Li, L. Review—Recent Developments in the Doped $LiFePO_4$ Cathode Materials for Power Lithium Ion Batteries. *J. Electrochem. Soc.* **163**, A2600–A2610 (2016).
5. Shenouda, A. Y. and Liu, H. K. Studies on electrochemical behaviour of zinc-doped $LiFePO_4$ for lithium battery positive electrode. *J. Alloys Compd.* **477**, 498–503 (2009).
6. Padhi, A. K., Nanjundaswamy, K. S., Masquelier, C., Okada, S. and Goodenough, J. B. Effect of structure on the Fe^{3+}/Fe^{2+} redox couple in iron phosphates. *J. Electrochem. Soc.* **144**, 1609–1613 (1997).
7. Islam, M. S., Driscoll, D. J., Fisher, C. A. J. and Slater, P. R. Atomic-scale investigation of defects, dopants, and lithium transport in the $LiFePO_4$ olivine-type battery material. *Chem. Mater.* **17**, 5085–5092 (2005).
8. Wagemaker, M., Ellis, B. L., Lützenkirchen-Hecht, D., Mulder, F. M. and Nazar, L. F. Proof of supervalent doping in olivine $LiFePO_4$. *Chem. Mater.* **20**, 6313–6315 (2008).
9. Wang, D., Li, H., Shi, S., Huang, X. and Chen, L. Improving the rate performance of

$LiFePO_4$ by Fe-site doping. *Electrochim. Acta* **50**, 2955–2958 (2005).

10. Shu, H., Wang, X., Wu, Q., Hu, B., Yang, X., Wei, Q., Liang, Q., Bai, Y., Zhou, M., Wu, C., Chen, M., Wang, A. and Jiang, L. Improved electrochemical performance of $LiFePO_4$/C cathode via Ni and Mn co-doping for lithium-ion batteries. *J. Power Sources* **237**, 149–155 (2013).

11. Yiming, W., Giuli, G., Moretti, A., Nobili, F., Fehr, K. T., Paris, E. and Marassi, R. Synthesis and characterization of Zn-doped $LiFePO_4$ cathode materials for Li-ion battery. *Mater. Chem. Phys.* **155**, 191–204 (2015).

12. Zhao, Y., Chen, L., Chen, X., Kuang, Q. and Dong, Y. Crystal structure and electrochemical properties of $LiFe_{1-x}Zn_xPO_4$ ($x \leq 1.0$) . *Powder Diffr.* **26**, 238–243 (2011).

13. Bilecka, I., Hintennach, A., Rossell, M. D., Xie, D., Novák, P. and Niederberger, M. Microwave-assisted solution synthesis of doped $LiFePO_4$ with high specific charge and outstanding cycling performance. *J. Mater. Chem.* **21**, 5881–5890 (2011).

14. Baster, D., Zheng, K., Zając, W., Świerczek, K. and Molenda, J. Toward elucidation of delithiation mechanism of zinc-substituted $LiFePO_4$. *Electrochim. Acta* **92**, 79–86 (2013).

15. Shannon, R. D. Revised effective ionic radii and systematic studies of interatomic distances in halides and chalcogenides. *Acta Crystallogr. Sect. A* **32**, 751–767 (1976).

16. Chantrasuwan, P., Wiriya, N., Kaewmala, S., Pongha, S., Limphirat, W., Nash, J., Srilomsak, S. and Meethong, N. Electrochemical property investigation of cobalt doped $LiFePO_4$ /C during charge-discharge by an in-situ x-ray near edge structure technique. in *AIP Conference Proceedings* **2097**, 020004 (2019).

17. Jugović, D., Cvjetićanin, N., Mitrić, M. and Mentus, S. Comparison between different $LiFePO_4$ synthesis routes. in *Materials Science Forum* vol. 555 225–230 (2007).

18. Yang, M.-R. and Ke, W.-H. The Doping Effect on the Electrochemical Properties of $LiFe_{0.95}M_{0.05}PO_4$ ($M=Mg^{2+}$, Ni^{2+}, Al^{3+}, or V^{3+}) as Cathode Materials for Lithium-Ion Cells. *J. Electrochem. Soc.* **155**, A729 (2008).

19. Zhang, L. L., Liang, G., Ignatov, A., Croft, M. C., Xiong, X. Q., Hung, I. M., Huang, Y. H., Hu, X. L., Zhang, W. X. and Peng, Y. L. Effect of vanadium incorporation on electrochemical performance of $LiFePO_4$ for lithium-ion batteries. *J. Phys. Chem. C* **115**, 13520–13527 (2011).

20. Gao, H., Jiao, L., Yang, J., Qi, Z., Wang, Y. and Yuan, H. High rate capability of Co-doped $LiFePO_4$/C. *Electrochim. Acta* **97**, 143–149 (2013).

21. Lu, Y., Shi, J., Guo, Z., Tong, Q., Huang, W. and Li, B. Synthesis of $LiFe_{1-x}Ni_xPO_4$/C composites and their electrochemical performance. *J. Power Sources* **194**, 786–793 (2009).

22. Gibot, P., Casas-Cabanas, M., Laffont, L., Levasseur, S., Carlach, P., Hamelet, S., Tarascon, J. M. and Masquelier, Christian. Room-temperature single-phase Li-insertion/extraction in nanoscale Li_xFePO_4. Nat. Mater. **7**, 741–747 (2008).

23. Liu, Z. and Huang, X. Factors that affect activation energy for Li diffusion in $LiFePO_4$: A first-principles investigation. *Solid State Ionics* **181**, 907–913 (2010).

24. Burba, C. M. and Frech, R. Raman and FTIR Spectroscopic Study of Li_xFePO_4 ($0 \leq x \leq 1$). *J. Electrochem. Soc.* **151**, A1032 (2004).

25. Paraguassu, W., Freire, P. T. C., Lemos, V., Lala, S. M., Montoro, L. A. and Rosolen, J. M. Phonon calculation on olivine-like $LiMPO_4$ (M = Ni, Co, Fe) and Raman scattering of the iron-containing compound. *J. Raman Spectrosc.* **36**, 213–220 (2005).

26. Wu, J., Krishna Phani Dathar, G., Sun, C., Theivanayagam, M. G., Applestone, D., Dylla, A. G., Manthiram, A., Henkelman, G., Goodenough, J. B. and Stevenson, K. J. In situ Raman spectroscopy of $LiFePO_4$: size and morphology dependence during charge and self-discharge. *IOP Publ. Nanotechnol. Nanotechnol.* **24**, 424009–424018 (2013).

27. Bai, Y., Yin, Y., Yang, J., Qing, C. and Zhang, W. Raman study of pure, C-coated and Co-doped $LiFePO_4$: thermal effect and phase stability upon laser heating. *J. Raman Spectrosc.* **42**, 831–838 (2011).

28. Jugović, D., Mitrić, M., Milović, M., Cvjetićanin, N., Jokić, B., Umićević, A. and Uskoković, D. The influence of fluorine doping on the structural and electrical properties of the $LiFePO_4$ powder. *Ceram. Int.* **43**, 3224–3230 (2017).

29. Popovic, L., de Waal, D. and Boeyens, J. C. A. Correlation between Raman wavenumbers and P-O bond lengths in crystalline inorganic phosphates. *J. Raman Spectrosc.* **36**, 2–11 (2005).

30. Yang, C. C., Hu, H. C., Lin, S. J. and Chien, W. C. Electrochemical performance of V-doped spinel $Li_4Ti_5O_{12}$/C composite anode in Li-half and $Li_4Ti_5O_{12}$/$LiFePO_4$-full cell. *J. Power Sources* **258**, 424–433 (2014).

31. Marx, N., Croguennec, L., Carlier, D., Bourgeois, L., Kubiak, P., Le Cras, F. and Delmas, C. Structural and electrochemical study of a new crystalline hydrated iron(iii) phosphate $FePO_4 \cdot H_2O$ obtained from $LiFePO_4(OH)$ by ion exchange. *Chem. Mater.* **22**, 1854–1861 (2010).

32. de Faria, D. L. A. and Lopes, F. N. Heated goethite and natural hematite: Can Raman spectroscopy be used to differentiate them? *Vib. Spectrosc.* **45**, 117–121 (2007).

33. Popovic, L., Manoun, B., de Waal, D., Nieuwoudt, M. K. and Comins, J. D. Raman spectroscopic study of phase transitions in Li_3PO_4. *J. Raman Spectrosc.* **34**, 77–83 (2003).

34. Haas, O., Deb, A., Cairns, E. J. and Wokaun, A. Synchrotron X-ray absorption study of

$LiFePO_4$ electrodes. *J. Electrochem. Soc.* **152**, (2005).

35. Deb, A., Bergmann, U., Cairns, E. J. and Cramer, S. P. X-ray absorption spectroscopy study of the Li_xFePO_4 cathode during cycling using a novel electrochemical in situ reaction cell. *J. Synchrotron Radiat.* **11**, 497–504 (2004).

36. Delacourt, C., Poizot, P., Bonnin, D. and Masquelier, C. Lithium-Insertion Mechanism in Crystalline and Amorphous $FePO_4 \cdot nH_2O$. *J. Electrochem. Soc.* **156**, A595 (2009).

37. Glatzel, P., Mirone, A., Eeckhout, S. G., Sikora, M. and Giuli, G. Orbital hybridization and spin polarization in the resonant 1s photoexcitations of α- Fe_2O_3. *Phys. Rev. B - Condens. Matter Mater. Phys.* **77**, 115133 (2008).

38. Kelly, S. D., Hesterberg, D. and Ravel, B. *Analysis of Soils and Minerals Using X-ray Absorption Spectroscopy*, 387–463 (2015).

39. Wilke, M., Farges, F., Petit, P. E., Brown, G. E. and Martin, F. Oxidation state and coordination of Fe in minerals: An Fe K-XANES spectroscopic study. *Am. Mineral.* **86**, 714–730 (2001).

40. Griffith, J. S. and Orgel, L. E. Ligand-field theory. *Q. Rev. Chem. Soc.* **11**, 381–393 (1957).

41. Deb, A., Bergmann, U., Cairns, E. J. and Cramer, S. P. Structural investigations of $LiFePO_4$ electrodes by Fe X-ray absorption spectroscopy. *J. Phys. Chem. B* **108**, 7046–7051 (2004).

42. Nam, K., Nam, Bak, S., Hu, E., Yu, X., Zhou, Y., Wang, X., Wu, L., Zhu, Y., Chung, K. and Yang, X. Combining In Situ Synchrotron X-Ray Diffraction and Absorption Techniques with Transmission Electron Microscopy to Study the Origin of Thermal Instability in Overcharged Cathode Materials for Lithium-Ion Batteries. *Adv. Funct. Mater.* **23**, 1047–1063 (2013).

43. Zhao, T., Chu, W., Zhao, H., Liang, X., Xu, W., Yu, M., Xia, D. and Wu, Z. XAS study of $LiFePO_4$ synthesized by solid state reactions and hydrothermal method. in *Nuclear Instruments and Methods in Physics Research, Section A: Accelerators, Spectrometers, Detectors and Associated Equipment* **619**, 122–127 (2010).

44. Keating, J., Sankar, G., Hyde, T. I., Kohara, S. and Ohara, K. Elucidation of structure and nature of the PdO-Pd transformation using in situ PDF and XAS techniques. *Phys. Chem. Chem. Phys.* **15**, 8555–8565 (2013).

45. Calvin, S. *XAFS for Everyone*. (CRC Press, 2013).

46. Ravel, B. and Newville, M. ATHENA, ARTEMIS, HEPHAESTUS: Data analysis for X-ray absorption spectroscopy using IFEFFIT. in *Journal of Synchrotron Radiation* **12**, 537–541 (2005).

47. Demeter: XAS Data Processing and Analysis. (2018) at http://bruceravel.github.io/demeter/.

48. Kelly, S. D. and Ravel, B. EXAFS energy shift and structural parameters. in *AIP Conference Proceedings* **882**, 132–134 (2007).

49. Zhao, T., Chu, W., Zhao, H., Liang, X., Xu, W., Yu, M., Xia, D. and Wu, Z. XAS study of $LiFePO_4$ synthesized by solid state reactions and hydrothermal method. in *Nuclear Instruments and Methods in Physics Research, Section A: Accelerators, Spectrometers, Detectors and Associated Equipment* **619**, 122–127 (2010).

50. Tabassam, L., Giuli, G., Moretti, A., Nobili, F., Marassi, R., Minicucci, M., Gunnella, R., Olivi, L and Di Ci, Andrea. Structural study of $LiFePO_4$-$LiNiPO_4$ solid solutions. *J. Power Sources* **213**, 287–295 (2012).

51. Minicucci, M., Tabassam, L., Natali, Ri., Mancini, G., Rezvani, S. J. and Di Cicco, A, Double-edge X-ray absorption study of $LiFe_{1-x}Ni_xPO_4$ cathode materials. *J. Mater. Sci.* **52**, 4886–4893 (2017).

Chapter 8

Co-doping with Zn^{2+} and Co^{2+} using a low cost and low energy synthetic route

8.1. Introduction

Co-doping the $LiFePO_4$ structure is another way in which the poor electronic and ionic conductivity can be improved.[1–5] Co-doping can either occur on the M1 and M2 site, only the M2 site or on both the M2 and the oxygen in PO_4^{3-} sites. Co-doping on the M1 site increases the possibility of causing blockage in the Li^+ diffusion channel[6] that can lead to poor electrochemical performance. Co-doping on the M2 site has yielded positive improvements to not only the electrochemical performance of $LiFePO_4$ but also to the stability of the structure.[2–4,7–9] Table 1.2 contains a summary of the different co-dopants on the different sites and how it improved the stability of the structure and electrochemical performance.

Zinc (Zn^{2+}) as a single dopant has been shown to improve conductivity, rate capability and capacity, reduce electrode polarization and to stabilize the structure by acting as a pillar during intercalation and de-intercalation.[10–13] Cobalt (Co^{2+}) as a single dopant has also been studied by several groups. Wang *et al.*[14], Yang *et al.*[15] and Chantrasuwan *et al.*[16] investigated the electrochemical performance and changes in the structure of $LiFe_{0.99}Co_{0.01}PO_4$. The samples were synthesised using either a solid state or hydrothermal synthetic route. $LiFe_{0.99}Co_{0.01}PO_4$ showed improved electrochemical performance, improved electrode reaction kinetics as well as higher energy density. Gao *et al.*,[17] investigated $LiFe_{1-x}Co_xPO_4$ with x = 0.005, 0.010 and 0.020 using a oxalic acid assisted sol-gel synthetic route. $LiFe_{0.99}Co_{0.01}PO_4$ exhibited the best electrochemical performance with improved rate capability as well as improved structure stability. Song *et al.*[18] used a hydrothermal synthetic route to synthesise $LiFe_{1-x}Co_xPO_4$ (x = 0.005, 0.01, 0.015, 0.02 and 0.025). $LiFe_{0.99}Co_{0.01}PO_4$ showed improved cycle retention as well as the lowest energy barrier for Li^+ diffusion.

Zn^{2+} has not been used as a co-dopant in $LiFePO_4$ whereas Co^{2+} has been used as a co-dopant with zirconium (Zr^{4+}), nickel (Ni^{2+}) and magnesium (Mg^{2+}). Gao *et al.*[19] investigated co-doping with Zr^{4+} on the M1 site and Co^{2+} on the M2 site. The concentration of Zr^{4+} was kept constant whereas the Co^{2+} concentration was varied. First-principle calculations were used to study the electrochemical properties of $Li_{0.99}Zr_{0.0025}Fe_{1-x}Co_xPO_4$ (x = 0.005, 0.01, 0.015, 0.02). Co-doped samples showed enhanced electrochemical properties as well as improved structure stability. Co-doping with Co^{4+} and Mg^{2+} on the M2 site was investigated by Ding *et al.*[9]

$LiFe_{0.99}Mg_{0.005}Co_{0.005}PO_4$ was synthesised using a solid state synthetic route. This sample showed improved ionic mobility, improved initial discharge capacity and discharge efficiency as well as improved cycling performance and rate capability. This chapter focuses on the possibility of co-doping $LiFePO_4$ with Zn^{2+} and Co^{2+}. $LiFePO_4$ and $LiFe_{1-x-y}Zn_xCo_yPO_4$ (x = 0.025, 0.03, 0.04; y = 0.035, 0.03, 0.02, respectively) was synthesised. The doping range was based on the individual doping percentages that other research groups investigated.[10,11, 15, 17,18,20] The effects of these co-dopants had on the $LiFePO_4$ structure was fully explored using synchrotron powder X-ray diffraction with Rietveld analysis, Raman spectroscopy and X-ray absorption spectroscopy.

8.2. Sample preparation

The co-dopants were prepared in a similar manner as the samples discussed in sections 5.2 and 7.2 with a molar ratio of $3_{Li}: 1-x-y_{Fe}: x_{Zn}: y_{Co}: 1_{PO_4}$. The co-dopant precursors were $Zn(NO_3)_2$•$6H_2O$ (98%, Sigma Aldrich) and $Co(NO_3)_2 \cdot 6H_2O$ (puriss, Riedel-de Haën) and both dopants were dissolved in unpurged deionised water before the start of the experiment. The Zn^{2+}/Co^{2+}-solution was then added separately to the purged $FeSO_4/H_3PO_4$ solution followed by LiOH which was added dropwise (one Li^+ drop every 3 seconds). The Teflon bombs were filled to 25% of the total volume and placed in the oven. The oven temperature was 120°C and the synthesis time was 48 hours.

8.3. Results and discussion

8.3.1. Powder X-ray powder diffraction

The PXRD diffractograms were collected for $LiFePO_4$ and the co-doped $LiFe_{1-x-y}Zn_xCo_yPO_4$ (x = 0.025, 0.03, 0.04; y = 0.035, 0.03, 0.02, respectively) samples. The $LiFePO_4$ sample will be referred to as the undoped sample whereas the co-doped samples will be coded 2.5Zn-3.5Co (x = 0.025 and y = 0.035), 3Zn-3Co (x = 0.03 and y = 0.03) and 4Zn-2Co (x = 0.04 and y = 0.02). The $LiFePO_4$ sample was the same sample used in the Chapter 7 for the single dopant study. Rietveld refinements were performed on all samples (Fig. 8.1 – 8.2) using an X-ray wavelength determined to be 0.166316(1) Å and the reliability factors for the refinements are in Table 8.1. It was assumed that Zn^{2+} and Co^{2+} prefer the M2 site and was successfully incorporated into the structure during the refinement process by keeping the occupancy of the M2 site fixed to the co-doping concentration. This assumption was based on the occupancy

errors the small doping percentages produced during the refinement and the preference of Co^{2+} and Zn^{2+} to occupy the M2 site.[4] $LiFePO_4$ was identified as the major phase in all co-doped samples. Minor phases present in the samples are lithiophosphate (Li_3PO_4), the Fe- impurity[20] ($I4_1/a$, #88), as discussed in section 4.1.2 and tavorite ($LiFePO_4(OH)$). The total impurity phases in each sample constitutes less than 13% with 3Zn – 3Co having the highest total percentage (Table 8.2). The total percentage of impurities in co-doped samples are twice as high as the total percentage impurities in Zn^{2+} single doped samples (Table 7.3). A possible explanation for this observation is that the two different solutions were added separately to the $FeSO_4/H_3PO_4$ solution allowing for more oxygen to enter the purged solution. An unidentified phase was present in small percentages (indicated by *) as visible in the peak intensity. This phase was present in the 2.5Zn – 3.5Co sample. The unidentified impurity phase has been previously observed in other undoped samples (sections 4.2.1, 4.2.2 and 6.3.1) using this synthetic route. None of the impurity phases contained any of the dopants and it is possible that both metal ions were incorporated into the structure.

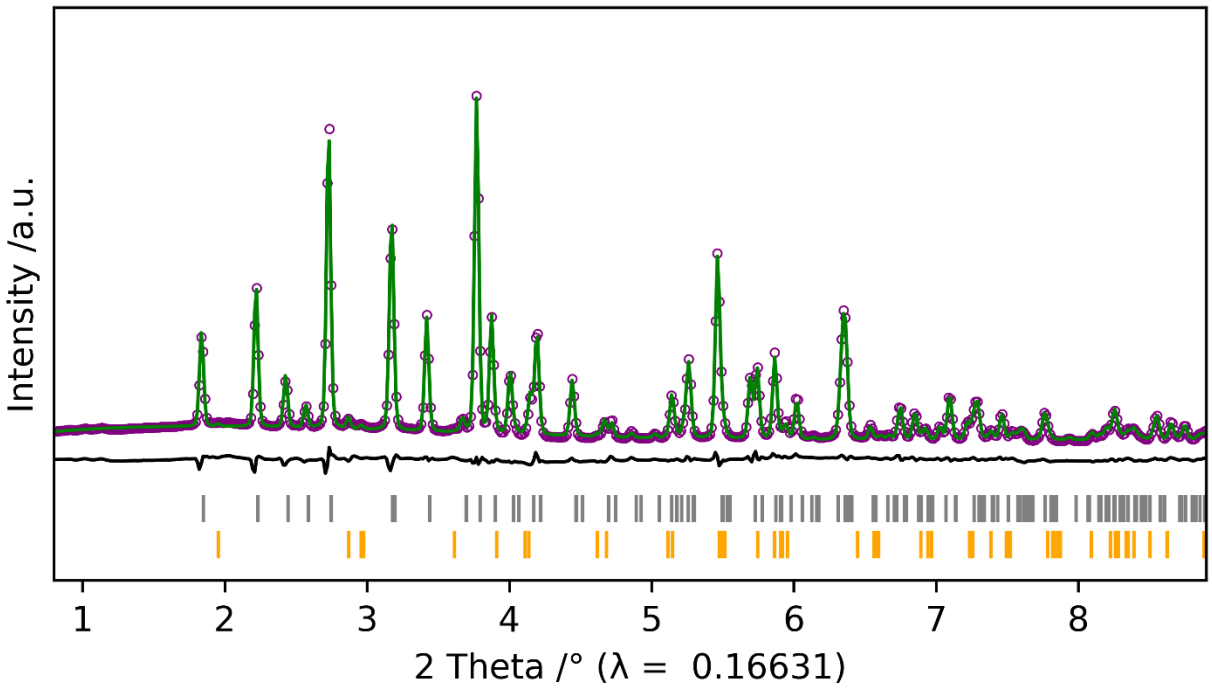

Figure 8.1: Synchrotron diffractogram of the undoped $LiFePO_4$ showing the observed (purple), calculated (green) and difference (black) plots generated from a Rietveld refinement analysis. Bragg reflections for $LiFePO_4$ and the Fe-impurity are indicated with the grey and yellow markers.

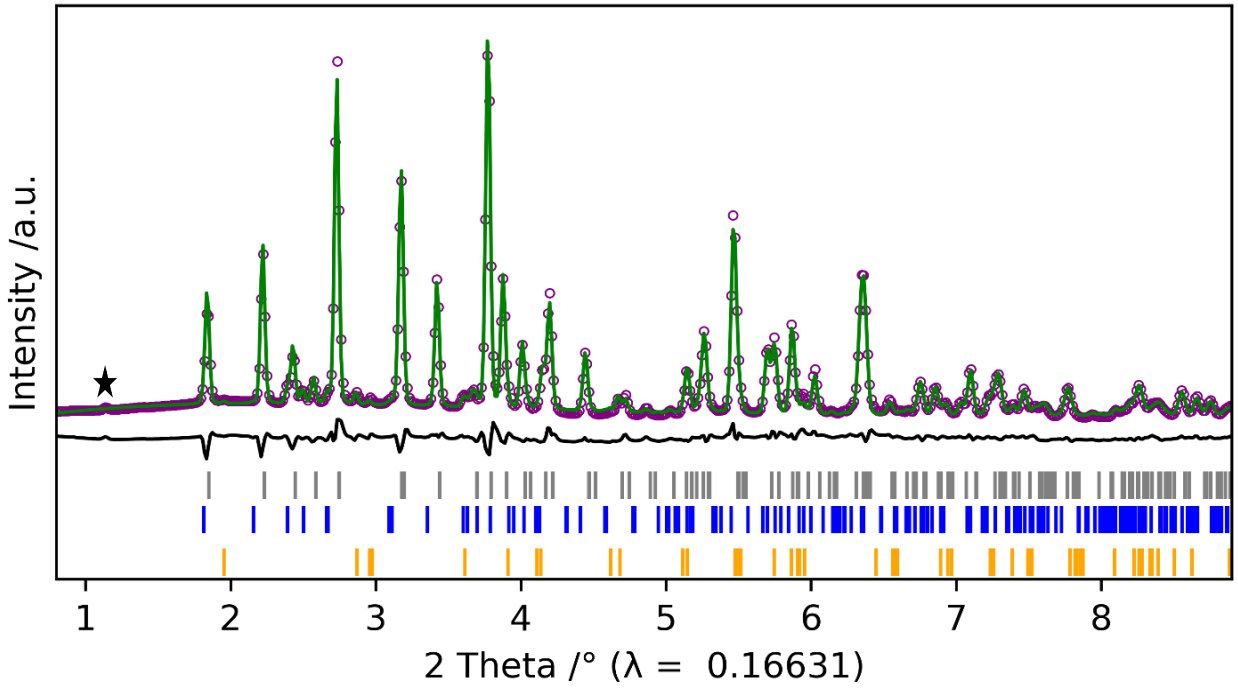

Figure 8.2: Synchrotron diffractogram of 2.5Zn – 3.5Co showing the observed (purple), calculated (green) and difference (black) plots generated from a Rietveld refinement analysis. Bragg reflections for $LiFePO_4$, Li_3PO_4 and the Fe-impurity are indicated with the grey, blue and yellow markers respectively. (*) indicates the unidentified impurity.

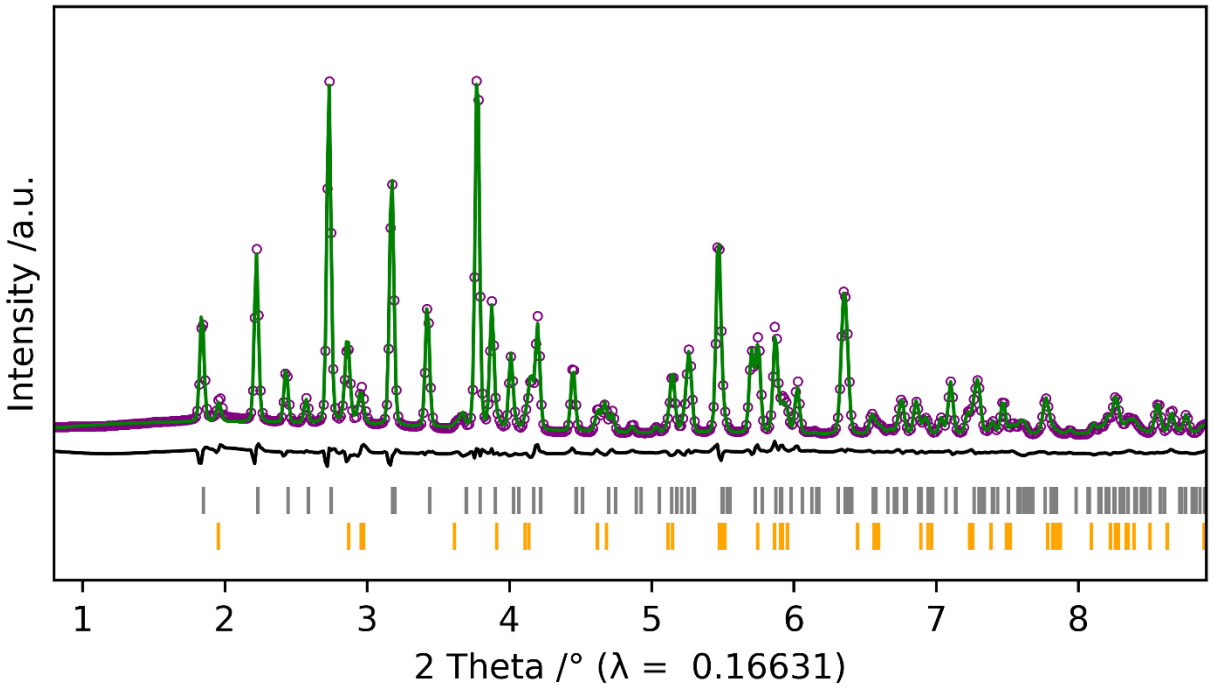

Figure 8.3: Synchrotron diffractogram of 3Zn – 3Co showing the observed (purple), calculated (green) and difference (black) plots generated from a Rietveld refinement analysis. Bragg reflections for $LiFePO_4$ and the Fe-impurity are indicated with the grey and yellow markers.

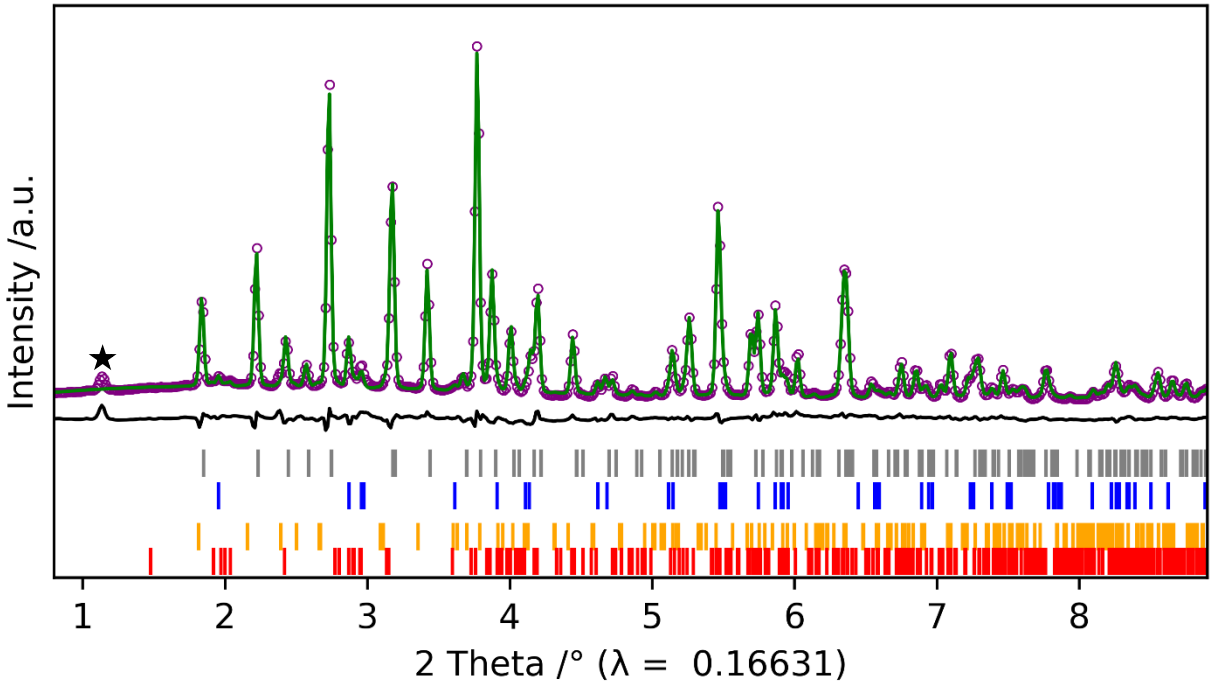

Figure 8.4: Synchrotron diffractogram of 4Zn – 2Co showing the observed (purple), calculated (green) and difference (black) plots generated from a Rietveld refinement analysis. Bragg reflections for $LiFePO_4$, Li_3PO_4, the Fe-impurity and $LiFePO_4(OH)$ are indicated with the grey, blue, yellow and red markers respectively. (*) indicates the unidentified impurity.

Table 8.1: Reliability factors for each Rietveld refinement.

	R_{wp}	R_p	R_{exp}	GOF
Undoped	5.06	3.94	16.92	0.30
4Zn – 2Co	5.63	4.20	15.84	0.36
3Zn – 3Co	5.12	3.96	16.44	0.31
2.5Zn – 3.5Co	6.54	4.93	15.39	0.43

Table 8.2: Multiphase analysis (%) for the undoped $LiFePO_4$ as well as the doped $LiFe_{1-x-y}Zn_xCo_yPO_4$.

	$LiFePO_4$	Fe-impurity	Li_3PO_4	$LiFePO_4(OH)$
Undoped	98.65	1.35	-	-
4Zn – 2Co	90.72	5.26	1.27	2.75
3Zn – 3Co	87.83	12.17	-	-
2.5Zn – 3.5Co	93.450	1.25	5.31	-

As mentioned in the introduction, Yang *et al.*[15] Chantrasuwan *et al.*[16] and Gao *et al.*[17] all determined the change in lattice parameters when doping with Co^{2+}. All three studies showed a decrease in these parameters. The a-lattice constant decreased from 10.321 to 10.295 Å,[15] 10.3328 to 10.3184 Å[16] and 10.3229 to 10.3002 Å.[17] The b-lattice constant decreased 5.984 to 5.960 Å,[15] 6.0093 to 6.0013 Å[16] and 6.0014 to 5.9893 Å.[17] Unlike the c-lattice parameters for the Zn^{2+} that either remained constant or increased the Co^{2+} dopant parameter showed a decrease from 4.692 to 4.685 Å,[15] 4.6949 to 4.6924 Å[16] and 4.6893 to 4.6791 Å.[17] The lattice parameters and the cell volume were extracted from the refinements for the $LiFePO_4$ phase and can be found in Table 8.3. The lattice parameters for the co-doped samples showed a slight decrease compared to that of the undoped sample. This is could be an indication that both Zn^{2+} and Co^{2+} successfully replaced some of the Fe^{2+} in the structure. The decrease in lattice parameters was due to the replacement of Fe^{2+} (0.78Å) in a high spin octahedral environment with Zn^{2+} (0.74Å) and Co^{2+} (0.75Å).[8, 10, 17,20] Both dopant metal ions have smaller ionic radii (as indicated in brackets) than that of the Fe^{2+} ion and this decrease in the lattice parameters was also observed for the individual dopants in other studies.[10,11, 14,17]

Table 8.3: Lattice parameters and volume for the $LiFePO_4$ phase of the undoped and Zn^{2+} - Co^{2+} co-doped $LiFePO_4$ samples.

	a (Å)	**b (Å)**	**c (Å)**	**Volume (Å^3)**
Undoped $LiFePO_4$	10.367(45)	6.0029(3)	4.7132(2)	293.31(2)
2.5Zn – 3.5Co	10.354(7)	6.0002(4)	4.7114(3)	292.70(3)
3Zn – 3Co	10.351(4)	6.0019(2)	4.7078(2)	292.47(2)
4Zn – 2Co	10.362(5)	6.0019(3)	4.7125(2)	293.08(3)

The decrease in the b-lattice indicates a shortening in the Li^+ diffusion pathway.[16,21] The 2.5Zn-3.5Co and 3Zn-3Co samples showed a decrease in the b-lattice parameter. A shorter pathway is electrochemically more favourable. The cell volume (Table 8.3) for the co-doped samples is smaller compared to that of the undoped sample. The shrinking cell volume also indicated that the Fe^{2+} atom was replaced with smaller ionic radii metals.[4, 10,11, 14,17] The cell volume for 4Zn – 2Co only decreases by 0.23Å^3. This is anomalous to the almost linear decrease in volume for 2.5Zn – 3.5Co and 3Zn – 3Co. The unit cell volume for the co-dopants is larger than the cell volume determined for the single dopant. This could be an effect of the higher percentage of impurity phases present.

The M2 site was only refined for the undoped $LiFePO_4$ sample but was kept fixed for the co-doped samples (Table 8.4). The M1 site showed the presence of antisite defects for all the synthesised samples. Fe on this site could possibly be the cause of amorphous Fe-containing impurities or the Fe-impurity detected with XRD. The 3Zn – 3Co sample had the highest percentage of Li^+ on the M1 site and therefore also the lowest degree of antisite defects present. The 4Zn – 2Co had the highest degree of antisite defects present on this site of all the samples. The occupancy on the M1 for the Zn^{2+} (Table 7.4) ranged between 89.97 – 94.64 %. There is a slight increase in the M1 site occupancies for the co-doped samples (90.90 – 94.74 %).

Table 8.4: Occupancy of Fe^{2+} on the M2 and Li and Fe^{2+} and/or Fe^{3+} on the M1 sites.

	M2 site	**M1 (Li^+) site**	**M1 (Fe^{2+}/Fe^{3+}) site**
Undoped $LiFePO_4$	99.14(7)	92.07(4)	7.93(34)
2.5Zn – 3.5Co	94	91.23(9)	8.77(78)
3Zn – 3Co	94	94.74(6)	5.26(56)
4Zn – 2Co	94	90.90(5)	9.10(43)

Individual and average interatomic bond distances can be found in Table 8.5 .Shortening of the average M2-O (Fe-O) and P-O interatomic bond distances stabilizes the $LiFePO_4$ structure and allows for better cyclic performance.[4, 17,22] The 2.5Zn – 3.5Co sample exhibited shortening of both the M2-O and P-O interatomic bond distance. All the co-doped samples showed shortening of the average P-O interatomic bond distance and not for M2-O. Shortening of these interatomic bond distances can provide information on the structural and thermal stability. A shorter distance indicates an increase in stability.[4, 17,23] The shortening of the M2-O bonds can also be an indication of the presence of Fe^{3+}-O bonds. Better electrochemical performance can be predicted by the widening of the Li^+ diffusion channel which allows for easier diffusion.[4, 17, 22,24] The widening of the diffusion channel is caused by the lengthening of the average M1-O interatomic bond distance. The 3Zn – 3Co and 4Zn – 2Co samples exhibited an increase in M1-O interatomic bond distance and could therefore exhibit better electrochemical performance. The M2-O interatomic bond distances for the co-doped samples were slightly longer than those determined for the Zn^{2+} single doped samples (Table 7.5). This could indicate that the co-doped samples have more Fe^{2+}-O bonds than the single doped samples. The average P-O and Li-O interatomic bond distances are shorter than those for the for the Zn^{2+} single doped samples.

Table 8.5: The individual and average interatomic bond distances (Å) of M2-O, P-O and M1-O.

	Undoped	**2.5Zn – 3.5Co**	**3Zn – 3Co**	**4Zn – 2Co**
M2–O(1)	2.177	2.171	2.158	2.178
M2–O(2)	2.069	2.057	2.092	2.083
M2-O(3) (×2)	2.044	2.038	2.043	2.043
M2-O(3) (×2)	2.228	2.218	2.240	2.239
Average M2–O	**2.132**	**2.123**	**2.136**	**2.138**
P – O(1)	1.550	1.523	1.554	1.544
P – O(2)	1.629	1.637	1.606	1.620
P – O(3) (×2)	1.602	1.608	1.596	1.594
Average P – O	**1.600**	**1.594**	**1.588**	**1.588**
M1-O (1) (×2)	2.184	2.110	2.184	2.188
M1-O (2) (×2)	2.010	2.102	2.080	2.083
M1-O(3) (×2)	2.202	2.171	2.158	2.178
Average M1-O	**2.132**	**2.128**	**2.141**	**2.150**

8.3.2. Raman Spectroscopy

Raman spectroscopy was used to ascertain if co-doping causes any structural changes to $LiFePO_4$. Raman analysis was performed on the undoped, 2.5Zn – 3.5Co, 3Zn – 3Co and 4Zn – 2Co $LiFePO_4$ (Fig. 8.5) samples. The characteristics of the most intense peak caused by the symmetric stretching of the PO_4^{3-} vibrational mode (Fig 8.5 inset) was used to determine these changes as it is difficult to identify any changes in the fingerprint region.[25] Raman spectroscopy was also used to determine if any other amorphous or low concentration

impurities were present in the samples. All the vibrational modes for $LiFePO_4$ could be assigned for the undoped and co-doped samples[26–28] (Table 8.6).

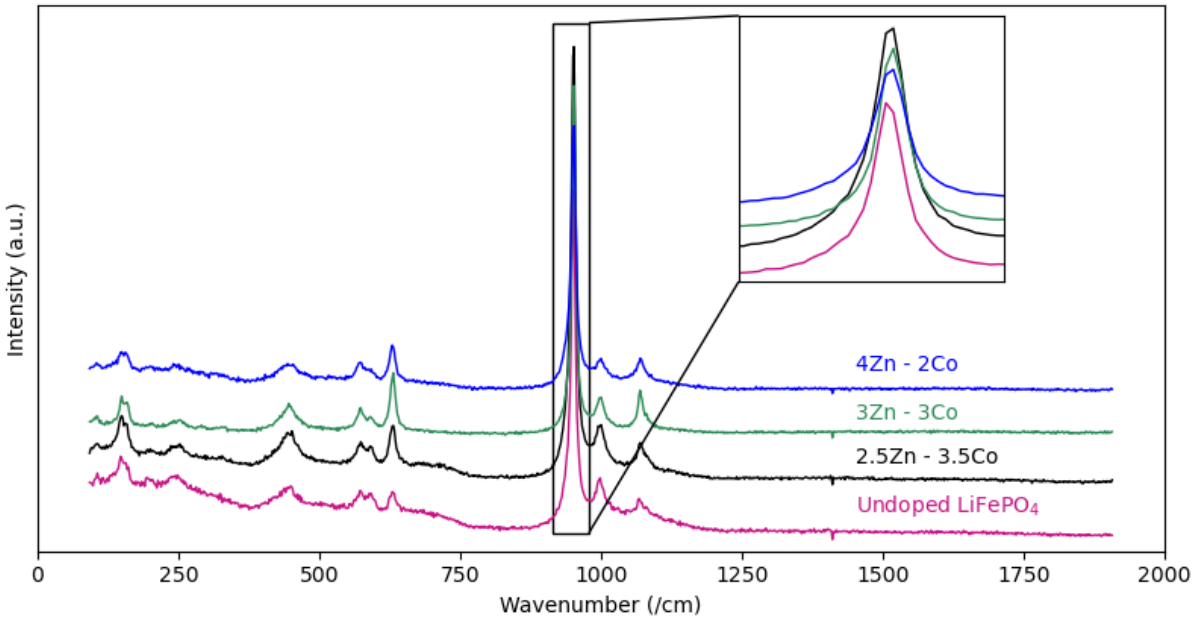

Figure 8.5: Raman spectra for the undoped and Zn^{2+} - Co^{2+} co-doped $LiFePO_4$ samples. The peaks due to symmetric stretching of PO_4^{3-} (950 – 951 cm^{-1}) are given in the inset (879 – 1118 cm^{-1}).

Table 8.6: Raman modes of the undoped and Zn^{2+}- Co^{2+} co-doped $LiFePO_4$ samples showing the assigned vibrational modes.

Wavenumbers (/cm)				Assignment
Undoped $LiFePO_4$	**2.5Zn – 3.5Co**	**3Zn – 3Co**	**4Zn – 2Co**	
103	103	102	104	PO_4^{3-} rotational and Fe^{2+} translational motion
150	149	152	153	
197	198	200	200	
243	249	249	245	
446	446	445	443	υ_2 (PO_4^{3-})
572	570	572	571	υ_4 (PO_4^{3-})
591	591	592	589	
630	630	630	629	
950	951	951	951	υ_1 (PO_4^{3-})
998	997	998	998	υ_3 (PO_4^{3-})
1068	1071	1069	1070	

The peak position for the most intense peak at ~950 cm^{-1} is caused by the symmetric stretching of the P-O vibration and it showed a minor blue shift (to higher wavenumbers) for the co-doped samples (Table 8.6). This shift suggests that the P-O bond distances of the tetrahedra are shorter[29,30] which improves the structure stability.[4, 17,23] All three co-doped samples also have

shorter average P-O interatomic bond distances (Table 8.6) as determined by XRD (Table 8.5), supporting what was found with Raman spectroscopy. Using the FWHM of the same peak any changes in the degree of ordering could be probed.[25,31] The FWHM for the undoped, 2.5Zn – 3.5Co, 3Zn – 3Co and 4Zn – 2Co $LiFePO_4$ samples were 7.91, 9.62, 8.60 and 9.82 cm^{-1}, respectively. The FWHM is larger for the co-doped samples than for the undoped sample. This increase for the co-doped samples suggests that co-doping decreases the degree of order of the structure caused by the perturbation of the PO_4^{3-} vibrations.[15,32,33] Previous studies showed that this decrease in the degree of order is accompanied by a decrease in crystallinity (decrease in peak intensity).[25, 31,34] The 2.5Zn – 3.5Co and 3Zn – 3Co samples showed an increase in intensity whereas 4Zn – 2Co showed a decrease in the intensity indicating a possible slight decrease in crystallinity although this was not really observed with XRD (Figs. 8.2 – 8.4). The Zn^{2+} single doped samples showed a shift to slightly lower wavenumbers for all the peaks including the intense peak at ~950 cm^{-1} indicating slightly less structure stabilization.

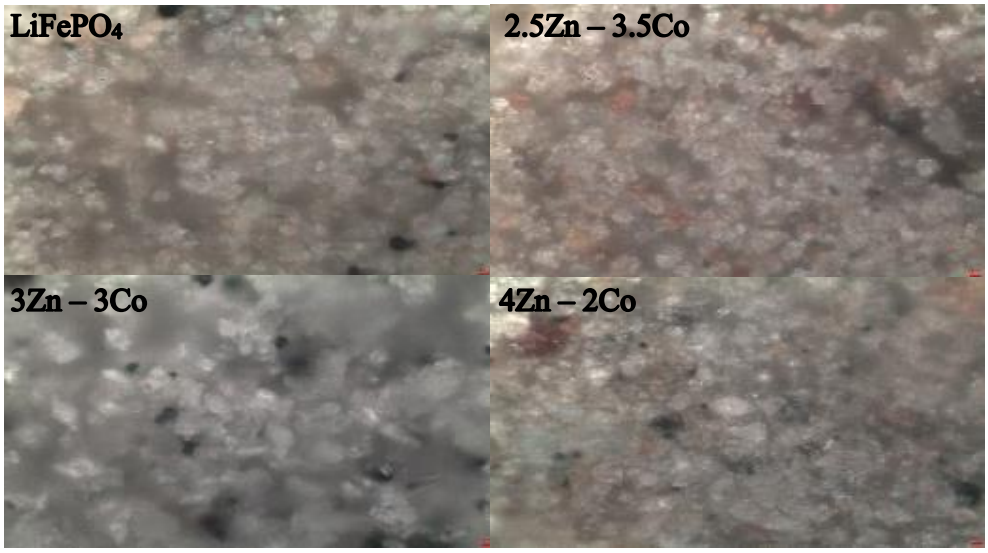

Image 8.1: Raman microscopic images of the undoped and Zn and Co co-doped $LiFePO_4$ samples.

The microscopic images (Image 8.1) again pointed to three different phases being present – shown as white, reddish brown and black. $LiFePO_4$ was identified as the white phase. The 2.5Zn – 3.5Co and 4Zn – 2Co images showed the pronounced red phase more than the undoped and 3Zn – 3Co samples. The undoped sample showed small reddish-brown crystals whereas the 3Zn – 3Co sample exhibited predominately the white and black phase. The impurity phases shown as black, light white and reddish brown in the samples were identified as $LiFePO_4(OH)$[35], Li_3PO_4[36] and a poorly crystalline phase that could possibly be α-Fe_2O_3,[37] respectively. For α-Fe_2O_3 only a broad peak between 1250 cm^{-1} – 1400 cm^{-1} could be

identified[37] and no other sharp peaks were visible. $LiFePO_4(OH)$ was present in the undoped, 4Zn – 2Co samples and possibly in the 3Zn – 3Co samples. $LiFePO_4(OH)$ was also detected in the 4Zn-2Co sample using XRD. In the 3Zn – 3Co sample the black particles produced poorly crystalline Raman spectra with only a few low intense peaks and the rest of the peaks were very broad making it difficult to fully identify the phase as $LiFePO_4(OH)$. Li_3PO_4 was present in the 2.5Zn – 3.5Co sample and was also detected using PXRD in the 2.5Zn – 3.5Co and 4Zn – 2Co. The possible Fe_2O_3 phase was present in all the samples except for the 3Zn – 3Co samples. Similar phases were identified in the Zn^{2+} single doped samples (section 7.3.1.2).

8.3.3. X-ray absorption spectroscopy

XAS for the Fe K-edge were collected for the undoped and co-doped samples. Before aligning and merging the data the spectra were truncated at 7708 eV to remove a peak caused by the Co K-edge and to ensure that the edge was not included in any further analyses. The normalized spectra (Fig. 8.6) were used for further analysis.

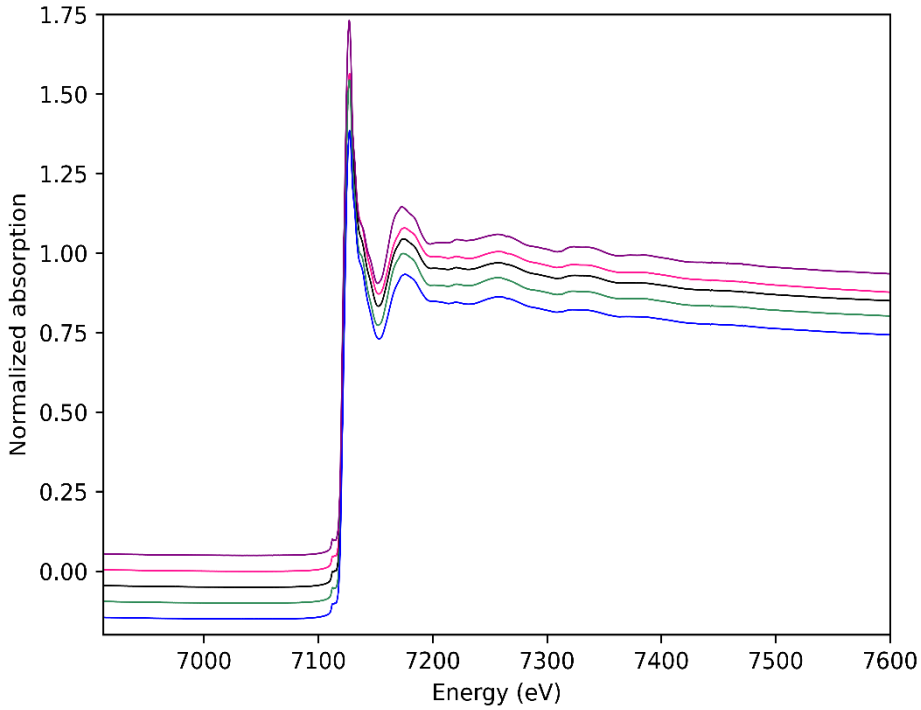

Figure 8.6: Normalized Fe K-edge spectra for the different Zn-doped samples compared to that of the $LiFePO_4$ – standard (purple). The spectra for undoped, 2.5Zn – 3.5Co, 3 Zn – 3Co and 4Zn – 2Co $LiFePO_4$ samples are indicated in pink, black, green and blue, respectively.

(i) XANES:

The same three standards ($LiFePO_4$, $FePO_4 \bullet 4H_2O$ and α-Fe_2O_3) used in section 7.3.2.1 were utilised in this section to compare the peak positions and peak intensities. A more detailed

description of the standards used can be found in section 2.2.3.1. All samples display both the t_{2g} (~7112 eV) and e_g (~7114 eV) peaks present in the $LiFePO_4$ standard (Fig. 8.7).[38,39] Only minor peak shifts occurred, indicating that some Fe^{2+} has been oxidised to Fe^{3+} causing the shift to slightly higher energy values (Table 8.7). The t_{2g} peak of the samples generally showed slight a decrease in peak intensity whereas the e_g peaks of the samples showed an increase in the intensity (Fig. 8.7 and Table 8.7). This could indicate that the orbitals situated between the axes experience a decrease in distortion[40] and the e_g orbitals that are along the axes might experience more distortion due to the repulsion present.[40] The 3Zn-3Co could experience similar distortion to that of the $LiFePO_4$ standard based on the similarity in the intensity whereas the lower doping percentage showed an increase in the distortion. The extent to which the e_g peak increased in intensity is higher for the Zn^{2+}-doped samples (Table 7.8) than was observed for the co-doped samples (Table 8.7). The changes in the intensity can also be indicative of changes in Fe^{2+} and Fe^{3+} concentrations.

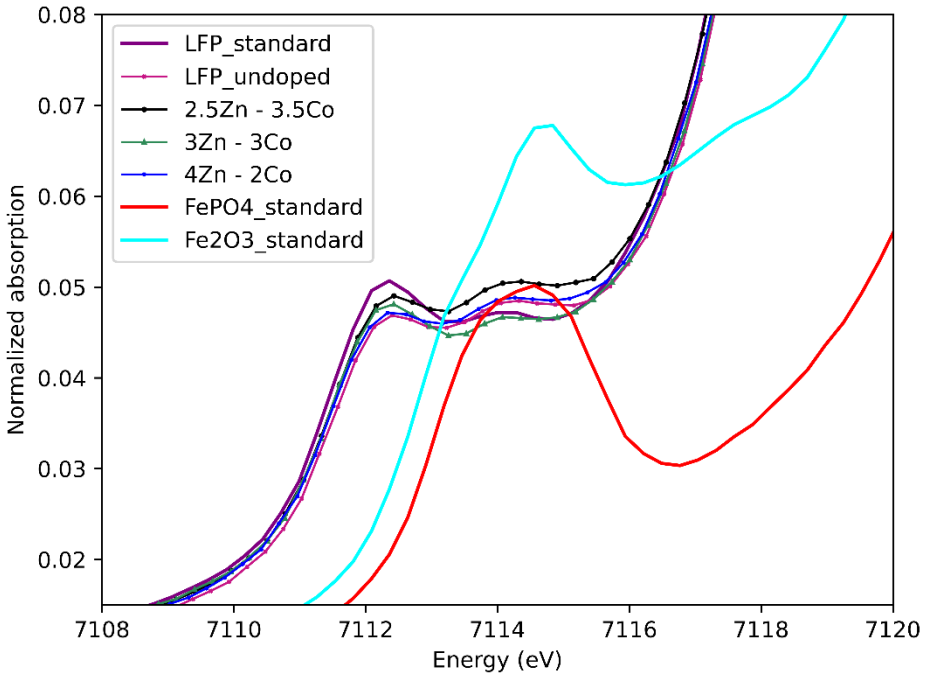

Figure 8.7: Comparison normalized Fe K-edge XANES pre-edge region of the different undoped and Zn^{2+}- Co^{2+} co-doped $LiFePO_4$ samples.

Table 8.7: The different pre-edge peak intensities and peak positions for the undoped and Zn^{2+}-Co^{2+} co-doped $LiFePO_4$ samples.

Sample	Peak position 1 (eV)	Peak intensity 1 (au)	Peak position 2 (eV)	Peak intensity 2 (au)
$LiFePO_4$	7112.19	0.050	7114.09	0.047
$FePO_4$	-	-	7114.27	0.050
Fe_2O_3	-	-	7114.43	0.067
Undoped	7112.21	0.045	7114.07	0.048
2.5Zn – 3.5Co	7112.45	0.047	7114.28	0.050
3Zn – 3Co	7112.37	0.046	7114.08	0.045
4Zn – 2Co	7112.39	0.045	7114.31	0.048

The rising absorption edge (Fig. 8.8) showed a shift to higher energies for the undoped and co-doped samples compared to the standard. This slight shift indicates that some of the Fe^{2+} was oxidised to Fe^{3+}.[39,41] This shift gives the trend of $LiFePO_4$ > 3Zn-3Co > 2.5Zn-3.5Co > undoped > 4Zn-2Co ranging from the highest Fe^{2+} content to the lowest. The main edge (Fig. 8.8 and Table 8.8) showed no major peak shift to higher energies but the slight shift did suggest that some of the Fe^{2+} was oxidised to Fe^{3+},[39,42,43] although this was minute because the peak positions are not close to that of the Fe^{3+} standards. The shift in peak positions for the main edge follow the same trend as described above which is expected. This trend is from the highest Fe^{2+} content to the lowest.

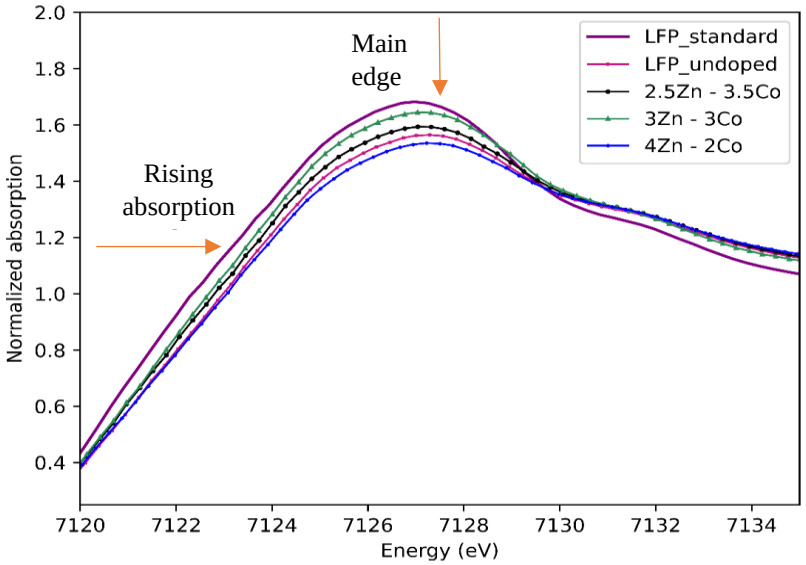

Figure 8.8: Comparison of the $LiFePO_4$ standard with the different undoped and Zn^{2+}- Co^{2+} co-doped $LiFePO_4$ samples.

Table 8.8: The different main edge peak intensities and peak positions for undoped and Zn^{2+}-Co^{2+} co-doped $LiFePO_4$ samples.

Sample	Peak position (eV)	Peak intensity (au)
$LiFePO_4$	7126.97	1.68
$FePO_4$ (not shown)	7131.92	1.54
Fe_2O_3 (not shown)	7133.75	1.53
Undoped	7127.26	1.56
2.5Zn – 3.5Co	7127.18	1.55
3Zn – 3Co	7127.12	1.61
4Zn – 2Co	7127.38	1.50

Linear combination fitting (LCF)

All three standards with the different bonding environments were used to perform LCF analysis on all the samples (Figs. 8.9 – 8.12). The fitting range used was between 7100 – 7153 eV. The LCF fitting procedure described in section 2.2.3.1 was also applied here. The R-factors and reduced chi-square factors are given in Table 8.9.

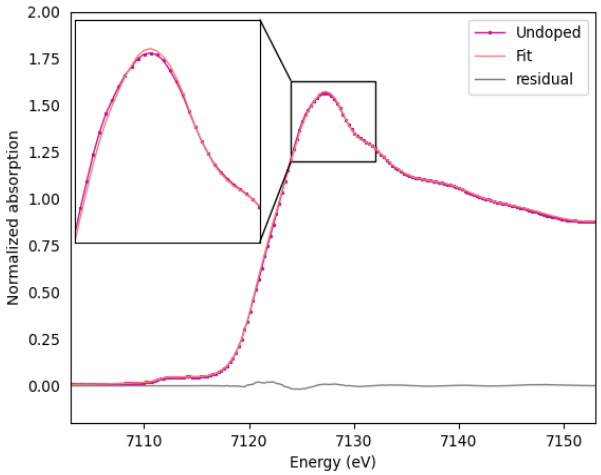

Figure 8.9: LCF best fit (coral) of the undoped $LiFePO_4$ sample of the normalized Fe K-edge XANES spectrum (pink) along with the residual spectrum (grey).

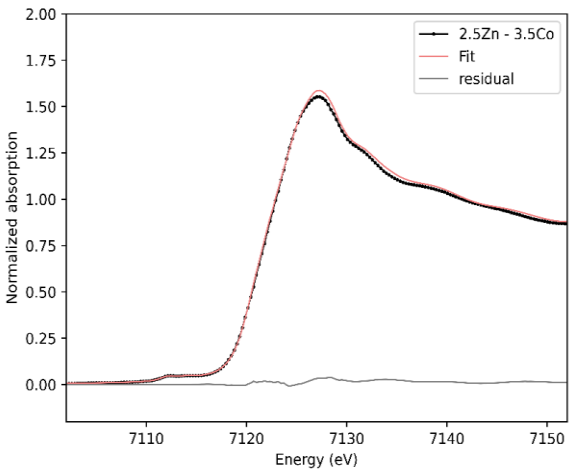

Figure 8.10: LCF best fit (coral) of the 2.5Zn-3.5Co $LiFePO_4$ sample of the normalized Fe K-edge XANES spectrum (black) along with the residual spectrum (grey).

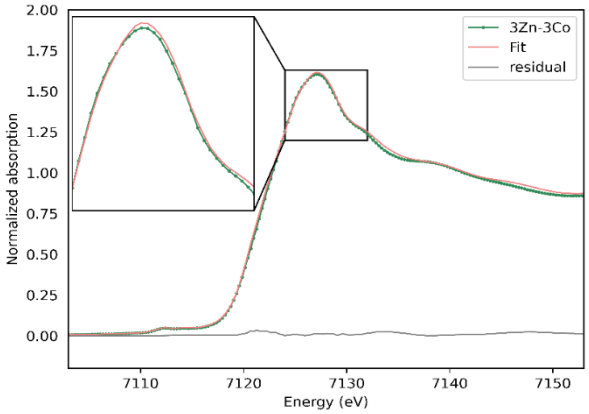

Figure 8.11: LCF best fit (coral) of the 3Zn-3Co $LiFePO_4$ sample of the normalized Fe K-edge XANES spectrum (green) along with the residual spectrum (grey).

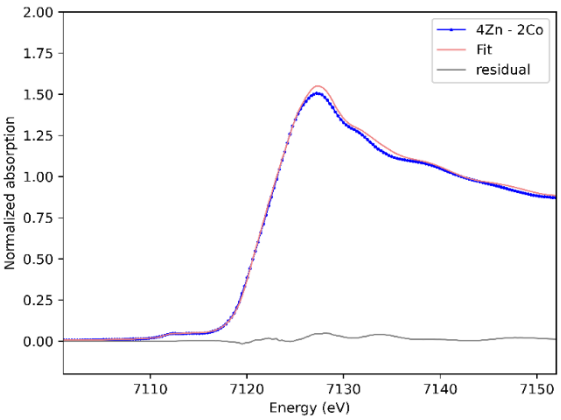

Figure 8.12: LCF best fit (coral) of the 4Zn-2Co $LiFePO_4$ sample of the normalized Fe K-edge XANES spectrum (blue) along with the residual spectrum (grey).

Table 8.9: LCF goodness of fit parameters for the undoped and Zn^{2+}- Co^{2+} co-doped $LiFePO_4$ samples.

Sample	R-factor	Reduced chi-square
Undoped	0.00012	0.000033
2.5Zn-3.5Co	0.00073	0.00020
3Zn-3Co	0.00052	0.00016
4Zn-2Co	0.00111	0.00031

All the samples showed mismatch between the fit and the experimental data. This mismatch can be described as under fitting compared to the fitted curve. Under fitting indicated that a bonding environment or different environment was missing from the set of standards used for the analysis. The results for the fit could be improve if other standards with different bonding environments were added and included as possible constituents present in the sample.[44] The undoped and 3Zn-3Co samples showed the least amount of mismatch indicating that the standards were suitable in describing the environments present in those samples. The different standard weightings for each sample were determined through LCF analysis (Table 8.10). The undoped sample had displayed similar environments to all three standards, whereas the co-doped samples only had environments similar to $LiFePO_4$ and Fe_2O_3. The 3Zn-3Co sample had the highest amount of Fe^{2+} present and the 4Zn-2Co sample had the lowest amount of Fe^{2+} present. This is somewhat surprising as the 3Zn-3Co sample had the highest percentage of impurities present as detected by XRD although the Fe-impurity phase contains both Fe^{2+} and

Fe^{3+}. The trend predicated using the rising absorption edge and the main absorption edge was confirmed with the quantitative analysis. The highest Zn^{2+} single doped sample (0.77) and co-doped samples (0.803) shows an increase in the Fe^{2+} weighting. This can also be seen with the increase in the Fe-O interatomic bond distances for the 4Zn-2Co sample.

Table 8.10: LCF weight percentage of the different components present in the undoped and Zn^{2+}- Co^{2+} co-doped $LiFePO_4$ samples.

Sample	$LiFePO_4$ ($Fe^{2+}O_6$)	Fe_2O_3 ($Fe^{3+}O_6$)	$FePO_4$ ($Fe^{3+}O_6$)
Undoped	85(1)	8(1)	7(1)
2.5Zn-3.5Co	86(1)	14(3)	-
3Zn-3Co	90(1)	10(1)	-
4Zn-2Co	80(1)	20(1)	-

(ii) EXAFS

The same procedure that was used for the doped samples (section 8.3.2.1 (i)) and outlined in the Artemis User Guide[45] for the co-doped sample set. For the co-doped sample set each atom was individually considered to determine how many Fe atoms had to be replaced. Using equation 1, the replacement of the amount of Fe atoms was determined (Table 8.11). The total doping percentage of 6% gave a Fe^{2+} replacement of 0.24 atoms. This value is much lower than the value of 1 and would lead to a high overestimation.

$$\text{Amount of iron atoms to be replaced} = (\text{dopant percentage}) \times (\text{nr of nearest neighbour iron atoms}) \quad \textbf{(1)}$$

Table 8.11: The amount of Fe to be replaced by the co-dopants in the feff.inp file.

Doping percentage	Replacement (Zn^{2+})	Replacement (Co^{2+})
2.5Zn – 3.5Co	0.1	0.14
3Zn – 3Co	0.12	0.12
4Zn – 2Co	0.16	0.08
Total doping percentage of 6%	0.24	

The individual replacement values (Table 8.11) are also still very low and because of the co-doping, two Fe^{2+} sites will have to be replaced, one for each dopant and 50% of the available sites. The modified feff.inp file can be found in Appendix A8.2. Including these atoms were

attempted and two Fe^{2+} sites were replaced with Zn^{2+} and Co^{2+} with the overestimation of each dopant to 1. This inclusion led to very high (disorder ± error) values and showed no improvement to the fit. The dopants were not included in the refinements when using an underestimation to zero dopants in the structure. All the FT-EXAFS are phase corrected. EXAFS analysis was used to determine if any changes in the local structure occurred upon co-doping $LiFePO_4$ with Zn^{2+} and Co^{2+}. As a comparison tool between the undoped and different co-doped samples, the Fe k^3-weighted $[k^3\chi(k)]$ spectra (Fig. 8.13) as well as the magnitude of the Fourier Transform (Fig. 8.14) was examined. The k-range used for fitting was 3 – 12.350 $Å^{-1}$. The k-range had to be shortened due to the truncation of the data.

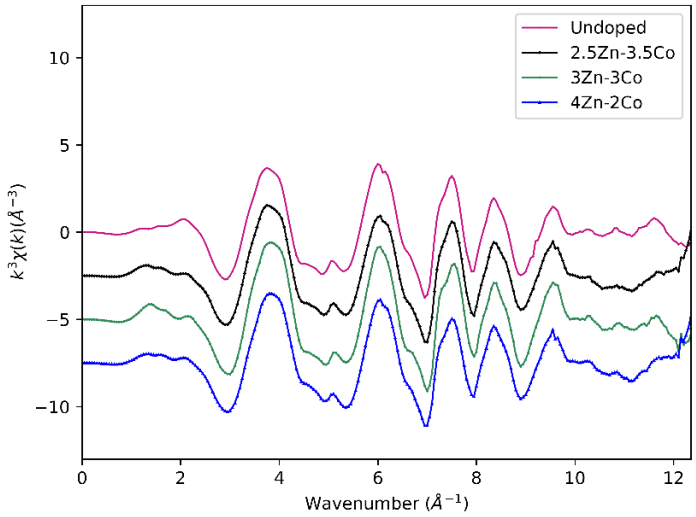

Figure 8.13: Comparison of the Fe k^3-weighted $[k^3\chi(k)]$ spectrum of the different synthesised samples (undoped and Zn^{2+}-Co^{2+}co-doped samples).

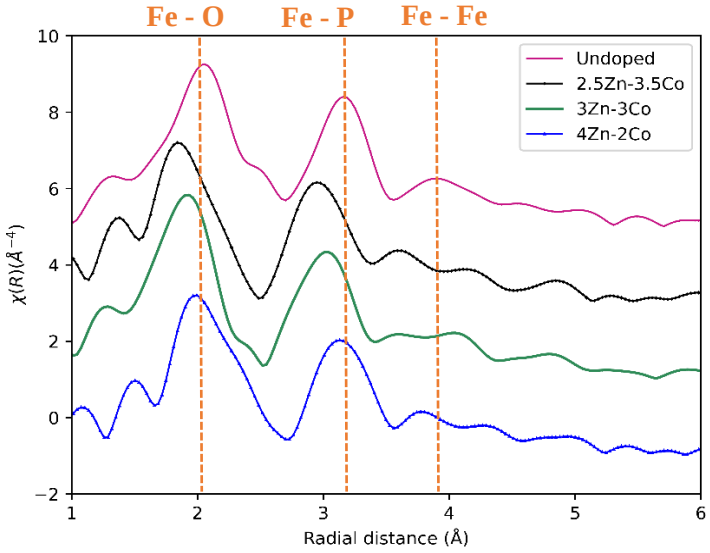

Figure 8.14: Phase corrected FT magnitude EXAFS $k^3\chi(k)$ data comparing radial distance of the different coordination shells of the undoped and Zn^{2+}-Co^{2+} co-doped samples.

There were no major changes in the local structure for either the Fe k^3-weighted $[k^3\chi(k)]$ spectra or the FT magnitude spectra. The Fe k^3-weighted $[k^3\chi(k)]$ spectra show slight changes in the intensity of some features but no major changes indicating no changes in local structure between samples. The small difference in features could be due to the addition of the co-dopants. The FT magnitude showed the presence of all three coordination shells previously noted. The peak positions show that there are possible changes in the interatomic distances or the changes in the bonding distribution for the first coordination shell due to the shouldering present for the undoped and 3Zn-3Co samples. There also seems to be a possible correlation between the co-doping concentration and the peak positions observed in Figure 8.14. All the co-doped samples show a shorter radial distance compared to the undoped sample. As co-doping concentration increases for zinc and decreases for cobalt the radial distance increases. These changes can only be properly investigated by performing EXAFS analysis and determining the local structure.

Local structure determination

The local structure was determined for the undoped and three co-doped $LiFePO_4$ samples (Figs. 8.15 – 8.18). The fitting method as described in section 2.2.3.2 was used for the undoped and co-doped samples. This method allowed for the use of a distorted Fe-O octahedra as shown by a pre-edge region of Figure 8.7. Only scattering paths that improved the fit were added. To determine if the fit improved, the reduced χ^2- value was monitored– a decrease in this value indicated that the fit was improved. To determine the quality of the fit the R-factor, ΔE_o (Table 8.12) and the size of the calculated errors were used. The R-factors were all less than 2% indicating a good fit.[44] These R-factors although acceptably low are higher than the R-factors determined for the fitted data in section (section 4.2.4) and (section 8.3.2.1 (ii)). The ΔE_0 as determined from the fits (Table 8.12) are within the acceptable range of $-10 < \Delta E_0 < 10$. The S_o^2 for the samples were between 0.76 – 0.83 and 14 variables were refined using 22 independent points for each fit. The experimental data together with the fits were presented in k-space, FT magnitude and real space of the Fourier Transform (FT real) as shown in Figures 8.15 – 8.18.

Table 8.12: The reliability factor and energy shift of the undoped and Zn^{2+}- Co^{2+} co-doped $LiFePO_4$ samples.

Sample	R-factor (%)	E_0 (eV)	ΔE_0 (eV)
Undoped	0.59	7122.83	-2.4(9)
2.5Zn-3.5Co	0.78	7122.00	-1.8(8)
3Zn-3Co	0.82	7120.90	-1.3(9)
4Zn-2Co	0.73	7121.93	-1.4(8)

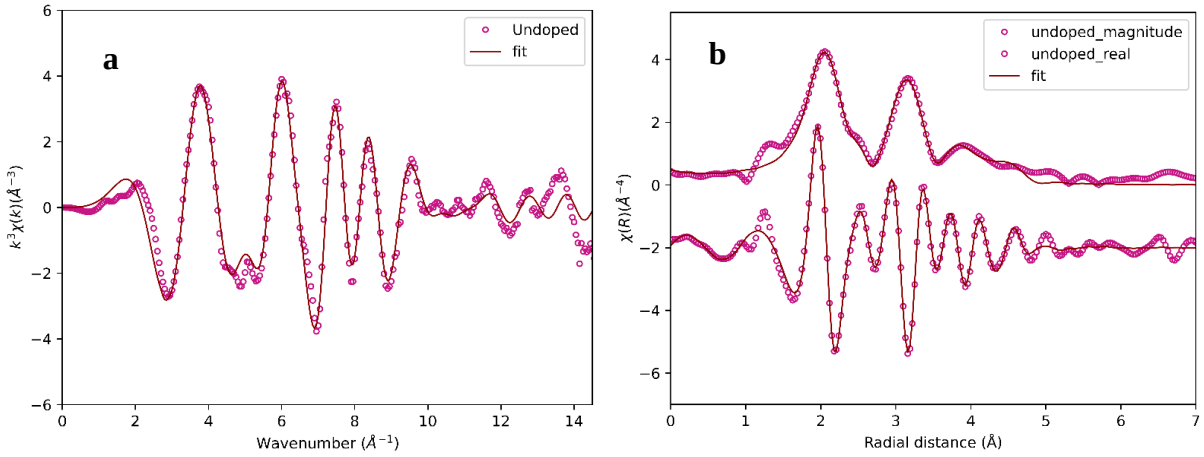

Figure 8.15: (a) The experimental Fe k^3-weighted $[k^3\chi(k)]$ spectrum and (b) the experimental FT magnitude (top) and FT real (bottom) of the EXAFS $k^3\chi(k)$ data (pink) and the theoretical FEFF fit (maroon) of the undoped sample. The fitting range for (a) was 3 – 12.350 Å $^{-1}$ and for (b) 1.3 – 5 Å.

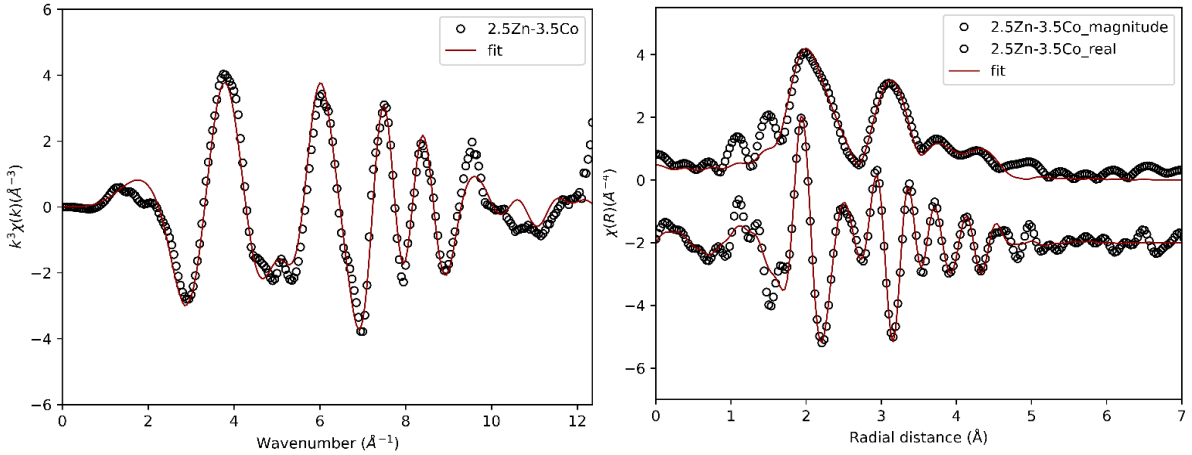

Figure 8.16: (a) The experimental Fe k^3-weighted $[k^3\chi(k)]$ spectrum and (b) the experimental FT magnitude (top) and FT real (bottom) of the EXAFS $k^3\chi(k)$ data (black) and the theoretical FEFF fit (maroon) of the 2.5Zn-3.5Co sample. The fitting range for (a) was 3 – 12.350 Å $^{-1}$ and for (b) 1.3 – 5

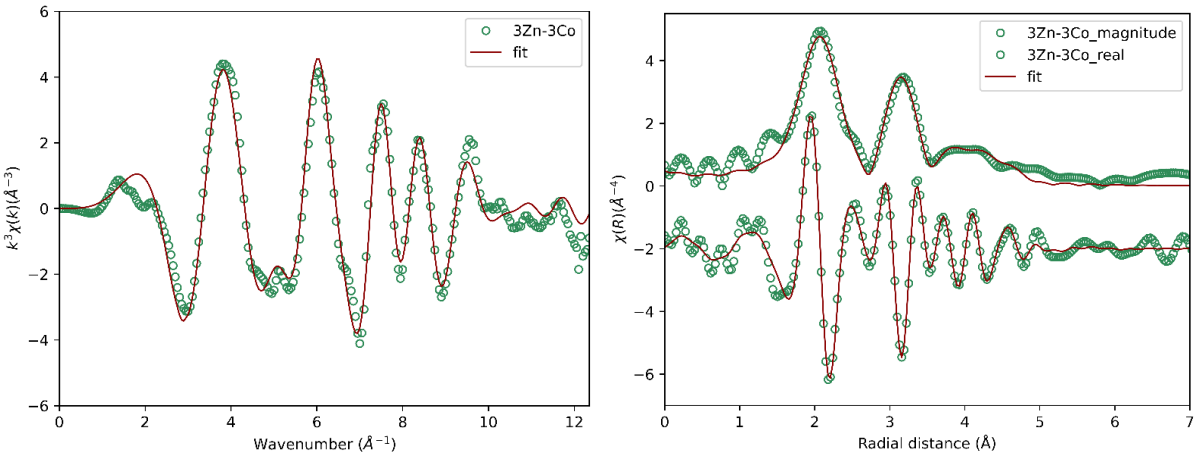

Figure 8.17: (a) The experimental Fe k^3-weighted $[k^3\chi(k)]$ spectrum and (b) the experimental FT magnitude (top) and FT real (bottom) of the EXAFS $k^3\chi(k)$ data (green) and the theoretical FEFF fit (maroon) of the 3Zn-3Co sample. The fitting range for (a) was 3 – 12.350 Å $^{-1}$ and for (b) 1.3 – 5 Å.

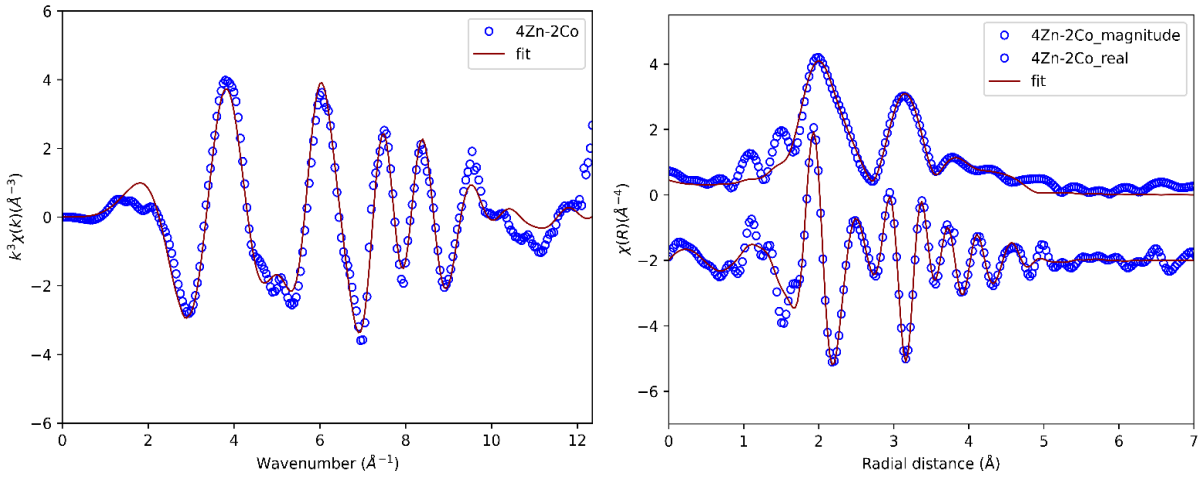

Figure 8.18: (a) The experimental Fe k^3-weighted $[k^3\chi(k)]$ spectrum and (b) the experimental FT magnitude (top) and FT real (bottom) of the EXAFS $k^3\chi(k)$ data (blue) and the theoretical FEFF fit (maroon) of the 4Zn-2Co sample. The fitting range for (a) was 3 – 12.350 Å $^{-1}$ and for (b) 1.3 – 5 Å

Description of the coordination shells:

All three coordination shells were present in the undoped and co-doped samples. The individual peaks showed no splitting or flattening indicating the local structure remained the same (Fig. 8.14).[46] The coordination shells were once again Fe-O, Fe-P and Fe-Fe. The different shells, coordination numbers, interatomic distances and Debye-Waller factors describing the disorder is given in Table 8.13. The average interatomic distances and Debye-Waller factors are in Table 8.14. As seen with the Zn^{2+} single doped EXAFS FT magnitude (Fig. 7.15) and structural parameters obtained from the fits (Table 7.15 and Table 7.16) the FT magnitude (Table 8.14) showed more peak feature changes and changes in the radial distance for all three coordination shells. These changes were again not reflected in the structural parameters (Table 8.13 and

Table 8.14) that showed almost no deviation with doping percentage. This can be an effect of the dopants that was not taken into account when doing the EXAFS modelling. As already mentioned, including such low doping percentages especially replacing two atoms with low percentages, led to a decrease in the quality in the fit and large disorder errors.

Table 8.13: Structural parameters determined using FEFF for the first, second and third coordination shells of the undoped and Zn^{2+}- Co^{2+} co-doped samples.

Sample	Shell	Coordination number	Average interatomic distance (Å)	Debye-Waller factor ($Å^2$)
Undoped	Fe-O2	4	2.09(1)	0.013(5)
	Fe-O3	2	2.05(1)	0.011(6)
	Fe-P1	1	2.823(8)	0.007(2)
	Fe-P2	4	3.248(8)	0.007(1)
	Fe-Fe1	2	3.82(1)	0.009(1)
	Fe-Fe2	2	4.64(1)	0.012(4)
2.5Zn-3.5Co	Fe-O1	4	2.13(1)	0.008(2)
	Fe-O3	2	1.99(1)	0.005(2)
	Fe-P1	1	2.820(9)	0.007(2)
	Fe-P2	4	3.244(9)	0.008(1)
	Fe-Fe1	2	3.82(2)	0.009(2)
	Fe-Fe2	2	4.64(2)	0.012(5)
3Zn-3Co	Fe-O1	4	2.12(1)	0.007(1)
	Fe-O3	2	1.98(1)	0.005(2)
	Fe-P1	1	2.825(9)	0.009(3)
	Fe-P2	4	3.249(9)	0.008(1)
	Fe-Fe1	2	3.82(2)	0.011(3)
	Fe-Fe2	2	4.64(2)	0.010(4)
4Zn-2Co	Fe-O1	4	2.12(1)	0.008(1)
	Fe-O3	2	1.98(1)	0.005(1)
	Fe-P1	1	2.828(8)	0.008(2)
	Fe-P2	4	3.253(8)	0.008(1)
	Fe-Fe1	2	3.82(2)	0.009(2)
	Fe-Fe2	2	4.64(2)	0.012(5)

The two reported studies by Tabassam *et al.*[47] and Minicucci *et al.*[48], as described in section 7.3.2.1 (ii), where $LiFePO_4$ was doped with Ni^{2+} (0.69 Å)[20] was used here as the comparative study as well. In both studies the effect of doping was investigated using the Fe K-edge and the Ni K-edge and the focus was on the Fe-O and Fe-P shells. Both co-dopant radii (Zn^{2+}- 0.74 Å and Co^{2+}- 0.75 Å)[20] used in this work and Ni^{2+} are smaller than Fe^{2+} (0.78 Å).[20] No EXAFS

modelling for these co-dopants using the Fe K-edge was found and this above mentioned study will be used.

In this work only the Fe K-edge was used to investigate the effect of co-dopants on the $LiFePO_4$ structure. The average size of the octahedra were not really affected by the addition of co-dopants or by the concentration range of the co-dopants and the average interatomic distance remained almost constant (Table 8.14). The longer interatomic distances are longer for the co-doped samples than for the undoped samples and the shorter distances are slightly shorter for the co-doped samples than for the undoped samples (Fig. 8.19). The actual position (axial or equatorial) of the different distances cannot be determined from this work and would be speculation. For the longer interatomic distances Minicucci *et al*.[48] determined that the longer interatomic distance is affected by the Ni^{2+} dopant. Co-doping with Zn^{2+} and Co^{2+} in this data set affected both the shorter and longer interatomic distances to some extent. The shorter and longer interatomic distances are more or less constant for the 3Zn-3Co and 4Zn-2Co samples (Table 8.13 and Fig. 8.19). Minicucci *et al*.[48] determined that the degree of disorder increases over a doping concentration range of $LiFe_{1-x}Ni_xPO_4$ where $x = 0.03, 0.05, 0.01, 0.015$. There is no change in disorder between the co-doped samples around the shorter interatomic distance (Fig. 8.20) whereas the disorder around the longer interatomic distance show slightly more variation (Fig. 8.20). There is less disorder for the co-doped than for the undoped samples. Tabassam *et al*.[47] observed the same trend regarding constant disorder around the shorter interatomic distances. Comparing the Fe-O shells for the Zn^{2+} single doped and co-doped studies showed that interatomic distances (2.08 – 2.09 Å) are similar but that the disorder (0.010 – 0.011 $Å^2$) has decreased quite a bit for the co-doped samples (0.006 – 0.007 $Å^2$).

Table 8.14: The average interatomic distance and average Debye-Waller factor of the first coordination shell.

Shell	Sample	Average interatomic distance (Å)	Average Debye-Waller factor (Å^2)
Fe-O	Undoped	2.08	0.012
	2.5Zn-3.5Co	2.08	0.007
	3Zn-3Co	2.07	0.006
	4Zn-2Co	2.07	0.007
Fe-P	Undoped	3.160	0.007
	2.5Zn-3.5Co	3.159	0.008
	3Zn-3Co	3.164	0.008
	4Zn-2Co	3.168	0.008
Fe-Fe	Undoped	4.23	0.011
	2.5Zn-3.5Co	4.23	0.011
	3Zn-3Co	4.23	0.011
	4Zn-2Co	4.23	0.011

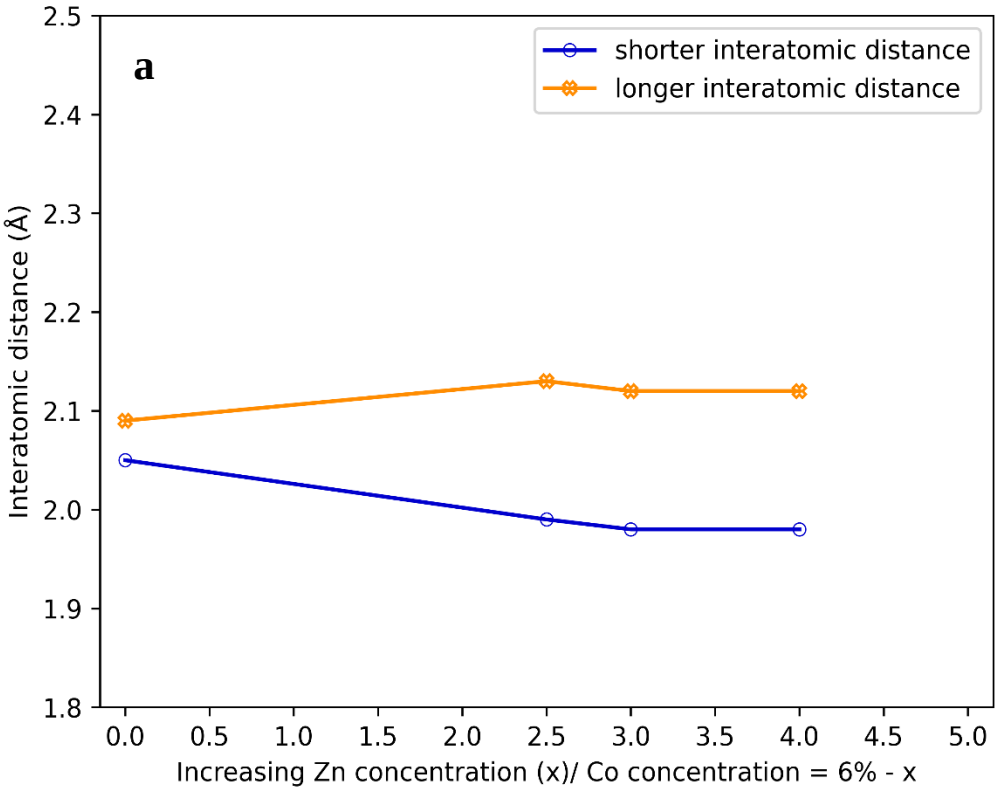

Figure 8.19: The changes in the interatomic distance of the first (Fe-O) coordination shell.

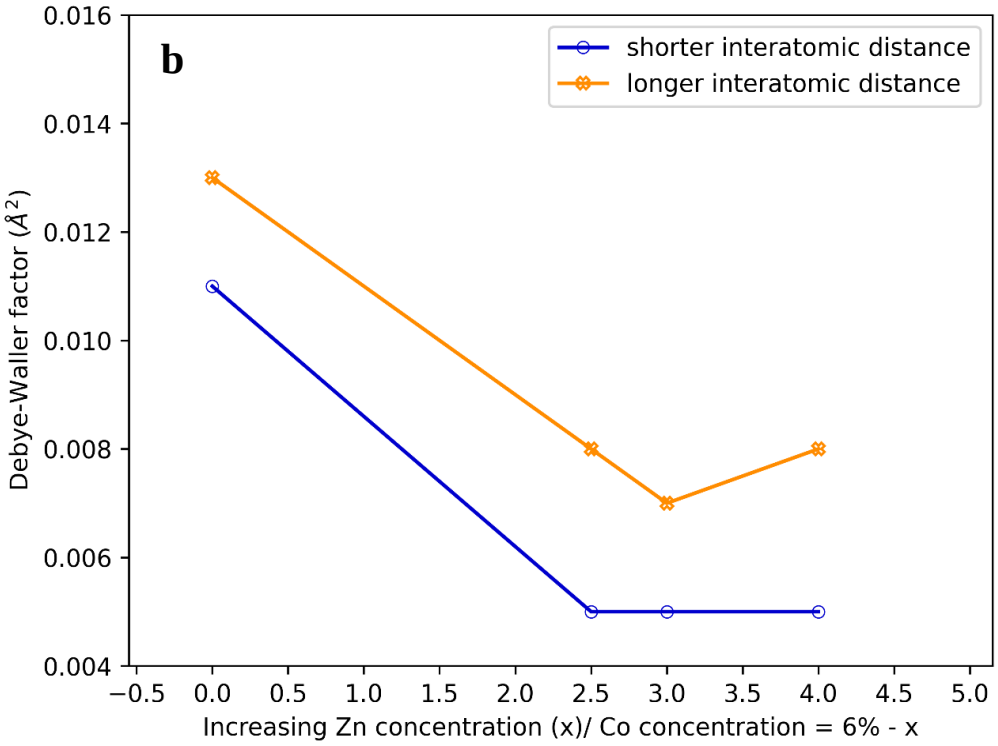

Figure 8.20: The changes in the disorder of the first (Fe-O) coordination shell.

For the Fe-P coordination shell Minicucci *et al.*[48] determined that this shell showed no significant change for either the interatomic distance or the disorder present in this shell. Co-doping with Zn^{2+} and Co^{2+} had some effect on the shorter interatomic distance but had very little effect on the longer interatomic distance (Table 8.13 and Table 8.14). The shorter interatomic distance showed that the disorder was not constant over the co-doping concentration range whereas the disorder around the longer interatomic distance was the same for all the co-doped samples (Fig. 8.21). The disorder was either the same or larger for the co-doped samples compared to the undoped samples (Fig. 8.22). Comparing the Zn^{2+} single doped samples to that of the co-doped showed that there were similar trends for the interatomic distances but the disorder had slightly more variation. The average interatomic distances (3.159 – 3.160 Å) and disorder (0.007 $Å^2$) were similar. The Fe-Fe coordination shell showed no changes in the interatomic distance over the co-doping concentration range. The interatomic distance was the same for the undoped and co-doped samples (Table 13 and Fig. 8.23). The disorder was constant for the undoped and co-doped samples but for the 3Zn-3Co sample the disorder around the shorter interatomic distance increased and the disorder around the longer interatomic distance decreased (Fig. 8.24). The interatomic distances (4.23 Å) and disorder (0.009 – 0.011 $Å^2$) for Fe-Fe coordination shell was the same for the single Zn^{2+} doped and the

co-doped samples. Figure 8.20a: The changes in the interatomic distance for the second (Fe-P) coordination shell.

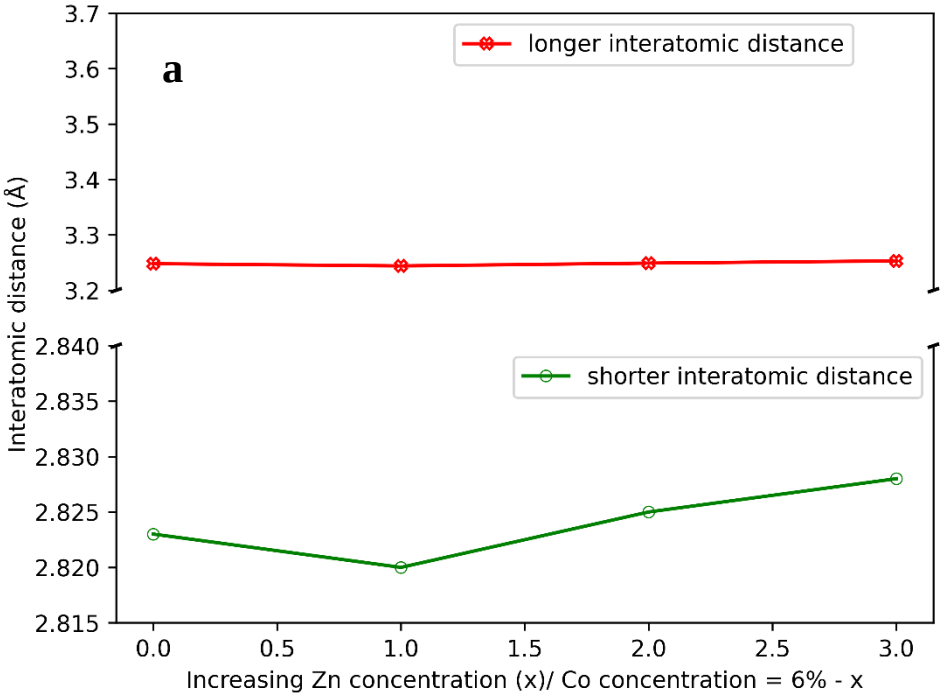

Figure 8.21: The changes in the interatomic distance of the second (Fe-P) coordination shell.

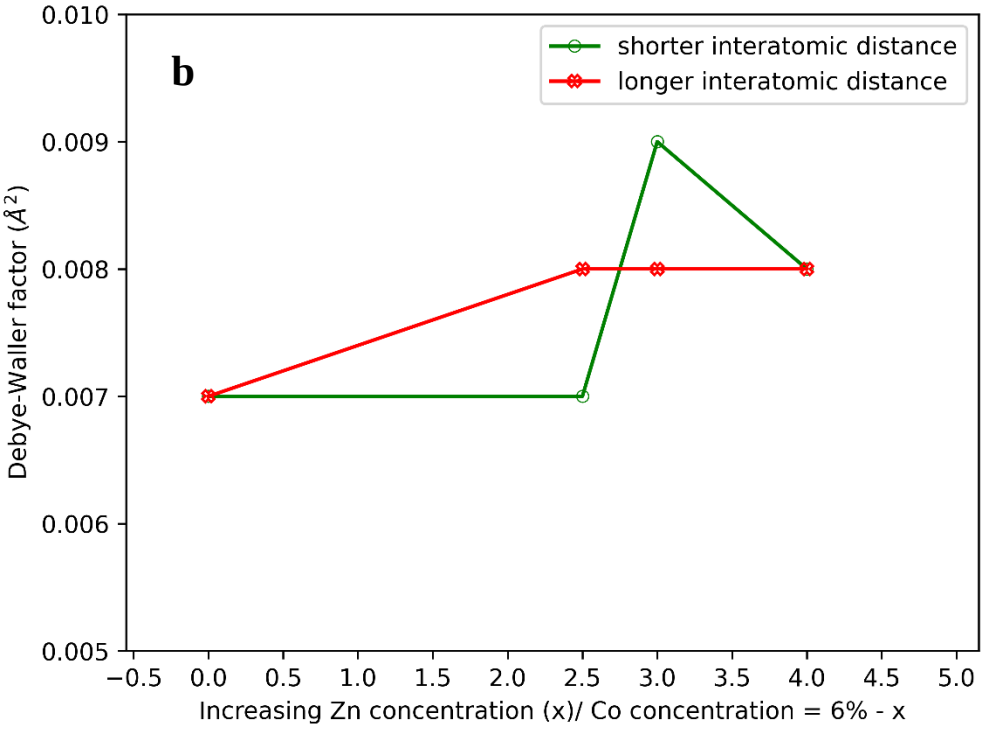

Figure 8.22: The changes in the disorder of the second (Fe-P) coordination shell

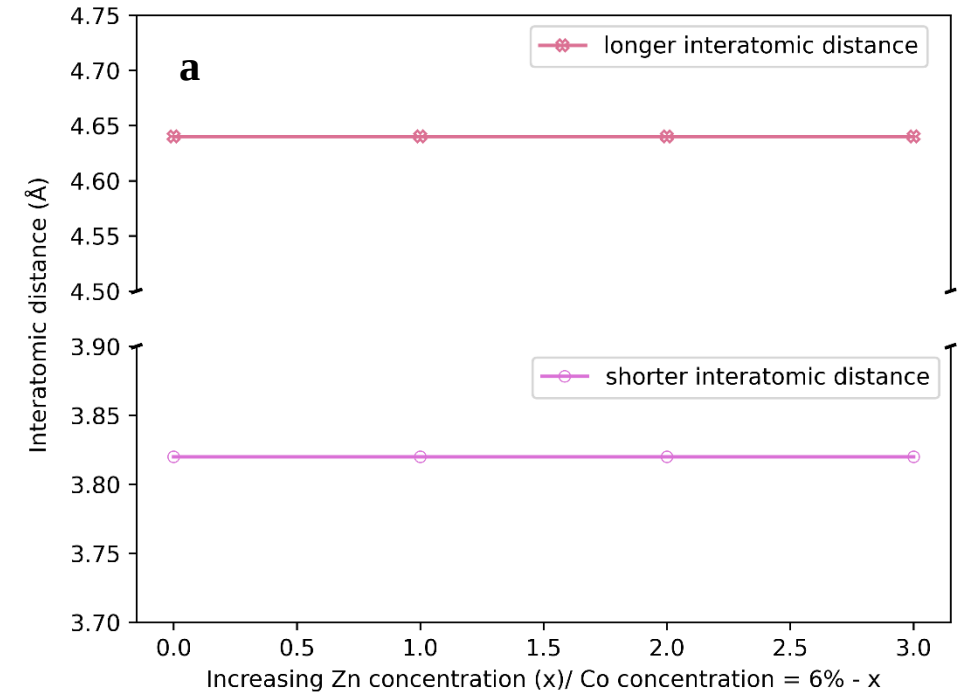

Figure 8.23: The changes in the interatomic distance of the third (Fe-Fe) coordination shell.

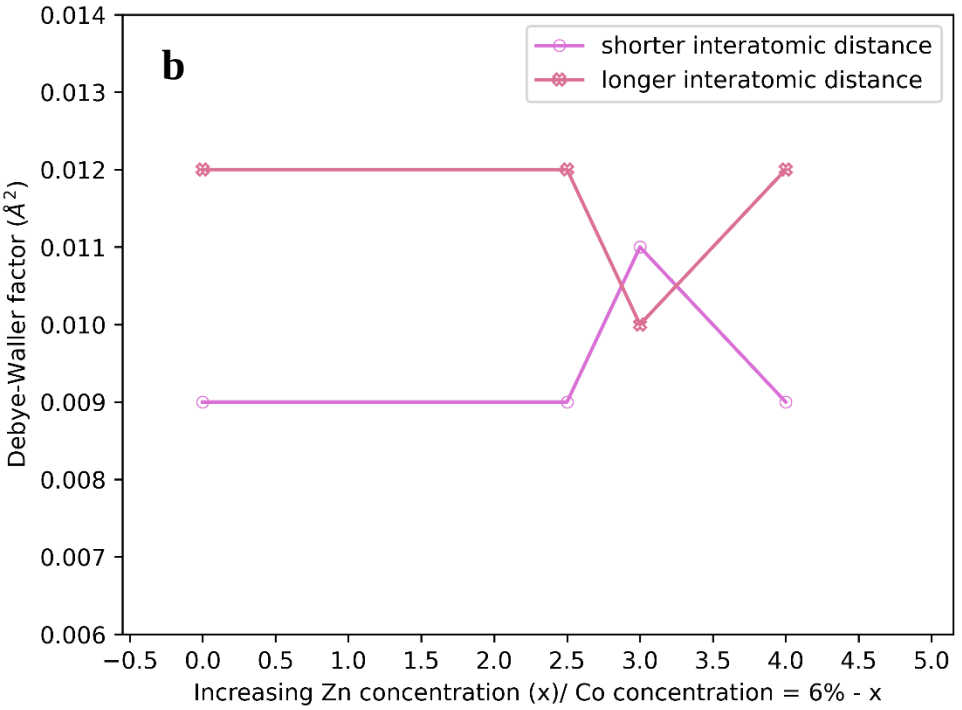

Figure 8.24: The changes in the disorder of the third (Fe-Fe) coordination shell

8.4. Conclusion

Co-doping with Zn^{2+} and Co^{2+} on the M2 site of $LiFe_{1-x-y}Zn_xCo_yPO_4$ (where, x = 0.025, 0.03, 0.04; y = 0.035, 0.03, 0.02, respectively) using a low cost, low energy hydrothermal synthesis in Teflon bombs was investigated. No impurity phases containing the dopants were identified in any of the doped samples but it is possible that the some of the dopants was lost in the filtrate that was not analysed. The impurities could possibly be reduced or eliminated with additional purging of the doping solutions. The same undoped sample was used in both the Zn^{2+} single doped (Chapter 7) and this study and the same defects were observed and the sample was not without defects. In the 2.5Zn-3.5Co sample two impurities in small percentages were detected and this sample had the highest percentage of $LiFePO_4$ present. LCF determined that 85.9% Fe^{2+} was present but this was not the highest Fe^{2+} content as was indicated with XRD. Both Raman spectroscopy and XRD detected the present of Li_3PO_4 in the sample. The pre-edge region only showed a small increase in the intensity of the e_g peak. The 3Zn-3Co sample had the lowest percentage of $LiFePO_4$ present as detected with XRD although LCF determined that this sample had the highest Fe^{2+} (90.3%) content. The Fe-impurity detected in the sample has both Fe^{2+} and Fe^{3+} present and there is a possibility that Fe^{2+} is in a similar environment in $LiFePO_4$ and therefore shows a higher Fe content. The 3Zn-3Co sample also had the least amount of defects on the M1 site. The 4Zn-2Co sample had the highest amount of impurity phases present, the highest impurity content as well as $LiFePO_4(OH)$ which is a source of Fe^{3+}. This additional Fe^{3+} phase could be reason for this sample having the lowest Fe^{2+} content. The 4Zn-2Co sample had the highest percentage of defects on the M1 site as well as an increase in both the lattice parameters and volume compared to the other co-doped samples. EXAFS modelling of the Fe K-edge for the co-doped samples showed only slight variations in the interatomic bond distances and disorder. The effect of doping was more noticeable for the disorder of the Fe-O coordination shell and showed a decrease in the disorder. To fully understand the effect that co-doping has on the M-O, M-P and M-M/M-Fe interatomic distances and disorder, the Zn K-edge and Co K-edge will have to be examined. Compared to the Zn^{2+} single doped samples, the co-doped samples had a higher percentage of impurities that is possibly an effect of the addition two unpurged solutions to the $FeSO_4/H_3PO_4$ solution, compared to one unpurged solution, introducing more oxygen. The co-doped samples had a smaller percentage of defects on the M1 sites. The Fe^{2+} content for the Zn^{2+}-doped samples ranged between 77.0 – 93.6% and for the co-doped samples between 80.3 – 90.3%. The co-doped samples exhibited improved structure stability based on the P-O bond distances and less

distortion as shown by the decreased e_g peak intensity of the pre-edge. Again, the Fe-O coordination shell showed almost no change in the interatomic distances but the co-doped samples had a lower disorder than the Zn^{2+} doped samples. This study thus showed that co-doping is possible using this synthetic route although there are still defects that need to be reduced/eliminated.

8.5. References

1. Yang, X., Hu, Z. and Liang, J. Effects of sodium and vanadium co-doping on the structure and electrochemical performance of $LiFePO_4$/C cathode material for lithium-ion batteries. *Ceram. Int.* **41**, 2863–2868 (2015).
2. Long, Y. F., Su, J., Cui, X. R., Lv, X. Y. and Wen, Y. X. Enhanced rate performance of $LiFePO_4$/C by co-doping titanium and vanadium. *Solid State Sci.* **48**, 104–111 (2015).
3. Fan, C. L., Zhang, K. H. and Han, S. C. Comprehensive methods to enhance the electrochemical performances of $LiFe_{0.94}Mg_{0.03}Cu_{0.03}PO_4$/C cathode for lithium ion batteries. *Mater. Res. Bull.* **48**, 2497–2503 (2013).
4. Shu, H., Wang, X., Wu, Q., Hu, B., Yang, X., Wei, Q., Liang, Q., Bai, Y., Zhou, M., Wu, C., Chen, M., Wang, A. and Jiang, L. Improved electrochemical performance of $LiFePO_4$/C cathode via Ni and Mn co-doping for lithium-ion batteries. *J. Power Sources* **237**, 149–155 (2013).
5. Lv, Y. J., Huang, B., Tan, J. X., Jiang, S. Q., Zhang, S. F., and Wen, Y. Z. Enhanced low temperature electrochemical performances of $LiFePO_4$/C by V^{3+} and F^- co-doping. *Mater. Lett.* **229**, 349–352 (2018).
6. Wagemaker, M., Ellis, B. L., Lützenkirchen-Hecht, D., Mulder, F. M. and Nazar, L. F. Proof of supervalent doping in olivine $LiFePO_4$. *Chem. Mater.* **20**, 6313–6315 (2008).
7. Lv, X. Y., Cui, X. R., Long, Y. F., Su, J. and Wen, Y. X. Optimization of titanium and vanadium co-doping in $LiFePO_4$/C using response surface methodology. *Ionics (Kiel).* **21**, 2447–2455 (2015).
8. Kiani, G. R., Boroomand, S., Khodabakhshi, R. and Esmaeili, M. A novel co-doped $LiFePO_4$/C cathode material, modified for enhanced high power density battery applications. *Microelectron. Eng.* **136**, 77–80 (2015).
9. Ding, Y. H. and Zhang, P. Effect of Mg and Co co-doping on electrochemical properties of $LiFePO_4$. *Trans. Nonferrous Met. Soc. China (English Ed.* **22**, s153–s156 (2012).
10. Yiming, W., Giuli, G., Moretti, A., Nobili, F., Fehr, K. T., Paris, E. and Marassi, R. Synthesis and characterization of Zn-doped $LiFePO_4$ cathode materials for Li-ion battery. *Mater. Chem. Phys.* **155**, 191–204 (2015).
11. Zhao, Y., Chen, L., Chen, X., Kuang, Q. and Dong, Y. Crystal structure and electrochemical properties of $LiFe_{1-x}Zn_xPO_4$ ($x \leq 1.0$) . *Powder Diffr.* **26**, 238–243 (2011).
12. Bilecka, I., Hintennach, A., Rossell, M. D., Xie, D., Novák, P. and Niederberger, M.

Microwave-assisted solution synthesis of doped $LiFePO_4$ with high specific charge and outstanding cycling performance. *J. Mater. Chem.* **21**, 5881–5890 (2011).

13. Shenouda, A. Y. and Liu, H. K. Studies on electrochemical behaviour of zinc-doped $LiFePO_4$ for lithium battery positive electrode. *J. Alloys Compd.* **477**, 498–503 (2009).

14. Wang, D., Li, H., Shi, S., Huang, X. and Chen, L. Improving the rate performance of $LiFePO_4$ by Fe-site doping. *Electrochim. Acta* **50**, 2955–2958 (2005).

15. Yang, J., Bai, Y., Qing, C. and Zhang, W. Electrochemical performances of Co-doped $LiFePO_4$/C obtained by hydrothermal method. *J. Alloys Compd.* **509**, 9010–9014 (2011).

16. Chantrasuwan, P., Wiriya, N., Kaewmala, S., Pongha, S., Limphirat, W., Nash, J., Srilomsak, S. and Meethong, N. Electrochemical property investigation of cobalt doped $LiFePO_4$/C during charge-discharge by an in-situ x-ray near edge structure technique. in *AIP Conference Proceedings* **2097**, 020004 (2019).

17. Gao, H., Jiao, L., Yang, J., Qi, Z., Wang, Y. and Yuan, H. High rate capability of Co-doped $LiFePO_4$/C. *Electrochim. Acta* **97**, 143–149 (2013).

18. Song, J., Shao, G., Shi, M., Ma, Z., Song, W., Wang, C. and Liu, S. The effect of doping Co on the electrochemical properties of $LiFePO_4$/C nanoplates synthesized by solvothermal route. *Solid State Ionics* **253**, 39–46 (2013).

19. Gao, L., Xu, Z. and Zhang, S. The co-doping effects of Zr and Co on structure and electrochemical properties of $LiFePO_4$ cathode materials. *J. Alloys Compd.* **739**, 529–535 (2018).

20. Baster, D., Zheng, K., Zając, W., Świerczek, K. and Molenda, J. Toward elucidation of delithiation mechanism of zinc-substituted $LiFePO_4$. *Electrochim. Acta* **92**, 79–86 (2013).

21. Schmid-Beurmann, P. Synthesis and phase characterization of a solid solution series between β-$Fe_2(PO_4)O$ and $Fe4(PO_4)_3(OH)_3$. *J. Solid State Chem.* **153**, 237–247 (2000).

22. Shannon, R. D. Revised effective ionic radii and systematic studies of interatomic distances in halides and chalcogenides. *Acta Crystallogr. Sect. A* **32**, 751–767 (1976).

23. Jugović, D., Mitrić, M., Cvjetićanin, N., Jančar, B., Mentus, S. and Uskoković, D. Synthesis and characterization of $LiFePO_4$/C composite obtained by sonochemical method. *Solid State Ionics* **179**, 415–419 (2008).

24. Zhang, L. L., Liang, G., Ignatov, A., Croft, M. C., Xiong, X. Q., Hung, I. M., Huang, Y. H., Hu, X. L., Zhang, W. X. and Peng, Y. L. Effect of vanadium incorporation on electrochemical performance of $LiFePO_4$ for lithium-ion batteries. *J. Phys. Chem. C* **115**, 13520–13527 (2011).

25. Lu, Y., Shi, J., Guo, Z., Tong, Q., Huang, W. and Li, B. Synthesis of $LiFe_{1-x}Ni_xPO_4$/C composites and their electrochemical performance. *J. Power Sources* **194**, 786–793 (2009).

26. Yang, M.-R. and Ke, W.-H. The Doping Effect on the Electrochemical Properties of $LiFe_{0.95}M_{0.05}PO_4$ (M=Mg^{2+}, Ni^{2+}, Al^{3+}, or V^{3+}) as Cathode Materials for Lithium-Ion Cells. *J. Electrochem. Soc.* **155**, A729 (2008).

27. Bai, Y., Yin, Y., Yang, J., Qing, C. and Zhang, W. Raman study of pure, C-coated and

Co-doped $LiFePO_4$: thermal effect and phase stability upon laser heating. *J. Raman Spectrosc.* **42**, 831–838 (2011).

28. Burba, C. M. and Frech, R. Raman and FTIR Spectroscopic Study of Li_xFePO_4 ($0 \leq x \leq 1$). *J. Electrochem. Soc.* **151**, A1032 (2004).

29. Paraguassu, W., Freire, P. T. C., Lemos, V., Lala, S. M., Montoro, L. A. and Rosolen, J. M. Phonon calculation on olivine-like $LiMPO_4$ (M = Ni, Co, Fe) and Raman scattering of the iron-containing compound. *J. Raman Spectrosc.* **36**, 213–220 (2005).

30. Wu, J., Krishna Phani Dathar, G., Sun, C., Theivanayagam, M. G., Applestone, D., Dylla, A. G., Manthiram, A., Henkelman, G., Goodenough, J. B. and Stevenson, K. J. In situ Raman spectroscopy of $LiFePO_4$: size and morphology dependence during charge and self-discharge. *IOP Publ. Nanotechnol. Nanotechnol.* **24**, 424009–424018 (2013).

31. Popovic, L., de Waal, D. and Boeyens, J. C. A. Correlation between Raman wavenumbers and P-O bond lengths in crystalline inorganic phosphates. *J. Raman Spectrosc.* **36**, 2–11 (2005).

32. Yang, C. C., Hu, H. C., Lin, S. J. and Chien, W. C. Electrochemical performance of V-doped spinel $Li_4Ti_5O_{12}$/C composite anode in Li-half and $Li_4Ti_5O_{12}$/$LiFePO_4$-full cell. *J. Power Sources* **258**, 424–433 (2014).

33. Jugović, D., Mitrić, M., Milović, M., Cvjetićanin, N., Jokić, B., Umićević, A. and Uskoković, D. The influence of fluorine doping on the structural and electrical properties of the $LiFePO_4$ powder. *Ceram. Int.* **43**, 3224–3230 (2017).

34. Galinetto, P., Mozzati, M. C., Grandi, M. S., Bini, M., Capsoni, D., Ferrari, S. and Massarotti, V. Phase stability and homogeneity in undoped and Mn-doped $LiFePO_4$ under laser heating. *J. Raman Spectrosc.* **41**, 1276–1282 (2010).

35. Bini, M., Mozzati, M. C., Galinetto, P., Capsoni, D., Ferrari, S., Grandi, M. S. and Massarotti, V. Structural, spectroscopic and magnetic investigation of the $LiFe_{1-x}Mn_xPO_4$ (x=0-0.18) solid solution. *J. Solid State Chem.* **182**, 1972–1981 (2009).

36. Galinetto, P., Mozzati, M. C., Grandi, M. S., Bini, M., Capsoni, D., Ferrari, S. and Massarotti, V. Phase stability and homogeneity in undoped and Mn-doped $LiFePO_4$ under laser heating. *J. Raman Spectrosc.* **41**, 1276–1282 (2010).

37. Marx, N., Croguennec, L., Carlier, D., Bourgeois, L., Kubiak, P., Le Cras, F. and Delmas, C. Structural and electrochemical study of a new crystalline hydrated iron(iii) phosphate $FePO_4 \cdot H_2O$ obtained from $LiFePO_4(OH)$ by ion exchange. *Chem. Mater.* **22**, 1854–1861 (2010).

38. Popovic, L., Manoun, B., de Waal, D., Nieuwoudt, M. K. and Comins, J. D. Raman spectroscopic study of phase transitions in Li_3PO_4. *J. Raman Spectrosc.* **34**, 77–83 (2003).

39. de Faria, D. L. A. and Lopes, F. N. Heated goethite and natural hematite: Can Raman spectroscopy be used to differentiate them? *Vib. Spectrosc.* **45**, 117–121 (2007).

40. Haas, O., Deb, A., Cairns, E. J. and Wokaun, A. Synchrotron X-ray absorption study of $LiFePO_4$ electrodes. *J. Electrochem. Soc.* **152**, (2005).

41. Deb, A., Bergmann, U., Cairns, E. J. and Cramer, S. P. X-ray absorption spectroscopy study of the Li_xFePO_4 cathode during cycling using a novel electrochemical in situ reaction cell. *J. Synchrotron Radiat.* **11**, 497–504 (2004).

42. Griffith, J. S. and Orgel, L. E. Ligand-field theory. *Q. Rev. Chem. Soc.* **11**, 381–393 (1957).

43. Nam, K., Bak, S., Hu, E., Yu, X., Zhou, Y., Wang, X., Wu, L., Zhu, Y., Chung, K. and Yang, X. Combining In Situ Synchrotron X-Ray Diffraction and Absorption Techniques with Transmission Electron Microscopy to Study the Origin of Thermal Instability in Overcharged Cathode Materials for Lithium-Ion Batteries. *Adv. Funct. Mater.* **23**, 1047–1063 (2013).

44. Deb, A., Bergmann, U., Cairns, E. J. and Cramer, S. P. Structural investigations of $LiFePO_4$ electrodes by Fe X-ray absorption spectroscopy. *J. Phys. Chem. B* **108**, 7046–7051 (2004).

45. Wong, J., Lytle, F. W., Messmer, R. P. and Maylotte, D. H. K-edge absorption spectra of selected vanadium compounds. *Phys. Rev. B* **30**, 5596–5610 (1984).

46. Calvin, S. *XAFS for Everyone*. (CRC Press, 2013).

47. Demeter: XAS Data Processing and Analysis. (2018) . at http://bruceravel.github.io/demeter/.

48. Hsu, K. F., Hu, S. K., Chen, C. H., Cheng, M. Y., Tsay, S. Y., Chou, T. C., Sheu, H. S., Lee, J. F. and Hwang, B. J. Formation mechanism of $LiFePO_4$/C composite powders investigated by X-ray absorption spectroscopy. J. Power Sources 192, 660–667 (2009).

49. Tabassam, L., Giuli, G., Moretti, A., Nobili, F., Marassi, R., Minicucci, M., Gunnella, R., Olivi, L and Di Ci, Andrea. Structural study of $LiFePO_4$-$LiNiPO_4$ solid solutions. *J. Power Sources* **213**, 287–295 (2012).

50. Minicucci, M., Tabassam, L., Natali, Ri., Mancini, G., Rezvani, S. J. and Di Cicco, A, Double-edge X-ray absorption study of $LiFe_{1-x}Ni_xPO_4$ cathode materials. *J. Mater. Sci.* **52**, 4886–4893 (2017).

Chapter 9

General conclusions

The main aim of this thesis was to develop a method using homemade Teflon bombs which require the use of moderate temperatures in order to synthesize $LiFePO_4$ and with the goal to produce a pure product with few defects and with very little cation distribution between the M2 and M1 site. Different synthetic modifications were applied in an attempt to reduce the defects that were formed at the moderate reaction temperatures and to minimize the Fe^{3+} content. It was important to determine how each modification affected the product, so they were thoroughly characterized. In this process it was attempted to exclude the additional heat-treatment step under an inert atmosphere at temperatures ranging between 450 - 800°C. Using homemade Teflon bombs as the reaction vessel it was shown that it was possible to produce phase pure samples without a further heat-treatment step or by including a reductant, although reproducibility was problematic.

Although the Teflon bombs were able to produce phase pure $LiFePO_4$ it was not defect free as seen with the presence of antisite defects, Fe^{3+} content and possible amorphous phases. The optimal pressure was reached when the Teflon bombs were filled to 25% and not to higher percentages such as 50% or 75%. The 3:1:1 ratio of the precursors ($Li:Fe:PO_4$) was the highest ratio that was considered and was also the optimum ratio here as well as that used in literature. One of the major synthetic challenges was preventing the oxidation of Fe^{2+} to Fe^{3+}. In an attempt to prevent this from occurring all the solutions were purged with nitrogen throughout the synthesis. This seem to be the main issue resulting in the variability between samples. The Fe^{3+} appears to be incorporated into the structure and could affect the performance of the battery. Thus, although the $LiFePO_4$ was phase pure, incorporated Fe^{3+} would also act as an impurity.

Many methods in literature stated that the Li^+ must be added dropwise to the $Fe\text{-}PO_4$ solution, particularly when using a solution-based synthesis. It was found that the rate at which the addition occurs does have an effect of the $LiFePO_4$ product, especially when looking at a system with Li^+ in excess. It was also seen that it possibly affects the formation of Li_3PO_4 as an impurity phase. For the system investigated here it was suggested to use an addition rate of on drop every 3 seconds. It appeared that longer addition times should be avoided as it increases the Fe^{3+} content possibly due to the increasing probability of exposure to air. This factor could be mitigated by working in a glovebox. Another aspect that could be important but was not

investigated here is the drop size. The drop size could have an effect on the addition rate and the formation of certain impurity phases.

To further investigate the effect of air on the samples, once all the precursors were mixed but before placing them in the sealed bombs and into the oven, samples were left in air under continuous stirring for between 3 minutes and 4 hours. By 4 hours all the Fe^{2+} had been oxidized to Fe^{3+}. This clearly showed that the impurities, defects and Fe^{3+} content increases with exposure time. A comparison between the purged sample and the sample exposed to air for 3 minutes showed that even at short exposure times there was about a 10% difference in Fe^{2+} content indicating the oxidation occurs rapidly in air.

The commercial $LiFePO_4$ (C-LFP) sample was fully characterize since it was used as a standard to analyze the XANES region. C-LFP was quoted to be >97% pure as determined using X-ray fluorescence, a technique not applied in this thesis. Both Fe_2O_3 and Fe_3O_4 were found to be present in the sample as amorphous phases together with an unidentified phase. The local structure was similar to the results reported in literature indicating that the presence of the impurity phases did not affect the local structure of $LiFePO_4$. The XANES region of the C-LFP sample showed that the intensity was lower for all the synthesized samples for the t_{2g} peak but for the e_g peak the intensities were either similar or higher for the synthesized samples. The EXAFS region of the more promising synthesized samples compared to that of C-LFP showed similarities in the average interatomic distances as well as the disorder for the Fe-O coordination shell. The disorder for the Fe-P and Fe-Fe coordination shells tend to be smaller than the determined values for the synthesized samples.

Since doping is often to for improve the ionic conductivity and structure stability in $LiFePO_4$, it was of interest to investigate whether doping could be successfully achieved on the M2 site using this synthetic procedure and if this had any effect on the Fe^{3+} content. Both single doped (with 1 – 3% Zn^{2+}) and co-doped (with a total Zn^{2+} and Co^{2+} doping percentage of 6% with varying ratios) samples were considered. A slight decrease in the lattice parameters were observed and the Raman spectra showed slight peak shifting for some of the samples, to higher wavenumbers for the PO_4^{3-} vibrational modes, indicating that the metals ions were most likely incorporated into the structure. This was expected due to the smaller radii of both Zn^{2+} (0.74 Å) and Co^{2+} (0.75 Å) compared to that of Fe^{2+} (0.78 Å). There was no real indication that either doping or co-doping had any effect on the Fe^{2+} content. The mid-range of the co-doping concentrations had a higher percentage of the Fe-impurity phase ($Fe_{3.44}(PO_4)_{1.98}O_{2.08}$) present

that the other synthesized samples. The XANES region showed that the distortion around the Fe atom was more pronounced for the doped than the co-doped samples, but from the EXAFS data no changes in the local structure was observed even for a co-doping percentage as high as 6%.

Different characterization techniques were used and considered to get a full picture of both the average and local structure. This was deemed necessary since different techniques highlight different aspects within the structure and are therefore complementary. PXRD is a reliable technique for determining the average structure and for phase identification but cannot be used to determine amorphous phases or accurately determine the percentage of defects present or the Fe^{2+} content. Raman spectroscopy compliments PXRD really well and was useful for identifying similar impurity phases detected using PXRD, amorphous phases and any changes in the crystallinity. The weakness of this technique is that it can be difficult to identify and assign the fingerprint region together with different phases due to the overlap of some peaks with that of $LiFePO_4$. Another possible limitation with this technique is that different spots will have to be sampled to get the full picture of the sample and the impurity phases, however, this does highlight the inhomogeneity within the sample.

As the oxidation of Fe^{2+} to Fe^{3+} due to exposure of the precursors to air played an important role in this thesis, the Fe K-edge and Mössbauer spectroscopy was both used to assess the different Fe environments. These techniques provide complimentary information, especially when determining the Fe^{2+} content, and they are able to detect both crystalline and amorphous phases. The pre-edge region using XAS is sensitive to changes in the oxidation state as well as the distortion, but references are generally needed especially when gauging the changes in the distortion. To obtain quantitative data on changes in the Fe^{2+} content LCF can be used, but to effectively use LCF a large library of standards is needed consisting of the different components present in the sample. Mössbauer spectroscopy in this regard could be considered a superior technique as no library of standards is needed to evaluate the Fe^{2+} content. Mössbauer spectroscopy is also very beneficial when it comes to identifying different Fe^{2+} and Fe^{3+} environments as seen in this thesis. In this case a proper understanding of the possible environments is required to adequately identify these different types of environments. Even though the techniques have their strengths and weaknesses, it was really important to use the information gained from all of them to get an overall picture of the structural changes that occur with each synthetic modification.

Future improvements, problems and additional work into the investigation of this methodology and work would be:

- One of the most important observations was that air has to be excluded completely during the synthesis especially when not using a reductant or a heat-treatment step. Purging did not appear to be completely sufficient in doing so. A solution to this would be to conduct the synthesis entirely in a glovebox which could also improve the reproducibility. Unfortunately, one was not available for this work.
- Using homemade Teflon bombs posed certain challenges such as determining the exact temperature at which the reaction occurs inside the bombs. Incorporating a thermocouple to determine this would be difficult especially with the design of the Teflon bombs.
- As this is a hydrothermal synthesis which requires filtration to separate the product from the solvent, there is a possibility that either some of the Li^+-ions, dopants or the co-dopants remained in the filtrate and was not incorporated into the structure. Thus, it would be beneficial to analyze the filtrate as well. This would provide additional insights into the plausibility of the synthesis and the incorporation of the ions into the structure.
- The electrochemical performance of cells incorporating the synthesised materials would be very beneficial in determining how successful the synthetic modifications were and especially to see the effect of the incorporated dopants. In order to fully understand how these changes affect the electrochemical performance, however, the reproducibility of the method still needs to be refined.

Appendix A

A1. Synchrotron PXRD calibration using LaB_6

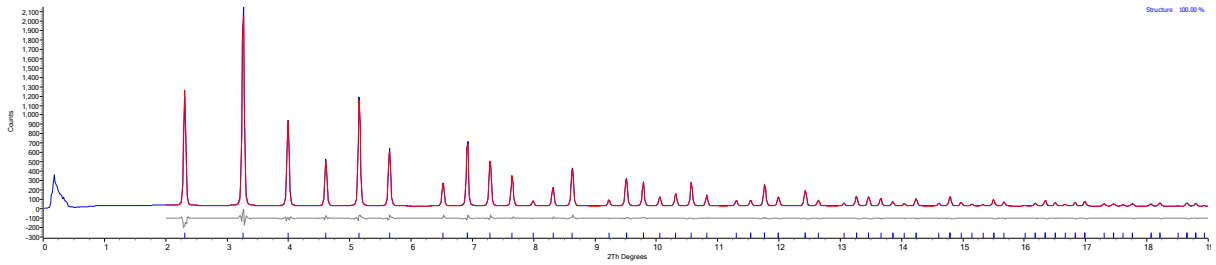

Figure A1: The Rietveld refinement plot for the calibration of 28-ID-1 at BNL of NIST 660c (LaB_6) with a wavelength of 0.167057(4) Å.

Table A1: Rietveld error indices for the calibration of 28-ID-1 at BNL of NIST 660c from the refinement of Figure A1.

R_{wp}	4.06
R_p	2.99
R_{exp}	12.99
GOF	0.31

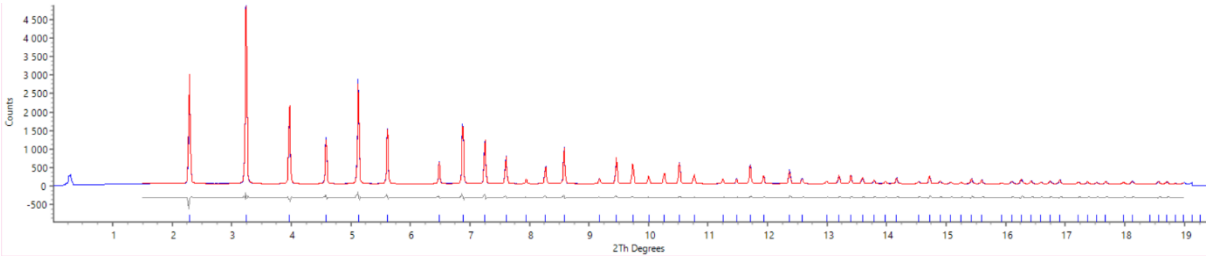

Figure A2: The Rietveld refinement plot for the calibration of 28-ID-1 at BNL of NIST 660c (LaB_6) with a wavelength of 0.166316(1) Å.

Table A2: Rietveld error indices for the calibration of 28-ID-1 at BNL of NIST 660c from the refinement of Figure A2.

R_{wp}	5.63
R_p	3.75
R_{exp}	9.38
GOF	0.60

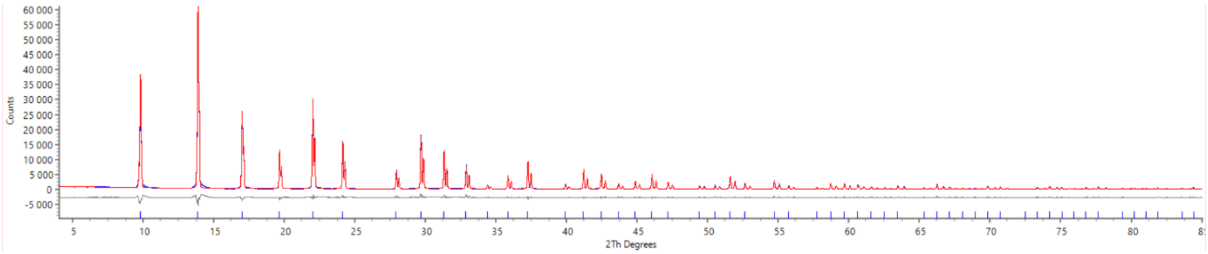

Figure A3: The Rietveld refinement plot for the calibration of the Bruker D8 Advance of NIST 660c (LaB_6) with a wavelength of 0.709313(4) Å.

Table A3: Rietveld error indices for the calibration of the Bruker D8 Advance of NIST 660c (LaB_6) from the refinement of Figure A3.

R_{wp}	11.29
R_p	6.82
R_{exp}	3.51
GOF	3.22

A2. Experimental components for XAS

XAS beamlines typically have a setup that contains slit, collimating mirrors, double toroidal mirrors, a monochromator, harmonic rejection mirrors and ionization chambers.[1,2] The slits block unwanted X-rays and also defines the profile of the X-rays. Primary and secondary slits were present for this experiment. The Si collimating mirrors coated in Pt[2] were used to filter the X-rays and the double toroidal mirrors, also coated in Pt[2], was used to focus the horizontal and vertical branched beams onto the sample. A monochromator is used to select the energy of the X-ray and the monochromator used in this experiment was a Si double crystal (crystals that are placed parallel to each other) monochromator with the atomic plane (111).[1,2] Harmonic rejection mirrors are needed to reduce the harmonic content in the X-rays. The measurement can be influenced by the harmonic X-ray intensity and it therefor has to be reduced. The mirrors are placed such that the harmonic X-rays are reflected away from the sample and only the fundamental energy X-rays are directed towards the sample.[1,2] Ionization chambers are used for X-ray absorption measurements. These detectors are spaces filled with gas with a plate on each side parallel to each other where the gas particles are ionized by some of the X-rays. A current is created by applying a voltage that separates the gas. A change in the X-rays of incident produces a linear detector response.[1]

A3. ^{57}Co decay scheme and the description of a Mossbauer spectrometer.

A3.1. Decay of ^{57}Co to ^{57}Fe

The parent isotope of ^{57}Fe is ^{57}Co and mostly decays to the 136.3 keV excited energy level of ^{57}Fe. The excited nucleus of ^{57}Fe can now decay in one of two ways to the ground state (Fig. A4). The first deexcitation is from the excited state directly to the ground state the second occurs via the 14.4 keV energy level where the release of a $\gamma-$ ray of the same energy occurs. The 14.4 keV $\gamma-$ ray is in turn absorbed by the sample of the same energy. [3]

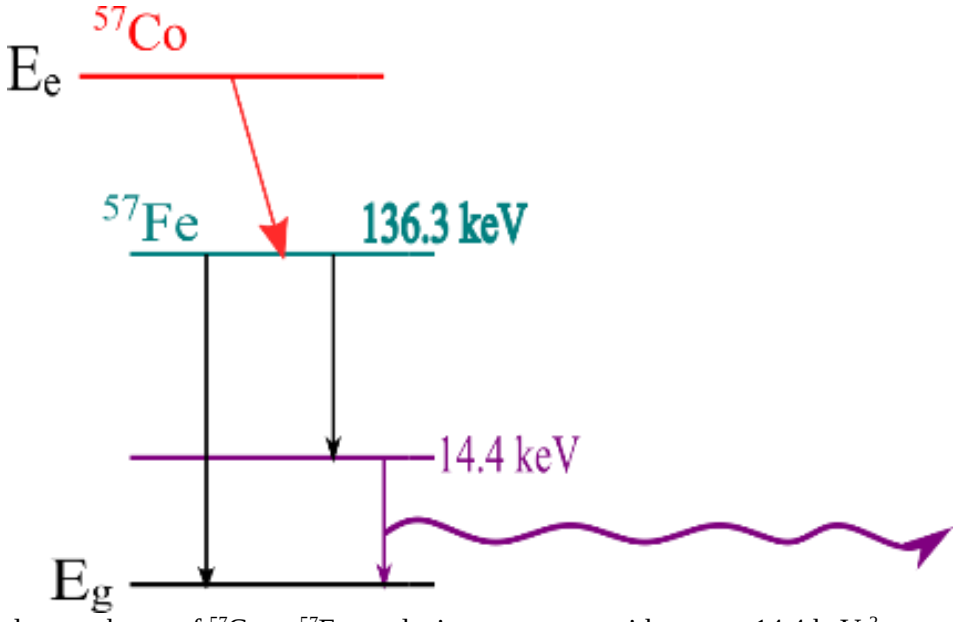

Figure A4: The decay scheme of ^{57}Co to ^{57}Fe producing a $\gamma - ray$ with energy 14.4 keV.[3]

A3.2 Experimental setup

A Mössbauer spectrometer set up for transmission experiments consist of four major parts: (1) the Mössbauer source and absorber, (2) the drive system, (3) the $\gamma-$ ray detector and (4) the data acquisition system.[4,5] A schematic of the setup is shown in Figure A5.

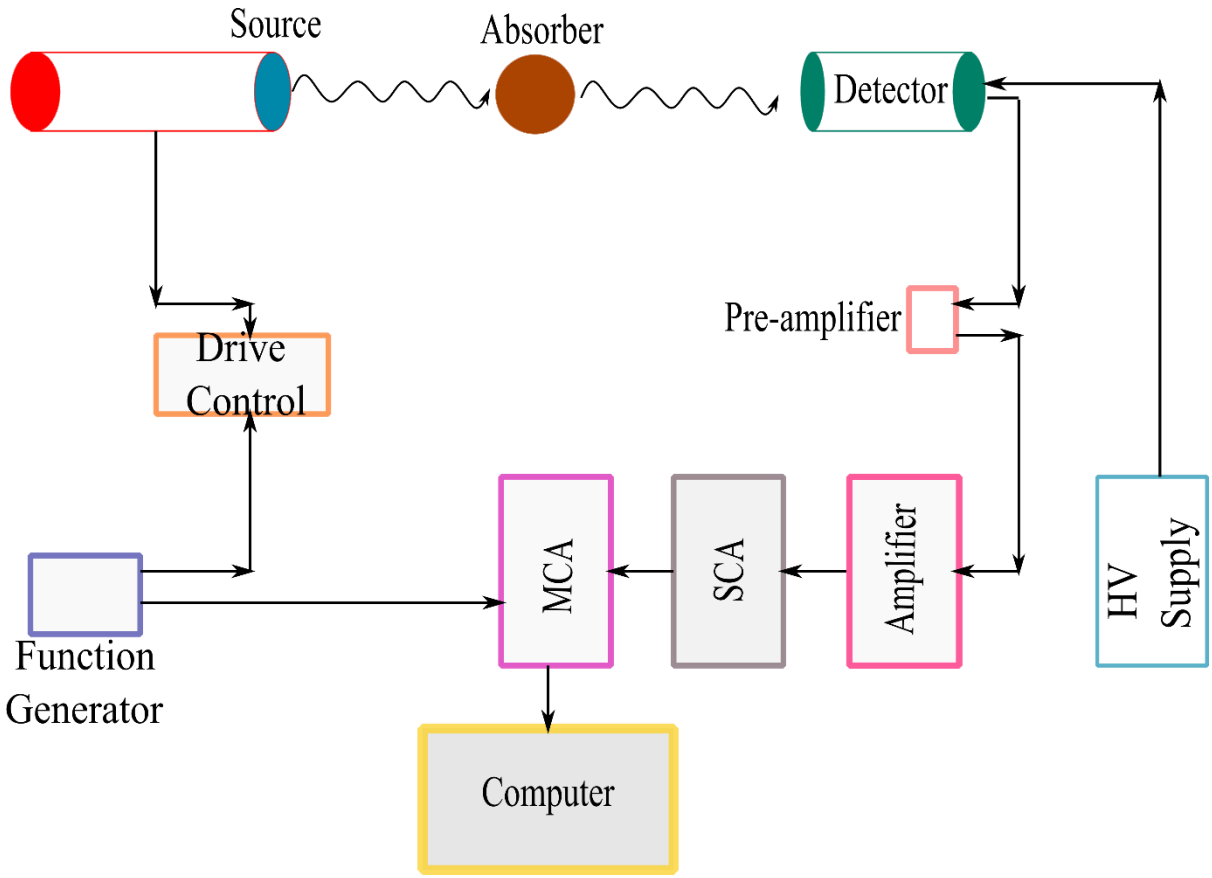

Figure A5: A schematic of the experimental setup for transmission measurements.[4,5]

A3.2.1 The Mössbauer source and absorber

The source consists of the radioactive parent isotope such as ^{57}Co embedded in an Rh matrix and the decay of the isotope should include the Mössbauer isotope that is present in the absorber. The absorber contains the same Mössbauer isotope, as found in the source, but is stable and not radioactive.

A3.2.2 The drive system

Most Mössbauer spectrometers with a transmission setup are operated in constant-acceleration mode.[5] This mode allows for the drive velocity to linearly sweep up-and-down (the mode being either triangular or saw-tooth). The source is attached to the one end of the drive and with the up-and-down sweeping the source is moved relative to the absorber and is responsible for the modulation of the $\gamma-$ray emission and is powered by the drive control unit.[5] The function generator connected to the drive control unit provides the reference voltage. The sweeping at constant acceleration creates a waveform as the voltage increases with time and the source and the drive would be at the same velocity increment for the same amount of time. The drive is also synchronized with the multi-channel analyzer (discussed in the data acquisition section)

such that the velocity, when moving from –v to +v, changes linearly and increases with the channel number.[4]

A3.2.3 The $\gamma - ray$ detector

The detector is responsible for converting the transmitted photons into electric pulses and is sensitive to the photon from the Mössbauer atom. Common detectors are proportional counters that are filled with gas such as Ar, Kr or Xe.[5] These gases can detect the transmitted $\gamma -$ rays, where the electric pulses are proportional to the incident $\gamma -$ ray energy. The voltage also changes with that of the electric pulses.[4] The pre-amplifier and amplifier are connected to the detector and are responsible for amplifying and shaping the pulses from the detector. After amplifying the pulses, they pass through a discriminator that is responsible for rejecting background radiation that did not undergo resonant absorption.[4]

A3.2.4 Data acquisition

The single-channel analyser (SCA) is responsible for the discrimination between pulses. The pulses with the correct radiation will go to the MCA where the rest of the pulses will be rejected. The multi-channel analyser (MCA) receives pulses from the SCA and is the central for storing the pulses and data acquisition.[5] The data acquisition module that was used was CMCA-550. The data is acquired in Pulse-Height mode (PHA)[6] and spectrum containing the pulse height stochastic frequency is collected. The pulse height is proportional to the incident photon energy.[5] The height of the input pulses can be determined digitally and is then allocated to a channel number based on the pulse height. The channel number and voltage have a linear relation, i.e. pulses with a higher voltage (amplitude) would be stored in higher channel numbers. Upper levels (UL) and lower levels (LL) of the voltage can be set, thus all the input pulses outside the set range would be discarded. The software Wissoft2003 can discriminate between pulses inside and outside the set window.[6] For ^{57}Co, the pulse height spectrum shows three peaks: 6 keV, 14.4 keV and 21 keV as shown in Figure A6.

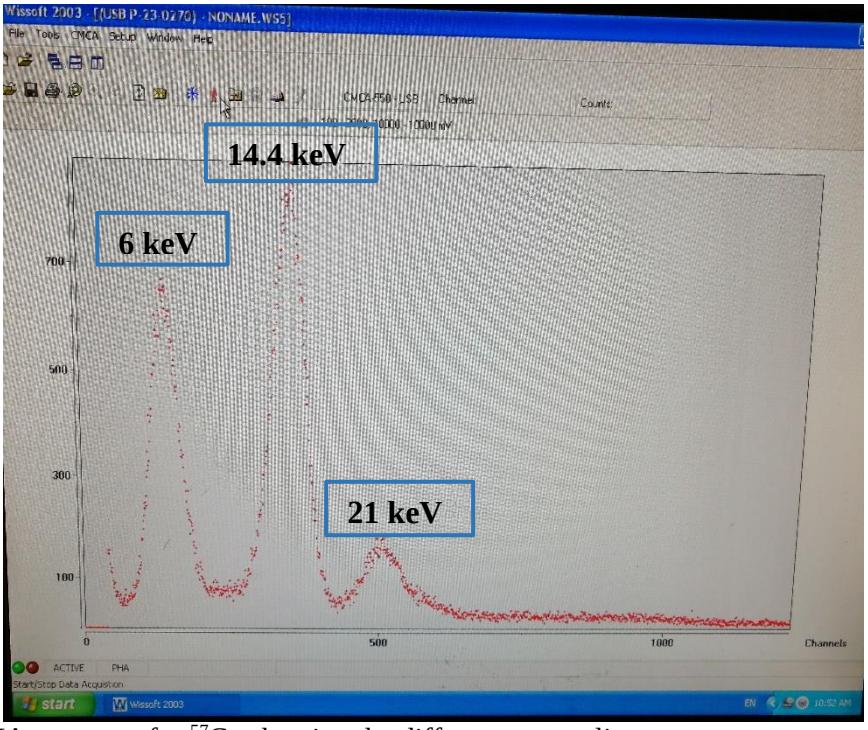

Figure A6: PHA spectrum for ^{57}Co showing the different energy lines.

For Mössbauer spectroscopy the 14.4 keV is selected (Figure A7). Switching the mode to Multi-Channel Scaling (MCS), the digital values of the analog pulses are obtained by feeding these pulses into the analogue digital converter (ADC) from the main amplifier. In this mode only the pulses within the selected range (Figure A7) are counted.[6]

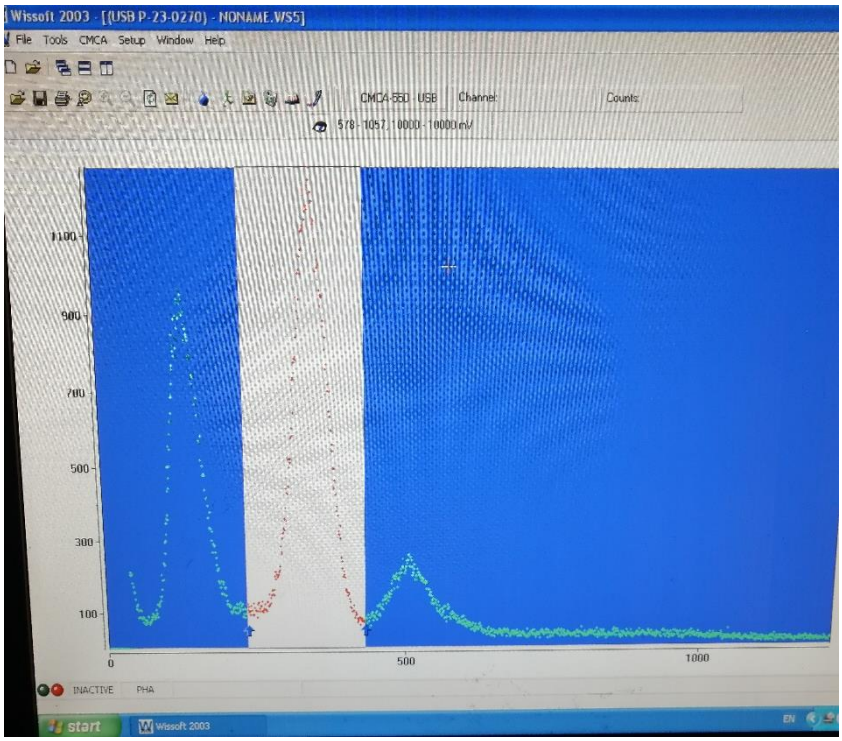

Figure A7: PHA spectrum for ^{57}Co showing the selected 14.4 keV.

Each channel corresponds to a velocity range increment and the counts stored in these channels produces the Mössbauer spectrum given as the counts vs. the Doppler velocity. The produced spectrum is doubled relating to the up and down motion of the velocity sweep (triangular mode) where the velocity values appeared twice and was folded around the point of symmetry to give the final spectrum.[5,6]

A.4. Mössbauer spectroscopy calibration

The Mössbauer spectra calibration for ^{57}Fe was performed using α-Fe foil. The thickness of the standard was $12\mu m$ with a purity of 99.99%. After a few hours of running the measurement a reasonable Mössbauer spectrum was obtained. The number of channels used to record the spectrum was 512. The resulting spectrum consisted of mirror images of the same spectrum but opposite velocity scales (as described above). The spectrum has to be folded around the point of symmetry to obtain the average structure. Folding reduces the length of the data to the use of 216 channels (half the amount of channels) and leads to an increase in the signal-to-noise ratio.[5] The spectrum obtained for the α-Fe foil consists of six lines with positions (Fig. A8) at (-5.3, -3.1, -0.8, 0.8, 3.1 and 5.2) mm/s[7] with hyperfine splitting of D_1 = 1.677 mm/s, D_2 = 6.167 mm/s and D_3 = 10.657 mm/s and with the zero velocity in the center.[5]

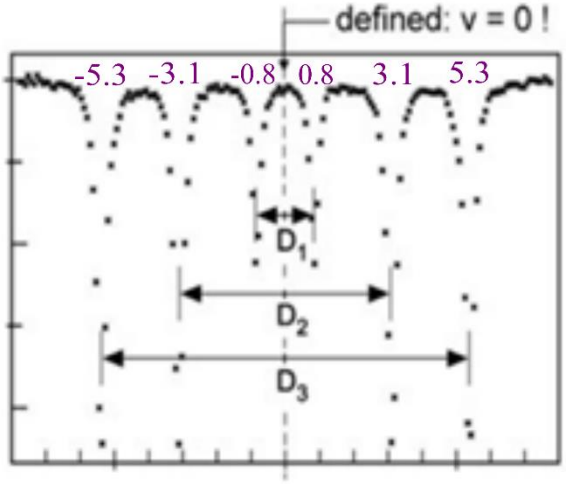

Figure A8: The Mössbauer spectrum of α-Fe foil showing the six line positions and the hyperfine splittings.[5]

The spectrum of α-Fe foil in transmission mode is shown in Figure A9. The spectrum was fit using Vinda[8], a Microsoft excel Add-In. A summary of the fitting process used for the samples can be found in section A5. The spectrum shows six different line positions with intensities of 3:2:1:1:2:3. A theoretical spectrum was used to compare the α-Fe foil and the determined hyperfine parameters were the magnetic field, Bh_f = 32.9T, $\Delta E_Q = 0\ mm/s$ and $\delta = 0\ mm/s$.

These values were in good agreement with cited values (Bh_f = ~33T, $\Delta E_Q = 0\ mm/s$ and $\delta = 0\ mm/s$).[9]

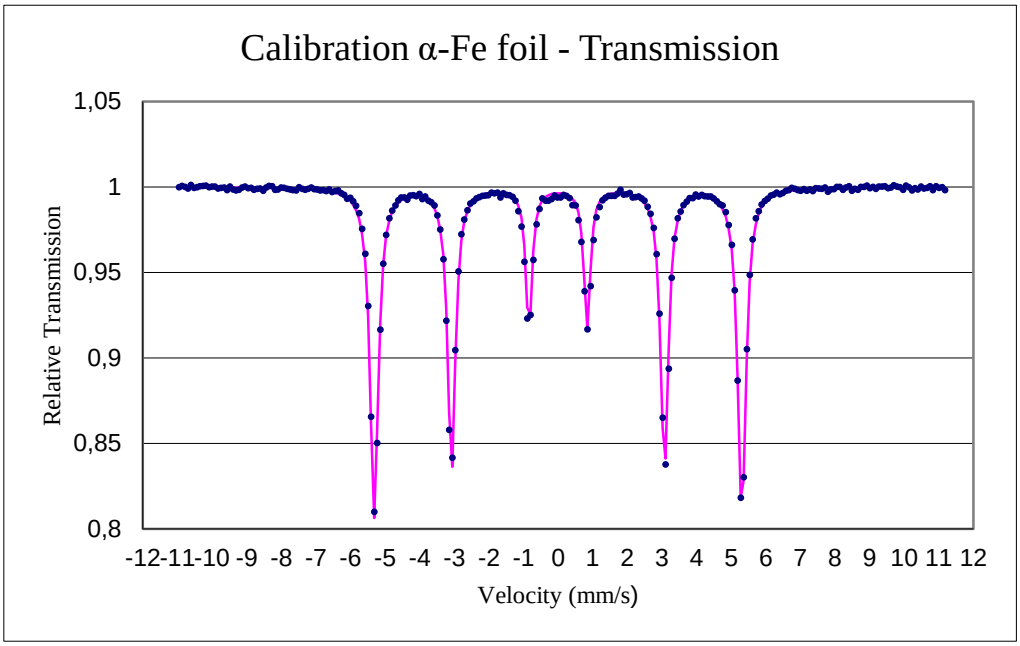

Figure A9: The calibration spectrum of the α-Fe foil recorded in transmission mode.

A5. Mössbauer data analyses using VindaD and χ^2- values for fits

A5.1 Data analysis using Vinda

Individual Mössbauer spectra fitting were performed using Vinda[8] which allows for analysis of the data using an Excel Add-In called VindaD (Fig. A10). To load the Mössbauer spectrum a 'Spec-sheet' has to be opened (Fig. A10 – 1). The 'Spec-sheet' contains the measurement information, the plotting window as well as data columns. Next the spectrum from the chosen measurement can be added (Fig. A10 – 2). By loading the spectrum the measurement information and the data columns are replaced with the spectrum data (Fig. A11) and it allows you to choose the calibration file that was used to determine calibration spectrum (Fig. A9). The desired model for the analysis can then be chosen from the model list built into the program. A model can be added for every environment present in the spectrum (Fig A11). The model used for the samples was a Voigt doublet. By solving the background, hyperfine parameters (ΔE_Q and δ) line widths and the areas the chi-squared (Fig A11) value can be minimised. This can be done by using the Solver Add-In in Excel.

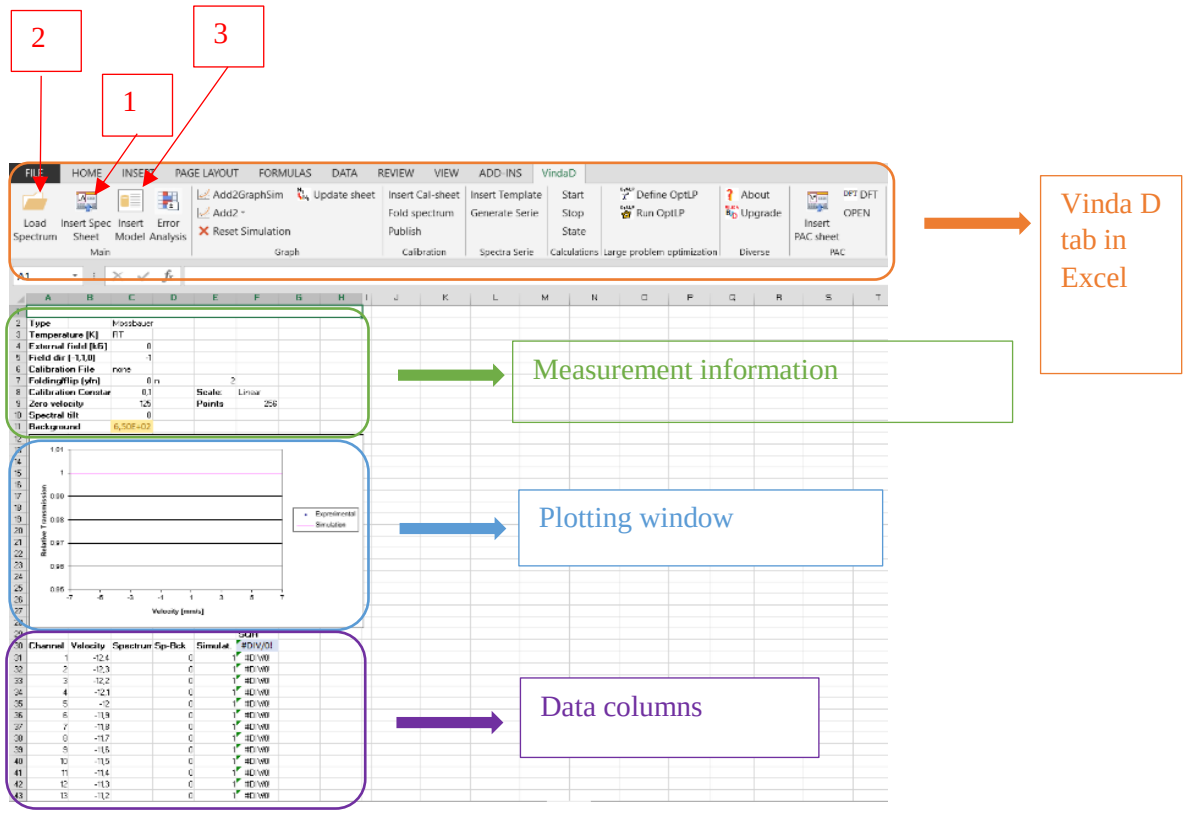

Figure A10: A description of the different fields provided in the Vinda ‘Spec-sheet’.

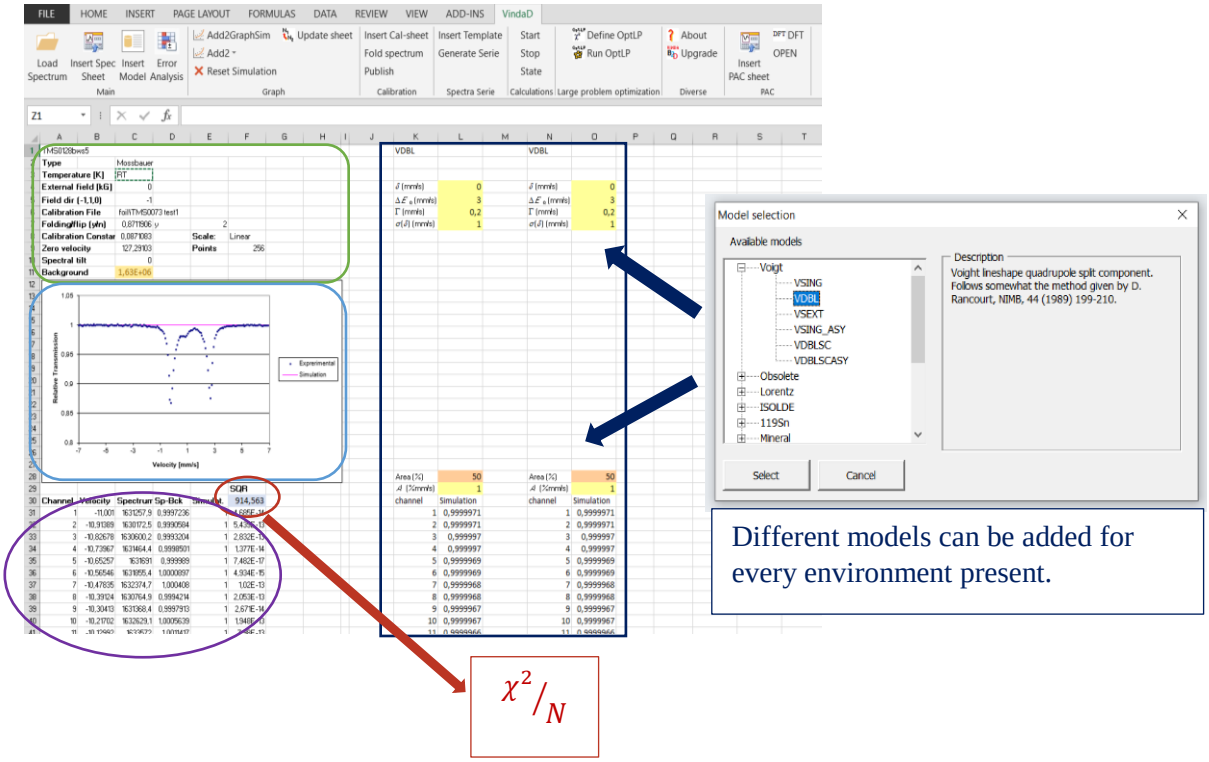

Figure A11: After loading of the spectrum the spectrum information as well as the plot is added to the different fields. Different models can be selected to account for the different environments. The objective is to minimize the chi-square by solving different parameters.

A5.2 Error Analysis

To perform error analysis on the parameters (Figure A12) such as the isomer shift, quadrupole splitting and, line width and area of the doublet it is based in the chi-square value in F30 and normalized by the number of points (256 points). Three iterations would provide a good analysis and using more than three made no difference in error values.

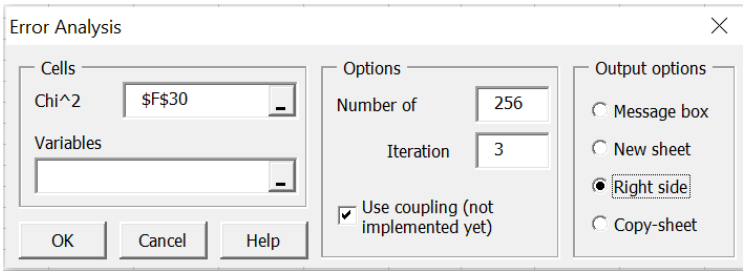

Figure A12: Error analysis box in Venda.

The chi-square value determined from the minimisation is used to assess the difference between the calculated (simulated) and the measured (data) spectrum for each channel (i) and can be mathematically expressed as:[8]

$$\chi^2 = \sum_{i=1}^{N} \frac{(data_i - simulation_i)^2}{data_i} \quad \text{(A1)}$$

Ideally χ^2 should be close to 1 as 1 represents the perfect fit. The χ^2 determined for all the samples used in this thesis can be found in Table A4.

Table A4: The determined χ^2 value along with the sample name and the chapter the data was used in.

Chapter	Sample	χ^2
Chapter 4	12hours-25	1.51
	48hours-25	1.11
	LFP-3b	1.34
	LFP-P1	1.83
	LFP-P2	1.11
	LFP-1	1.40
	LFP-2	1.21
	LFP-3	1.22
Chapter 5	1sec	1.43
	3sec-1	1.25
	3sec-2	1.36
	4sec	1.04
	Purged	1.68
Chapter 6	3min	1.29
	30min	1.92
	1hour	1.28
	4hours	1.02

A6. Scripts used for PDF Gaussian fitting

The command shell iPython (v7.19.0) was used to run the scripts written in Notepad++ (saved as a python file) as shown in Figure A12. The directory name and the python file changes for different scripts.

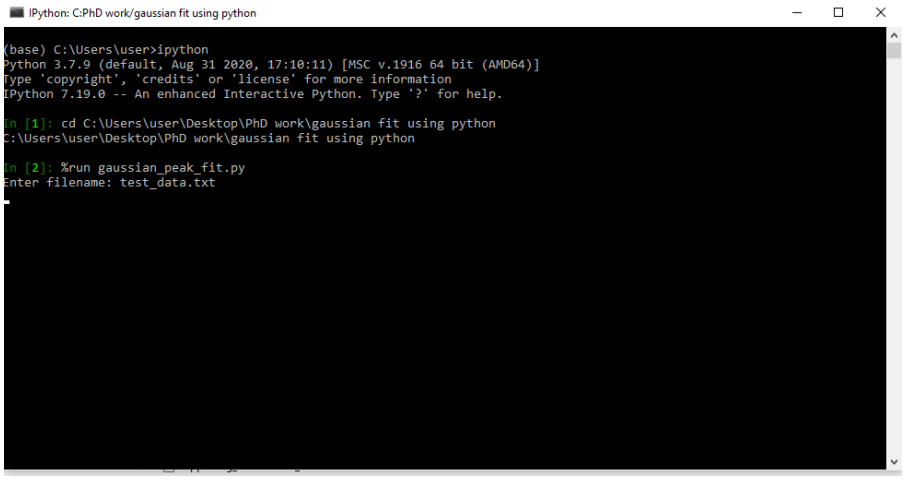

Figure A13: An example of the Ipython window.

PDF Gaussian fitting

To determine the peak position, the peak integral intensity and the full width at half maximum that was used for the model independent analysis, an in-house python script was developed. The script uses NumPy[10] which is allows for the use of mathematical functions. Figure A14, Figure A15 and Figure A16 is an example of the script in notepad++, the fitted peak and the information output, respectively.

```python
from numpy import loadtxt
from lmfit.models import GaussianModel
from lmfit.models import LorentzianModel
import numpy as np
import matplotlib.pyplot as plt
import csv
from scipy.optimize import curve_fit
from scipy import asarray as ar,exp
import pandas as pd

x=[]
y=[]


with open(input("7: "), 'r') as csvfile:  #Opening data of single peak and normalizing##
    plots= csv.reader(csvfile, delimiter=',') #Change delimiter as needed##
    for row in plots:
        x.append(float(row[0]))
        y.append(float(row[1])+ 0.5)  #Change normalization value for row[1]##
zip(x,y)

with open('7.txt', 'w') as f:  #Writing normalized data to a temp txt file for further fitting##
    writer = csv.writer(f, delimiter='\t')
    writer.writerows(zip(x,y))

data = loadtxt('7.txt')
x = data[:, 0]
y = data[:, 1]

mod = GaussianModel() #Gaussian fitting - change to LorentizianModel() if required##
pars = mod.guess(y, x=x)
out = mod.fit(y, pars, x=x)

print(out.fit_report(min_correl=0.25), file=open("Gaussian output ynorm.txt", "a")) #Export txt file with fitting stats##

plt.plot(x,y, marker='o', linewidth=0.0, markersize=3, color="blue", mfc='none', markeredgewidth=0.3, label='Observed data')
plt.plot(x, out.best_fit, color='red', label='Gaussian fit')
#plt.plot(x, out.init_fit, color='black', label='Initial fit') #Use to check if fitting actually occurs##
plt.legend(loc='best', frameon=False)
plt.xlabel('r ($\AA$)')
plt.ylabel('G ($\AA^{-2}$) normalized')
plt.savefig('Test.png', dpi=300, bbox_inches='tight')
plt.show()
```

Figure A14: The script used for fitting a Gaussian model to a PDF peak.

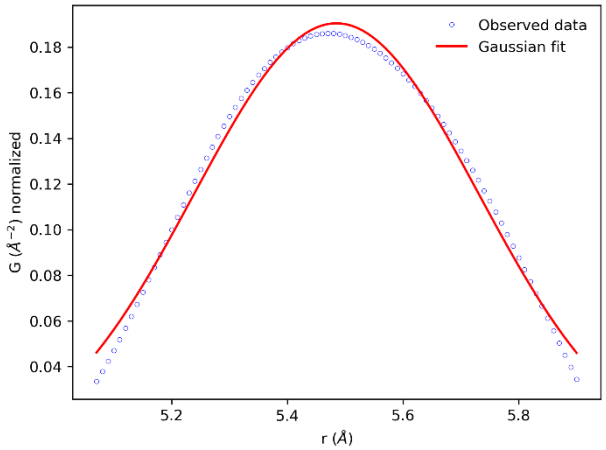

Figure A15: The individual PDF peak and the Gaussian fit.

Gaussian output ynorm - Notepad

File Edit Format View Help

```
[[Model]]
    Model(gaussian)
[[Fit Statistics]]
    # fitting method   = leastsq
    # function evals   = 21
    # data points      = 84
    # variables        = 3
    chi-square         = 0.00206529
    reduced chi-square = 2.5497e-05
    Akaike info crit   = -885.517514
    Bayesian info crit = -878.225063
[[Variables]]
    amplitude:  0.11761954 +/- 6.6799e-04 (0.57%) (init = 0.1212524)
    center:     5.48481736 +/- 0.00149100 (0.03%) (init = 5.485)
    sigma:      0.24636780 +/- 0.00177498 (0.72%) (init = 0.265)
    fwhm:       0.58015181 +/- 0.00417975 (0.72%) == '2.3548200*sigma'
    height:     0.19046081 +/- 9.8430e-04 (0.52%) == '0.3989423*amplitude/max(2.220446049250313e-16, sigma)'
[[Correlations]] (unreported correlations are < 0.250)
    C(amplitude, sigma) =  0.702
```

Figure A16: The information output after executing the script shown in Figure A14.

A7 Integrating the 2-dimensional PXRD data to a 1-dimensional diffractogram

Data had to be integrated for both the calibrant (Fig. A17) and the samples (Fig. A18) using Fit2D.[11] The beam stop has to be masked properly in both cases. The next step was to determine and define the geometric and instrumental parameters for the calibrant. The starting values for

the sample to detector distance and the wavelength was chosen as 405 mm and 0.166350 Å. The refineable parameters were the XY beam centre and the sample to detector distance. The wavelength was not set to refine as this was refined when refining the LaB_6 structure in TOPAS. Next the coordinates were chosen for the inner ring and this allows the coordinates on the outer rings to be chosen automatically. The image can now be integrated and the parameters refined. The refined values for the sample to detector distance was 409.4343 mm, for the X-pixel coordinate of the direct beam was 1009.038 and for the Y-pixel coordinate of the direct beam was 1030.653.

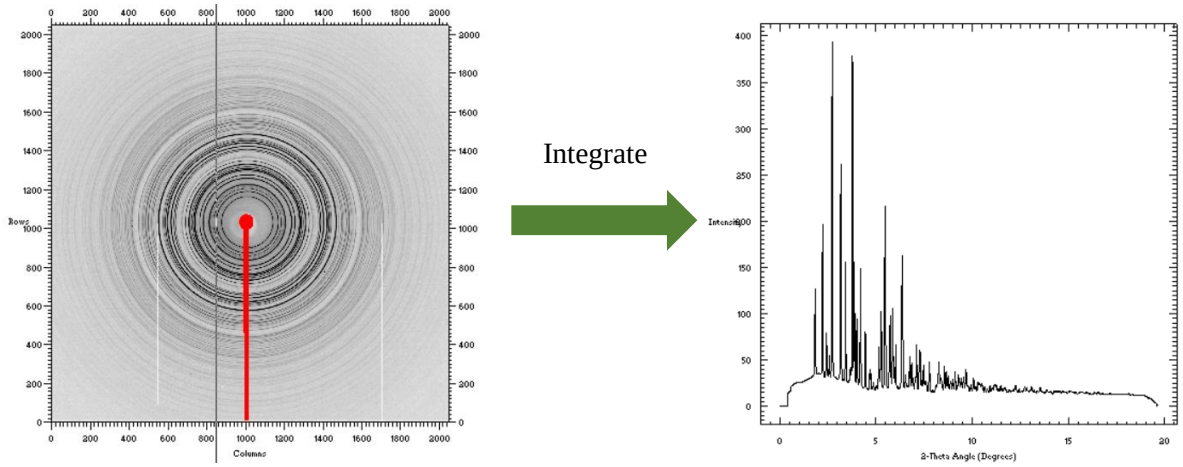

Figure A17: Integrating the 2-Dimensional data to produce a 1-Dimensional powder pattern for the calibrant LaB_6. The masked beam stop is shown in red.

Integrating the 2-Dimensional data to produce the 1-Dimensional diffractogram for the samples (Fig. A18) only needed the beam stop to be masked and then to use the geometric and instrumental parameters that was refined for the calibrant and use it as the sample parameters.

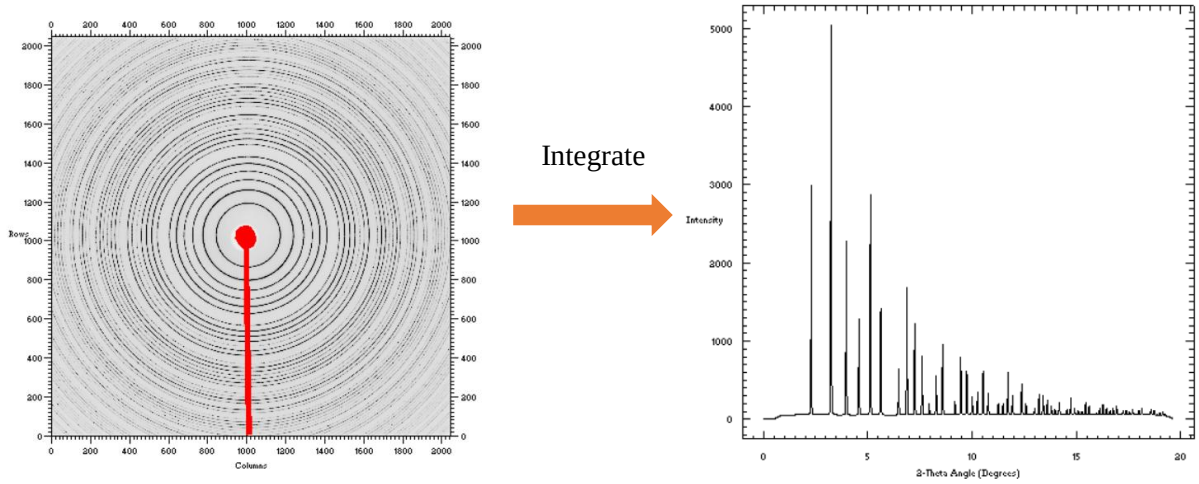

Figure A18: Integrating the 2-Dimensional data to produce a 1-Dimensional powder pattern for the $LiFePO_4$ sample. The masked beam stop is shown in red.

A8. Modifying the FEFF.inp to account for doping and co-doping by adding a single scattering path for the dopant

To calculate the scattering paths used for the EXAFS signal fitting an undoped $LiFePO_4$ CIF[12] is used (Fig. A19 and A20). To account for the dopants or co-dopants the FEFF.inp has to be modified to include the dopants (Fig. A21) and co-dopants (Fig. A23) and to allow for the scattering path for the dopant (Fig. A22) and co-dopants (Fig. A24) to be calculated. Using the calculation shown in Chapter 7 and Chapter 8 the amount of neighbouring Fe atoms that have be replaced by the dopants was calculated. All replacements shown here was an overestimation of the dopant amount.

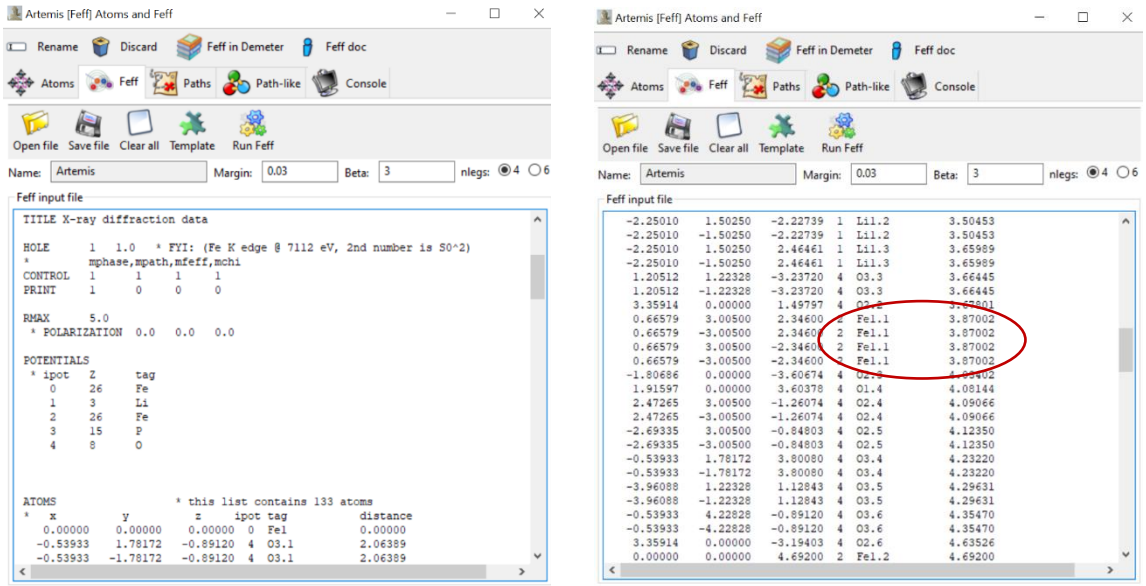

Figure A19: The FEFF.inp of the undoped $LiFePO_4$ resulting in four different nearest neighbour Fe atoms (indicated in red).

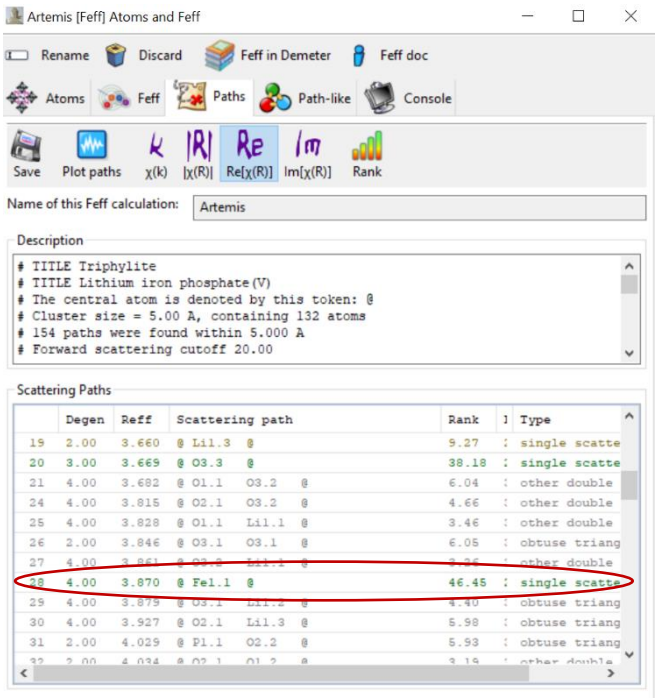

Figure A20: The undoped $LiFePO_4$ produces one Fe scattering path (indicated in red) with a high ranking.

A8.1 Modification of the FEFF.inp to determine the Zn scattering path

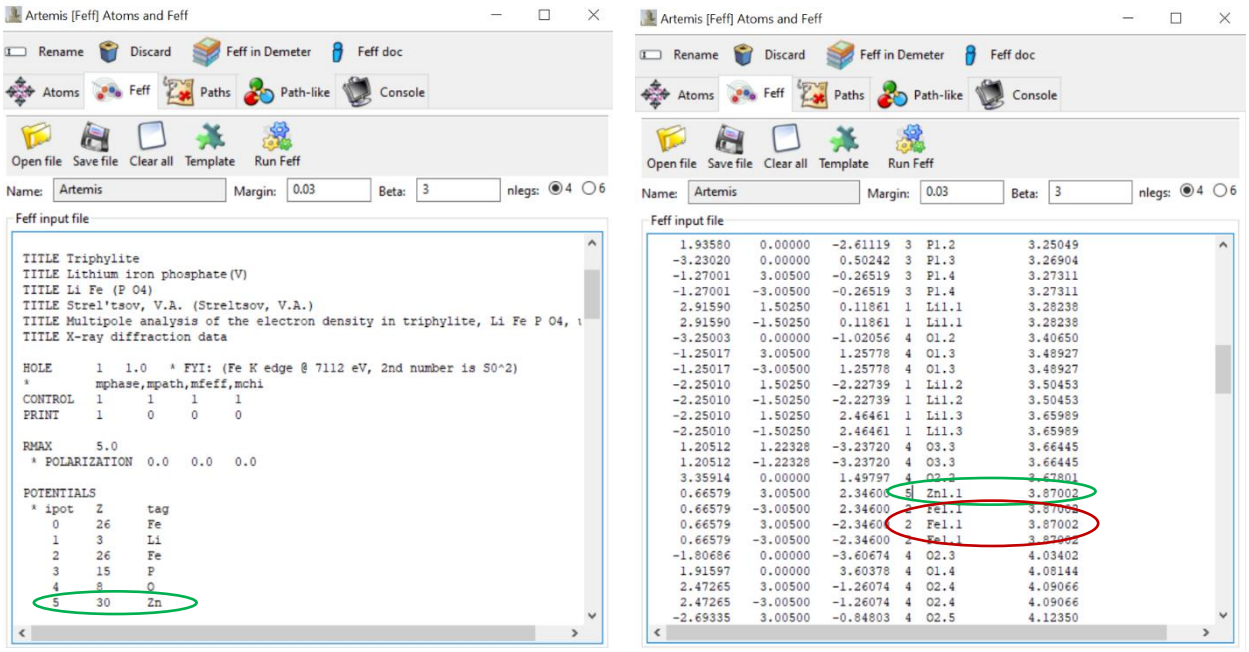

Figure A21: Adding Zn to the atom list (indicated in green) produces one Zn nearest neighbour (indicated in green) and three Fe nearest neighbours (indicated in red).

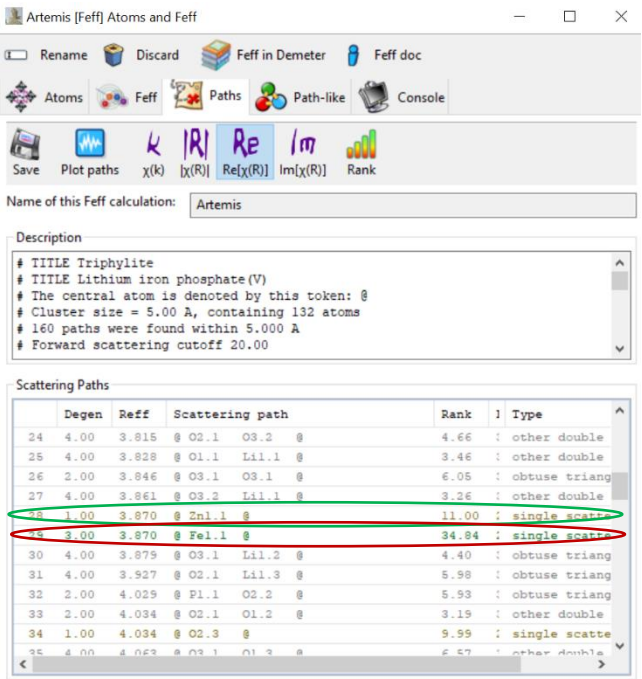

Figure A22: The Zn doped $LiFePO_4$ produces one Zn scattering path (indicated in green) with a very low ranking and one Fe scattering path (indicated in red) with a higher ranking.

A8.2 Modification of the FEFF.inp to determine the Zn and Co scattering path

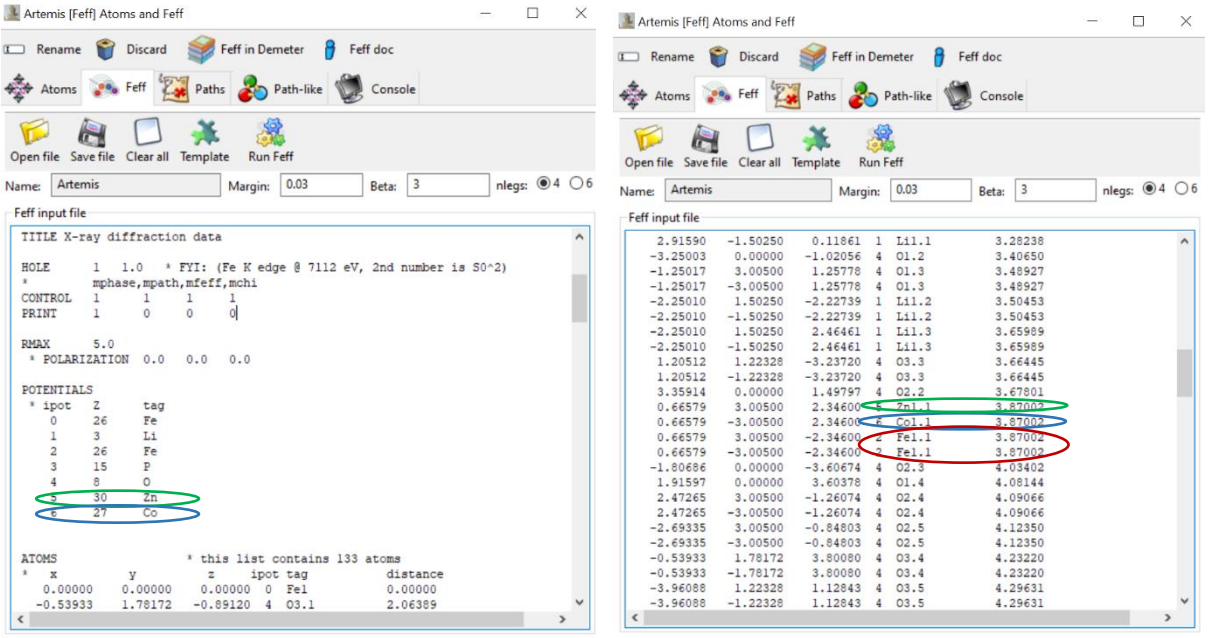

Figure A23: Adding Zn (indicated in green) and Co (indicated in blue) to the atom list leads to one Zn nearest neighbour (indicated in green) one Co nearest neighbour (indicated in blue) and two Fe nearest neighbours (indicated in red).

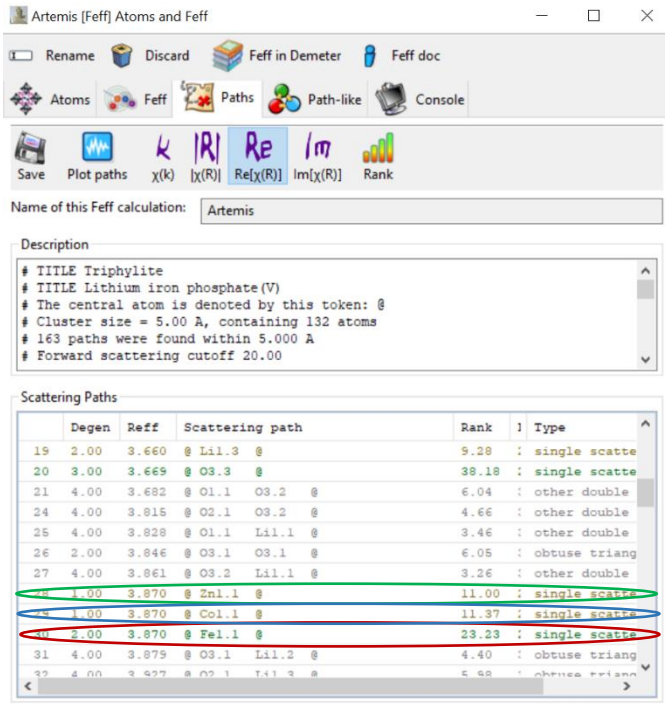

Figure A24: The Zn doped and Co co-doped $LiFePO_4$ produces one Zn scattering path (indicated in green) and one Co scattering path (indicated in blue) both with a very low ranking and one Fe scattering path (indicated in red) with a higher ranking.

A9. References

1. Kelly, S. D., Hesterberg, D. and Ravel, B. *Analysis of Soils and Minerals Using X-ray Absorption Spectroscopy* 387–463 (John Wiley & Sonds, Ltd, 2015).

2. B18 - Diamond Light Source. (2018) at https://www.diamond.ac.uk/Instruments/Spectroscopy/B18.html.

3. Dyar, M. D., Agresti, D. G., Schaefer, M. W., Grant, C. A. and Sklute, E. C. Mössbauer spectroscopy of Earth and planetary materials. *Annual Review of Earth and Planetary Sciences* **34**, 83–125 (2006).

4. Gibb, T. C. *Principles of Mössbauer Spectroscopy* Chapters 1–21 (Springer Netherlands, 1976).

5. Gütlich, P., Bill, E. & Trautwein, A. X. *Mössbauer Spectroscopy and Transition Metal Chemistry* 25–71 (Springer Berlin Heidelberg, 2011).

6. *Data Acquisition Module CMCA-550 Instruction Manual (2021)*. at www.wissel-instruments.de.

7. Shechter, H., Ron, M., Niedzwiedz, S. and Herber, R. H. Mössbauer spectrometer calibration using ^{57}Fe enriched metallic iron. *Nucl. Instruments Methods* **44**, 268–272 (1966).

8. Gunnlaugsson, H. P. Spreadsheet based analysis of Mössbauer spectra. *Hyperfine Interact.* **237**, 79 (2016).

9. Longworth, G. and Window, B. The preparation of narrow-line Mössbauer sources of ^{57}Co in metallic matrices. *J. Phys. D. Appl. Phys.* **4**, 835–839 (1971).

10. Oliphant, T. E. Guide to NumPy. (2006). at NumPy. https://numpy.org/.

11. Hammersley, A. P. FIT2D: A multi-purpose data reduction, analysis and visualization program. *J. Appl. Crystallogr.* **49**, 646–652 (2016).

12. Streltsov, V. A., Belokoneva, E. L., Tsirelson, V. G. and Hansen, N. K. Multipole analysis of the electron density in triphylite, $LiFePO_4$, using X-ray diffraction data. *Acta Crystallogr. Sect. B* **49**, 147–153 (1993).